

Lecture Notes in Electrical Engineering 435

Sabyasachi SenGupta

Ahmed F. Zobaa

Karma Sonam Sherpa

Akash Kumar Bhoi

Editors

Advances in Smart Grid and Renewable Energy

Proceedings of ETAEERE-2016

Lecture Notes in Electrical Engineering

Volume 435

Board of Series editors

Leopoldo Angrisani, Napoli, Italy
Marco Arteaga, Coyoacán, México
Samarjit Chakraborty, München, Germany
Jiming Chen, Hangzhou, P.R. China
Tan Kay Chen, Singapore, Singapore
Rüdiger Dillmann, Karlsruhe, Germany
Haibin Duan, Beijing, China
Gianluigi Ferrari, Parma, Italy
Manuel Ferre, Madrid, Spain
Sandra Hirche, München, Germany
Faryar Jabbari, Irvine, USA
Janusz Kacprzyk, Warsaw, Poland
Alaa Khamis, New Cairo City, Egypt
Torsten Kroeger, Stanford, USA
Tan Cher Ming, Singapore, Singapore
Wolfgang Minker, Ulm, Germany
Pradeep Misra, Dayton, USA
Sebastian Möller, Berlin, Germany
Subhas Mukhopadhyay, Palmerston, New Zealand
Cun-Zheng Ning, Tempe, USA
Toyoaki Nishida, Sakyo-ku, Japan
Bijaya Ketan Panigrahi, New Delhi, India
Federica Pascucci, Roma, Italy
Tariq Samad, Minneapolis, USA
Gan Woon Seng, Nanyang Avenue, Singapore
Germano Veiga, Porto, Portugal
Haitao Wu, Beijing, China
Junjie James Zhang, Charlotte, USA

About this Series

“Lecture Notes in Electrical Engineering (LNEE)” is a book series which reports the latest research and developments in Electrical Engineering, namely:

- Communication, Networks, and Information Theory
- Computer Engineering
- Signal, Image, Speech and Information Processing
- Circuits and Systems
- Bioengineering

LNEE publishes authored monographs and contributed volumes which present cutting edge research information as well as new perspectives on classical fields, while maintaining Springer’s high standards of academic excellence. Also considered for publication are lecture materials, proceedings, and other related materials of exceptionally high quality and interest. The subject matter should be original and timely, reporting the latest research and developments in all areas of electrical engineering.

The audience for the books in LNEE consists of advanced level students, researchers, and industry professionals working at the forefront of their fields. Much like Springer’s other Lecture Notes series, LNEE will be distributed through Springer’s print and electronic publishing channels.

More information about this series at <http://www.springer.com/series/7818>

Sabyasachi SenGupta · Ahmed F. Zobaa
Karma Sonam Sherpa · Akash Kumar Bhoi
Editors

Advances in Smart Grid and Renewable Energy

Proceedings of ETAEERE-2016

 Springer

Preface

Advances in Smart Grid and Renewable Energy is a compilation of papers presented in the two-day International Conference on ‘Emerging Trends and Advances in Electrical Engineering and Renewable Energy–ETAEEERE 2016,’ organized by the Department of Electrical and Electronics Engineering (EEE) of Sikkim Manipal Institute of Technology (SMIT), Majhitar, Sikkim, India, during December 17–18, 2016. This was a very unique conference which combined renewable energy, electronics, computing, communication, systems, controls, and automations under one roof. Moreover, it is a matter of honor for SMIT to learn that Springer was associated with ETAEEERE-2016 as a major publication sponsor for the event. The proceedings of this conference come out with four different book volumes titled under Lecture Notes in Electrical Engineering (LNEE). This volume offers state-of-the-art chapters on energy management systems (EMS), renewable energy resources, micro-generation, green communications architectures and frameworks, green computing and education as well as energy-aware process optimization.

Eminent speakers like former Jadavpur University vice-chancellor Prof. A Chakrabarti; Prof. A Rajaraman of IIT Chennai; Prof. Gyoo-Shee Chae of Baekseok University, South Korea; Prof. Avinash Konkani of University of Virginia, USA; Prof. Kamani KK (the global economic advisor of Karnataka); Prof. Manjesh of Bangalore University; and Dr. Amitanshu Patnaik of DRDO Delhi shared their knowledge and experience. The conference attended and presented by participants from institutes such as IISc, IITs, NITs, NEHU, BIT, VIT, MIT Manipal, IEST Kolkata, and abroad deliberated on their research works. In addition, the paper presentations were accompanied by 6 keynote addresses from leading academic and industry researchers around the globe. The paper presentations were taken place in 3 different tracks with 18 parallel sessions. Through the platform of ETAEEERE-2016, we got the opportunity to promote the national campaign ‘Make In India’.

The review committee has done an excellent job in reviewing the articles and approving the high-quality research articles to be published in the conference proceedings in the Lecture Notes in Electrical Engineering (LNEE), Springer. The

editors are thankful to all of the faculty and students of these various committees for their dedication in making this a very successful conference and also to the editors and support staff at Springer for making the compilation possible. We sincerely hope that this volume will inspire researchers.

Majhitar
Sikkim, India

Karma Sonam Sherpa
Akash Kumar Bhoi
Mohammed Nasir Ansari
Amit Kumar Singh

Editorial Board

Chief Patron

Prof.(Dr.) Somnath Mishra, Vice-Chancellor, Sikkim Manipal University

Patron

Prof.(Dr.) Ashis Sharma, Registrar, SMU

Prof.(Dr.) Amik Garg, Director, SMIT

Prof.(Dr.) Sadasivan Thekkey Veetil, Joint Director, SMIT

Programme Chair

Dr. Rabindranath Bera, SMIT

Dr. Karma Sonam Sherpa, SMIT

Dr. Kalpana Sharma, SMIT

Dr. H.K.D Sarma, SMIT

Dr. Tejbanta Singh Chingtham, SMIT

Dr. Utpal Deka, Physics, SMIT

Dr. B.B Pradhan, SMIT

Dr. Samarjeet Borah, Dept. of CA, SMIT

Dr. Gobinda Chandra Mishra, SMIT

Prof. Om Prakash Singh, SMIT

Special Session Chairs

Dr. Sabyasachi Sen Gupta, IIT Kharagpur
Dr. Samrat Paul, NEHU, Shillong
Dr. Swagatam Das, ISI, Kolkata
Dr. Abhijit Chakrabarti, IEST, Shibpur
Prof. Kamani K.K, Dept. of Higher Education, Govt. of Karnataka (Global Economic Adviser)
Dr. GS Chae, Baekseok University, South Korea
Prof. Natarajan Gajendran, Editor IJST, President (iSee)
Dr. Manjesh, Dept. of Electronic Science, Bangalore University
Dr. Amitanshu Patnaik, DTRL, DRDO

International Advisory Committee

Dr. Avinash Konkani, AHFP, Clinical Engineer, University of Virginia Health System, USA
Dr. P. Sanjeevikumar, Dept. of EEE, University of Johannesburg, South Africa
Dr. Ahmed Faheem Zobaa, BU, UK
Dr. Akhtar Kalam, VU, Australia
Dr. David YU, UWM, USA
Dr. Atilla Elci, Chairman, Dept. of EEE, Aksaray University, Turkey
Dr. Dmitri Vinnikov, TUT, Estonia
Dr. Hussain Shareef, UKM, Malaysia
Dr. Seshadev Sahoo, Purdue University, USA
Dr. Anil Kavala, Sr. Engineer, Samsung Electronics, Seoul, South Korea
Dr. Kamran Morovati, University of New Brunswick, Canada
Dr. Joseph Olorunfemi Ojo, TTU, USA
Dr. Mohamed A. Zohdy, OU, MI
Dr. Murad Al-Shibli, Head, EMET, Abu Dhabi
Dr. Nesimi Ertugrul, UA, Australia
Dr. Omar Abdel-Baqi, UWM, USA
Dr. Richard Blanchard, LBU, UK
Dr. Shashi Paul, DM, UK

National Advisory Committee

Dr. Sabyasachi Sen Gupta, IIT Kharagpur
Prof. Kamani K.K, Dept. of Higher Education, Govt. of Karnataka (Global Economic Adviser)

Dr. Manjesh, Dept. of Electronic Science, Bangalore University
 Dr. Amitanshu Patnaik, DTRL, DRDO
 Dr. Swagatam Das, ISI, Kolkata
 Dr. Ajoy Kr. Ray, SMIT
 Dr. Ajeya Jha, SMIT
 Dr. Rabindranath Bera, SMIT
 Dr. Karma Sonam Sherpa, SMIT
 Dr. Kalpana Sharma, SMIT
 Dr. B.B Pradhan, SMIT
 Dr. H.K.D Sarma, SMIT
 Dr. Debabrata Pradhan, IIT Kharagpur
 Prof. C.J Thomas, SMIT
 Dr. Bidita Khandelwal, SMIMS
 Dr. Sangeeta Jha, SMIT
 Dr. Vinod Kumar Sayal, SMIT
 Dr. Arun Baran Samaddar, Director, NIT Sikkim
 Dr. Gobinda Chandra Mishra, SMIT
 Dr. V K Manoharr, CEO & MD, TechMaven Private Limited
 Dr. Anjan Kumar Ray, NIT Sikkim
 Dr. Ashok Kumar Pradhan, IIT Kharagpur
 Dr. Bhim Singh, IIT Delhi
 Dr. Ganapati Panda, IIT Bhubaneswar
 Dr. Debashish Jena, NITK, India
 Dr. N.P. Padhy, IIT Roorkee
 Dr. C. Subramani, IIT Roorkee
 Dr. Patnaik S.K, Anna University
 Dr. G. Uma, Anna University
 Dr. Avik Bhattacharya, IIT Roorkee
 Dr. Smarajit Ghosh, Thapar University
 Dr. Sandeep Chakravorty, Baddi University
 Dr. Krishnendu Chakraborty, KGEC
 Dr. Urmila Kar, NITTTR, Kolkata
 Dr. Abhijit Chakrabarti, IEST, Shibpur
 Er. Kunal Munshi, Managing Partner at Sunrator Technologies LLP
 Er. Bikash Rai, Assistant Engineering, Power & Energy Department, Govt. of Sikkim

Reviewer Committee

Dr. Ahmed Faheem Zobia, Dept. of ECE, BU, UK
 Dr. Avinash Konkani, AHFP, Clinical Engineer, University of Virginia Health System, USA

Dr. Atilla Elci, Chairman, EEE, Aksaray University, Turkey
Dr. Kamran Morovati, CS, University of New Brunswick, Canada
Dr. Karma Sonam Sherpa, HOD EEE, SMIT
Dr. Chandrashekar Bhuiyan, CE, SMIT
Dr. Seshadev Sahoo, ME, Purdue University, USA
Dr. Akhtar Kalam, Leader–Smart Energy Research Unit, VU, Australia
Dr. Richard Blanchard, Renewable Energy, LBU, UK
Dr. Utpal Deka, Physics, SMIT
Dr. Nitai Paitya, ECE, SMIT
Dr. N.K. Bhattacharyya, Chemistry, SMIT
Dr. A. Senthil Kumar, EEE, VEC, Chennai
Dr. Samarjeet Borah, Dept. of CA, SMIT

Organizing Committee

(Sikkim Manipal Institute of Technology)

Overall Incharge

Prof. Karma Sonam Sherpa—Convenor
Prof. Akash Kumar Bhoi—Secretary
Prof. Mohammed Nasir Ansari—Convenor
Prof. Amit Kumar Singh—Convenor

Publicity

Prof. Pradeep Kumar Mallick
Prof. Himangshu Pal

Hall and Stage Arrangements

Prof. Shabbiruddin
Prof. Sandip Kumar Gupta

Caterings and Refreshment

Prof. Sunam Saha
Prof. Roshan Pradhan

Transport

Prof. Arunava Tikader
Prof. Arijit Ghosh

Help Desk and Registration

Prof. Chitragada Roy
Prof. Dibyadeep Bhattacharya

Sponsorship

Prof. Saikat Chatterjee
Prof. Anirban Sengupta

Guest Hospitality

Prof. Moumi Pandit
Prof. Bijay Rai
Prof. Rahul Kumar

Printing

Prof. Pratik Pradhan
Prof. Rajiv Pradhan

Student Organizing Committee

(Sikkim Manipal Institute of Technology)

Yupphung Keimba Limbu
Kunglho Lepcha
Sagar Pradhan
Avinash Gupta
Avinash Pradhan
Tshering Sangmo Sherpa
Sisir Chettri
Deepika Chettri
Suyog Pradhan
Shristi Shresta
Pankaj Kumar
Biswas Pradhan
Ritika Pradhan
Aruna Chettri
Ashish Lamichaney
Neeta Lamichaney
Ashutosh Mukherjee
Amit KR. Singh
Gyan Shree
Dheeraj Kumar
Raval Parth Pradip
Srihari K
Saurabh Bhowmik
Madhura Pardhe

Contents

Clustered Prosumer Penalty Framework on Smart Grid	1
Sreenithya Sumesh, Vidyasagar Potdar and Aneesh Krishna	
Critical Evaluation of Offline MPPT Techniques of Solar PV for Stand-Alone Applications	13
Mohammad Asim, Mohd Tariq, M.A. Mallick, Imtiaz Ashraf, Supriya Kumari and Akash Kumar Bhoi	
Design of Permanent Magnet Synchronous Generator for Wind Energy Conversion System	23
Abhishek Sahu, Sanjeev Gupta, Vinod Kumar Singh, Akash Kumar Bhoi, Amik Garg and Karma Sonam Sherpa	
Design and Development of Buck-Boost Regulator for DC Motor Used in Electric Vehicle for the Application of Renewable Energy	33
Manjesh, K.C. Manjunatha, Akash Kumar Bhoi and Karma Sonam Sherpa	
The Particle Swarm Optimization Algorithm for Maximum Power Extraction of Solar PV Array	39
B. Dhanalakshmi and N. Rajasekar	
Analysis of Voltage Stability in Radial Distribution System for Hybrid Microgrid	49
Kuldip Singh, Swetalina Bhuyan, M. Narendra Kumar and Satyasis Mishra	
PV-Fed Eleven-Level Capacitor Switching Multi-Level Inverter for Grid Integration	57
K. Mohana Sundaram, P. Anandhraj and V. Vimalraj Ambeth	
Daylight Harvesting Concepts and Its Application: A Review	65
Amiya Ranjan Behera, Siddhartha and Jyoti Devi	
Smart Switching Algorithm Between IC and PO Algorithms for Grid-Connected PV System	83
A. Ambikapathy, Gajendra Singh and Prabhakar Tiwari	

A Novel Educational Proposal and Strategies Toward Promoting Cloud Computing, Big Data, and Human–Computer Interaction in Engineering Colleges and Universities	93
Prantosh K. Paul and Mrinal Kanti Ghose	
Why Green Computing and Green Information Sciences Have Potentialities in Academics and <i>iSchools</i>: Practice and Educational Perspectives	103
Prantosh K. Paul and Mrinal Kanti Ghose	
Annual Energy, Exergy, and Environmental Benefits of <i>N</i> Half Covered Concentrated Photovoltaic Thermal (CPVT) Air Collectors	113
Rohit Tripathi and G.N. Tiwari	
An Experimental Realization of Grid-Connected PV System with MPPT Using dSPACE DS 1104 Control Board	125
Neeraj Priyadarshi, Amarjeet Kumar Sharma and Shrikshitish Priyam	
Cascaded Voltage Control of Three-Phase Four-Leg Inverter for OFF Grid Solar Photovoltaic Applications	135
Ikkurti Sai Chaitanya and Hanumath Prasad Ikkurti	
Study on the Effect of Tilt on the Variation of Aperture Area Shading in a Linear Fresnel Reflector Field for Two Different Configurations	147
Gaurab Bhowmick and Subhasis Neogi	
Design Analysis and Implementation of MPPT Using PSIM	157
R. Shivrudraswamy, Aditya Nandan Shukla and C.B. Chandrakala	
Kinematical Synthesis and Numerical Analysis of Rail-Based Dual-Axis Solar Tracking System	167
Arun A. Yadav, Chetan O. Yadav and Paladugula V. Ramana	
Application of Artificial Intelligence-Based Techniques in Controlling the STATCOM Used for Compensation for Voltage Dips in DFIG-Based Grid-Connected Wind Power System	177
Bineeta Mukhopadhyay and Rajib Kumar Mandal	
Micro-grid for Village Empowerment Using Solar PV-Operated Micro-hydel Power Plant	191
T.K. Rana and S. Chakraborty	
A Design for High-Torque, Low-Speed Vertical Axis Wind Turbine	203
Rajesh Dommeti, Avinash Kathi and Mallikarjunarao Pasumarthi	
Single-Stage Boost Inverter Topologies for Nanogrid Applications	215
P. Sriramalakshmi and V.T. Sreedevi	

Investigation of Failure and Degradation Types of Solar PV Plants in a Composite Climate: Abstract After 4–6 Years of Field Operation 227
 Bhaveshkumar V. Dobaria, Vikrant Sharma and Alpesh Adeshara

A New Switching Pattern Scheme-Based Compact Integrated 15-Level Smart Inverter for Micro-grid System Using Fuzzy Logic Controller 237
 Kshatriya Vamshi Krishna Varma, Kalahasti Sirisha and A. Ram Kumar

Modeling of Energy Consumption in Foundries by Integrating Renewable Energy Sources: Kolhapur Foundry Sector 249
 Dhanashri P. Patil, Nilkanth N. Shinde and Mahesh M. Wagh

Analysis of Ripple Voltage at the Output of Five-Phase Converter with Five-Phase Inverter Drive for Renewable Energy Applications 259
 Manjesh

A Novel Six-Switch Power Converter for Single-Phase Wind Energy System Applications 267
 K. Kumar, K.R. Prabhu, N. Ramesh Babu and P. Sanjeevikumar

Fuzzy Logic-Based Pitch Angle Controller for PMSG-Based Wind Energy Conversion System 277
 Ramji Tiwari, N. Ramesh Babu and P. Sanjeevikumar

Experimental Investigation of VFD-Fed Scalar Control of Induction Motor for Pumping Application 287
 Vishnu Kalaiselvan Arun Shankar, Subramaniam Umashankar, Shanmugam Paramasivam, Padmanaban Sanjeevikumar and K.N. Dileep Sailesh

Comparison Between PI Controller and Fuzzy Logic-Based Control Strategies for Harmonic Reduction in Grid-Integrated Wind Energy Conversion System 297
 Ramji Tiwari, N. Ramesh Babu, R. Arunkrishna and P. Sanjeevikumar

Direct-Coupled Permanent Magnet DC Motor-Driven Solar Photovoltaic Water Pumping System—A Literature Review 307
 R. Sivapriyan, S. Umashankar, P. Sanjeevikumar and Atif Iqbal

Decoupled Active and Reactive Power Control of Cascaded H-Bridge PV Inverter for Grid-Connected Applications 315
 V. Sridhar, S. Umashankar and P. Sanjeevikumar

Fuzzy-Based Microgrid Energy Management System Using Interleaved Boost Converter and Three-Level NPC Inverter with Improved Grid Voltage Quality	325
Swaminathan Ganesan, V. Ramesh, S. Umashankar and P. Sanjeevikumar	
Impact of Power Quality Disturbances on Grid-Connected Double Fed Induction Generator	339
Karthik Tamvada, S. Umashankar and P. Sanjeevikumar	
Health Monitoring System of Solar Photovoltaic Panel: An Internet of Things Application	347
Prutha M. Badave, B. Karthikeyan, S. M. Badave, S.B. Mahajan, P. Sanjeevikumar and Gurjit Singh Gill	
Design and Implementation of Solar-Powered Low-Cost Model for Greenhouse System	357
Shrivardhan Suryawanshi, Sudha Ramasamy, S. Umashankar and P. Sanjeevikumar	
Sustainable Organic Farming in Sikkim: An Inclusive Perspective	367
Jitendra Kumar, Meghan Pradhan and Niti Singh	
Investigations of Microgrid Stability and Optimum Power Sharing Using Robust Control of Grid Tie PV Inverter	379
G. Swaminathan, V. Ramesh, S. Umashankar and P. Sanjeevikumar	
Design and Graphical Analysis of 8-kW Off-Grid Solar Photovoltaic Power System	389
Nikhil Kumar Yadav and Dharmendra Kumar Singh	
An Internet of Things to Maximum Power Point Tracking Approach of Solar PV Array	401
Himanshu Manghani, J. Prasanth Ram and N. Rajasekar	
Energy Storage Considerations for High Renewable Power Penetration: A Case Study	411
James R. Doyle and Hannah Johlas	
Development and Implementation of Renewable Energy Potential Geospatial Database Mapping in India for Cloud SDI Using Open Source GIS	419
Rabindra K. Barik, K. Muruga Perumal, P. Ajay-D-Vimal Raj and S. Rajasekar	
A Robust Controller Design for Standalone Microgrid System Feeding Composite Loads	429
Md. Asif Hasan, Raj Kumar Mishra and Md. Ashique Hassan	

Maximum Power Point Tracking of Direct-Drive PMSG with High-Efficiency Boost Converter 437
 J. Barsana Banu, M. Balasingh Moses and S. Ganapathy

PEM Fuel Cell System Identification and Control 449
 Pinagapani Arun Kumar, Mani Geetha, K.R. Chandran and P. Sanjeevikumar

Lightweight Microwave Absorber from Industrial Waste Fly Ash Cenosphere 459
 Pritom J. Bora, K.J. Vinoy, Kishore, Praveen C. Ramamurthy and Giridhar Madras

Concrete Solar Collector 467
 Pratik M. Waghmare, Shrishail B. Sollapur and Shweta M. Wange

Power Quality Improvement of Microgrid with Cascaded Controller-Based PMSG Used in Wind Turbines 477
 W.J. Praiselin and J. Belwin Edward

Experimental Investigation and Fabrication of Biogas Digester 485
 Jeetendra Bhandari, Premendra Mani Pradhan and Rohit Kumar Choudhary

Validation of an Inverter Topology for Transformerless Grid-Connected Photovoltaic System 495
 Asim Datta, Rishiraj Sarker, Sanjay Debbarma and Amit Kumar

Harvesting Insolation Using Mo–W–Sulfide Compound Nanoparticle Semiconductor as Photocatalyst: A Pollution Controlling Material 505
 Debabrat Kalita, Lakhi Chetia and Gazi A. Ahmed

Visible Light Harvesting Titania-Coated Diatom Frustules with Superior Photocatalytic Activity 515
 Lakhi Chetia, Debabrat Kalita and Gazi A. Ahmed

A Review on Grid Codes and Reactive Power Management in Power Grids with WECS 525
 K.V. Ramana Reddy, N. Ramesh Babu and P. Sanjeevikumar

PEM Fuel Cell Modeling Using Genetic Algorithm—A Novel Approach 541
 K. Priya, Sashang Roy Choudhury, K. Sathish Kumar and N. Rajasekar

Renewable Energy Capacity Estimation for Indian Energy Sector Using Energy Demand Forecasting Through Fuzzy Time Series 551
 Shibabrata Choudhury, Aswini Kumar Patra, Adikanda Parida and Saibal Chatterjee

Performance Analysis of Combined Biogas-Diesel Run Dual-Fuel Engine	559
Diwakar Gurung, Ankur Rajvanshi, S. Lalhriatpuia and Premendra Mani Pradhan	
Photovoltaic System-Based Marx Multilevel Converter for Hybrid Modulation Strategy	567
Akbar Ahmad and P. Samuel	
Thermal Performance Analysis of a Box-Type Solar Cooker with Finned Pot: An Experimental Approach	575
Jayashree Nayak, Sudhansu S. Sahoo, Ranjan K. Swain, Antaryami Mishra and Sanju Thomas	
Design of Energy Efficient Voltage Multiplier Circuit for RF Energy Harvesting	583
Asmita Rajawat and P.K. Singhal	
Integrated Model of Renewable Energy Sources Feeding Both AC and DC Load	593
Sisir Chettri, Suyog Pradhan, Karma Sonam Sherpa and Saikat Chatterjee	
Investigating Effects of Shading on Performance of Solar Conversion Devices	605
K.J. Shruthi, P. Giridhar Kini, C. Viswanatha, Mohan Divekar and A. Amruthakala	
An Unrestricted Placement of Wind Turbines Toward Maximizing the Energy Output Using Teacher-Artificial Bee Colony Algorithm	613
Jaydeep Patel, Vimal Savsani, Vivek Patel and Rajesh Patel	
Fault Diagnosis in Smart Distribution System Using Smart Sensors and Entropy	623
Mangal Hemant Dhend and Rajan Hari Chile	
Topologies of a DC–DC Converter for Micro-grid Application and Implementation of Parallel Quadratic Boost Converter	633
T. Arunkumari, V. Indragandhi and S. Sreejith	
Quantum Streaming Instabilities in Multi-component Plasma with Dust Particles	645
U. Deka, K. Choudhury and P.K. Karmakar	
5.8-GHz Antenna Array Design for Satellite Solar Power Station	659
Deepak Kumar and Kalpana Chaudhary	
Development of Wireless Data Acquisition and Control System for Smart Microgrid	667
Lipi Chhaya, Paawan Sharma, Govind Bhagwatikar and Adesh Kumar	

Real-Time Implementation of Maximum Power Point Methods for Photovoltaic Systems 675
Akbar Ahmad and Paulson Samuel

Deterministic Node Deployment for Connected Target Coverage Problem in Heterogeneous Wireless Sensor Networks for Monitoring Wind Farm 683
M. Vergin Raja Sarobin and R. Ganesan

Kinetic Instability of the Ion Acoustic Mode in Permeating Plasma of Electron–Positron and Ion 695
U. Deka and K. Shah

Comparative Study and Yield Productivity of Nano-paint and Nano-fluid Used in a Passive-Type Single Basin Solar Still 709
Amrit Kumar Thakur, Deepak Agarwal, Prashant Khandelwal and Saty Dev

About the Editors

Prof. (Dr.) Sabyasachi SenGupta received his undergraduate degree from Calcutta University (B.E. College) in the year 1974 and his M.Tech and Ph.D. degrees from IIT Kharagpur. He is currently working as Professor in the Department of Electrical Engineering, IIT Kharagpur. Professor S. SenGupta was the Vice-Chancellor, West Bengal University of Technology till June 2012. He is the Chairman, Eastern Regional Committee, AICTE and also member of All India Council for Technical Education. He has guided six Ph.D. students (three ongoing) with more than 30 M.Tech students for their thesis work and taught different courses in UG and PG level. His primary research focus is on Elementary Particle Physics and Newtonian Dynamics. He was also past member of National Steering Committee of NaMPET, MoDIT. He convened Second National Power Electronics Conference (NPEC05) at IIT Kharagpur, December 2005 and performed as selection committee member of several IITs, NITs and several government and private technical institutes. He has published several research papers and attended invited lectures on various topics. Professor S. SenGupta is engaged with several sponsored research and industrial consultancy projects as Principal Investigator. He has also filed two patents in connection with the SMES-UPS project.

Ahmed F. Zobaa received his B.Sc. (Hons), M.Sc., and Ph.D. degrees in electrical power and machines from Cairo University, Egypt. Also, he received a Postgraduate Certificate in Academic Practice from University of Exeter, UK. He was an instructor, a teaching assistant, and an assistant professor at Cairo University during 1992–2007. He moved to UK as a Senior Lecturer in renewable energy at University of Exeter in 2007. He was Associate Professor (on leave) at Cairo University during 2008–2013. He was promoted to Full Professor (on leave) at Cairo University in 2013. Currently, he is a Senior Lecturer (Associate Professor) in power systems, an M.Sc. Course Director—Sustainable Electrical Power—and a Full Member of the Institute of Energy Futures at Brunel University London, UK. His main areas of expertise are power quality, (marine) renewable energy, smart grids, energy efficiency, and lighting applications. Dr. Zobaa is the Editor-In-Chief of the International Journal of Renewable Energy Technology and Technology and

Economics of Smart Grids and Sustainable Energy. He is also an Editorial Board member, Editor, Associate Editor, and Editorial Advisory Board member for many international journals. Dr. Zobia is a registered Chartered Engineer, Chartered Energy Engineer, European Engineer, and International Professional Engineer. He is also a registered member of the Egypt Syndicate of Engineers and the Egyptian Society of Engineers. He is a Senior Fellow of the Higher Education Academy of UK. He is a Fellow of the Institution of Engineering and Technology, the Energy Institute of UK., the Chartered Institution of Building Services Engineers, the Institution of Mechanical Engineers, the Royal Society of Arts, the African Academy of Sciences, and the Chartered Institute of Educational Assessors. He is a senior member of the Institute of Electrical and Electronics Engineers. Also, he is a member of the International Solar Energy Society, and the European Power Electronics and Drives Association.

Prof. (Dr.) Karma Sonam Sherpa has completed his B.E. (Electrical Engineering) from MREC, Jaipur, and M.Tech (Power Electronics and Machine Drives) from IIT Kharagpur in the year 1996 and 2003, respectively. He is a doctorate from Sikkim Manipal University. He has been serving SMIT, Sikkim for the last 18 years. Presently, Prof. K.S. Sherpa is Dean (Research and Development). He is head and professor in the Department of Electrical and Electronics Engineering. His areas of research are DC power conversion and nonlinear dynamics, voltage stability and load management in power distribution systems and electromagnetic levitation systems. He is life member of ISTE, IEI and System Society of India (SSI). His areas of interests are Electric Power Distribution System, Power Electronics and Electrical Drives. Professor K.S. Sherpa is a member of Academic Senate since and University Research Committee (2013 onwards). He has published several papers in national and international journals and conferences.

Akash Kumar Bhoi has completed his B.Tech (Biomedical Engineering) from TAT, Bhubaneswar and M.Tech (Biomedical Instrumentation) from Karunya University, Coimbatore in the year 2009 and 2011, respectively. He is pursuing Ph.D. (Biomedical Signal Processing) from Sikkim Manipal University, India. He is working as R&D Faculty Associate and Assistant Professor in the Department of Electrical and Electronics Engineering at Sikkim Manipal Institute of Technology (SMIT), India since 2012. He is member of ISEIS and IAENG, Associate member of UACEE and Editorial Board member of IJAEEEE, IJAEEEE, ITSII-TEEE, IJECCE, and IJCTT, and Reviewer of IJET, IJCT, IJBSE, IJMI, AJBLS. His areas of research are biomedical signal processing, medical image processing, sensors and transducers, and medical instrumentation. He has published several papers in national and international journals and conferences.

Clustered Prosumer Penalty Framework on Smart Grid

Sreenithya Sumesh, Vidyasagar Potdar and Aneesh Krishna

Abstract The smart grid regulators and retailers generally have a legally binding contract on purchasing energy from prosumers (energy producers). A hefty portion of them incorporate incentives strategies for energy effectiveness in their legal contract. In the event that the prosumers that supply energy meet or go past its objective, they will get a financial motivation, regularly an extent of the investment funds in energy rate that customers get. On the off chance that it misses the mark regarding the objective, it might be liable to a punishment. Thus, smart grid regulators reward well-performed prosumers or prosumer community groups using money earned from penalized poorly performed prosumers or prosumer community groups. Dissemination of punishments (penalties) assumes an essential part in prosumers. This can prompt fortifying existing non-dynamic energy sharing prosumers to end up dynamic prosumers. This paper proposes a performance-based penalty function technique that decidedly influences the way of the prosumers' state of mind, along these lines bringing about a predictable energy sharing conduct.

Keywords Smart grid · Prosumer · Incentive · Penalty · Regulator

1 Introduction

Smart grid is a bidirectional energy information infrastructure. To enable this energy exchange, the idea of goal-oriented prosumer community groups [1] has been introduced in the literature. Different prosumer community groups have

S. Sumesh (✉) · A. Krishna
Department of Computing, Curtin University, Bentley, Australia
e-mail: s.sumesh@postgrad.curtin.edu.au

A. Krishna
e-mail: a.krishna@curtin.edu.au

V. Potdar
School of Information Systems, Curtin University, Bentley, Australia
e-mail: v.potdar@curtin.edu.au

different minimum energy thresholds to join the group. Also, the groups have different energy targets to achieve. Goal-oriented prosumer groups have several advantages over other techniques of forming energy sharing communities such as VPPs or microgrids. VPPs and microgrids are not flexible as they are fixed in its architecture. It is very complex to add new prosumers or remove any prosumer from the grid. Whereas, goal-oriented prosumer community groups are very flexible as new members could be easily added into the group. The prosumers in each group share energy to achieve some goal.

There are different frameworks introduced in [1–5] intending to fulfilling the purpose of these groups. Defining and characterization framework aims at forming the different prosumer community groups based on the minimum and maximum energy threshold that individuals can share. To add the new prosumers to the existing groups, another framework was designed for the recruitment of the prosumers. The new prosumers are added into the groups based on their energy sharing pattern. As different prosumers have different goals, a mutual goal definition framework aims at solving the problem of managing multiple goals. With an aim to identify the outstanding prosumers regarding energy sharing, member assessment and ranking framework was introduced in the literature. All the frameworks mentioned above work in an integrated manner to achieve the goal of prosumer community groups. However, for the continuous and positive growth of these groups, there exists no penalty framework. The prosumers in the group who do not actively participate and their energy sharing remains negative should be penalized. This penalty would act as a driving force to motivate them to produce enough energy.

Dissemination of rewards and penalties shows a crucial part in retaining prosumers. It is one of the vital main thrusts for motivating prosumers. Motivating prosumers can occur in various forms; first of all, it is a key to bring issues to light of the energy sharing procedure among prosumers by publicizing about the guidelines and rules and the feed-in tariff methods. Moreover, it promotes monetary welfares to green energy distribution. This can lead to invigorating existing non-dynamic energy sharing prosumers to end up dynamic prosumers. Besides, to build the size of dynamic prosumers, one conceivable technique is to publicize for added rewards, for example, exceptional offers for greater energy providers. The prosumer inspiration emphatically influences the way of the prosumers' state of mind, subsequently bringing about a steady energy sharing conduct. So in order to initiate the energy sharing process and to enhance their performance in the energy sharing procedure, it is necessary to motivate the prosumers.

2 Requirements

This section represents the conceptual process where requirements are elicited and prioritized. The following conditions are laid down for the proposed solution:

1. Determine the energy behavior profile:

The solution should prepare the prosumers' daily energy generation profiles. In fact, prosumers' daily energy profiles show that the hourly energy variations are the most useful choice to capture the prosumers' features for generating significant PCGs and empowering significant exchange of energy between them.

2. Based on the similarity of the prosumer's behavior, we grouped prosumers to create prosumer community group (PCG):

The framework should guarantee that the prosumers having the energy profiles with related energy conducts are grouped in the same PCG. Making PCGs with homogeneous energy profiles will make it easy for the prosumer community coordinator to manage such groups rather than managing the groups having extremely diverse prosumers.

3 Design Rationale

This section provides a design rationale to fulfill the requirements that are outlined (Fig. 1).

4 Overview of the Prosumer Penalty Framework in Energy Sharing Network

In many past study on prosumer involvement [1–5], each prosumer was straightforwardly associated with the smart grid. This structure encourages direct exchange of energy among prosumers and the utility grid. Because of their unreliable and inefficient behavior, these individual prosumers are regularly rejected from the wholesale energy market. This is one of the detriments of the older structure. Not just the prosumers' individual frameworks are very smaller, however, all the more critically, their supplying is capricious as it relies upon fluctuating atmosphere situations [5, 6]. To overcome this situation, these individual prosumers that have similar behavior are joined in the form of a prosumer community group (PCG). Here, a PCG is defined as a collection of distributed energy resources with a combined capability. PCGs can communicate with the energy market furthermore negotiate with the other prosumer community groups. Thus, a PCG is motivated to satisfy the demand of energy of its individuals while detaching from the main grid [6]. In the PCG architecture [3, 6], prosumer community coordinator manages the power flow information, analyzes it, and makes appropriate decisions for controlling each prosumer in different PCGs.

The constant motivation of prosumers is important to urge them to stay dynamic and to enhance their part. The basic power for this inspiration is the award (reward)

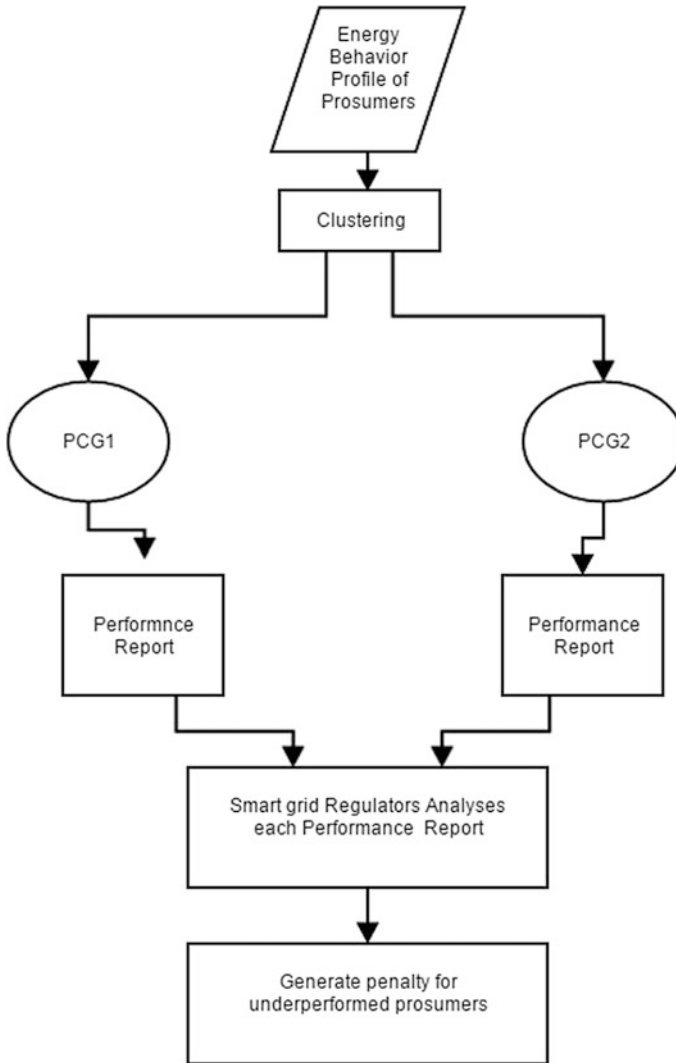


Fig. 1 Design of penalty calculation for prosumers

or other nonmonetary motivating forces. A portion of the nonmonetary prizes incorporates social appreciation, status and ubiquity in production, and efficient sharing of green energy [7].

Due to the unexpected change, involved in climate and uncertain prosumer behaviors, prosumers could not meet the required target. In that case, prosumer community group coordinator imposes some penalty and then requests the required energy from other prosumers within their group, or it has to reduce their power consumption to achieve a minimum energy target required by the utility companies.

In some cases, those simple groups may not be able to meet the minimum energy threshold. If the group of prosumers in a group cannot attain the least amount of energy [7] demanded by the utility companies, then they are allowed to request the required energy from other prosumer community groups. The prosumer groups that supply lower amount of energy than agreed should pay a higher penalty to the utility grid. These behaviors can affect unfavorably all the members of the prosumer groups.

In a prosumer classification [6], the prosumers who supply energy between 1 and 5 kWh over the domestic solar panels added to one community group, and those who provide energy between 6 and 10 kWh added to another community and so on. All the communities and prosumer should satisfy a minimum energy supply target value. The number of prosumers of the communities can change according to their minimum energy supply objective. If one of the communities fails to meet the goal, then either it can request to other communities that have the surplus energy supply or it has to reduce their power consumption. In either way, the community has to pay a penalty.

If the other community who has surplus energy has accepted their request, then they can do energy sharing. This energy sharing is called inter-PCG energy sharing [3], where the PCGs having excess energy than the threshold energy limit can share their energy with the other PCGs who could not meet the threshold energy limit after paying the penalty imposed by the PCG coordinator as analogous to intra-PCG energy sharing. In intra-PCG local energy distribution [3], those prosumers that have excess energy than threshold energy limit can share their energy with those local prosumers within the community who could not achieve the threshold energy limit after paying the penalty imposed by the PCG coordinator. For assessing this energy sharing [3], we should think through several components: How much surplus energy the prosumer or PCG will share, how much more energy the prosumer PCG need to meet the threshold energy limit. In this case, in spite of the fact that the energy sharing not only rises the aggregate energy of the buying prosumer or PCG but it also makes social support inside the group by helping those prosumers or PCGs, who can get punishments because of the break of agreement. In this way, the selling prosumer or PCG who sells their energy to the companion buying prosumer or PCG, who required energy to meet their requirement, ought to be dealt fairly.

Key objectives of the energy sharing process:

- Aims to maintain energy offered by individual prosumers
- Aims to keep energy provided by the prosumer community groups
- Aims to satisfy the shortage of energy of its members
- Aims to fulfill the demands of energy buyers
- Aims to achieve higher incentives
- Aims to decrease the cost related with penalty.

5 Performance Metrics and Performance Mechanisms for Prosumer Motivation

A performance metric [8] is that which determines prosumer's behavior and performance. It can measure prosumer's activities and performance based on how much energy they are generating and supplying. Here, we concentrate on the performance-based mechanisms for prosumer motivation that utilize financial penalties for those prosumer or PCGs who are not supplying enough energy to the utility grid.

The following requirements are set down for the proposed solution

1. Analyze the performance (amount of energy supplied) report.
2. Establish threshold energy limit (performance target) that provides PCGs or prosumers about the threshold energy level (minimum level of energy supply) anticipated by utility grid.
3. Determine those PCGs or prosumers who fail to accomplish the threshold energy level.
4. Compute penalties for keeping up or enhancing their performance.

Firstly, amount of energy supplied is analyzed in order to observe PCG's or prosumer's performance. Secondly, targets are established for providing information about the amount of energy supply anticipated by the utility grid. The target characterizes the exact level of performance that a prosumer or a PCG should accomplish in a specific period. It is used directly to lead a prosumer without a penalty and offers PCGs or prosumer to achieve the desired outcomes. Once performance targets have been defined retailers or utility grid can review the performance report to monitor PCGs or prosumers who fail to meet the performance goal. Finally, financial penalties are applied to improve the PCG's or prosumer's inspiration in order to accomplish the specific targets.

6 Specific Objectives of the Research

- (a) Describe the penalty formulas
- (b) Ensure a reasonable magnitude for the penalty
- (c) Presentation of penalties in several different equivalent units
- (d) Develop an algorithm and MATLAB code for the penalty formula
- (e) Observation, results, and discussion.

6.1 Penalty Formulas

6.1.1 Linear Penalty Formula

It calculates penalties for those PCGs or prosumers who are not supplying the requested amount of energy that means their performance is lower than the specified target. It is easy to comprehend and oversee. This penalty function varies linearly according to the supply of energy.

$$P(x) = \frac{\left[Target - \frac{\left(\sum_{i=0}^M x_i \right)}{M} \right]}{\sqrt{\left(\sum_{i=0}^M \left(x_i - \frac{\left(\sum_{i=0}^M x_i \right)}{M} \right) \right)^2}} \times Max\ Penalty$$

6.1.2 Quadratic Penalty Formula

It also calculates penalties for PCGs or prosumers who are not satisfying the performance (supplying the minimum amount of energy demanded by the utility company). As compared to the linear formula, this penalty function [8] increases more slowly as performance goes astray from target, thus brings about an increased slope. So there will be little incentive around the target. Thus it is more favorable to prosumers and PCGs than utility grid regulators.

$$P(X) = \left[\frac{\left[Target - \frac{\left(\sum_{i=0}^M x_i \right)}{M} \right]}{\sqrt{\left(\sum_{i=0}^M \left(x_i - \frac{\left(\sum_{i=0}^M x_i \right)}{M} \right) \right)^2}} \right]^2 \times Max\ Penalty$$

6.2 Ensure a Reasonable Magnitude for the Penalty

While setting up the proper formulas for penalty calculations, utility company or regulator should follow certain points. The calculated penalty value should catch PCG's or prosumer's attention. It should offer an adequate inspiration to achieve the sought result. Then again, calculated penalty value ought not to be unbalanced to the

expenses. In order to guarantee that the penalty value will stay inside a sensible bound, most such methods incorporated a cap on the maximum penalty [9–11].

6.3 *Presentation of Penalties*

Depending on the circumstances, penalty values are specified in a few diverse proportional units [7]. For instance, it can be represented as dollars, pennies per share, and percent of aggregate income. In any case, penalty calculations are least difficult when calculated as dollars, as different proportional units are officially mind boggling.

6.4 *Algorithm: Prosumer Penalty Framework*

Input: 500 prosumers with their energy supply performance to grid on an average winter day and an average summer day

Output: Display the penalty of each prosumer in each cluster.

1. Load the 500 prosumer's energy behavior profiles in the form of time series data.
 2. Cluster these prosumers into four clusters using k-means clustering algorithm.
 3. Set the target of each prosumer in each cluster.
 4. Set the maximum penalty to each prosumer (max_penalty hourly).
 5. Calculate the standard deviation of each prosumer energy supply in each cluster during the given 48 hour time series
 6. Calculate the penalty rate for each prosumer on average daily basis whose energy supply is less than the target.
 7. For each prosumer, i , compute the average daily energy they have to supply.
 8. For each prosumer daily average energy supplied $<$ target, calculate their penalty
 9. Display the daily penalty of each prosumer during the 24-hour duration.

6.5 *Verification and Results*

Research studies on PCGs [1, 7–9] are deficient in addressing the key aspects of developing penalty framework in managing prosumers. This opening motivated us to address the key challenges of developing penalty frameworks for prosumers and prosumer community groups to manage them in the smart grid. None of the existing

works [1–5] address any motivational schemes to grow or sustain PCGs that should be incentive driven. In this section, by applying different values for each parameter, we verify the proposed prosumer penalty framework for prosumers and PCG. For this, we extensively used MATLAB to verify the concepts we used in developing penalty frameworks for prosumers and prosumer community groups.

In this section, we discussed the experimental setting used to test the proposed framework and illustrated the simulation parameters used for the verification.

As shown in Table 1, the key simulation parameters of the verification are the prosumer energy data set. Obtaining a prosumer energy data set is challenging as actual energy data are publicly inaccessible. Therefore, to produce the prosumer energy data set, we model the average prosumers’ energy generation data during the 48-h time series (winter periods) in Australia. Here, our concern is only with the solar energy generation profiles which are prominent in the Australian domestic environments compared to the other renewable energy sources. In this section, we first discuss the generation of prosumer energy data set. In this section, the theoretical aspects used by the proposed framework are evaluated. Firstly, we verify the time series clustering [1] and the penalty calculation of the hourly energy sharing behaviors of 500 prosumers. The time series data set that we used results in four clusters. Figures 2, 3, 4, and 5 illustrate the penalty profiles owed to each prosumer in each cluster on an average winter day.

Table 1 Simulation parameters used to test the penalty frameworks for prosumers and prosumer community groups

Simulation parameter	Value
Number of prosumers’ energy profiles	500
Minimum number of prosumers anticipated in each PCG	70
Target energy expected from each prosumer community	100

Fig. 2 Cluster 1

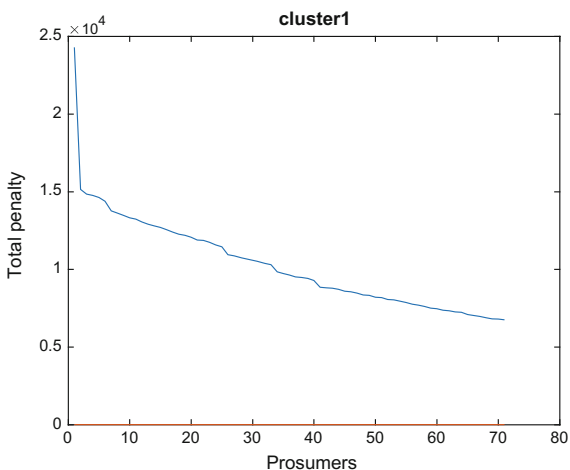


Fig. 3 Cluster 2

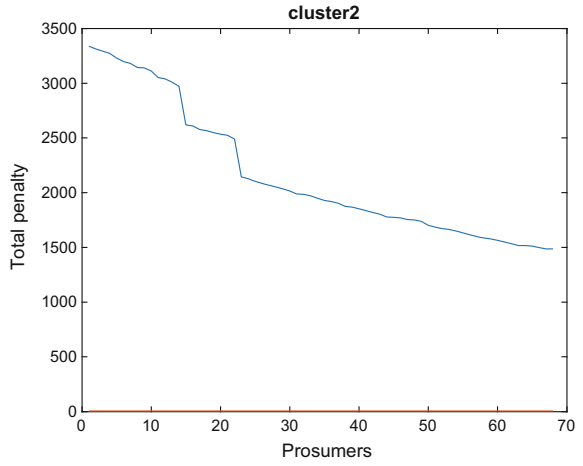


Fig. 4 Cluster 3

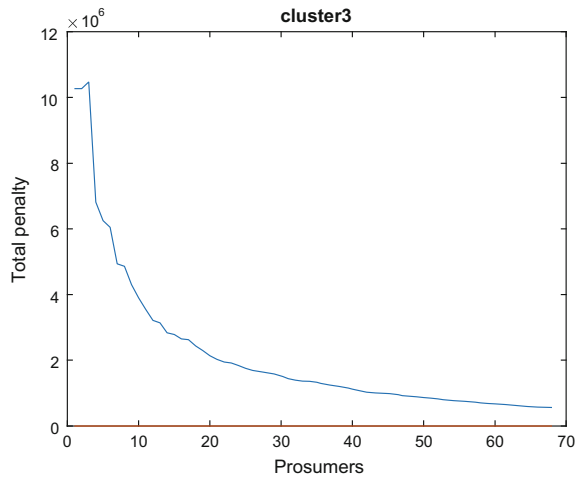
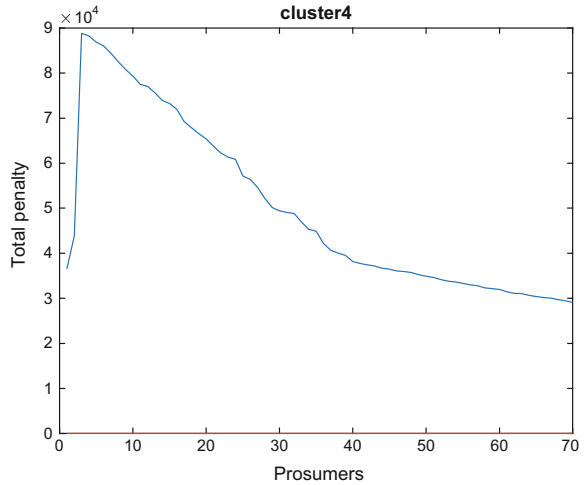


Fig. 5 Cluster 4



7 Conclusion and Future Work

In this research, a clustered prosumer penalty framework on the smart grid was proposed to determine the penalty owed to each prosumer in each cluster on an average winter day. A performance-based target is defined for each prosumer and PCG, i.e., they should maintain the minimum performance target in order to avoid paying penalties. Moreover, MATLAB simulations are present to verify the penalty framework. Future work depending on some external factors such as climate change, change in the number of family members, and the prosumer's energy profile can vary. So such factors should be considered while developing the penalty framework. At times when the prosumer does not obey as stated on contract, perhaps purposefully supplying very low quantity of energy than concurred during a period. It is important to consider those undesirable practices and investigates the related issues.

References

1. Rathnayaka, A.D., Potdar, V.M., Dillon, T.S., Kuruppu, S.: Formation of virtual community groups to manage prosumers in smart grids. *Int. J. Grid Util. Comput.* **6**(1), 47–56 (2014)
2. Rathnayaka, A.J.D., Potdar, V.M., Dillon, T., Hussain, O., Kuruppu, S.: Analysis of energy behaviour profiles of prosumers. In: *IEEE 10th International Conference on Industrial Informatics*, pp. 236–241 (2012)
3. Rathnayaka, A.J.D., Potdar, V.M., Dillon, T.S., Hussain, O.K., Chang, E.: A methodology to find influential prosumers in prosumer community groups. *IEEE Trans. Ind. Inform.* **10**(1), 706–713 (2014)

4. Rathnayaka, A.J.D., Potdar, V.M., Kuruppu, S.J.: An innovative approach to manage prosumers in Smart Grid. In: 2011 World Congress on Sustainable Technologies (WCST), pp. 141–146 (2011)
5. Rathnayaka, A.J.D., Potdar, V.M., Dillon, T., Kuruppu, S.: Framework to manage multiple goals in community-based energy sharing network in smart grid. *Int. J. Electr. Power Energy Syst.* **73**, 615–624 (2015)
6. Rathnayaka, A.J.D., Potdar, V.M., Dillon, T., Hussain, O., Kuruppu, S.: Goal-oriented prosumer community groups for the smart grid. *IEEE Technol. Soc. Mag.* **33**(1), 41–48 (2014)
7. Rathnayaka, A.J.D., Potdar, V., Ou, M.H.: Prosumer management in socio-technical smart grid. In: Proceedings of the CUBE International Information Technology Conference, New York, USA, pp. 483–489 (2012)
8. Whited, M., Woolf, T., Napoleon, A.: Performance incentives for utilities. Western inter-state energy board www.synapse-energy.com (2015)
9. Jooshaki, M., Abbaspour, A., Fotuhi-Firuzabad, M., Moeini-Aghtaie, M., Ozdemir, A.: A new reward-penalty mechanism for distribution companies based on concept of competition. In: Innovative Smart Grid Technologies Conference Europe (ISGT-Europe), IEEE PES, pp. 1–5 (2014)
10. Mohammadnezhad-Shourkaei, H., Fotuhi-Firuzabad, M.: Impact of penalty-reward mechanism on the performance of electric distribution systems and regulator budget. *Gener. Transm. Distrib. IET* **4**(7), 770–779 (2010)
11. Mohammadnezhad-Shourkaei, H., Fotuhi-Firuzabad, M.: Principal requirements of designing the reward-penalty schemes for reliability improvement in distribution systems. In: Presented at the Proceedings 21st International Conference Electricity Distribution (CIRED) (2011)

Critical Evaluation of Offline MPPT Techniques of Solar PV for Stand-Alone Applications

Mohammad Asim, Mohd Tariq, M.A. Mallick, Imtiaz Ashraf, Supriya Kumari and Akash Kumar Bhoi

Abstract This paper critically presents the analysis of the performance of offline maximum power point tracking techniques such as voltage- and current-based MPP technique, look-up table method, and curve fitting-based MPP technique. Based on the analysis presented in the paper, authors have selected offline voltage-based MPPT technique for using in their modeling and simulation study for stand-alone applications. An offline voltage-based MPPT technique which is capable of tracking MPP has been selected because of numerous advantages it offers such as simple and low cost of implementation. The modeling has been done in MATLAB[®]/SIMULINK simulation environment, and MPPT technique is developed and implemented by taking a variable resistance as a load. To remove the limitation of the momentarily interruption in power delivery to the load due to measurement of the open circuit voltage (V_{oc}), a pilot PV panel of same rating to that of main PV panel is used in the paper to calculate V_{oc} . It resulted in an increase in efficiency as more energy can be delivered to the load as the main panel is never disconnected to calculate V_{oc} . The simulation results are presented and discussed in the paper, and the results shows that the MPP is tracked under changing atmospheric conditions such as variation in temperature and insolation. The study presented in the paper will help the researchers/engineers/professionals in the industry to implement the

M. Asim · M.A. Mallick · S. Kumari
Department of Electrical Engineering, Integral University, Lucknow, India
e-mail: asimamu@gmail.com

M. Tariq (✉)
School of Electrical and Electronic Engineering, Nanyang Technological University,
Singapore, Singapore
e-mail: tariq.iitkgp@gmail.com

I. Ashraf
Department of Electrical Engineering, Aligarh Muslim University, Aligarh, India

A.K. Bhoi
Research & Development Section, Department of Electrical & Electronic
Engineering, Sikkim Manipal Institute of Technology, Sikkim Manipal University,
Rangpo, Sikkim, India
e-mail: akash730@gmail.com

MPP technology at large scale thus making India a self-reliant country on tapping solar energy resources.

Keywords MPPT • Offline technique • Constant voltage • Photovoltaic Look-up table • Curve fitting

1 Introduction

The world relies on coal, oil, and gas for most of the current energy needs. The energy demand is continuously on the rise [1, 2]. The conventional energy sources are depleting, which may cause devastating consequence on the global quality of life.

The security of global energy is an issue as most of the gas and oil reservoirs are with few nations. The security concerns have led leaders all over the world to look for alternative energy sources. Moreover, an issue such as global temperature rise due to greenhouse gas emissions, which is primarily caused by burning of fossil fuels, has aggravated the issue to for renewable energy resources. The increase use of renewable energy resources and improving overall conversion efficiency is one of the best possible conditions to energy crisis [3, 4].

Renewable energy is energy that is generated from natural process that are continuously republished which includes wind, sunlight, tides, water, geothermal heat, and various form of biomass. These energies have low environmental impact and are being seen as an answer to the global warming issue [5, 6]. Most renewable energy ultimately comes from sun. The solar power is a complete renewable energy source. It produces no noise pollution as compared to other, and very little maintenance is required, as there is no moving part. The solar-powered panels are easy to install.

The drawbacks of solar are being high initial cost, weather dependent, and occupy a lot of space. To maximize the efficiency of a solar PV array, the PV array is made to operate at MPP, irrespective of changing atmospheric conditions [7, 8]. Maximising the efficiency is required especially when the electrical drives are operated from PV [8]. Maximum power generation can be achieved by matching PV source with load for any given atmospheric condition. The MPP can be tracked in two ways i.e., mechanical tracking and electrical tracking. In mechanical tracking, the PV panel orientation is changed physically according to the movement of sun. The positions of PV panels are precalculated according to the length of the day and seasons. The electrical tracking is done by tracking P-V or I-V curve of PV panel, and the panel is made to operate around MPP with the help of power electronic devices [7].

This paper aims to assess the various offline MPPT techniques such as voltage- and current-based MPPT techniques, look-up table method, and curve fitting method. These methods are discussed in terms of tracking speed, applications, number of sensors required, complexity, and cost. The effect due to various weather

conditions, variation in isolation, and variation in temperature is discussed. Finally, the MATLAB[®]/Simulink for voltage-based MPPT for resistive load is discussed.

2 Offline MPPT Techniques

MPPT techniques are broadly classified as offline method, online method, and hybrid method on the basis of technique used to track MPP. Offline control technique calculates MPP using technical data of PV panels such as open circuit voltage, short circuit current, and P–V and I–V curves. Offline methods have low cost compared with online method, but performance wise online methods are better.

Online method used real-time data such as voltage and current to track MPP. This method does not require the measurement of solar insolation and temperature. Online methods do not rely on model of solar cell and are also called model-free method.

Offline method uses reference signal such as open circuit voltage (V_{oc}), short circuit current (I_{sc}), solar insolation, and temperature which is used to generate the control signal to track MPP. The instantaneous value of voltage and current of PV panel is used to generate control signal to track MPP in case of offline method (Fig. 1).

Hybrid method is a combination of offline and online method. The MPP is tracked in two steps. The first step which is offline method places the operating point close to MPP and in second step which is online method fine-tunes the operating point to MPP.

2.1 Curve Fitting-Based MPPT

It is an offline method where in addition to technical data, panel characteristics other details such as output equation of PV panel in terms of the voltage corresponding to the MPP is calculated based on the mathematical model and equation used. The operating point is made to move to MPP. This method though simple has the disadvantage that prior knowledge of PV model and mathematical equation are required. It requires large number of calculation; hence, speed is less, and large memory is required.

2.2 Constant Voltage Method

The maximum power point voltage V_{mpp} and open circuit voltage V_{oc} have linear relationship for different values of solar insolation and temperature. Equation (1) is

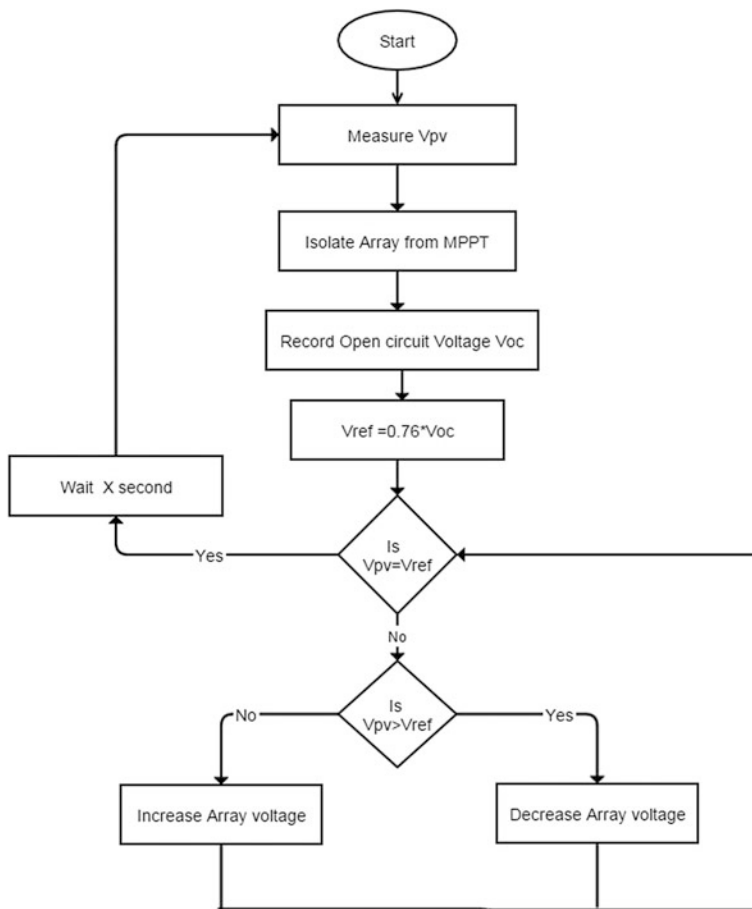


Fig. 1 Constant voltage algorithm

the basis of constant voltage method where K is called voltage factor whose value varies from 0.7 to 0.95.

$$V_{mpp} = K \cdot V_{oc} \tag{1}$$

There are basically two types of constant voltage technique available in the literature [9–11]. In one method, we isolate the solar panel to calculate V_{oc} , then by using Eq. (1), correct operating point is calculated for a particular value of K whose value is depend upon the material of solar cell. Then, the array voltage is adjusted till V_{mpp} is reached.

The drawback of this method is it is difficult to choose optimal value of K which varies in the range of (73–80)%. Its efficiency is relatively low.

The other constant voltage method is the use of pilot panel to calculate open circuit voltage. A pilot solar panel of same characteristic as that of main solar panel is used to calculate V_{oc} , which eliminates the loss of PV power during V_{oc} measurement as in previous method of constant voltage. The drawback of this method is that it is costlier as an extra pilot panel is being used.

$$I_{MPP} = K_I I_{sc} \tag{2}$$

The current-based MPPT method is based on Eq. (2) where K_I is called current factor whose value varies from 0.7 to 0.9 which depends upon characteristics of panel and cell material.

The voltage-based MPPT works on the principal that MPP generally lies from 0.7 to 0.95 of V_{oc} [12]. The pilot panel of same rating of main panel is used to calculate V_{oc} . This value is used as reference voltage. The error signal obtained is based through a PI block and then compared with a high-frequency triangular wave. The output obtained due to pulse width modulation (PWM) is fed to a DC-DC step-down converter. The duty cycle of the converter keeps charging till the PV panel voltage becomes equal to MPP voltage. The complete MATLAB model is shown in Fig. 2. The model in Fig. 3 shows that a pilot panel is being used to calculate V_{oc} .

The simulation was carried out up to 20 s for constant temperature 26 °C, $N_s = 4$, $N_p = 4$, and various insolation conditions of PV modules. The different outputs for different insulations from 100 to 30 mW/cm^2 for PV array are shown in Table 1.

Here, N_s is the number of series connected modules, and N_p is the number of parallel connected modules. The motor efficiency or load matching factor is tabulated in Table 1. The array efficiency is calculated as $(P_{max}/P_{Array}) \times 100$ where P_{max} is the output power of the array and P_{array} is output power of the PV array. The motor efficiency tabulated in Table 1 is given by $(P_{motor}/P_{Array}) \times 100$, where P_{motor} is the motor power that PV array can generate at the given ambient

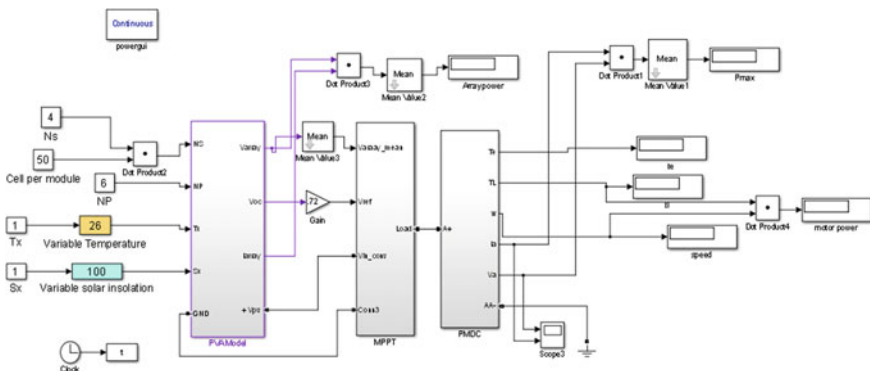


Fig. 2 Simulink model of constant voltage MPPT

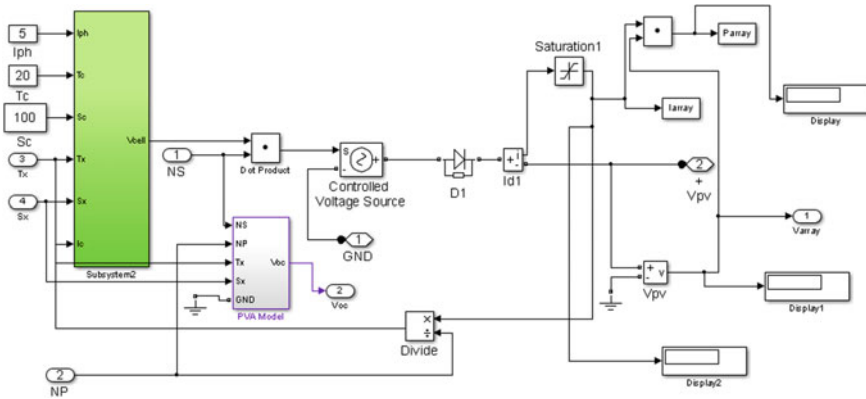


Fig. 3 Details of PVA block

Table 1 Variation of output parameters (WMPPT) at 26 °C

S_x (W/m ²)	P_a	P_{max} (WMPPT)	P_m (WMPPT)	Eff_A (WMPPT)	Eff_M (WMPPT)
100	1646	1579	1088	95.92	68.9
95	1562	1494.8	1028.44	95.7	68.83
90	1526	1459	1004	95.6	68.81
85	1361	1253.4	862.39	92.1	68.8
80	1275	1148.39	790.78	90.07	68.86
75	1240	1088.72	747.9	87.8	68.71
70	1065	935.07	641.7	87.8	68.63
65	998.1	863.9	592.2	86.6	68.54
60	963.8	834.3	571.7	86.6	68.52
55	821.7	676.4	461.9	82.1	68.28
50	797.3	655.3	447	82.2	68.21
45	648.5	615.8	419.9	82.33	68.18
40	565.7	424.6	281.9	75.07	66.39
35	483.7	329.4	211	68.1	64.05
30	403.9	176.2	98.67	43.62	55.98

conditions. The array efficiency indicates the extent of utilization of PV array and has been plotted in Fig. 4.

At low insolation, a very low array voltage is observed whereas the array current is observed to be very near (proximate/closed) to the array short circuit current. With the above observation, it is stated that the PV array is not operating at the MPP (maximum power point) condition which results in a very poor array efficiency. It is further observed that the highest array efficiency is at the solar insolation of 100 mW/cm². At low insolation, the efficiency of the motor is also observed to be lower. Hence, the poor utilization of the motor and array will take place at less

Fig. 4 Array efficiency versus solar efficiency at 26 °C

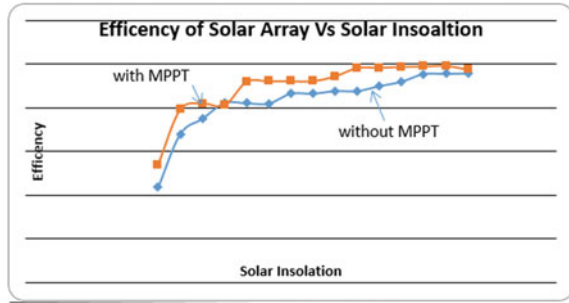


Table 2 Variation of output parameters (WMPPT) at 26 °C

S_x (W/m ²)	P_a	P_{max} (MPPT)	P_m (MPPT)	Eff _A (MPPT)	Eff _M (MPPT)
100	1646	1608.47	1157.45	97.72	71.96
95	1562	1553	1106	99.42	71.21
90	1526	1513.02	1087.71	99.15	71.89
85	1361	1347	944.5	98.97	70.11
80	1275	1256.51	877.54	98.55	69.84
75	1240	1220.9	852.43	98.46	69.82
70	1065	1007.49	694.16	94.6	68.9
65	998.1	922.1	626.2	92.38	67.91
60	963.8	890.2	604.3	92.36	67.88
55	821.7	758.75	514.74	92.34	67.84
50	797.3	734.31	497.64	92.1	67.77
45	648.5	527.1	346.3	81.27	65.69
40	565.7	464.7	297.9	82.14	64.1
35	483.7	384	245.2	79.38	63.85
30	403.9	218.6	126.9	54.12	58.05

WMPPT Without maximum power point tracking
 MPPT Maximum power point tracking

insolation. Poor utilization implies that the motor will be running at low speed at low insolation. The motor speed will increase on increasing the solar insolation. The motor will start to run at the rated speed for the insolation of 100 mW/cm² (Tables 2 and 3).

2.3 Look-up Table Methods

In this method, previous knowledge of PV panel material, panel characteristics, and technical data are stored. The output of PV panel is compared with the previously stored data in the look-up table to track the V_{PV} or I_{PV} to the V_{MPP} or I_{MPP} with the

Table 3 Summary of the major characteristics

MPPT technique	PV AD	Sensor	Complex	TA	Econ.	ETF	ECSR	TTS
Curve fitting	Yes	V	C	Low	NE	Low	Two	Slow
Look-up table	Yes	V, I	S	High	NE	Low	One	Faster
VMPPT	Yes	V	S	Low	NE	High	Two	Slow
CMPPPT	Yes	I	S	Low	NE	High	Two	Slow

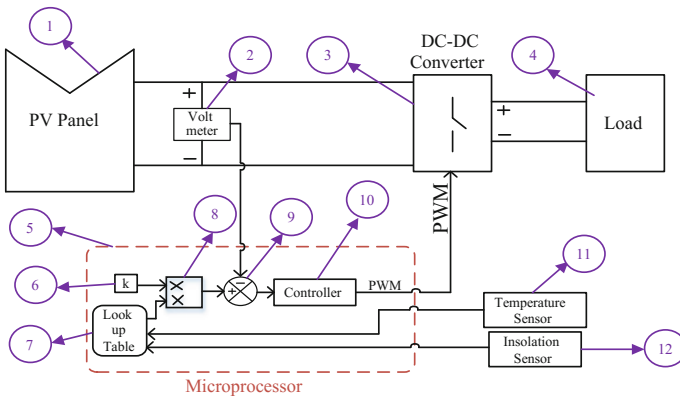


Fig. 5 Look-up table method

help of some converter [13, 14]. A large amount of data need to be stored. For varying atmospheric conditions, the system becomes complex, making the system slow. The block diagram for a look-up table for PV module is shown in Fig. 5.

At solar insolation of 100 mW/cm², the array power is 1646 W, whereas at 30 mW/cm², the array power is 403.9 W only. The efficiency is in the range 95–82% for solar insolation 100–45 W/m², and in the range of 75–43% for solar insolation 40–30 W/m² for a directly connected system. The efficiency is seen to increase after MPPT is implemented and is in the range 99–82% for solar insolation 100–45 W/m² and in the range of 81–54% for solar insolation 40–30 W/m² for a MPPT connected system.

3 Conclusion

The use of energy from PV panels is slowly becoming a reality, and its use is becoming a solution to environmental and energy problems very soon. Various offline techniques have been reviewed with their advantages and disadvantages. An

open circuit voltage-based MPPT has been designed and simulated for PMDC load. The efficiency is seen to increase at various solar insolation and temperature. The advantage of this MPPT algorithm is that the loss of energy which takes place when V_{oc} is calculated by disconnecting the load has been avoided by implementing the pilot panel. The pilot panel calculates V_{oc} and sends it as reference signal. The error in calculating MPP between sampling periods is also removed. The setup though bit costly due to addition of pilot panel gives higher efficiency.

References

1. Tariq, M., Shamsi, K.: Application of RET to Develop educational infrastructure in Uttar Pradesh. *International Journal of Recent Trend Inengineering, ACEEE*. **4**, 187–190 (2010)
2. Tariq, M., Bhardwaj, S., Rashid, M.: Effective battery charging system by solar energy using C programming and microcontroller. *Am. J. Electr. Power Energy Syst.* **2**, 41–43 (2013)
3. Yongxiu, H., Xu, Y., Pang, Y., Tian, H., Wu, R.: A regulatory policy to promote renewable energy consumption in China: review and future evolutionary path. *Renew. Energy* **89**, 695–705 (2016)
4. Tariq, M., Yuvarajan, S.: Modeling and analysis of self excited induction generator with electronic load controller supplying static loads. *Can. J. Electr. Electron. Eng.* **4**(1), 9–13 (2013)
5. Khare, V., Nema, S., Baredar, P.: Solar-wind hybrid renewable energy system: a review. *Renew. Sustain. Energy Rev.* **58**, 23–33 (2016)
6. Tariq, M., Yuvarajan, S., Wakode, P.: Digital simulation of electronic load controller with reduced THD for self-excited induction generator. *IUP J. Electr. Electron. Eng.* **6**(4), 36 (2013)
7. Ramli, M.A.M., Twaha, S., Ishaque, K., Al-Turki, Y.A.: A review on maximum power point tracking for photovoltaic systems with and without shading conditions. *Renew. Sustain. Energy Rev.* **67**(January), 144–159 (2017)
8. Tariq, M., Iqbal, M.T.: Power quality improvement by using multi-pulse AC-DC converters for DC drives: Modeling, simulation and its digital implementation, *Journal of Electrical Systems and Information Technology*, **1**(3) ,255–265, (2014)
9. Elgendy, M.A., Zahawi, B., Atkinson, D.J.: Comparison of directly connected and constant voltage controlled photovoltaic pumping systems. *IEEE Trans. Sustain. Energy* **1**(3), 184–192 (2010)
10. Tariq, A., Asghar, M.S.J.: Development of an analog maximum power point tracker for photovoltaic panel. In: *Proceedings of “the sixth international conference on power electronics and drive systems-PEDS 2005”*, Kuala Lumpur, Malaysia, Nov 28–Dec 01 (2005)
11. Ahmad, J.: A fractional open circuit voltage based maximum power tracker for photovoltaic arrays. In: *International Conference on Software Technology and Engineering*, pp. 247–250 (2012)
12. Asim, M., Tariq, M., Mallick, M.A., Ashraf, I.: An improved constant voltage based MPPT technique for PMDC motor. *Int. J. Power Electron. Drive Syst. (IJPEDS)* **7**(4), 1330–1336 (2016)
13. Tariq, A., Asim, M., Tariq, M.: Simulink based modeling, simulation and performance evaluation of an MPPT for maximum power generation on resistive load. In: *2nd international conference on environmental science and technology, IPCBEE vol. 6* (2011)
14. Asim, M., Tariq, A., Sarwar, A.: Simulation and analysis of a directly coupled solar PV based water pumping system. *J. Electr. Eng.* **2**(3), 72–81 (2009)

Design of Permanent Magnet Synchronous Generator for Wind Energy Conversion System

Abhishek Sahu, Sanjeev Gupta, Vinod Kumar Singh,
Akash Kumar Bhoi, Amik Garg and Karma Sonam Sherpa

Abstract It describes about the power and potential of wind energy that can be used to meet energy demand in future. The detailed illustration of generator and wind turbine has focused on interconnection of the generators and the troubles allied with it. For the generation of power from the wind, wind turbine, and PM synchronous generator are designed using MATLAB/Simulink. The results of this simulation authenticate the validity of developed WECS.

Keywords AC/DC and DC/AC converter · PMSG · Pitch controller
2-mass drive train · Wind turbine and WECS

A. Sahu · S. Gupta · V.K. Singh (✉)
Department of Electrical Engineering, SRGI, Jhansi, UP, India
e-mail: singhvinod34@gmail.com

A. Sahu
e-mail: mr.abhisheksahu88@gmail.com

A.K. Bhoi · K.S. Sherpa
Department of Electrical & Electronics Engineering, Research
& Development Section, Sikkim Manipal Institute of Technology,
Sikkim Manipal University, Rangpo, Sikkim, India
e-mail: akash730@gmail.com

K.S. Sherpa
e-mail: karmasherpa23@gmail.com

A. Garg
Research & Development Section, Sikkim Manipal Institute of Technology,
Sikkim Manipal University, Rangpo, Sikkim, India
e-mail: amikkarg@gmail.com

Table 1 All renewable energies installed capacity in India (till 31 Dec 2014)

S. No.	Source power	Total install capacity (MW)
1	Wind	22465.03
2	Solar (SPV)	3062.68
3	Small hydro power	3990.8
4	Biomass	1365.2
5	Biogases cogeneration	2800.35
6	Waste to power	107.58
	Total	33791.74

1 Introduction

Recently, the injurious effect of global warming and emission of carbon is considerably augmented. Due to which clean and extensive renewable sources such as wind, sun, ocean, and biomass energy come in more demand. Among all sources, wind energy has the maximum growth in the last decade. The reason that wind energy is free from toxic waste and continuously available natural source of energy, which is endless source and having great potential [1–4].

There are two factors which stimulate interest for the research in PMSG technology for wind turbine. First one is the significant growth trend of wind generation demonstrates its importance in meeting global requirements for electrical power in future and second, as wind generation technology progresses, the PM synchronous generator has potential to supplant this technology as primary means to the generation of electricity for large scale wind turbines [5–8].

This paper aims to simulate the controller of three-phase PMSG system, which will be built-in in a small wind turbine of fixed pitch variable speed. The wind turbine will be used to provide electricity for farm, business industries with the main electric supply in the India. The whole system consists PMSG, AC/DC convertor, DC link, PWM inverter and LC filter, and 3-phase load, and objective of the system is to develop the simulation model (Table 1).

2 Proposed Methodology

Figure 1 explains the main components of wind energy conversion system (WECS) such as Wind turbine system, generation system, DC/AC converter, and the load. Figure 2 shows PMSG system.

1. Wind turbine system: it converts the potential of wind energy into the rotation of the turbine, which is responsible for generating mechanical energy.
2. Generation system: the generation system converts the mechanical energy output into electric energy.

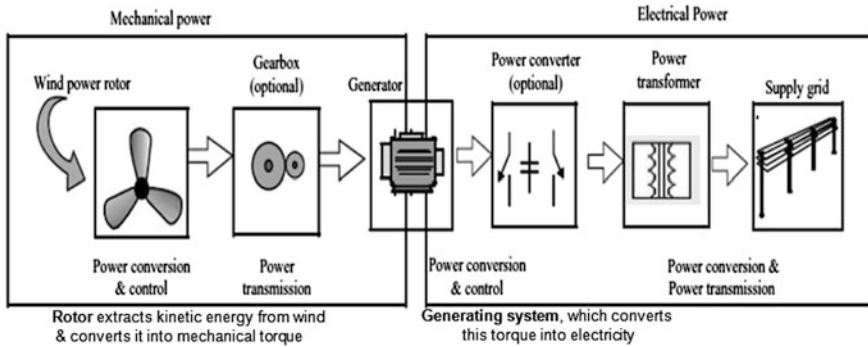


Fig. 1 Main components of a WECS

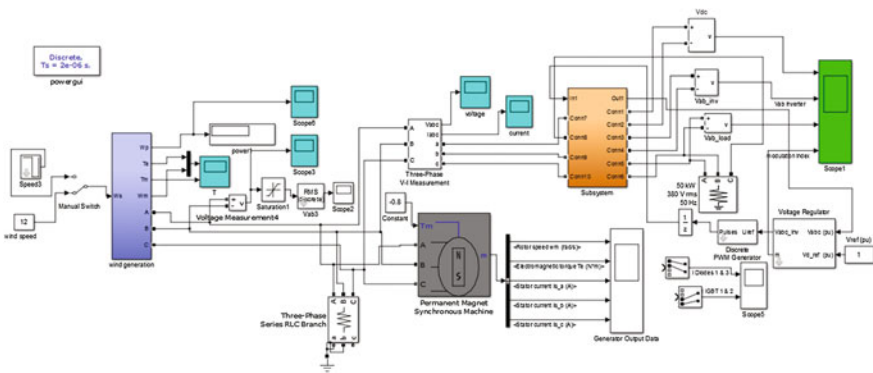


Fig. 2 Proposed system of a variable speed PMSG-based WECS

3. AC/DC converter: this AC/DC converter, i.e., rectifier is a full-bridge converter circuit.
4. DC/AC inverter: the PWM is selected to implement DC/AC converter. The controller takes voltage signal and current signal, in order to generate a signal to control the IGBT to attain a closed loop full-bridge voltage source inverter.
5. The load: a three-phase load is connected to the output end to measure the output results.

3 Modeling of the System

The turbine blades of wind extract kinetic energy and convert it into mechanical energy. Hence, the kinetic energy associated with an object having mass m rotating with velocity v is equal to the following:

$$E = \frac{1}{2}mv^2 \quad (1)$$

$$P_m = \frac{dE}{dt} = \frac{1}{2}\rho Av^3 \quad (2)$$

where

P_m mechanical power

T_w mechanical torque

A rotor area; $A = \pi r^2$

v wind speed in m

C_P coefficient of power

α speed ratio of tip

β pitch angle of rotor blade in radian

Air density $\rho = \rho_0 - 1.194 * 10^{-14}$ (where $\rho_0 = 1.225 \text{ kg/m}^3$ known as the air density at $T = 298 \text{ K}$).

4 Extraction of the Power from Wind

The power that contained by the wind can be calculated as

$$P_{\text{wind}} = \frac{1}{2}\rho_{\text{air}}\pi R^2 V_{\text{wind}}^3 \quad (3)$$

where $\rho_{\text{air}} = 1.225 \text{ kg/m}^3$ is the density of air.

The extracted power from the wind is

$$P_{\text{blade}} = C_P(\alpha, \beta)P_m \quad (4)$$

$$P_{\text{blade}} = \frac{1}{2}C_P(\alpha, \beta)\rho Av^3 \quad (5)$$

The rated speed is the point on power curve, wherever the power output begins to level out. Typical height of turbine is around 50 m, now increased up to 80–100 m. The manufacturers are also trying to increase the length of blades of

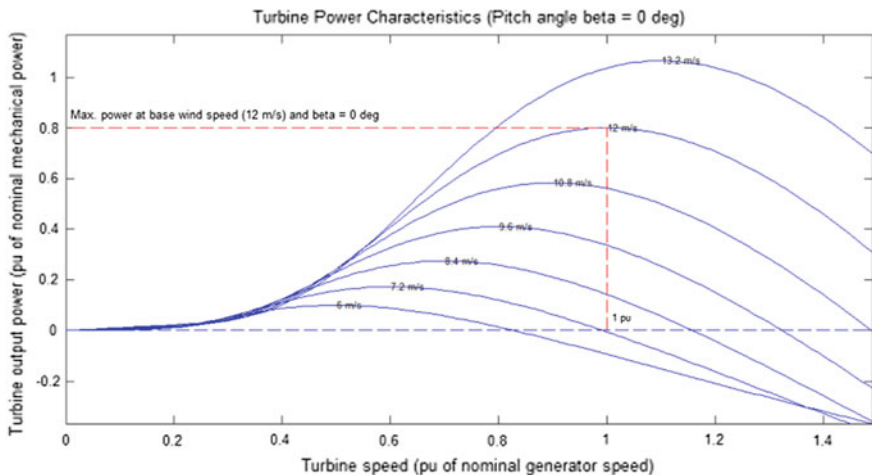


Fig. 3 Typical power curve between turbine output power versus turbine speed

rotor. The motive for this is the indirect relationship between the output mechanical power and tip-speed ratio (λ) of the rotor which is shown in Fig. 3.

$$\lambda = \frac{\omega_{\text{turb}}R}{v_{\text{wind}}} \tag{6}$$

$$P_{\text{mech}} = C_p^{1/2} \rho_{\text{air}} \pi R^2 (\omega_{\text{turb}}R/\lambda)^3 \tag{7}$$

where ω_{turb} is the turbine rotational speed, as the turbine’s rotor radius increases, the tip-speed ratio decreases, allowing for better output. After this stage, the output has given to the power convertor. AC voltage at fundamental frequency is related with DC voltage by Eq. (8)

$$V_B = \frac{1}{2\sqrt{2}} m_B V_B \angle \delta_B \tag{8}$$

m_g modulation index.
 $\angle \delta$ Phase angle.

The primary stage is rectification, also known as AC to DC conversion. The essential form of a rectifier is three-phase diode bridge, in which upper group diode will pass the positive cycle of a sine wave, and the lower group diode will pass negative cycle of a sine wave. A one-phase DC output can be calculated as given in Eq. (9). In the stage of inversion the output of DC link converted back into

alternating current output, which is achieved by three-phases switching circuits, (MOSFET or IGBTs).

$$V_{dc} = \frac{2V_{peak}}{\pi} \tag{9}$$

For a three-phase bridge converter, this will have to be multiply by three.

5 Results and Discussion

The WECS is built via MATLAB/Simulink with base wind speed is supposed as 8–12 m/s. The simulation results for the proposed system are given in Figs. 4 and 5. The output voltage wave forms of wind turbine are shown in Figs. 6 and 7. The output voltage waveforms of the wind turbine are shown in Fig. 8. The output waveforms of the AC-DC-AC convertor subsystem are shown in Fig. 9, which

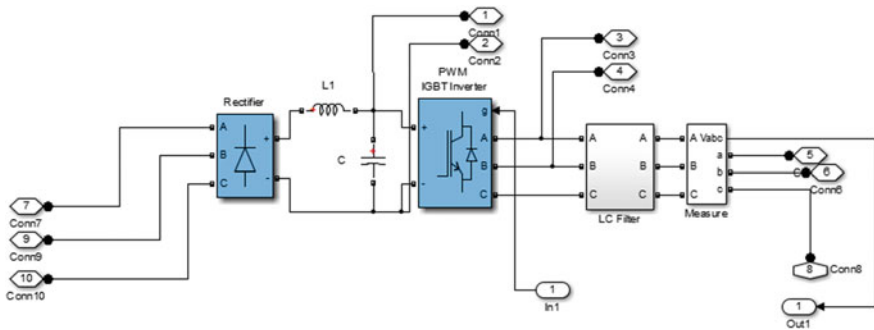


Fig. 4 AC-DC-AC converter model subsystem

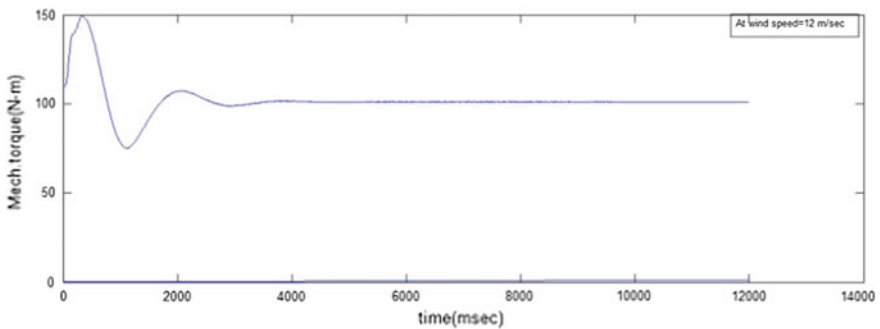


Fig. 5 Mechanical torque at wind speed 12 m/s

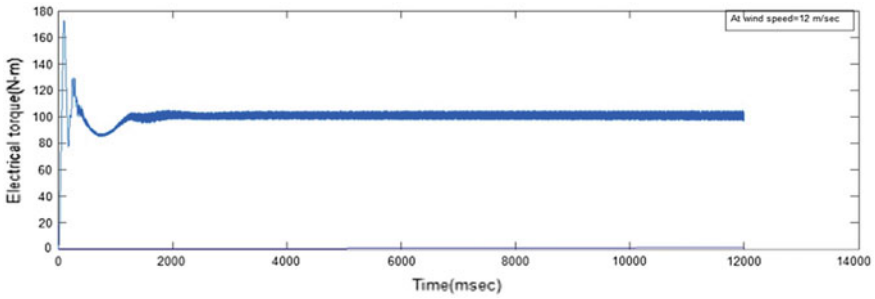


Fig. 6 Electrical torque of the generator at 12 m/s

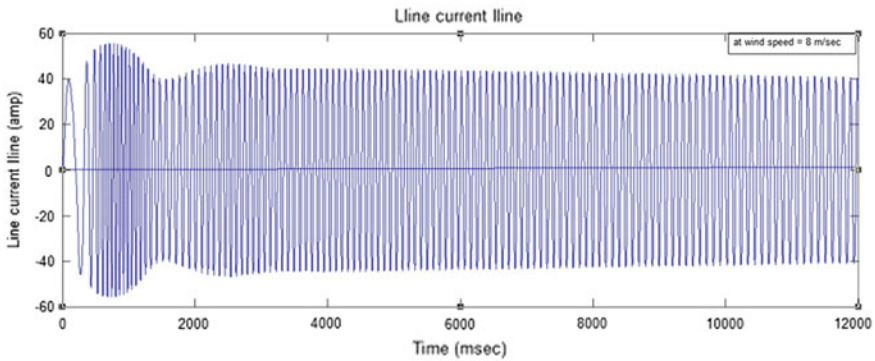


Fig. 7 Output current I_a of the generator at wind speed 8 m/s

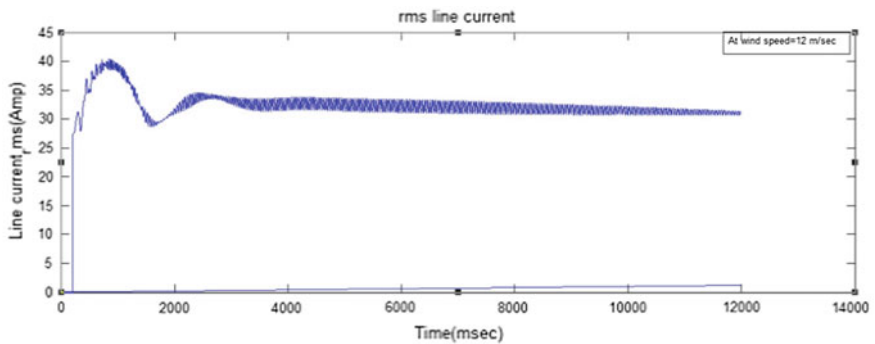


Fig. 8 RMS line current at 12 m/s

shows the RMS output voltage at wind speed 10 m/s. Also Figs. 10 and 11 show output line current at wind speed 12 m/s and three-phase output voltage on load (Fig. 12), respectively. Figure 13 describes the output RMS current on load at wind speed 12 m/s, and Fig. 14 shows the modulation index.

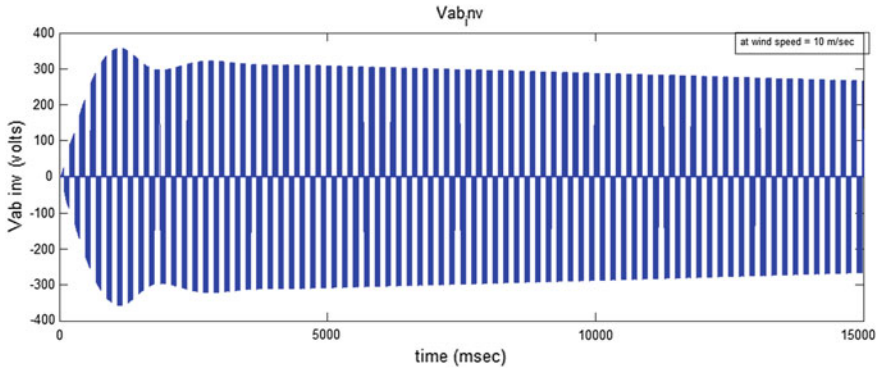


Fig. 9 Inverter output voltage V_{ab} at wind speed 10 m/s

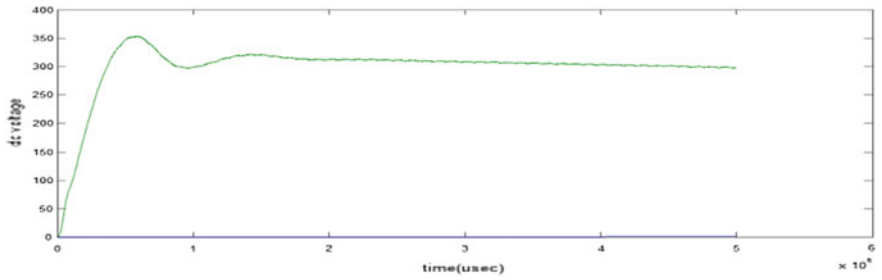


Fig. 10 RMS output voltage at wind speed 10 m/s

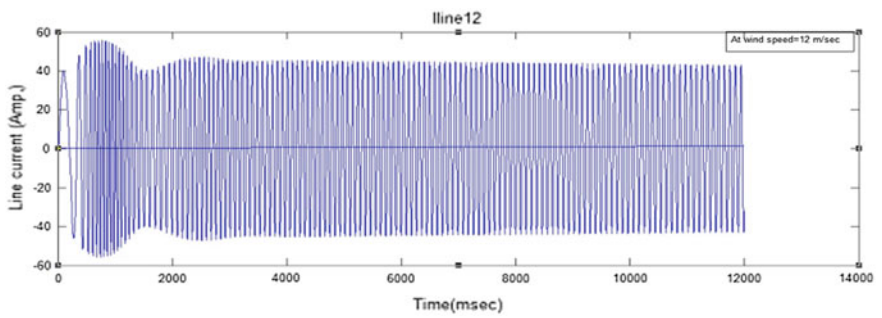


Fig. 11 Output line current at wind speed 12 m/s

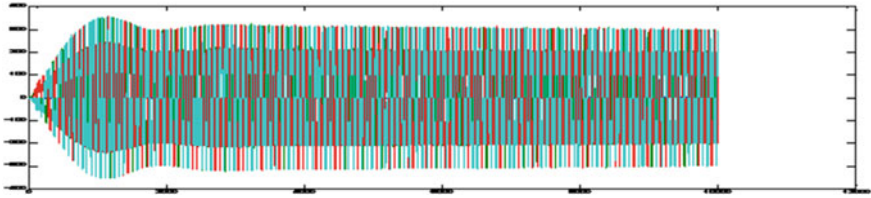


Fig. 12 Three-phase output voltage on load

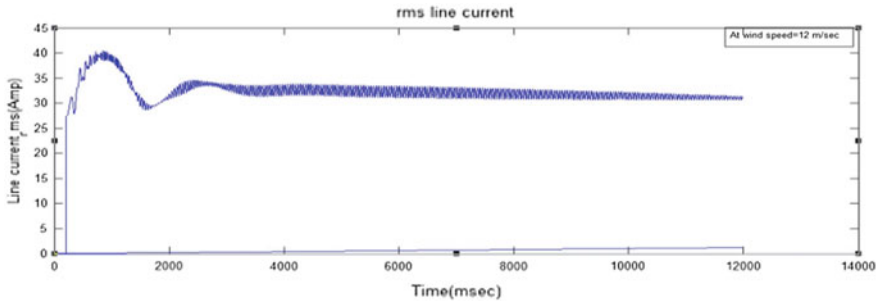


Fig. 13 Output RMS current at load at wind speed 12 m/s

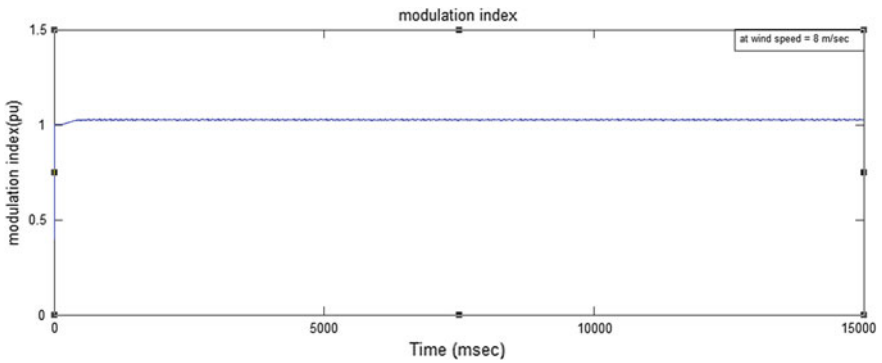


Fig. 14 Modulation index

6 Conclusions

This paper tries to maximize the yield of wind turbine by means of PMSG. The variable speed has been selected because of higher energy gain to reduce stress. A variable speed WECS has been developed using the MATLAB/SIMULINK. PMSG generator along with its controls has been discussed. The wind turbine

model is changed to a stall wind turbine model by adding a controller for strike angle. All results prove that the model is developed, and controllers demonstrate the effectiveness to obtain the maximum power output.

References

1. Pinto, A., Carvalho, B., Oliveira, J., Guimaraes, G., Moraes, A.: Analysis of a WECS connected to utility grid with synchronous generator. In: IEEE 2006 IEEE PES Transmission & Distribution Conference and Exposition, Latin America, Caracas doi:[10.1109/TDCLA.2006.311373](https://doi.org/10.1109/TDCLA.2006.311373), pp. 1–6 (2006)
2. Mesemanolis, A. Mademlis, C. Kioskeridis, I.: Maximum efficiency of a wind energy conversion system with a PMSG. In: IET 7th Mediterranean Conference and Exhibition on Power Generation, Transmission, Distribution and Energy Conversion. ISBN: 978-1-84919-319-1, pp. 1–9 (2010)
3. Ni, B., Sourkounis, C.: Energy yield and power fluctuation of different control methods for wind energy converters. *IEEE Trans. Ind. Appl.* **47**(3), 1480–1486 (2011)
4. Zahedi, A.: Current status and future prospects of the wind energy. In: IEEE 2012 10th IPEC Conference, Ho Chi Minh City (2012.12.12–2012.12.14) (2012)
5. Parikh, K., Maheshwari, A., Agarwal, V.: Modelling, simulation and performance analysis of AC-DC-AC PWM converters based WECS **2**(4) (2013)
6. Ahmed, A.A., Abdel-Latif, K.M., Eissa, M.M., Wasfy, S.M., Malik, O.P.: Study of characteristics of wind turbine PMSG with reduced switches count converters. In: 26th IEEE Canadian Conference of Electrical and Computer Engineering, doi:[10.1109/CCECE.2013.6567673](https://doi.org/10.1109/CCECE.2013.6567673), pp. 1–5 (2013)
7. Jayalakshmi, N.S., Gaonkar, D.N., Sai Kiran Kumar, K.: Dynamic modeling and performance analysis of grid connected PMSG based variable speed wind turbines with simple power conditioning system. In: 2012 IEEE International Conference on Power Electronics, Drives and Energy Systems, 16–19 Dec 2012, Bengaluru, India doi:[10.1109/PEDES.2012.6484474](https://doi.org/10.1109/PEDES.2012.6484474), pp. 1–5 (2012)
8. Research on the directly driven permanent magnet synchronous generator connected to DC grid. doi: [10.1049/cp.2013.1830](https://doi.org/10.1049/cp.2013.1830). ISBN: 978-1-84919-758-8, pp. 1–4 (2013)

Design and Development of Buck-Boost Regulator for DC Motor Used in Electric Vehicle for the Application of Renewable Energy

Manjesh, K.C. Manjunatha, Akash Kumar Bhoi
and Karma Sonam Sherpa

Abstract This paper presents design and development of buck-boost regulator for DC motor used in electric vehicle for the application of renewable energy. The proposed work is used to study electric vehicle with DC motor energized from buck-boost regulator Hybrid and Electric Vehicle Solutions by TEXAS INSTRUMENTS [1], with energy generated by renewable source. Present work depicts six-phase generator to generate the power from wind fans, and six-phase converter (rectifier) is used to convert AC to DC. The DC is again amplified or regulated by using buck-boost regulator.

Keywords Six-phase generator · Six-phase converter · Buck-boost regulator

1 Introduction

Transportation system contributes to more than 25% of worldwide greenhouse gas (GHG) generation, it is the highest contributor of GHG generation. GHG emissions from transportation system have grown up 30% from 2005 and show no sign of declination. Hence, reducing GHG generation from transportation gas system is the right step to eradicate global warming. To cut GHG emissions drastically and to maximize renewable energy adoption, it is essential to replace the internal

Manjesh (✉) · K.C. Manjunatha
Department of Electronic Science, Bangalore University, Bangalore, India
e-mail: manjesh1972@gmail.com

K.C. Manjunatha
e-mail: manjunathakc9@gmail.com

A.K. Bhoi · K.S. Sherpa
Department of Electrical & Electronics Engineering, Research & Development Section,
Sikkim Manipal Institute of Technology, Sikkim Manipal University, Rangpo, Sikkim, India
e-mail: akash730@gmail.com

K.S. Sherpa
e-mail: karmasherpa23@gmail.com

combustion engine (ICE) with hybrid system and hybrid-powered vehicles (PVs) [2,3]. By flipping the transportation system to electrified transportation, hence power can be derive from renewable energy. An electric vehicle is cleaner than petroleum-fuelled vehicles and seems to be a promising solution to global warming. In the twentieth century, the powered vehicles promise of minimizing global warming by the implementation of renewable energy technology. The renewable energy system offers energy free of cost and reliable operation towards the growth of electrical energy system wind turbines convert mechanical force into electrical energy. Therefore, source of mechanical force can be widely used in internal combustion engines.

A six-phase generator system is used to generate the power; the system has six electrical conductors working with alternating currents for a definite time offset in each conductor. Six-phase converters and inverters are used to provide power to linear and nonlinear loads [4]. Power generation using wind turbine is economical and highly efficient than other renewable energies such as solar cells and fuel. The power generated from all sources is very effectively utilized for the applications; in power electronics system, most of the 60% energy is wasted; in various conversions of energies for different applications, the use of converters and inverters in transforming energies to the load will generate additional harmonics with fundamental harmonics. This does not contribute extra energy for the load instead it is simply dissipated as heat in the devices and therefore the efficiency deteriorates. Since six-phase generator generates more power to weight ratio, these systems offer better voltage, frequency and improved reliability. Six-phase rectifier circuit is used to convert the generated AC into DC. In this work, a traditional rectifier circuit is used for converting AC into DC. The buck-boost converter is a type of DC-to-DC converter [5,6] that has an output voltage magnitude which can be either greater than or less than the input voltage magnitude. It is equivalent to a flyback converter using a single inductor instead of a transformer. The buck-boost converter circuit is constructed for the purpose of supplying stabilized/constant voltage to the DC motor applications.

2 Circuit Diagram

A six-phase converter is constructed with power diodes with 6 legs. In each leg, two diodes are employed to convert the AC voltage generated by wind turbine to a DC output voltage. The practical use of wind turbine is complex for the power electronics system in generation of power, since the power generated by the wind turbine depends on the capacity of the wind. If the generated wind is less, the speed of rotation of wind turbine is less; hence, the power generated by the wind turbine is

minimum. Also, in power electronics, it is most challenging work to operate instantaneously with loads. This situation can be overcome by designing buck-boost converters and inverters. In this work, the model has been created and simulated with Simulink/MATLAB software. The rectified output from rectifier is fed into buck-boost regulator. This buck-boost regulator is designed to work for the voltage between DC 150 and DC 250 V. This means the subsystem which is designed to work within the input voltage, but always greater than DC 150 V and less than DC 250 V, gives the proper constant DC voltage (Fig. 1).

If the applied DC voltage is less than 150 V, it is required to boost the applied voltage, and if the voltage is greater than 250 V, it is required to buck (regulate) the out voltage for constant DC output to drive DC motor.

Parameters used for simulation of circuit:

1. Input voltage = AC 120 V (from wind turbines to rectifier).
2. Frequency = 50 Hz.
3. DC input for buck-boost = 249.2 and 154 V (from rectifier to buck-boost).
4. DC output from buck-boost = 199.7 and 207.7 (from buck-boost regulator).

3 Results

For the buck-boost regulator, the output voltage vs time has been measured using Simulink and shown in Figs. 2 and 3. Simulation carried out by initializing 50 Hz as frequency. Output voltage is measured and plotted for both input of DC 249.2 and 154 V.

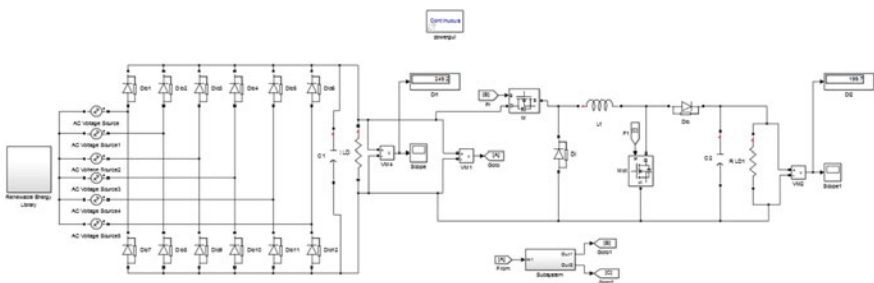


Fig. 1 Six-phase generator with buck-boost regulator for DC motor

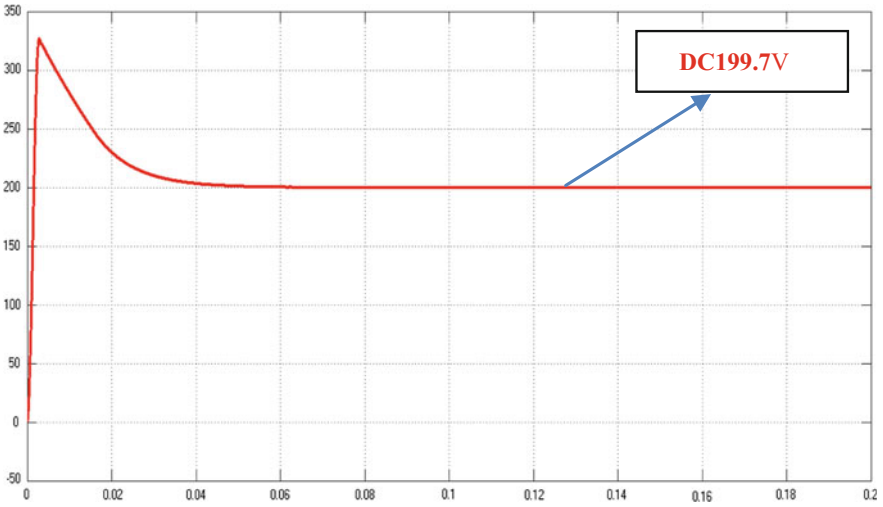


Fig. 2 Output voltage of buck-boost converter for the DC input of 249.2 V

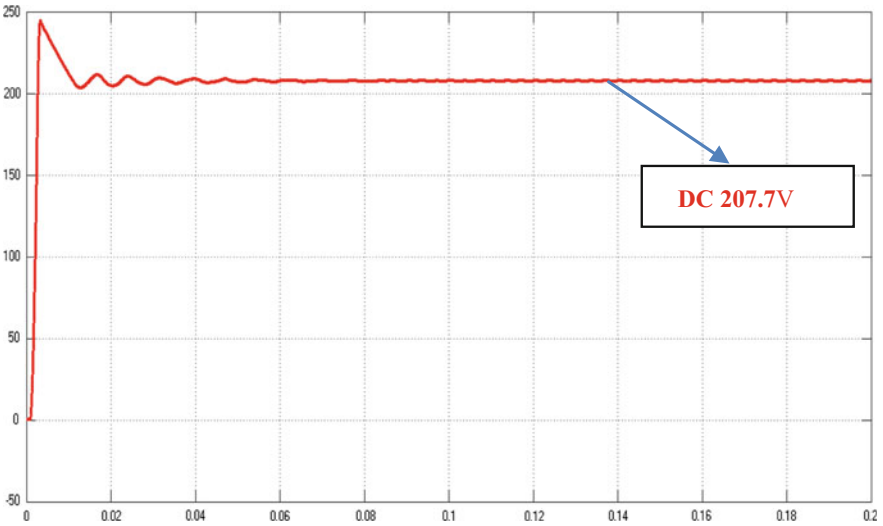


Fig. 3 Output voltage of buck-boost converter for the DC input of 154 V

4 Conclusion

The output response of a buck-boost regulator for DC motor has been simulated by creating a power source of six-phase generator. The simulated result is studied and this work is proposed to generate renewable energy for electric vehicles under low wind energy and high wind energy generation system.

References

1. Hybrid and Electric Vehicle Solutions by TEXAS INSTRUMENTS
2. Jayareshma, B.J., Preethi, N., Kumar, N.: Hybrid multi-port converter based electric vehicles using renewable energy with microcontroller. *J. Environ. Sci. Comput. Sci. Eng. Technol. Int. Peer Rev. E-3 J. Sci. Technol. JECET*; **3**(2), 1048–1060. E-ISSN: 2278-179X, 9 March 2014–May 2014
3. Shiau, J.-K., Ma, C.-W.: Li-ion battery charging with a buck-boost power converter for a solar powered battery management system. *Energies*, **6**, 1669–1699 (2013); doi:[10.3390/en6031669](https://doi.org/10.3390/en6031669)
4. Ananda, A.S., Manjesh: Analysis and study of total harmonic distortion in five phase PWM inverter using LC filter with neutral point DC link capacitor voltage balancing scheme. In: *International Conference on Magnetic, Machines and Drives* (2014)
5. Kumar, A., Gaur, P.: Operation of DC/DC converter for hybrid electric vehicle. *Int. J. Electron. Electr. Eng.* **7**(4), 335–340 (2014). ISSN 0974-2174
6. Dawood, N.B.: Review of different DC to DC converters based for renewable energy applications. *Int. Res. J. Eng. Technol. (IRJET)* **3**(03), e-ISSN: 2395-0056, www.irjet.net p-ISSN: 2395-0072, (Mar-2016)

The Particle Swarm Optimization Algorithm for Maximum Power Extraction of Solar PV Array

B. Dhanalakshmi and N. Rajasekar

Abstract The utilization of renewable energy nowadays has a tremendous growth over the past few years. The important factor which reduces the power output of solar PV array is partial shading. Further the mismatch losses in solar PV array are created by uneven shading. This affects the characteristics of PV array by creating multiple peaks which further reduces the output power. To reduce the effect of partial shading, the shading pattern has to be distributed uniformly which can reduce the mismatch losses as well as to increase the output power. In this article, the PSO algorithm has been proposed to mitigate the problems by partial shading to increase the output yield.

Keywords Array reconfiguration · Partial shading · Mismatch losses
Particle swarm optimization · Global maximum power point
Power enhancement

1 Introduction

From the last few decades, the renewable energy has turned out to be more competitive and widespread. In order to meet out the rising power crisis, renewable energy is extensively used. The non-conventional energy resources like solar, wind and biomass are abundant in nature, pollution-free and restorable [1, 2]. Due to the growth of power semiconductor technology, cost of solar PV panels has drastically reduced in recent years. This scenario attracted the interest of researchers and practitioners by large extent.

The installed capacity of solar power in India till March 2016 is 6763 MW. The government of India has raised subsidies and introduced new schemes to reach the

B. Dhanalakshmi · N. Rajasekar (✉)
Solar Energy Research Cell, School of Electrical Engineering,
VIT University, Vellore, India
e-mail: nrjasekar@vit.ac.in

B. Dhanalakshmi
e-mail: dhanalakshmi.b2015@vit.ac.in

target of 1,00,000 MW by the year 2020. The efficiency of solar PV system depends upon climatic conditions [3]. Further single solar PV module alone cannot meet out the energy demand; hence, interconnection of solar PV modules is mandatory.

The solar photovoltaic modules are connected either in series or parallel fashion [4]. In series connection, the panels are linked such that the array output voltage is sum of panel voltages connected in series. Accordingly, amperage is limited to the every single module current, whereas incase of parallel connection, the voltage of each panel is same and the amperage of each panel is added. Thus, the generated power is greater than the power from single module and applicable only to medium loads.

In order to serve high power loads in an efficient way, a number of interconnection schemes like series–parallel (SP), bridge linked (BL), total cross tied (TCT) and honey comb (HC) were introduced [4]. Generally TCT connection scheme is the most preferred configuration. It is been illustrated in [5] that incorporation of cross ties increases the life of PV array, even though losses will be more. A common phenomenon that occurs in PV array is partial shading (PS). The occurrence of partial shading may be due to building shade, birds, tress, etc. [5]. If any one panel is subjected to shading, then the array power reduces. Thus, the shadow is concentrated on the solar PV array and it affects the P–V and I–V characteristics. The consequences of PS are steps and multiple peaks in I–V and P–V characteristics [5]. Further this creates mismatch losses and reliability issues.

In order to mitigate this problem, array reconfiguration method was introduced. The concept behind array reconfiguration technique is to disperse the shade uniformly with minimum row current difference. In this article, the problem of array reconfiguration is framed as a optimization task and solved using particle swarm optimization algorithm. This method is a population-based search method. It is simple in structure and easy to implement with good convergence characteristics. The main focus of this article is to arrive global solution through iterative procedure by minimizing the row current difference and to maximize the energy yield of PV array [5, 6]. In this technique, the physical location remains unchanged; however, the circuit connections are varied. The proposed technique is analyzed with different shading pattern, and also obtained results are compared with TCT method [6].

2 PV Array Reconfiguration Technique

In practical, one of the recent methods to maximize power is array reconfiguration. In this article, aforementioned task is carried out using PSO technique. To appreciate the modeling simplicity, the single diode PV model is used.

2.1 TCT Array Interconnection Scheme

A 9×9 TCT configuration of solar photovoltaic array is depicted in Fig. 1. In TCT configuration, every row is connected in a series-parallel (SP) configuration. Due to large interconnection in TCT arrangement, a number of loops formed are more. Thus, the dissimilar values of current flows through the strings of the solar PV module connected in the PV array. The generated module current in any row at an irradiance of G is given by

$$I = SI_m \tag{1}$$

where I_m is the maximum current by the module at STC of G_0 (1000 W/m^2), $T = 25 \text{ }^\circ\text{C}$ and $S = G/G_0$. Applying Kirchhoff's Voltage Law, the array voltage for nine rows is given by

$$V_{\text{array}} = \sum_{i=1}^9 V_{mi} \tag{2}$$

where V_{array} is the PV array voltage and V_{mi} is the array voltage of the PV panels at the i th row. Kirchhoff's current law is applied for calculating current at every node in the array. Therefore, the total current of a PV array is given by

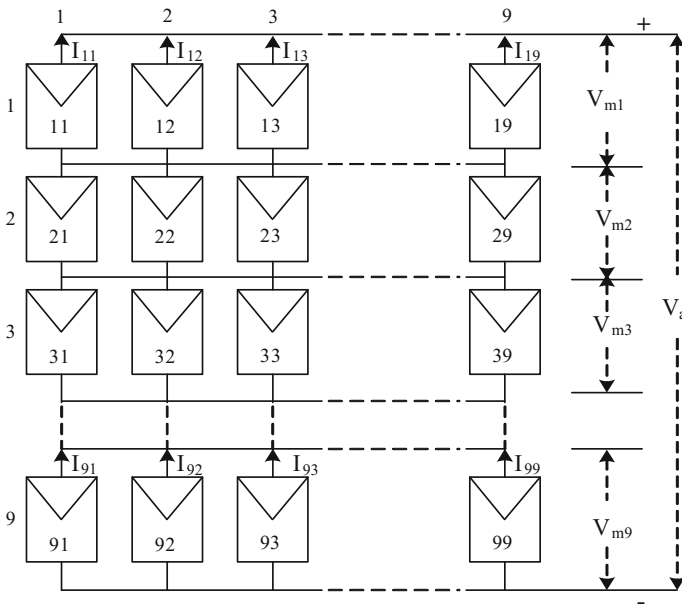
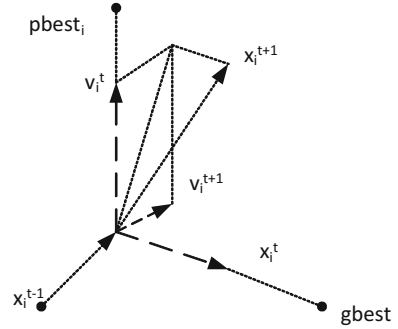


Fig. 1 PV array connected in TCT configuration

Fig. 2 PSO particle movement in the search space



$$I_a = \sum_{j=1}^9 (I_{ij} - I_{(i+1)j}) = 0, \quad i = 1, 2, 3, \dots, 8 \quad (3)$$

Instead of aiming better performance with conventional method like series, parallel, series–parallel and TCT, a new reconfiguration method based on swarm intelligence (PSO) is utilized for meeting the challenges like effective shade dispersion, row current minimization and maximum power extraction. The movement of particle in search space in case of the PSO method is represented in Fig. 2.

3 PSO-Based Technique

PSO technique was proposed by Kennedy [7], and it was extended by many authors to solve various optimization problems [8, 9]. Further, due to its higher adaptability and simple in structure, it is one of the most common optimization techniques used for solving MPP problem [9]. It is achieved by natural selection based on social behavior of swarm, fishes, birds, etc. In this technique, particles are initialized randomly in the search space at different position and are updated from P_{best} and g_{best} . The particle movements are governed by their own best position P_{best} , and the best position over the entire swarm is g_{best} . The process of search is continued till we attain the best values.

3.1 Process of Search

Initialize input parameters: irradiation parameters, population size, maximum number of iterations, swarm size, velocity weight w , and position weight, c_1 , c_2 .

Start: Generate initial swarm size

For iter= 1:N,

For each particle=1:pop

Initialize velocity vector, $Vel(i) = 1 + round(rand()*8)$

Initialize position vector, $Pos(i) = 1 + round(rand()*8)$

end

For each particle = 1:pop, swap the modules in each column according to the velocity initiated. Calculate the individual row currents, panel output power and individual position of each particle $Position(q) = sum(P) + (10/E_e) + (10*P_a)$

end

For each particle = 1:pop

Find P_{best} and g_{best}

End

Update the position and velocity of other particles as follows

For each particle = 1:pop

$Vel(i+1) = w*Vel(i) + c_1*rand()*[P_{best}(i)Present(i)] + c_2*rand()*[G_{best}(i)-Present(i)]$

$Present(i+1) = present(i) + v(i)$

end

Repeat for N iterations until convergence is reached

End

4 Problem Formulation

The problem of array reconfiguration is a maximization problem since the objective is to enhance the power output of a solar PV array for a given pattern by minimizing the row current difference. Therefore, the objective of output power maximization through row current difference minimization can be defined as

$$\text{Maximize Fitness } (i) = \text{Sum}(P) + \left(\frac{W_e}{E_e}\right) + (W_p * P_a) \quad (4)$$

where Fitness (i) = i th element in the current position fitness.

(i) $\text{sum}(P) = \sum_{k=1}^9 I_k * V_k$ where V_k and I_k are k th row voltage and current, respectively.

(ii) $E_e = \sum_{k=1}^9 |I_m - I_k|$

where I_m is the maximum possible current without bypassing.

P_a = output power of the panel when not bypassed.

W_e and W_p are the weights considered for E_e and P_a .

5 Results and Discussion

Optimization of PV array reconfiguration is the most important for effective shade dispersion. Therefore, applying suitable optimization technique is the best solution for reconfiguration pattern. At the same time, the proposed technique takes shorter time to find the best reconfiguration pattern for solving main issues like maximum power output of PV array and also for minimizing row current difference. Since TCT is a conventional method for solving array reconfiguration problem, PSO plays a vital role due to its simple in structure, system independency, very less number of tuning parameters, high adaptability which all leads the system to converge at a faster rate. The proposed method is tested on 9×9 matrix in MATLAB/SIMULINK, and the corresponding P-V and I-V characteristics are plotted and compared with conventional TCT interconnection scheme.

5.1 Case Study

Case 1

Short and Wide Shadow

Figure 3 shows the shading pattern considered for short and wide shadow condition. In this, the below half of the solar PV panel alone receives different irradiation level like 200, 400, 600 and 800 W/m², respectively. The remaining half of the panel remains unshaded. The considered shading pattern is tested with TCT and PSO technique. In TCT arrangement, the calculation of row current is important for tracking global peak power. Hence, for a given row, the output current is addition of panel current. The current limit calculation for any row, for instance, is:

$$I_{Rn} = \sum_{n=1}^9 I_{1n} * g_{1n} \quad (5)$$

where $g_{1n} = (G_{in}/G_{on})$, n represents column index. G_{1n} is the insolation level and I_{1n} is the current limit at full irradiance ($G_{1n} = G_0$) of the panel labeled $1n$. Let the current limit of the solar PV panel experiencing full insolation $g_m = 1$ at normal temperature be I_m ; then, the individual row current limits for first row with the shade pattern shown in Fig. 3 can be calculated as follows:

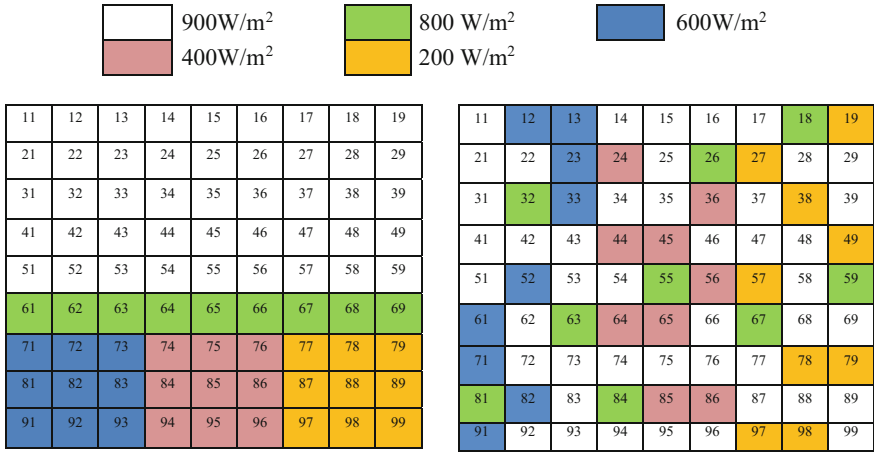


Fig. 3 Shading pattern for TCT and PSO

- Row 1 to row 5 of the panel experience an equal insolation of 900 W/m². Therefore, the current limit of the respective rows is:

$$I_{R1} = 9 \times 0.9 I_m = 8.1 I_m \tag{6}$$

and

$$I_{R1} = I_{R2} = I_{R3} = I_{R4} = I_{R5} \tag{7}$$

where

$$g_{1n} = 900/1000 = 0.9$$

- The complete row 6 experiences an insolation of 800 W/m² and the rows 7, 8, 9 experience shade of three different insolation, i.e., 600, 400 and 200 W/m². Thus, the calculation of the row currents for R6–R9 can be carried out in a similar fashion by the following Eqs. (8) and (9). Thus, the current contribution of rows 6, 7, 8 and 9 is calculated as follows:

$$I_{R6} = 9 \times 0.8 I_m = 7.2 I_m \tag{8}$$

Table 1 Position of GP IN TCT and PSO arrangement

TCT arrangement				PSO arrangement			
R. No.	Current	Voltage	Power	R. No.	Current	Voltage	Power
IR9	$3.6 I_m$	$9 V_m$	32.4 W	IR4	$6.4 I_m$	$9 V_m$	57.6 W
IR8	–	–	–	IR5	–	–	–
IR7	–	–	–	IR7	–	–	–
IR6	$7.2 I_m$	$6 V_m$	43.2 W	IR9	–	–	–
IR5	$8.1 I_m$	$5 V_m$	40.5 W	IR2	$6.5 I_m$	$5 V_m$	32.5 W
IR4	–	–	–	IR3	–	–	–
IR3	–	–	–	IR6	$6.6 I_m$	$3 V_m$	19.8 W
IR2	–	–	–	IR8	–	–	–
IR1	–	–	–	IR1	$6.7 I_m$	1 m	6.7 W

$$I_{R7} = I_{R8} = I_{R9} = 3 \times 0.6 I_m + 3 \times 0.4 I_m + 3 \times 0.2 I_m = 3.6 I_m \quad (9)$$

Individual rows limit is a function of the insolation received by them. When no panels are bypassed, then the array terminal voltage is $9 V_m$. When unshaded, the maximum solar PV array power output is given by

$$P_t = V_t I_m = (9 V_m) I_m \quad (10)$$

Equation (9) is suited only for the case when no panels in the row are bypassed.

On the other hand, when the power drawn by the load increases, the load current also increases, simultaneously the row which has lowest current limit will be bypassed. The terminal voltage of the array drops when any of the row is bypassed, therefore the array voltage is $V_t = 8 V_m + V_d$. Since diode drop is less than that of row voltage the array voltage reduces to $V_t = 8 V_m$. The above characteristics curve is shown for TCT and PSO for short and wide case. It is observed from graph that in TCT, occurrence of global peak is far away from nominal array voltage. It is clear from Table 1 that only when rows 6, 5, 4, 3, 2 and 1 are bypassed in TCT case, then we are able to receive maximum voltage, i.e., $9 V_m$. The maximum power voltage can be achieved at v_a (array voltage) of 112.56 V which is away from array voltage. For further power enhancement, PSO method is applied for the same case by executing the PSO code to evaluate the optimal reconfiguration pattern in order to achieve uniform distribution of shade all over the array. For dispersed PSO shading pattern, the PV array row currents are calculated using the following.

$$\left. \begin{aligned}
 I_{R1} &= 0.9 \times 5 + 0.4 \times 2 + 0.2 + 0.8 = 6.3 I_m \\
 I_{R2} &= I_{R4} = I_{R9} = 0.9 \times 5 + 0.4 + 0.6 \times 2 + 0.2 = 6.3 I_m \\
 I_{R5} &= I_{R6} = 0.9 \times 5 + 0.8 + 0.6 + 0.4 + 0.2 = 6.5 I_m \\
 I_{R7} &= 0.9 \times 3 + 0.8 \times 4 + 0.4 + 0.2 = 6.5 I_m \\
 \\
 I_{R3} &= 0.9 \times 7 + 0.4 + 0.2 = 6.9 I_m \\
 I_{R8} &= 0.9 \times 5 + 0.8 \times 2 + 0.6 + 0.2 = 6.9 I_m \\
 I_{R7} &= I_{R9} = 0.9 \times 6 + 0.6 + 0.2 \times 2 = 6.4 I_m
 \end{aligned} \right\} \quad (11)$$

$$\left. \begin{aligned}
 I_{R4} &= 0.9 \times 6 + 0.4 \times 2 + 0.2 = 6.4 I_m \\
 I_{R5} &= 0.9 \times 4 + 0.8 \times 2 + 0.6 + 0.4 + 0.2 = 6.4 I_m \\
 I_{R2} &= I_{R3} = 0.9 \times 5 + 0.8 + 0.6 + 0.4 + 0.2 = 6.5 I_m \\
 I_{R6} &= I_{R8} = 0.9 \times 4 + 0.8 \times 2 + 0.6 + 0.4 \times 2 = 6.6 I_m \\
 I_{R1} &= 0.9 \times 5 + 0.8 + 0.6 \times 2 + 0.2 = 6.7 I_m
 \end{aligned} \right\} \quad (12)$$

It is noted that the global point for the PSO arrangement occurs at a voltage around 188 V which is closer to the nominal array voltage. The maximum power extracted using PSO technique is 4879 W and for TCT 3847 W as shown in Fig. 4 which ensures that there is increase in power of 21.1% when compared to TCT technique shown in Table 2. It is noticed from the table that the maximum power coefficient for PSO scheme is almost closer. The maximum power coefficient not only depends on maximum power extraction from solar PV array, and it also depends on P-V and I-V characteristics, locality of v_{mpp} in the I-V curve.

The values of row 4 in Table 1 are maximum for PSO case, and hence, it is not bypassed. However, there is increase in load current due to increase in power demand. The rows with lower current are being bypassed from protecting them from excessive current which in turn reduces the array output voltage. Hence, when the load current demand increases, then the solar PV array should provide the excessive current with minimal bypass diode and it is also possible to find out the maximum power extraction only after plotting I-V and P-V characteristics as

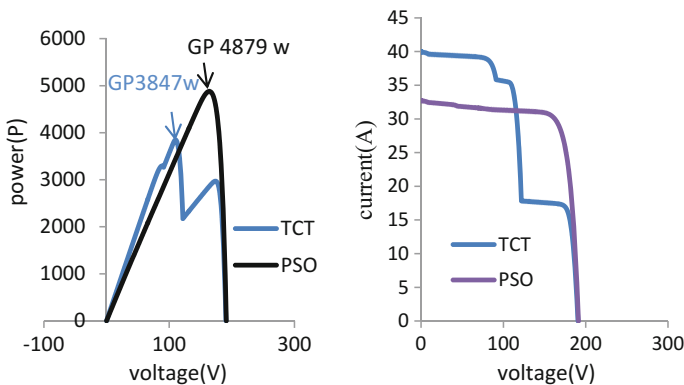


Fig. 4 P-V characteristics and I-V characteristics

Table 2 Maximum values for different methods

S. No.	Method	Maximum power (W)
1	TCT	3847
2	PSO	4879

depicted in Fig. 4. From the above results, we can conclude that under PSO technique, current extraction from the array at fixed voltage is comparatively higher than TCT. The evidence indicates that there is decrease in mismatch by equalizing the row current as closer as can.

6 Conclusion

A PSO-based array reconfiguration technique for maximum power extraction under partial shaded condition is presented. The proposed method has been tested with short and wide shade pattern. From the obtained results, by comparing with TCT methods, PSO method generates higher power with minimum bypass. In addition, this proposed method reduces the multiple peaks and minimized the difference in row current.

References

1. Rajasekar, N., Neeraja, K., Venugopalan, R: Bacterial foraging algorithm based solar PV parameter estimation. *Solar Energy* **97**, 255–265 (2013)
2. Sudhakar Babu T., Rajasekar, N., Sangeetha, K.: Modified particle swarm optimization technique based maximum power point tracking for uniform and under partial shading condition. *Appl. Soft Comput.* **34**, 613–624 (2015)
3. Sahu, H.S., Nayak, S.K., Mishra, S: Maximizing the power generation of a partially shaded PV array. *IEEE J. Emerg. Sel. Top. Power Electron.* **04**, 626–637(2016)
4. Indu Rani, B., Saravana Ilango, G., Nagamani, C.: Enhanced power generation from PV array under partial shading conditions by shade dispersion using Su Do Ku configuration. *IEEE Trans. Sustain. Energy* **43**, 594–601 (2013)
5. Sahu, H.S., Nayak, S.K.: Power enhancement of partially shaded PV array by using a novel approach for shade dispersion. In: *IEEE Conference on Innovative Smart Grid Technologies—Asia (ISGT ASIA)*, pp. 498–503 (2014)
6. Vijayalekshmy, S., Bindu G.R., Rama Iyer, S.: A novel Zig-Zag scheme for power enhancement of partially shaded solar arrays. *Solar Energy*, **135**, 92–102 (2016)
7. Kennedy, J., Eberhart, R.: Particle swarm optimization. *IEEE Int. Conf. Neural Netw.* **4**, 1942–1948 (1995)
8. Rajasekar, N., Vysakh, M., Thakur, H.V., Mohammed Azharuddin, S., Muralidhar, K., Paul, D., Jacob, B., Balasubramanian, K., Sudhakar Babu, T.: Application of modified particle swarm optimization for maximum power point tracking under partial shading condition. *Energy Procedia.* **61**, 2633–2639 (2014)
9. Ishaque, K., Salam, Z., Amjad, M., Mekhilef, S.: An improved particle swarm optimization (PSO)-based MPPT for PV with reduced steady-state oscillation. *IEEE Trans. Power Electron.* **27**, 3627–3638 (2012)

Analysis of Voltage Stability in Radial Distribution System for Hybrid Microgrid

Kuldip Singh, Swetalina Bhuyan, M. Narendra Kumar
and Satyasis Mishra

Abstract The hybrid microgrid is growing in India for rural electrification due to potential benefits in providing shape, reliable and sustainable electricity from renewable energy resources. As we know, the renewable energy resources are depending on nature and on the other hand, the loads on microgrid are variable. Due to instability in generation and load, voltage instability problem occurs. In this paper, we are discussing voltage stability by radial distribution network in microgrid with computational recursive method and implementing load flow analysis on 10-node system with simulation approach for voltage stability index (VSI). The critical node in microgrid is identifying with help of VSI.

Keywords Microgrids · Radial distribution · Voltage stability
Renewable energy · VSI · Load flow

1 Introduction

The microgrid has been growing rapidly in India for rural electrification due to several potential and economic advantages. The main advantage in microgrid is required less capital cost due to no transmission required only distribution is

K. Singh
EEE, CUTM, Paralakhemundi, India
e-mail: ksmann3@gmail.com

S. Bhuyan (✉)
EE, MEMS, Balasore, Odisha, India
e-mail: bhuyan_swetalina@yahoo.co.in

M. Narendra Kumar
EEE, GNIT, Kolkata, India
e-mail: vp.gnit@gniindia.org

S. Mishra
ECE, CUTM, Paralakhemundi, India
e-mail: s.mishra@cutm.ac.in

existing. The most commonly used power generation in microgrid from PV system along with wind generation to fulfill the power demand in isolated and non-isolated mode. The microgrid will operate in either grid synchronize mode or Islanded mode. In grid synchronize mode, the power is import/export from main grid. As we know in microgrid, the amount of generated energy is not fixed the different times of a day due to natural resources and the loads on microgrid does not remain same in specific time. The voltage stability problem is occurring in microgrid due to instability in generation and loads.

In this paper, we are discussing the active and reactive power flows from different sources in microgrid, which are connected to load in different branches, buses and networks. The flow of reactive power and active power in microgrid is called power flow or load flow in microgrid. In this paper, the main focus on improvement of voltage stability in microgrid with radial distribution system.

The paper is as follow. We briefly described the load flow study in Sect. 2. Section 3 described the radial distribution system, Sect. 4 radial distribution for voltage stability, and Sect. 5 will provide the simulation results. Finally, we conclude this paper in Sect. 6.

2 Power or Load Flow in Microgrid

The active and reactive power flows from different sources in hybrid microgrid with help of power electronics devices connected between load and sources. The flow of reactive and active power in microgrid is called power flow or load flow. The analysis of power flow study help to identify the bus voltages, phase angle, active power and reactive power in microgrid with mathematical approach, when load in steady state condition. Power flow analysis is helpful for planning and operations of hybrid microgrid. The load flow study is analyze with different methods like Newton Rapshon, Gauss–Seidel and fast decoupled method etc. [1]

The hybrid microgrid have major challenge with ever growing load demand, due to sudden changes in load, the hybrid microgrid experience voltage collapse. Therefore, the distribution utilities are keeping close vigil on the load pattern to take appropriate decision regarding system monitoring and future planning of load on microgrid. In this paper we are considering the stability index to determine critical loads, which may push the network. The microgrid has significantly impact on the distribution system for power flow and voltage condition at customers and utility equipment. The microgrid defines as a small-scale generation units, which is near to load centers at distribution side. In this paper hybrid microgrid and shunt capacitor are connected at selected nodes to analyze the voltage stability with radial distribution network.

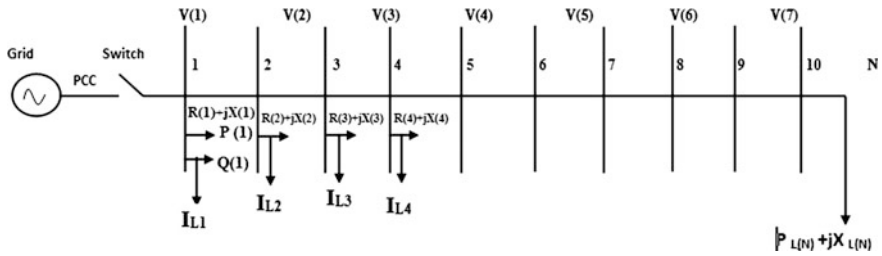


Fig. 1 Microgrid with radial system

3 Radial Distribution for Hybrid Microgrid

A 23 kV radial distribution with 10 nodes is shown in Fig. 1. Based on availability of resources, microgrid sources (DG) are connected at node-6. The radial distribution system is most frequently used in microgrid because it is the simplest and least expensive system.

Here $P_L(1) = 0$ and $Q_L(1) = 0$ (As slack bus)

Here N = Number of nodes

jj = Branch Number.

$jj = 1, 2, 3, 4, 5 \dots (N - 1)$

k = Node no.

$P_L(k)$ = active power load at k th node

$Q_L(k)$ = reactive power load at k th node

$V(k)$ = voltage k th node

$R(jj)$ = resistance at jj th branch

$X(jj)$ = reactance at jj th branch

$Z(jj)$ = impedance at jj th branch

$I(jj)$ = current flows at ' jj ' branch

Table 1 10-node system: base voltage = 23 kV; base MVA = 100.0

Branch number	Sending end node	Receiving end node	Resistance (R) (Ω)	Reactance (X) (Ω)	Active load P_L (kW)	Reactive load Q_L (KVAR)
1	1	2	0.1233	0.4127	1840.0	460.0
2	2	3	0.0140	0.6051	980.0	340.0
3	3	4	0.7463	1.2050	1790.0	446.0
4	4	5	0.6984	0.6084	1598.0	1840.0
5	5	6	1.9831	1.7276	1610.0	600.0
6	6	7	0.9053	0.7886	780.0	110.0
7	7	8	2.0552	1.1640	1150.0	60.0
8	8	9	4.7953	2.7160	980.0	130.0
9	9	10	5.3434	3.0264	1640.0	200.0

$I_L(k)$ = load current at 'kth' node

$P(k + 1)$ = total active power at load fed through $(k + 1)$ node

$Q(k + 1)$ = total reactive power at load fed through $(k + 1)$ node

As shown in Fig. 1, the radial distribution system under microgrid with following data shown in Table 1.

4 Analysis of Voltage Stability in Radial Distribution System for Hybrid Microgrid

The analysis of voltage stability of hybrid microgrid with radial distribution network for analyzed 10 node system to identify more sensitive node in critical load conditions, when microgrid is in isolated mode. Under normal condition the voltage at different buses is equal to the nominal value i.e. 1 pu at all time and in case of unbalance voltage level means instability in voltage. If voltage change more than nominal value, the phenomena known as voltage collapse. The system instability is occurring due to sudden changes in generation and load in microgrid. Consider Fig. 2 to analyze the voltage stability and more sensitive node in hybrid microgrid.

From Fig. 2, we derive the active and reactive power for particular node.

$$I_{jj} = \frac{V_{M1} - V_{M2}}{R_{jj} + jX_{jj}} \quad (1)$$

$$P_{M2} - jQ_{M2} = V_{M2}^* I_{jj} \quad (2)$$

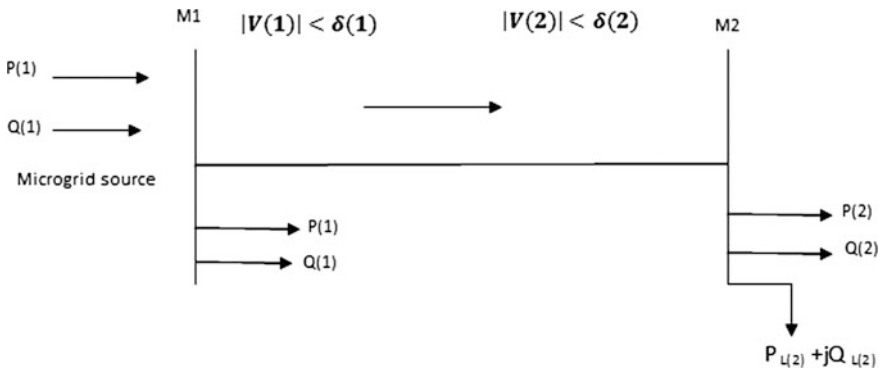


Fig. 2 Equivalent circuit for microgrid

From Eqs. (1) and (2), we get

$$P_{M2} - jQ_{M2} = \frac{V_{M2}^*}{R_{jj} + jX_{jj}} \cdot [V_{M1} - V_{M2}] \quad (3)$$

$$\begin{aligned} \Rightarrow P_{M2} - jQ_{M2} &= \frac{V_{M2}^* V_{M1} - V_{M2}^2}{R_{jj} + jX_{jj}} \\ \Rightarrow [P_{M2} - jQ_{M2}] \cdot [R_{jj} + jX_{jj}] &= V_{M2}^* V_{M1} - V_{M2}^2 \\ \Rightarrow V_{M2}^4 + (2P_{M2} \cdot R_{jj} + 2Q_{M2} - V_{M1}^2) + [R_{jj}^2 + X_{jj}^2] \cdot [P_{M2}^2 + Q_{M2}^2] &= 0 \end{aligned} \quad (4)$$

Roots of the Eq. (4) will be real and positive if

$$\begin{aligned} \Rightarrow [(2P_{M2} \cdot R_{jj} + 2Q_{M2} - V_{M1}^2)]^2 - 4[R_{jj}^2 + X_{jj}^2] \cdot [P_{M2}^2 + Q_{M2}^2] &\geq 0 \\ \Rightarrow 4 \cdot [P_{M2} \cdot X_{jj} - R_{jj} \cdot Q_{M2}]^2 + 4 \cdot [P_{M2} \cdot R_{jj} + Q_{M2} \cdot X_{jj}] \cdot [V_{M1}^2 - V_{M2}^4] &\leq 0 \\ \Rightarrow SI_{M2} = \frac{4 \cdot [P_{M2} \cdot X_{jj} - R_{jj} \cdot Q_{M2}]^2 + 4 \cdot [P_{M2} \cdot R_{jj} + Q_{M2} \cdot X_{jj}] \cdot [V_{M1}^2 - V_{M2}^4]}{V_{M1}^4} \end{aligned}$$

Hence, in general, stability index (SI) for microgrid having any number of node can be expressed as

$$SI_{k+1} = \frac{4 \cdot [P_{k+1} \cdot X_k - R_k \cdot Q_{k+1}]^2 + 4 \cdot [P_{k+1} \cdot R_k + Q_{k+1} \cdot X_k] \cdot [V_{M1}^2 - V_{M2}^4]}{V_{M1}^4} \quad (5)$$

and

$$VSI = \text{MAX} \{SI_{k+1}\} \text{ for } k = 1, 2, 3, \dots, N \quad (6)$$

or

$$VSI = \text{MAX} \{SI_2, SI_3, SI_4, \dots, SI_{NB}\}$$

The stability operation of the microgrid with radial distribution network $SI_{(M2)} \leq 1$ for $M2 = 2, 3, 4, \dots, N$. With help of voltage stability index, we are analyzing the stability of microgrid and implement the proper action for poor stability. After load flow study in microgrid, all node voltages are known in radial distribution system with branch currents. With help of voltage and currents of different branch or node, we are calculating the VSI (voltage stability index) by using Eqs. (5) and (6). From VSI index, we are sensitive node with minimum VSI value for voltage collapse.

5 Simulation Results

By analyzing the load flow study in microgrid with 10 nodes, we calculate the voltage index and find the sensitive node with sources (DG). The simulations results for VSI are shown in Fig. 3 for 10-node radial system, when source are not connected at sensitive node. Figure 4 shows VSI and load factor, when the source is connected to sensitive node. In this system, we observed the sensitive node-9. It was seen that by increasing the critical loading limit, voltage drops as well as the stability index is most sensitive node become instable. The placement of shunt capacitor ($Q_C = 2000$ KVAR) at node-9 increases the critical loading limit from 2.4 to 2.7 as shown in Fig. 5.

Fig. 3 VSI and loading factor for 10-node system

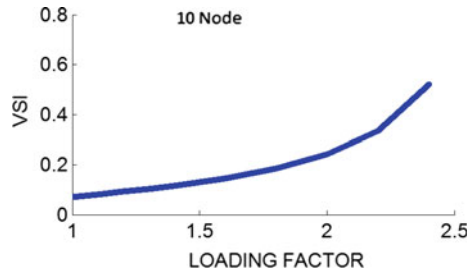


Fig. 4 VSI and factor of acceleration

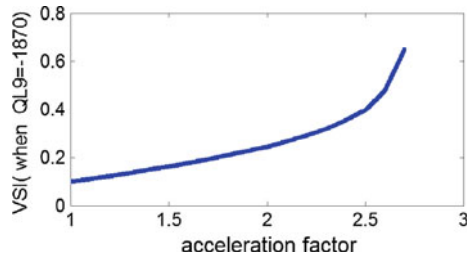
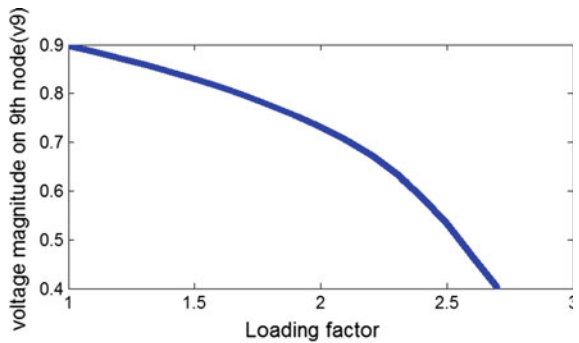


Fig. 5 VSI and load factor for sensitive node-9



6 Conclusion

The analysis of load flow in radial distribution network for hybrid microgrid is implemented to improve the voltage stability for the 10th node networks. In microgrid, sources are natural, so the generation is not constant all the time; on the other hand, load also not constant on microgrid. Due to sensitive loads, the voltage instability or voltage collapse occurs in microgrid. In this paper, we analyze, with help of Voltage stability index, the sensitive load or node can be identified in microgrid. After identifying the sensitive node, the shunt capacitor is helping to improve the stability of particular node.

References

1. Das, D., Kothari, D.P., Kalam, A.: Simple and efficient method for load flow solution of radial distribution networks. *Electr. Power Energy Syst.* **17**(5), 335–346 (1995)

PV-Fed Eleven-Level Capacitor Switching Multi-Level Inverter for Grid Integration

K. Mohana Sundaram, P. Anandhraj and V. Vimalraj Ambeth

Abstract This paper presents new photo-voltaic electrical power generation system, and this system consists of a DC (direct current)-to-DC power converter and multi-level inverters. This DC-to-DC converter combines a boost (step-up) converter and isolated converter (forward) with a coupled inductor to convert the output voltage of the solar panel fed PV array into different voltage sources. This eleven-level multi-level inverter is constructed using a full-bridge power converter and a capacitor selection circuit. These circuits are connected one by one, i.e. cascade. The capacitor selection circuit (CSC) is the combination of capacitor and transistor switches which helps to produce five levels of DC voltage from DC-to-DC converter output voltage. Then, H-bridge inverter converts this stepped level of DC power into AC power. By this way, the proposed solar power-fed eleven-level inverter produces a nearly sinusoidal output power and it produces very low THD which is less than twelve percentage. The important feature of this inverter is that only eight power electronics are used. The power produced from this multi-level inverter is same phase with the utility power.

Keywords Photo-voltaic (PV) array · Capacitor selection circuit
Multi-level inverter (MLI) · Maximum power point tracker (MPPT)
Total harmonic distortion (THD) · Amplitude (Amp)

K. Mohana Sundaram (✉) · P. Anandhraj · V. Vimalraj Ambeth
EEE, Veltech Multitech Dr.Rangarajan Dr.Sakunthala Engineering College,
Chennai, India
e-mail: kumohanasundaram@gmail.com

P. Anandhraj
e-mail: anandpannerselvam@gmail.com

V. Vimalraj Ambeth
e-mail: vimalrajambeth@veltechmultitech.org

1 Introduction

The application of renewable energy system is amplifying worldwide due to low cost, higher reliability, gas emission also very low compared with non-renewable energy system. The solar panel cost is reducing yearly, so this usage is increasing yearly. The integration of renewable energy sources with utility grid requires some consideration, i.e. voltage profile, frequency matching, voltage stability, and economical aspects network investment postponement. These are all the big challenges while integrating renewable energy sources with power grid [1]. The consolidation of power is very important in utility grid integrated solar energy system because this converts the DC power produced from solar panel using photovoltaic effect into AC power, and then, this power is connected to the utility grid. An H-bridge voltage source inverter is needed to convert DC power into AC power. This proposed multi-level inverter is designed using active and passive devices. The active devices are power semiconductor switches, and passive devices are inductors and capacitors [2, 3]. There are two losses in this circuit switching loss and conduction loss. The main reason for switching loss is owing to changes in voltage and current for each switching frequency and conduction loss due to power transistor switches. The normal inverter produces square wave AC waveform which has higher harmonic distortion. This normal inverter output power does not synchronize with utility power. The primary aim of this paper is to reduce the total harmonic distortion (THD) by producing multi-level AC power [4, 5]. This capacitor switching multi-level inverter uses less number of transistor switches compared with conventional multi-level inverters, i.e. diode-clamped multi-level inverter, flying capacitor multi-level inverter, and cascaded multi-level inverter. So this multi-level inverter is important research area for past some decades [6, 7].

2 Materials and Methodology

Figure 1 represents circuit diagram of eleven-level inverter. It consists of two stages of power conversion, DC–DC power conversion (boost) and DC–AC power conversion (inverter). Boost operation is done with the help of boost converter and current-fed forward converter with a transformer to convert PV array voltage into four different voltage sources with multiple relationships. The combination of capacitor selection circuit and full-bridge voltage source inverter produces eleven-level AC powers from four different capacitors. There are four modes of operation in positive half cycle of voltage source inverter and another four modes in the negative cycle of voltage source inverter.

Voltage source inverter switches S7 and S8 are ON in the first half of the cycle, and S9 and S10 switches are ON in the next half of the cycle.

Table 1 illustrates switching states in eleven-level inverter.

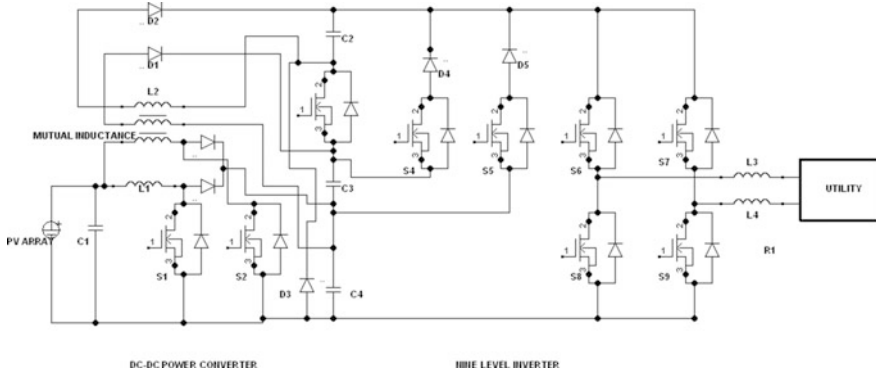


Fig. 1 Circuit diagram of eleven-level inverter

Table 1 Switching states of positive cycle operation

Voltage levels	S1	S2	S3	S4	S5	S6	S7	S8	S9	S10
$V_0 = V_{dc}/5$	ON	OFF	OFF	OFF	OFF	OFF	ON	ON	OFF	OFF
$V_0 = 2V_{dc}/5$	ON	OFF	OFF	OFF	OFF	ON	ON	ON	OFF	OFF
$V_0 = 3V_{dc}/5$	ON	OFF	OFF	OFF	ON	OFF	ON	ON	OFF	OFF
$V_0 = 4V_{dc}/5$	OFF	ON	OFF	ON	OFF	OFF	ON	ON	OFF	OFF
$V_0 = V_{dc}$	OFF	ON	ON	OFF	OFF	OFF	ON	ON	OFF	OFF

2.1 Modes of Operation

In mode 1, switch S1 in the DC-to-DC converter is turned ON and inductor L1 and capacitor C5 also charge. Capacitor switching circuit switches S3, S4, S5, and S6 are turned off. The capacitor C2 delivers its stored energy to the load. Voltage source inverter is operated in positive half cycle. The maximum value of stepped voltage available in this mode is $V_0 = V_{dc}/5$.

In mode 2, the operation of DC converter is same as mode 1 and switch S6 alone from capacitor switching circuit turned ON. The capacitor C5 discharges via switch S6. The maximum value of stepped voltage available in this mode is $V_0 = 2V_{dc}/5$.

In mode 3, switch S5 alone from capacitor switching circuit turned ON. The capacitors C5 and C4 discharge its energy to the load via switch S5. The maximum value of stepped voltage available in this mode is $V_0 = 3V_{dc}/5$.

In mode 4, switch S2 in the DC-to-DC converter is turned ON and inductor L1 discharges its energy to the capacitors C2 and C5. Switch S4 alone from capacitor

switching circuit turned ON. The capacitors C5, C4, and C3 discharge its energy to the load via switch S4. The maximum value of stepped voltage available in this mode is $V_0 = 4V_{dc}/5$.

In mode 5, the operation of DC converter is same as mode 4, and switch S3 alone from capacitor switching circuit turned ON. The capacitors C5, C4, C3, and C2 discharge via switch S3. The maximum value of stepped voltage available in this mode is $V_0 = V_{dc}$.

Where V_0 represents output voltage and V_{dc} represents output of DC-to-DC converter voltage. The operation of negative cycle is same as positive cycle, except alternate switches in the voltage source inverter turned ON. The five-level stepped DC is given as input to the voltage source inverter, and this inverter converts five-level DC into eleven-level AC output.

3 Simulation Results and Discussion

Figure 2 is the Simulink diagram which is designed using MATLAB/Simulink. Simulink and Simpower system components are used to design this circuit. Transistor (MOSFET) switches are used here, and the different switching frequencies are used in DC-to-DC converter, capacitor switching circuit, and voltage source inverter, i.e. 10 kHz, 100 Hz, and 20 kHz, respectively. Single-diode model-based solar panel is designed. Powergui block is used to run Simpower system elements. Scope is used to show the output in graphical view. Pulse generator and PWM generator block are used to provide gate pulses to the transistor switches.

Figure 3 represents five-level DC voltage obtained from four different voltage sources of DC-DC boost converter using four capacitors and four transistor switches.

Figure 4 represents four different gate pulses which are given to power semiconductor switches in the capacitor switching circuit. Pulse width of switch S3 is low, and this switch turn ON time is 20% per cycle. Switch S4 turned ON 50% per cycle. Switch S5 turned ON 70% per cycle. Switch S8 turned ON 80% per cycle.

The output voltage of the eleven-level inverter has eleven level of voltage in peak to peak which is shown in Fig. 5. X-axis and Y-axis represent time period and amplitude of voltage, respectively. The output voltage is **440 V**.

The full-bridge voltage source inverter converts five-level DC current into eleven-level AC current which is shown in Fig. 6. The magnitude of this AC current is **0.45 A**.

Figure 7 represents the THD of eleven-level inverter which is only **11.41%**. By comparing this in three multi-level inverters, eleven-level inverter has low harmonic distortion. Table 2 illustrates total harmonic distortion in different multi-level inverters

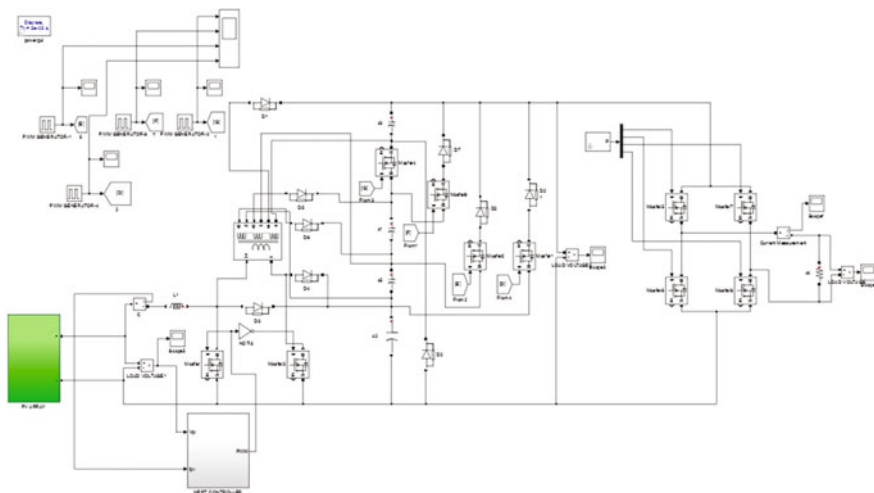


Fig. 2 Simulink circuit of eleven-level inverter

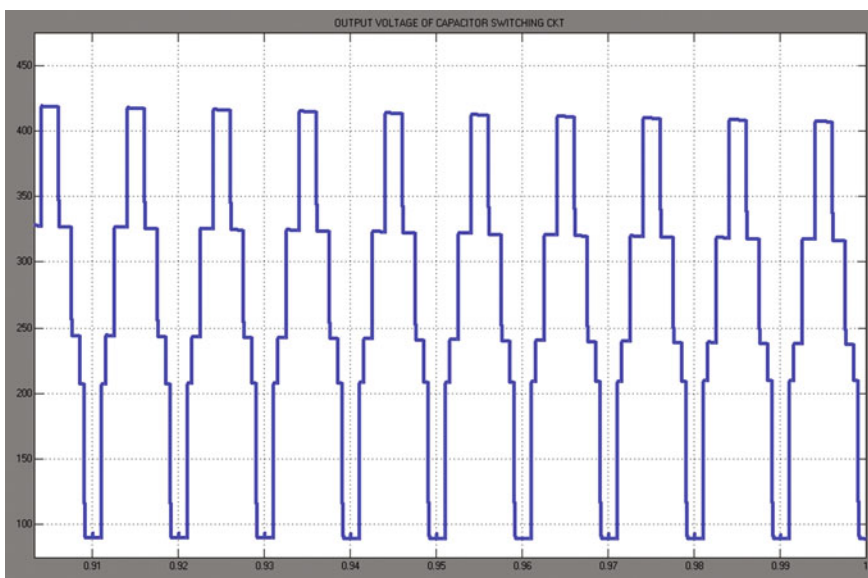


Fig. 3 Output voltage of capacitor switching circuit

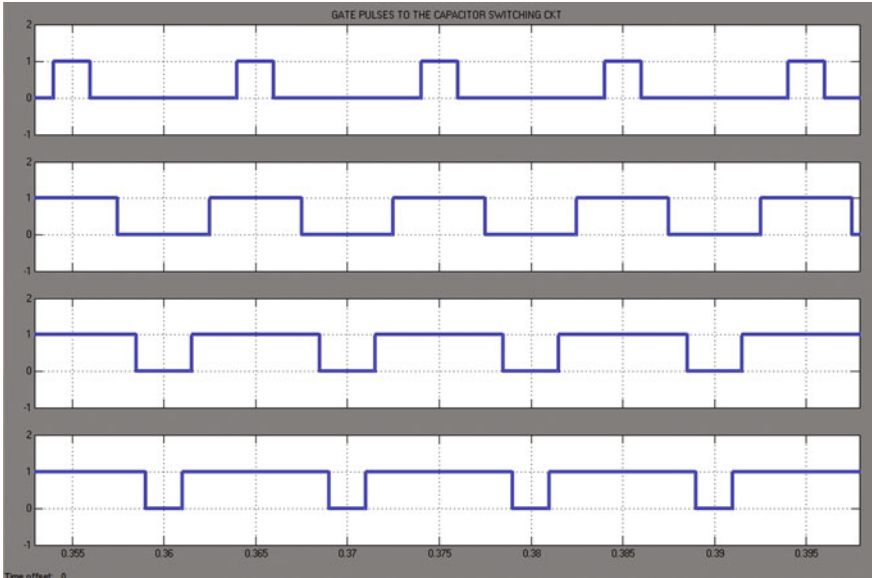


Fig. 4 Pulse signal given to switches in the capacitor selection circuit

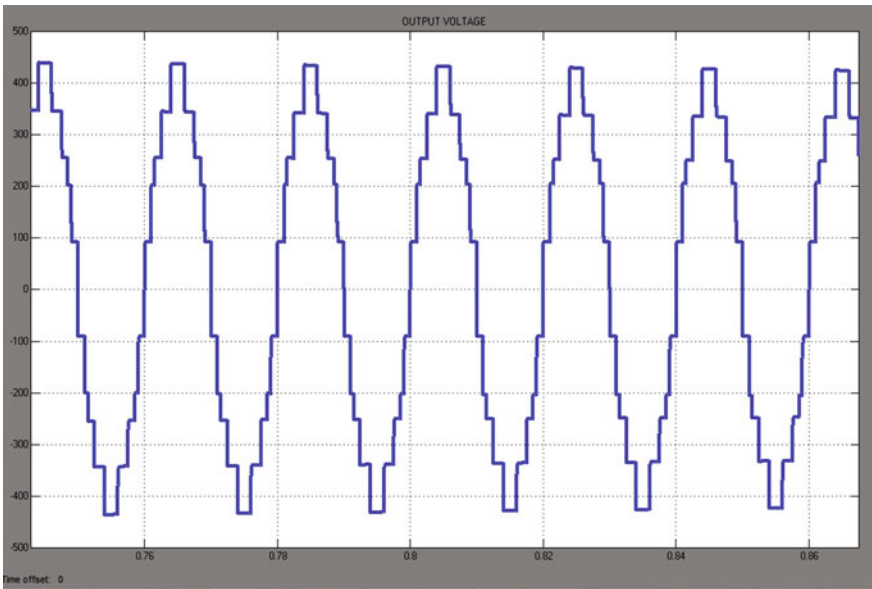


Fig. 5 Eleven-level AC output voltage

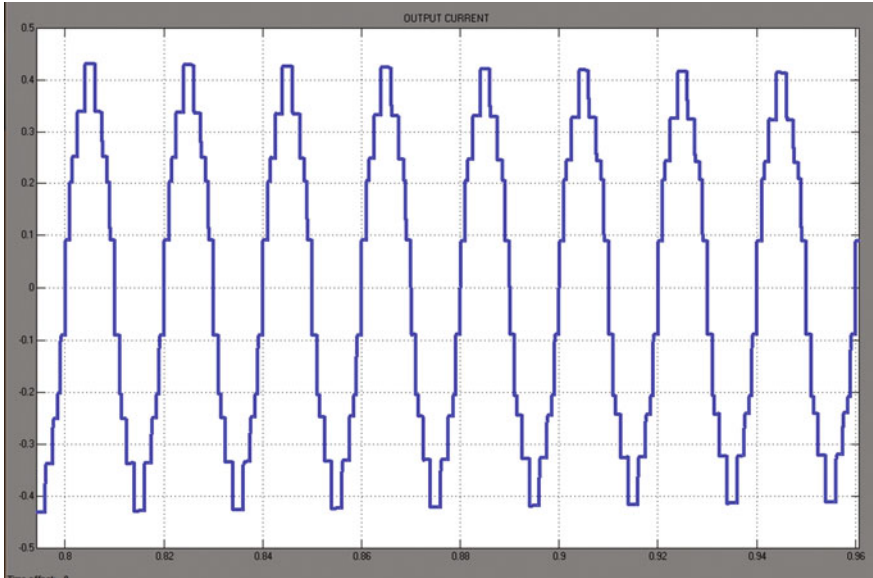


Fig. 6 Eleven-level AC output current

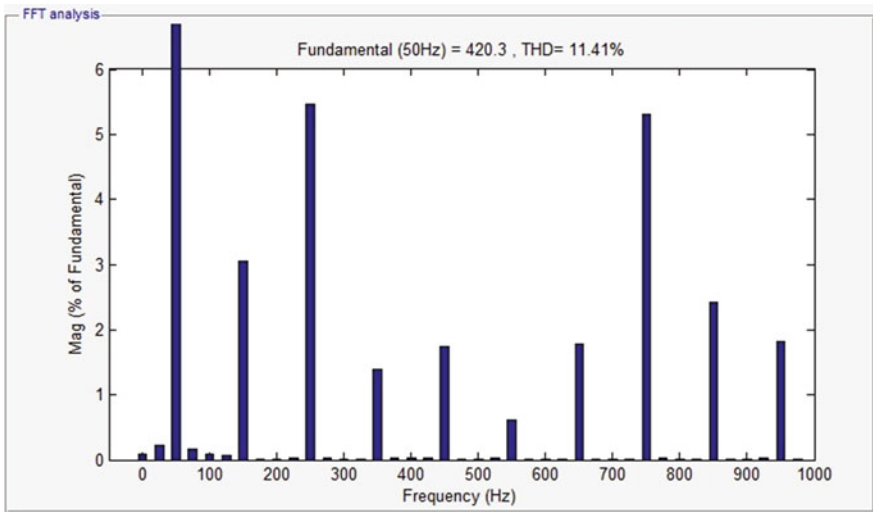


Fig. 7 THD of eleven-level inverter

Table 2 THD in three multi-level inverters

Multi-level inverters	THD (%)
Seven-level inverter	20.08
Nine-level inverter	13.91
Eleven-level inverter	11.41

4 Conclusion

This paper proposed a photo-voltaic (PV)-fed eleven-level capacitor switching multi-level inverter. Total harmonic distortion (THD) present in this inverter is only 11%, it produced a nearly sinusoidal waveform, and power produced from this inverter is in-phase with the utility power, and thus, grid integration was not critical. By comparing this in three multi-level inverters, eleven-level inverter has low harmonic distortion. This multi-level inverter (MLI) produces two extra levels while adding a switch and a capacitor in the existing circuit, so number of power electronic switches required for higher levels are very low. Only eight transistor switches are required to generate eleven-level output voltage and current, compared with conventional multi-level inverters which require more than double the times switches required in this MLI. Thus, efficiency of the system is improved, and circuit complexity and switching losses also reduced.

Acknowledgements Authors remit their graduate to DST-TSDP (No. DST/TSG/WM/2015/557/G) Government of India for financial assistance.

References

1. Miracle, D.M., Pouresmaeil, E., Bellmunt, O.G.: The control scheme of 3-level Neutral point clamped inverter for integration of inexhaustible energy resources into Alternating Current (AC) grid. *IEEE Trans.* **6**(2), 242–253 (2012)
2. Akagi, H., Hasegawa, K.: Low-modulation-index operation of a 5-level diode-clamped Pulse width modulation inverter with a (direct current) DC voltage-balancing circuit for a motor drive. *IEEE Trans. Power Electron.* **27**, 3495–3505 (2012)
3. Srikanthan, Mishra, M.K.: Direct current capacitor voltage equalization in neutral clamped inverters(NPC) for Distributed STATCOM application. *Inst. Electr. Electron. Eng. Trans. Ind. Electron.* **57**, 2768–2775 (2010)
4. Chaves, M., Silva, F., Pinto, F.: Novel approach in back-to-back m-level diode clamped MLC modelling and Direct Current (DC) bus voltages balancing. *Inst. Eng. Technol. Power Electron.* **3**, 578–589 (2010)
5. Jesus, G.A., Barros, Silva, A.: Predictive optimal control of Neutral point clamped multi-level converters. *IEEE Trans. Ind. Electron.* **60**(2), 619–627 (2013)
6. Hossaini, S.H., Gharehpetien, G.B.: Double flying capacitor multi-cell power converter based on the modified phase shifted pulse width modulation (PWM). *IEEE Trans. Power Electron.* **25** (2010)
7. Thielemans, S., Ruderman, A., Reznikov, B., Melkebeek, J.: Improved natural balancing with modified phase-shifted pulse width modulation for one leg five-level flying-capacitor multi-level inverters. *IEEE Trans. Power Electron.* **27**(4), 1658–1667 (2012)

Daylight Harvesting Concepts and Its Application: A Review

Amiya Ranjan Behera, Siddhartha and Jyoti Devi

Abstract Daylight has been an integral part of building design throughout architectural history. In fact, only during the past forty to fifty years daylight has been considered the primary interior illuminant during daytime hours in almost all buildings. Starting from dawn till dusk, daylight constantly changes its intensity and color, from day to day and season to season. The design and analysis of daylighting systems present unique problems that span both architecture and engineering; daylighting decisions affect the design of the building and the design and use of various environmental control systems that are to go in it. Daylight effects different factors like, the functional arrangement of spaces, building structure, energy use by the building, visual and thermal comfort of occupant, type and use of electric light as well as associated control systems. Therefore, it can be concluded that daylight is both art and science. In other words, daylight can be considered as both design element and environmental system. The purpose of this paper is to explain the science and technology of daylighting in a manner that is useful to architects, engineers, interior designers and lighting designers.

Keywords Daylight harvesting · Illumination · Visual comfort · Energy saving Artificial lighting

1 Introduction

Daylight is being considered as the primary source of light for building with the current movement toward the more sustainable and green buildings. Daylight is being configured/integrated with the article electric lighting where and when the

A.R. Behera · Siddhartha (✉) · J. Devi
Dept. of Electrical & Electronics Engineering, Manipal Institute of Technology,
Manipal University, Manipal 576104, India
e-mail: siddhartha.mit@manipal.edu

A.R. Behera
e-mail: amiyaranjan.1990@gmail.com

daylight fails to provide sufficient interior lighting [1]. Electric lighting energy can be saved by reducing or turning off some or all the electric lighting within the daylight space or area. Two major lines of actions in daylighting control principles are passive measure and active measure [2]. Passive measure is referred as by directing the diffuse daylight into the interior of the building by improving the depth of the daylight area. Active measure is referred as the control of artificial lighting output with respect to the available daylight.

2 Importance of Daylight

Daylight is a variable source. It changes constantly with respect to color and intensity. Sometimes daylight is considered exclusively as a design esthetics. However, most of the time it is considered as a design alternative because of energy conservation and energy use in the proposed building. Each building has its own requirements, needs and constraints. They are different from building to building and are as follows [3];

- Energy conservation resulting from the use of daylight as a primary or secondary illuminant.
- Daylighting apertures can be used as fire exits in case of emergencies.
- In some cases, daylight apertures can be used as visual communication channel to the outside.
- Peak demand cost can be reduced by use of daylight.
- The quality of daylight is very good. A study by Ehrenkrantz group in 1979 has been done and observed that same task can be performed with less amount of daylight than electric light. For example, reading with daylight from a side-lighting system requires about 35% as much light as is required of a fluorescent light system.
- Daylight provides a good visual environment. A good visual environment affects a person's ability to see objects in a room properly and to perform visual tasks.
- Daylight provides an esthetic quality to space as a design element.
- Daylight adds lesser amount of heat to a building as compared to electric light. Study says, an incandescent bulb emits only 10% of the input energy as light and the rest in terms of heat. But, a fluorescent bulb emits about 20–35% of the input energy as light. Coming to daylight, it also adds heat to a building, but 55% of the thermal energy in solar radiation lies in visible spectrum.

3 Concept of Daylight

Like any other lighting system, the main concept behind the daylighting is to provide required amount of light in different places inside a building by ensuring good visual performance, constant and visual comfort. According to requirement and orientation of daylighting apertures, the daylighting concept can be grouped into different categories as follows [4].

To improve and analyze the daylighting concept, some key proportional relationships are usually taken into account. Proportional relationships between the daylighting concept and the room or space being daylighted can be grouped into three areas;

- Spatial Proportions
- Aperture Proportions
- Spatial/Aperture Proportions

Size, volume and area relationships in the room and building being daylighted are illustrated by spatial proportions. Aperture proportions illustrate lighting performance characteristics either of an entire group of daylighting concept (for example, sidelighting concept) or of a specific daylighting concept (for example sidelighting using clerestories). The relationships between the aperture and the major surface areas of the room, such as the floor, ceiling and walls are being illustrated by spatial/aperture proportions. The impact of daylight upon a building size, volume and area can be described by using two basic spatial proportions [5];

- A ratio of envelope area to floor area, $a = \frac{e}{f}$
- A ratio of volume to floor area, $b = \frac{v}{f}$

where e = total envelope area of the building

f Total floor area of the building

v Volume of the building

As the surface area of the envelope can be increased by the daylight apertures, the envelope/floor ratio ‘ a ’ is often somewhat larger for daylighted buildings than for non-daylighted buildings. Similarly, the volume/floor area ratio ‘ b ’ is sometimes larger in daylighted buildings.

3.1 Sidelighting Concept

In case of sidelighting concept, the walls of the buildings are being used as the location for daylighting apertures. These are designed to provide light that sweeps across horizontal work planes. Sidelighting concept includes view and non-view apertures; one is known as windows and another is known as clerestory apertures,

respectively [6]. The rough opening of a window without framing is known as an aperture.

The positive aspects of sidelighting concept include the strong directionality of the light and their capacity to provide primary lighting on two-dimensional horizontal surfaces. Certain sidelighting can also provide excellent lighting quality and quantity on vertical two-dimensional surfaces [7]. The main negative aspects of sidelighting are it causes glare and high contrast in the space sometimes.

The distribution pattern of a sidelighting concept mainly depends on the penetration and the latitudinal spread of daylight into the room from the aperture. Penetration is defined as the distance into the room that daylight reaches along the task plane at a predetermined level of illuminance [8]. This distance is usually measured perpendicularly to the plane of the aperture. Latitudinal spread is the distance along which a predetermined level of illuminance extends parallel to the plane of the aperture along the work plane. The term vertical spread also comes into picture in case of sidelighting. It generally describes the extension of light from the top to the bottom of a vertical surface.

The characteristics of lighting patterns are specific but different for clear and overcast sky conditions. Therefore, the above two conditions should be considered separately when analyzing the performance of sidelighting concept [9]. Overcast sky generally provides a deeper penetration of skylight into the room along with softer set of shadow pattern and sometimes additional glare than the clear sky. Alternatively, clear sky condition delivers a source of light into the room that creates a high-pitched shadow pattern; in which the smallest details can be easily highlighted. In sidelighting concept, the daylight entering a building can be divided into different components which represent light from different specific source such as the ground, the sky, exterior reflecting surface and interior reflections around the room (Fig. 1).

In sidelighting concept, the proportional relationships which describe the penetration of daylight into the space are the aperture height to sill height ratio, i.e., \bar{H} and the ceiling height to aperture height ratio, i.e., \bar{V} . The proportional relationship which is used to describe the spread of daylight in a sidelighting concept is the aperture length to aperture height ratio, i.e., \bar{M} . Mathematically (Fig. 2);

$$\bar{H} = \frac{f}{h} = \frac{\text{Total aperture height above the floor}}{\text{Height of aperture from the sill to top plane}} \quad (1)$$

$$\bar{V} = \frac{H}{h} = \frac{\text{Floor to ceiling height}}{\text{Height of the aperture from sill to top plate}} \quad (2)$$

$$\bar{M} = \frac{l}{h} = \frac{\text{Aperure length}}{\text{Height of the aperture from sill to top plate}} \quad (3)$$

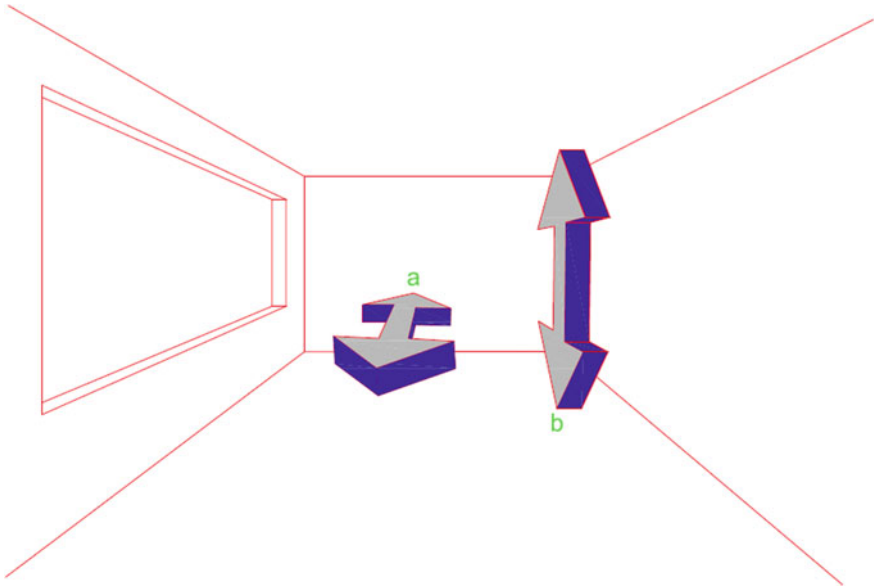


Fig. 1 Daylight spread from a vertical aperture: a latitudinal spread; b vertical spread

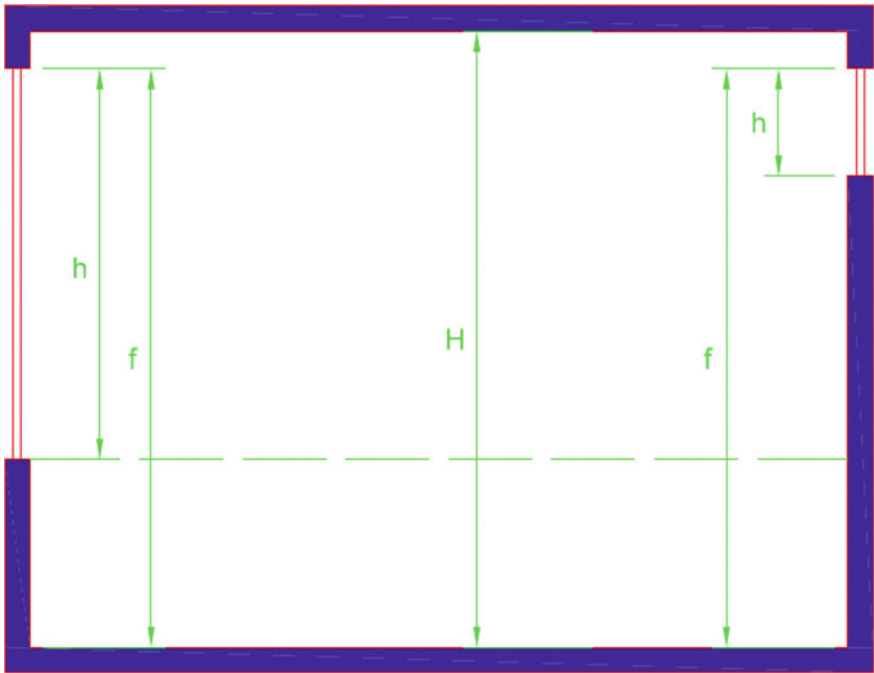


Fig. 2 Section and plan view, labeled for determining different aperture proportions

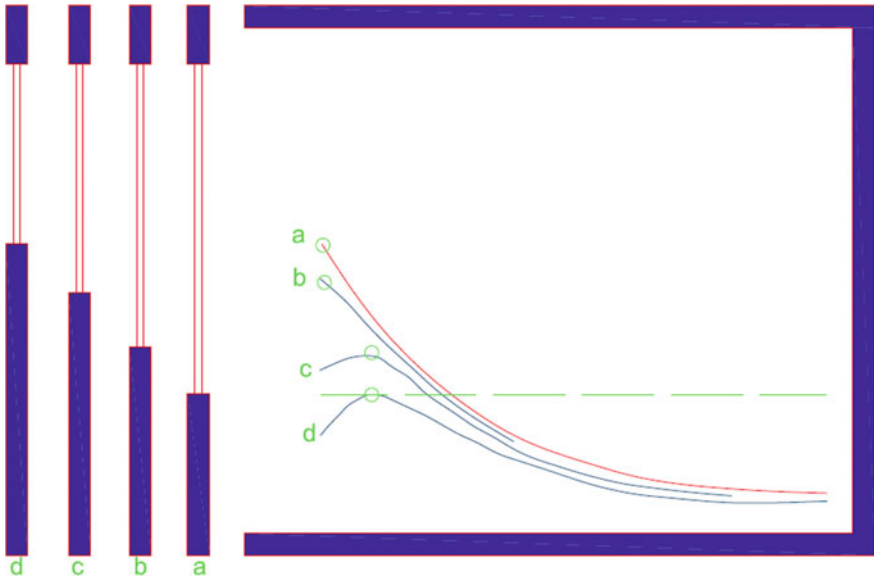


Fig. 3 Rate of change in slope for the base case room with window under overcast sky

In Fig. 3, it has been considered as $\bar{V} = 1:1$ and $\bar{M} = \infty:1$ [(a) $\bar{H} = 1.5:1$; (b) $\bar{H} = 1.6:1$; (c) $\bar{H} = 1.9:1$; (d) $\bar{H} = 2.4:1$]. From Fig. 3 we can observe that the point of maximum illuminance move away from the aperture as \bar{H} ratio increases. The point of maximum illuminance is marked by the open circle O in the figure. Therefore, the designer can move the point of maximum illuminance toward or away from the aperture in response to the lighting and design requirements of the room by increasing or decreasing the \bar{H} ratio. From the figure we can observe that lowest \bar{H} ratio provides about three times the illuminance of the case with the height \bar{H} ratio at the same observation point of in the room.

In Fig. 4, it has been considered as $\bar{H} = 1.5:1$ and $\bar{V} = 1:1$ [(a) $\bar{M} = \infty:1$; (b) $\bar{M} = 4:1$; (c) $\bar{M} = 2:1$; (d) $\bar{M} = 1:1$ (e) $0.5:1$].

From Fig. 4 we can see that by varying \bar{M} , the point of maximum illuminance remains the same in each case and the penetration decreases gradually. Also e can observe S changes as \bar{M} is varied. Where, S is the change in slope of the illuminance curve.

In Fig. 4, it has been considered as $\bar{H} = 2.4:1$ and $\bar{M} = \infty:1$ [(a) $\bar{V} = 1.5:1$; (b) $1.6:1$; (c) $\bar{V} = 2:1$; (d) $\bar{V} = 3.5:1$]. By varying the V ratio, we can observe the changes in the level of illuminance that is penetrating into the room from Fig. 5.

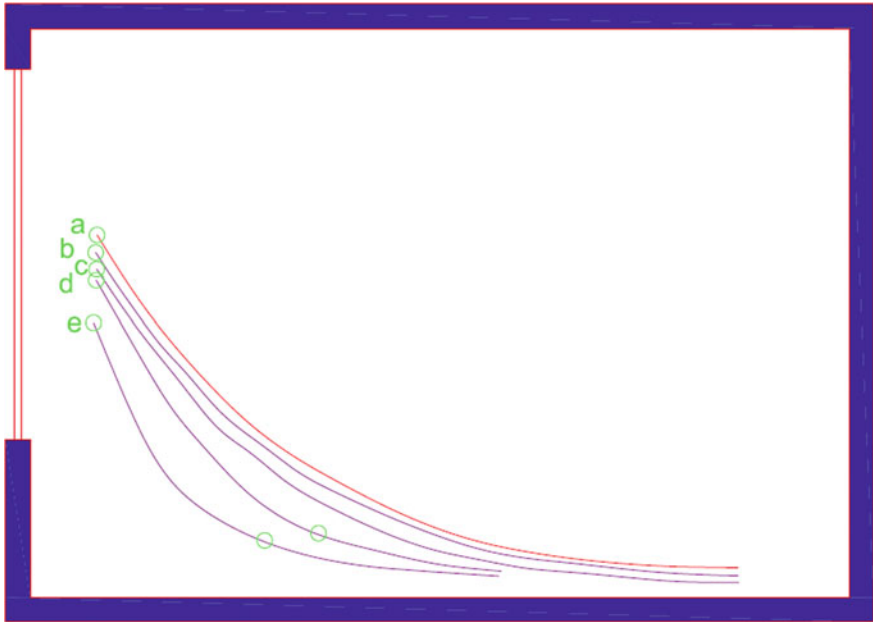


Fig. 4 Impact on penetration in the base case room with window at mentioned conditions

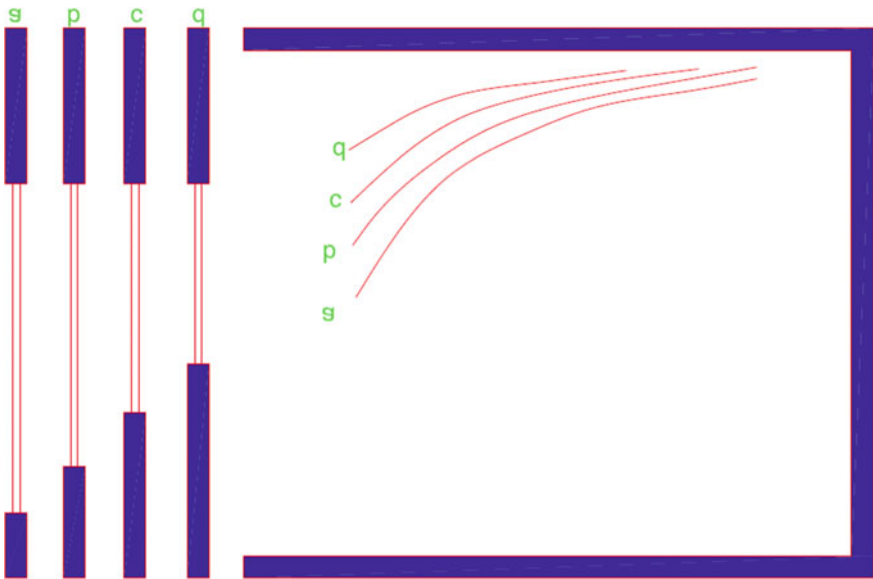


Fig. 5 Impact of illuminance in a room at mentioned conditions

3.2 *Toplighting Concept*

In case of toplighting concept, the daylight penetrates through the aperture that is positioned overhead to the ceiling line and generally includes portion of the roof of a building. As a total, there are five toplighting concepts, out of which four traditional toplighting concepts which use the clear or overcast sky to illuminate the interior and one newer concept that uses sunlight either directly or indirectly to illuminate the interiors of buildings. These concepts are [10];

- (a) Horizontal lights and light wells
- (b) Angled roof lights
- (c) Sawtooth lights
- (d) Monitor lights
- (e) Direct and Indirect beam lighting

A moderately even level of illuminance through a space is provided by horizontal lights, such as skylights. It allows for the practice of both skylight and sunlight as interior illuminants. Skylights are most frequently used to illuminate horizontal work planes, such as desk tops, drafting boards or work benches, and they are more efficient when accustomed to deliver wide-ranging illuminance or to illuminate three-dimensional display. Light wells are opening in the ceiling or floor of a room that allow daylight to penetrate to the floor below [11]. Sawtooth lights have vertical or angled apertures that work in conjunction with a sloped ceiling surface to help direct daylight into a room. A series of sawtooth apertures look like the teeth of a handsaw. An even illuminance throughout a space with less variation in brightness pattern can be generated with help of a regular sawtooth light aperture [12].

Monitor lights have conventionally been used in industrial applications where a central high bay area and part of the neighboring low bay areas. Both sawtooth and monitor apertures are typically used to illuminate horizontal and vertical task surfaces, to provide general lighting, and to illuminate three-dimensional objects [13]. Daylighting concepts that allow the direct component of daylight into a building are called direct or indirect beam concepts. Direct beam concepts use sunlight as an interior illuminant without attempting to control or distribute it. Indirect daylighting is the use of daylight to illuminate a room that does not have a direct view of the sky. Indirect daylighting is often used in areas where maintaining a specific level of illuminance is not critical [14]. The three types of indirect daylighting concepts are [15];

- Ceiling Washers
- Wall Washers
- Floor Washers

Toplighting concept is the easiest daylighting technique that can be integrated with electric lights as the light enters the space from the ceiling of the room in both cases. The main positive characteristics of toplighting are the evenness of light

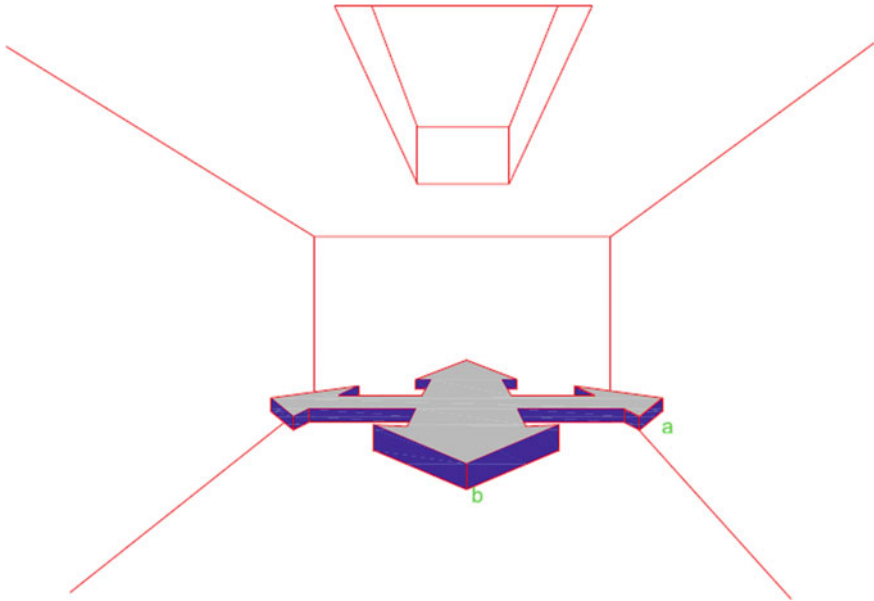


Fig. 6 Spread from toplighting concepts: **a** latitudinal spread; **b** longitudinal spread

dispersed throughout the space and the span of the area light able to the same illuminance level. The main negative characteristics of to-lighting are that many of the perceptions are limited to small or low-rise buildings [16].

In toplighting, penetration is often considerably less important than it is in sidelighting as in most of the cases; the space between the floor and ceiling is well in the ideal penetration range of 8–20 ft. In addition to this, toplighting apertures generally have a view of a larger portion of the sky dome, and thus the available exterior illuminance is often much greater than in sidelighting concepts [17]. In toplighting concepts, longitudinal spread is used to describe the distribution of daylight along the length of the aperture (same as sidelighting), while latitudinal spread describes the distribution of daylight normal to the primary apertures. Vertical spread is used to describe light distribution on vertical surfaces. Refer Fig. 6.

4 Horizontal Aperture Concept

Two of the aperture proportions used to describe sidelighting concepts are also used to describe toplighting concepts: the ceiling height to aperture height ratio (H) and the aperture length to aperture height ratio (M). In addition to M ratio, horizontal

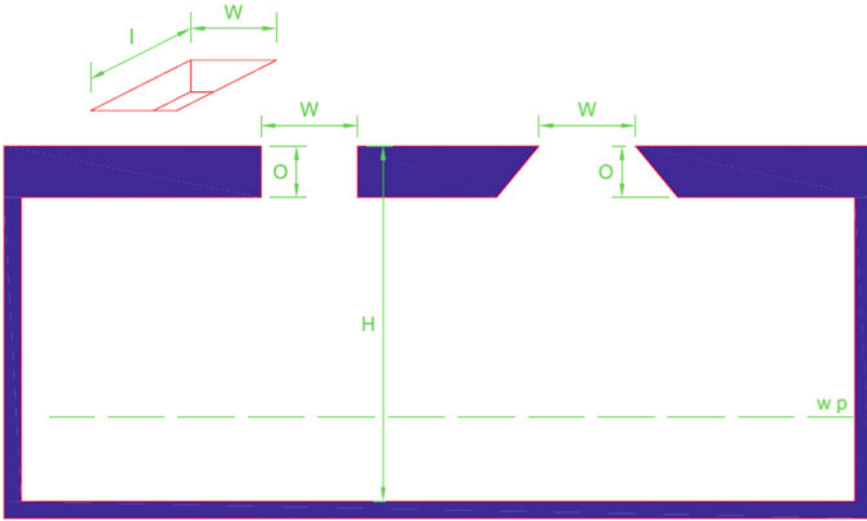


Fig. 7 Variables used to describe a horizontal aperture

aperture can be described in terms of the aperture height above the floor (H) to the width of the aperture (w). Mathematically;

$$\bar{N} = \frac{H}{W} \quad (4)$$

The height of the well (light-well) through which the daylight must penetrate can have a significant impact upon the distribution and quantity of natural light in the room [18]. The proportional relationship between the top-to-bottom height of the well (O) and the height of the bottom of aperture above the floor (H), called the O ratio, is described as (Fig. 7):

$$\bar{O} = \frac{H}{O} \quad (5)$$

The first parametric analysis is of the impact of varying \bar{N} , including determining the resulting change in the interior distribution pattern. If the floor-to-ceiling height is found and the width of the aperture is varied such that $\bar{N} = 2 : 1, 1:1, 0.5:1$ and $0.25:1$, the effect of interior distribution is to reduce the maximum illuminance in comparison with the case and to flatten the slope of the curve significantly. Refer Fig. 8.

From the above figure and analysis we can conclude that several small apertures spaced at fairly short intervals provide better, more even light distribution than large aperture spaced for apart. One of the advantages concepts is that the former can provide more even illuminance throughout a room or building.

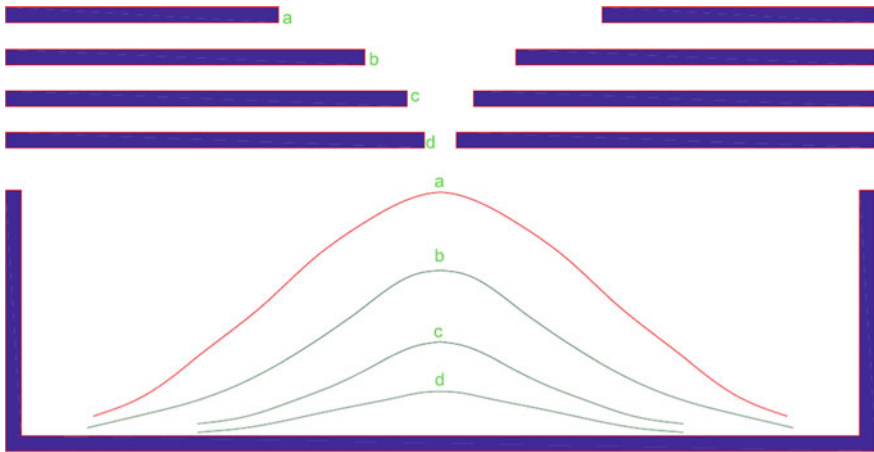


Fig. 8 Impact on illuminance in a room with horizontal aperture

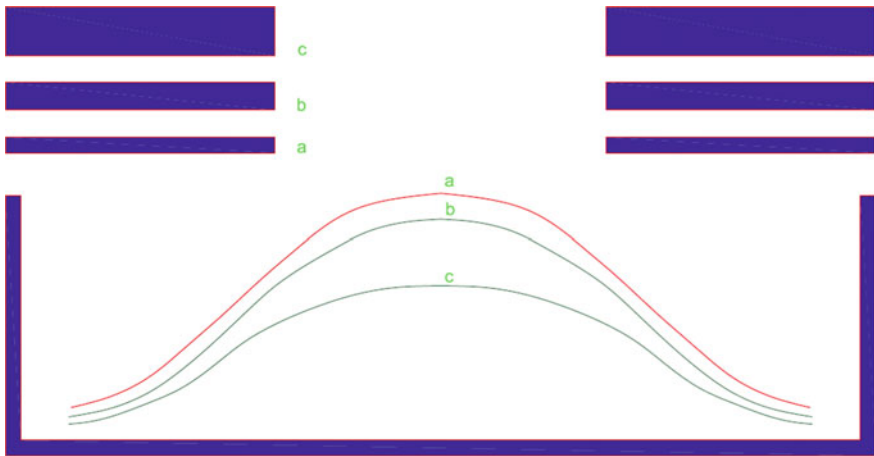


Fig. 9 Impact of illuminance in a room with horizontal aperture at different \bar{O} ratio

One of the most significant factors affecting daylight distribution from horizontal lights is the depth and slope of the light-well. The reduction in daylight because of the light-well is shown in Fig. 9. The \bar{O} ratio is varied from 16:1 to 4:1. We can observe from the figure that as the height of the well increases, the view of the sky is progressively reduced, especially for station points not directly under the aperture, and so is the daylight entering the room.

By varying the slope of the well distributes the daylight more evenly on an overcast day and flattens out the slope of the distribution curve [19]. On a clear day with sun, the change in slope has an even greater impact on the distribution of light

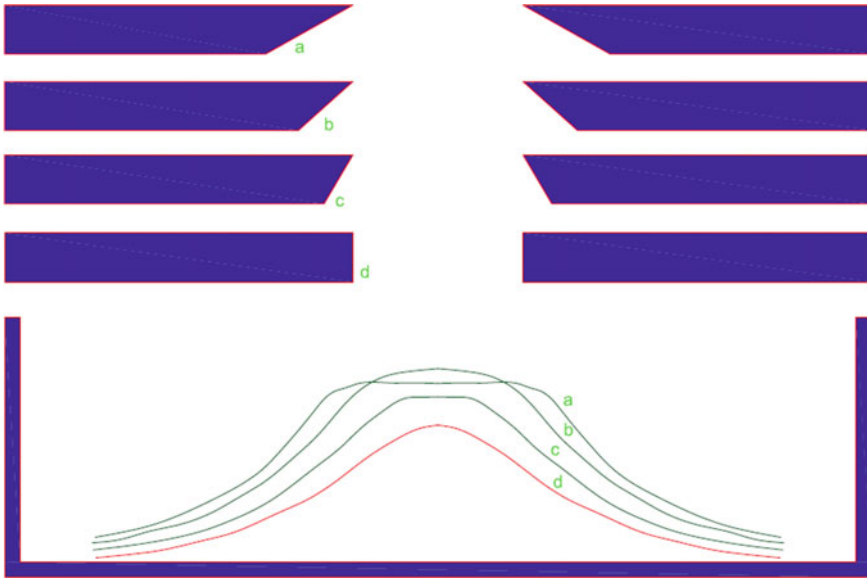


Fig. 10 Impact of illuminance in a room with horizontal aperture at different slope

in the space. The distribution of lights for different slopes of well [(a) 30° slope; (b) 45° slope; (c) 60° slope; (d) 90° slope] is illustrated in Fig. 10.

5 Angled Aperture Concept

Sometimes we need different illuminance level on either side of the point of maximum illuminance [20]. In this type of situation we need to use angled aperture. For angled aperture along with M ratio, one more ratio, i.e., \bar{G} , is used to describe the ratio of the distance from the floor to the mid-height of the aperture (G) to the width of the aperture (w). Mathematically,

$$\bar{G} = \frac{G}{w} \tag{6}$$

Angled aperture can also be used to illuminate vertical surface. The \bar{Q} ratio is described as (Fig. 11);

$$\bar{Q} = \frac{Q}{G} \tag{7}$$

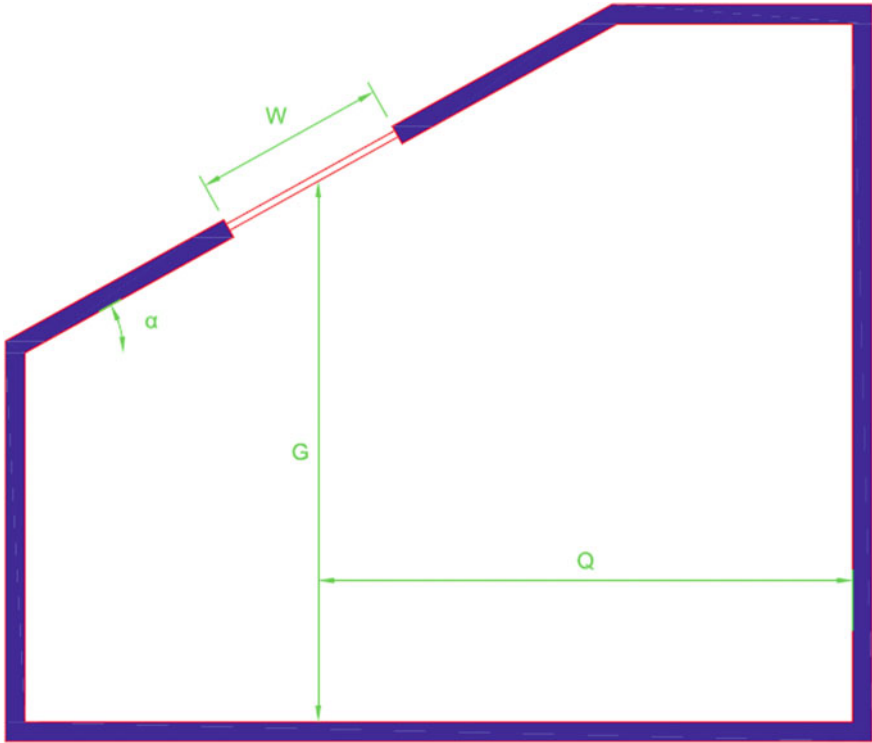


Fig. 11 Nomenclature used to describe an angled aperture

In this type of aperture, if the light-well height (top to bottom) is increased then the maximum illuminance and penetration will decrease. But increasing light-well slope increased the spread along the same axis and decreases the maximum illuminance.

6 Sawtooth Aperture Concept

Following are the some important characteristics to recognize the distribution pattern of a series sawtooth aperture [21].

- The distribution pattern of a single aperture is different than for a series of aperture.
- The end conditions are different, i.e., the daylight below the first aperture in series is significantly different from that under the last aperture in the series.

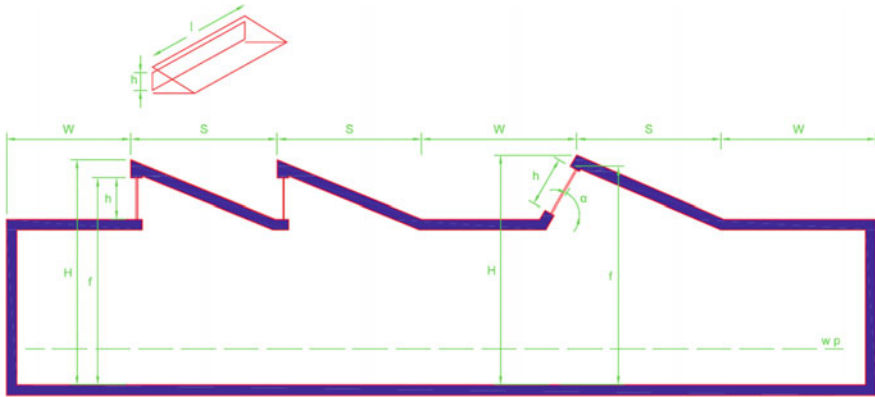


Fig. 12 Nomenclature used to describe a sawtooth aperture

- The pattern of illuminance is different in shape depending upon sky type.
- The characteristics pattern of light from a sawtooth cannot be established with fewer than three apertures in series.
- The location of the point of maximum illuminance for a series of sawtooth aperture under a clear sky is about two-thirds the distance from the plane of the aperture to the end of the sloped roof portion of the aperture.
- The point of minimum illuminance from the previous aperture is about one-third the distance from the aperture to the end of the sloped roof.
- The location of the maximum and minimum illuminance points varies with the orientation of the aperture to the sun (Fig. 12).

7 Monitor Aperture Concepts

Light distribution under a series of monitors is almost similar to that under one monitor. The point of peak distribution varies with sky types. Under an overcast sky, the point of peak illumination becomes a plane of peak illumination and similarly the point of minimum illuminance extends over a plane [22]. Under an overcast sky, the illuminance from each light is very similar to the distribution pattern from a sawtooth light, except that the light spreads an equal distance in both directions. Refer Fig. 13.

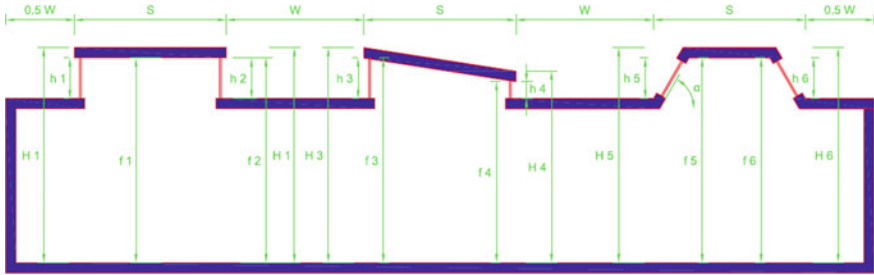


Fig. 13 Nomenclature used for a room with a monitor aperture

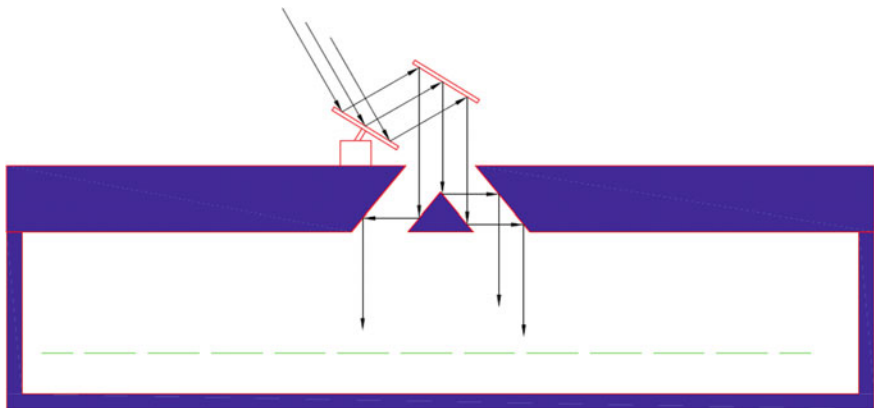


Fig. 14 One type of beam lighting concept (Heliostat)

8 Beam Lighting Concepts

Heliostats used for daylighting building interiors by reflecting the direct component of the visible spectrum into the building. Heliostats use the beam or direct component of sunlight instead of the diffuse sky as an interior illuminant [23]. This system uses a two-mirror combination to reflect sunlight into the building. The primary mirror tracks the sun and reflects the image of the solar disk to the secondary mirror. The secondary mirror is fixed in position, and it reflects the sunlight from the primary mirror into the building. In case of clear sky, the amount of illuminance in a room is directly proportional to the size of the primary and secondary reflectors [24]. Refer Fig. 14.

9 Conclusion

Daylight in interior offers a consideration contribution in building level energy saving. This paper gives review on the fundamental design approach to use a natural daylight strategy. Efficient utilization of daylighting can save artificial lighting energy. By following the discussed concepts during the building design process, the design team can begin to establish a method that includes daylighting design and analysis as part of the process. The method presented herein is simply an overview of some out of the many steps necessary to include daylighting in a building. Each designer and each member of the design team will have to develop an individualized, workable design process that allows for consideration of daylighting in each building project.

References

1. Ayaz, R., Nakir, I., Akca, H., Ajder, A., Tanrioven, M.: A new approach for relationship between daylight and indoor illumination level. In: 2014 International Conference on Renewable Energy Research Application, no. 3, pp. 833–836 (2014)
2. Campo, P.: Energy Saving by Compensation of Daylight Deficiencies in Buildings, pp. 2–5 (2010)
3. Robbins, C.L.: Daylighting Design & Analysis. Van Nostrand Reinhold Company (1986)
4. Schapire, A.B., Haar, A., Haar, A.H., Boost, F.: “: r I,” no. d, pp. 30–33 (2014)
5. Haq, M.A.U., Hassan, M.Y., Abdullah, H., Rahman, H.A., Abdullah, M.P., Hussin, F.: A method for evaluating energy saving potential in lighting from daylight utilization. In: 2014 IEEE International Power Energy Conference, pp. 177–181 (2014)
6. Matta, S., Mahmud, S.M.: An intelligent light control system for power saving. In: IECON 2010—36th Annual Conference of the IEEE Industrial Electronics Society, pp. 3316–3321 (2010)
7. Parise, G., Martirano, L., Member, S.: Combined electric light and daylight systems ecodesign. *IEEE Trans. Ind. Appl.* **49**(3), 1062–1070 (2013)
8. Parise, G., Martirano, L., Member, S.: Daylight impact on energy performance of internal lighting. *Ind. Appl. IEEE Trans.* **49**(1), 242–249 (2013)
9. Wang, L., Member, S., Lin, W., Lee, W.: Energy saving of green buildings using natural daylight. *Electr. Eng.*, 1–7 (2009)
10. The Institute for Market Transformation to Sustainability: ANSI Whole Systems Integrated Process Guide, [cited 28 September 2012]. Available from: www.delvingdeeper.org/pdfs/wsip.pdf (2007)
11. Whole Building Design Guide: Engage the Integrated Design Process, [cited 28 September 2012]. Available from: www.wbdg.org/design/engage_process.php (2012)
12. Whole Building Design Guide: Whole Building Design, [cited 28 September 2012]. Available from: www.wbdg.org/wbdg_approach.php (2012)
13. Whole Building Design Guide: Planning and Conducting Integrated Design Charettes, [cited 28 September 2012]. Available from: www.wbdg.org/resources/charrettes.php?r=engage_process (2012)
14. Whole Building Design Guide: Daylighting, [cited 28 September 2012]. Available from: www.wbdg.org/resources/daylighting.php (2012)
15. Bodart, M., Deneyer, A., De Herde., Wouters, A.: P. A Guide for Building Daylight Scale Models, University of Louvain: Louvain-du-Neuve, Belgium (2006)

16. Moore, F.: Concepts and Practice of Architectural Daylighting. Wiley, New York City, NY (1991)
17. Ander, G.D.: Daylighting Performance and Design. Wiley, New York City, NY (2003)
18. Baker, N., Steemers, K.: Daylight Design of Buildings: A Handbook for Architects and Engineers. Routledge, London (2002)
19. International Energy Agency (IEA): Daylight in Buildings: A Source Book on Daylighting Systems and Components, [cited 28 September 2012]. Available from: <http://archive.iea-shc.org/publications/downloads/8-8-1%20Application%20Guide.pdf>
20. Advanced Buildings: Daylighting Pattern Guide, [cited 28 September 2012]. Available from: <http://patternguide.advancedbuildings.net/>
21. Advanced Lighting Guidelines: Daylighting, [cited 28 September 2012]. Available from: www.algonline.org/index.php?daylighting-strategies
22. Illuminating Engineering Society (of North America): The Lighting Handbook, Illuminating Engineering Society, New York City, NY (2011)
23. Lawrence Berkeley National Laboratory: Lighting Research Group, [cited 28 September 2012]. Available from: <http://lighting.lbl.gov>
24. Rensselaer Polytechnic Institute: Lighting Research Center, [cited 28 September 2012]. Available from: www.lrc.rpi.edu

Smart Switching Algorithm Between IC and PO Algorithms for Grid-Connected PV System

A. Ambikapathy, Gajendra Singh and Prabhakar Tiwari

Abstract As we know that n number of methods are available to increase the output power to the level of maximum power from the PV cells, but among all of those methods there are two methods which are majority in use which are P and O method and IC methods, in this paper we have analysed each method under less step size and more step size vice versa. As the result says that the IC method tracks the maximum power point efficiently within short span of time with reduced ripples when its step size is less, in the same way the P and O method is able track the maximum level of power more efficiently within short span of time with reduced ripples when its step size is more. Hence, in this paper we have developed a new algorithm which can smartly switch over the technology between P and O and IC methods according to the step size which is demanded by the system so as to improve the efficiency, cut the ripples and improve the power quality when the output power generated from PV is connected to the utility grid. The output from this technique is utilized to change the width of the pulse of Zeta (DC–DC) converter which converts the variable DC to fixed DC to make the output compatible to inverter circuit which is compatible to connect it directly to the commercial grid.

Keywords Smart switching algorithm · Commercial grid · Prediction control Efficiency · Reliable · Power quality

A. Ambikapathy (✉)
Department of Electrical & Electronics Engineering, Galgotias College
of Engineering & Technology, Greater Noida, India
e-mail: jesus.ami.phd@gmail.com

G. Singh · P. Tiwari
Sharada University, Greater Noida, India
e-mail: gajendra.singh3@sharda.ac.in

P. Tiwari
e-mail: profptiwari@gmail.com

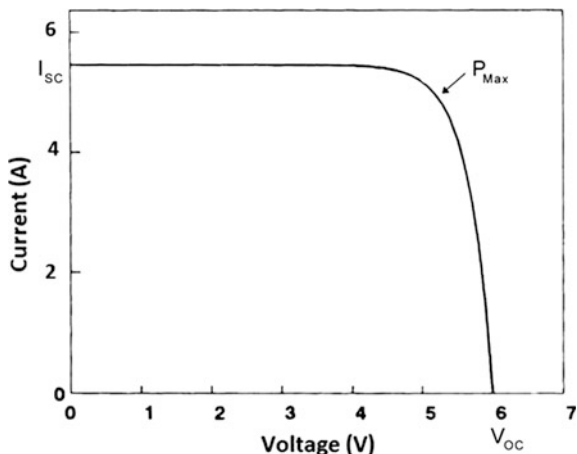
1 Introduction

The unavailability of nonrenewable sources in long run and its side effects which produce the global warming encourage the humans to use renewable sources to adopt green energy and clean environment. Not only the unavailability issues are there but also the different types of losses which are occurred in the power system network which makes the system with very less efficiency. Hence, the generation should be twice as the demand so as to satisfy the losses. Therefore, the renewable energy generation has become more popular because it has numerous advantages as it does not require fuel and it does not require maintenance and it has many environmental benefits. But it has some disadvantages as when it is processed, the conversion efficiency is very less. The solar energy is the major source of renewable energy source among all the renewable energy sources, which can generate electricity throughout the day. But storing the energy is the biggest problem. Hence, the best solution will be connecting the output of PV to the utility grid. As the grid needs the constant voltage and frequency, the output of PV has to be maintained constant before it is inverted using inverter [1–6]. As we know that the irradiance of the sun is not stable throughout the day, therefore there is always fluctuation at the end of PV system and it becomes very tedious to connect it to the utility grid. To achieve the greatest efficiency and to avoid fluctuation of output of PV arrays, the tracking of largest power is important; hence, there is a necessity for maximum power point (MPP) technique. This MPPT system helps and ensures the greatest output point is taken or generated from PV. So the purpose of maximum power point tracking is to control the output of PV with automatic technology algorithms which are adjusted and ensure the maximum output according to suitability of the utility grid system [7–10]. Several techniques, algorithms and methods are available to achieve maximum power, and among all only two methods yield the best result and they are incremental conductance method (IC) and perturb and observe method (P and O) [11–14]. Therefore, this paper is first going to analyse the performance of P and O method and IC method in different situation such as less step size and broad step size. After finding the method gives best output with less step size and which method is giving best result with more step size the new prediction algorithm is created switch between P and O method and IC method according to the requirement needed by the step size of PWM circuit.

2 Introduction to MPPT Technique

The magnitude of the output of PV module in terms of power is proportional to the operating voltage of the PV cell and its maximum power point (MPP). Not only it had the above said quantities, it also depends on solar irradiance. Generally the

Fig. 1 Characteristics of PV panel under operating condition with MPP mentioned



characteristics of PV array are nonlinear, and in right side of the curve it has a maximum point at which the photovoltaic operates at its maximum possible high efficiency. As we know that the product of current and voltage is power, MPP is obtained by multiplying the voltage corresponding to maximum power (V_{MPP}) and current corresponding to maximum power (I_{MPP}) which can be written in general equation and which is given in Eq. (1) [15].

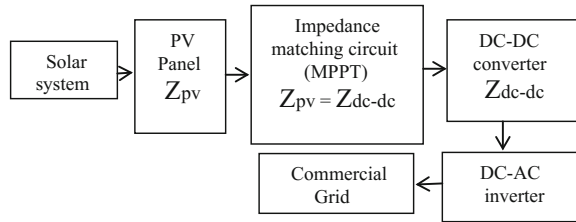
$$I = Ish - I_o \left(e^{q \left(\frac{V + IR_s}{K_n T} \right)} - 1 \right) - \frac{V + IR_s}{Rsh} \quad (1)$$

The point where the maximum power, voltage and current are obtained is represented in Fig. 1 which is obtained by observing the operational characteristics of PV array. The working of these algorithms is exactly same as the theorem called maximum power transfer, i.e. the load may receive maximum power only when the impedances of internal source and load are equal. This matching of impedances achieved by different methods of MPPT algorithm techniques as we discussed in the introduction there are different methods are used to achieve this task such as incremental conductance method (IC) and perturb and observe method [16].

$$Z_{Source} = Z_{Load} \quad (2)$$

The algorithm of MPPT is same as maximum power transfer theorem, i.e. impedance matching network which interfaces the impedances of PV and DC-DC converter. Hence match the impedances of source and load. The representation of this technique is clearly explained in Fig. 2.

Fig. 2 Block diagram showing the concept of MPPT algorithm



2.1 Perturb and Observe Method

The P&O algorithm technique is very unique the output always does not depend on different environmental conditions. It calculates the output values of voltage, current and power of PV array automatically and corrects the value of width of the pulse (duty cycle) according to the requirement of maximum power point. This process is repeated even after the perturb action, and the output is further calculated and result is being compared to ensure whether the duty cycle width has been adjusted according to the efficiency and reliability. Once it is being observed that duty cycle was increased, then the same action is carried out; otherwise, the action can be reversed to get the desired output [17].

The perturbation is kept in the same direction if it found that there is a slight increment in the power. In opposite to the first case, if the power start decreases, then immediately perturb action is changed to other direction. These are the two basic requirement facts in which the algorithm is implemented [18]. This variation of process is continued to repeat until the attempt is success to reach the point of

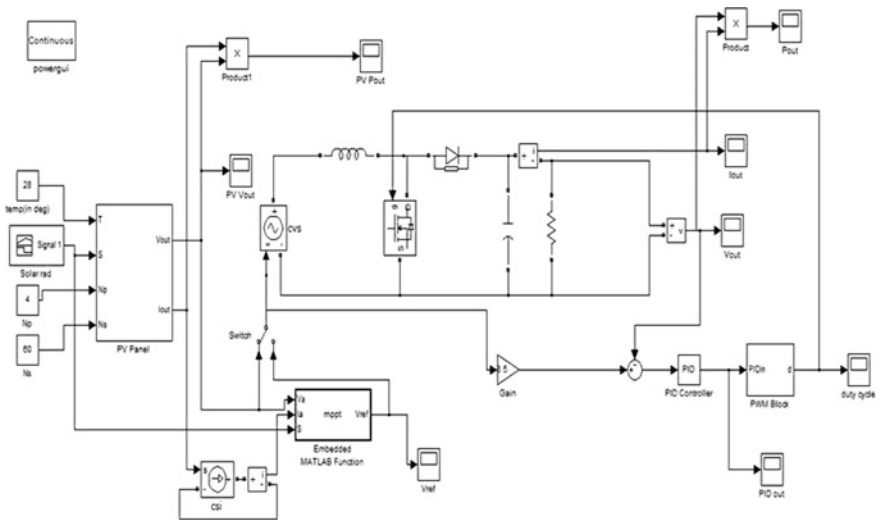


Fig. 3 SIMULINK model of MPPT algorithm using P and O method

MPP. The most important drawback of this method is that the output is not steady as the perturbations are fixed, and hence, the operating point keep oscillates around the greatest power point region instead of settling at one point which makes the system to move towards the unstable region. It is also having one more drawback that the tracking is slow and less efficient when the irradiance get changed within short span (fast changing condition of irradiance) of solar irradiance. From Fig. 3, it is understood that the maximum point is fixed, and till the point is being shifted to the desired point, the process will be repeated to achieve the desired (maximum) point by changing width of the duty cycle of the DC–DC Zeta converter [19].

3 Incremental and Conductance Method

As the first method is having some disadvantages, this method has been adopted to resolve the problem created by the previous model and this method is capable of identifying whether the maximum power point has been reached or not and also it decides when the action of shifting has to be done within the maximum operating point. This method operates by the principal of dI/dV and $-I/V$ characteristics. The MPPT has to be in right side of the MPP if the value of dP/dV is negative, and it should be in left of the MPP when the value is positive; when it is then these values are fed to the algorithm for the correct decision. This method can track even when the irradiance is keep on oscillating between increasing and decreasing nature rapidly with better accuracy than P&O method. The incremental conductance value for every environmental condition is obtained by comparing the value of conductance at any instant with the standard conductance (predefined), and hence, the duty cycle is adjusted according to the requirement [20]. Equations (3)–(5) show the relation and fundamental working of incremental conductance method how does it work, etc.

$$\text{The value of } I/V \text{ is negative at MPP which is equal to } \Delta I/\Delta V \quad (3)$$

$$\text{The value of } I/V \text{ is negative at left which is less than } \Delta I/\Delta V \quad (4)$$

$$\text{The value of } I/V \text{ is negative at right which is greater than } \Delta I/\Delta V \quad (5)$$

The output of duty cycle of MPPT is adjusted and improved according to the width of the pulse. As the duty cycle has been changed according to the requirements, now the output of the converter may directly converted into AC using inverter so that the output may have suitability to connect it to the utility grid [21]. The simulation realization of INC method is given in Fig. 4.

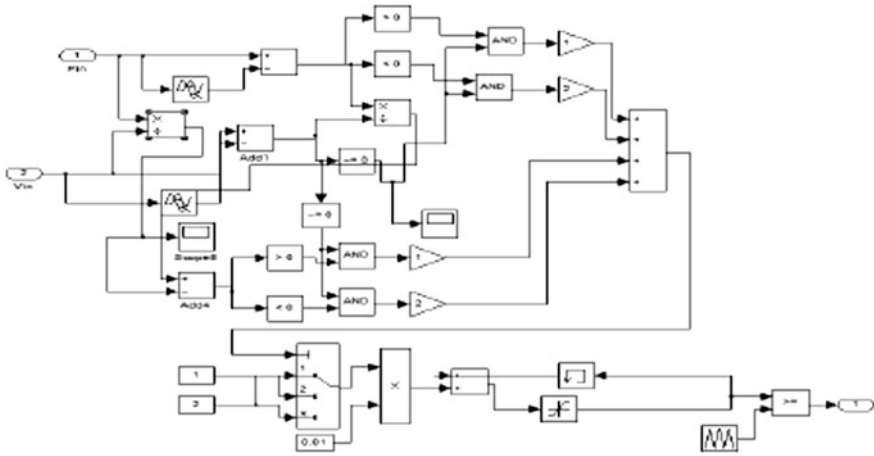


Fig. 4 SIMULINK model of MPPT algorithm using IC method

4 Result Comparison with Smaller and Larger Step Sizes

When we compare the output power curve of P&O and INC methods at smaller step size (duty cycle), we can see from Fig. 5 the P&O method tracks the greatest power point quickly as compared to the INC method, and the ripple content in both the cases is same as shown in Fig. 5.

At larger step size (duty cycle), it is shown in Fig. 6 that the P&O method is failed to track maximum power at all, whereas IC method is easily able to track the required point. However, the ripple increases in case of INC method. From the result of simulation graph of both the methods, it is clear that INC method

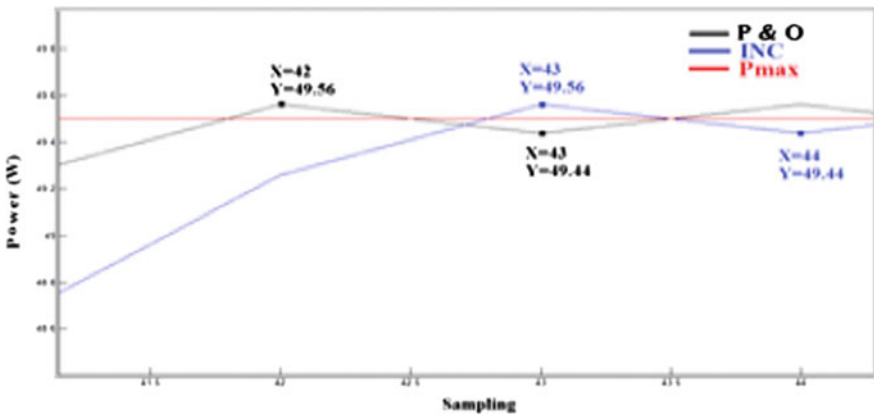


Fig. 5 Simulation result with small step of INC and P&O methods

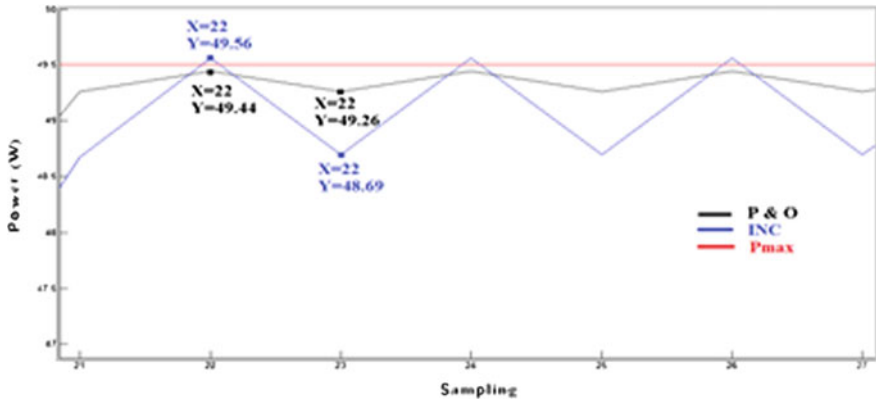


Fig. 6 Simulation result with large step of INC and P&O methods

performance is better when the duty cycle step size is large and P&O method performance is not better when the duty cycle step size is large, but it is better for smaller size of step size. Hence, we introduce a new technology called prediction control technique which can smartly switch the different MPPT algorithm according to the step size which is being decided by the atmospheric conditions of the solar irradiance. Let us see the simulation result of both the methods of P&O and INC individually.

5 Proposed Prediction Control to Switch Between P&O

5.1 Proposed Prediction Control Method to Switch Between P&O Method and IC Method

As we know that the both the methods of algorithms are tracking efficiently in different situations, we need to design a new algorithm which can switch between two different algorithms as per the efficient level of the particular situation. For implementing this technique, we need to follow the following steps

- Design identifier to predict all possible switching actions performed by power electronics devices using its duty cycle.
- Model the identifier using discrete time and state space analysis.
- Calculate the step size for which MPPT is going to work.
- Design new algorithm to provide control scheme.

Figure 7 shows the technique that how it switches between the two different algorithms according to the step size of the pattern of the solar irradiance is demanding according to the climatic conditions (Fig. 8).

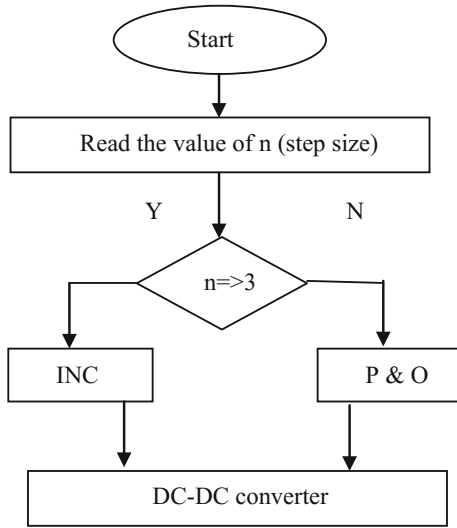


Fig. 7 Flowchart algorithm of smart switching between INC and P&O methods

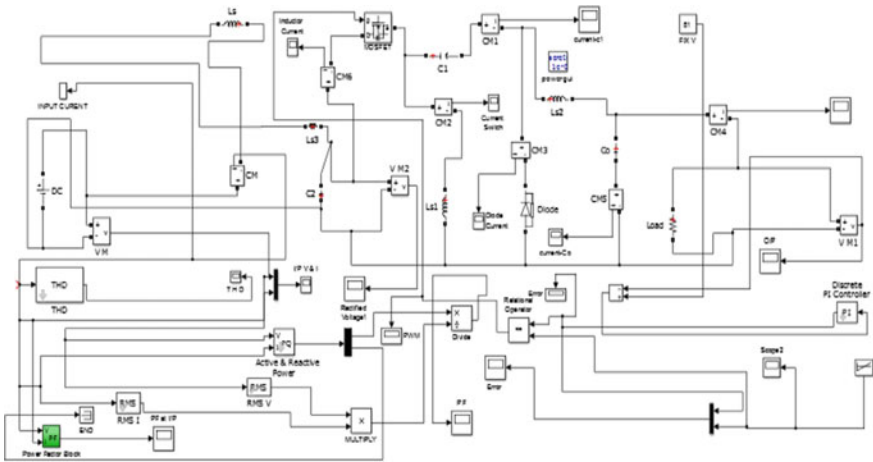


Fig. 8 Simulation realization of MPPT with new proposed technology

6 Simulation Execution and Its Results of Proposed Method

6.1 Comparative Result

As we can see from Figs. 5, 6 and 9, it is clear that the maximum point line (red line) is being tracked by both INC and P&O method in different step size scenarios.

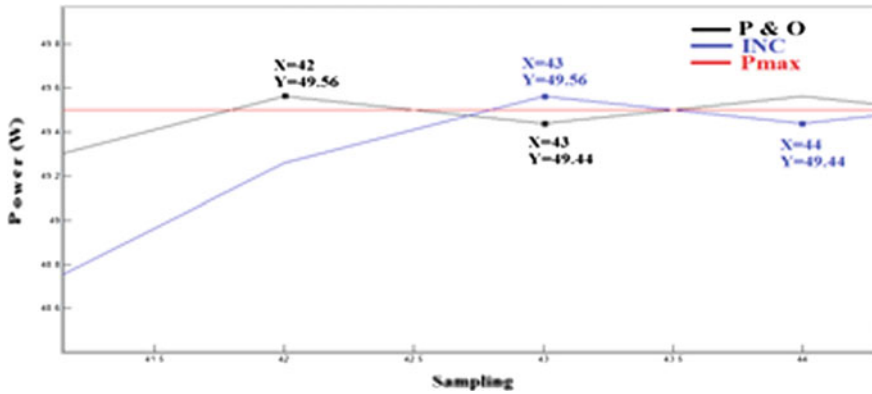


Fig. 9 Simulation result of proposed system

The new algorithm which is proposed can smartly switch to different algorithm (either INC or P&O) which is demanded by the desired output.

7 Conclusion

Here one of the critical requirements of photovoltaic system is presented, i.e. ensuring the efficiency and reliability of commercial grid-connected PV system under both smaller step size of the duty cycle and larger size of the duty cycle as the environmental conditions change the step size of the duty cycle of the converter of MPPT. The basic traditional principle of greatest (maximum) power point tracking system is compared with individual algorithm and smart switching algorithm (hybrid), and in addition to it the soft switching technique also has been added to make the system more reliable and to reduce the switching losses. The results are discussed with help of simulation results. The new method which is being proposed in this paper gives the better efficiency with reduced switching losses. Boost converter topology is implemented for this proposed algorithm.

References

1. Ambikapathy, A., Singh, G., Tiwari, P.: Significance of saving one unit of electricity. 1st UPCON-ICEEE 2015, 26–28th, IEEE Explore, pp. 1–6, (March, 2015)
2. Peng, Z., Yang, W., Weidong, X., Wenyuan, L.: Reliability evaluation of grid connected photovoltaic power system. *IEEE Trans. Sustain. Energy*, **3**, 379–389 (2012)
3. Kasper, M., Bortis, D., Friedl, T., Kolar, J.W.: Classification and comparative evaluation of PV panel integrated DC-DC converter concepts. In: *IEEE Power Electronics and Motion Control Conference (EPE/PEMC)*, pp. LS1e4–LS1e.4-8 (2012)

4. Farhangi, B., Farhangi, S.: Comparison of z source and Boost Buck inverter topologies as a single phase transformer less photovoltaic grid connected power conditioner. In: IEEE Power Electronics Specialist Conference (PESC), pp. 1–6 (2006)
5. Behjati, H., Davoudi, A.: A multiple input multiple output DC–DC converter. IEEE Trans. Ind. Appl. **49**, 1464–1479 (2013)
6. Keyhani, H., Toliyat, H.A.: A new generation of buck-boost resonant AC-Link DC-DC converter. In: IEEE Applied Power Electronics Conference and Exposition (APEO), pp 1383–1390 (2013)
7. Shenoy, P.S., Kim, K.A., Jhonsons, B.B., Krein, P.T.: Differential power processing for increased energy production and reliability of photovoltaic systems. IEEE Trans. Power Electron. **28**, 2968–2979 (2013)
8. Hamzeh, M., Farhangi, S., Farhangi, B.: A new control method in PV grid connected inverters for anti-islanding protection by impedance monitoring. In: IEEE Workshop on Control and Modeling for Power Electronics, pp. 1–5 (2008)
9. Kashyap, A.R., Ahmadi, R., Kimball, J.W.: Input voltage control of SEPIC for maximum power point. In: IEEE Power and Energy Conference at Illinois (PECI), pp. 30–35 (2013)
10. Ahmadi, A., Kashyap, A., Berrueta Irigoyen, A., Rayachoti, A., Wright, C., Kimmall, J.: Selective source power converter for improved photovoltaic power utilization. In: IEEE Power and Energy Conference at Illinois, pp. 247–252 (2013)
11. Sera, D., Kerekes, T., Teodorescu, R., Laabjerg, F.B.: Improved MPPT algorithm for rapidly changing environmental conditions. In: IEEE Power Electronics and Motion Control Conference (EPE-PEMC), pp. 1614–1619 (2006)
12. Kim, K.A., Li, R.M., Krein, P.T.: Voltage offset resistive control for DC-DC converters in photovoltaic applications. In: IEEE Applied Power Electronics Conference and Exposition (APEC), pp. 2045–2052 (2012)
13. Femia, N., Petrone, G., Pagnodo, G.S., Vitelli, M.: Optimization of perturb and observe maximum power point tracking methods. IEEE Trans. Power Electron. **20**, 963–973 (2005)
14. Bidram, A., Davoudi, A., Balog, R.S.: Control and circuit techniques to mitigate partial shading effects in photovoltaic arrays. IEEE J. Photovoltaics **2**, 532–546 (2012)
15. Kim, T.Y. et al.: A novel based maximum power point tracking controller of photovoltaic power system rapidly changing solar radiation. IEEE Int. Symp. Ind. Electron. **2**, 1011–1014 (2002)
16. Coelho, R.F., Martins, D.C.: An optimized maximum power point tracking method based on PV surface temperature measurement. In: Book on Sustainable Energy-Recent Studies, INTECH Publication (2012)
17. Florea, M.-L., Blttanu, A.: Modeling photovoltaic arrays with MPPT perturb & observe algorithm. In: Proceedings IEEE Advanced Trends in Electrical Engineering Conference, pp. 1–4 (2013)
18. Atallah, A.M., Abdelaziz, A.Y., Jumaah, R.S.: Article on implementation of perturb and observe MPPT of PV system with direct control method using buck and buck boost converters. An International Journal of Emerging Trends in Electrical and Electronics and Instrumentation Engineering, Vol. 1 (2014)
19. Safari, A., Mekhilef, S.: Incremental conductance MPPT method for PV systems. In: Proceedings of 24th Canadian Conference, IEEE Electrical and Computer Engineering, pp. 000345–000347 (May 2011)
20. Vedasangamithra, I. Selvarani, N.: Design and analysis of MPPT algorithms for CHBMLI. Int. J. Adv. Res. Electr. Electron. Instrum. Energy, **2** (2012)
21. Abdi, B., Safaei, A., Moghani, J.S., Abyanesh, H.A.: An overview of soft switching converter for Photovoltaic. Int. J. Commun. Electr. Eng. **5**(1) (2013)

A Novel Educational Proposal and Strategies Toward Promoting Cloud Computing, Big Data, and Human– Computer Interaction in Engineering Colleges and Universities

Prantosh K. Paul and Mrinal Kanti Ghose

Abstract Cloud computing is an important name in current Information Technology domain and responsible for the development in many perspectives. The advancement of information processing, management, delivery to software-related matter may be solved with cloud platforms. The virtualization of hardware, software, applications, etc., is in many ways dedicated for solid information infrastructure building and side by side solid information technology management. The related field of cloud computing is Big Data, which is responsible for managing large amount of data only rather software, hardware, etc. The application of Big Data is also called as Big Data Management. The complex and huge data generation results this domain and helps in data and information solutions in most of the organizations, institutions, associations, etc. Apart from these two, another important technology is human–computer interaction and partially related with the earlier mentioned technologies. It is worthy to note that these tools and technologies become common name in today’s world, but the educational opportunities are very much limited in India. The university and college level education as a full-fledged domain or specialization is more or less absent. This paper talks about cloud computing, Big Data, HCI as an overview including its current educational scenario with special focus on possible degrees, etc., in Indian context.

Keywords Cloud computing · Big Data · Human–computer interaction
Usability Engineering · Universities · Emerging Educational Programs
India · MSc

P.K. Paul (✉)

Raiganj University, PG Building, Raiganj 733134, West Bengal, India
e-mail: prantoshkpaul@gmail.com

M.K. Ghose

SMIT, Sikkim Manipal University, Gangtok, Sikkim, India

© Springer Nature Singapore Pte Ltd. 2018

S. SenGupta et al. (eds.), *Advances in Smart Grid and Renewable Energy*,

Lecture Notes in Electrical Engineering 435, https://doi.org/10.1007/978-981-10-4286-7_10

1 Introduction

The virtualization of software, hardware, applications, systems and other Information Technology services is called as cloud computing. It is a kind of remote-based computing and higher than the grid computing fundamentals. Moreover, the cloud computing is responsible for the remote information technology and computing infrastructure availability anytime and anywhere with adequate network and Internet backup [1, 2]. Companies and institutes are no longer using separate hardware, software, applications. They are using the common integrated systems either as public cloud, private cloud or hybrid cloud computing. The collaborations among the companies are very much common in this context. Information transfer cycle becomes easy with the adoption of cloud computing etc. The large amount of data creation was responsible for the creation of data management as a tool and later on as a field of study and research [3, 4]. The continuation of this promotion brings ‘Big Data Management.’ The modern education and research has created a domain called *Data Science*. Managing with large amount of data, data complexity, etc., many ways are possible to solve by the cloud computing applications and thus today both the domains also termed as cloud-big data or cloud-analytics. The easiness and beautification of IT and Computing products are also very much important and valuable for healthy IT products and service creations. The HCI or human–computer interaction is a kind of model and concept for the creation of an interactive and sophisticated information systems and computing products. The HCI is also known as Human-Centered Computing and closely related with the Usability Engineering. The HCI is dedicated for designing, development of tools, technologies and systems which are much more interactive, reliable and sophisticated. However, the applications of HCI are most common in interface creations of the computer, laptop, mobile, tablet, etc. The user-friendliness is the main agenda for the HCI in many contexts. Though cloud computing, Big Data Management, human–computer interaction have important role and continuous applications these days, but it is fact that in India, educational opportunities and programs on these domain are more or less nil. Most the universities, Institute of National Importance, etc., do not have any full-fledged program on these fields. Though there are huge potentialities to offer the program including as a specializations, degrees, major, etc., in several disciplines.

2 Objectives and Agendas

This is a conceptual study and deals with many aim, agenda and objectives. The following are the major among these:

- To learn about the cloud computing, Big Data and human–computer interaction and their basic features along with characteristics.

- To know about the Indian education systems in brief manner with few information on universities, colleges, engineering colleges, etc.
- To find out the potentialities of introducing the cloud computing, Big Data Management and human–computer interaction and allied programs in Indian Universities, Colleges, etc.
- To draw a possible degrees and educational programs on cloud computing, Big Data Management and human–computer interaction and allied fields.

3 Methodologies Undertaken

The present study is conceptual in nature, and thus various tools as well as techniques have been used for this study. Though, the review of literature played an important role, but the web review, etc., to find out latest is also used to learn about the cloud computing, Big Data Management and human–computer interaction, etc. Moreover, the web review is conducted to know about the running courses in the field of Information Science and Technology and specifically cloud computing, Big Data Management and human–computer interaction, etc. UGC (*Government of India*), AICTE (*Government of India*) and their official web played a great role. MHRD (*Ministry of Human Resource Development*) and its sub-link also played an important role to know more about education systems in India. Related Journals of cloud computing, Big Data Management and human–computer interaction (*of national and international level*) have been handled to learn more on these areas and to design programs in this design.

4 Emerging Fields and IT

The Domain of Information Science and Technology is changing rapidly, today many universities, research centers, industrial units have designed and developed several information systems and technology products, and thus many new areas have been emerged. Among the new concepts and tools, few important are in Networking and Telecommunications (such as Wi-Fi, Li-Fi, 5G) in Computing—cloud computing, Green Computing, in Information Science—human–computer interaction, Usability Engineering, Data Science, etc., have played imperative role [5, 6].

4.1 Cloud Computing: An Overview

Cloud computing is kind of virtualization technology which permits hardware, software, application and packages anytime and anywhere available with

remote-based services. The cloud computing uses the Internet. Ultimately, cloud computing is helpful for the low-cost infrastructure for higher business units. Public cloud computing is provides to the user from common and general Internet services. Private cloud computing is run by the organization's own server infrastructure. Hybrid cloud computing is the Combination of Public cloud computing and Private cloud computing users depending upon need and mainly for confidential data. In many areas such as Defense, Bank and others commercial firms, hybrid services are useful. cloud computing is a kind of Architecture and model for virtualization than that of Technology and run without comprising the privacy [7, 8]. cloud computing promotes Green Computing and promotes centralization accordingly; client does not need own infrastructure. Hassle-free deployment of hardware, software, IT Infrastructure is possible with cloud computing.

4.2 Big Data Management: An Overview

'Big' means something very large in nature. On the other hand, Data means the raw information. In the recent past, the technology is changing emerging continuously. The social media has become very popular geographical boundaries. Every foundation of information is only a few second away from the user. Big Data is a word for the data sets which are so large (or complex) that of traditional data processing, and ultimately applications are inadequate. In traditional settings, the issues include analysis, capture, sharing, storage, visualization, querying, information, etc. It is the data sets with huge sizes beyond the common traditional data systems ability. One of the related fields is Business Intelligence and responsible for the descriptive statistics with high information density to measure things, detect trends and so on. The Big Data is also called as Data Sciences. Big data uses inductive statistics along with concepts from nonlinear scheme identification toward infer from large sets of data with low information compactness to divulge relationships moreover dependencies, even or to perform predictions and guess of the outcomes and behaviors [9, 10].

4.3 HCI and UE: An Overview

Human-computer interaction is the computing system which is responsible for the users particularly for the computers rather including other kind of machines and deals with the planning, designing and development of Human Computer Devices and systems for the computer systems, computer interface, webpage, interfaces of the mobile and ATM and so on. HCI is accountable for methodologies and process for designing and implementing interfaces and close to Usability Engineering (UE) which is needed for creation of better, healthy usability as well as

instructiveness. Usability Engineering is a broad field with principles of Human Computing along with man–machine interaction. Human Interactive Design is the most recent word. It is related with *User Centered Design*—User Centric Design (also called as User Driven Design). *Usability Testing* is also important tool and concept for user interest seeking. It helps in better usability practice. *Interaction Design* is a field and concept responsible for the creation of healthy and interactive digital products, services and systems.

5 Indian Education Systems

India is one of the important nations these days in the world. Regarding education and training, India holds popularity. India holds highest number of higher educational institutes (HEIs) in the world. It holds more than 40,000 HEIs. Among these categories important are Universities, Engineering Colleges, Management & other technical colleges under AICTE, General colleges and so on. Table 1 depicts more regarding this.

Many colleges are offering UG and PG programs with MA/MSc/MCom nomenclature. Moreover, universities are also getting tie-up with the foreign universities. Thus, huge potentialities are awaiting for offering these programs and study.

6 Engineering Education and Potentialities of Cloud, Big Data Management and Human–Computer Interaction

As far as Engineering colleges are concerned, India is one of the largest in the world with many colleges (6375 as on 2015) offering Engineering degrees, whereas around 4276 institutes are offering polytechnic, i.e., Diploma in Engineering. Most of them are offering lots of specializations and subjects and all come under the jurisdiction of AICTE. However, apart from these India also holds 93 Institute of National Importance (INI), which categorized as super specialty, and higher than central university (*See Table 2 for details*). Among these, many are categorized as

Table 1 Depicted the Universities and HEIs at a glance with approximate numbers

Universities	Numbers	Remarks
Central Universities	46	Pan India with 28 States and UT
State Universities	342	Pan India with 28 States and UT
State Private Universities	239	Except some states and UT
Deemed Universities	125	Except some states and UT
Colleges (HEIs)	33,000 (including technical)	Pan India with 28 States and UT

Table 2 Depicted the category of Universities and HEIs at a glance with approximate numbers

Universities and others Higher Educational Institutions (HEIs)	The numbers
Indian Institute of Technology (IITs)	23
Indian Institute of Information Technology (IIITs) <i>established as INI</i>	04
Indian Institute of Information Technology (IIITs) <i>established by other means with core from GoI</i>	17
National Institute of Technology (NITs)	31
School of Planning and Architecture (SPAs)	03
Indian Institute of Management (IIMs)	19
Indian Institute of Science Education and Research (IISERs)	07
Academy of Scientific and Innovative Research	01
Indian Institute of Engineering Science and Technology (IIST), Shibpur	01

Table 3 Depicted the nomenclature offered in computing & technologies in India

Streams	Remarks
Computer Science and Engineering/IT/ISE	It is offered in most of the institutions under the AICTE (the approximate number is: 6375)
Computer Applications (CA)	Offered in 1469 institute and with about 1 Lakh + Seats
Computer Science (CS)/IT/CA	The CS/IT/CA/SE are also offered in Universities and not under the Technical Fields

Engineering based. Apart from these, some other Institutes also have the potentiality to offer Cloud, Big Data and HCI programs and many of these fall under the AICTE (these are Architecture Schools, Management, Designing & Applied Arts, etc.). All of these have the potentiality to offer programs on Cloud, Big Data and human-computer interaction with various approaches, etc.

The Information Technology and Computing is among the highest offered subject in the Science and Technology field, as it comes with different flavors and levels (BTech/MCA/MSc-IT/CS/CA/SE etc.). The details are depicted in Table 3. But surprisingly it is a fact that cloud computing, Big Data and human-computer interaction all fall under the field of computing and information technology!

Due to the total intake possibilities regarding Computing field is over 2.5 Lakh thus there are huge potentialities on offering Cloud, Big Data and HCI related fields and handsome amount of output annually for he industries, academia, government sector etc.

6.1 Cloud Computing (CC) Programs: Proposed

Cloud computing programs may be offered in different flavors and levels. The program directly may be on CC or any specific areas [4]. The CC may also offer

Table 4 Depicted cloud computing as a full-fledged program

Engineering/technology: cloud computing	
BTech/BE-Cloud Computing (CC)	MTech/ME-Cloud Computing
BTech/BE-Cloud Computing & Virtualization	MTech/ME-Cloud Computing & Virtualization
BTech/BE-Cloud & Green Computing	MTech/ME-Cloud & Green Computing
BTech/BE-Cloud & Enterprise Computing	MTech/ME-Cloud & Enterprise Computing
BTech/BE-Cloud Computing & Informatics	MTech/ME-Cloud Computing & Informatics

Table 5 Depicted cloud computing as a specialized program in other related branches

Science	Commerce	Social Science	Management	Architecture
BSc/MSc-Cloud Computing	B.Com. (Cloud Management)	BA (Digital Humanities & Cloud)	BBA (Cloud Management)	B.Arch. (Cloud Designing)
BSc/MSc-IT (CC)	B.Com (E-Commerce & Cloud)	BA (Social Informatics with Cloud)	MBA (Cloud Business)	M. Arch. (Cloud Architecture)
BSc/MSc-CS (CC)	B.Com (Cloud Business Marketing)	BA-Economics (Cloud & Internet Economy)	PGBDA (Cloud & Big Data)	
BSc/MSc-SE (SaaS)	B.Com (Cloud & Green Accounting)		PGDM (Cloud & Digital Marketing)	
BSc/MSc-Networking (IaaS)				

jointly with other related fields. Table 4 depicts CC fully as Engineering Program, whereas Table 5 depicts the cloud computing possibilities in different branches such as in Science, Commerce, Social Science, Management, Architecture etc.

6.2 Big Data Programs: Proposed

Big Data Management is one of the important and valuable tool, mechanism and procedure for healthy and sophisticated data management [11]. Today in many countries, the Big Data become popular as a branch and also called as Data Science. Many more proposed nomenclatures have been proposed and depicted in Table 6 in Indian context.

Table 6 Showing the possible programs of Big Data Management

Science	Commerce	Social Science	Management	Engineering
BSc/MSc-Data Science	B.Com. (Cloud Management)	BA (Social Informatics with Analytics)	PGBDA (Cloud & Big Data)	BE/BTech/ME/MTech (Big Data Analytics Systems)
BSc/MSc-IT (Big Data)	B.Com (E-Commerce & Big Data/Data Science)	BA-Economics (Big Data Management)	PGDM (Cloud & Digital Marketing)	BE/BTech/ME/MTech (Data Science & Emerging Data)
BSc/MSc-CS/IT/IS (Data Analytics)				

Table 7 Showing the possible programs of HCI/Usability Engineering etc.

Science	Commerce	Social Science	Management	Architecture
BSc/MSc-HCI BSc/MSc-IT (HCI) BSc/MSc-CS/IT/SE (HCI & Usability Engineering)	B. Com. HCI & Image Systems Management/Content Management & Usability Management	BA (Digital Interaction) BA (Interaction Systems Management) BA-Economics (HCI Systems & Management)	BBA (HCI Management) MBA (HCI Systems & Content Management) PGBDA (HCI & Usability Management)	B. Arch. (HCI & Interaction) M. Arch. (Interaction Management)

6.3 HCI and Related Programs: Proposed

Like cloud computing and Big Data Management another highlighted area *HCI or human-computer interaction* also become popular and available in aboard. Though its availability in Indian market is nil, and surprisingly we have world largest educational institutes. Table 7 depicts several programs in this regard. cloud computing, Big Data and human-computer interaction—all these three are practically employed in industries, academic, government, health and other places but the skills are basically outsourced from the IT/CSE, etc., with post-training in the concerned field. Though, the oceans of opportunities are waiting for.

7 Findings (with Tenability of Hypothesis)

- Cloud computing is actually a virtualization technology and dedicated to the creation of hardware, software, systems majorly in public-private hybrid model and for all kinds of establishments. Similarly the large data management has been also evolved. Human-computer interaction and Usability Engineering are responsible for good usability, better interface development, image management and good branding. Thus, cloud computing, Big Data (*refer Data Science in academia*), HCI are emerging fields for study and research.
- Several areas such as Virtualization, Cloud Systems, Cloud Information Systems, etc., are considered as most important and deemed as **cloud computing**. Human-Centered Computing, User Experience Designing, Usability Engineering, etc., are considered as **human-computer Interaction**. Big Data is also referred as Data Science, Big Data Management, Data Analytics, Business Analytics, etc.
- Though our the globe many universities, the cloud computing, Big Data Management and human-computer interaction treated as an academic domain and offers as Master's and Doctoral programs (Bachelor is little bit limited) either full-fledged degree or specialization in Computing & IT program.

- In India, Computing Field is most popular and intake is over 2.5 Lakh (*perhaps the highest intake than any other fields of Applied Science & Engineering*) in BTech/MSc level. But only a few are offered cloud computing, Big Data (around 10 institutes) out of 40,000+ potential institutes. Even HCI program is purely absent in UG/UG either full-fledged degree or specialization. Initially if UG/PG courses are tough, then research-based degrees may be started, but the growth is very much limited and offers only in few institutes.

8 Suggestions

Cloud computing, Big Data Analytics, human–computer interaction—all these three are emerging name, and thus institutes, companies as well as government need to affiliate their products, services, etc., with these. All these technologies have potentialities in flexibility, elasticity, cost saving, collaborative environment and thus all whether Health, Medical, Education, Government, Business needs proper steps towards their implementation. The HCI can also be considered as vital. All these programs may be started as full-fledged program in Bachelors level (such as BSc, MSc, BTech, B.Com., BBA etc.) and Masters as well. In India, Computing is highly practiced and available degrees, but there are no specializations in the field of *cloud computing, Big Data Analytics, human–computer interaction, etc.*, and thus, universities may start these programs either specialization or major. Universities may be started program on cloud computing, Big Data Analytics, human–computer interaction as a specialization in their Bachelors or preferably in Masters of Computer Application, Information Technology, Information Systems. The program may be started in Engineering level too (*in BE/BTech & ME/MTech*). Moreover, in India there are total 1469 institutes offering MCA program and thus in such department all these three program may be started either full-fledge degree or specialization.

9 Conclusion

The society is changing rapidly, there are many tools and technologies are emerging rapidly, and among theme cloud computing, Data Analytics and human–computer interaction are important. The organizations and institutions are especially moving for healthy Information Technology practice. The increasing rate of data creation and generation needs better Big Data Principle adaptation. Moreover, the Information Systems Management of an organization also needs proper and healthy information transfer cycle and its better dissemination. And in this regard, HCI and Usability Engineering technologies may be deployed. The creation of right man-power is an urgent task for the emerging domain, particularly for its rapid

development. Thus, universities, industries and engineering institutes need proper step for healthy manpower creation in this field. India is moving toward its best and thus in future creation of solid manpower and their adaptation is no doubt beneficial.

References

1. Altbach, P.G.: Research and training in higher education: the state of the art. *HEE* **27**(1–2), 153–168 (2002)
2. Annand, D.: The problem of computer conferencing for distance-based universities. *Open Learning* **14**(3), 47–52 (1999)
3. Bhattacharya, I., Sharma, K.: India in the knowledge economy-an electronic paradigm. *IJEM* **21**(6), 543–568 (2007)
4. www.en.wikipedia/big_data (Accessed on 05-08-2016)
5. Buyya, R., et al.: Modeling and simulation of scalable Cloud computing environments and the CloudSim toolkit: Challenges and opportunities. In: *HPCS-09. HPCS'09. International Conference*, vol 9, pp. 1–11 (2009)
6. McFarlane, D.C., Latorella, K.A.: The scope and importance of human interruption in HCI design. *HCI* **17**(1), 1–61 (2002)
7. Subashini, S., Kavitha, V.: A survey on security issues in service delivery models of cloud computing. *IJCA* **34**(1), 1–11 (2011)
8. www.mhrd.gov.in (Accessed several section on 05-08-2016)
9. www.ugc.ac.in (Accessed several section on 05-08-2016)
10. www.aicte-india.org (Accessed several section on 05-08-2016)
11. www.en.wikipedia/Cloud_Computing (Accessed on 05-08-2016)

Why Green Computing and Green Information Sciences Have Potentialities in Academics and *iSchools*: Practice and Educational Perspectives

Prantosh K. Paul and Mrinal Kanti Ghose

Abstract Green computing is responsible for the designing and developing the Computing Systems and IT infrastructure which are less energy consumed and eco friendly. The policies on environment, power management, consumption, recycling etc. have wider prospects in building and solid practice of Green computing and Green technology. Ultimately Green Computing is dedicated to the healthy and sophisticated Green Systems building. The integration of Green Computing with Informatics and Information Sciences have the potentiality to launched Green Informatics and Green Information Science respectively. The organization, association, government, educational institutes etc. have the healthy potentialities of introducing Green Computing and similar systems for healthy output and solid benefit. In the academics computers and similar devices become very common and thus the principles and their applications of Green Computing many ways would lead the sustainability. The *iSchools* are the consortium of information and computing related branches into one single academic wing and common in many countries. Thus they not only practice the Green Computing but also teach and engage the Green Computing and Green Information Sciences. The paper is described and reported Green Computing and allied branches their practice related issues and possibilities of the areas as academics subjects in Indian universities etc. The paper also highlighted the potentialities of *iSchools* regarding offering Green Computing and related branches including practicing Green Computing principles.

Keywords Green computing · Cloud computing · Green information science Academics · Emerging degrees · Energy management

P.K. Paul (✉)

Raiganj University, PG Building, Raiganj 733134, West Bengal, India
e-mail: prantoshkpaul@gmail.com

M.K. Ghose

SMIT, Sikkim Manipal University, Gangtok, Sikkim, India

© Springer Nature Singapore Pte Ltd. 2018

S. SenGupta et al. (eds.), *Advances in Smart Grid and Renewable Energy*,

Lecture Notes in Electrical Engineering 435, https://doi.org/10.1007/978-981-10-4286-7_11

1 Introduction

Green Computing is an emerging concept, practice field and research areas in modern Energy Science. In the Computing and Information Sciences the concept and its practices are increasing day by day in most of the modern countries and advance institutes etc. Worldwide, Green Computing is growing and promoting sustainability in many contexts [1–3]. Green Computing and its application in Informatics and Information Systems already created two domains *Green Computing* and *Green Information Systems*. Similarly the Green Computing into Information Science may positively bring Green Information Science which may be for the wider solutions of manual information management and computation information management with sustainability practices. Energy Management, Green Systems and Recycling are the common name in Green Computing and Allied Sciences [4–6]. The real practices in the field are become obstacle due to less manpower, though there are huge possibilities to offer the programs and their final manpower production.

2 Objectives and Agendas

The present study is conceptual in nature and deals with several objectives. Among them following are the major:

- To learn about the Green Computing, Eco Informatics and their basic features along with characteristics.
- To learn about the Indian education systems in brief manner as well as data regarding universities, colleges, engineering colleges etc.
- Find out pertaining to the potentialities of starting programs on Green Information Science, Green Computing and allied subjects in Indian Universities, Colleges.
- To draw a proposed degrees furthermore educational programs on Eco Informatics, Green Information Science, Green Computing and allied fields.

3 Methodologies Undertaken

Various tools and techniques have been used for this conceptual study. However literature (*secondary and primary*) played an imperative role including the web review for learning latest also used to learn about the Green Information Science, Green Computing etc. Web review conducted to know about the running courses in the field of Information Technology and Computing specifically Eco Informatics, Green Information Science, Green Computing etc. Websites and sub link of UGC,

AICTE (*Government of India*) have also played a big role. Ministry of Human Resource Development's website is also played an important role to know more about education systems in India. Related National and International Journals of Eco Informatics, Green Information Science, Green Computing have been consulted to learn about running program and to design possible programs in Indian context.

4 Green Computing: The Foundation with Cloud Perspectives

Green computing is a field of study and research responsible for Eco Friendly less consuming computing and informatics system. Green Computing is dedicated to designing furthermore developing the Computing, IT infrastructure and also based policy on Environment, Power Management, Consumption, recycling etc. Integration of Green computing as well as green technology bring many practices and emerging academic fields of study and research. Green computing and Green technology and their integration in informatics and information science make available emerging domain Green Informatics [3, 7, 8]. Green Computing is purely a Computing practice that engaged for design, development of Energy consumed and Friendly Information Infrastructure designing and building. Ultimately it helps in better IT products which are less power consumed and therefore also less carbon emission based. Design and development of information systems and IT system in an organization is possible with less hardware and technology with Green Computing. Green Computing is comes with many devices and many service providers and hence it does not needs much equipments and machines and ultimately it supports Green Computing principles as it uses centralized machines with very less carbon emission systems. The less machines and products and centralize service are basically rendered by the Cloud Computing services and thus indirectly Cloud Computing also helps in promotion of Green Computing.

5 Green Information Science?

Green Information Science (GISc) may be deemed as the combination of Green Computing and Information Science and should be responsible for the overall greening and energy management of the Information Systems, Centers, Networks (in Information Foundations and MNCs) and whole information infrastructure hence the scope is enormous by means of larger users. Fields such as Geo Informatics, Energy Informatics, Green IT, Green computing may be jointly called as Green Information Science. So that GISc is accountable for green information system buildings (for the organizations, MNC, academic information foundations).

GISc possible to offer in Information Science/IT or related departments (computing, IT, Geo Informatics, MIS, information systems) or Environment related departments or (*iSchools*) information schools. The program may be combined with *information, computing* along with green fundamentals for the designing of sophisticated information infrastructure. Among the new concepts and tools of *Information Science and Technology* few important are (in) Networking & Telecommunications (*such as Wi-Fi, Li-Fi, 5G* etc.), Computing-(*Cloud Computing, Green Computing*), Information Science (*Human Computer Interaction, Usability Engineering, Data Science*) etc. have played imperative role.

6 Educational Opportunities in India and Aboard in Green Computing (with Cloud Related Subjects)

In regard to education it is worthy that India is largest education system in universe having 40,000+ Higher Educational Institutes (HEIs) with the colleges, universities, research centers, polytechnics etc. of several kinds. India also holds many Engineering Colleges, Management Colleges, Architecture Colleges, Polytechnic Colleges and so on [3, 9, 10]. Thus there are huge potentialities to offer the Educational programs on Green and Eco Informatics or Computing. Many universities around the world offers many programs on the related to Green Computing/Eco Informatics etc. (jointly may be called as Green Information Science) [6]. These programs are depicted as follows with core structures (*which ultimately helps in the proposed programs on Green Information Science in Indian context*).

- **University of Leicester**, MSc-Environmental Informatics (having focus Course on Earth Observation and Remote Sensing, Programming for Spatial Scientists, Ecosystem and Biodiversity Conservation, Environmental Economics etc.) with Duration: 1–2 years.
- **Cranfield University**, UK MSc-Environmental Data Science (having Fundamentals of Environment, GIS Fundamentals, Spatial Data Management, Modeling Environmental Process, Applied Environmental Informatics, Programming with Java, Environmental Resource Survey, Spatial Data and Internet) with Duration of 1–3 years.
- **University of Northampton**, UK, MSc-Environmental Informatics (having coursework from Database, Media Technology, Java Programming, Water Resource Management, Energy Resource Management, Sustainable Urban Informatics, Climate Change, Geo Informatics) with Duration: 1–2 years.
- **Technical University of Denmark**, UK, MSc-Environmental Informatics offered as 2 years program.
- **Indian Institute of Information Technology and Management, Kerala** offers a flagship MPhil-Ecological Informatics.

- **University of Technology, Malaysia** offers PhD-Information Technology (Green Computing, 2–5 years).
- **Leeds Beckett University, UK** offers an MSc Sustainable Computing, 1–2 years with Coursework.
- **University of West England, UK** offers MSc Sustainable Development in Practice, 1–2 years.
- **Technical University of Munich, Germany with NTU, Singapore** offers MSc-Green Electronics, a 20 Month program.

Like Green Computing and Allied Branches, Cloud Computing may also consider as a parallel branch (*as it helps in minimizing resources and equipments etc.*). So that an account of popular **MSc program on Cloud Computing** also under taken and some popular programs in this regard are:

- University of Newcastle
- Cork Institute of Technology
- University of Essex
- University of Leicester
- National University of Ireland
- Anglia Ruskin University
- Nottingham Trent University

Most of these programs are offered with MSc-Cloud Computing nomenclature except Nottingham Trent University which offers MSc-Cloud & Enterprise Computing. The duration of the programs are normally 1 year or 2 years in case of part time study.

7 *iSchools* and Green Information Sciences

Information Schools (iSchools) is an imperative educational advancement in recent years in the universities. *iSchools* is combination of some related academic departments which are related and deal with information and computers [11]. *iSchools* interested to work from a single umbrella and helps in interdisciplinary research. Among the related departments few important are information technology, information systems, librarianship, computer science, communication, management information systems etc., apart from the flagship discipline information science. Thus *iSchools* depends and deals with many IT and Electronics Gadgets. Hence here Green Computing principle and strategies in may be used. The *iSchools* taught the strategies of Green system building and Development. Regarding training, education and research *iSchools* uses many Electronics gadgets such as Servers, computer, Laptop, Networks Devices. Thus hence here relevance of Green Computing is exists for building Eco-Friendly *iSchools* creation. Regarding advance networking, the smart Wireless Information Infrastructure is another

alternative for building healthy eco friendly Information Systems. Following belongings may be helpful for creating a healthy *iSchools*:

- It is essential to purchase and upgrade the electronic products and computers with Green and energy efficient systems.
- *iSchools* uses several devices such as servers, NIC, Router, Switch along with other Network Devices. Therefore it is important to check that such devices are energy related aspects.

iSchools is a combination of some schools in one umbrella and all the departments concerned with computers and similar devices for better information practice. Thus in every sub department/section lab related to the computer is common. So, it is essential all the computing devices should be 'switch off' mode if computers/devices not active.

8 Potential Programs in Green Information Science: Indian and International Context

Green computing and its combination with Information Science may be called as *Green Information Science* that is responsible for the sustainable manual and computation information solutions that we already reported [12]. Though, the all related Green and Energy field in relation to Computing & Information may also designate as *Green Information Sciences* instead of Green Information Science. India is leading educational hub in the world that we already mention and with several institutes (listed in Table 1). Thus there are healthy possibilities of offering emerging programs.

8.1 GIS and Science, Engineering and Management Stream: Some Possibilities

Green Information Sciences (*may be deemed as combination of Green Computing, Green Informatics, Green Information Systems, Green IT, Green Electronics, Energy Informatics, Energy Management etc.*) have the wider possibilities to offer programs on Green Information Sciences in the Science, Engineering and Management and few possible are depicted in Table 2.

Table 1 Depicted the Universities and HEIs at a glance with approximate numbers [12–15]

Universities	Numbers	Remarks	GIS and these Institutes: a remarks
Institute of National Importance	93	Pan India with 28 States and UTs	Possible in most INI as they either deal Technology, Management or Designing
Central Universities	46	Pan India with 28 States and UTs	Possible in most Universities including Agricultural except languages
State Universities	342	Pan India with 28 States and UTs	Possible in most Universities including Agricultural except languages
State Private Universities	239	Except some states and UTs	Possible in most Universities
Deemed Universities	125	Except some states and UTs	Possible in most Deemed Universities including
Engineering Colleges	6375	Pan India with 28 States and UTs	Possible in most Engineering Colleges
Management Colleges	3217	Pan India with 28 States and UTs	Possible in most Management Colleges
Polytechnic Colleges	4276	Pan India with 28 States and UTs	Possible in most Polytechnic Colleges
Architecture Colleges	177	Except some states and UTs	Possible in most Architecture Colleges
General Colleges (UG/PG)	33,000+	Pan India with 28 States and UTs	Possible in some General Colleges in Science Faculties

Table 2 Showing some possible GIS, Green Computing related programs in Science, Engineering and Management domain

In Science	In Engineering	In Management
BSc/BS/MSc/MS-Green Computing/Green Informatics/Energy Informatics/Eco Informatics BSc/BS/MSc/MS-IT or Computer Science or Information Science (Green Computing/Green Informatics/Energy Informatics/Eco Informatics)	BE/BTech/ME/MTech- Green Computing/Green Informatics/Energy Informatics/Eco Informatics BE/BTech/ME/MTech-IT or Computer Science or Information Science (<i>Green Computing/Green Informatics/Energy Informatics/Eco Informatics</i>)	BBA/MBA in Management/Green Informatics/Energy Informatics/Eco Informatics BBM/MBM in Eco Management/Green Informatics/Energy Informatics/Eco Informatics

8.2 GIS and Humanities Stream: Some Possibilities

In few Humanities and Social Science stream also, the Green Information Sciences may be positively possible to offer with Masters, Bachelors etc. with specialization and full-fledged degree. More are depicted in Table 3.

Table 3 Showing some possible GIS, green computing related programs in Humanities, Designing and Architecture domain

In Humanities	In Designing	In Architecture
BA/MA -(Green Information Management) MA -Environmental Studies (Green Computing)	BA/MA -Green Information Designing B.Des/M.Des -(Green Computing Designing/Green)	B.Arch/M.Arch (Green Information Designing/Eco Computing Architecture)

Table 4 Showing some possible Green Information Science related programs with research focus

In Masters Research	In Doctoral Research	In Post Doctoral Level
MPhil/MS (Research) (Eco Informatics) MPhil/MS (Research) -Green Computing/Green Informatics/Energy Informatics/Eco Informatics MPhil/MS (Research)- IT/CS/IS (<i>Green Computing/Green Informatics/Energy Informatics/Eco Informatics</i>)	PhD/DPhil (Eco Informatics) PhD/DPhil Green Computing/Green Informatics/Energy Informatics/Eco Informatics PhD/DPhil-IT/CS/IS (<i>Green Computing/Green Informatics/Energy Informatics/Eco Informatics</i>)	DSc (Research) (Eco Informatics) DSc (Research) -Green Computing/Green Informatics/Energy Informatics/Eco Informatics D.Engg (Research) -IT/CS/IS (<i>Green Computing/Green Informatics/Energy Informatics/Eco Informatics</i>)

8.3 GIS and Few Other Streams: Some Possibilities

Green computing is a research oriented domain and field and the domain has the potentiality to offer in Research level also with several flavor as PhD, D.Sc, D.Phil. etc. Refer Table 4 for more.

9 Tenability of Hypothesis (with Major Findings)

- Green Computing and Similar domains such as Green Informatics, Green Information Systems, Ecological Informatics are rising as a practicing field and popular in many context in the developed countries.
- The combination of Green Sciences in relation to Computing and Informatics may be considered as Green Information Science with possible academic programs.

- In the United Kingdom most of the Eco or Green Informatics or Computing related programs have been offered with Masters (MSc) and beyond.
- In India only one Institute i.e. IIITD Kerala offers MPhil program on the domain (Ecological Informatics).

10 Recommendation

- NGOs, Associations, Institutes and Government etc. should establish joint and collaborative efforts for real practice of Green Computing and Green systems for solid sustainable society building.
- Proper planning and implementation are very much important for a solid and healthy Green Computing practice and these are need to take care by the Ministries and Concerned department with research units.
- Education is the ultimate solution for every successful event and regarding better Eco Informatics and Green Computing practice solid manpower and trained are required. The Universities need to start the programs on the domain with various levels as proposed.
- *iSchools* are the future academic innovations and thus the universities need to establish school by combining other related department which will saves the manpower, money and obviously energy. Moreover the established *iSchools* need to obey the depicted principles as much as possible.

11 Conclusion

Green Computing and Green Information System are most valuable these days for healthy sustainability and ecological promotions. The right implementation of Green world many ways possible with the development of Green Information Science by combining all related departments and its practice in the Computing related schools and other academic units. Though creation of solid manpower very much important and needed for its real practice. Government, Ministries, Associations, Universities need to establish policies for the promotion of programs and research in the Green Information Sciences. India also needs healthy steps for solid Green and Eco Practices.

References

1. Altbach, P.G.: Research and training in higher education: the state of the art. *High Educ. Europe* **27**(1–2), 153–168 (2002)
2. Hooper, A.: Green computing. *Commun. ACM* **51**(10), 11–13 (2008)
3. Paul, P.K., Chatterjee, D., Kumar, K., Ghosh, M.: Green computing: wider prospects, opportunities and challenges in 21st century for healthy energy management. *Int. J. Embed. Syst. Comput. Eng.* **4**(2), 123–126 (2012)
4. Buyya, R., et al.: Modeling and simulation of scalable Cloud computing environments and the CloudSim toolkit: challenges and opportunities. In *HPCS-09. HPCS'09. International Conference*, pp. 1–11. IEEE (2009)
5. Interconnect, E.E., Living, S., Computing, G.: Technology with the environment in mind. *Intel Technol. J.* **12**(1) (2008)
6. Watson, R.T., Boudreau, M.C., Chen, A.J.: Information systems and environmentally sustainable development: energy informatics and new directions for the IS community. *MIS Q.* 23–38 (2010)
7. McFarlane, D.C., Latorella, K.A.: The scope and importance of human interruption in HCI design. *HCI* **17**(1), 1–61 (2002)
8. Murugesan, S.: Harnessing green IT: principles and practices. *IT Prof.* **10**(1), 24–33 (2008)
9. Subashini, S., Kavitha, V.: A survey on security issues in service delivery models of cloud computing. *IJCA* **34**(1), 1–11 (2011)
10. Williams, J., Curtis, L.: Green: the new computing coat of arms?. *IT Prof. Mag.* **10**(1), 12 (2008)
11. www.ischools.org home page (Accessed on 05-08-2016)
12. www.en.wikipedia.org/green_computing (Accessed on 05-08-2016)
13. www.ugc.ac.in (Accessed several section on 05-08-2016)
14. www.aicte-india.org (Accessed several section on 05-08-2016)
15. www.mhrd.gov.in (Accessed several section on 05-08-2016)

Annual Energy, Exergy, and Environmental Benefits of N Half Covered Concentrated Photovoltaic Thermal (CPVT) Air Collectors

Rohit Tripathi and G.N. Tiwari

Abstract In current study, the N identical concentrated photovoltaic thermal (PVT) has been designed where a series connection of N collectors has been adopted for higher outlet temperature of fluid. Here, air has been chosen as a fluid for proposed system. The low concentrator or compound parabolic concentrator (CPC) has been also implemented with photovoltaic thermal (PVT) to increase higher input energy or solar radiation to get much higher temperature from PVT. The air flow rate and no. of collector for CPVT (50% covered by PV module) air collector have been optimized for achieving 97 °C of outlet air temperature as eight number of collector ($N = 8$ at mass flow rate of 0.06 kg/s). The analysis has been carried out for a clear day condition for New Delhi, India. The proposed system has been useful for space heating or drying an object. Here, the net annual overall energy and exergy have been calculated as 1309.42 and 272.75 kWh, respectively. The electrical gain has also been found as 89.97 kWh. The enviroeconomic study also examined CO₂ emission per annum is reduced by energy production and earned carbon credits. For present system, the earned carbon credits are as 38.73 and 8.06 \$/year on the basis of overall thermal energy and overall exergy, respectively.

Keywords PVT · CPC · Overall energy · Overall exergy · Carbon credits

R. Tripathi (✉) · G.N. Tiwari
Centre for Energy Studies, Indian Institute of Technology Delhi, Hauz Khas,
New Delhi 110016, India
e-mail: rohittripathi30.iitd@gmail.com

G.N. Tiwari
e-mail: gntiwari@ces.iitd.ac.in

1 Introduction

A hybrid solar system produces two energy sources in order to enhance the overall efficiency of the system. One of the typical hybrid systems is the photovoltaic thermal (PVT). Conventional PV systems generate a voltage and current in combination of series connection for increase in voltage and parallel for increase in current and heat from solar radiation. By this heat, the temperature of PV module increases which effects negatively on electrical efficiency of PV cells. To reduce the temperature of PV module, a fluid having strong heat capacity is used to carry the heat or temperature of PV module out. By this principal, thermal gain can also be achieved from PV system. Now, the PVT systems can deliver not only the electrical power but also the thermal energy by solar radiation, the extraction of energy via a heat transfer fluid applies for space heating, cools the photovoltaic module, and increases electrical yield as well as overall efficiency [1, 2]. The associations between energy and exergy, energy and sustainable development, exergy and the environment in detail are presented [3]. The energy performance of a PVT water collector has been studied at range of 400–800 W/m² solar radiation [4]. It is observed that the maximum overall efficiency of PVT collector is 68.4%, thermal efficiency is 52%, and PV efficiency is 13% at a solar radiation level of 800 W/m² and mass flow rate of 0.041 kg/s. Different types of series and parallel combination of connections can be designed to make PVT air collector that can be integrated into building for space heating in cold climatic condition. Overall annual thermal energy, exergy gain, and exergy efficiency of unglazed hybrid PVT tiles air collector have been improved by 32, 55.9 and 53%, respectively, over conventional PVT air collector [5, 6]. The exergetic and enviroeconomic analysis of semi-transparent PVT array based on optimum air flow configuration and its comparative study have been analyzed [7]. They have compared three systems: opaque PVT array, solar cell tile-based PVT array and semitransparent PVT array with series and parallel combination. They have concluded that semitransparent PVT array is best sable for delivering lower solar cells temperature and higher electrical efficiency of PV module, and the outlet air temperature has been found higher in this case. The study has analyzed the performance of PVT with CPC and phase change materials [8]. In this study, PV solar collector with CPC has analyzed for two different weather conditions: One is clear day condition and second is semi cloudy day condition. The thermal modeling, outlet fluid temperature, and electrical efficiency of PV module at *N*th collector of partially covered photovoltaic thermal (PVT)–compound parabolic concentrator (CPC) collectors have derived. Here, water has taken as a fluid for proposed system and comparative study for summer and winter season performance of present system. Further, annul energy, exergy, and enviroeconomic parameters have been calculated for considering all four weather type for New Delhi, India. Energetic and exergetic analysis have been taken for four different PVT collectors for New Delhi, India [9–13].

In present paper, annual performance of N concentrated photovoltaic thermal (PVT) air collectors has been evaluated for New Delhi, India. The analysis has been carried for evaluation of overall energy and exergy for the proposed system. The enviroeconomic analysis has also evaluated for reducing CO₂ emission or mitigation and their respective earned credits by generating green energy.

2 System Description

A partially covered (25% covered by PV) N number of photovoltaic (PVT)–compound parabolic concentrator (CPC) collector connected in series has been presented [9]. Here, the cross-section view and front view of first basic collector of N -number half covered of CPVT collector have been shown in Figs. 1 and 2. N number of collectors are connected in series to increase a much higher temperature of fluid (air) for space heating or building heating. The configuration has been considered as series connection of collectors where final inlet of N th collector is the

Fig. 1 Cross-section view of first concentrator photovoltaic thermal (PVT) air collector

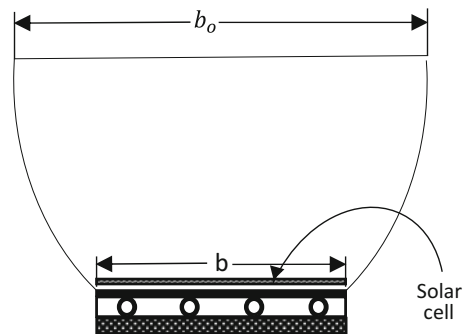
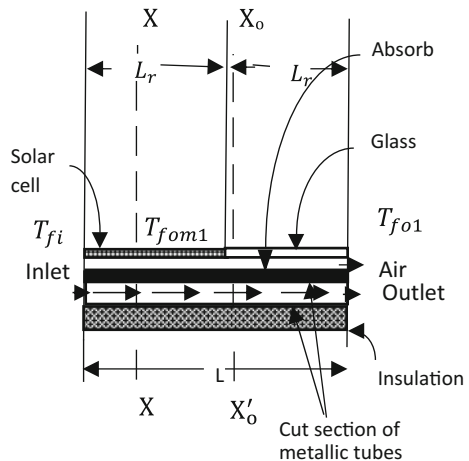


Fig. 2 Cut section view of first concentrated photovoltaic thermal (PVT) air collector



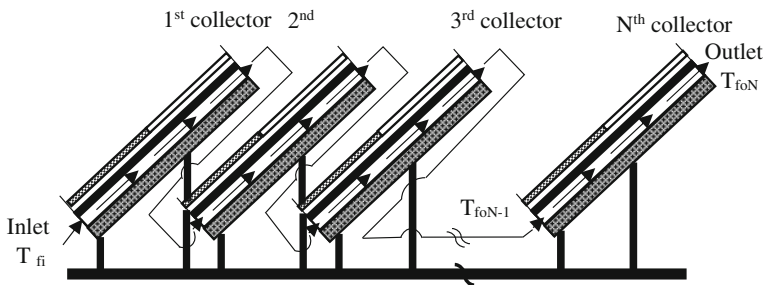


Fig. 3 Diagram of series connected of N half covered concentrated photovoltaic thermal (PVT) air collector

Table 1 Input values of parameters for proposed system

$A_r = 1 \text{ m}^2$ $A_{rm} = 0.5 \text{ m}^2$ $A_{rc} = 0.5 \text{ m}^2$	$U_{rc,p} = 5.58$ $U_{rp,a} = 4.8$ $U_{rp,a} = 4.8$ $U_{rc,a} = 9.17$	$K_g = 0.816 \text{ W/m}^\circ\text{C}$ $L_g = 0.003 \text{ m}$
$A_a = 2 \text{ m}^2$ $A_{am} = 1 \text{ m}^2$ $A_{ac} = 1 \text{ m}^2$	$PF_1 = 0.3782$ $PF_2 = 0.9512$ $PF_c = 0.9842$	$K_i = 0.166 \text{ W/m}^\circ\text{C}$, $L_i = 0.100 \text{ m}$
$U_{L1} = 3.47$ $U_{L,m} = 7.87$ $U_{Lc} = 4.7$	$h_{pf} = 100$ $F' = 0.9680$ $FF = 0.8$	$K_p = 6 \text{ W/m}^\circ\text{C}$, $L_p = 0.002 \text{ m}$
$h_i = 5.7$ $h'_i = 5.8$ $h_0 = 9.5$	$F_{rc} = 0.86 \text{ m}^2$ $F_{rm} = 0.81 \text{ m}^2$	$\rho = 0.84$ $\tau_g = 0.95$ $\alpha_p = 0.8$
$\dot{m}_f = 0.06 \text{ kg/s}$ $c_f = 1000 \text{ J/kg K}$	$\eta_a = 0.15$ Tube diameter = 0.0125 m	$\alpha_c = 0.9$ $\beta_c = 0.89$

Note All heat transfer coefficients are in $\text{W/m}^2 \text{ }^\circ\text{C}$

outlet of previous collectors. The configuration of connections has been shown in Fig. 3. The area of each collector is same or equal to 1 m^2 . In PVT, 50% of receiver area is covered by PV module and rest area is covered by glass. Total number of collector has been taken eight to study the proposed system. Air is considered as fluid for N-CPVT air collector connected in series, and mass flow rate has been optimized at 0.06 kg/s in present study. The values of parameters for proposed system have been given in Table 1.

3 Thermal Modeling

Thermal modeling of partially covered N photovoltaic thermal (PVT)–compound parabolic concentrator (CPC) collector connected in series has been presented. The final outlet temperature from N th collector of CPVT collector is derived as follows [9].

$$T_{foN} = \frac{I_b(AF_R(\alpha\tau))_1(1 - K_k^N)}{\dot{m}_f C_f(1 - K_k)} + \frac{T_a(AF_R U_L)_1(1 - K_k^N)}{\dot{m}_f C_f(1 - K_k)} + T_{fi} K_k^N \quad (1)$$

Expressions for $(AF_R U_L)_1$, $(AF_R(\alpha\tau))_1$ and K_k have been given in Appendix.

Through Eq. (1), the rate of available thermal energy and useful exergy has evaluated as followed

$$\dot{E}_{eth,N} = \dot{m}_f c_f (T_{foN} - T_{fi}) \quad (2)$$

$$\dot{E}_{xth,N} = \dot{m}_f c_f (T_{foN} - T_{fi}) - \dot{m}_f c_f (T_a + 273) \ln \frac{(T_{foN} + 273)}{(T_{fi} + 273)} \quad (3)$$

where

- \dot{m}_f flow rate of air,
- c_f specific heat of air,
- T_{fi} inlet air temperature, and
- T_a ambient air temperature.

Analytical expression of electrical efficiency of solar cell (η_{cN}) of half covered N-CPVT collectors has been followed, like as [9],

$$\eta_{cN} = \frac{\eta_0 \left[1 - \frac{\beta_0}{(U_{c,p} + U_{c,a})} \{ (XI_b + YT_a + ZT_{fi}) - T_0 \} \right]}{\left[1 - \frac{\eta_0 \beta_0 I_b}{(U_{c,p} + U_{c,a})} (\alpha + \beta\gamma) \right]} \quad (4)$$

where X , Y , Z , α , β , and γ have been given in Appendix.

When the air has been considered as fluid, then electrical efficiency of solar cell (η_{cN}) of half covered N-CPVT air collector is same as Eq. (4) as above. But, the specific heat (c_f) is different for air.

Now, electrical efficiency of series connection of PV modules of half covered N-CPVT air collectors has been obtained as

$$\eta_{mN} = \tau_g \beta_c \eta_{cN} \quad (5)$$

where η_{mN} is electrical efficiency of N —number of glass (semitransparent) PV modules.

The rate of useful electrical gain from N -identical CPVT collectors is obtained by Eq. (5)

$$\dot{E}_{ele,N} = A_{rm} I_b \sum_1^N \eta_{mN} \quad (6)$$

The rate of available overall thermal energy gain and exergy has been calculated from Eqs. (2), (3), and (5) by using the following expression

$$\sum \dot{Q}_{ith,overall,N} = \sum \dot{E}_{eth,N} + \sum \frac{\dot{E}_{ele,N}}{0.38} \tag{7}$$

and

$$\sum \dot{E}_{ux,overall,N} = \sum \dot{E}_{xth,N} + \sum \dot{E}_{ele,N} \tag{8}$$

3.1 Enviroeconomic Analysis

The average CO₂ emits in environment is 0.980 kg CO₂/kWh approximately for electrical power generation in coal-based power plant. Two losses introduced in power supply: One is distribution losses (L_d) which are 20%, ($(\frac{1}{1-0.2}) = 1.25$ kg) and second one is transmission losses (L_t) which are 40% ($(\frac{1.25}{1-0.4}) = 2.08$ kg) by the disordered transmission and electrical instruments [13]. Then, the amount CO₂ per kWh comes to be 2.08 kg. Therefore, CO₂ mitigation per year from half covered N-CPVT air collector is given as

$$\varnothing_{CO_2} = \frac{\psi_{CO_2} \times \dot{Q}_{u,overall}}{10^3} \tag{9}$$

where \varnothing_{CO_2} is CO₂ emission per year (tCO₂/year), ψ_{CO_2} is 2.08 kg CO₂/kWh and ($\dot{Q}_{ith,overall,N}$) is annual overall energy or exergy gain ($\dot{E}_{ux,overall,N}$) from half covered N-CPVT air collectors per annum.

Now, carbon credits can be evaluated by following expression

$$Z_{CO_2} = P_{CO_2} \times \varnothing_{CO_2} \tag{10}$$

where Z_{CO_2} is the carbon credits (CO₂ mitigation price per annum in \$/annum), and P_{CO_2} is the carbon price per tCO₂e (average price has been taken as 14.5 \$/tCO₂e) by [14, 15]. The numerical computation of carbon credits evaluation has given in Table 2.

Table 2 Enviroeconomic analysis (carbon credits) for half covered N-CPVT air collectors

Annual carbon credits: (clear day sky)	CO ₂ emission (tCO ₂ e/annum)	Carbon credits (\$/annum)	Carbon credits (Rs./annum) (1\$ = 67.28 INR on 01/06/2016)	Life cycle (n , in years)	Carbon credits (Rs./annum)
By overall thermal energy	2.67	38.73	2605.93	30	78178.15
By overall exergy	0.55	8.06	542.81	30	16284.47

4 Result and Discussions

The inputs for the proposed system as the total, direct beam radiation, and ambient temperature to hourly variation for a clear day have been shown in Fig. 4. Flow rate variation of outlet air temperature for N-CPVT air collector has been shown in Fig. 5. Here, T_{foN} for the N number of collector variation to respective mass flow rate has been presented. It is seen that the outlet air temperature has not been very much changed after eighth collector with mass flow rate 0.06 kg/s. With these parameters, the maximum outlet air temperature has been found as 97 °C for a typical day. Average solar cell temperature and ambient air temperature to the variation of hour have been shown in Fig. 6. It is observed that electrical efficiency of PV module of N th collector decreases with increase in the average solar cell temperature of N th collector of CPVT collector. Hourly variation of outlet fluid temperature of different number of collectors has been shown in Fig. 7. Here, pattern is noted that maximum number of collector has been delivered maximum T_{foN} , which is expected. Hourly variation of electrical gain, overall thermal energy, and exergy have been presented in Fig. 8. The daily maximum gain in a typical day for electrical gain, overall thermal energy, and exergy has been found as 2.19, 4.89, and 33.64 kWh, respectively. Monthly variation of overall thermal energy and exergy has been shown in Fig. 9. Overall energy and exergy have been found maximum in month of September and minimum in month of June in a year. The annual overall thermal energy and exergy gain for proposed system have been found as 1309.42 and 272.75 kWh, respectively. The overall thermal energy gain is found 4.8 times higher than overall exergy. The CO₂ emission by the proposed system on the basis of overall thermal energy and exergy has been 2.67 and

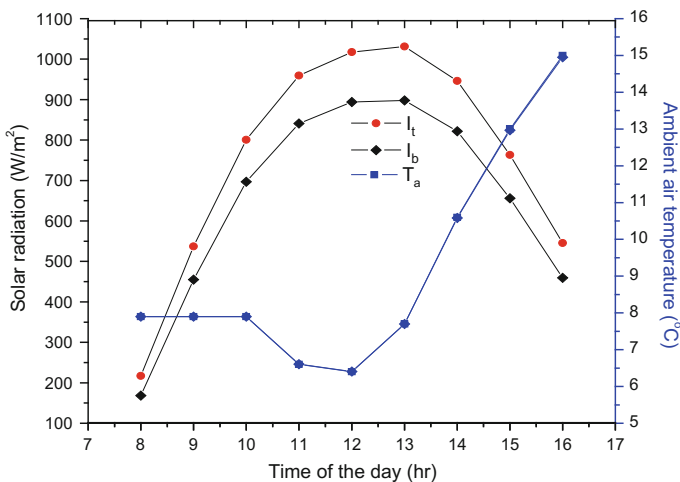


Fig. 4 Time variation of total solar radiation, beam radiation, and ambient air temperature to hours for a clear day

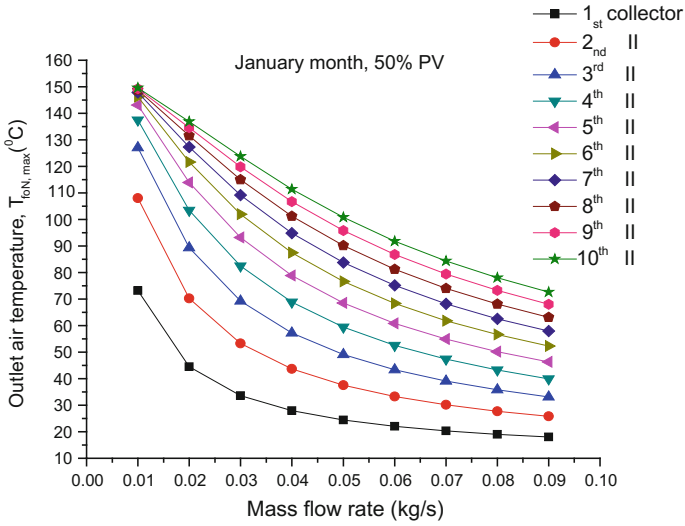


Fig. 5 Flow rate variation of maximum outlet temperature of half covered N-CPVT air collector for a clear day in January

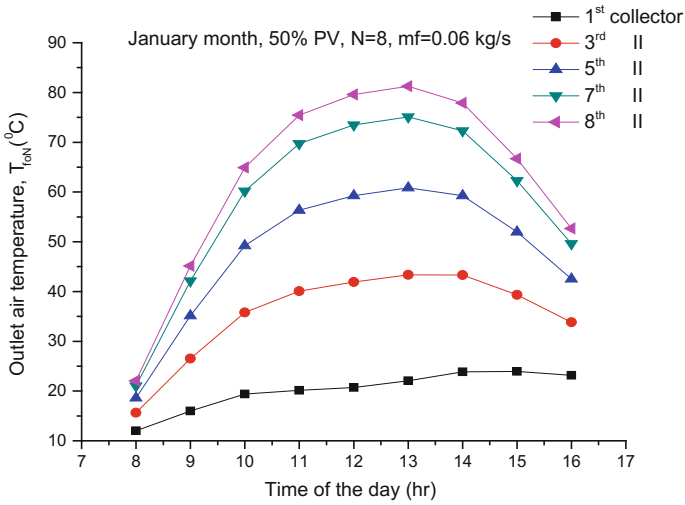


Fig. 6 Sunshine time variation of max. outlet temperature to hours of half covered N-CPVT air collector for a clear day

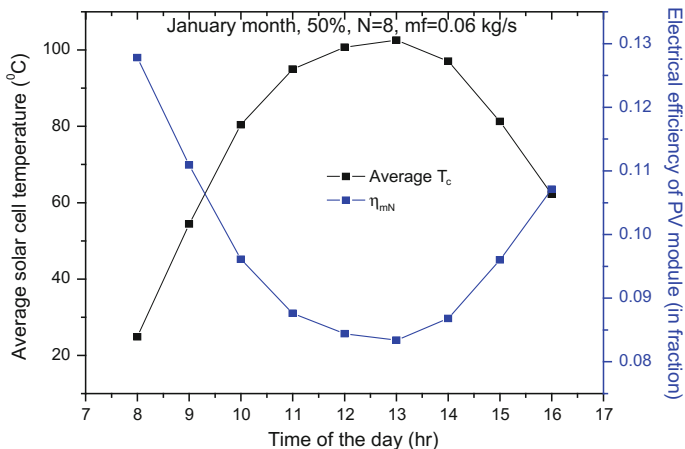


Fig. 7 Sunshine time variation of solar cell temperature to electrical efficiency of PV module with hour for a clear day

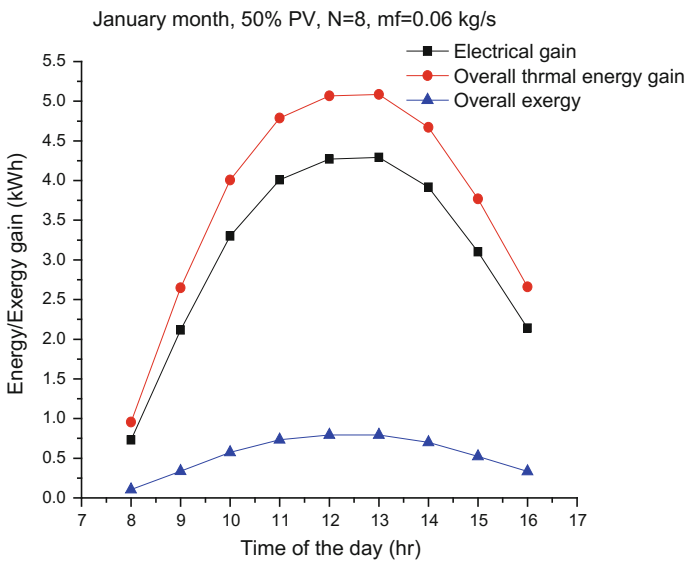


Fig. 8 Sunshine time variation of electrical gain, overall thermal energy, and exergy to hours of half covered N-CPVT air collector for a clear day in January

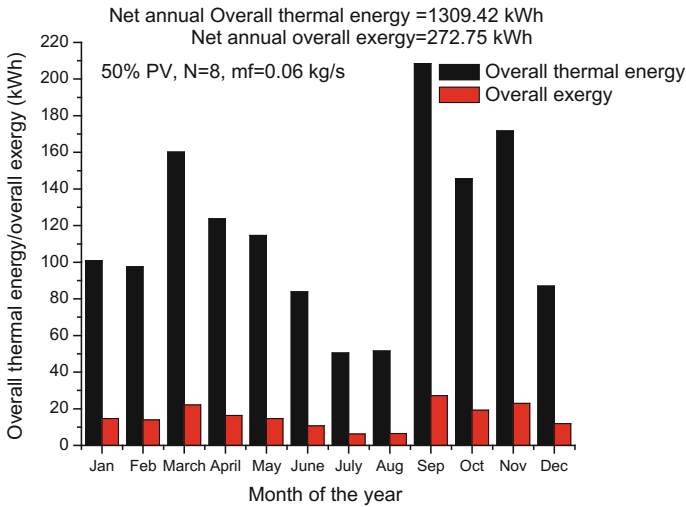


Fig. 9 Monthly variation of thermal energy and exergy of half covered N-CPVT air collector for a clear day condition for New Delhi, India

0.55 tCO₂/annum, and the environmental cost has been 38.73 and 8.06 \$/annum, respectively. For 30 years of life cycle, the environmental cost by the proposed system on the basis of overall thermal energy and exergy has been 78178.15 and 16284.47 Rs./annum, respectively, when one dollar rate is 67.28 INR in India as shown in Table 2.

5 Conclusions

- The maximum outlet air temperature (T_{foN}) for proposed system has been obtained 97 °C with mass flow rate (0.06 kg/s) and $N = 8$ in January, at New Delhi, India.
- The net electrical gain for half covered N-CPVT air collector has been obtained 89.97 kWh/year for clear day condition only.
- The net annual overall thermal energy and exergy for proposed system have been found 1309.42 and 272.75 kWh, respectively, at New Delhi, India.

Appendix

$$U_{tc,a} = \left[\frac{1}{h_o} + \frac{L_g}{K_g} \right]^{-1}; \quad U_{tc,p} = \left[\frac{1}{h_i} + \frac{L_g}{K_g} \right]^{-1};$$

$$U_{tp,a} = \left[\frac{1}{U_{tc,a}} + \frac{1}{U_{tc,p}} \right]^{-1} + \left[\frac{1}{h'_i} + \frac{1}{h_{pf}} + \frac{L_i}{K_i} \right]^{-1}$$

$$h_0 = 5.7 + 3.8V \text{ W/m}^2 \text{ K}; \quad V = 1 \text{ m/s}; \quad h_i = 5.7 \text{ W/m}^2 \text{ K};$$

$$h'_i = 2.8 + 3V' \text{ W/m}^2 \text{ K}; \quad V' = 1 \text{ m/s}; \quad (AF_R(\alpha\tau))_{m1} = PF_2(\alpha\tau)_{m,\text{eff}} A_m F_{Rm};$$

$$U_{L1} = \frac{U_{tc,p} U_{tc,a}}{U_{tc,p} + U_{tc,a}}; \quad U_{L2} = U_{L1} + U_{tp,a};$$

$$U_{L,m} = \frac{h_{pf} U_{L2}}{F' h_{pf} + U_{L2}}; \quad U_{L,c} = \frac{h_{pf} U_{tp,a}}{F' h_{pf} + U_{tp,a}};$$

$$PF_c = \frac{h_{pf}}{F' h_{pf} + U_{tp,a}}; \quad PF_1 = \frac{U_{tc,p}}{U_{tc,p} + U_{tc,a}};$$

$$PF_2 = \frac{h_{pf}}{F' h_{pf} + U_{L2}}; \quad (\alpha\tau)_{c,\text{eff}} = PF_c \alpha_p \tau_g \frac{A_{ac}}{A_{rc}};$$

$$(\alpha\tau)_{1,\text{eff}} = (\alpha_c - \eta_c) \tau_g \beta_c \frac{A_{am}}{A_{rm}}; \quad (\alpha\tau)_{2,\text{eff}} = \alpha_p \tau_g^2 (1 - \beta) \frac{A_{am}}{A_{rm}};$$

$$(\alpha\tau)_{m,\text{eff}} = \left[(\alpha\tau)_{1,\text{eff}} + PF_1 (\alpha\tau)_{1,\text{eff}} \right];$$

$$A_c F_{Rc} = \frac{\dot{m}_f c_f}{U_{L,c}} \left[1 - \exp\left(\frac{-F' U_{L,c} A_c}{\dot{m}_f c_f} \right) \right];$$

$$A_m F_{Rm} = \frac{\dot{m}_f c_f}{U_{L,m}} \left[1 - \exp\left(\frac{-F' U_{L,m} A_m}{\dot{m}_f c_f} \right) \right];$$

$$(AF_R U_L)_1 = \left[A_c F_{Rc} U_{L,c} + A_m F_{Rm} U_{L,m} \left(1 - \frac{A_c F_{Rc} U_{L,c}}{\dot{m}_f c_f} \right) \right];$$

$$(AF_R(\alpha\tau))_1 = \left[A_c F_{Rc} (\alpha\tau)_{c,\text{eff}} + PF_2 (\alpha\tau)_{m,\text{eff}} A_m F_{Rm} \left(1 - \frac{A_c F_{Rc} U_{L,c}}{\dot{m}_f c_f} \right) \right];$$

$$K_k = \left(1 - \frac{(AF_R U_L)_1}{\dot{m}_f c_f} \right);$$

References

1. Chow, T.T.: A review on photovoltaic/thermal hybrid solar technology. *Appl. Energy* **87**, 365–379 (2010)
2. Aste, N., Chiesa, G., Verri, F.: Design, development and performance monitoring of a photovoltaic-thermal (PVT) air collector. *Ren. Energy* **33**, 914–927 (2008)
3. Dincer, I.: The role of exergy in energy policy making. *Energy Policy* **30**, 137–149 (2002)
4. Fudholi, A., Sopian, K., Yazdi, M.H., Ruslan, M.H., Ibrahim, A., Kazem, H.A.: Performance analysis of photovoltaic thermal (PVT) water. *Energy Convers. Manag.* **78**, 641–651 (2014)
5. Agrawal, S., Tiwari, G.N., Pandey, H.D.: Indoor experimental analysis of glazed hybrid photovoltaic thermal tiles air collector connected in series. *Energy Build.* **53**, 145–151 (2012)
6. Agrawal, S., Tiwari, G.N.: Overall energy, exergy and carbon credit analysis by different type of hybrid photovoltaic thermal air collectors. *Energy Convers. Manag.* **65**, 628–636 (2013)
7. Rajoria, C.S., Agrawal, S., Tiwari, G.N., Chaurasia, G.S.: Exergetic and enviroeconomic analysis of semitransparent PVT array based on optimum air flow configuration and its comparative study. *Sol. Energy* **122**, 1138–1145 (2015)
8. Al Imam, M.F.I., Beg, R.A., Rahman, M.S., Khan, M.Z.H.: Performance of PVT solar collector with compound parabolic concentrator and phase change materials. *Energy Build.* **113**, 139–144 (2016)
9. Tripathi, R., Tiwari, G.N., Al-Helal, I.M.: Thermal modelling of N partially covered photovoltaic thermal (PVT)—compound parabolic concentrator (CPC) collectors connected in series. *Sol. Energy* **123**, 174–184 (2016)
10. Tripathi, R., Tiwari, S., Tiwari, G.N.: Performance of partially covered N—number of photovoltaic thermal (PVT)—compound parabolic concentrator (CPC) series connected water heating system. *Int. J. Electr. Comput. Eng. Electron. Commun. Eng.* **10**(1), 35–42 (2016)
11. Tripathi, R., Tiwari, G.N., Dwivedi, V.K.: Overall energy, exergy and carbon credit analysis of N partially covered photovoltaic thermal (PVT) concentrating collector connected in series. *Sol. Energy* **136**, 260–267 (2016)
12. Tripathi, R., Tiwari, G.N.: Energetic and exergetic analysis of N partially covered photovoltaic thermal-compound parabolic concentrator (PVT-CPC) collectors connected in series. *Sol. Energy* **137**, 441–451 (2016)
13. Tripathi, R., Tiwari, S., Tiwari, G.N.: Energy analysis of partially covered Number (N) of photovoltaic thermal-compound parabolic concentrator collectors connected in series at constant collection temperature mode. In: *International Conference on IEEE Emerging Trends in Electrical Electronics & Sustainable Energy System (ICETEESES-2016)*, pp. 12–17 (2016)
14. Den Elzen, M.G.J., Hof, A.D., Beltran, A.M., Grassi, G., Roelfsema, M., van Ruijven, B., van Vliet, J., van Vuuren, D.P.: The Copenhagen accord: abatement costs and carbon prices resulting from the submissions. *Environ. Sci. Policy* **14**(1), 28–39 (2011)
15. Caliskan, H., Dincer, I., Hepbasli, A.: Exergoeconomic, enviroeconomic and sustainability analyses of a novel air cooler. *Energy Build.* **55**, 747–756 (2012)

An Experimental Realization of Grid-Connected PV System with MPPT Using dSPACE DS 1104 Control Board

Neeraj Priyadarshi, Amarjeet Kumar Sharma
and Shrikshitish Priyam

Abstract This paper presents the experimental realization of grid-connected photovoltaic (PV) system using dSPACE DS 1104 control board. To obtain high tracking efficiency, an adaptive Neuro-Fuzzy inference system (ANFIS)-based maximum power point tracking (MPPT) algorithm is proposed. The performance of the system is improved by fuzzy logic control (FLC), which generates the switching signal to the power switches of inverter. The proposed controller tracks optimal power from PV array as well as injects sinusoidal inverter current to the utility grid. Experimental results are validated using dSPACE DS 1104 control board under abrupt weather conditions.

Keywords dSPACE DS 1104 · FLC · MPPT · PV

1 Introduction

Due to climate change and rapid depletion of conventional energy sources, the renewable energy technology is becoming more popular day by day. The photovoltaic (PV) system becomes promising energy sources among all renewable energy sources because of its eco-friendly nature. As it is intermittent in nature, the effective control of maximum power point tracking (MPPT) is compulsory [1–3]. Various MPPT algorithms have been employed to control the MPPT such as perturb and observe (P and O), incremental conductance (INC), fuzzy logic control (FLC), and artificial neural network (ANN) [4–7]. Here, an adaptive neuro-fuzzy inference system (ANFIS) has been proposed to get maximum power point tracking

N. Priyadarshi (✉) · A.K. Sharma · S. Priyam
Millia Institute of Technology, Purnea 854301, Bihar, India
e-mail: neerajrjd@gmail.com

A.K. Sharma
e-mail: maxeramar@gmail.com

S. Priyam
e-mail: vanduyam@gmail.com

(MPPT) as it gives fast transient response and better tracking efficiency compared to all MPPT algorithms under variable weather conditions. There are several dc–dc converters for MPPT as discussed to optimize the effectiveness of solar panel [8–10]. In this work, SEPIC buck–boost converter is employed as it has high power tracking capability and low input current ripple compared to other dc–dc converters.

There are two modes, grid-connected and standalone in which PV system is operated. In grid-connected mode, the maximum extracted power from PV system is fed to the electric grid. The battery cost is minimized, and stable grid operation is performed in this mode. In my work, a fuzzy logic controller for voltage source inverter is proposed to ensure the grid requirements and to supply stable PV power to the grid. The simulation is performed using MATLAB/Simulink environment and then interfaced with dSPACE DS 1104 controller kit. The novelty of this paper is such control system using dSPACE software neither developed nor discussed before by author's best knowledge.

2 Control System

Figure 1 presents the proposed structure of the grid-connected PV system and its control. The SEPIC converter performs the MPPT functions. The ANFIS-based controller for MPPT and FLC-based inverter control have been employed to generate gating pulses to the inverter power switches. The real-time dSPACE DS 1104 control board is interfaced with MATLAB/Simulink model to control the inverter and MPPT.

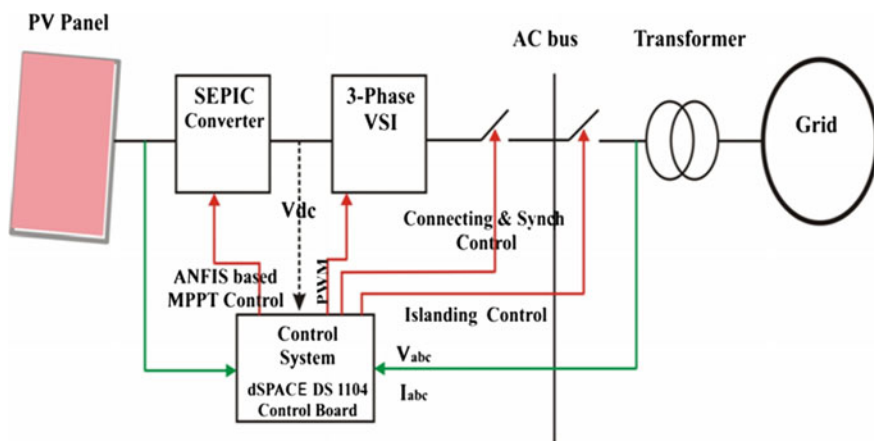


Fig. 1 Proposed grid-connected PV system structure and control

2.1 Adaptive Neuro-Fuzzy Inference System (ANFIS)-Based MPPT Controller

The ANFIS-based MPPT integrates the advantages of FLC and ANN in one package. By assigning fuzzy inference rules and membership functions, the linguistic variables are converted to numerical variables using fuzzy logic. To remove the disadvantages of individual intelligent methods, an ANFIS integrates the ANN and FLC. Therefore, ANFIS-based MPPT has better tracking efficiency with high accuracy compared to all MPPT methods, which tracks peak power from the PV system. By embedding the overall system knowledge, the ANFIS has optimal fuzzy inference system. It has similar training data as ANN. Firstly, ANFIS-based MPPT method is simulated using MATLAB/Simulink environment and after that dSPACE DS 1104 real-time board is used to interface with hardware. Figure 2 shows the structure of ANFIS-based MPPT controller to obtain the required duty ratio for power switch of SEPIC converter.

2.2 Inverter Control Strategy

Figure 4 depicts the fuzzy logic-based three-phase inverter control strategy of grid-connected PV system. Voltage and current control, system protection, detection of grid changes, and generation of PWM gating signal are the major controlling components. The input dc voltage V_{dc} is compared with V_{dref} and then regulated using FLC in voltage control mode. In current control loop, the reference current I_{dref} has been tracked. There are five trapezoidal- and triangular-shaped membership functions which are assigned as negative big (NB), negative small (NS), zero (ZE), positive small (PS), and positive big (PB). Figure 3 presents the basic structure of

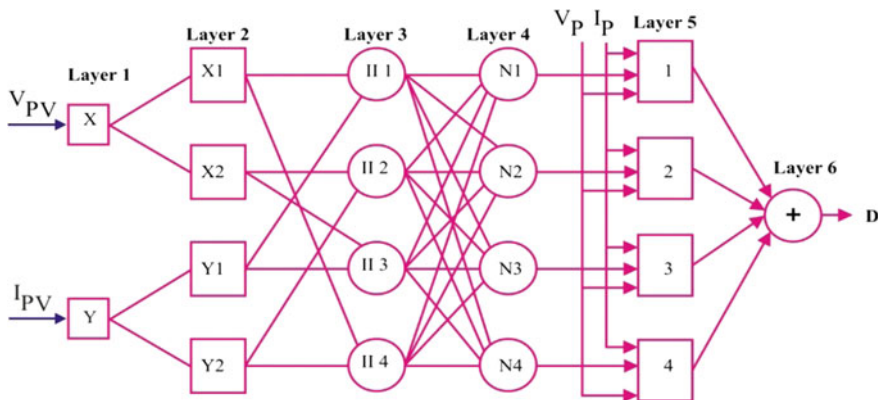


Fig. 2 Structure of ANFIS-based MPPT controller

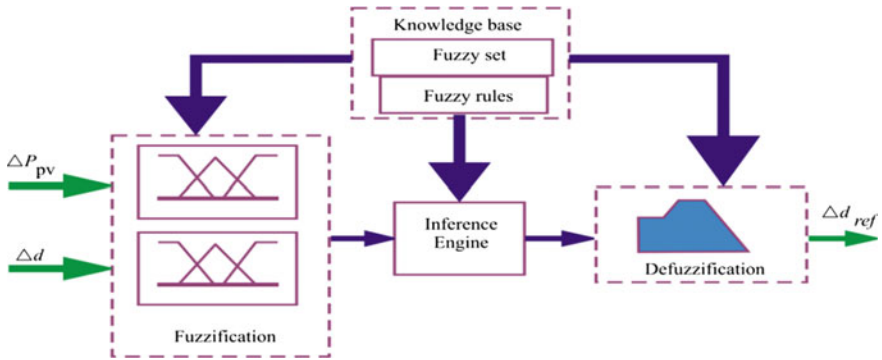


Fig. 3 Structure of fuzzy logic controller

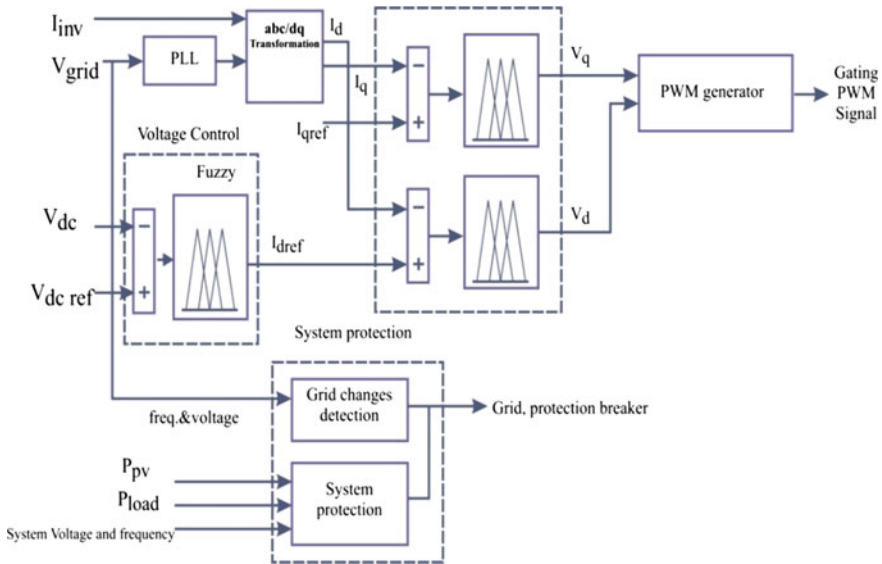


Fig. 4 Inverter control strategy

FLC controller. The input and output of FLC is related using 25 generated fuzzy inference rules which is shown in Table 1.

The output switching PWM signals for inverter are obtained using PWM generator. The real-time inverter control is implemented using dSPACE DS 1104 controller board. The system is protected by over/under voltage and frequency. The inverter is isolated from grid using breaker under system protection.

In grid connection mode, the inverter follows the grid frequency and grid voltage. For grid synchronization purpose, the phase-locked loop (PLL) has been employed. When grid is synchronized, the grid connection is controlled by breaker.

Table 1 Inference rules for fuzzy logic controller

ΔP_{pv}	Δd				
	NB	NS	ZE	PS	PB
NB	NB	NS	NS	ZE	ZE
NS	NS	ZE	ZE	ZE	PS
ZE	ZE	ZE	PB	PS	PS
PS	ZE	PS	PB	PS	PB
PB	PS	ZE	PB	PB	PB

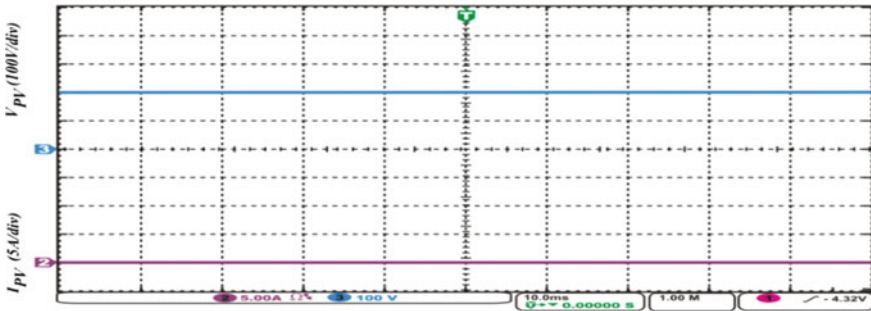


Fig. 5 Practical response of PV voltage and current during steady-state condition

3 Experimental Control Scheme and Results

To validate the effectiveness of the proposed grid-connected PV system, a hardware model is built. The practical components inverter, dSPACE DS 1104 kit, personal computer, programmable dc voltage source for PV simulator have been employed to test the MPPT as well as inverter control. The switching frequency of SEPIC converter and inverter has been maintained 20 and 15 kHz, respectively. LA25NP and LV25P sensors are used for current and voltage measurement of the components employed in the proposed experimental model. Using dSPACE control board, the gating signals to IGBT switch have been generated, which is connected to the power converter by interfacing card. The experimental results are depicted under steady as well as dynamic conditions.

3.1 Steady-State Operation

Under standard insolation and environmental temperature, the steady-state performance of the proposed PV power system is investigated. PV voltage and current which realizes the effectiveness of the proposed controller has been presented by Fig. 5.

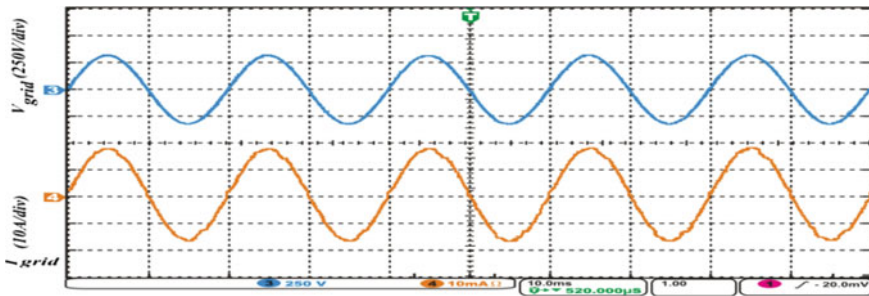


Fig. 6 Practical response of grid voltage and current under steady-state condition

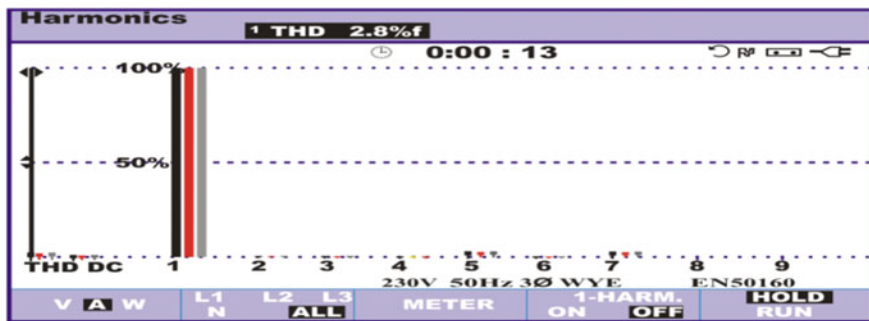


Fig. 7 THD spectrum of grid current under steady-state condition

The unity power factor is achieved by purely sinusoidal grid current, which is in phase with grid voltage. Figure 6 depicts the experimental responses of current injected by the inverter to the grid. Figure 7 depicts the experimental THD spectrum of grid current. It shows that grid current has 2.8% THD under steady-state condition which satisfy the IEEE 519 standard.

3.2 Dynamic Operation

The dynamic performance of grid-connected PV system is observed under variable environmental conditions. The experimental waveform of grid voltage and current has been demonstrated using Fig. 8. From practical results, it depicts the small variations in grid current during dynamic state. It also shows that the grid current has less harmonic distortion and high tracked power efficiency in small transient time which makes it in phase with grid voltage.

Figure 9 depicts the practical results of PV voltage and current under changing weather conditions. Initially, the PV system is disconnected and current through inverter has been controlled. The proposed MPPT method is compiled at this

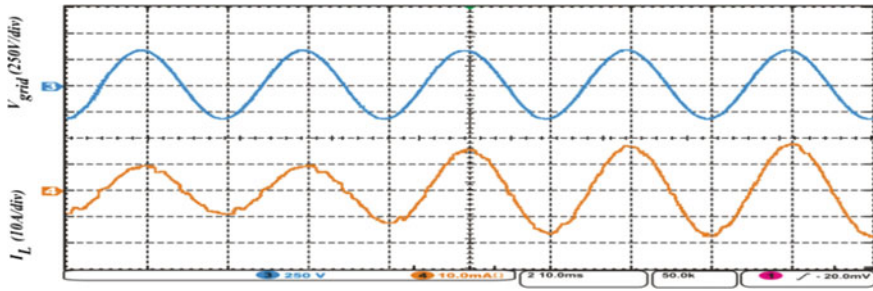


Fig. 8 Experimental response of grid voltage and current under dynamic condition

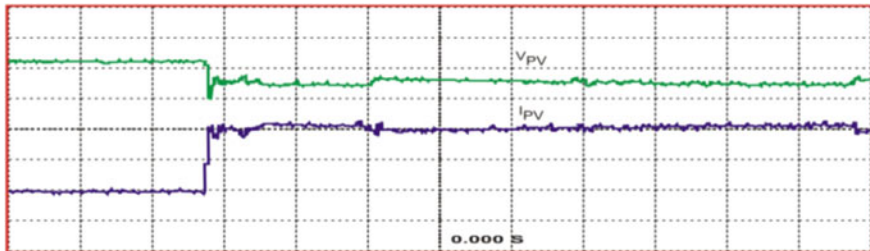


Fig. 9 Experimental result of PV voltage and current under dynamic-state condition



Fig. 10 Experimental performance of proposed controller

moment so that the PV operating point gets shifted to peak power point zone periodically with least oscillation around MPP.

At abrupt weather conditions, the proposed operation has been validated effectively using Fig. 10. Figure 11 depicts the experimental THD spectrum of grid current. It shows that grid current has 3.2% THD under variable weather condition which satisfy the IEEE 519 standard.

Also, Fig. 12 shows the comparison curve of experimental tracking efficiency of proposed and conventional grid-connected PV system control. The proposed controller makes the system high tracked efficient. The experimental results confirm that the proposed control algorithm working efficiently under steady and dynamic conditions.



Fig. 11 Practical THD spectrum of grid current under variable environmental condition

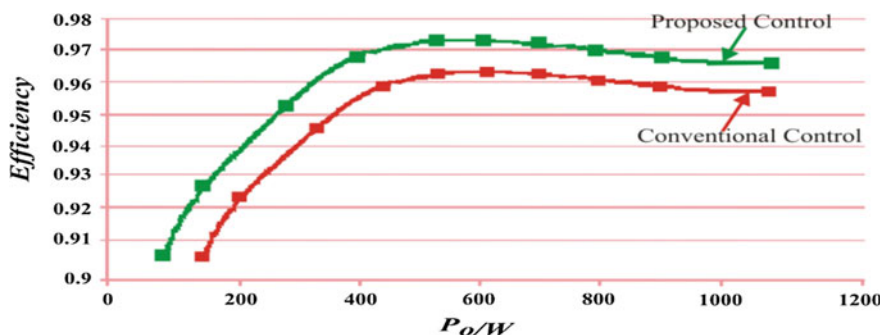


Fig. 12 Measured tracking efficiency curve

4 Conclusion

In this research work, the working capability of the proposed system with MPPT has been realized using dSPACE DS 1104 control board. The experimental response confirms that the proposed controller works efficiently under steady state as well as changing atmospheric conditions. The pure sinusoidal current injected to the grid justifies the stable and satisfactory operation of PV system at MPP.

References

1. Maiti, A., Mukherjee, K., Syam, P.: Design Methodology, Control and Performance of a Three-Phase Grid-Tie PV Inverter Under Maximum Power Point Tracking, pp. 382–386 (2016)
2. Sangwongwanich, A., Yang, Y., Blaabjerg, F.: Sensor Less Reserved Power Control Strategy for Two-Stage Grid-Connected Photovoltaic Systems (2016)

3. Singh, B., Jain, C., Goel, S., Chandra, A., Al-Haddad, K.: A Multifunctional Grid Tied Solar Energy Conversion System with ANF Based Control Approach (2016)
4. Skik, N., Abbou, A.: Nonlinear Control for MPPT and UPF of PV System Connected to the Grid (2016)
5. Mhiri, N., Ammous, K., Alahdal, A., Ammous, H.G.A.: Design of a New Analog Circuit for Maximum Power Point Tracking of Photovoltaic Panels (2016)
6. Lee, H.H., Dzung P.Q., Khoa, L.D., Phuong, L.M., Vu, N.T.D.: The New Maximum Power Point Tracking Algorithm Using ANN-Based Solar PV Systems, pp. 2179–2184 (2010)
7. Vinay, P., Mathews, M.A.: Modelling and Analysis of Artificial Intelligence Based MPPT Techniques for PV Applications, pp. 56–65 (2014)
8. Farswan, R.S., Fernandes, B.G.: A Low Cost and Reliable Single Stage Four Switch Photovoltaic System, pp. 1912–1918 (2014)
9. Saravanan, S., Babu N.R.: Performance Analysis of Boost & cuk Converter in MPPT Based PV System (2015)
10. Andrade, A.M.S.S., Schuch, L., Martins, M.L.D.S.: Photovoltaic battery charger based on the zeta converter. Analysis, Design and Experimental Results, pp. 379–384 (2015)

Cascaded Voltage Control of Three-Phase Four-Leg Inverter for OFF Grid Solar Photovoltaic Applications

Ikkurti Sai Chaitanya and Hanumath Prasad Ikkurti

Abstract Solar photovoltaics (PV) is one of the popular renewable energy sources in tropical countries like India which can help in supplementing the rising demand of electrical energy. DC input from solar PV strings needs to be converted into AC component both for ON and for OFF grid applications. Three-phase inverters are used for the above inversion when power levels are high. In OFF grid applications, task of maintaining stable terminal voltage across the loads lies with the inverter in the absence of utility grid. It also has to supply variety of balanced and unbalanced loads. In this paper, cascaded voltage control scheme, for a three-phase four-leg inverter, is developed. Parameters of the proportional resonant controllers (PR) are tuned using bode plot techniques. Simulations results are presented for operation under different loading conditions.

Keywords Cascaded voltage control · Four-leg inverter · PR controller
Solar inverter

1 Introduction

The constant growth of population and sharp rise in industrialization throughout the world is causing steep rise in energy demand, and the conventional energy sources cannot meet this in the long run due to their rapid depletion. Non-conventional sources are playing a key role in bridging this gap, and solar photovoltaics is one of the popular sources of energy because of its ease of harness and simplicity [1].

The electrical energy produced by the solar PV modules is DC (through photovoltaic effect) and has to be converted into AC, a task achieved through inverters.

I.S. Chaitanya (✉) · H.P. Ikkurti
CSIR-Central Mechanical Engineering Research Institute (CSIR-CMERI),
Durgapur, West Bengal, India
e-mail: isaichaitanya@gmail.com

H.P. Ikkurti
e-mail: hp_ikkurti@cmeri.res.in; hye.prasad@gmail.com

There are single-phase and three-phase inverters, and generally, the latter are used for higher-power applications. The conventional three-phase inverters consist of three legs with two power electronic switches in each leg and can be used for ON grid applications or for balanced loads in OFF grid applications. But in case of unbalanced loads, there is no path for the neutral current flow. Addition of an extra leg and connection of its midpoint to the neutral point of the load can provide the path for neutral current flow [2, 3].

The schematic of three-phase four-leg inverter is given in Fig. 1.

In the absence of utility grid, inverter has to maintain sinusoidal voltage at the load terminals, within the acceptable limits of THD for which an LC filter is added in each phase to filter out the high frequency switching harmonics, the design of which is given in the sections below.

In the available literature, voltage control of three-phase inverters is mainly performed in a-b-c or d-q-o coordinate systems [4]. References [5, 6] have utilized d-q-o rotating coordinate system, also called as synchronous reference frame control for achieving output voltage control. Independent per-phase control, also known as natural reference frame control, is introduced in Refs. [6, 7]. The authors in Ref. [6] have stated that in case of unbalance and nonlinearity in the system, the best strategy is to use the actual AC voltage and current for controller design. But the limitation of stationary reference frame comes from the fact that PI controller cannot remove the steady-state error since the steady-state variables in a-b-c coordinate are sinusoidal and the absence of the DC operating point makes it difficult for the controller to track the reference signal due to the time varying characteristics of the reference signal [6]. When it comes to d-q-o coordinate, the positive-sequence component shows constant DC values in channels d and q [5]. Hence, design of controllers in the d-q-o coordinate system is easier. But the drawback of d-q-o coordinate system is inability to perform in case of unbalanced and non-linear systems, where in the negative-sequence component travels in channels d and q at a frequency that is twice that of the fundamental. Reference [8] use proportional resonant (PR) controllers for a four-leg voltage source inverter. Reference [9] uses control scheme called scalar resonant-filter-bank-based output-voltage control. PR controllers can be tuned to provide high gain at the

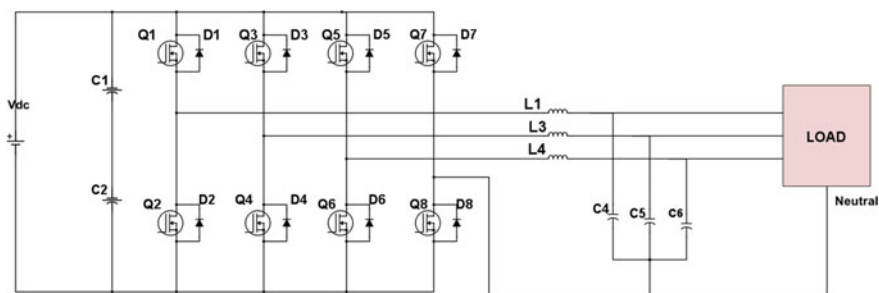


Fig. 1 Three-phase four-leg inverter

required frequency and can help in reducing steady error at the grid frequency. Reference [10] uses grid voltage feedforward control for current regulation in three-phase four-leg inverters. Sinusoidal PWM is the simplest PWM switching scheme and is simple to execute both in analogue or digital circuits [11–13].

Traditionally voltage control has been achieved using single feedback of the terminal voltage. While it is simple in implementation, it suffers from drawbacks like huge inrush currents because of absence of control on device currents. In this paper, cascaded voltage control is developed for the three-phase four-leg inverter wherein there will be an outer voltage loop providing reference to the inner current loop. This is a very robust control scheme wherein we have a control over the current that can potentially avoid damage caused by large current transients in case of direct voltage control. PR controllers are used in both the loops to obtain reference tracking.

The rest of paper is organized in the following lines. Section 2 covers the design of *LC* filter. Section 3 discusses the proposed control scheme and the design of controllers. Section 4 explains the simulation results. Section 5 contains conclusion. This is followed by references.

2 Design of *LC* Filter

Design specifications of the envisaged three-phase four-leg inverter are given in Table 1.

Filter inductor has been designed to keep the maximum possible ripple in one cycle of sinusoid to be 20% of the rated current at 37 A, as given in Eq. (1).

$$L = \frac{V_{dc}}{4 * F_{sw} * \Delta i_{p-p}} \quad (1)$$

Here the V_{dc} is the DC bus voltage of 720 V, F_{sw} Switching frequency and Δi_{p-p} is maximum current ripple taken as 20% of the rated current, i.e., 37 A. With these parameters, the value of inductor is obtained as 1.5 mH.

Table 1 Design specifications

Rated power	20 kW
Output voltage (per phase)	230 V
Rated current	37 A
Switching frequency	10 kHz
Output frequency	50 Hz
Voltage THD	<5%
Power factor	0.8 to unity
DC bus voltage	720 V

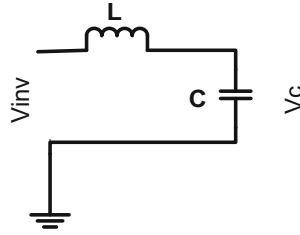


Fig. 2 LC filter circuit

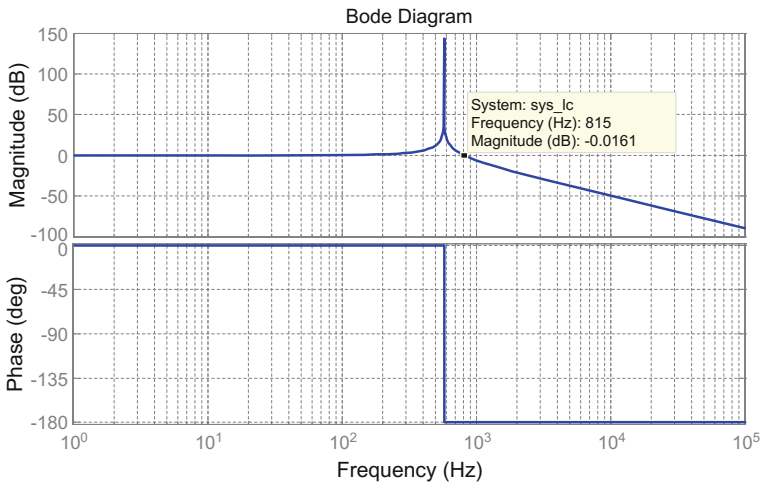


Fig. 3 Bode plot of LC filter circuit

For the output LC filter circuit shown in the Fig. 2 where L and C are filter inductor and capacitor, respectively, the transfer function between output and input voltage is obtained as

$$\frac{V_c(s)}{V_{inv}(s)} = \frac{1}{1 + s^2LC} \tag{2}$$

The value of the capacitor is selected in such a way that the cut-off frequency is decade lesser than the switching frequency (10 kHz), i.e., less than the 1000 Hz. We have selected a capacitance of 50 μF that provides a cut-off frequency of 815 Hz as can be seen in the bode plot of Fig. 3.

3 Proposed Control Scheme

As mentioned in the above sections, cascaded control scheme has been used in this paper, consisting of an inner current control loop and an outer voltage control loop. Mathematical modeling of three-phase four-leg inverter is represented by the equations governing the dynamics of different states as given in the below sections.

3.1 Mathematical Modeling of Three-Phase Four-Leg Inverter

Figure 4 shows the circuit diagram of the plant, where r_l is series resistance of the filter inductor (0.03Ω in our system), L is the filter inductance, C is the filter capacitance, $V_{inv}(t)$ is fundamental component of the inverter output voltage, $i_L(t)$ is inductor current, $V_c(t)$ is capacitor voltage, $i_c(t)$ is capacitor current, and $i_o(t)$ is load current. Plant transfer function can be derived from the following equations

$$V_{inv}(t) = r_l i_L(t) + L \frac{di_L(t)}{dt} + V_c(t) \tag{3}$$

$$i_L(t) = i_c(t) + i_o(t) = C \frac{dV_c(t)}{dt} + i_o(t) \tag{4}$$

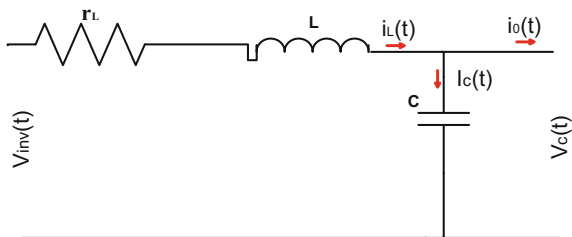
And applying Laplace transforms to the above Eqs. 3 and 4

$$\frac{V_{inv}(s) - V_c(s)}{r_l + sL} = I_L(s) \tag{5}$$

$$\frac{I_L(s) - I_o(s)}{Cs} = V_c(s) \tag{6}$$

Figure 5 shows the block diagram representation of the plant given by Eqs. 5 and 6. The block diagram parameters are represented in S domain.

Fig. 4 Circuit diagram of plant



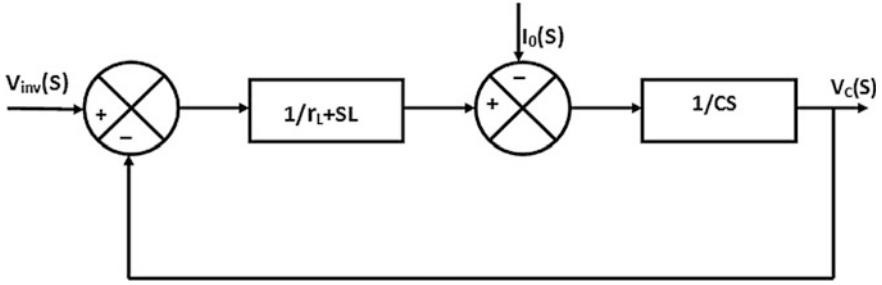


Fig. 5 Block diagram of the plant

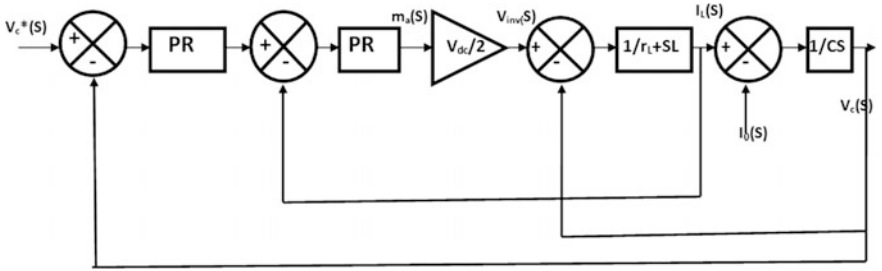


Fig. 6 Cascaded voltage control scheme of three-phase four-leg inverter

Figure 6 shows a cascaded voltage control scheme. Here, the actual capacitor voltage is taken as feedback from the plant and compared to reference voltage $V_c^*(s)$. The error is given to a controller whose output is the reference inductor current $I_L^*(s)$. This is in turn compared to the feedback of actual inductor current $I_L(s)$ and the error is given to a controller, whose output is modulation index $m_a(s)$. This modulation index multiplied by half the DC input voltage $V_{dc}/2$ gives the fundamental of the inverter output voltage $V_{inv}(s)$. Here, the states are inductor current $I_L(s)$ and capacitor voltage $V_c(s)$. Inductor current $I_L(s)$ is also the control input for outer voltage loop, whereas the output current $I_o(s)$ is the disturbance input. Modulation index is the control input for inner current loop, and the capacitor voltage $V_c(s)$ is the disturbance input.

This control scheme is used in all the three phases of four-leg inverter, independently. Modulation index obtained from the output of the controller is compared to a common high frequency carrier signal (its frequency is same as the switching frequency) to generate PWM signals. Fourth leg of inverter is always given a constant modulation index of zero, to ensure its potential difference is zero with respect to the midpoint of the DC bus. In this way, we can ensure that the fundamental of inverter pole voltage is same as the fundamental of inverter phase voltage, since the loads are connected between the midpoints of first three legs and the fourth leg.

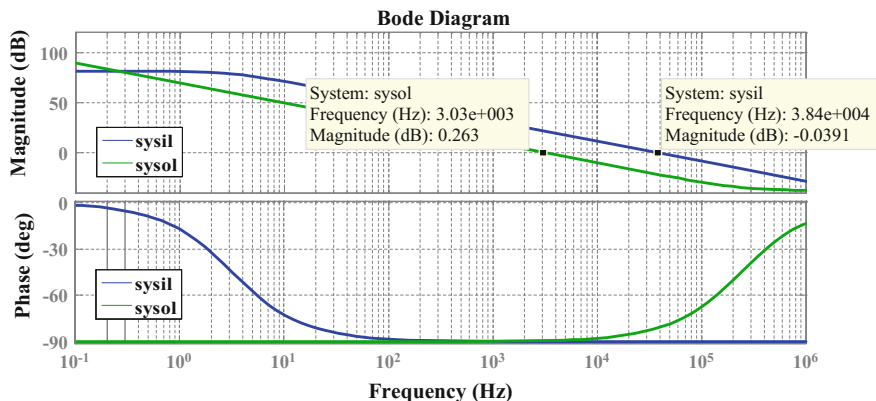


Fig. 7 Bode plot for the inner (sysil) and outer loop (sysol) plants

Table 2 Parameters of inner and outer loop PR controller

Parameter	Inner loop	Outer loop
K_p	0.0245	0.155
K_i	7.5	2.222
ω_c	$2 * \pi * 0.1$	$2 * \pi * 0.1$
ω_0	$2 * \pi * 50$	$2 * \pi * 50$

3.2 Design of Controller

Bode plots of inner and outer loop plants are given in Fig. 7. Blue color plot is for the inner loop transfer function between $I_L(s)$ and $m_a(s)$, while the red color plot is for the outer loop transfer function between $V_c(s)$ and $I_L(s)$. Effect of disturbance inputs is neglected while deriving the transfer function gains. Bandwidths of inner and outer loop plants are 38 and 3 kHz as can be seen from the bode plots.

In a cascaded control, inner loop gain bandwidth is generally taken to be less than a decade of the switching frequency, while the outer loop gain bandwidth to be further less than the inner loop gain bandwidth (at least by half). In our case, as the switching frequency is 10 kHz, inner loop bandwidth is chosen to be less than 1 kHz and the outer loop bandwidth to be less than 500 Hz. Proportional resonant (PR) controller is introduced in the system to achieve the above objectives.

PR controller provides very high gain at resonant frequency and almost no gain at other frequencies [9]. The structure of PR controller is taken as

$$K_p + \frac{2K_i\omega_c s}{s^2 + 2\omega_c s + \omega_0^2} \tag{7}$$

where K_p is proportional gain, K_i is integral gain, ω_c is the 3 dB gain frequency, and ω_0 is the resonant frequency of the system. Parameters of the inner and outer loop PR controllers are given in Table 2.

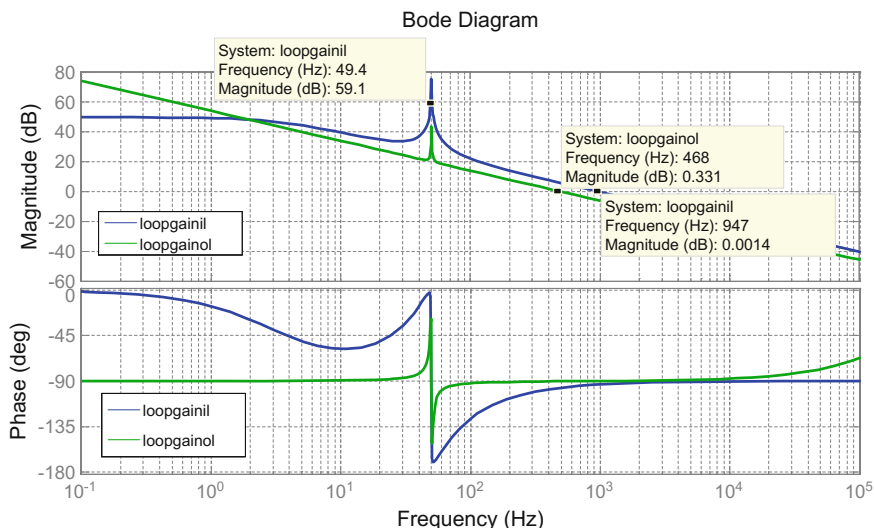


Fig. 8 Bode plot for the inner (loopgainil) and outer loop (loopgainol) gains with PR controllers

Bode plots of inner and outer loop gains are given in Fig. 8. Blue color plot is for the inner loop gain, while the red color plot is for the outer loop gain. Bandwidths of inner and outer loop gain plots are 947 and 468 Hz as can be seen from the bode plots, which are according to the selected criteria. Also we can observe a peak at the power frequency, i.e., 50 Hz.

4 Simulation Results

The simulation of three-phase four-leg inverter has been carried out using the PSIM software. Sinusoidal pulse width modulation has been used for the switching operation by including a dead time of 5 μ s between two switches of the same leg.

Figure 9 shows the reference and actual voltage and current wave forms of 'R' phase. Reference voltage (VC_Rref) of 325 V is given, and AC load resistance of 12 Ω /phase is considered. Initially, the inverter was started at no load and a load of 12 Ω is applied at 0.1 s. After 0.1 s, there is a momentary dip in the actual voltage (VC_R), but outer loop controller increases the current reference of inner loop (IL_Rref) and allows the actual voltage (VC_R) to settle to its reference value at around 0.4 s. At 0.6 s again the load is removed and we can see there is momentary swell in the voltage which again settles back to its reference value at around 0.8 s. This establishes the efficacy of the developed control algorithms in maintaining the tracking of voltage under different load disturbances. The change in loading is reflected in the load current $I(RL_R)$ which turned to zero on sudden turn OFF. It can also be observed that the inner loop is faster than outer loop as reflected in the

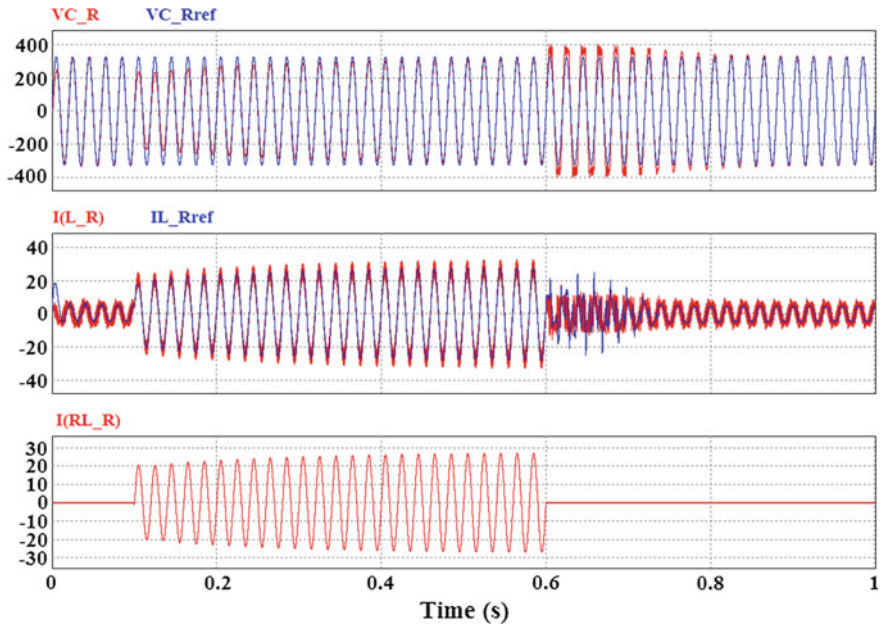


Fig. 9 Reference and actual 'R' phase voltage and currents

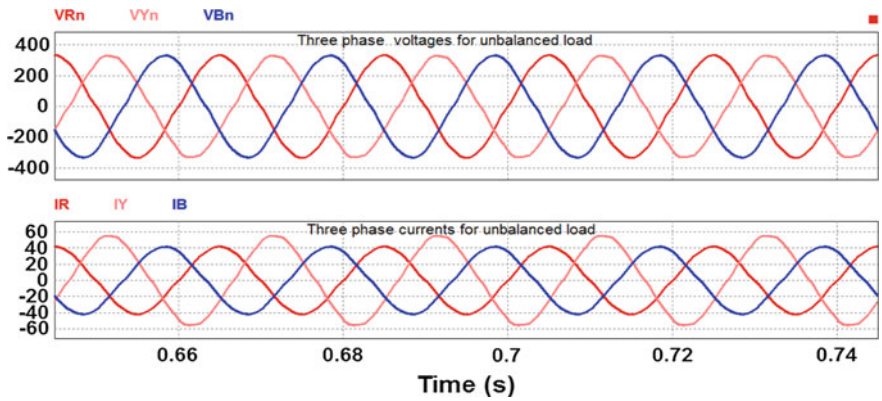


Fig. 10 Three-phase voltages and currents of unbalanced resistive load (V_{Rn} , V_{Yn} , V_{Bn} , I_R , I_Y , I_B)

fast tracking of currents in comparison with the voltages. Also there are no inrush currents because of inherent control on the phase currents.

Figure 10 shows the output voltages and currents of the three-phase four-leg inverter for unbalanced load under steady state. The change of the current in the unbalanced phase can be observed, but the magnitudes of the voltages are equal in

Table 3 % THD under balanced and unbalanced loads

Phase	% THD balanced loads	% THD unbalanced loads
V_{Rn}	4.57	4.32
V_{Yn}	4.34	4.42
V_{Bn}	4.46	4.62

all phases, because the controller has been designed and operated in closed loop mode in order to maintain the voltage irrespective of the disturbances.

Table 3 shows the total harmonic distortion percentage three-phase voltages with balanced and unbalanced loads.

5 Summary/Conclusion

A cascaded voltage control scheme has been developed for the voltage control of three-phase four-leg inverter. Bode-plot-based techniques are used to tune the inner and outer loop PR controllers. The outer loop bandwidth (468 Hz) is designed to be half of the inner loop bandwidth (947 Hz). The efficacy of the developed control scheme has been verified through numerical simulation by PSIM software. It can be observed that the voltage at the load is being maintained at the reference value irrespective of load disturbances due to control action of the PR controllers. The main objective of the closed loop control has been fulfilled, and the total harmonic distortion is also observed to be less than 5%.

Acknowledgements The authors express their gratitude to Council of Scientific and Industrial Research (CSIR), New Delhi, for funding this project under TAPSUN program.

References

1. Akhtar, M.A., Ikkurti, H.P.: A new controller for maximum power extraction from photovoltaic system using phase modulated converter. In: Proceedings of IEEE International Conference on Advances in Power Conversion and Energy Technologies, pp. 1–6. Andhra Pradesh, India (2012)
2. Zhang, R., Boroyevich, D., Prasad, V.H., Mao, H.C., Lee, F.C., Dubovsky, S.: A three-phase inverter with a neutral leg with space vector modulation. In: Proceedings of Twelfth Annual Applied Power Electronics Conference and Exposition, vol. 2, pp. 857–863 (1997)
3. Griffith, D.C.: Neutral wire current monitoring for three-phase four-wire power distribution system. Patent US 5182547A (1993)
4. Blaabjerg, F., Teodorescu, R., Liserre, M., Timbus, A.V.: Overview of control and grid synchronization for distributed power generation systems. *IEEE Trans. Industr. Electron.* **53** (5), 1398–1409 (2006)
5. Vechiu, I., Curea, O., Camblong, H.: Transient operation of a four-leg inverter for autonomous applications with unbalanced load. *IEEE Trans. Power Electron.* **25**(2), 399–407 (2010)

6. Zhang, R.S.: High performance power converter systems for nonlinear and unbalanced load/source. Ph.D. Dissertation, Virginia Polytechnic Institute and State University (1998)
7. Zhou, K., Wang, D.: Relationship between space-vector modulation and three-phase carrier-based PWM: a comprehensive analysis [three-phase inverters]. *IEEE Trans. Industr. Electron.* **49**(1), 186–196 (2002)
8. De, D., Ramanarayanan, V.: A proportional multiresonant controller for three-phase four-wire high-frequency link inverter. *IEEE Trans. Power Electron.* **25**(4), 899–906 (2010)
9. Demirkutlu, E., Çetinkaya, S., Hava, A.M.: Output voltage control of a four-leg inverter based three-phase UPS by means of stationary frame resonant filter banks. In: *Proceedings of IEEE International Electric Machines & Drives Conference*, vol. 1, pp. 880–885. Antalya-Turkey (2007)
10. Dong, G., Ojo, O.: Current regulation in four-leg voltage-source converters. *IEEE Trans. Industr. Electron.* **54**(4), 2095–2105 (2007)
11. Hava, A.M., Cetin, N.O.: A generalized scalar PWM approach with easy implementation features for three-phase, three-wire voltage-source inverters. *IEEE Trans. Power Electron.* **26**(5), 1385–1395 (2011)
12. Kim, J.H., Sul, S.K.: A carrier-based PWM method for three-phase four-leg voltage source converters. *IEEE Trans. Power Electron.* **19**(1), 66–75 (2004)
13. Holtz, J.: Pulsewidth modulation for electronic power conversion. *Proc. IEEE* **82**(8), 1194–1214 (1994)

Study on the Effect of Tilt on the Variation of Aperture Area Shading in a Linear Fresnel Reflector Field for Two Different Configurations

Gaurab Bhowmick and Subhasis Neogi

Abstract Linear Fresnel reflector (LFR) consists of parallel rows of reflectors that direct the incident solar radiation on to a common focus. A linear receiver placed at the common focus absorbs the reflected solar radiation. Due to continuous change in Sun's position in sky, continuous tracking of reflectors is required that leads to variable shading losses. Portion of reflector area gets shaded due to adjacent reflector row, and the amount of shading varies throughout the day and year. In this work, analytical expression has been used to determine the shaded aperture areas for two different system configurations. Monthly and yearly average values of shading loss factor at different system tilt angles have been plotted and compared.

Keywords Linear Fresnel reflector · Shading · Tilt · MATLAB
Shading factor

1 Introduction

In a linear Fresnel reflector (LFR), parallel rows of horizontal reflectors direct the incident solar beam radiation on to a common focal plane. A linear receiver placed at the common focal plane intercepts the reflected solar radiation from the reflector field [1]. Advantages of linear Fresnel reflector (LFR) over parabolic trough collectors (PTC) include easy maintenance, fixed receiver, no requirement of high pressure fluid joints, low structural requirement, flat reflectors, high ground utilization and many more [2]. Annual performances of linear Fresnel reflectors (LFR) are less as compared to parabolic trough collectors (PTC) due to enhanced optical and thermal losses [3]. Portion of reflector area gets shaded by adjacent reflector rows due to daily variation of Sun's position in the sky [4]. Thus, shading loss forms an important part in the

G. Bhowmick (✉) · S. Neogi
School of Energy Studies, Jadavpur University, Kolkata, India
e-mail: gaurabh.bhowmick@gmail.com

S. Neogi
e-mail: neogi_s@yahoo.com

overall optical efficiency of the system. It has been estimated that the North–South-oriented LFR system attains the highest annual available energy than East–West-oriented LFR system [5]. Estimation of monthly and annual average shading loss for different system configuration and tilt angles has been carried out in this work.

2 Methodology

Linear Fresnel reflector (LFR) consisting of n number of parallel reflector rows and an elevated linear receiver at a height H above reflector plane has been considered for this study. The system parameters mainly pitch P (center-to-center distance between adjacent reflector rows), width of each reflector row W and length of each reflector L were defined for this study (Fig. 1). The system was considered to be south facing (N–S oriented), and individual reflector tracked the Sun (E–W) throughout the day.

Total n rows of reflectors divided into section of $n/2$ rows were placed on both the sides of the receiver. Each half is denoted by East field and West field, respectively (Fig. 2). The angle λ_t is the angle in transversal plane at any instant of time t between the vertical to the plane of reflectors and the projection of incident ray on the transversal plane as shown in Fig. 2. Its expression [5] can be defined as in Eq. (1).

$$\lambda_t = \tan^{-1} [\sin(\gamma_{\text{sun},t}) \tan(\theta_{\text{zen},t})] \quad (1)$$

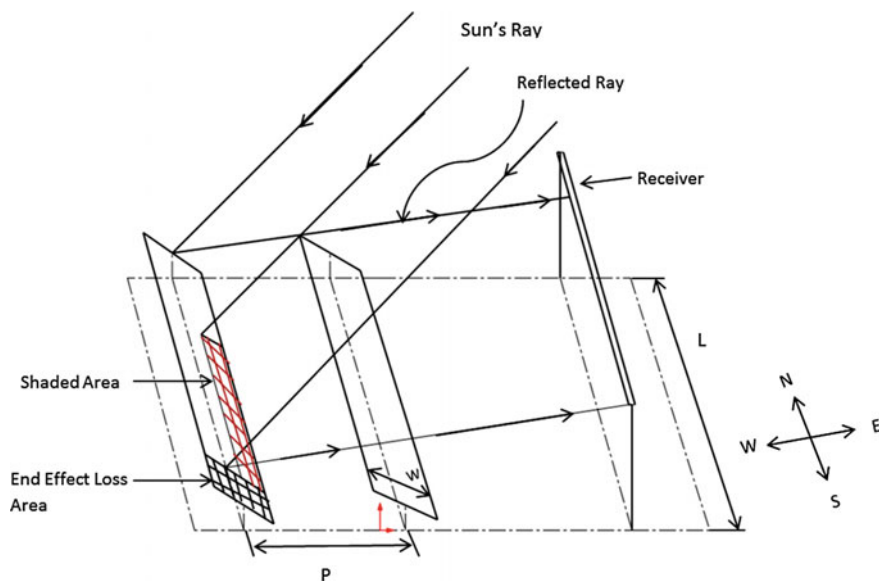


Fig. 1 Shading of one reflector row due to adjacent reflector row

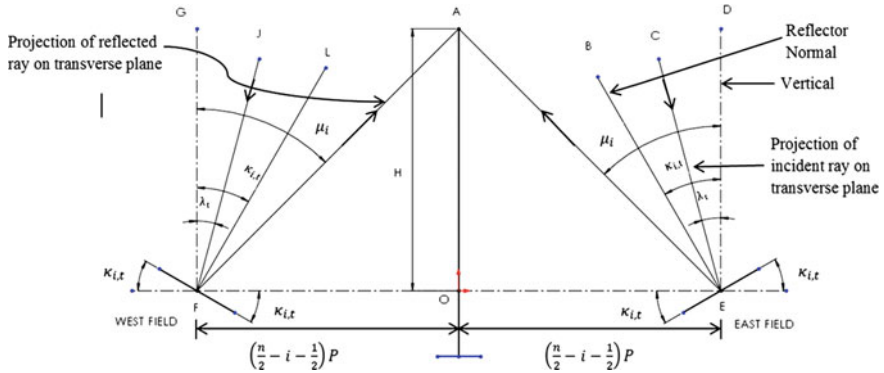


Fig. 2 View of LFR along the tracking axis

The angle μ_i is the angle in transversal plane between the vertical to the plane of reflectors and the projection of the reflected ray of the i th reflector on transversal plane as shown in Fig. 2. The expression [5] can be defined as in Eq. (2).

$$\mu_i = \tan^{-1} \left[\frac{(\frac{n}{2} - i + \frac{1}{2})P}{H} \right] = \tan^{-1} \left[\frac{(\frac{n}{2} - i + \frac{1}{2})P/W}{H/W} \right] \quad (2)$$

As the individual reflectors are tracking the Sun, tracking angle ($\kappa_{i,t}$) can be written as in Eq. (3).

$$\kappa_{i,t} = \left| \frac{\lambda_t + \mu_i}{2} \right| \quad (3)$$

The surface azimuth angle ($\gamma_{\text{surface},i,t}$) of the i th reflector row can be obtained from Eq. (4).

$$\gamma_{\text{surface},i,t} = \begin{cases} 90^\circ, & \text{if } \lambda_t + \mu_i > 0^\circ \\ 270^\circ (-90^\circ), & \text{if } \lambda_t + \mu_i < 0^\circ \end{cases} \quad (4)$$

Let $L_{\text{shade},i,t}$, $W_{\text{shade},i,t}$ and $A_{\text{shaded},i,t}$ be defined as the length, width and area of the shaded portion of the i th reflector row at any instant of time t , respectively.

Following [5], the expressions in equation number (5), (6), (7) and (8) for $A_{\text{shaded},i,t}$, $L_{\text{shade},i,t}$, $W_{\text{shaded},i,t}$ and shading factor have been derived, respectively.

$$A_{\text{shaded},i,t} = \begin{cases} 0, & \text{if } \gamma_{\text{sun},t} < 180^\circ \text{ and } i = n \\ 0, & \text{if } 180^\circ < \gamma_{\text{sun},t} < 360^\circ \text{ and } i = 1 \\ L_{\text{shade},i,t} W_{\text{shade},i,t}, & \text{otherwise} \end{cases} \quad (5)$$

$$L_{\text{shade},i,t} = [L_{\text{mirror}} - P |\tan(\gamma_{\text{sun},t} - 90)| - L_{\text{end-length},i,t}]^+ \quad (6)$$

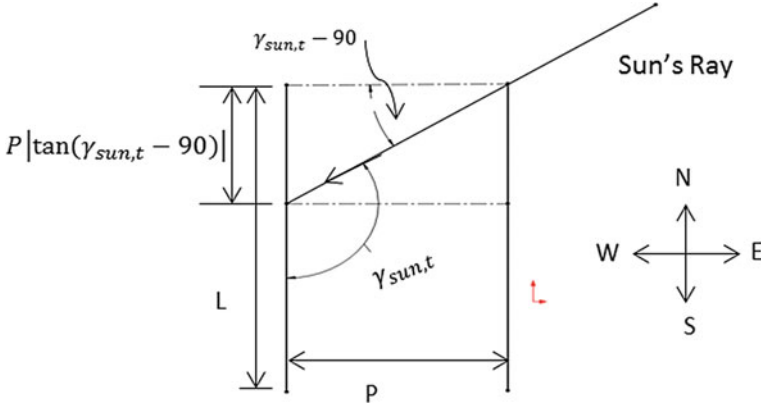


Fig. 3 Estimation of $P|\tan(\gamma_{sun,t} - 90)|$ term

where $L_{end-length,i,t}$ is the end effect loss length for i th reflector at any instant of time t . The term $P|\tan(\gamma_{sun,t} - 90)|$ can be obtained as seen in Fig. 3.

$$W_{shaded,i,t} = \begin{cases} \left[\frac{W}{2} - \frac{2P \cos \lambda_t - W \cos \{ \kappa_{i+1,t} \sin(\gamma_{surface,i+1,t}) - \lambda_t \}}{2 \cos \{ \kappa_{i,t} \sin(\gamma_{surface,i,t}) - \lambda_t \}} \right]^+, & \text{if } (\gamma_{sun,t} \leq 180^\circ) \\ \left[\frac{W}{2} - \frac{2P \cos \lambda_t - W \cos \{ \kappa_{i-1,t} \sin(\gamma_{surface,i-1,t}) - \lambda_t \}}{2 \cos \{ \kappa_{i,t} \sin(\gamma_{surface,i,t}) - \lambda_t \}} \right]^+, & \text{if } (180^\circ < \gamma_{sun,t} \leq 360^\circ) \end{cases} \quad (7)$$

$$\text{Shading Factor (SF)} = \frac{\left[\int_{t_1}^{t_2} (\sum_{i=1}^n A_{shaded,i}) dt \right]}{\left[\int_{t_1}^{t_2} (\sum_{i=1}^n A_{reflector,i}) dt \right]} \quad (8)$$

Positive sign in the above equations denotes that only the positive output values have to be considered. In this study, two different configurations (Case 1: constant width and pitch reflectors, Case 2: variable width and pitch reflectors) as shown in Table 1 were considered for the analysis of monthly and annual average shading factor at different system tilt angles throughout the year at given latitude (ϕ). A total of $n = 22$ reflectors was considered. Subsequently the value of width and pitch of i th reflector was calculated [6]. The incidence angle of the system at different tilt angles can be obtained by considering the system to be at a fictitious latitude ($\phi - \beta$), where β is the system tilt angle [7]. The expression for incidence angle (tilted system) can be given as in Eqs. (9) and (10).

Table 1 Dimension parameters for LFR system configuration

Case	Width (W) (m)	Pitch (P) (m)	Length (L) (m)
Case 1	0.05	0.075	1.8
Case 2	0.0553	0.1641	1.8
	0.062	0.1732	1.8
	0.0698	0.182	1.8
	0.0788	0.1902	1.8
	0.0894	0.1972	1.8
	0.1018	0.2026	1.8
	0.1165	0.2055	1.8
	0.1336	0.205	1.8
	0.1528	0.2009	1.8
	0.1722	0.1949	1.8
	0.1875	0.3941	1.8
	0.1875	0.3941	1.8
	0.1722	0.1949	1.8
	0.1528	0.2009	1.8
	0.1336	0.205	1.8
	0.1165	0.2055	1.8
	0.1018	0.2026	1.8
	0.0894	0.1972	1.8
0.0788	0.1902	1.8	
0.0698	0.182	1.8	
0.062	0.1732	1.8	
0.0553	0.1641	1.8	

$$\cos \theta = \cos(\varnothing - \beta) \cos \delta \cos \omega + \sin(\varnothing - \beta) \sin \delta \text{---Northern hemisphere} \quad (9)$$

$$\cos \theta = \cos(\varnothing + \beta) \cos \delta \cos \omega + \sin(\varnothing + \beta) \sin \delta \text{---Southern hemisphere} \quad (10)$$

In order to obtain the year round variation of shading effect loss, a MATLAB code was written in MATLAB script and compiled using MATLAB compiler.

3 Results and Discussion

In this study, shading factor (SF) has been calculated for two system configurations on monthly and yearly average for different system tilt angles. Kolkata (22.53°N, 88.33°E), India, has been chosen as the site location for this study. In order to analyze the monthly variation of shading, shading factor (SF) has been plotted for

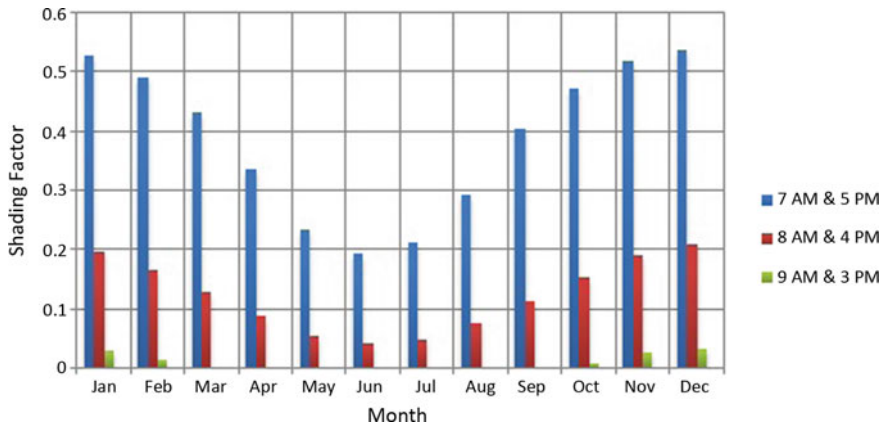


Fig. 4 Case 1 (Tilt = 0°), monthly variation of shading factor

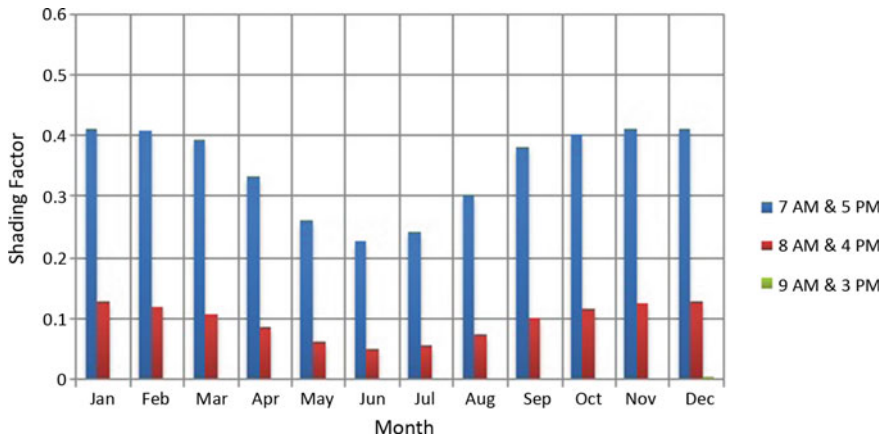


Fig. 5 Case 1 (Tilt = 10°), monthly variation of shading factor

the two different system configurations with different tilt angles as shown in Figs. 4, 5, 6, 7, 8 and 9. Figures 10 and 11 show the yearly average variation of shading factor (SF) with time of day and different system tilt angles for fixed and variable width, pitch reflector system. It is seen that for horizontal system with constant width and pitch reflector, the monthly shading factor (SF) decreases from January to June and then increases from July to December as shown in Fig. 4. Similarly, the system with 10° tilt follows the same trend as the horizontal system as shown in Fig. 5.

While for the system with 22.5° tilt, the change of monthly shading factor (SF) is relatively less throughout the year as shown in Fig. 6. For both horizontal and 10° tilt system with variable width and pitch reflectors, there is a decrease in shading

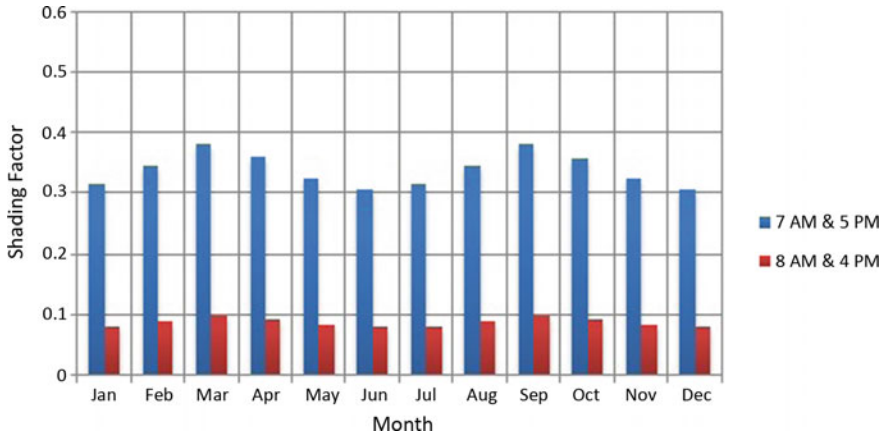


Fig. 6 Case 1 (tilt = 22.5°), monthly variation of shading factor

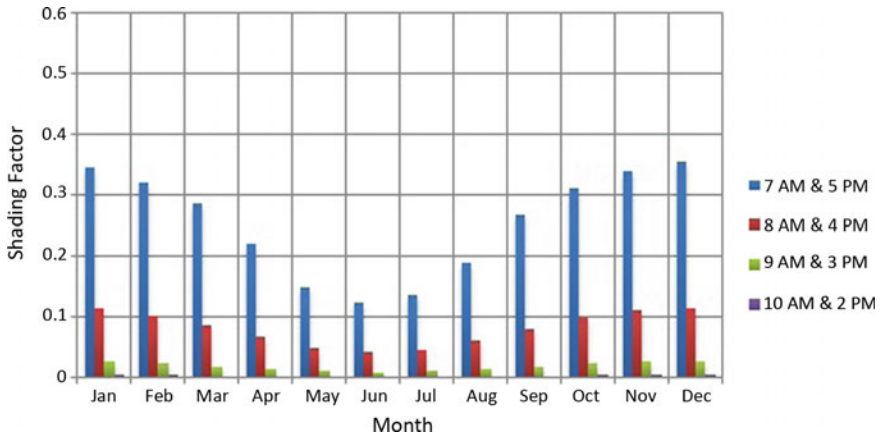


Fig. 7 Case 2 (tilt = 0°), monthly variation of shading factor

factor (SF) from January to June and increase from July to December as shown in Figs. 7 and 8. While the monthly shading factor (SF) does not change much for 22.5° tilt as shown in Fig. 9.

It is also seen that for both the system configurations, maximum shading loss occurs around 0700 and 1700 h, while it is relatively less around 0800 and 1600 h. Shading losses tend to zero after 0900 and up to 1500 h. For both the systems with tilt, the shading factor (SF) decreases significantly as compared with the horizontal system. Even the maximum values of shading factor (SF) for system with constant width and pitch reflectors are relatively higher than variable width and pitch reflector system. This is because the variable width and pitch reflector system optimize the spacing in between adjacent reflector rows to reduce shading and

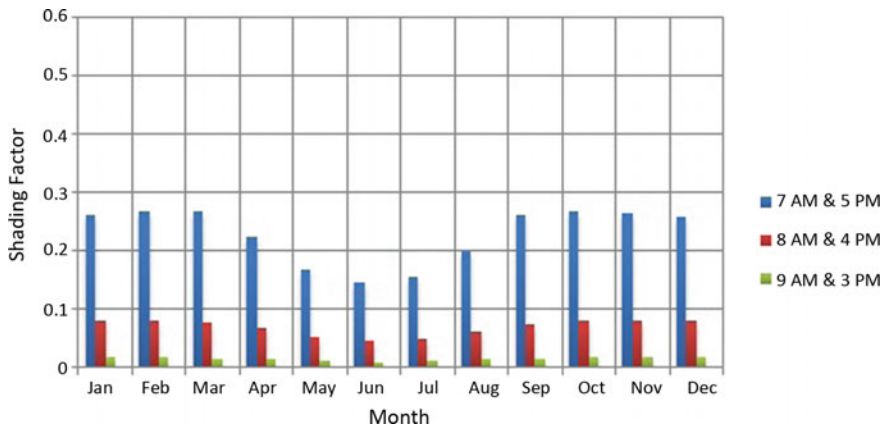


Fig. 8 Case 2 (tilt = 10°), monthly variation of shading factor

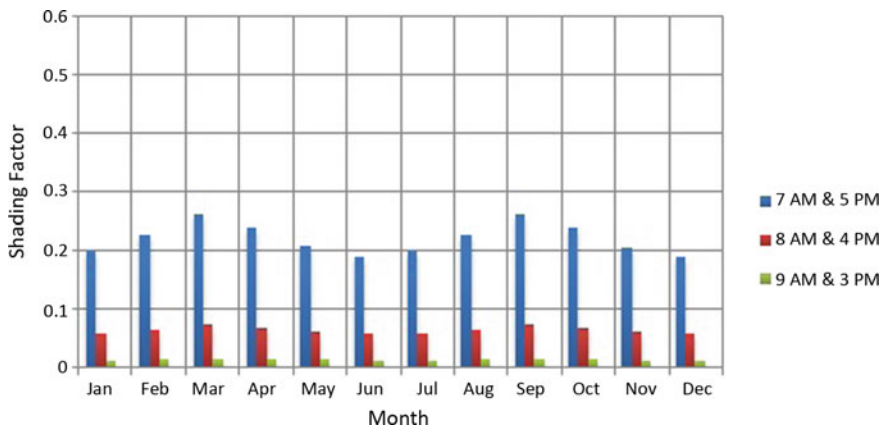


Fig. 9 Case 2 (tilt = 22.5°), monthly variation of shading factor

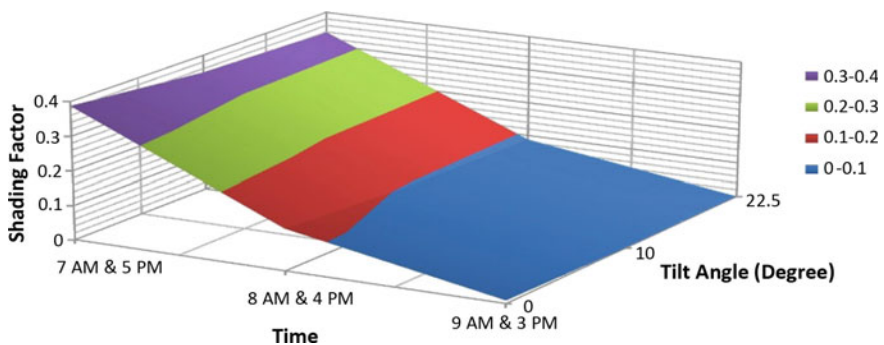


Fig. 10 Case 1 (yearly average shading factor)

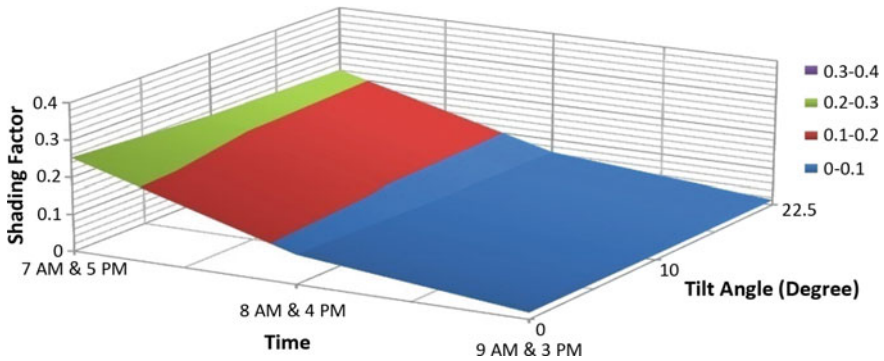


Fig. 11 Case 2 (yearly average shading factor)

blocking effects. The reason for decrease in shading factor (SF) with tilt is because of the change in incidence angle of Sun's rays. The angle of incidence decreases with increase in tilt which in turn reduces shaded length of reflector and vice versa. The change of shaded reflector length changes the shaded area which subsequently changes the shading factor (SF).

4 Conclusion

In this present work, the variation of monthly and yearly average shading loss in North–South-oriented linear Fresnel reflector (LFR) fields has been analyzed. It is seen that for both the system configuration, monthly shading factor (SF) decreases gradually from January to June and again increases from July to December. The shading loss decreases with increase in tilt angle and vice versa for a given latitude. For the system with constant width and pitch reflectors, shading loss is higher as compared to the variable width and pitch reflector system. Thus, an optimum system configuration can be selected based on given latitude with reduced shading losses.

References

1. Manikumar, R., Palanichamy, R., Valan Arasu, A.: Heat transfer analysis of an elevated linear absorber with trapezoidal cavity in the linear fresnel reflector solar concentrator system. *J. Ther. Sci.* **24**, 90–98 (2015)
2. Moghimi, M.A., Craig, K.J., Meyer, J.P.: Optimization of a trapezoidal cavity absorber for the linear Fresnel reflector. *Sol. Ener.* **119**, 343–361 (2015)
3. Montes, M.J., Rubbia, C., Abbas, R., Martinez-Val, J.M.: A comparative analysis of configurations of linear Fresnel collectors for concentrating solar power. *Energy* **73**, 192–203 (2014)

4. Sharma, V.: Hourly and monthly variation in shading and blocking of aperture area in a linear Fresnel reflector field. *Ener. Proc.* **48**, 233–241 (2014)
5. Sharma, V., Nayak, J.K., Kedare, S.B.: Effects of shading and blocking in linear Fresnel reflector field. *Sol. Ener.* **113**, 114–138 (2015)
6. Mathur, S.S., Kandpal, T.C., Negi, B.S.: Optical design and concentration characteristics of linear Fresnel reflector solar concentrators-I, mirror elements of varying width. *Ener. Conv. Manage.* **31**(3), 205–219 (1991)
7. Duffie, J., Beckman, W.: *Solar Engineering of Thermal Processes*, 2nd edn. Wiley (1991)

Design Analysis and Implementation of MPPT Using PSIM

R. Shivrudraswamy, Aditya Nandan Shukla and C.B. Chandrakala

Abstract Solar energy is one of the highly available non-conventional and clean energy sources. Harnessing the power from the solar panel is costlier than other sources. The maximum power point tracking (MPPT) helps maximum power utilization and also improves the system efficiency of PV panel and therefore reduces the overall cost of system. Normally, the voltage and current relationship is nonlinear and maximum power point (MPP) varies according to the solar irradiance. The MPPT consists of a DC–DC converter and a MPPT algorithm. This paper presents a simulation of perturb and observe (P&O) MPPT algorithm and SEPIC converter by using a simulation software powersim (PSIM). The simulation shows that the DC–DC converter extracts maximum power from the panel using MPPT algorithm.

Keywords DC–DC converter • Fossil fuel • MPPT • Photovoltaic P&O • SEPIC

1 Introduction

The main power source in India is the thermal power plant. These power plants need fossil fuel. If it takes thousands of years with favorable condition to create fossil fuel, and this supply of fossil fuel is also limited. Renewable energy is one of the alternate sources which can meet energy demands. This alternate source is available and is a clean source of energy. The type of renewable energy available in abundance is solar energy. Converting the solar energy into electrical energy is

R. Shivrudraswamy (✉) · A.N. Shukla
Department of Electrical & Electronics, MIT, Manipal, India
e-mail: shivarudraswamy.r@manipal.edu

A.N. Shukla
e-mail: aditya.shukla581@gmail.com

C.B. Chandrakala
Department of I&CT, MIT, Manipal, India
e-mail: chandrakala.cb@manipal.edu

costlier; at the same time, efficiency of PV is very low to increase the efficiency of the overall PV system and also per unit cost of energy generation the algorithm is applied to extract maximum power available from the PV module; this algorithm is known as maximum power point tracking (MPPT) algorithm. Power generation from photovoltaic module totally depends upon irradiance levels, temperature and also on load condition, so current and power characteristic of photovoltaic module is highly nonlinear [1].

In recent years, many techniques to track maximum power have been proposed such as hill-climbing, fractional open circuit voltage control, perturb and observe, incremental conductance (INC), neural network control and fuzzy control based. These algorithms are varying in terms of emerging speed, simplicity, effectiveness, sensor required and cost. The most common algorithm used to track maximum power point (MPP) due to its simplicity, effectiveness and merging speed based on current and voltage sensing incremental conductance (INC) and perturb and observe (P&O) is used to [2].

There are also many converters which can be used as DC–DC converter for MPPT, and some of the commonly used converters are buck, boost, buck-boost, Cuk and SEPIC converter [3]. As SEPIC converter has lot of advantages over other converter like less ripple and input and out isolation.

From the above discussion it can be concluded that one of the most efficient and simple algorithms to track maximum power from PV panel is perturb and observe (P&O), and converter which can be used to implement that algorithm is SEPIC converter for having advantages over other converters.

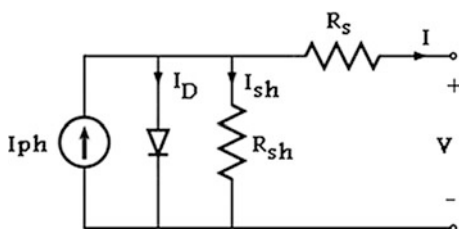
2 PV Module Characteristics

R_s series resistance introduced as to consider the voltage drop and internal losses due to flow of current (Fig. 1).

R_{sh} shunt resistance across diode takes into account the leakage current to the ground when diode is in reversed-biased condition.

This model neglects recombination effect of diode. So the equivalent model output current is given by:

Fig. 1 PV cell equivalent model [4]



$$I = I_{\text{ph}} - I_0 \left(e^{\frac{V + IR_s}{nV_T}} - 1 \right) - \frac{V + IR_s}{R_{\text{sh}}} \quad (1)$$

where

I Output current of PV cell

I_{ph} Incidence of light generates photocurrent

I_0 Diode reverse bias saturation current

V_t Thermal Voltage of PV module = $\frac{kT}{q}$

k Boltzmann's constant = 1.381×10^{-23}

T Temperature

q Charge of electron = 1.602×10^{-19}

n Ideality factor, which is a measure of how closely diode follow ideal diode equation.

The light generated by the module depends linearly on solar irradiation and is also influenced by temperature according to equation,

$$I_{\text{ph}} = (I_{\text{ph},n} + K_i \Delta T) \frac{G}{G_n} \quad (2)$$

where,

$I_{\text{ph},n}$ Light generated current of module at STC

ΔT $T_a - T_r$

T_a ambient temperature (K)

T_r Room temperature (K)

K_i Short circuit temperature coefficient

G Irradiance (W/m^2)

G_n Irradiance at STC ($1000 \text{ W}/\text{m}^2$).

The diode saturation current is given by,

$$I_0 = I_{0,n} \left(\frac{T_a}{T_r} \right)^{\frac{3}{n}} \left[\frac{qE_g}{nk} \left[\frac{1}{T_r} - \frac{1}{T_a} \right] \right] \quad (3)$$

where,

E_g Band gap energy (1.12 for poly-Si at STC)

$I_{0,n}$ Nominal saturation current at STC.

The nominal saturation current is given by,

$$I_{0,n} = \frac{I_{\text{sc},n}}{\left[e^{\frac{V_{\text{oc},n}}{nV_{T,n}}} - 1 \right]} \quad (4)$$

Fig. 2 Expected P-V and I-V curves [5]

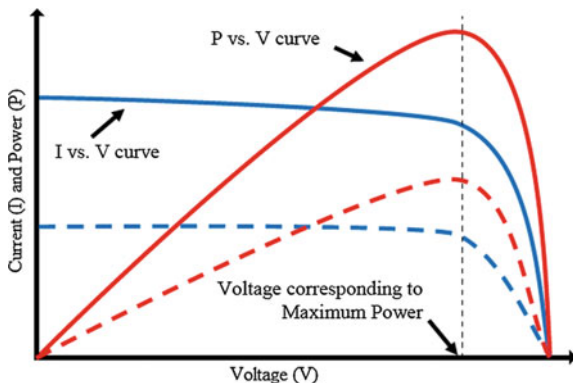


Table 1 Parameters used in the model

Parameters	Value
Maximum power of module	50 W
Open circuit voltage of module (V_{oc})	22.1 V
SC current of module (I_{sc})	2.95 A
Number of cells in series in a module	36
Standard temperature	25 °C
Temperature coefficient	0.034
Shunt resistance of the module (R_{sh})	1000 Ω
Series resistance of the module (R_s)	0.0058 Ω

where,

$I_{sc,n}$ Short circuit current at STC

$V_{oc,n}$ Open circuit voltage at STC

$V_{T,n}$ Thermal Voltage at STC.

Typically, short circuit current, open circuit voltage, maximum power point voltage and current are provided by the manufacturer. Using these values, the other unknown parameter of PV panel is considered. The expected P-V and I-V curves from the solar module is given in Fig. 2 (Table 1).

3 Single-Ended Primary Inductance Converter (SEPIC)

The output of SEPIC converter can be higher or lower than the input voltage and also the output is not inverted as in Cuk converter. Inductors are used to transfer energy from input to output, and both input and output are isolated by coupling capacitor. The SEPIC converter is shown in Fig. 3. And its design parameters are

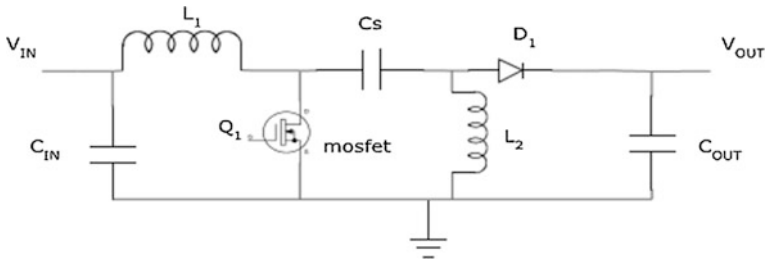


Fig. 3 SEPIC converter [6]

Table 2 SEPIC converter design parameter

Parameters	Values
Input voltage	5–25 V
Output voltage	15 V
Frequency	100 kHz
Series inductor	47 μ H
Shunt inductor	47 μ H
Series capacitor	10 μ F
Output capacitor	33 μ F
Input capacitor	1000 μ F

given in Table 2. The analysis is performed with the assumption that all components are ideal and C_s and C_{OUT} are large enough so that voltage is constant across them.

4 Perturb and Observe (P&O) Algorithm

In this method, the controller perturbs voltage by small amount and then measures corresponding power. If the power increases, further adjustments are made in the same direction till the power no longer increases. This method is called P&O method (Fig. 4).

The voltage to the cell is initially increased, if power output from the PV module increases, the voltage is increased continuously until the power output starts decreasing. As the power starts decreasing the voltage to the cell is decreased till it reaches the maximum power [8, 9]. This power is continued till MPPT is reached, resulting in oscillation around the maximum power point. The output power curve of the PV module is a function of voltage, at constant temperature and irradiance. If the operating point of PV module is away from MPP, the operating voltage is perturbed by small amount and change in power is observed. If the change in power is positive, then voltage is further perturbed in same direction to move operating

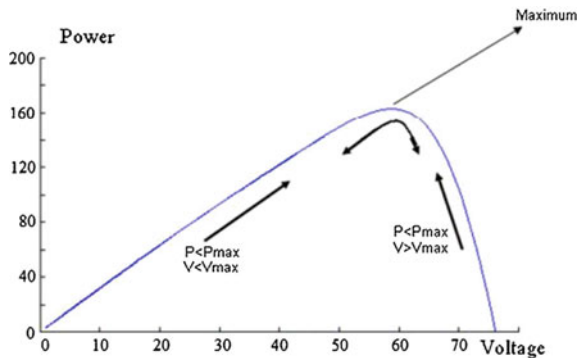


Fig. 4 P&O power curve [7]

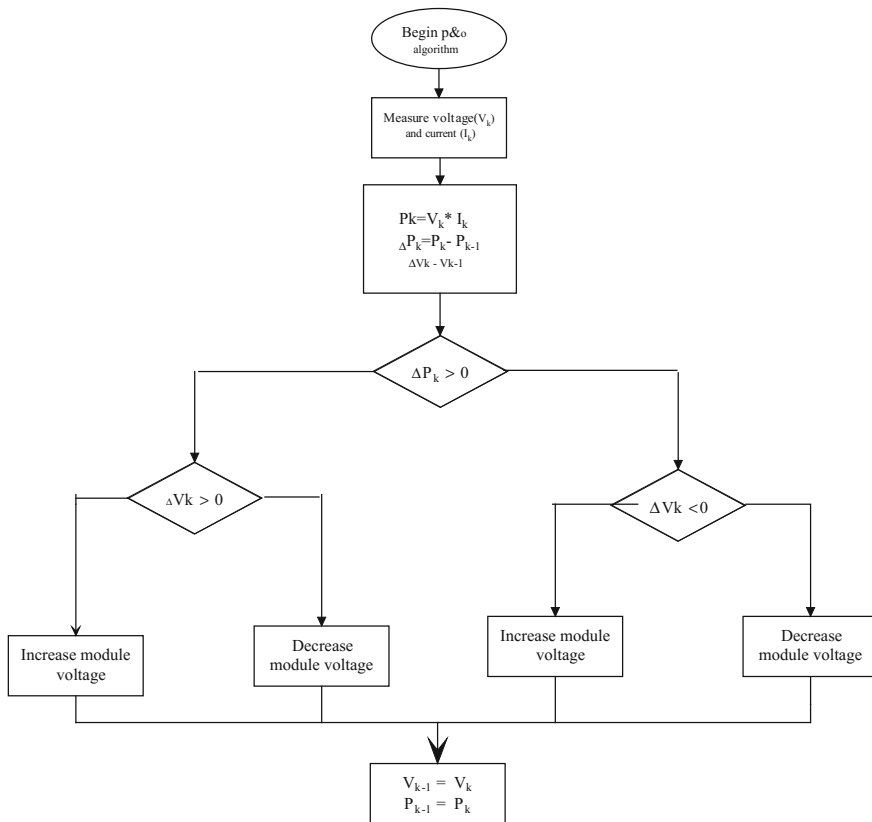


Fig. 5 Flowchart of perturb and observe algorithm [10]

point toward MPP. If the change in power is negative, the voltage is perturbed in opposite direction that is back toward MPP. The flowchart of P&O algorithm is given by (Fig. 5).

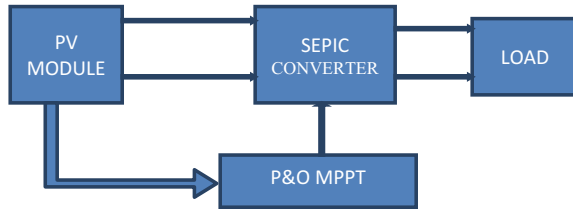


Fig. 6 Block diagram of MPPT [11]

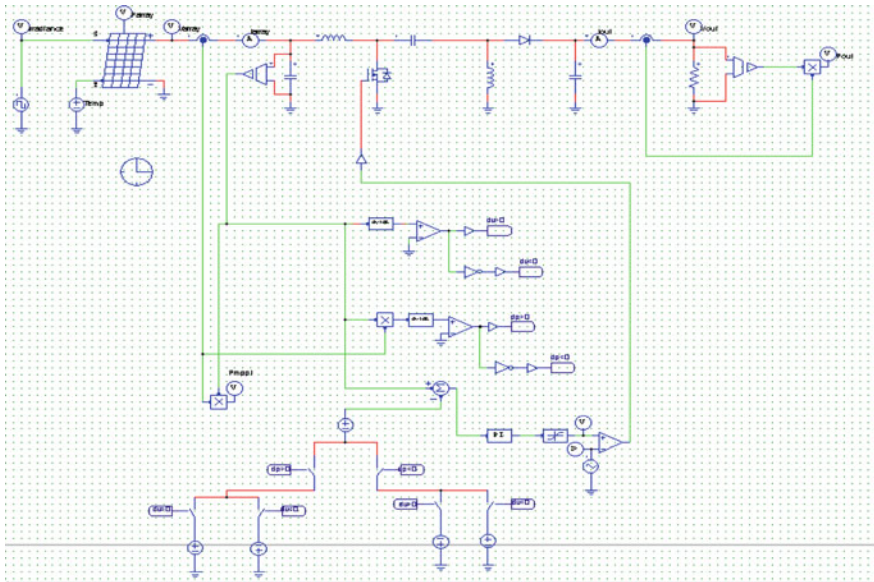


Fig. 7 Simulation diagram of MPPT system

Figure 6 shows the overall system block diagram of PV panel output connected to the SEPIC converter, and output of converter is connected to the load. The duty cycle to the SEPIC converter is controlled by P&O MPPT algorithm.

5 Simulation Result

The simulation diagram of P&O MPPT algorithm with SEPIC converter using PSIM with specified component value and load of 12 Ω is shown in Fig. 7. The irradiance profile varying from 1000 to 800 W/m² and temperature 25 °C used to test MPPT method are given in Fig. 8.

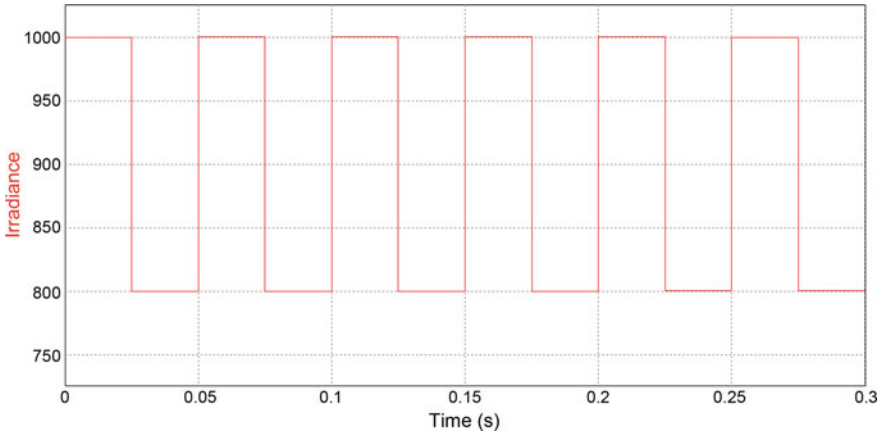


Fig. 8 Irradiance profile

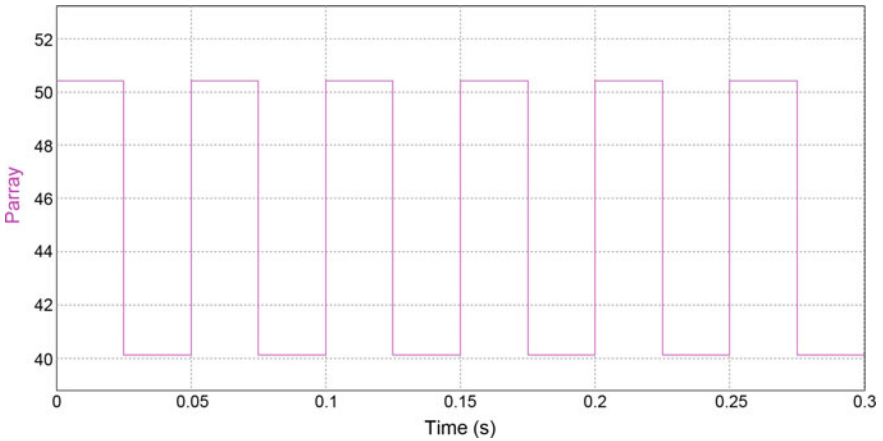


Fig. 9 Power output at different irradiance

Figure 9 shows the power generated by the PV module with changing irradiance from 1000 to 800 W/m^2 . Power generated at 1000 W/m^2 is approximately 50.5 W, and at 800 W/m^2 is approximately 40.1 W. Figure 10 shows the one of the best method for small and medium loads, i.e., P&O method, because this method tracks maximum power accurately and quickly. One of the disadvantages of this method is that it oscillates around MPP and never reaches it, but this drawback can be easily rectified by taking very small perturbations (step size). The power generated from the PV module is transferred to the load of 12 Ω with some losses due to system components as shown in Fig. 11.

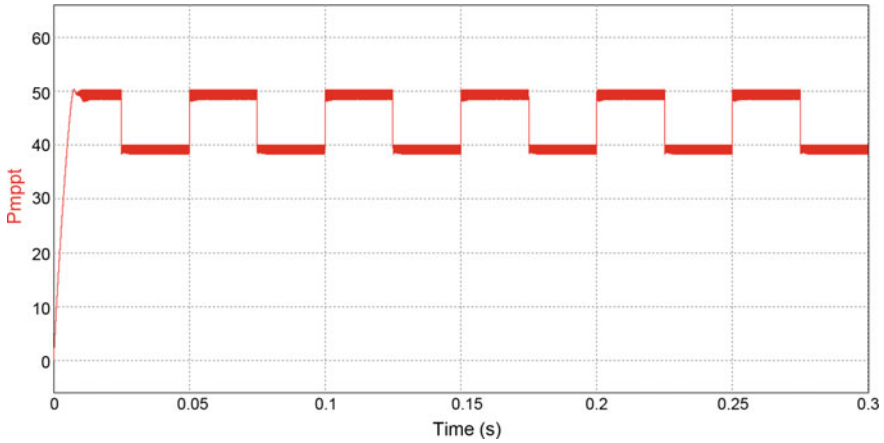


Fig. 10 Maximum PV output at different irradiance

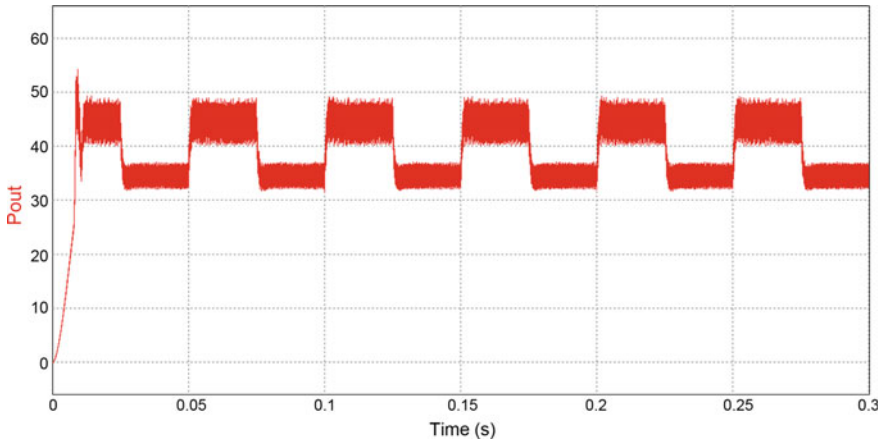


Fig. 11 Power output of SEPIC at 12 Ω load

6 Conclusion

In this paper, the novel perturb and observe MPPT algorithm is implemented using SEPIC converter. The SEPIC converter is chosen as it provides the dc isolation between input and output, also perform buck and boost operation with less stress on components and less ripples. It can also be seen that P&O is simplest method to achieve MPPT. From the above simulation result, we can see that the P&O method tracks the maximum power from the PV module with changing irradiance. Initially the output has some lag as the passive components of dc-dc converter need some

time to attain steady state in initial stages. As P&O never attains steady state as it keeps on oscillating around MPP point, which can be seen in the results. The losses at the output are due to the passive components used and the load condition.

7 Future Work

The panel is modeled by not considering the effect of shading. As shading causes lot of power variation, modeling of PV module with shading effect may be considered to simulate real-time result. The model can be integrated with wind energy and can be modeled for distributed system with load balancing and with secondary power source like battery or fuel cell to store PV power, to supply power to load at night or low irradiance condition.

References

1. Chung, H.S., Tse, K.K., Hui, S.Y.R., Mok, C.M., Ho, M.T.: A novel maximum power point tracking technique for solar panels using a SEPIC or Cuk converter. *IEEE Trans. Power Electron.* **18**(3), 717–724 (2003)
2. Mihnea, R.-H., Sergiu, O.: Practical Guide to Implementing Solar Panel MPPT Algorithms. AN1521 Microchip Technology Inc. (2013)
3. Hua, C., Shen, C.: Study of maximum power tracking techniques and control of DC/DC converters for photovoltaic power system. In: 29th Annual IEEE PESC, pp. 86–93. IEEE Computer Society Press, New York, USA (1998)
4. Handoko, S., Sukmadi, T.: Maximum Power Point Tracking Simulation for a Photovoltaic System. ICITACEE, Indonesia (2015)
5. Zhang, H., Ji, H., Ren, J., Shan, L., Gao, Y.: Research on MPPT Control and Implementation Method for Photovoltaic Generation System and Its Simulation. *IPENC* (2009)
6. Dos Santos, W.M., Martins, D.C.: Digital MPPT Technique for PV Panels with a Single Voltage Sensor. *Intelec* (2012)
7. Bonkougou, D., Koalaga, Z., Njomo, D.: Modelling and Simulation of Photovoltaic Module Considering Single Diode Equivalent Model MATLAB, *IJETAE*, vol. 3, Issue 3 (2013)
8. Bourdouden, H., Gastli, A.: Analytical modelling and simulation of photovoltaic panels and arrays. *J. Eng. Res.* **4**(1) (2007)
9. Masoum, M.A.S., Mousavi, S.M., Fuchs, E.F.: Microprocessor controlled new class of optimal battery chargers for photovoltaic application. In: *IEEE Transaction on Energy Conversion*, vol. 19, No. 3 (2004)
10. Erickson, R.W.: *Fundamental of Power Electronics*, 2nd edn. Kluwer Academic Publishers. ISBN 0-7923-7270-0
11. Hart, D.W.: *Power Electronics*. McGraw-Hill. ISBN 978-0-07-338067-4

Kinematical Synthesis and Numerical Analysis of Rail-Based Dual-Axis Solar Tracking System

Arun A. Yadav, Chetan O. Yadav and Paladugula V. Ramana

Abstract This paper focuses on effective design of dual-axis solar tracking system employing the rail-based azimuth axis mounting mechanism for 500 W_p power output. The photovoltaic panels are mounted on four-wheeled rolling platform that locates east–west direction by horizontal axis. The vertical axis is located by leadscrew and nut mounting mechanism in north–south direction. This type of mounting arrangement causes minimum load on driving motor shaft that helps to decrease the consumption of power from motors. In present paper, the kinematical synthesis of proposed mounting mechanism has been reported to determine the optimal geometric dimensions. The synthesis and numerical analysis have been carried out to determine the optimum geometry dimensions of the mounting mechanism and also to find out the starting tilt angle so as to provide adequate stability. The reported mounting mechanism for solar power system is stable, feasible and efficient for tracking the solar energy through solar photovoltaic modules.

Keywords Rolling platform · Solar energy · Transmission angle
Numerical simulation · Tilt angle

1 Introduction

It is estimated that considering average 10% efficient energy conversion of solar systems would give 20 TW of power from solar energy, nearly twice the consumption rate of fossil fuels [1]. As per research studies, based on movement capability two types of sun trackers are available: single-axis tracker [2, 3] and dual-axis tracker [4, 5]. The various methods and mechanisms have been presented

A.A. Yadav (✉) · C.O. Yadav · P.V. Ramana
Department of Mechanical Engineering, Sardar Vallabhbhai Patel
Institute of Technology (SVIT), Vasad, Gujarat, India
e-mail: arun.140410708011@gmail.com

© Springer Nature Singapore Pte Ltd. 2018

S. SenGupta et al. (eds.), *Advances in Smart Grid and Renewable Energy*,

Lecture Notes in Electrical Engineering 435, https://doi.org/10.1007/978-981-10-4286-7_17

by previous studies [6–9]. The solar tracking system which is designed nowadays, uses rotating actuators for tilt angle of photovoltaic panels [10]. The disadvantages of such a system are their costs and their complication. A substitute to this system is the linear actuator solution, having negative aspect of small transmission angles, thus small angular strokes. One accessible way out is a two-contour linkage [11] in which four-bar mechanism of 4R type performs high angular strokes. This can be achieved with the help of an amplification delivered by a linear actuator. The another novel type of a triangular linkage fitted with a planetary gear pair capable to get to high angular strokes is used as essential mechanism for azimuth tracking of photovoltaic systems [12, 13]. The main contribution of this paper is synthesis and numerical simulation of rail-based dual-axis solar tracking system comprised of rolling platform and leadscrew and nut arrangement. The kinematical synthesis for elevation movement for photovoltaic platform is carried out to determine the optimal geometrical dimensions of mounting structures. The azimuth axis is controlled by rolling platform, and elevation axis is controlled by leadscrew and nut mechanism.

2 Mechanism Design of the Solar Tracker

The dual-axis solar tracking and mounting mechanism for installing solar PV panels of 500 Wp output is designed, and its structural stability, tracking capabilities were studied. Figure 1 depicts the CAD model of the proposed solar tracking mechanism and its components installed on two-frame support (2). The entire structure is mounted on chassis-based rolling platform consisting of two rail bars (3), crossbar (14), solid bases (6), U-brackets (7), V-grooved guiding wheels (9), wheel forks (8) and V-grooved circular rail (12). When DC motor M1 (15) drives the leadscrew to move, the alternation support (2), which holds the two PV panels, will revolve about vertical axis. The rotation of horizontal axis is implemented by attaching the DC motor M2 (15) to one of the guiding wheels (9). When motor M2 is actuated, it rolls on the rolling platform. The diameter of V-grooved circular rail (12) is 2575 mm.

3 Kinematical Synthesis

The novel type of dual-axis solar tracking system for 500 Wp solar photovoltaic panels is proposed with leadscrew and nut mechanism rolling on a rail-based platform mounting arrangements. Figure 2 shows the triangular arrangement for

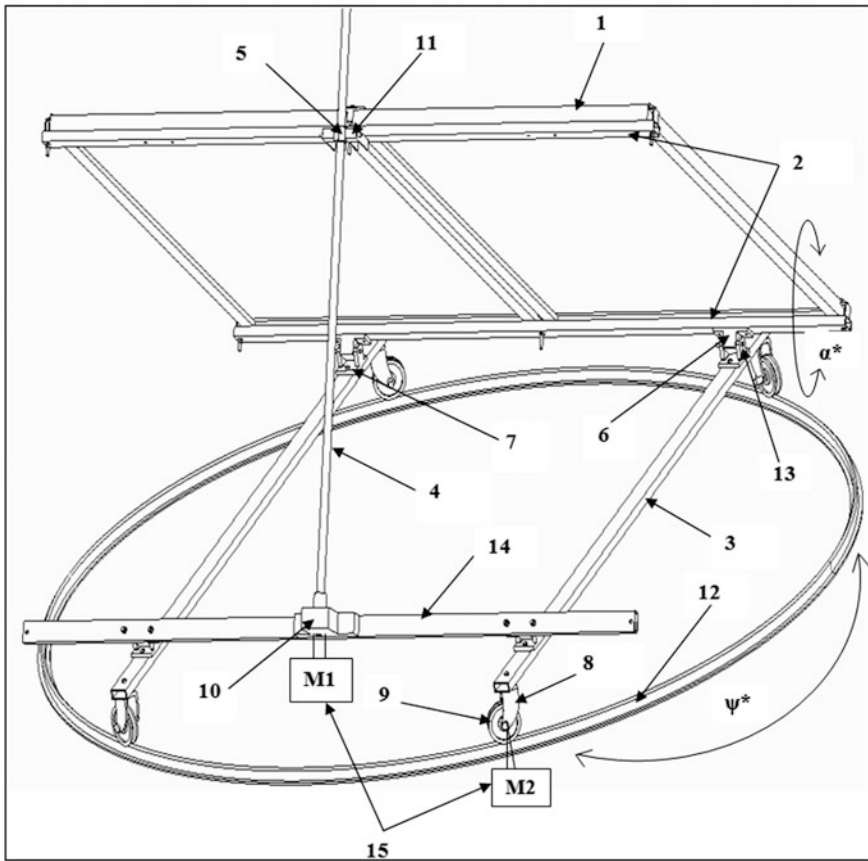


Fig. 1 CAD model (1) PV modules, (2) PV support frame, (3) rail bar, (4) leadscrew, (5) nut, (6) solid base, (7) U-bracket, (8) wheel fork, (9) guiding wheel, (10) leadscrew holder, (11) nut support, (12) circular ring, (13) pin joint, (14) crossbar, (15) PMDC geared motor

vertical axis. The components of this arrangement are (Fig. 2): a bottom ($AB = b$), photovoltaic panels ($BC = r$) and leadscrew and nut attachment ($AC = s_0 + s$).

Using the Sinus theorem in Fig. 2, the subsequent equations are found:

$$\frac{b}{\sin \gamma_m} = \frac{r}{\sin(C_2AB)} = \frac{AC_2}{\sin(ABC_2)} \tag{1}$$

$$C_2AB = \sin^{-1}\left(\left(\frac{r}{b}\right) \sin \gamma_m\right) \tag{2}$$

$$\frac{b}{\sin \gamma_m} = \frac{r}{\sin(C_1AB)} = \frac{AC_1}{\sin(ABC_1)} \tag{3}$$

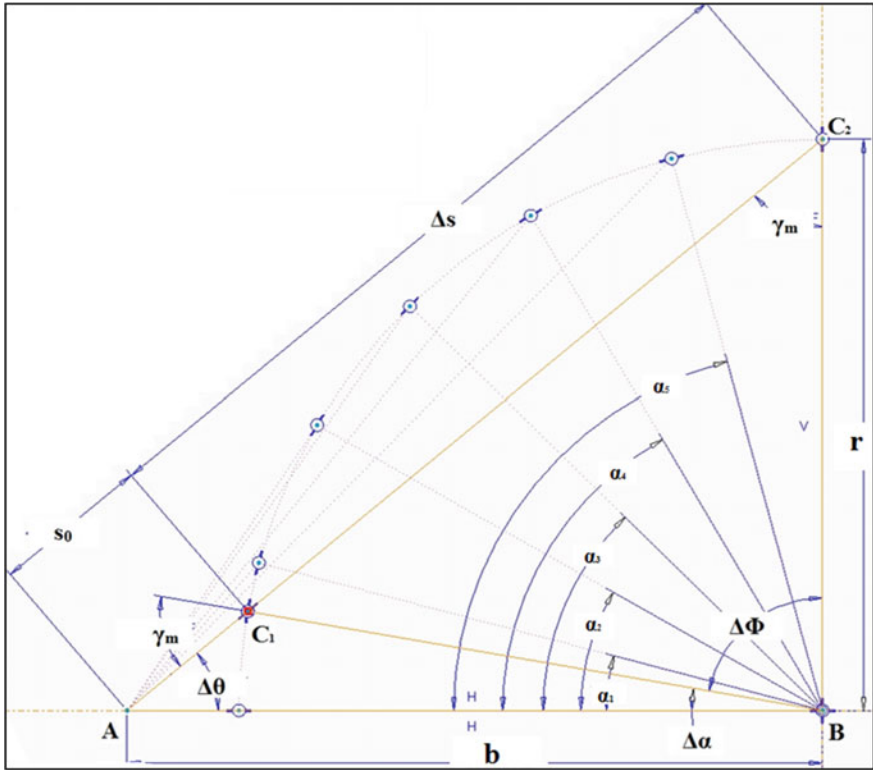


Fig. 2 First and last position of triangle-type arrangement for a minimum admitted value of the transmission angle (γ_m)

$$\angle C_1AB = \sin^{-1}\left(\left(\frac{r}{b}\right) \sin \gamma_m\right) = \angle C_2AB \tag{4}$$

According to relations from (2) and (4), it is accomplished that C_2, A and C_1 are collinear (Fig. 4). Therefore, the photovoltaic panels' angular stroke C_1BC_2 and the stroke length Δs of the linear actuator happen to;

$$\Delta\Phi = C_2BC_1 = 180^\circ - 2\gamma \tag{5}$$

$$\Delta S = C_1C_2 = 2r \cos \gamma_m \tag{6}$$

The leadscrew actuator's internal speed ratio is defined by the subsequent equation:

$$i_0 = \frac{AC_1}{C_1C_2} \tag{7}$$

$$AC_1 = \frac{r \times \sin \Delta\alpha}{\sin \Delta\theta} \quad (8)$$

$$C_1C_2 = \frac{r \times \sin \Delta\Phi}{\sin \gamma_m} \quad (9)$$

Now putting the value of (8) and (9) into (7), the internal speed ratio is finally given by,

$$\therefore i_0 = \frac{AC_1}{C_1C_2} = \frac{\sin \Delta\alpha}{\sin \Delta\theta} \times \frac{\sin \gamma_m}{\sin \Delta\Phi} \quad (10)$$

The altitude angle is continuously changing when sun moves from east to west direction. The changing of altitude angle (α^*) of photovoltaic modules during the tracking period depends on internal speed ratio which is given by:

$$\alpha^* = ABC_1^* = \sin^{-1} \left(\frac{AC_1}{r} \times \sin C_1AB \right) \quad (11)$$

$$= \sin^{-1} \left(\frac{i_0 \times \Delta s}{r} \times \sin \Delta\theta \right) \quad (12)$$

The b/r ratio of the triangle-type geometry of linear actuator depends on the ratio $K_a = AC_1/r$ as shown in Fig. 2. By applying the cosine law of triangle to ΔABC_1 , the following equation is determined.

$$AB^2 = AC_1^2 + BC_1^2 - 2AC_1BC_1 \cos AC_1B \quad (13)$$

Here, $AC_1B = 180^\circ - \gamma_m$ and divide the above Eq. (13) by BC_1^2 . Now the equation becomes,

$$\frac{AB^2}{BC_1^2} = \frac{AC_1^2}{BC_1^2} + 1 - 2 \frac{AC_1}{BC_1} \cos(180^\circ - \gamma_m) \quad (14)$$

As we know that $AB = b$ and $AC_1 = AC_2 = r$, the equation becomes,

$$\left(\frac{b}{r} \right)^2 = 1 + K_a^2 + 2K_a \cos \gamma_m \quad (15)$$

From Eq. (15) it can be concluded that by knowing the values of angle γ_m and K_a , the ratio b/r can be determined.

4 Numerical Simulation and Results

The numerical simulations are made considering the above-described geometric models in Fig. 3 for the condition of $b > r$. The various graphical outcomes, obtained by numerical simulations using (15), are illustrated in Figs. 3 and 4. As example, the subsequent hypothetical in-practice demands are well thought-out:

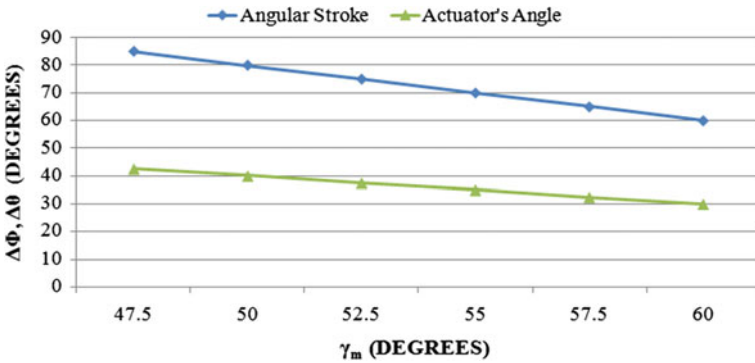


Fig. 3 Variation of angular stroke ($\Delta\Phi$) and actuator's angle ($\Delta\theta$)

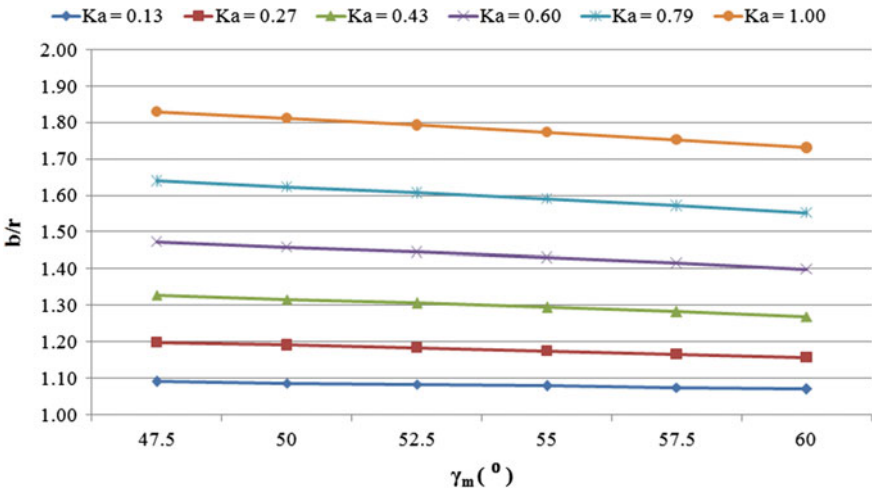


Fig. 4 Variation of the ratio b/r for different values of K_a

Table 1 Calculus examples

$\Delta\alpha$ (°)	$\Delta\phi$ (°)	γ_m (°)	$\Delta\theta$ (°)	K_a	b/r	b (mm)	s (mm)	AC_1 (mm)	AC_2 (mm)	i_0
5	85	47.5	42.5	0.13	1.09	1818.12	2251.1	214.9	2466.0	0.1
10	80	50	40	0.27	1.19	1985.5	2141.8	450.1	2591.8	0.21
15	75	52.5	37.5	0.43	1.30	2171.17	2028.4	708.3	2736.7	0.35
20	70	55	35	0.60	1.43	2379.29	1911.2	993.4	2904.6	0.52
25	65	57.5	32.5	0.79	1.57	2615.1	1790.3	1310.4	3100.7	0.73
30	60	60	30	1.00	1.73	2885.6	1666.0	1666.0	3332.0	1.00

Bold values indicate the optimal geometrical dimensions for designing the 500 Wp power output photovoltaic based dual axis solar tracking system

- solar tracker’s angular stroke (Fig. 2): $\Delta\Phi \leq 90^\circ$;
- admitted minimum transmission angle: $\gamma_m \geq 45^\circ$;
- PV panels’ length: $r = 1666$ mm;
- actuator’s minimum angle (Fig. 2): $s_0 = 450$ mm ($K_a = AC_1/r = 0.27$);
- actuator’s stroke (Fig. 2): $\Delta s = C_1C_2 = 2150$ mm.

From above considered example, the synthesis algorithm is developed in two steps.

Step 1: Estimating the values of sizes i_0 , γ_m and $\Delta\theta$ versus the imposed size $\Delta\Phi$.

Based on Fig. 3 and on the imposed values of $\Delta\Phi$, the values for the i_0 ratio (with discrete variations of 0.10, 0.21, 0.35, 0.52, 0.73, 1.0) for the minimum transmission angle γ_m (through values from 45° to 60°) and for the linkage stroke $\Delta\Phi$ can be estimated.

Step 2: Calculating the b/r ratio.

By means of the data in Fig. 4, the b/r ratio (that depends on the ratio K_a) can be calculated, for each preceding estimated pair of values sets for γ_m . In Table 1, there are available six probable solutions, while remaining solutions can be expected through interpolation by considering constant transmission angle as shown in Table 2. According to Table 1, the most satisfactory stroke (considering the imposed value of 2150 mm) is $s = 2141.77$ mm; hence, the requisite arrangement with $b > r$ (Fig. 4) works on the following parameters: $\gamma_m = 50^\circ$; $i_0 = 0.21$; $K_a = 0.27$; $r = 1666$ mm; $b = 1985.27$ mm and $\Delta\alpha = 9.99^\circ$. The further synthesis values can be estimated as shown in Table 2.

5 Conclusion

The paper presents a new type of proposed design for solar tracking mechanism for holding flat photovoltaic modules for 500 Wp power output. The kinematical synthesis of the proposed design leads to the optimal geometrical dimensions. Based on numerical simulation and hypothetical examples, the results obtained are validated for the $b > r$ condition. Based on obtained dimensions, the rolling

Table 2 Examples of synthesis solutions

γ_m	i_0	K_a	b/r	b	s	α^*
47.5	0.1	0.13	1.09	1819.34	2251.07	5.00
	0.21	0.27	1.20	1997.62	2251.07	11.05
	0.35	0.43	1.33	2213.91	2251.07	18.63
	0.52	0.60	1.47	2454.57	2251.07	28.34
	0.73	0.79	1.64	2733.22	2251.07	41.79
	1.00	1.00	1.83	3049.82	2251.07	65.90
50	0.1	0.13	1.09	1812.82	2141.07	4.53
	0.21	0.27	1.19	1985.27	2141.07	9.99
	0.35	0.43	1.32	2196.15	2141.07	16.81
	0.52	0.60	1.46	2432.21	2141.07	25.45
	0.73	0.79	1.62	2706.78	2141.07	37.10
	1.00	1.00	1.81	3019.82	2141.07	55.73
52.5	0.1	0.13	1.08	1806.80	2028.39	4.06
	0.21	0.27	1.18	1972.39	2028.39	8.95
	0.35	0.43	1.31	2177.58	2028.39	15.04
	0.52	0.60	1.45	2408.80	2028.39	22.67
	0.73	0.79	1.61	2679.07	2028.39	32.76
	1.00	1.00	1.79	2988.38	2028.39	47.83
55	0.1	0.13	1.08	1798.99	1911.16	3.60
	0.21	0.27	1.18	1958.21	1911.16	7.94
	0.35	0.43	1.60	2158.21	1911.16	13.31
	0.52	0.60	1.43	2384.35	1911.16	20.01
	0.73	0.79	1.59	2650.12	1911.16	28.71
	1.00	1.00	1.77	2955.52	1911.16	41.15
57.5	0.1	0.13	1.08	1791.70	1790.28	3.16
	0.21	0.27	1.17	1945.04	1790.28	6.96
	0.35	0.43	1.28	2138.05	1790.28	11.66
	0.52	0.60	1.42	2358.88	1790.28	17.47
	0.73	0.79	1.57	2619.93	1790.28	24.93
	1.00	1.00	1.75	2921.25	1790.28	35.27
60	0.1	0.13	1.07	1784.18	1666.00	2.74
	0.21	0.27	1.16	1930.62	1666.00	6.03
	0.35	0.43	1.27	2117.13	1666.00	10.08
	0.52	0.60	1.40	2332.40	1666.00	15.07
	0.73	0.79	1.55	2588.53	1666.00	21.41
	1.00	1.00	1.73	2885.60	1666.00	30.00

Bold values indicate the optimal geometrical dimensions for designing the 500 Wp power output photovoltaic based dual axis solar tracking system

platform-based dual-axis solar tracking system can be developed to obtain the minimum torque condition on motor shafts in order to maximize the output of photovoltaic panels.

References

1. Hossein, M., Alireza, K., Arzhang, J., Karen, A., Ahmad, S.: A review of principle and sun-tracking methods for maximizing solar systems output. *Renew. Sustain. Energy Rev.* **13**, 1800–1818 (2009)
2. Huang, B., Huang, Y., Chen, Y., Hsu, P., Li, K.: Improving solar PV system efficiency using one-axis 3-position sun tracking. *Energy Procedia* **33**, 280–287 (2013)
3. Creanga, N., Hermenean, I., Diaconescu, D.: 4-bar Geared Linkage Used for Photovoltaic Azimuth Orientation, vol. 10, pp. 1139–1148. Product Design Centre for Sustainable Development, Transilvania University of Brasov (2010)
4. Abu-Khadra, M., Badranb, O., Abdallah, S.: Evaluating multi-axes sun tracking system at different modes of operation in Jordan. *Renew. Sustain. Energy Rev.* **12**, 864–873 (2008)
5. Visa, I., Diaconescu, D., Popa, V., Burduhos, B.: Synthesis of Linkages for Tracking Systems with Increased Angular Stroke, pp. 193–206. Department of Product Design and Robotics, Transilvania University of Brasov, Romania (2010)
6. Guillon, L., Quesada, G., Rouse, D.: An experimental validation of the concept critical solar radiation for solar tracking systems. *Int. J. Appl. Sci. Technol.* **5**, 1–11 (2015)
7. Kelly, N., Gibson, T.: Increasing the solar photovoltaic energy capture on sunny and cloudy days. *Sol. Energy* **85**, 111–125 (2011)
8. Yao, Y., Hu, Y., Gao, S., Yang, G., Du, J.: A multipurpose dual-axis solar tracker with two tracking strategies. *Renew. Energy*, **72**, 88–98 (2014)
9. Loschi, H., Iano, Y., Moretti, A., Conte, F., Braga, H.: A review on photovoltaic systems: mechanisms and methods for irradiation tracking and prediction. *Smart Grid Renew. Energy* **6**, 187–208 (2015)
10. Blackman, S., Popoli, R.: Design and Analysis of Modern Tracking Systems. Artech House Publishers, Boston (2000)
11. Visa, I., et al.: The synthesis of a linkage with linear actuator for solar tracking system with large angular stroke. In: Proceedings of EUROMES, Cassino, Italy, pp. 457–464 (2008)
12. Creanga, N., Visa, I., Diaconescu, D., Hermenean, I., Butuc, B.: Geared Linkage Driven by Linear Actuator Used for PV Platform Azimuth Orientation, pp. 1–6. Transilvania University of Brasov, Romania (2011)
13. Visa, I., Dorin, D., Radu, S., Monica, V., Bogdan, B.: New linkage with linear actuator for tracking PV systems with large angular stroke. *Chin. J. Mech. Eng.* **24**(5) (2011)

Application of Artificial Intelligence-Based Techniques in Controlling the STATCOM Used for Compensation for Voltage Dips in DFIG-Based Grid-Connected Wind Power System

Bineeta Mukhopadhyay and Rajib Kumar Mandal

Abstract Severe voltage sag in weak power systems connected to DFIG-based wind farms may lead to voltage instability. In such cases, FACTS devices like static synchronous compensator (STATCOM) can provide voltage support at the point of common coupling (PCC) by dynamic injection of reactive power. In this research attempt, three artificial intelligence-based techniques have been used to control the STATCOM—fuzzy logic, particle swarm optimization (PSO) and a combination of fuzzy logic and PSO. The STATCOM, controlled by the three proposed techniques—fuzzy-PI, PSO-PI and fuzzy PSO-PI, provides voltage compensation in the DFIG-based grid-connected wind power system in five test cases, namely simultaneous occurrence of step change (drop) in wind speed and dip in grid voltage, single-line-to-ground (SLG) fault, line-to-line (LL) fault, double-line-to-ground (DLG) fault and sudden increase in load by more than a thousand times. A performance comparison regarding the amount of voltage compensation offered is done among all the three artificial intelligence-based STATCOM control techniques in all the five test cases.

Keywords Static synchronous compensator (STATCOM) · Fuzzy logic Particle swarm optimization (PSO) · Grid-connected · Point of common coupling (PCC) · Doubly fed induction generator (DFIG)

B. Mukhopadhyay (✉) · R.K. Mandal
National Institute of Technology, Patna, India
e-mail: bineeta2010@gmail.com

R.K. Mandal
e-mail: rajib.k.mandal@gmail.com

1 Introduction

DFIG is considered to be highly suitable for grid-connected wind power plants owing to its advantages which include independent supervision of active and reactive power, better voltage regulation, maximum power extraction at low wind speeds and the ability to ride-through faults [1]. Voltage instability may occur due to severe faults in weak power systems associated with grid-connected wind farms. Under such circumstances, FACTS devices like the STATCOM may be harnessed to provide dynamic reactive power support at the PCC, thus enabling enhanced transient and steady-state voltage stability [2, 3]. In this work, the STATCOM employed for voltage compensation is controlled using three artificial intelligence-based techniques—fuzzy logic, PSO and a combination of fuzzy logic and PSO. In terms of voltage compensation offered at the PCC, a performance comparison is done among the three techniques used to control the STATCOM, namely fuzzy-PI, PSO-PI and fuzzy PSO-PI, in five test cases—simultaneous occurrence of step change (drop) in wind speed and grid voltage dip, SLG, LL, DLG faults and sudden load change.

2 Fuzzy-PI Controller for STATCOM

The voltage, current and frequency regulators in the STATCOM control system shown in Fig. 1 are equipped with fuzzy logic controllers. Mamdani fuzzy inference system and Center of Area (COA) defuzzification method are used. The membership functions used are NL (negative large), NIL (zero), PL (positive large), NEL (negative extremely large) and PEL (positive extremely large).

The fuzzy controller adjusts the gain constants of the PI controller, K_{PROP} and K_{INT} , in the fuzzy voltage regulator block and current regulator block. The inputs to the fuzzy logic controllers in the current and voltage supervisors are the error between the reference and measured values (voltage/reactive current) and the first derivative of this error. The outputs are the desirable changes in proportional and integral gains, ΔK_{PROP} and ΔK_{INT} , respectively. The fuzzy rules stated in Tables 1 and 2 are based on the fact that greater magnitude of error and its derivative call for a larger ΔK_{PROP} and smaller errors require a larger ΔK_{INT} for steady-state error reduction [4, 5]. The final values of K_{PROP} and K_{INT} are obtained as shown in Eqs. (1) and (2), where K_{PROP} (PI) and K_{INT} (PI) are the proportional and integral gains, respectively, in the conventional PI controllers, and ΔK_{PROP} (fuzzy) and ΔK_{INT} (fuzzy) are the respective increments in proportional and integral gains obtained from fuzzy controllers (all in the voltage and current regulator blocks of the STATCOM control system).

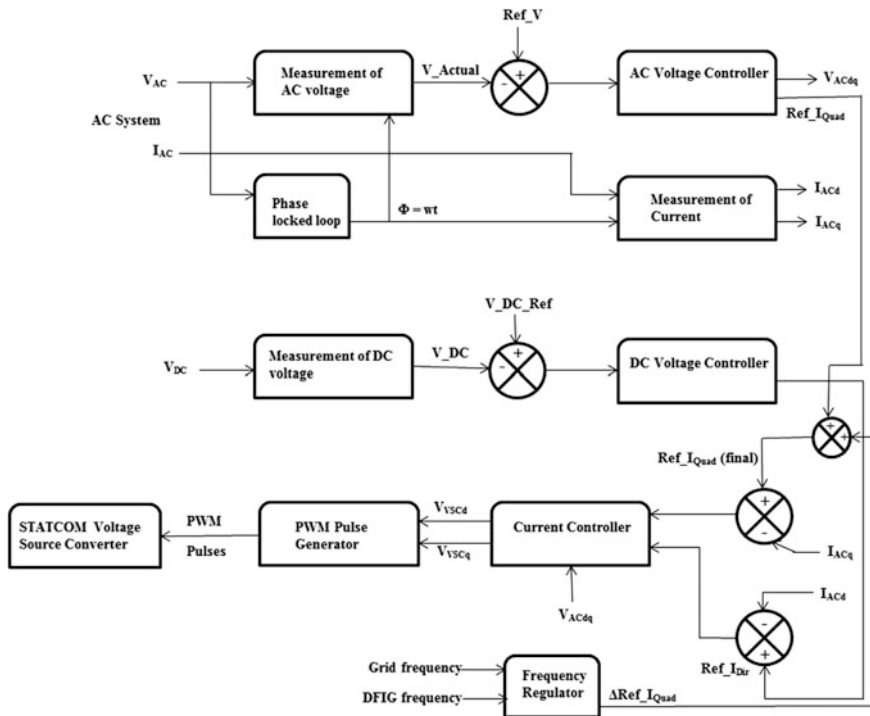


Fig. 1 STATCOM control system: block schematic representation

Table 1 Table for fuzzy rules for ΔK_{PROP} : voltage and current regulators

de/dt	e				
	NEL	NL	NILL	PL	PEL
NEL	NL	NL	NL	PL	NIL
NL	NL	NL	NIL	NIL	PL
NIL	NL	NL	NIL	PL	PL
PL	NL	NL	NI	PL	PL
PEL	NIL	NL	PL	PL	PL

Table 2 Table for fuzzy rules for ΔK_{INT} : voltage and current regulators

de/dt	e				
	NEL	NL	NIL	PL	PEL
NEL	NIL	NL	NL	NL	NIL
NL	NIL	NL	NL	NIL	NIL
NIL	NIL	NIL	NIL	PL	NIL
PL	NIL	NIL	PL	PL	NIL
PEL	NIL	PL	PL	PL	NIL

Table 3 Table for fuzzy rules for $\Delta\text{Ref_I}_{\text{Quad}}$: frequency regulator

de/dt	e				
	NEL	NL	NIL	PL	PEL
NEL	NEL	NL	NL	NL	NL
NL	NL	NL	NL	NL	NL
NIL	NL	NL	NIL	PL	PL
PL	PL	PL	PL	PL	PL
PEL	PL	PL	PL	PL	PEL

$$K_{\text{PROP}}(\text{final}) = K_{\text{PROP}}(\text{PI}) + \Delta K_{\text{PROP}}(\text{fuzzy}) \quad (1)$$

$$K_{\text{INT}}(\text{final}) = K_{\text{INT}}(\text{PI}) + \Delta K_{\text{INT}}(\text{fuzzy}) \quad (2)$$

The inputs of the fuzzy frequency regulator are the error (f) between reference and DFIG frequency and the first derivative of error (df/dt), and the output is the desired change in reference reactive current of the STATCOM, $\Delta\text{Ref_I}_{\text{Quad}}$, respectively. The fuzzy rules for $\Delta\text{Ref_I}_{\text{Quad}}$ stated in Table 3 follow the fact that the STATCOM must supply greater capacitive current in response to the fast rising high frequency error [6].

3 PSO-PI Controller for STATCOM Voltage Regulator

The PI gains of the STATCOM voltage regulator are supervised using PSO. In the PSO algorithm for STATCOM control, the PI controller gains, K_{PROP} and K_{INT} , are the positions/searching points and the increments in controller gains, ΔK_{PROP} and ΔK_{INT} , are the velocities, as shown in the flowchart in Fig. 2. In the PSO objective function for STATCOM control, stated in Eq. (3), $K = [K_{\text{PROP}}K_{\text{INT}}]$, and ss_{err} , t_{set} , t_{ri} , g and Os stand for the error at steady-state, settling time, rise time, weighting factor (assumed 1.2) and the peak overshoot, respectively [7].

$$\text{In}(K) = (1 - e^{-g}).(Os + ss_{\text{err}}) + e^{-g}.(t_{\text{set}} - t_{\text{ri}}) \quad (3)$$

The controller gains and their increments are altered using Eqs. (4)–(5):

$$w^i = w_{\text{max}} - (w_{\text{max}} - w_{\text{min}})/\text{max_iter} \times i \quad (4)$$

$$K_c^{i+1} = K_c^i + V_c^{i+1} = K_c^i + \Delta K_c^{i+1} = K_c^i + \text{cog_ckt} \times r1 \times (K_{c(\text{pbest})} - K_c^i) + \text{soc_ckt} \times r2 \times (K_{g\text{best}} - K_c^i) + w^i \Delta K_c^i \quad (5)$$

In Eqs. (4) and (5), K_c^i and K_c^{i+1} denote the positions of the particle c at iterations i and $i + 1$, respectively, $V_c^{i+1} = \Delta K_c^{i+1}$ is the velocity of c th particle at

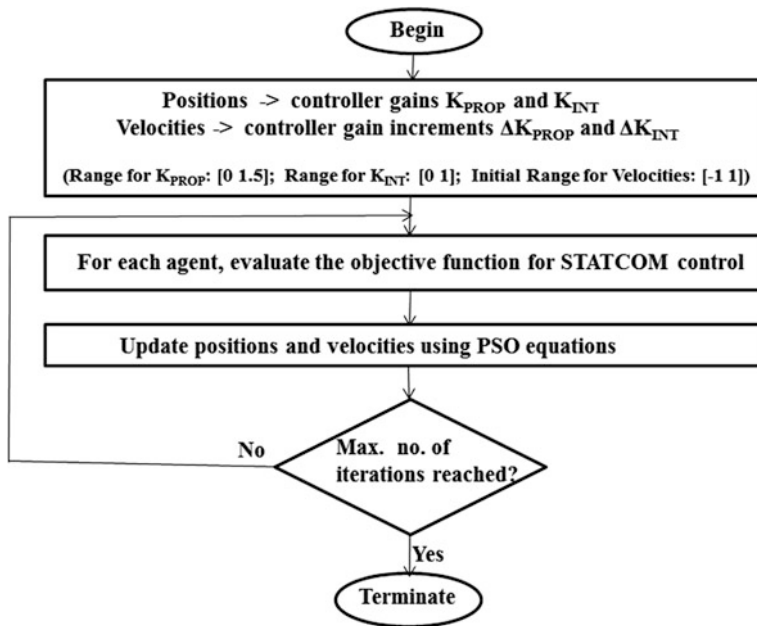


Fig. 2 Flowchart for PSO for STATCOM control

iteration $i + 1$, $r1$ and $r2$ are sequences of random numbers within 0 and 1, and cog_ckt , soc_ckt , max_iter , w_{max} and w_{min} denote the individual behavior constant, social behavior constant, maximum number of iterations, maximum inertia weight and minimum inertia weight, respectively [8]. $K_{c(pbest)}$ represents the best position (personal) of particle c , and K_{gbest} stands for the best global position. The values considered for cog_ckt , soc_ckt , max_iter , w_{max} and w_{min} in the PSO program for STATCOM control are 2, 2, 24, 1.5 and 0.5, respectively.

4 Fuzzy PSO-PI Controller for STATCOM

In fuzzy PSO-PI controller for STATCOM, both the fuzzy-PI control technique and the PSO-PI control technique are implemented. The current regulator and frequency regulator are the same as described in the fuzzy-PI controller section. In case of the STATCOM voltage regulator, besides the fuzzy controller, the PSO program is implemented for STATCOM control.

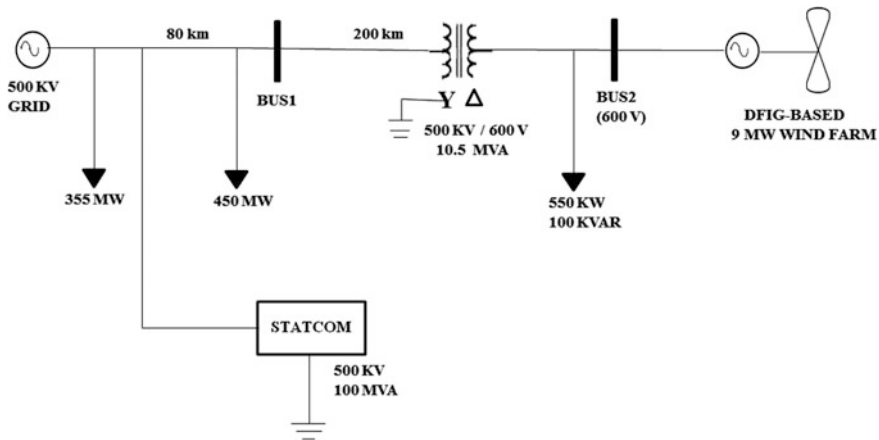


Fig. 3 Schematic representation of test system

5 Description of Test System and Test Cases

In the test system displayed in Fig. 3 (simulated using MATLAB/SIMULINK), the voltage dip at the PCC, which is the bus labeled ‘BUS2’ (at 600 V), and its subsequent improvement after including 48 pulse GTO-based 500 kV, 100 MVA STATCOM, has been observed in five test cases. In the first test case, the speed of the wind falls sharply as a step from 22 to 3 m/s at time $t = 0.1$ s, and at the same instant, the voltage of the grid reduces to 0.1 pu (restored to 1 pu at time $t = 0.14$ s). In the second, third and fourth test cases, the effects of SLG, LL and DLG faults at the terminals of the bus named ‘BUS1’ at time $t = 0.1$ s for 2 cycles are investigated. The fifth test case examines the consequence of a sudden increase in load at the bus named ‘BUS2’. In this test case, the load at BUS2 is initially a 500 KW resistive load. At time $t = 0.1$ s, an extra 500 MW resistive load is switched on at BUS2. Hence, the total load at time $t = 0.1$ s at BUS2 is 500 KW + 500 MW (extra load removed after 2 cycles). The wind speed is 15 m/s in all the cases, except the first. In all the five test cases, the positive sequence voltage at BUS2 (PCC) is observed, first without the STATCOM, and later after incorporating the fuzzy-PI, PSO-PI and fuzzy PSO-PI-controlled STATCOM. The total simulation time is 0.2 s.

6 Results and Analysis

A performance comparison among the three STATCOM control techniques described earlier can be derived from Table 4 and the simulation results obtained for the different test cases shown in Figs. 4, 5, 6, 7, 8, 9, 10, 11, 12.

Table 4 Positive sequence voltage at BUS2 (PCC) in all the test cases using STATCOM controlled by all the three techniques

Test case	BUS2 (PCC) Voltage (pu): no STATCOM	BUS2 (PCC) Voltage (pu): fuzzy-PI STATCOM	BUS2 (PCC) Voltage (pu): PSO-PI STATCOM	BUS2 (PCC) Voltage (pu): fuzzy PSO-PI STATCOM
Dip in wind speed and grid voltage	0.68	0.92	0.95	0.94
SLG fault	0.75	0.98	0.995	0.99
LL fault	0.55	0.78	0.79	0.8
DLG fault	0.4	0.575	0.586	0.591
Sudden load rise	0.69	0.89	0.86	0.897

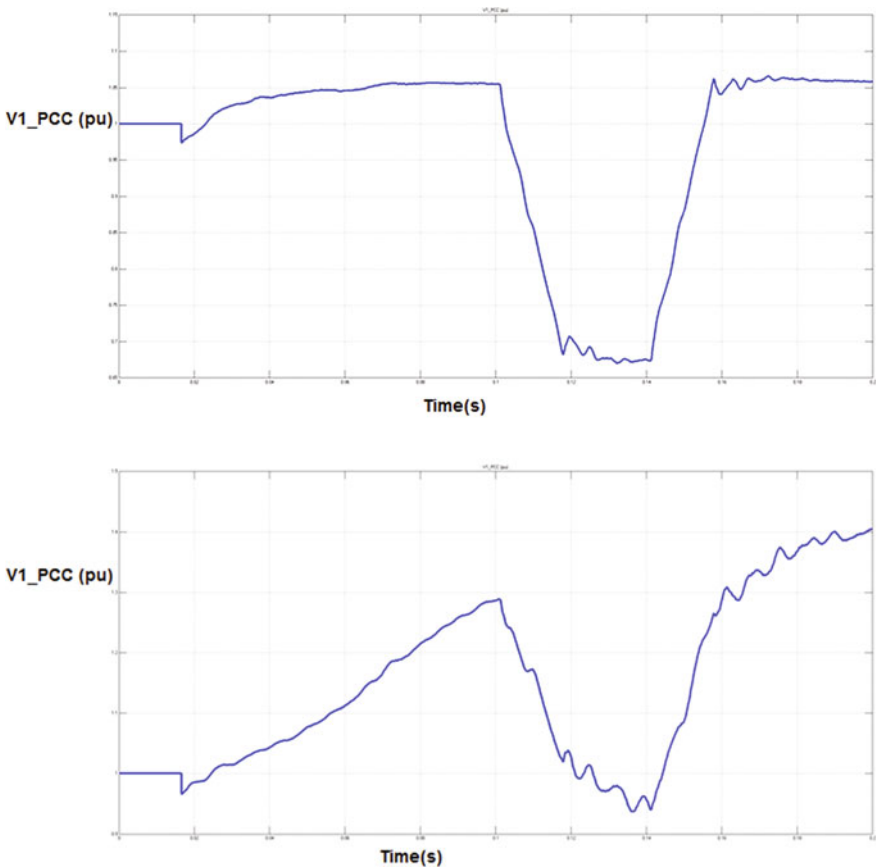


Fig. 4 Positive sequence voltage (pu) at BUS2 (PCC) under the impact of step change (drop) in wind speed and voltage dip on the grid when STATCOM is absent (*top*) and when PSO-PI-controlled STATCOM is included in the system (*bottom*)

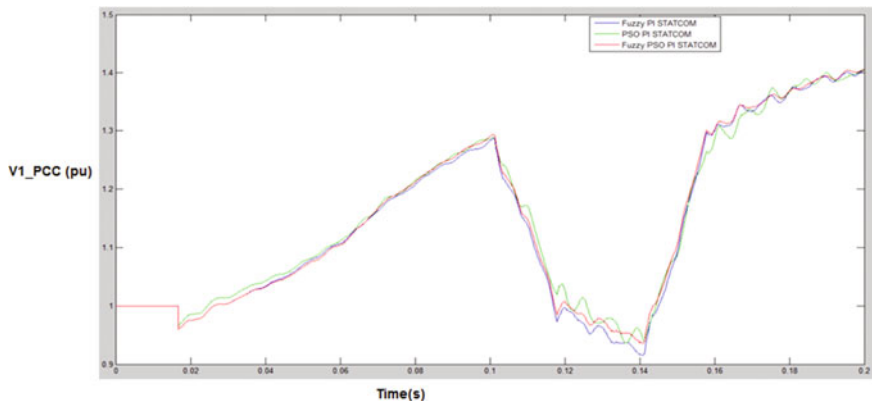


Fig. 5 Positive sequence voltage (pu) at BUS2 (PCC) for simultaneous occurrence of step change (drop) in wind speed and grid voltage dip: fuzzy-PI (blue), PSO-PI (green) and fuzzy PSO-PI (red)-controlled STATCOM

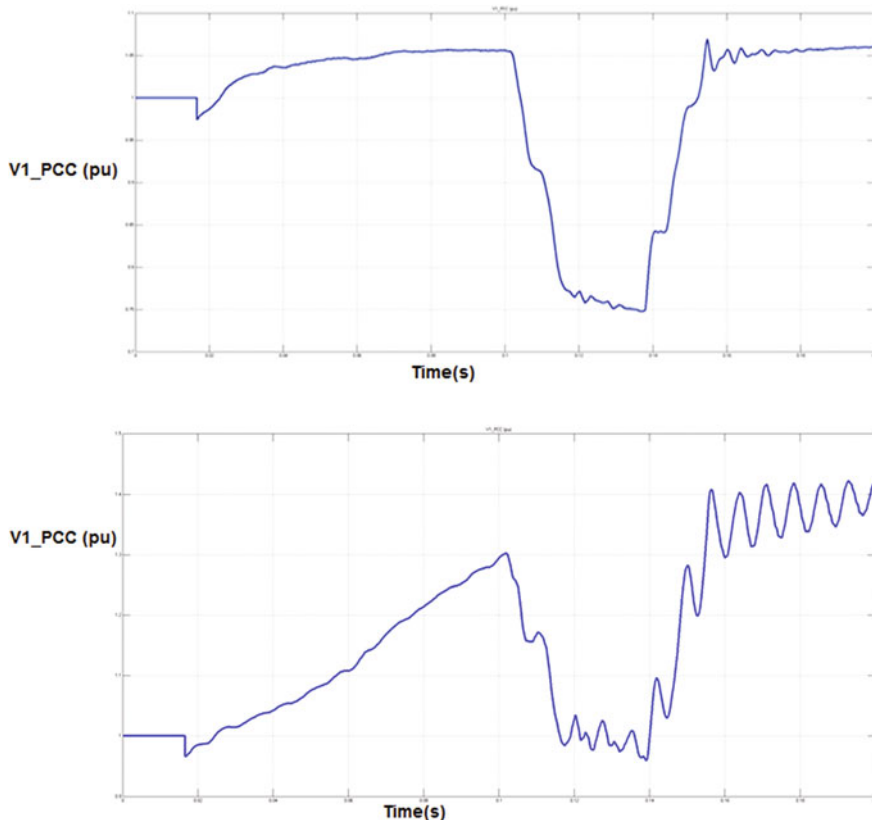


Fig. 6 Positive sequence voltage (pu) at BUS2 (PCC) when an SLG fault occurs at BUS1 and STATCOM is absent (top) and when PSO-PI-controlled STATCOM is present (bottom)

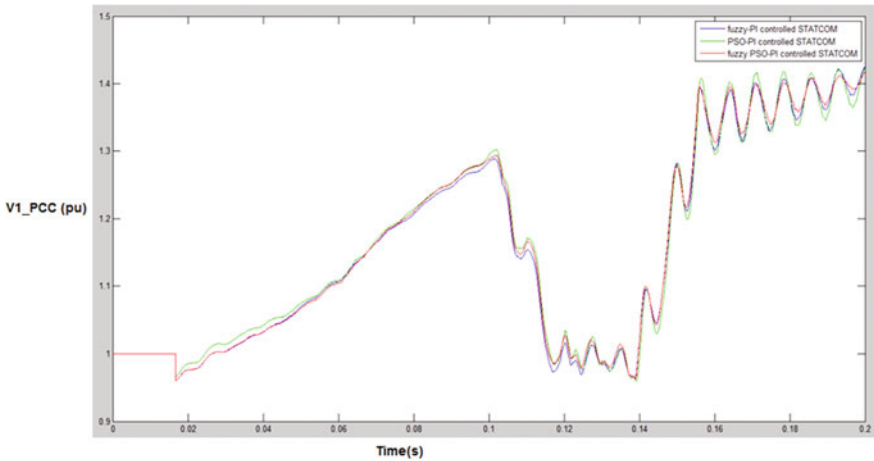


Fig. 7 Positive sequence voltage (pu) at BUS2 (PCC) for SLG fault: fuzzy-PI (blue), PSO-PI (green) and fuzzy PSO-PI (red)-controlled STATCOM

Simultaneous Occurrence of Step Change (Drop) in Wind Speed and Dip in the Grid Voltage

See Figs. 4 and 5.

Single-Line-to-Ground Fault

See Figs. 6 and 7.

Line-to-Line Fault

See Figs. 8 and 9.

Double-Line-to-Ground Fault

See Figs. 10 and 11.

Sudden Increment in Load

See Fig. 12.

From the figures and Table 4, it is observed that the inclusion of STATCOM in the power system certainly improves the voltage profile at the PCC in all the test cases. From the plots and table, it is also clear that in the first two test cases, namely simultaneous occurrence of step change (drop) in wind speed and grid voltage dip and SLG fault, the PSO-PI-controlled STATCOM offers the highest voltage compensation among the three techniques. In the remaining test cases, namely LL fault, DLG fault and sudden increment in load, the fuzzy PSO-PI-controlled STATCOM provides the maximum voltage improvement, compared to the other

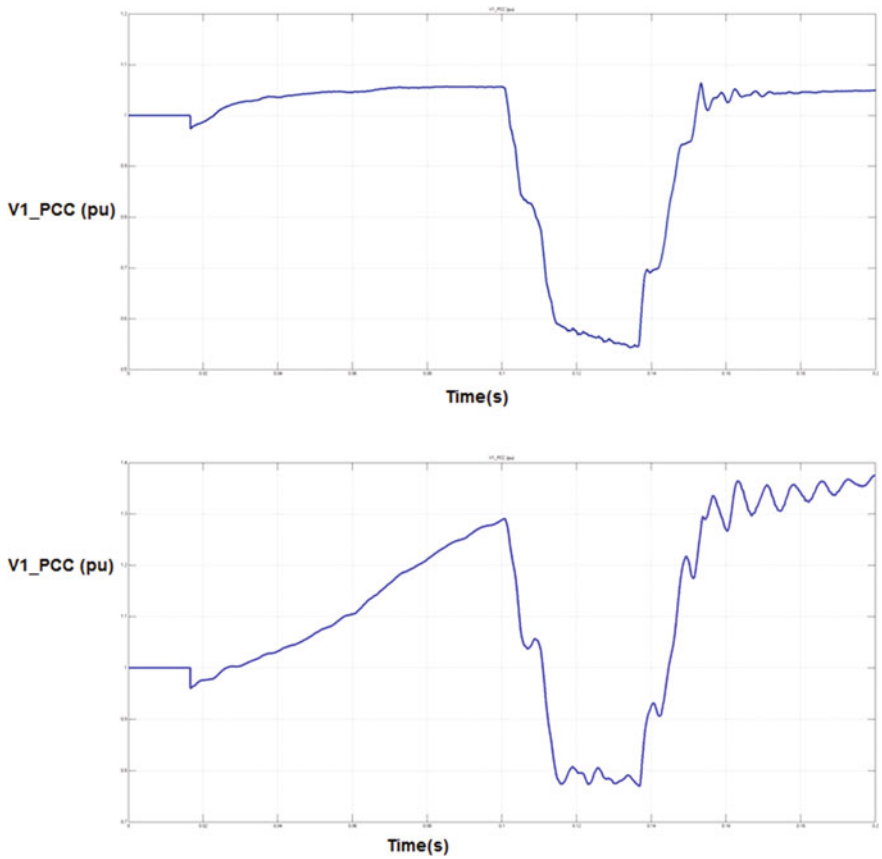


Fig. 8 Positive sequence voltage (pu) at BUS2 (PCC) when an LL fault occurs at BUS1 and STATCOM is absent (*top*) and when fuzzy PSO-PI-controlled STATCOM is present in the system (*bottom*)

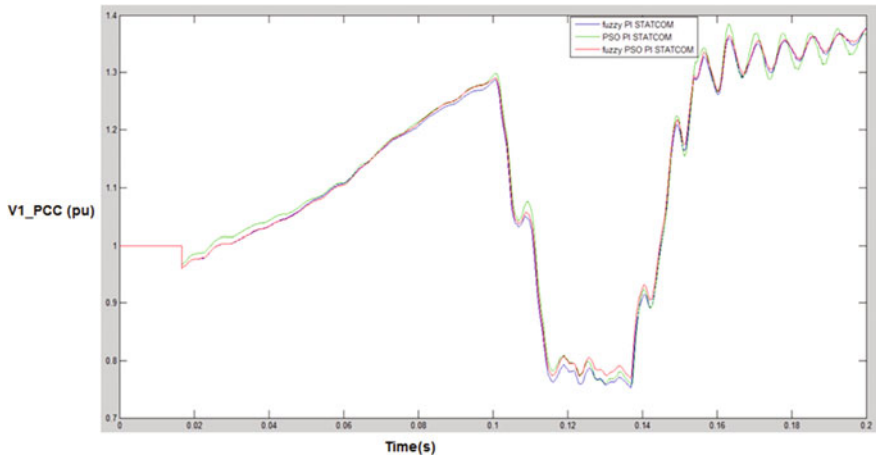


Fig. 9 Positive sequence voltage (pu) at BUS2 (PCC) for LL fault: fuzzy-PI (blue), PSO-PI (green) and fuzzy PSO-PI (red)-controlled STATCOM

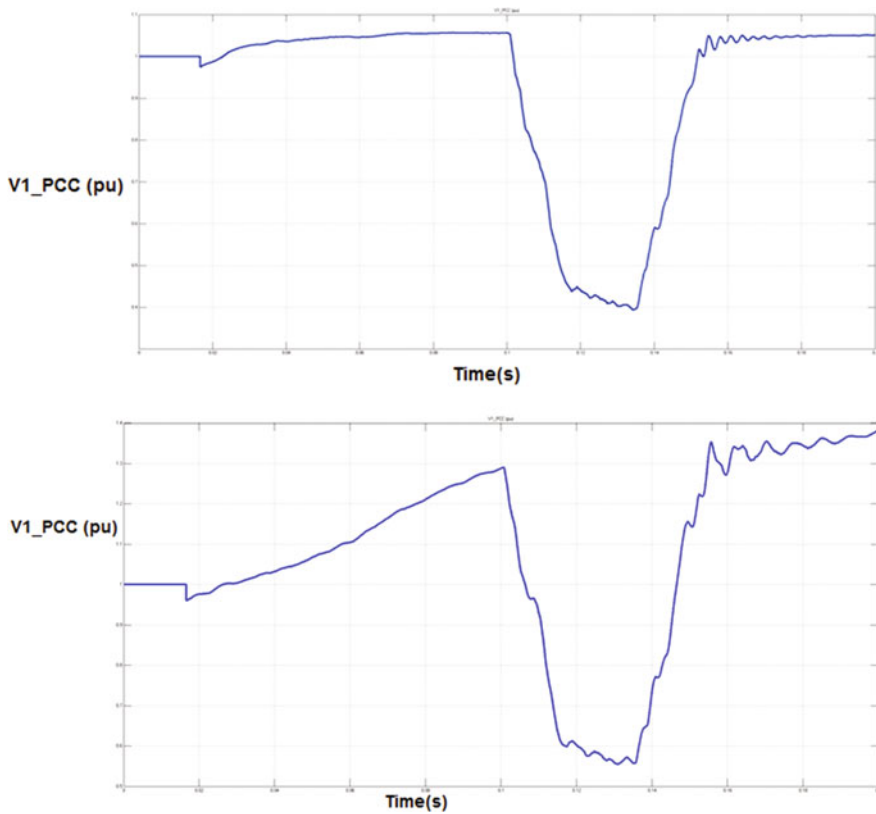


Fig. 10 Positive sequence voltage (pu) at BUS2 (PCC) when a DLG fault occurs at BUS1 and STATCOM is absent (top) and when fuzzy PSO-PI-controlled STATCOM is present in the system (bottom)

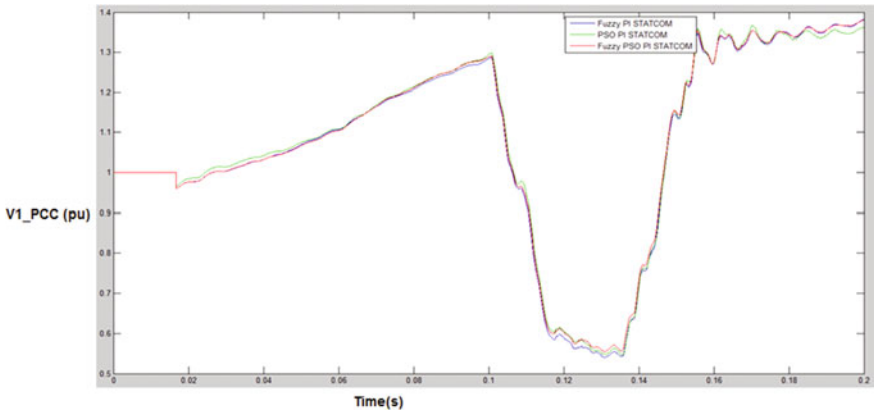


Fig. 11 Positive sequence voltage (pu) at BUS2 (PCC) for DLG fault: fuzzy-PI (blue), PSO-PI (green) and fuzzy PSO-PI (red)-controlled STATCOM

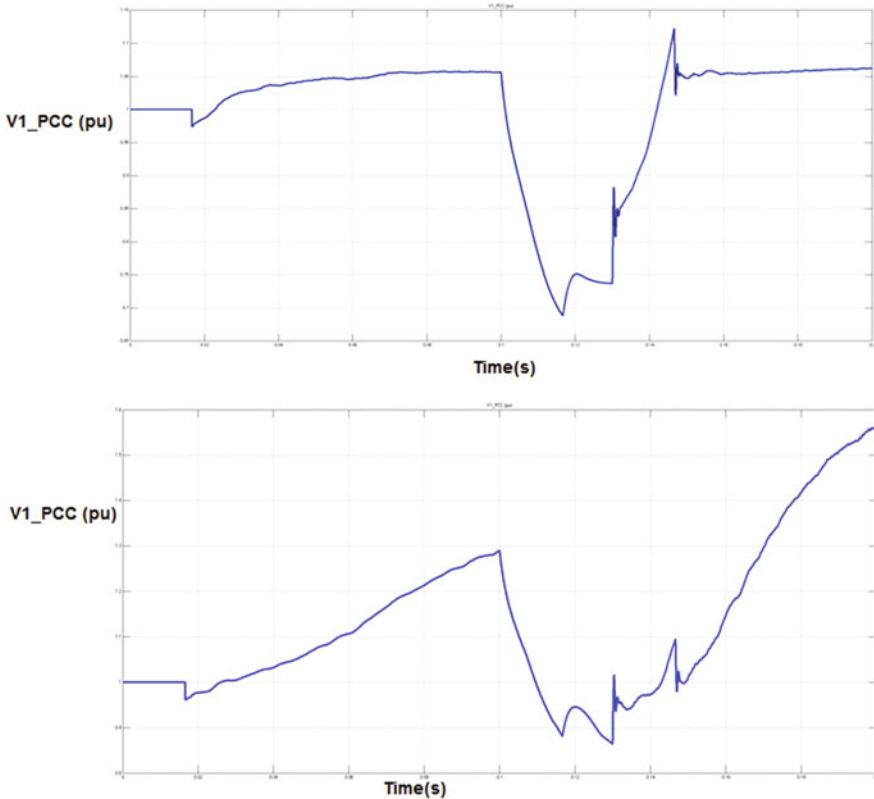


Fig. 12 Positive sequence voltage (pu) at BUS2 (PCC) under the impact of a sudden increment in load at the PCC when STATCOM is absent (top) and when fuzzy PSO-PI-controlled STATCOM is included (bottom)

techniques. In all the cases, it is additionally seen that whenever fuzzy PSO-PI-controlled STATCOM is incorporated in the system, the voltage response becomes smoother with comparatively fewer oscillations.

7 Conclusion

The STATCOM, controlled using all the three soft computing techniques—fuzzy-PI, PSO-PI and fuzzy PSO-PI methods, is able to provide voltage compensation at the PCC in all the five test cases. A performance comparison among the three STATCOM control techniques indicates better performance by the PSO-PI-controlled STATCOM in the first two test cases (wind speed change as well as grid voltage dip and SLG fault) and superior voltage compensation by fuzzy PSO-PI-controlled STATCOM in the remaining test cases (LL fault, DLG fault, sudden load increment).

References

1. Ahuja, H., Bhuvanewari, G., Balasubramanian, R.: Performance comparison of DFIG and PMSG based WECS. In: IET Conference on Renewable Power Generation (2011)
2. Qiao, W., Venayagamoorthy, G.K., Harley, R.G.: Real-time implementation of a STATCOM on a wind farm equipped with doubly fed induction generators. *IEEE Trans. Ind. Appl.* **45**(1), 98–107 (2009)
3. Qiao, W., Venayagamoorthy, G.K., Harley, R.G.: Coordinated reactive power control of large wind farm and a STATCOM using heuristic dynamic programming. *IEEE Trans. Energy Convers.* **24**(2), 493–503 (2009)
4. Luo, A., Tang, C., Shuai, Z., Tang, J., Xu, X.Y., Chen, D.: Fuzzy-PI-based direct-output-voltage control strategy for the STATCOM used in utility distribution systems. *IEEE Trans. Ind. Electron.* **56**(7) (2009)
5. Chauhan, S., Chopra, V., Singh, S.: Power system transient stability improvement using fuzzy PI based STATCOM controller. In: 2nd International Conference on Power, Control and Embedded Systems (2012)
6. Ghafouri, A., Zolghadri, M.R., Ehsan, M., Elmatboly, O., Homaifar, A.: Fuzzy controlled STATCOM for improving power system transient stability. In: Power Symposium, NAPS, IEEE Conference Publications (2007)
7. Gaing, Z.-L.: A particle swarm optimization approach for optimum design of PID controller in AVR system. *IEEE Trans. Energy Convers.* **19**(2) (2004)
8. Liu, C.-H., Hsu, Y.-Y.: Design of a self-tuning PI controller for a STATCOM using particle swarm optimization. *IEEE Trans. Ind. Electron.* **57**(2) (2010)

Micro-grid for Village Empowerment Using Solar PV-Operated Micro-hydel Power Plant

T.K. Rana and S. Chakraborty

Abstract Day and night empowerment in remote and isolated places through electric power and water supply has been designed in a smart and efficient way. Solar photovoltaic power with Maximum Power Point Tracking (MPPT) controller generates electricity during day time which is used to run domestic appliances. It also simultaneously pumps water and stores it in an overhead tank. Along with the normal utilization of water in daily life from the water tank, potential energy in the form of stored water in overhead tank is used to run a micro-turbine coupled with a generator for producing electricity at night. The centralized electric power is distributed to different homes in the village through a micro-grid.

Keywords MPPT · Potential energy · Micro-grid · Photovoltaic Renewable energy

1 Introduction

In remote locations, islands or in similar places, due to non-availability of commercial grid power supply, people lead the lives of an ancient world. They do not enjoy the TV, fan or light. Sometime oil or gas is used to meet their certain demands. On the other hand, conventional energy resources used in different sectors are insufficient to meet the future demand due to the limited availability which will last not more than two centuries. The conventional energy sources also cause pollution, thereby degrading the environment. Different studies have been done in

T.K. Rana

Electronics and Communication Engineering Department, Institute of Engineering and Management, Kolkata, India
e-mail: tkrana@rediffmail.com

S. Chakraborty (✉)

Electronics and Communication Engineering Department, Sikkim Manipal Institute of Technology, Rangpo, India
e-mail: swastika1971@gmail.com

© Springer Nature Singapore Pte Ltd. 2018

S. SenGupta et al. (eds.), *Advances in Smart Grid and Renewable Energy*,

Lecture Notes in Electrical Engineering 435, https://doi.org/10.1007/978-981-10-4286-7_19

the area of solar power-operated energy systems. It is renewable and causes no pollution. In this paper, an efficient and useful concept is implemented to meet the day and night demand of power for the people staying in isolated places. Referring to Fig. 1, solar energy is extracted through solar photovoltaic (PV) panels. DC electrical energy is processed to operate electrical utilities. Extra energy is used to run water pump to store water in an overhead tank. Electrical energy is thus converted to potential energy in the form of stored water in the overhead tank. At night, the stored water is released. The potential energy of the stored water in the overhead tank is converted to kinetic energy which, in turn, rotates a turbine coupled with a generator to produce electricity [1]. In addition to the electric power, the water is also used for normal uses. System view is shown in Fig. 1.

The potential energy in the form of stored water in an overhead tank is thus converted to kinetic energy, and finally, electric energy is made available. Normally, battery is used to store energy from PV panel during the day and the stored battery energy [2, 3] is used at the night. Life of battery is in the order of 3–5 years, and it is also very expensive. Storing PV energy in the form of potential energy in overhead tank serves two purposes simultaneously. In one form, it provides water required for daily normal household needs, and in other form, it produces electricity. Periodic replacement as is required for a battery is nil here. Thus, energy storing in an overhead tank will work better than storing energy in conventional way in battery.

To empower the village houses, a basic scheme has been designed. Power for lamps, fan and TV set will give the people comfort, and they will see the world through various TV programs. The micro-grid is a DC grid which is simpler in implementation. AC micro-grid for this type of application has been designed [4–7]. Complexity is less in DC grid system. In a different type of application, solar power is converted to national grid quality power [8]. Power is fed to the grid. Energy efficient hybrid micro-grid for a building has been analyzed also [9]. Hybrid AC/DC micro-grid design is available in the literature [10]. Hybrid micro-grid with battery, wind, solar, fuel cell and national grid has been studied and optimized [11–14]. We have presented a very simple and efficient system. Converter shown in Fig. 2 regulates the DC voltage level. Here, an inverter can also be connected for AC voltage operated loads.

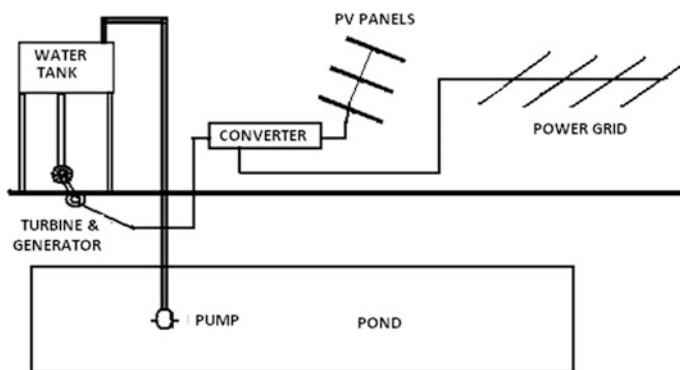


Fig. 1 System view

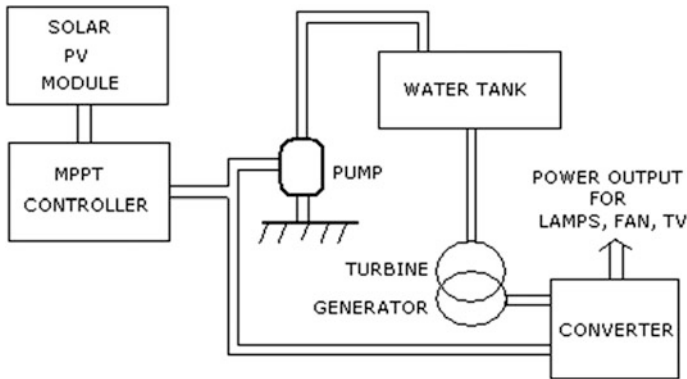


Fig. 2 Basic scheme of operation

In remote and isolated places, national grid is absent. Local grid serving a local area for DC operated utilities is efficient. Referring to Fig. 2, our design approach is unique, efficient and simple. It meets the basic need of electrically powered utilities and simultaneously water supply through water distribution.

2 Load Distribution from the Scheme

The calculation is based on the total consumption of power in the village. Loads are mainly fans, lights and TVs.

- (i) Total fan load = F W for H1 h during day and H2 h at night
- (ii) Total TV load = T W for H3 at day and H4 h at night
- (iii) Total LED lamp load = L W for H5 h at night

$$\text{Total energy required} = (F.H1 + F.H2 + T.H3 + T.H4 + L.H5)WH \quad (1)$$

Considering overall efficiency of N1%, energy required

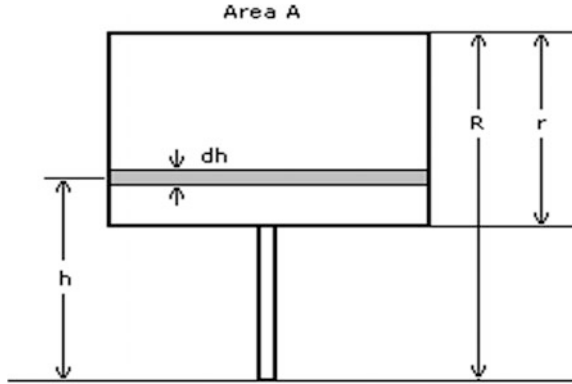
$$= (F.H1 + F.H2 + T.H3 + T.H4 + L.H5)/0.N1WH = E$$

Assuming H6 h availability of proper sunlight, the required size of the solar PV panel

$$= E/H6W$$

Requirement of storage energy for night is seen from the above figure

Fig. 3 Overhead tank details



$$= E_{\text{night}} = (F.H2 + T.H4 + L.H5)/0.NWH$$

$$\text{Peak power requirement at night} = E_{\text{night}}/H2$$

Referring to Fig. 3, we see that potential energy in mass of water stored in incremental head dh above the head h is given by Eq. (2)

$$dw = dm.g.h \quad (2)$$

Total potential energy of water stored is shown in Eq. (3) below,

$$PE = \int_0^R \rho.A.g.h.dh = \frac{1}{2}.\rho.A.g.R^2 J \quad (3)$$

Replacing bottom height by 'r'

$$\begin{aligned} PE &= \frac{1}{2}.\rho.A.g.(R^2 - r^2); \quad \rho = 1000 \text{ kg/m}^3 \\ &= \frac{1}{2}.1000.A.(9.8).(R^2 - r^2) \\ &= (F.H2 + T.H4 + L.H5)/0.NWH \end{aligned}$$

With storing efficiency and extra water required for normal house hold uses, another efficiency factor of N2% is considered.

Actual potential energy (PE) required

$$= (F.H2 + T.H4 + L.H5)/(0.N2)WH$$

3 Alternator Details

When water is released from the tank, the stored potential energy gets converted to kinetic energy. This energy is used to rotate a water turbine. Water turbines are basically low speed prime movers. Its operating speed depends on the water head. Alternators coupled to this type of turbines require large number of poles as shown in the following Eq. (6). Frequency and output voltage are shown in Eqs. (4) and (5)

$$\text{Frequency of the alternator output} = (P/2) \times (N/60), \tag{4}$$

where

- N rotational speed in RPM
- P total number of magnetic poles

$$\text{RMS value of emf generated per phase} = 4.44.f.\phi.T \tag{5}$$

where

- ϕ flux/pole in webers

The alternator will generate 3-phase AC output which when rectified by a full wave rectifier will give V_{dc} .

Per phase ac voltage = $V_{dc}/2.34$

For f Hz output frequency number of poles

$$P = (2 \times f \times 60)/N \tag{6}$$

4 Turbine Details

The velocity of the water at the turbine point can be expressed as shown in Eq. (7) below

$$v = C_v(2gH)^{1/2} \tag{7}$$

where

- v outlet velocity (m/s)
- C_v velocity coefficient (water 0.9)
- g acceleration of gravity (9.81 m/s²)
- H height (m)

A reasonable rotational speed of a water turbine = N rps

Now the rotational speed of the turbine blades of radius ‘ R ’ and the speed of water flow are given by the following Eqs. (8) and (9)

$$v = 2.\pi R.N \text{ m/s} \quad (8)$$

$$R = v/(2.\pi.N) \quad (9)$$

Kinetic energy of a moving object or liquid is governed by equation $E = 1/2.m.v^2$ where m is mass and v the velocity of motion.

Now we will find the diameter of the discharging pipe.

Potential energy of water in the overhead tank will be converted to kinetic energy at the turbine blades. This kinetic energy per second has to meet the demand of electrical power generation. Mass of water and diameter of pipe will follow Eqs. (10) and (11).

$$\text{So, } E = 1/2.m.v^2 = (F + T + L)W$$

$$m = ((F + T + L) \times 2)/v^2 \text{ kg} \quad (10)$$

If ' d ' be the diameter of the discharge pipe, then
i.e.,

$$\rho.A.v = 1000.\pi.d^2 \quad (11)$$

from above equation ' d ' can be found out.

5 Results of a Case Study

We consider a small village of 50 houses. Load distribution is as given. We can assume an average of load per house as

- (i) 15 W solar fan for 6-h day and 6-h night use = 180 WH
- (ii) 14 in. 15 W LCD TV 6-h day and 6-h night = 180 WH
- (iii) 3×7 W LED lamps for 4 h at night = 48 WH

$$\text{Total} = 180 + 180 + 48 = 408 \text{ WH.}$$

Considering overall efficiency of 80% actual energy requirement = $408/0.8 = 510$ WH.

For 50 houses, energy to be extracted from solar panel = $50 \times 510 = 25500$ WH
And for one day extra power storage the energy requirement from the PV panel

$$= 2 \times 25,500 = 51,000 \text{ WH}$$

Assuming 5-h availability of proper sunlight, the average power supplied by the PV panel

$$= 25,500 \text{ WH}/5 \text{ H} = 5100 \text{ W}$$

Selected PV module: Model no-SS265P,
 Make—SovaPower (or equivalent),
 Watt—250 W,
 $V_{oc} = 37.05 \text{ V}$,
 $V(\text{optimum}) = 30.12 \text{ V}$,
 Short-circuit current—8.74 A,
 Optimum operating current—8.31 A.

We should take into consideration the power generation capacity of a PV panel with years of use with its aging characteristics when we design a system for long-term use. Figure 4 shows a typical PV output capacity with years.

The most important consideration in designing PV output-based system is its power generation capacity round the clock. A typical qualitative power generation pattern is shown in the graph in Fig. 5.

Graph in Fig. 6 shows insolation level with time.

Monthly insolation pattern with different ambient temperature is shown in Fig. 7.

Fig. 4 Power output versus age of PV panel

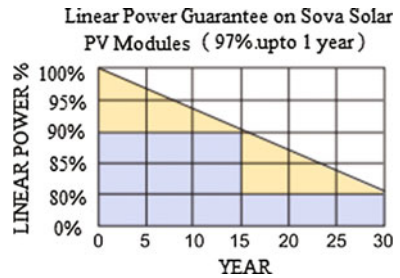
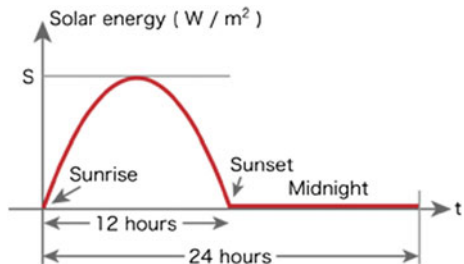


Fig. 5 Solar energy pattern throughout the day



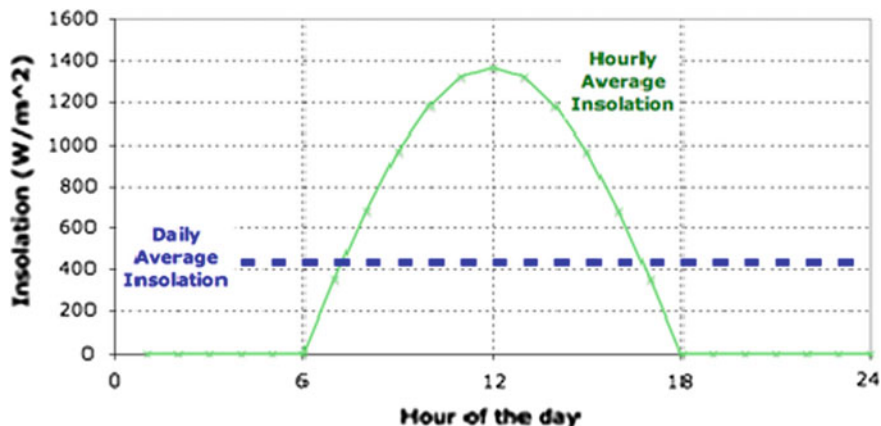


Fig. 6 Hourly insolation pattern

Fig. 7 Monthly insolation pattern

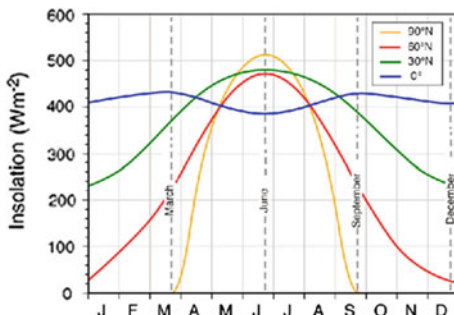


Table 1 Percent of solar energy with respect to time in summer and winter seasons

Time	Summer (%)	Winter (%)
8 a.m.–9 a.m.	10	5
9 a.m.–10 a.m.	25	10
10 a.m.–11 a.m.	70	40
11 a.m.–12 noon	100	70
12 noon–1 p.m.	100	70
1 p.m.–2 p.m.	90	60
2 p.m.–3 p.m.	60	45
3 p.m.–4 p.m.	20	10
4 p.m.–5 p.m.	5	2

Useful energy available from the solar panel is as given in the chart with respect to peak energy (Table 1).

With the realistic pattern of generation from PV modules based on time (Figs. 4 and 5), month (Fig. 7) and year (Fig. 4) of use, we can find out the size of PV panel

Table 2 Power available from solar panel in summer and winter seasons

Time	Summer	Winter
8 a.m.–9 a.m.	1.6 kW	800 W
9 a.m.–10 a.m.	4 kW	1.6 kW
10 a.m.–11 a.m.	11.2 kW	6.4 kW
11 a.m.–12 noon	16 kW	11.2 kW
12 noon–1 p.m.	16 kW	11.2 kW
1 p.m.–2 p.m.	14.4 kW	9.6 kW
2 p.m.–3 p.m.	9.6 kW	7.2 kW
3 p.m.–4 p.m.	3.2 kW	1.6 kW
4 p.m.–5 p.m.	800 W	320 W

based on an application. If P_p be the peak power available from the solar panel, the total energy available through out the day in summer

$$= P_p.(0.1 + 0.2 + 0.7 + 1.0 + 1.0 + 0.9 + 0.6 + 0.2 + 0.05) = 4.8P_pH$$

But total energy available in winter will be

$$= P_p.(0.05 + 0.1 + 0.4 + 0.7 + 0.7 + 0.6 + 0.45 + 0.1 + 0.02) = 3.12P_pH$$

Considering the winter situation $3.12P_pH = \text{energy requirement} = 51000 \text{ WH}$.

Peak power of the solar panel = $51,000/312 = 16346 \text{ W} = 16 \text{ kW}$ (approx).

Useful power available from the solar panel is as given in the following chart (Table 2).

5.1 PV Panel Details

Considering $250W_p$ panel, total number of 250 W panel will be = $16,346/250 = 65$ nos.

5.2 Overhead Tank Details

Overhead tank height be $R = 7 \text{ m}$ and $r = 5$.

$$\text{Area of tank} = 360 \text{ m}^2.$$

5.3 MPPT Controller

A buck converter as shown in Fig. 8 has been used to extract maximum power from the solar PV module

Fig. 8 Buck converter

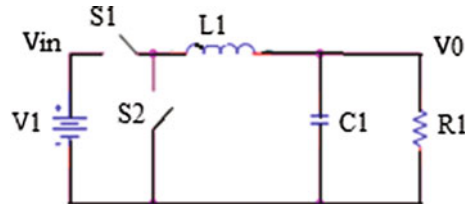
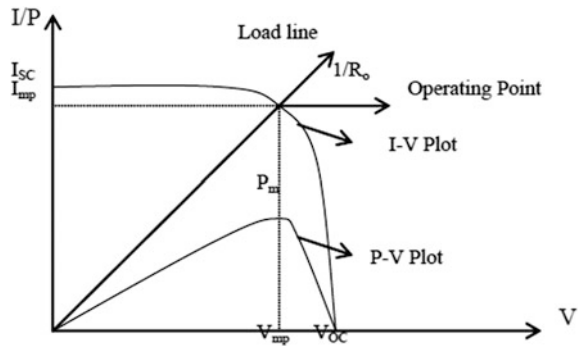


Fig. 9 V-I characteristics of PV module



$$V_0/V_{in} = I_{in}/I_0 = D$$

where

D is the duty cycle.

This expression of R_0 as derived in Eq. (12) below gives us input resistance value in terms of output load resistance,

$$\begin{aligned} V_{in} &= V_0/D \\ I_{in} &= I_0 \cdot D \\ V_0 &= V_{in} \cdot D \end{aligned}$$

$$R_{in} = V_{in}/I_{in} = (V_0/D)/I_0 \cdot D = (V_0/I_0)/D^2 = R_0/D^2 \tag{12}$$

where R_0 is the output resistance or load resistance of the converter. We know that D varies from 0 to 1. Hence, R_{in} would vary from ∞ to R_0 as D varies from 0 to 1 corresponding. A standard V/I characteristic of a PV cell is shown in Fig. 5. Maximum power from the solar cell is available at a particular point in the V/I curve. To extract the maximum power [15], the load resistance is to be selected to achieve the point. The formula as given in Eq. (1) will be used to do that. Here the duty cycle of the converter is constantly adjusted to receive the maximum power. It in turn adjusts the load resistance faced by the solar PV output.

By adjusting the duty cycle and calculating the output power generated continuously, the maximum power output can be extracted as shown in Fig. 9.

Fig. 10 Control scheme block diagram

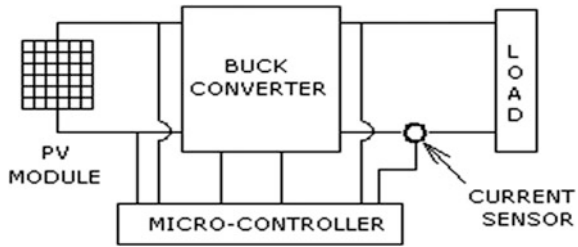
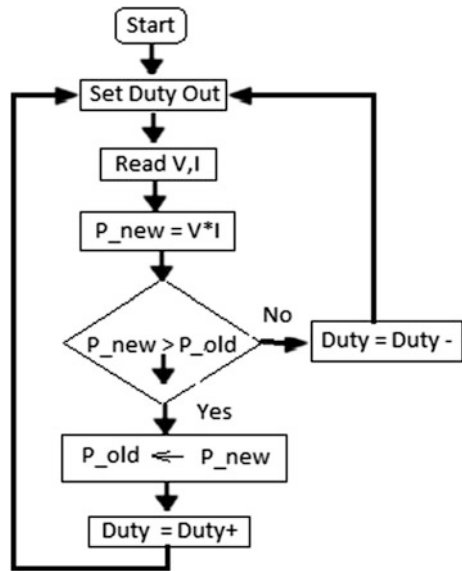


Fig. 11 Flow chart of MPPT controller



5.4 Control Scheme

The basic control scheme is shown in Fig. 10. The PV output is sent to a buck converter. The micro-controller monitors the input and output power by sensing input/output voltage and current constantly. The micro-controller generates pulse width modulated signal whose duty cycle is controlled to extract maximum power from the PV panel.

The duty cycle of the buck converter is varied following an algorithm as shown in flow chart in Fig. 11. The MPPT-based controller is designed using ATMEGA16 micro-controller (Fig. 6). Output voltage and current are sensed to calculate the power output. The micro-controller generates PWM signal for the buck converter. Duty cycle is constantly adjusted for MPPT.

6 Conclusion

Local grid providing electricity for round the clock to a remote village using pollution free resources has been presented. Along with electric power, the proposed system provides water to the villagers for their daily need. Necessary and useful design methodology has been formulated. A realistic case study of a small village has been analyzed. The scheme will be very much efficient and cost effective for empowerment of remote villages in future.

References

1. Kabalan, M., Anabaraonye, B.: Solar photovoltaic versus micro-hydroelectricity framework for assessing the sustainability of community-run rural electrification projects. In: IEEE Global Humanitarian Technology Conference, pp. 1–8 (2014)
2. Parida, B., Iniyar, S., Ranko, G.: A review of solar photovoltaic technologies. *Renew. Sustain. Energy Rev.* **15**, 1625–1636 (2011)
3. Dali, M., Belhadj, J., Roboam, X.: Hybrid solar wind system with battery storage operating in grid-connected and standalone mode: control and energy management-experimental investigation. *Energy* **35**, 2587–2595 (2010)
4. Prasad, D.R., Kamath, B.R., Jagadisha, K.R., Girish, S.K.: Smart DC Micro-grid for effective utilization of solar energy. *Int. J. Sci. Eng. Res.* **3**, 1–5 (2012)
5. Huang, R., Huang, T., Gadh, R.: Solar generation prediction using the ARMA model in a laboratory-level micro-grid. In: IEEE Smart Grid Communication Symposium, pp. 528–533 (2012)
6. Serban, E., Serban, H.: A control strategy for a distributed power generation micro-grid application with voltage and current-controlled Source converter. *IEEE Trans. Power Electron.* **25**, 2981–2992 (2010)
7. Khanh, L., Seo, J., Kim, Y., Won, D.: Power-management strategies for a grid-connected PV-FC hybrid system. *IEEE Trans. Power Delivery* **25**, 1874–1882 (2010)
8. Liu, X., Wan, P., Loh, P.C.: A hybrid AC/DC micro-grid and its coordination control. *IEEE Trans. Smartgrid* **2**, 278–285 (2011)
9. Xiaohong, G., Zhanbo, X., Jia, Q.: Energy-efficient buildings facilitated by micro-grid. *IEEE Trans. Smart Grid* **1** (2010)
10. Fu, Q., Montoya, F., Solanki, A., Nasiri, A., Bhavaraju, V., Abdallah, T., Yu, D.C.: Micro-grid generation capacity design with-renewables and energy storage addressing-power quality and surety. *IEEE Trans. Smart Grid* **3**, 2019–2027 (2012)
11. Huneke, F., Henkel, J., González, J.A.B., Erdmann, G.: Optimisation of hybrid off-grid energy systems by linear programming. *Sustain. Soc.* **2**, 2–19 (2012)
12. Lasseter, R.H.: Smart distribution coupled micro-grids. *Proc. IEEE* **99**, 1–8 (2011)
13. Su, W., Yuan, Z., Chow, M.U.: Microgrid planning and operation. *IEEE Solar Energy Wind Energy Conf.* 1–7 (2010)
14. Khatib, T., Mohamed, A., Sopian, K.: Optimization of a PV/wind micro-grid for rural housing electrification using a hybrid iterative/genetic algorithm: case study of Kuala Terengganu, Malaysia. *Energy Build.* **47**, 321–331 (2012)
15. Chen, C., Duan, S., Ca, T., Liu, B., Hu, G.: Smart energy management system for optimal micro-grid economic operation. *IET Renew. Power Gener.* **5**, 258–267 (2011)

A Design for High-Torque, Low-Speed Vertical Axis Wind Turbine

Rajesh Dommeti, Avinash Kathi and Mallikarjunarao Pasumarthi

Abstract Since last few years, there has been an enormous thrust on the development of alternative energy sources to cope up with the diminishing reserves of conventional energy resources. Because of its continuous availability, wind happened to be element for conversion into an alternative energy resource. The design of high-power wind turbine has geared up to the requirement, but unfortunately there are not much literature that contain any functional design for low-speed, high-torque micro-wind power generation system. In this paper, a methodology has been presented for the design of vertical axis wind energy conversion systems suitable for low-power domestic purposes. This design facilitates the manufacturer to easily select the turbine blade tilt angle and the ratio of overall L/D. This design is based on the Gorlov helical structure concept applied to Savonius turbine. A workbench for the simulation has been developed, and the design is simulated. The vertical axis turbine that is designed avoids the use of gearbox, and it is more suitable for direct mounted generation system.

Keywords Savonius helical turbine · Gorlov principle · Airfoil
Vertical axis wind turbine · Direct coupled generator · Tip speed ratio

R. Dommeti (✉) · A. Kathi · M. Pasumarthi
Department of Electrical Engineering, College of Engineering (A),
Andhra University, Visakhapatnam 530003, A.P, India
e-mail: rajesh.dommeti@gmail.com

A. Kathi
e-mail: aaronavi@gmail.com

M. Pasumarthi
e-mail: electricalprofessor@gmail.com

1 Introduction

Power generation through wind is a new swing from conventional energy sources, in which reliable power generation and cost saving are the main criteria. In the process, maximum effort is taken to reduce the noise level and meet the load demand. Based on the orientation of the axis, turbines are classified into horizontal axis and vertical axis turbine. The horizontal axis turbine is more common over the decade; in the installation the first and foremost problem is, it occupies a huge area, required large capacity of cranes to mount on the surface and needed more men power. The HAWT should be oriented towards the wind direction by the yaw mechanic control technique, and the aerodynamics of the horizontal axis is very complex. Many VAWT are proposed in recent times in which Darrieus and Savonius turbines are most common. Keeping with the view of a few aspects such as self-starting and uniform torque distribution along the turbine with vibration free, where the Darrieus and Savonius turbines fail to attain, a new Savonius helical turbine is designed.

Gorlov [1] developed a helical turbine designed for low fluid flow rates in the 1990s. It was initially developed for use in water either in a slow river or as a tidal generator. This turbine uses a vertical axis configuration having three blades that are swept along a helical path. Using this configuration, the turbine will always rotate in the same direction, regardless of the direction of the fluid flow. With its small size and intended to apply for low wind speeds, Gorlov helical turbine is a prime candidate to fill the need for a portable wind turbine. By using the idea of Gorlov helical turbine, a Savonius helical twist turbine is designed for self-start and uniform torque distribution. The turbine size as a function of power is required to drive a permanent magnet generator.

This paper is organized as follows. Second section elobertaes the Power calculation for VAWT from the literature. The next section gives an idea of the problems associated with VAWT design, particularly Savonius helical turbines. The obtained CFD analysis results for various designs are compared and the adaptable configuration is chosen from analysis data.

2 Power Equations of VAWT

The maximum power that can be extracted is given by [2] (Fig. 1)

$$P_{\max} = C_0 \rho R_0 H (V^3) \quad (1)$$

where C_0 = power coefficient = 0.3 ρ = density of air = 1.225.

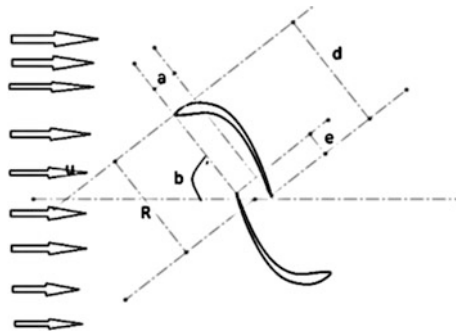


Fig. 1 Airfoil isometric view and wind force directions

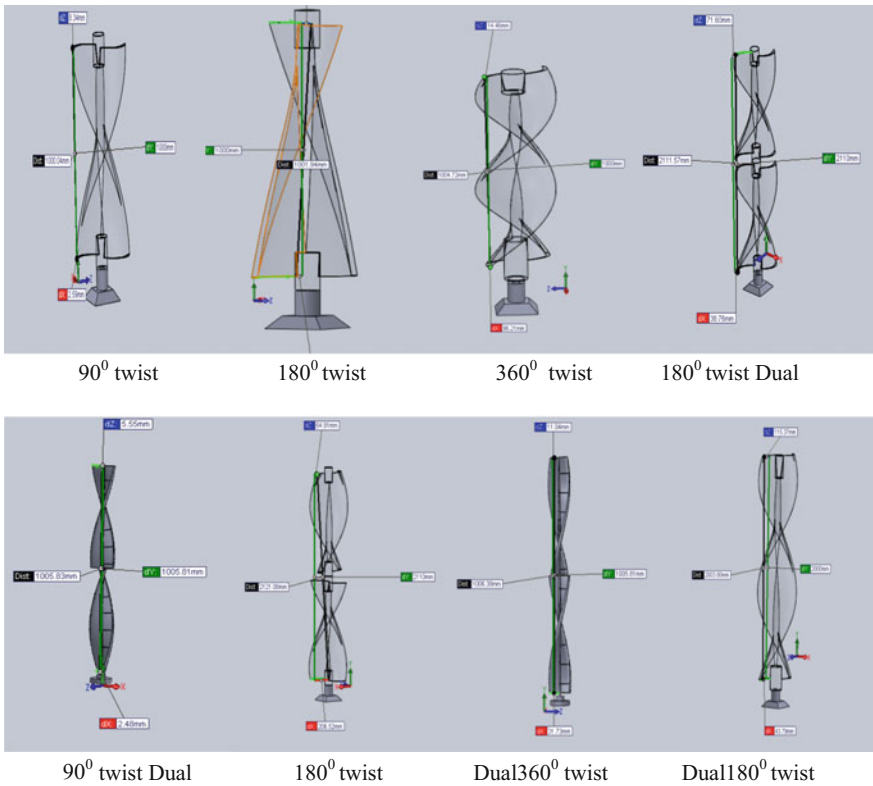


Fig. 2 Different combinations of Savonius helical twist turbines

Generally, Assuming tip speed ratio = 1 and we get

$$\lambda = \left(\frac{\omega r}{V_w} \right) \quad (2)$$

$$\text{Torque} = \left(\frac{P_{\max}}{\omega} \right) \quad (3)$$

For example, with diameter D of 480 mm, using the empirical relation $2d - e = D$; $m = e = (d/6)$; then $e = a = 51$ mm, $d = 265.5$ mm and $L = 1000$ mm.

The data considered for the simulation are shaft diameter D : 100 mm. Bearing type: roller.

The generator chosen was permanent magnet synchronizing generator with voltage rating of 12 V and 100 rpm so as to achieve direct drive generator.

2.1 *Designed Models of Savonius Helical Twist Turbines*

See Fig. 2.

3 Stated Problem

The problems identified in the literature [3, 4] existing on VAWT were as follows

- At low speeds, there is a lack of lift generated in the turbine and uneven torque distribution, and the Darrieus turbine fails to self-start
- The Savonius While self-starting has very low efficiency.

The uneven torque distribution of Darrieus turbine has been addressed in a design known as Quiet Revolution turbine, which is based on Dr Gorlov's Helical Turbine.

3.1 *Proposed Elucidation*

Savonius turbine blades to be twisted helical for solving the uneven torque distribution, and the assembly of 2 or 3 blades will be incorporated to provide the starting torque for the turbine which in turn makes the turbine self-starting [5–7]. With different wind velocities, the model is tested.

3.2 Steps to Be Taken

- Designing the blades based on the application in rural and domestic environment with the limitation of size.
- Designing the complete airfoil section of the blade where the angle attack is same throughout the blade in order to achieve noise-less rotation.
- Prototype manufacturing based on the newly proposed concepts.
- Testing using solid work flow simulation by creating a virtual wind tunnel where environmental pressure acts.

3.3 Flow Simulation

The design software for flow simulation is very much suitable for engineer who needs flow analysis [8]. A goal-oriented approach easily allows for gaining insight into the performance of design under real environmental conditions in less time.

4 Computational Fluid Dynamics Analysis

The wind tunnel environment is created for the design turbine model to study the flow simulation characteristics on the CFD work bench. The environment constraints like wind direction and environmental pressure are given as boundary conditions to flow simulation, the virtual environment is achieved equivalent to a real time scenario.

Objective of testing is

- To test the best helical twist turbine, the model of one blade with dimensions is tested at different wind velocities by creating a wind tunnel in CFD analysis.
- The testing is done in two phases; first phase includes the testing the best twist for a unique turbine, and the second phase includes by varying the L/D ratio of the turbine (Fig. 3).

Tip speed ratio impact on turbine dimensions

CFD flow analysis tip speed ratio of Savonius turbine is observed to be 1, since the wind tunnel environment is created bounded with environmental pressure acting

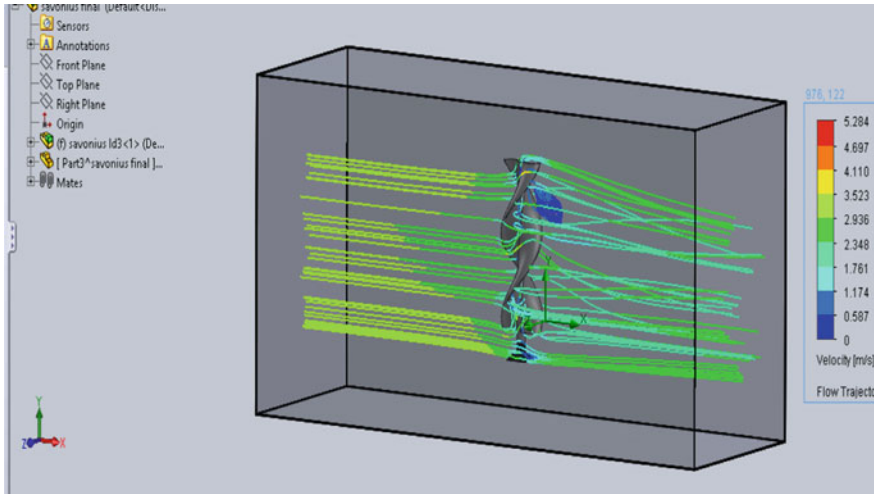


Fig. 3 Flow simulations for 360 twist blade turbine, $L/D = 3$

opposite to the direction of the wind flow. The tip speed ratio is (TPR) 0.833, which is near to 1.0; therefore, the tip speed ratio of Savonius turbine is confined to 1.0 [9, 10].

5 Results and Discussion

Case (i) Savonius turbine tested with different twist angles

In this the turbine dimensions of diameter 0.5 m and height 1.0 m with a helical twist of 90° , 180° , 360° are designed. The turbine is tested in a wind tunnel with the flow simulation tool. The turbine behaviour for different wind conditions is observed and conclusions are derived with a goal oriented to obtain a turbine which suits micro-power generator parameters (Table 1).

Figure 4a shows that wind power and shaft power developed by wind turbine with respect to wind speed. From Fig. 4b, the torque obtained by the 90° twist helical turbines is maximum as compared to that of 180° and 360° twist.

The 180° twist turbine attains high shaft speed at different wind velocities as that of 90° and 360° twist turbines as shown in Fig. 5a. Speed and torque characteristics of wind turbine with 360° helical twist have a large variety of operating conditions with variable wind velocities as shown in Fig. 6. Hence the turbine with blade twist of 360° is chosen for further analysis by varying the dimensions, i.e. L/D ratio of the turbine.

Table 1 Turbine shaft speed, torque variation for different configurations

Blade twist (deg)	Wind speed (m/s)	Wind power (w)	Power extracted (w)	Torque (Nm)	ω (rad/s)	Turbine speed (rpm)
90	3	24.14	7.24	1.42	5.09	48
180	3	24.14	7.24	0.415	17.44	166
360	3	24.14	7.24	0.729	9.93	94
90	5	111.78	33.53	4.04	8.29	79
180	5	111.78	33.53	2.93	11.44	109
360	5	111.78	33.53	2.133	15.71	150
90	7	306.72	92	7.904	11.63	111
180	7	306.72	92	3.297	27.90	266
360	7	306.72	92	4.144	22.2	212
90	10	894.25	268.27	16.03	16.73	159
180	10	894.25	268.27	6.699	40.04	382
360	10	894.25	268.27	8.384	31.99	305
90	15	3018	905.4	35.979	25.16	240
180	15	3018	905.4	14.749	61.38	586
360	15	3018	905.4	18.576	48.74	465

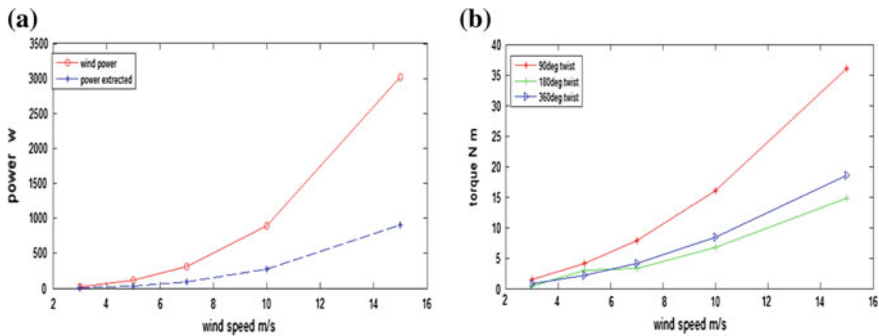


Fig. 4 a Wind power, shaft power extracted variation as a function of wind speed b turbine shaft torque versus wind speed for different twists

Case (ii) Testing of turbine with different L/D ratio

The Savonius two-blade turbines with 360° twist with different heights are considered by keeping the radius as constant. The turbine with more sweeping area acquires (turbine with high L/D ratio) more power and torque, but the limitation on shaft speed. So confining to size constraints for the different combinations of parameters, a suitable model has to be finalized. For L/D ratio 4, the turbine acquires high torque compared to other configurations as shown in Fig. 6a. For L/D

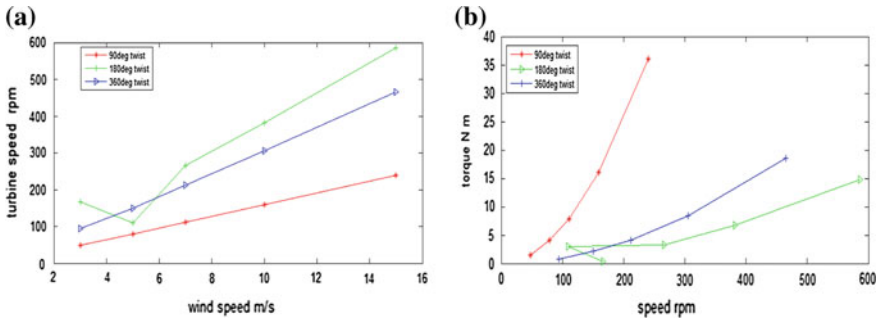


Fig. 5 a Turbine shaft speed versus wind speed for different twists b shaft speed, shaft torque cumulative variation for different twist angles

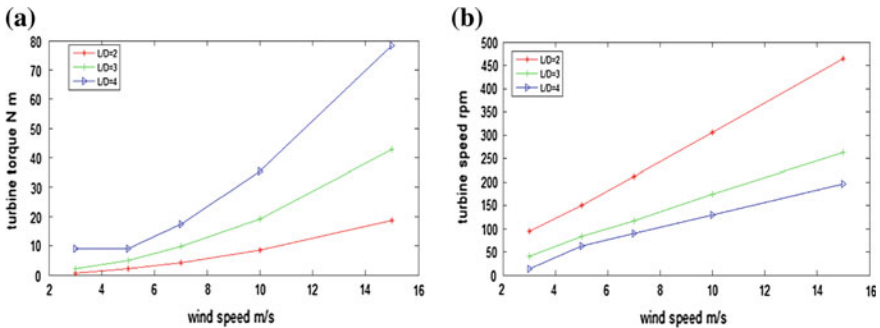


Fig. 6 a Torque versus wind velocities with different L/D ratios, b shaft speed variation w.r.t to wind velocities for different L/D ratio

ratio 2, the turbine attains high speed compared to other turbines for different wind velocities as shown in Fig. 6b (Table 2).

Therefore, when an average wind speed is in the range of 5 m/s and L/D as 3.0, i.e. dimensions of the turbine are optimum for a length of 1.5 m and a diameter of 0.5 m with a shaft torque of 4.973 Nm at shaft speed of 83 rpm. For the obtained turbine parameters, it is evident that the turbine can be used to drive direct coupled generator. The obtained torque is enough to drive the generator. Thus, with the considerable elimination of gear train, the turbine efficiency is improved (Fig. 7 and Table 3).

The designed Optimum turbine model is simulated with direct coupled Axial flux permanent magnet (AFPM) generator. For the Designed turbine shaft torque a AFPM machine is modelled using the dimensional equations and it is simulated in powergui template, to verify the specifications of Generator. The Matlab simulation incorporate with design turbine and AFPM with a three phase bridge rectifier and Buck boost converter.

Table 2 Turbine shaft speed, torque variation w.r.t to L/D ratio

L/D ratio	Wind speed (m/s)	Wind power (W)	Power extraction (w)	Torque (Nm)	w (rad/s)	Turbine speed (rpm)
2	3	24.14	7.242	0.729	9.93	94.91
3	3	31.42	9.42	2.243	4.199	40.12
4	3	42.99	12.897	9.028	1.428	13
2	5	111.78	33.53	2.133	15.71	150
3	5	145.46	43.63	4.973	8.77	83
4	5	199.06	59.718	9.048	6.6	63
2	7	306.72	92.016	4.144	22.20	212
3	7	399.16	119.74	9.731	12.30	117
4	7	546.22	163.866	17.516	9.355	89
2	10	894.25	268.27	8.384	31.99	305
3	10	1163.75	349.125	19.106	18.27	174
4	10	1592.5	477.75	35.345	13.51	129
2	15	3018	905.4	18.576	48.74	465
3	15	3927.65	1178.29	42.848	27.499	262.72
4	15	5374.68	1612.40	78.420	20.56	196

Fig. 7 Shaft torque and speed cumulative variation with L/D ratio variation

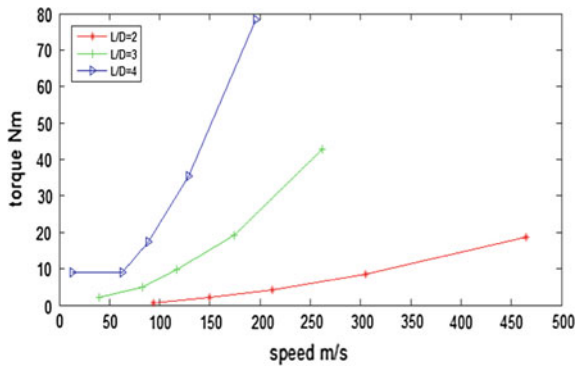


Figure 8a represents the voltage of the Simulink model, x axis and y axis represent time and DC voltage, respectively. As the wind velocity increases, the power generated also increases, The model designed as the survival speed to operate at 15 m/s. Figure 8b represents the current of the model, where x axis and y axis represent time (s) and current, respectively. The power obtained is nearly 814 W which serves the need of domestic and lighting usages. These models can be extended to the required design from end-to-end analysis.

Table 3 Slotted PMSG final design dimensions and specifications

Output power	P_{out} (W)	1000	Speed	N (rpm)	100
Output DC voltage	V_{dc}	24	Frequency	F (Hz)	15
Number of poles	P	18	Number of slots	N_s	162
Fundamental winding factor	K_{wl}	0.966	Air gap	g (mm)	1
Magnetic loading	B_g (T)	0.79	Electric loading	A (LA/m ²)	
Outer diameter	D_o (m)	0.25	Inner/outer diameter	L	0.53
Pole arc/pole pitch	α_p	0.65	Magnet thickness	L_{pm} (mm)	5
Stator core axial length	L_{cs} (mm)	50	Rotor core axial length	L_{cr} (mm)	25
Number of slots per pole phase (nspp)		3	Resistance per phase	R_{phase} (Ω)	0.043
Synchronous reactance per phase	X_{phase} (Ω)	0.3897	Efficiency	%	85

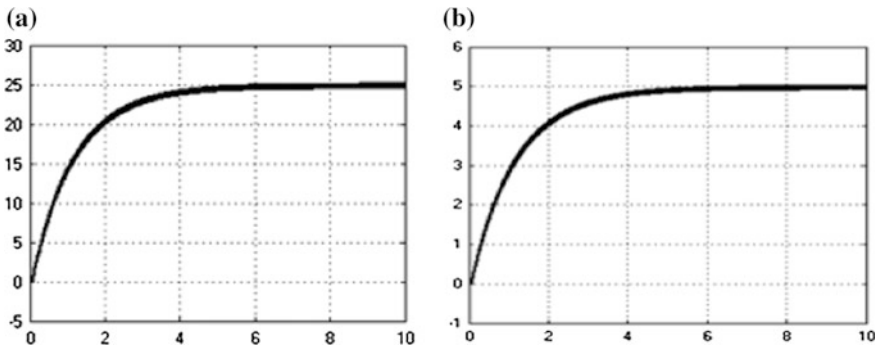


Fig. 8 a Output voltage of RE load b output current of the RE load at 15 m/s wind speeds

6 Conclusion

The helical two foil turbine with 3600 of twist gives Optimum shaft speed- torque characteristics than that of 900 and 1800 of twist turbines for same dimensions. In the helical 3600 twist turbine the angle of attack is same throughout the length of the blade and the tip speed ratio is near to 1.0, which are defined to be optimum design characteristics. The analysis for 3600 twist turbine with different dimensions by keeping constant radii of 0.5 m, The output torque obtained at shaft torque is proportional to the length of the turbine and wind speed. Variation in L/D ratio also affects the required generator input characteristics. For L/D of 3, best suitable turbine with linear speed and torque characteristics of direct coupled wind energy

system. The workbench has the feasibility to test the turbine model at high speeds rather than a manual wind tunnel to estimate the performance. The designed turbine model can archive rated performance at low wind speeds, which suits the requirement of Urban and Rural domestic power requirements.

References

1. Gorlov, A.: Development of the helical reaction hydraulic turbine (1990)
2. Schubel, P.J., Crossley, R.J.: Wind turbine blade design. *Energies* **5**(12), 3425–3449 (2012)
3. Johnson, G.L.: *Wind energy systems* (2001)
4. John, L.: The effect of cord length and taper on wind turbine blade design (2008)
5. Madani, N.: Design of a permanent magnet synchronous generator for a vertical axis wind turbine. Electrical Engineering Stockholm, Sweden (2011)
6. Sawin, J.L., Martinot, E.: Global Status Report. Technical Report, Renewable 2010. Renewable Energy Policy Network for the 21st century (2010)
7. Nathan Willard Northeastern University Efficiency.: Investigation of a helical turbine for harvesting wind energy (2011)
8. Hossain, A.: Design and development of a 1/3 scale vertical axis wind turbine for electrical power generation. *JUEE J. Urban Env. Eng.* **1**(2), 53–60 (2007)
9. Regheb, M.: Vertical axis wind turbine (2015)
10. McIntosh, S.C., Babinsky, H.: London Aerodynamic Modeling of Swept Bladed Vertical Axis Wind Turbine. Quiet Revolution Ltd (2012)

Single-Stage Boost Inverter Topologies for Nanogrid Applications

P. Sriramalakshmi and V.T. Sreedevi

Abstract The non-conventional energy source-based distribution generation systems are suitable for low-power applications. These renewable energy system (RES)-based networks very often experience vast changes in the inverter output voltage, due to certain power quality issues like fluctuations, voltage sags, etc. Usually, a conventional boost converter is connected between the DC source and inverter to boost up the DC voltage when the available voltage is less than the required voltage for a particular application. If a highly boosted voltage is needed, the duty ratio of the converter needs to be fixed at maximum which creates serious reverse recovery issues. In order to overcome the aforementioned problems, single-stage power inverters are the best solution. Impedance-source inverter (ZSI), switched boost inverter (SBI), quasi-switched boost inverter (QSBI) are some of the single-stage step-up inverter topologies. These converters can either buck or boost the available DC input voltage, which provides better electromagnetic interference immunity and need not to be operated at extreme duty cycle, and it can produce both direct and alternating voltages from a single DC source. Because of all the above-mentioned advantages, single-stage boost inverters are appropriate for nanogrid applications. This paper reviews the features and operations of single-stage boost inverter topologies like ZSI, QZSI, basic SBI and family of QSBI topologies. The MATLAB simulation studies are carried out with the same design parameters for all the topologies, and the results are presented in detail including performance comparison.

Keywords Nanogrid · VSI · ZSI · QZSI · SBI · Quasi-SBI · Shoot through

P. Sriramalakshmi (✉) · V.T. Sreedevi
School of Electrical Engineering, VIT University, Chennai, India
e-mail: sriramalakshmi.p@vit.ac.in

V.T. Sreedevi
e-mail: sreedevi.vt@vit.ac.in

1 Introduction

The power electronic converters play main role in connecting RES to the load [1]. The voltage-source inverter (VSI) [2, 3] is widely used in distributed generation, drive applications, uninterruptible power supplies and electric vehicles. But conventional VSI has drawbacks. It can provide the output voltage less than the input voltage, and its output cannot be more than the DC-link voltage. Both the switches in each phase cannot be turned on simultaneously. Otherwise short circuit will happen and damage the devices [4]. For applications where high voltage is needed, a DC–DC conventional boost converter is connected as shown in Fig. 1 which may increase the converter cost and reduces the efficiency [5]. To avoid two stage power conversions, the ZSI was proposed in 2002 [6] as shown in Fig. 2. The ZSI has an ability to overcome the aforementioned issues. ZSI has an X network which connects the inverter and the DC source. In ZSI, both the upper and lower switches can be fired simultaneously. It can increase or decrease the available source voltage. Also it has no dead time and hence improves the system reliability. Thus, it minimizes the harmonic content in the AC load voltage [7–10].

To have continuous source current and reduced capacitor voltage which is not possible with conventional ZSI, quasi-impedance-source inverter (QZSI) [11, 12] was proposed as shown in Fig. 3. But the lattice network with two symmetrical inductors and capacitors in the ZSI and QZSI maximizes the size and overall cost of the system. Also the implementation of perfect symmetrical X network is not feasible in practical. So this inverter cannot be used for low-power applications. A switched boost inverter (SBI) is suggested [13] as shown in Fig. 4.

Fig. 1 DC–DC boosted VSI

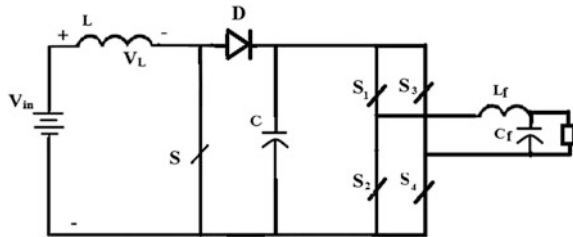


Fig. 2 Impedance-source inverter

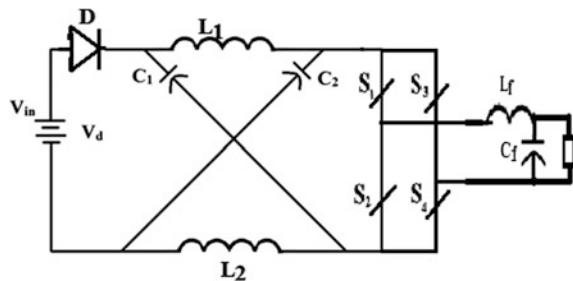


Fig. 3 Quasi-ZSI

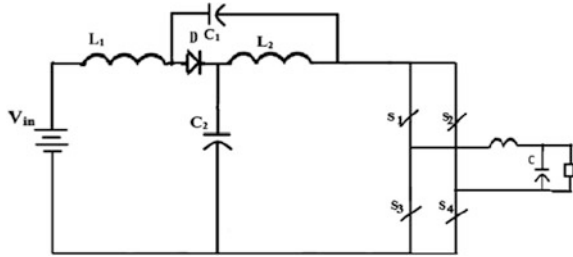
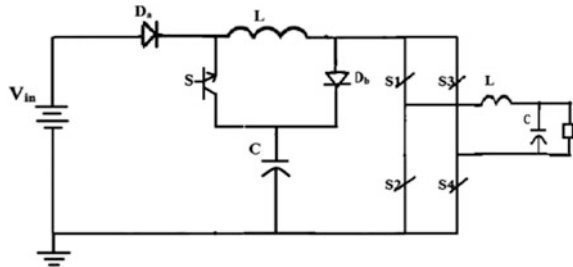


Fig. 4 Basic switched boost inverter



There are two major problems of ZSI, i.e., high magnetic requirement and poor transient response in case of asymmetrical impedance network. It can be eliminated with the help of SBI [14]. In addition, SBI can be used wherever both DC and AC voltages are required [15]. Also it is best suitable for nanogrid applications. In the SBI, the voltage across the capacitor is same as the inverter input voltage (DC-link voltage) when it is operated to have boosted voltage. The SBI uses reduced number of semiconductor devices. To produce high voltage gain, a high shoot-through duty ratio D must be used. The modulation index M is chosen such that it satisfies the condition, $M = 1 - D$. The low value of M leads to increment in the harmonic content of the inverter output voltage. A family of quasi-switched boost inverter (QSBI) is presented to overcome all the issues addressed under SBI [16]. Similar to conventional SBI, the QSBI family has same number of components. QSBI can be classified as embedded-type QSBI and DC-linked-type QSBI. The voltage stress across the capacitor in a DC-linked-type QSBI is low. A high boost with continuous source current is possible in an embedded-type QSBI [16].

In this paper, Sect. 2 explains various single-phase high boost inverter topologies, advantages and their boost ability, Sect. 3 briefs the PWM techniques and presents the simulation results, Sect. 4 analyzes the performance of the above-mentioned topologies and Sect. 5 concludes the paper. At the end, reference papers are listed out.

2 Analysis of Single-Stage Boost Inverter Topologies

2.1 Impedance-Source Inverter Topology

Figure 2 shows the ZSI [4] topology. The X network connects the source and load. It includes two inductors and two capacitors of same values. Depending upon the shoot-through duty ratio, ZSI can increase or decrease the available DC voltage. In ZSI, both the switches in a single leg can be turned on simultaneously. Shoot through cannot damage the device. Active state and Shoot-through state of ZSI are shown in Fig. 5a, b. During active state, diode gets turned on. During this state, the capacitor is getting charged. Also the DC voltage and the inductive energy are transferred to the load. During shoot-through state, the capacitors discharge through the inductors [17].

The boost factor (B) can be given by,

$$\frac{V_C}{V_{in}} = \frac{1 - \frac{T_0}{T}}{1 - \frac{2T_0}{T}} = \frac{1 - D}{1 - 2D} \tag{1}$$

$$V_C = BV_{in} \tag{2}$$

B is the boost factor.

2.2 Quasi-Z-Source Inverter Topology

The QZSI [11, 12] has two states namely shoot-through zero state and active state like ZSI. During shoot-through zero state, diode is reverse biased and inverter legs

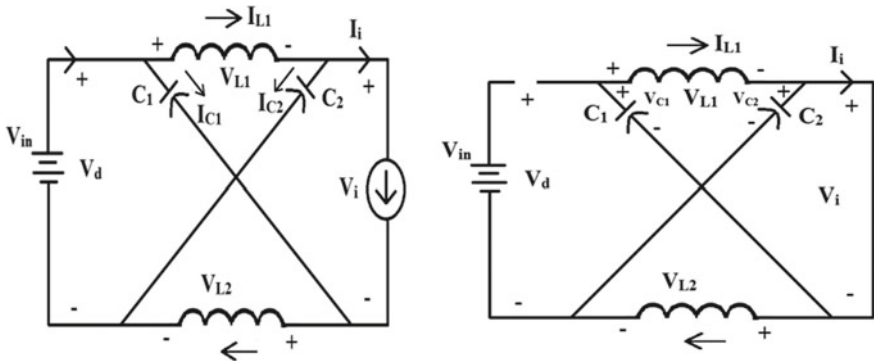


Fig. 5 a Active state, b shoot-through zero state

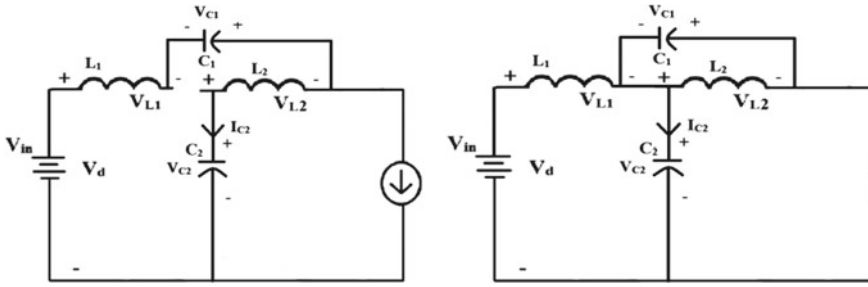


Fig. 6 a Active state, b shoot-through zero state

are shorted. Also no voltage will appear across the load. During active state, diode is in conduction state and the boosted voltage will be delivered to the load. Both the active state and shoot-through zero state are shown in Fig. 6a, b, respectively. During active mode (T_1), voltage across the inductor (V_{L1}) is difference between the source voltage and the voltage across capacitor (V_{C1}). The voltage across the inductor (V_{L2}) is equal to negative of capacitor voltage (V_{C2}). Similarly, during shoot-through state (T_0), inductor voltage (V_{L1}) is the addition of input voltage and capacitor voltage (V_{C2}). And the inductor voltage (V_{L2}) is equal to voltage across the capacitor (V_{C2}).

$$V_0 = V_{C1} + V_{C2} = BV_{in} \tag{3}$$

The boost factor B is given as,

$$B = \frac{1}{1 - 2\frac{T_0}{T}} \tag{4}$$

2.3 Switched Boost Inverter Topology

The switched boost inverter (SBI) is also a structure of single-stage step-up [13, 14] converter topology. Figure 4 shows the basic SBI topology. The operation of basic SBI topology is explained in two different states. Similar to ZSI, SBI too has shoot-through zero state in addition to active state, due to which the boost action takes place. By considering the circuit shown in Fig. 4, during shoot-through zero interval, S is turned on. Since voltage across capacitor is more than the input DC voltage, diodes D_1 and D_2 are reverse biased during this interval as shown in Fig. 7a. Now L and C are connected in parallel and the energy stored in C discharges through the inductor. During active state as shown in Fig. 7b, S is

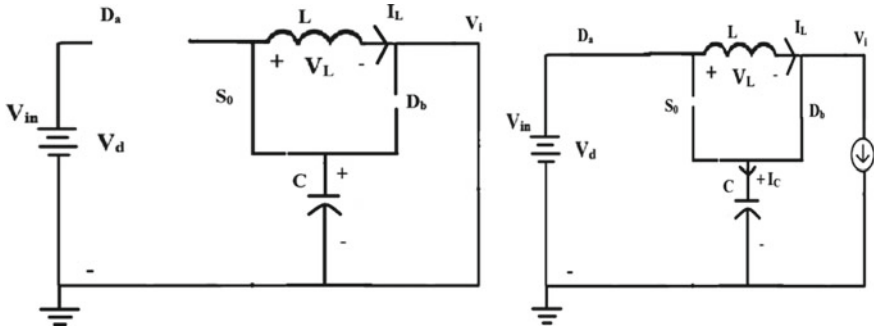


Fig. 7 a Shoot-through state, b active state

switched off and diodes D_1 and D_2 are forward biased and inductor current flows through the load [16, 17].

The boost factor (B) can be given by,

$$\frac{V_C}{V_{in}} = \frac{1 - D}{1 - 2D} \tag{5}$$

where ‘ D ’ is the shoot-through duty ratio.

2.4 Quasi-Switched Boost Inverter Topologies

In this topology, an inductor, a diode and a switch is connected directly to a DC source. So the voltage across the DC link is higher than source voltage. Thus, SBI topologies are extended to QSBI [18]. So the number of components used in QSBI is similar to that of basic SBI topologies. QSBI can also provide continuous source current. The voltage across the capacitor is same as that of DC-link voltage. QSBI topologies are further classified into embedded-type QSBI and DC-linked-type QSBI.

2.4.1 Embedded-Type Quasi-Switched Boost Inverter

When DC input is connected in series with the inductor, it draws a continuous source current and gives boosted voltage. But the capacitor voltage is same as the DC-link voltage. In other way, topology can be modified in such a way to share same common ground which is termed as CFSI (current-fed switched inverter) [18]. The embedded type-1 QSBI is shown in Fig. 8. During active state, the inductor voltage is the difference of the source voltage (V_{in}) and the voltage stress across the

Fig. 8 Embedded type-1 quasi-SBI

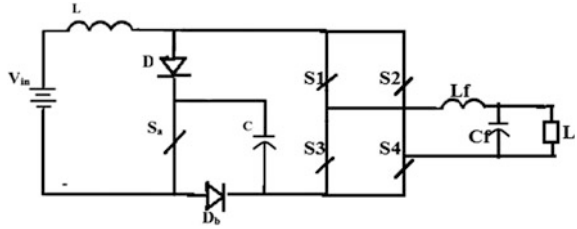
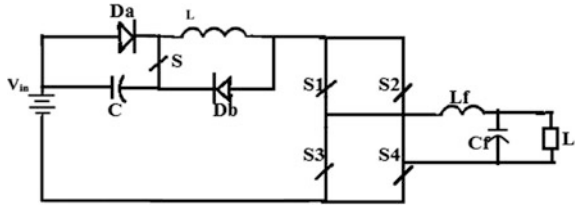


Fig. 9 DC-linked negative bus-type quasi-SBI



capacitor (V_C). Also the capacitor current (I_C) is the difference of the inductor current (I_L) and the inverter input current (I_{in}) as shown in Fig. 10a. Similarly, the shoot-through operation of the inverter is shown in Fig. 10b.

The capacitor voltage is given as,

$$V_C = \frac{1}{1 - 2D} V_{in} \tag{6}$$

The boost factor B is given by,

$$B = \frac{1}{1 - 2D} \tag{7}$$

2.4.2 DC-Linked-Type Quasi-Switched Boost Inverter

The n-type DC-linked QSBI [19] is shown in Fig. 9. It can reduce the voltage stress across capacitors. It can be further classified into positive terminal DC-linked-type QSBI and negative bus-type DC-linked QSBI. When the voltage source is connected between the boost cell and negative terminal of the DC bus, it is called as negative bus-type DC-linked QSBI. But in positive bus-type QSBI, voltage source is connected between positive terminal of the DC bus and switched boost cell. This type of inverter does not share the same ground. QSBI topologies have less

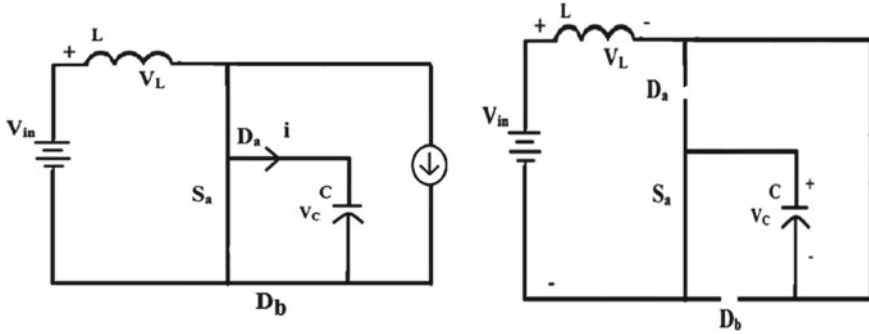


Fig. 10 a Active state, b shoot-through state

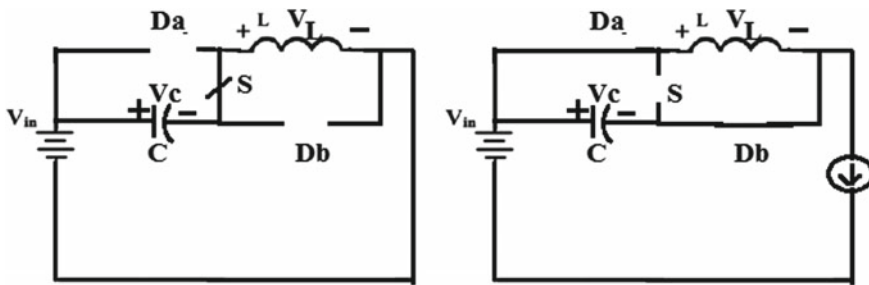


Fig. 11 a Shoot-through state, b active state

capacitor voltage stress with the same component count as that of SBI. The shoot through and active state of the converter are shown in Fig. 11a, b, respectively.

The peak DC-link voltage during active state is given as,

$$V_{PN} = \frac{1 - D}{1 - 2D} V_{in} \tag{8}$$

The boost factor B is expressed as

$$B = \frac{1 - D}{1 - 2D} \tag{9}$$

where D is the shoot-through duty ratio.

3 Simulation Results and Comparisons

To analyze the performance of all the above-mentioned single-stage high boost inverter topologies, the MATLAB/SIMULINK-based simulations are done with the same design parameters and their output voltage and current results are presented. Simple Boost Control (SBC) method [20] of pulse width modulation technique is used to produce the pulses to all the switches. Simple boost method is a modified method of conventional sinusoidal PWM (SPWM).

The shoot-through pulses which are responsible for boosted voltage can be produced by comparing the triangular carrier waves with the positive and negative envelopes. With the DC input voltage of 64 V, modulation index (M) of 0.5, carrier switching frequency for switches ($S_1, S_2, S_3,$ and S_4) is 10 kHz and for S which is 20 kHz. The inductance values are $L_1 = L_2 = L = 5.6$ mH, capacitance values are $C_1 = C_2 = C = 100$ μ F, filter inductor is 4.6 mH, filter capacitance of 10 micro-Farad and the star-connected resistive load of 100 Ω .

ZSI can provide peak load voltage of 230 V, and QZSI can provide the peak load voltage of 240 V. The load voltage and load current waveforms of ZSI and QZSI are presented in Fig. 12a, b. The advantage of using QZSI is that it can provide continuous input current with reduced voltage stress across the capacitor. With the DC source voltage of 64 V, the negative bus-type DC-linked SBI can boost the DC-link voltage up to 175 V and the AC peak voltage of around 85 V as shown in Fig. 13a. At the same time, embedded type-1 QSBI can provide the AC peak output voltage of about 280 V as shown in Fig. 13b. As shown in Fig. 14, both the type of QSBI topologies can provide DC voltage for powering DC loads as well. For example, embedded-type QSBI provides 500 V boosted DC voltage.

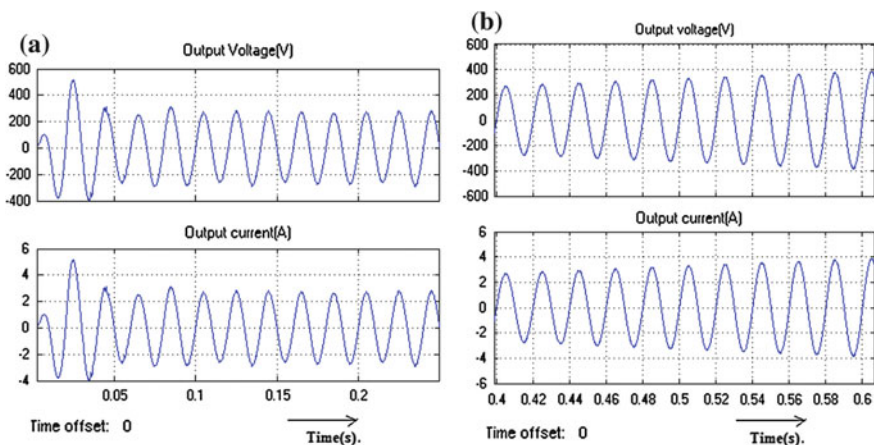


Fig. 12 Output voltage and load current waveforms of ZSI and QZSI

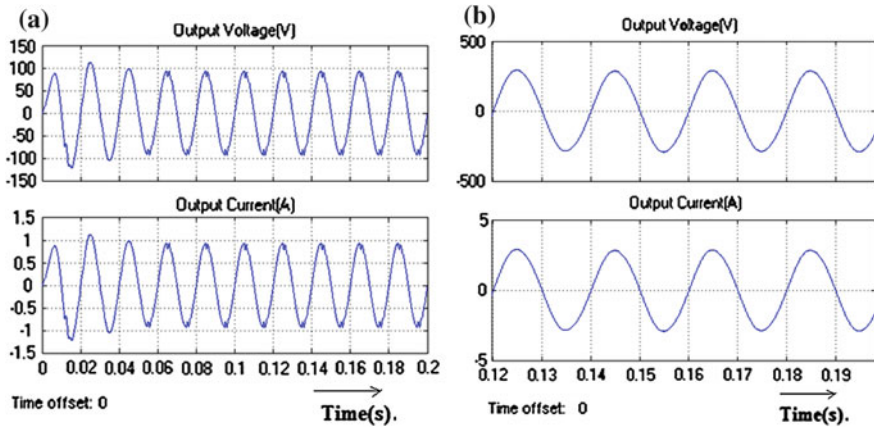
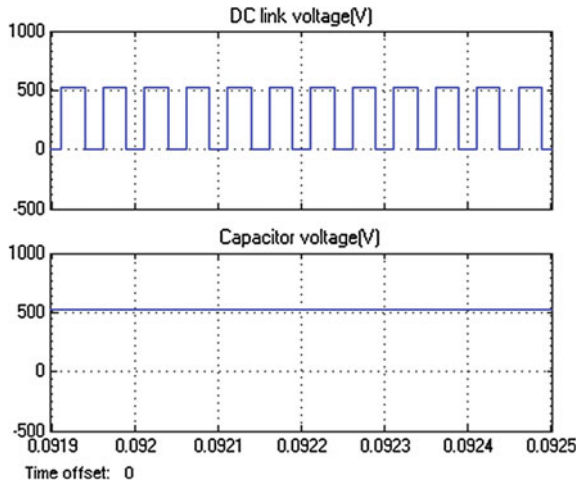


Fig. 13 Output voltage and load current waveforms of DC-linked negative bus-type and embedded type-1 quasi-switched boost inverter

Fig. 14 Capacitor voltage and DC-link voltage of embedded-type QSBI



4 Performance Analysis of High Boost Inverter Topologies

Table 1 lists out the number of semiconductor switches, inductors and capacitors used in the single-stage high boost inverter topologies. It is obvious that ZSI and QZSI use one additional inductor and capacitor when compared to other topologies. But SBI and its modified topologies have additional semiconductor devices compared to ZSI and QZSI topologies.

Table 1 Number of components used in different topologies

	ZSI	QZSI	SBI	Embedded-type QSBI	DC-linked type QSBI
Switches	4	4	5	5	5
Diode	5	5	6	6	6
Inductor	2	2	1	1	1
Capacitor	2	2	1	1	1

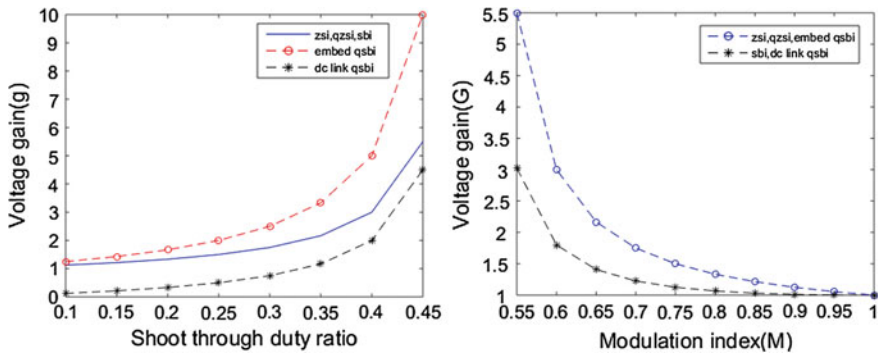


Fig. 15 **a** Shoot-through duty ratio versus voltage gain, **b** modulation index versus voltage gain

Figure 15a shows the relationship between voltage gain and shoot-through duty ratio of conventional ZSI, QZSI, SBI, embedded and DC-linked-type QSBI topologies. It is clear from Fig. 15a that voltage gain of embedded-type QSBI is higher than ZSI, QZSI, SBI and DC-linked-type QSBI. So device rating of embedded-type QSBI is higher than SBI. Also ZSI and QZSI have highest total device rating compared to other topologies. Wherever high voltage boost is demanded, embedded-type QSBI can be used. It is obvious from Fig. 15b that with lower modulation index, ZSI, QZSI, and embedded-type QSBI inverters can provide high voltage boost compared to SBI and DC-linked-type QSBI.

5 Conclusion

This paper reviews a few single-stage high boost inverter topologies available for nanogrid applications. The detailed working of converters available in the literature is discussed. All the inverter topologies are simulated with the same source voltage and other design parameters. The simulated load voltage and current waveforms are presented. The performance analysis reveals that the embedded-type QSBI can provide higher voltage boost among the inverters discussed in this work. It can be

used effectively where both DC and high boost AC voltages are desirable. The future work may be extended to design the control system for single-stage boost inverter topology used for producing both DC and AC voltages simultaneously in nanogrid applications.

References

1. Kroposki, B., Pink, C., Deblasio, R., Thomas, H., Simoes, M., Sen, P.K.: Benefits of power electronic interfaces for distributed energy systems. *IEEE Trans. Energy Convers.* **25**, 901–908 (2010)
2. Erickson, R.W., Maksimovic, D.: *Fundamentals of Power Electronics*. Kluwer, Norwell, MA, USA (2001)
3. Lazzarin, T.B., Baue, G.A.T.R., Barbi, I.: A control strategy for parallel operation of single-phase voltage source inverters: analysis, design and experimental results. *IEEE Trans. Ind. Electron.* **60**, 2194–2204 (2013)
4. Sriramalakshmi, P., Sreedevi, V.T.: Modified PWM control methods of Z source inverter for drive applications. *ARNP J. Eng. Appl. Sci.* **10**, 6932–6943 (2015)
5. Shen, M., Joseph, A., Wang, J., Peng, F.Z., Adams, D.J.: Comparison of traditional inverters and Z-source inverter for fuel cell vehicles. *IEEE Trans. PE* **22**, 1453–1463 (2007)
6. Peng, F.Z.: Z-source inverter. *IEEE Trans. Ind. Appl.* **39**, 504–510 (2003)
7. Peng, F.Z.: Z-source Networks for Power Conversion. In: *APEC 2008*, pp. 1258–1265 (2008)
8. Ellabban, O., Mierlo, J.V., Lataire, P.: A DSP-based dual-loop peak DC-link voltage control strategy of the Z-source inverter. *IEEE Trans. Power Electron.* **27**, 4088–4097 (2012)
9. Hanif, M., Basu, M., Gaughan, K.: Understanding the operation of a Z-source inverter for photovoltaic application with a design example. *IET Power Electron* **4**, 278–287 (2011)
10. Liu, J.B., Hu, J.G., Xu, L.Y.: Dynamic modeling and analysis of Z-source converter-derivation of AC small signal model and design-oriented analysis. *IEEE Trans. Power Electron.* **22**, 1786–1796 (2007)
11. Li, Y., Jiang, S., Cintron Rivera, G., Peng, F.Z.: Modelling and control of quasi z source inverter for distributed generation applications. *IEEE Trans. Ind. Electron.* **60** (2013)
12. Liu, H., Liu, P., Zhang, Y.: Design and digital implementation of voltage and current mode control for the quasi-Z-source converters. *IET Power Electron.* **6**, 990–998 (2013)
13. Upadhyay, S., Ravindranath, A., Mishra, S., Joshi, A.: A Switched-Boost Topology for Renewable Power Application, pp. 758–762. *IEEE IPEC 10* (2010)
14. Mishra, S., Adda, R., Joshi, A.: Inverse Watkins-Johnson topology based inverter. *IEEE Trans. Power Electron.* **27**, 1066–1070 (2012)
15. Adda, R., Ray, O., Mishra, S., Joshi, A.: Synchronous-reference-frame based control of switched boost inverter for standalone dc nanogrid applications. *IEEE Trans. Power Electron.* **28**, 1219–1233 (2013)
16. Ravindranath, A., Mishra, S., Joshi, A.: Analysis and PWM control of switched boost inverter. *IEEE Trans. Ind. Electron.* **60**, 5593–5602 (2013)
17. Rajakaruna, U., Jayawickrama, L.: Steady-state analysis and designing impedance network of Z-source inverters. *IEEE Trans. Ind. Electron.* **57**, 2483–2491 (2010)
18. Nag, S.S., Mishra, S.: Current-fed switched inverter. *IEEE Trans. Ind. Electron.* **61**, 4680–4690 (2014)
19. Nguyen, M.-K., Le, T.-V., Park, S.-J., Lim, Y.-C.: A class of quasi-switched boost inverter. *IEEE Trans. Ind. Electron.* **62**, 1526–1536 (2015)
20. Loh, P.C., Vilathgamuwa, D., Lai, M.X., Chua, Li, Y.W.: Pulse-width modulation of Z-source inverters. *IEEE Trans. Power Electron.* **20**, 1346–1355 (2005)

Investigation of Failure and Degradation Types of Solar PV Plants in a Composite Climate: Abstract After 4–6 Years of Field Operation

Bhaveshkumar V. Dobaria, Vikrant Sharma and Alpesh Adeshara

Abstract The chief objective of this study is the reliability and durability assessment of 4–6-year-old solar photovoltaic (PV) crystalline systems located in the city of Rajkot, Gujarat (having a composite climate condition). These all systems were originally installed during 2010–2012 with a rated capacity of 10 kWp (2 in numbers), 50 kWp (1) and 100 kWp (3) (fixed tilt, south orientation). This study only recognized the degradation and failure mechanisms. The observations obtained from the exclusive visual inspection and thermography made on 6 different solar plants were utilized to detect degradation and failure types. The encapsulant discoloration and delamination, corrosion of cell gridlines, back-sheet delamination and yellowing, snail track, hot spot, cell cracks and burn marks at back-sheet have been examined to be the degradation and/or failure types of these 4–6-year-old solar PV plants in this particular composite climate.

Keywords PV durability · PV degradation · Defects · PV module performance
PV reliability

1 Introduction

The reliability and durability of PV solar plants are critical for their commercial feasibility as it affects the financial aspect of PV electricity. Deducing the degradation and failure types of PV solar power plants is of quintessential for all

B.V. Dobaria (✉)

Darshan Institute of Engineering and Technology, Rajkot, Gujarat, India
e-mail: bhaveshkumar.dobaria@darshan.ac.in

V. Sharma

National Institute of Solar Energy, Gurgaon, Haryana, India
e-mail: sharma_vs1982@yahoo.co.in

A. Adeshara

VVP Engineering College, Rajkot, Gujarat, India
e-mail: alpeshsays@yahoo.com

© Springer Nature Singapore Pte Ltd. 2018

S. SenGupta et al. (eds.), *Advances in Smart Grid and Renewable Energy*,

Lecture Notes in Electrical Engineering 435, https://doi.org/10.1007/978-981-10-4286-7_22

stakeholder of PV industry. In this special case, PV manufacturers can be benefited from this know how with an objective to establish an appropriate guaranteed span of time, to define sufficient reliability tests and improve their module manufacturing mechanism. Investors need the most transparent and accurate estimate of life duration of PV modules with a view to devise impeccable models for the economical returns on investment. PV plant designers must know the degradation and failure types, so they can improve their PV plant designs. PV plant owners must be aware about degradation and failure of PV modules so that proper maintenance strategies can be devised and implemented [1].

This study describes the failure and degradation types which have been noticed on 6 different poly-crystalline silicon PV systems of 10, 50 and 100 kWp size after 4–6 years of field operation at various sites of the city of Rajkot, Gujarat, India. The most important ideas of the study are: (i) to identify different types of early age defects occurring on the field and (ii) to apprehend the degradation mechanisms behind every typical defect.

The PV systems under study are composed of poly-crystalline solar PV modules with a peak power of 10–100 kWp. Analyzed plants are connected to the utility day and night via various inverter classes.

The usual meteorological conditions at the site of the system as per the data by National Renewable Energy Laboratory, USA (NREL), are: 5.65 kWh/m²/day of annual average global horizontal irradiation, average daytime ambient temperature of around 27 °C, relative humidity of 60% and wind speed of 18 km/h.

2 Visual Inspection

Visual inspection is the result-oriented and shortest practice to find visible defects in PV plant panels. Snail tracks, cell cracks, delamination, encapsulant discoloration, back-sheet blistering, finger corrosion, back-sheet burning, back-sheet yellowing, semiconductor material delamination, hotspot and junction box and bypass diode failures observed by visual inspection of 6 solar PV plants. This is generally the starting phase in determining if a PV module should be considered for additional tests. The investigation must be carried out under the natural sunlight in order to obtain qualitative level [2, 3]. Reflections should not be taken into consideration as they may produce erroneous images.

2.1 *Snail Tracks*

Crystalline silicon solar PV modules at outdoor exposure may show the so-called snail track effect which comes out as brownish-colored gridlines on cell edges and/or microcracks as shown in Fig. 1. The existence of microcracks is accountable for the development of snail tracks, but snail tracks are not necessarily related to the

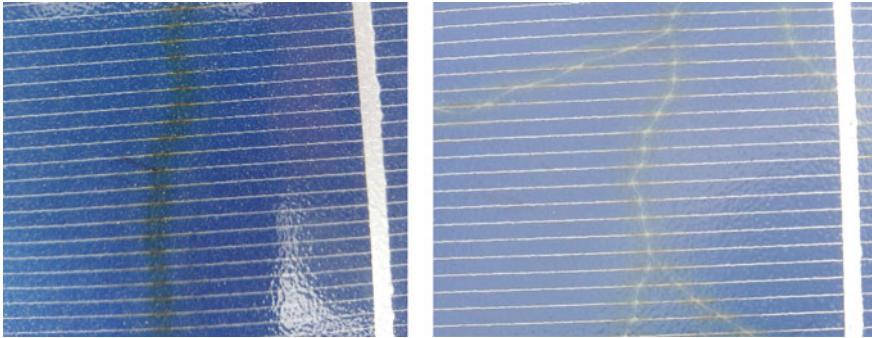


Fig. 1 Snail track along the bus bar (*left*), snail track with visible cell crack (*right*)

existence of microcracks. As per visual inspection, it has been noted that the development of snail tracks can vary with the module types and with modules from different manufacturers. The discoloring normally occurs after 1–2 years of operation of the modules. The speed of primary discoloring relies on the season and climatic conditions. In a hot climate, snail track may grow faster. Furthermore, the combination of UV radiation and temperature is critical for snail tracks [4].

As per the latest information, it is considered that humidity can diffuse through the back-sheet into the module. Humidity can spread out inside the module, pass through back-sided EVA and microcrack toward front side of cell. A chemical reaction at the interface between the PV cell with the silver fingers and the front EVA is suspected to cause the grid finger discoloration [1, 3, 5].

As per the literature, there is no instance where the discoloration leads to noticeable degradation of power of the PV modules. However, the snail tracks make solar cell cracks visible which can abate the PV module power. A tendency of high leakage currents have been observed in snail track affected solar PV modules.

2.2 Solar Cell Cracks

Solar PV cell consists of silicon, and this leads to brittleness of the cells. The cracks in PV cell at the silicon substrate are generally not visible. Cracks are generated in different dimensions in a solar cell as shown in Fig. 1. The wafer slicing, cell production, stringing and embedding are the processes of PV cell and module which generate cracks in the PV cells. Particularly, the stringing procedure of the PV cells has high prospect of cell cracks. After the production process, main roots of cell cracks are packaging, transportation and reloading and installation of PV modules [1, 3, 6–8].

As per the literature, there are PV modules having numerous cracked cells, but no significant power loss detected. However, the literature showing that in a solar

park, with almost half of PV modules, indicate 10% or more power loss after 6 years of field exposure [9, 10].

2.3 Hot Spot

‘Hot spot heating’ is produced in series connected cells when shadow covers one or more cells creating a reverse bias across the shaded cell/s ultimately that leads to dissipation of enormous power in the shaded/erroneous cell/s. Hence whole power generation of healthy series connected cells is dissipated in the shaded/erroneous cell/s. The huge power loss occurring in small space entails into local overheating or hot spot which consequently leads to damaging impacts [1, 3, 7, 11]. As per the literature review and visual inspection (Fig. 2), the hot spots produced due to the bypass diode failure and cracks in solar cell [12].

2.4 Back-Sheet Burning Marks/Front Side Yellowing/Blistering

The functions of the back-sheet encompass: (i) To furnish electrical insulation between the solar PV module and the surrounding environment and (ii) To act as a mechanical environmental road-block from stresses, viz. moisture, airborne chemicals, diffused UV light and dust. Back-sheet failures can increase degradation, lower system performance and unsafe operating conditions [1, 3, 13]. Back-sheet burn marks or burning is caused by hot spots, front side yellowing due to UV exposure damage and blistering due to heat and humidity (see Fig. 3) [14].

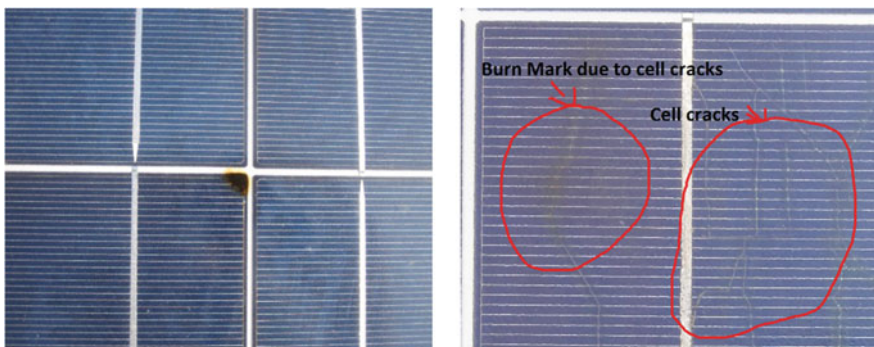


Fig. 2 Hot spot due to bypass diode failure (*left*), hot spot due to cell cracks (*right*)

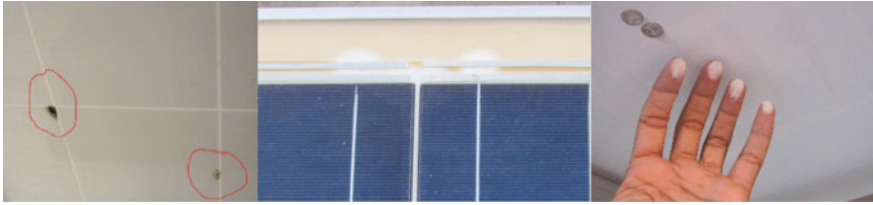


Fig. 3 Back-sheet burn marks (*left*), back-sheet front side yellowing (*middle*) and back-sheet blistering (*right*)

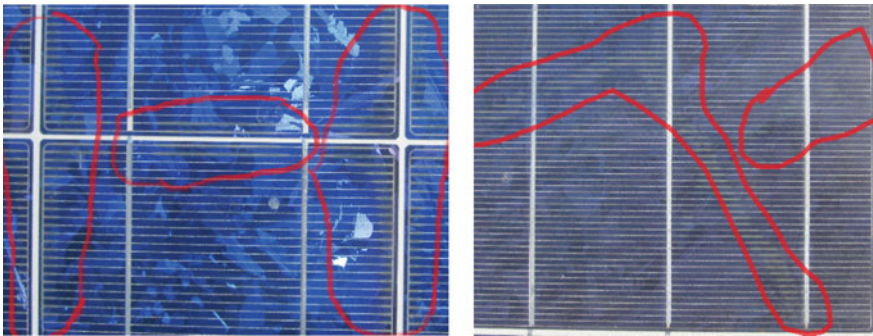


Fig. 4 Fingers corrosion on edges of cell (*left*), random pattern of fingers corrosion (*right*)

2.5 *Finger Corrosion*

As per the literature review, corrosion at fingers occurs due to inadequate adhesion or loss of adhesion among layers and driven by moisture, mechanical stress and UV radiation (see Fig. 4) [4].

As per the literature, minute power loss is detected by fingers corrosion [7, 9, 12–14].

2.6 *Delamination*

The adhesion among the glass, encapsulant, active layers and back layers is scraped due to various reasons. To be specific, if the adhesion is scraped due to contamination of environmental parameters, delamination will be formed come after moisture ingress and corrosion [1, 3, 10, 12, 15]. Here, Fig. 5 shows the delamination occurred throughout cell crack (*left*) and middle figure shows the white spot (delamination) on active layer. Right figure shows the delamination of active layer without any cracks or any other defect [9, 13, 14].

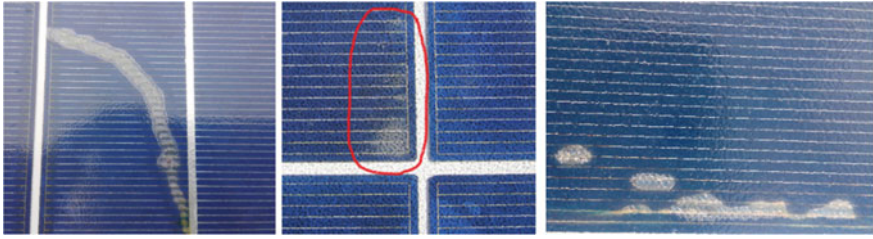


Fig. 5 Delamination along cell crack (*left*), white spot (*middle*) and delamination without cell crack (*right*)

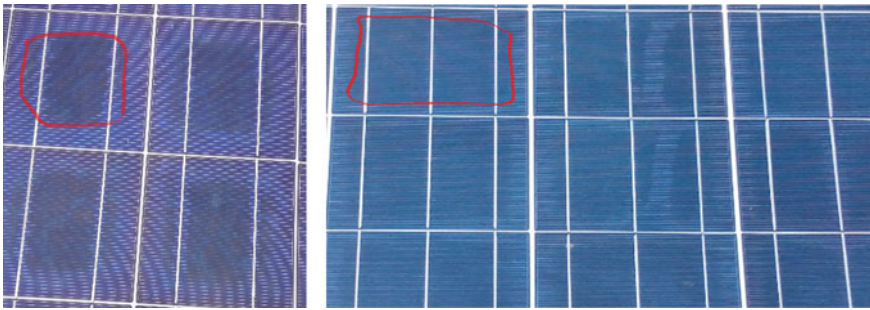


Fig. 6 Discoloration of encapsulant

2.7 Encapsulant Discoloration

Discoloration of encapsulant can cause a noticeable difference in the optical transmission of applied light on crystalline cells. As per the literature, at the starting stage performance losses attributed to optical losses at the encapsulant discoloration and the latter attributed to fill factor losses due to solder bond degradation and insufficient usage of bypass diodes [1, 3, 6, 9, 13, 15].

In this study, minor discoloration of encapsulant has been found which is shown in Fig. 6.

3 Infrared Analysis

The systems were analyzed with a thermal imaging camera Fluke Ti32. The modules were connected to the grid during the measurement and thus approximately at their peak capacity. The thermal photographs were taken from the front side of modules. Standard process was followed while capturing images and to avoid the reflection by the neighboring objects [2, 3, 6, 7].

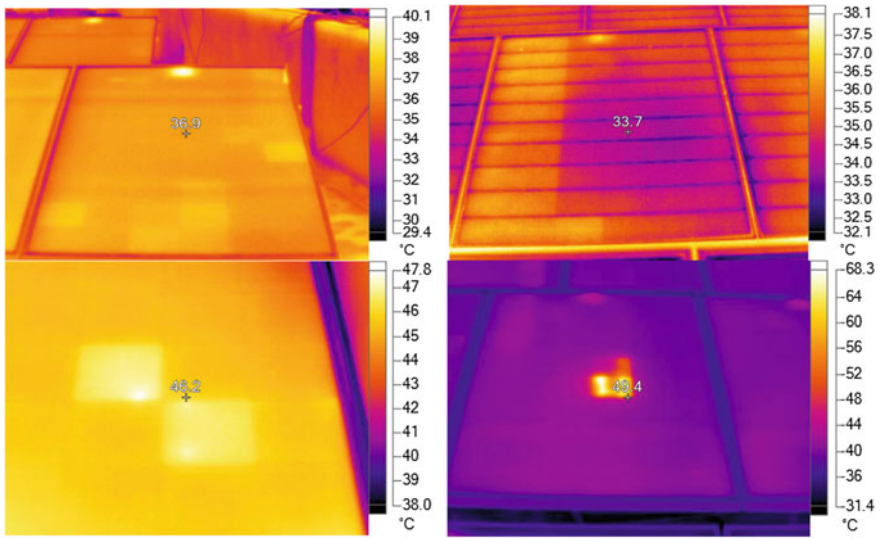


Fig. 7 Thermal image of modules with hot cells lying on junction box (*top left*), one bypass diode in operation (*top right*), uneven cell temperature (*bottom left*) and hot spot (*bottom right*)

One of the noticeable observations of infrared analysis was that a solar cell, lying immediately on the junction boxes, carrying the temperature approximately 2–4 °C higher than the remaining (Fig. 7 top left) [13].

Some modules were observed with two cell strings hotter than others. This indicated the on state of bypass diode of these particular strings (Fig. 7 top right) [11].

Few modules were observed with uneven cell temperature without any visible defect (Fig. 7 bottom left).

Two modules were observed with one particular cell heating around 30 °C higher than module temperature. This was due to lots of cracks in the cell (Fig. 7 bottom right).

4 Conclusion

The analysis of the failure and degradation types of 6 different poly-crystalline solar cell photovoltaic plants of different size after 4–6 years of operation has been presented. These plants have experienced the degradation types of snail tracks, cell cracks, back-sheet front side yellowing, back-sheet blistering, fingers corrosion (electro-chemical corrosion), delamination and discoloration of encapsulant and hot spot. It has been observed that different plants having different defects indicate that degradation and failure types depend on all module components materials, processing factors, transportation method, installation and design of PV plants

Table 1 Defect analysis of six different plants

Types of defect	Plant 1 50 kWp (%)	Plant 2 10 kWp (%)	Plant 3 10 kWp (%)	Plant 4 100 kWp (%)	Plant 5 100 kWp (%)	Plant 6 100 kWp (%)
Cell cracks	35.9	0.0	0.0	39.1	0.0	0.0
Snail tracks	20.9	0.0	0.0	5.7	0.0	0.0
Hot spot	2.3	0.0	0.0	0.0	0.0	0.0
Delamination	1.4	0.0	0.0	5.7	0.0	0.0
Encapsulant discoloration	2.3	2.9	25.9	0.7	1.2	3.0
Back-sheet burning marks	1.36	0.0	0.0	0.0	0.0	0.0
Back-sheet yellowing (front side)	0.0	0.0	18.5	0.0	0.0	0.0
Back-sheet blistering	0.0	0.0	64.8	0.0	0.0	0.0
Finger corrosion	0.0	84.3	0.0	0.0	39.9	35.0
Burn marks near bus bar	0.0	0.0	46.3	0.0	0.0	12.0
Bypass diode is in operation	0.0	0.0	1.9	0.7	1.2	0.0

(Table 1). Notwithstanding, scanty reliability- and durability-based lessons have been learnt from this study which are: (i) Fingers corrosion in a composite climate which would increase series resistance and degrade the module performance. (ii) Encapsulant discoloration resulted by ultraviolet radiation in a composite climate is a serious degradation.

References

1. Wohlgemuth, J., Silverman, T., Miller, D.C., McNutt, P., Kempe, M., Deceglie, M.: Evaluation of PV Module Field Performance. Submitted IEEE PVSC (2015)
2. Lopez, J., Pozza, A., Sample, T.: Analysis of Crystalline Silicon PV Modules After 30 years of Outdoor Exposure. Presented at EU PVSEC, Germany (2015)
3. International Energy Agency.: Review of failures of photovoltaic modules. Report IEA-PVPS T13-01 (2014)
4. Berghold, J., Roericht, M., Böttcher, A., Wendlandt, S., Hanusch, M., Koch, S., Grunow, P., Stegemann, B.: Electrochemical Corrosion Within Solar Panels. Presented at EU PVSEC, Germany (2012)
5. Liu, H.-C., Huang, C.-T., Lee, W.-K., Yan, S.-S., Lin, F.-M.: A defect formation as snail trails in photovoltaic modules. *Energy Power Eng.* **7**, 348–353 (2015)

6. Olakonu, K., Belmont, J., Tatapudi, S., Kuitche, J., TamizhMani, G.: Degradation and Failure Modes of 26-year-old 200 kW Power Plant in a Hot-Dry Desert Climate. Presented IEEE PVSC, USA (2014)
7. Sanchez-Friera, P., Piliouguine, M., Pelaez, J., Carretero J., Sidrach de Cardona, M.: Analysis of degradation mechanisms of crystalline silicon PV modules after 12 years of operation in southern Europe. *Progress in photovoltaics. Res. Appl.* **19**, 658–666 (2011)
8. Gabor, A.M., Janoch, R., Anselmo, A., Field, H.: Solar Panel Design Factors to Reduce the Impact of Cracked Cells and the Tendency for Crack Propagation. Presented at PV Module Reliability Workshop, NREL, USA (2015)
9. Silverman, T.J., Wohlgemuth, J., Miller, D.C., Kempe, M., McNutt, P.: Review of Observed Degradation Modes and Mechanisms from Fielded Modules. National Renewable Energy Laboratory (NREL), USA
10. Munoz, M.A., Alonso-Garcia, M.C., Vela, N., Chenlo, F.: Early degradation of silicon PV modules and guaranty conditions. *Solar Energy* **85**, 2264–2274 (2011)
11. Buerhop, C., Schlegel, D., Niess, M., Vodermayr, C., Weißmann, R., Brabec, C.J.: Reliability of IR-imaging of PV-plants under operating conditions. *Solar Energy Mat. Solar Cells* **107**, 154–164 (2012)
12. Ndiaye, A., Charki, A., Kobi, A., Kébé, C.M.F., Ndiaye, P.A., Sambou, V.: Degradations of silicon photovoltaic modules: a literature review. *Solar Energy* **96**, 140–151 (2013)
13. Chandel, S.S., Naik, M.N., Sharma, V., Chandel, R.: Degradation analysis of 28 years field exposed mono-c-Si photovoltaic modules of a direct coupled solar water pumping system in western Himalayan region of India. *Renew. Energy* **78**, 193–202 (2015)
14. Kuitche, J.M., Pan, R., Samy, G., Mani, T.: Investigation of dominant failure mode(s) for field-aged crystalline silicon PV modules under desert climatic conditions. *IEEE J. Photovoltaics* **4**, 814–826 (2014)
15. Shioda, T.: Delamination Failures in Long-Term Field-Aged PV Modules from Point of View of Encapsulant. Presented at PV Module Reliability Workshop, NREL, USA (2013)

A New Switching Pattern Scheme-Based Compact Integrated 15-Level Smart Inverter for Micro-grid System Using Fuzzy Logic Controller

Kshatriya Vamshi Krishna Varma, Kalahasti Sirisha
and A. Ram Kumar

Abstract The great demand for renewable energy utilization is increased owing to province of natural fuels, ultimatium energy, and several atmospheric issues. Planning of the futuristic energy generation strategies is utilized by superior energy management technologies. The superior technology is acquired by co-generation scheme with the use of primary energy sources. The intended primary energy sources are accommodated to micro-grid system by using recognized power conditioner with effective intelligent controller. The intelligent controller envisions the switching patterns of proposed 15-level smart inverter topology for regulation of sudden variations, intensifying the outcome responses and ameliorating stability index and low harmonic content. In this approach procure the sinusoidal grid voltage which is in-phase to grid current, then amalgamate to micro-grid system. A MATLAB/Simulink model is developed to validate the proposed scheme via intelligent controller with several modulation patterns with conferred results and several comparisons.

Keywords Asymmetrical multilevel inverter • Fuzzy controller
Fuel stacks • PI controller • PV arrays • Total harmonic distortions (THDs)

K.V.K. Varma (✉)

Department of Electrical & Electronics Engineering, GPREC, Kurnool,
Andhra Pradesh, India
e-mail: varmak418@gmail.com

K. Sirisha

Department of Mechanical Engineering, Mahatma Gandhi Institute of Technology,
Hyderabad, India
e-mail: sirivamshi.k@gmail.com

A. Ram Kumar

Department of Electrical & Electronics Engineering, Kalasalingam University,
Krishnakoil, Tamil Nadu, India
e-mail: ramkumar.manonmani@gmail.com

1 Introduction

The advents of low-rated power generation plants are attracted by modern offerings to on-site power production within a short period by using renewable energy resources (RES). The acceptance of renewable energy gains the acute ability of fabulous advantages to deform the micro-grid system with virtuous connectivity [1]. Grid-integrated renewable sources are highly interpreted of standby module to co-energy generation scheme [2]. Obtaining the safe, clean, reliable, renewable energy sources are fuel cell (FC) and photovoltaic (PV) considered as primary energy generators to look up co-generation scheme. It extends the appropriate versatility and superb scalability for superior energy management. The supreme power intensity is prevailed by impressive formation of FC-PV scheme which has ample stability index and minimizes the rapid step load changes by encouraging co-generation scheme. Moreover, it is mostly used in remote area applications and acceptable system for energy generation using recognized power conditioner.

The power conditioner plays an imperative role in grid-integrated RES system, which transforms the electrical power flow control coming from RES to respective micro-grid system [3]. It is comprised of couple of splices like (1) high-grade boost converter and (2) inverter topology. Utilization of high-grade power apparatus plays a key role in a grid-integrated system placed in a single unit [4]. The high-grade boost converter promotes the FC-PV voltage at DC link as well as inverter topology supported as girdle between the DC link to integrate micro-grid system. Generally, the unit ranges from 100 to 400 V from 50 to 200 V input and then interfaced to micro-grid system via intended asymmetric 15-level inverter. Terrific efficiency, current–voltage quality, reduced switch stress, low harmonic distortions ameliorated the aid of several MLI topologies [5–7]. The superior multilevel (MLI) inverter topologies have been reviewed few years ago, acquiring the optimal features by expanding the further voltage levels with succor of advanced topologies. Regular multilevel inverter topologies like cascaded H-bridge topology [8], flying capacitor topology [9], and diode-clamped topology [10] are vibrant fundamental topologies. The regular MLI topologies are un-usable due to generation of asymmetrical voltages and require extra clamping devices. The asymmetric approach is meticulously preferred in cascaded H-bridge topology, but demands ancillary components. The vital attraction is production of extreme voltage levels with limited switches by consisting of unequal DC sources, low space cost, acquired from asymmetrical voltage technique [11, 12].

In this paper, 15-level asymmetrical MLI topology has been explored by incorporating modulation technique to micro-grid associated system with intelligent fuzzy controller. It is a class of artificial linguistic nature that is developed under the Mamdani fuzzy system. It constituted the symbolic approach of inference network with respect to expertise comprehension to improve transient stability, qualified RMS voltage, and low THD content. Finally, the proposed module is formulated by MATLAB/Simulink tool; results are conferred with several comparisons.

2 Proposed Co-generation Scheme

The proposed configuration comprised as superior attitude of power production with ample flexibility and tidiness. The power transformation flow of FC-PV is in a self-reliant voltage device with myriad relationship under unique principle, which is interacted to 15-level inverter topology through high-grade DC link. This DC link provides the integrated barrier of intended modules. The schematic diagram of proposed 15-level asymmetrical MLI with PI fuzzy controller for micro-grid system with co-generation scheme is delineated in Fig. 1. The intended arrangement consists of dual conversion processes which is named as a level and polarity generation scheme. The primary act is a level generation which is formed by submodule multicells; it expands the dual switches per module and regulates the DC voltages with respect to proper switching sequence. Pertained 7-level DC voltage is V_{dc} , $2V_{dc}$, $3V_{dc}$, $4V_{dc}$, $5V_{dc}$, $6V_{dc}$, and $7V_{dc}$ by utilizing the 6 switches. The secondary act is polarity generation formed by full-bridge modules; it transforms the DC 7-level into AC 15-level voltage with the aid of series-parallel transformation. The pertaining voltage levels are 0 , $+V_{dc}/-V_{dc}$, $+2V_{dc}/-2V_{dc}$, $+3V_{dc}/-3V_{dc}$, $+4V_{dc}/-4V_{dc}$, $+5V_{dc}/-5V_{dc}$, $+6V_{dc}/-6V_{dc}$, $+7V_{dc}/-7V_{dc}$ by utilizing 4 switches. The final 15-level stair case output voltage directly interacted with micro-grid system via filter units for acquired voltage-current quality, reduced ripples, pure sinusoidal RMS voltage, low THD content in both voltage-current. The proposed topology requires only 10 switches for production of 15 voltage levels, and it has several advantages over the several classical topologies. The switching pattern selection of 15-level inverter is depicted in Table 1 for level generation and Table 2 for polarity generation.

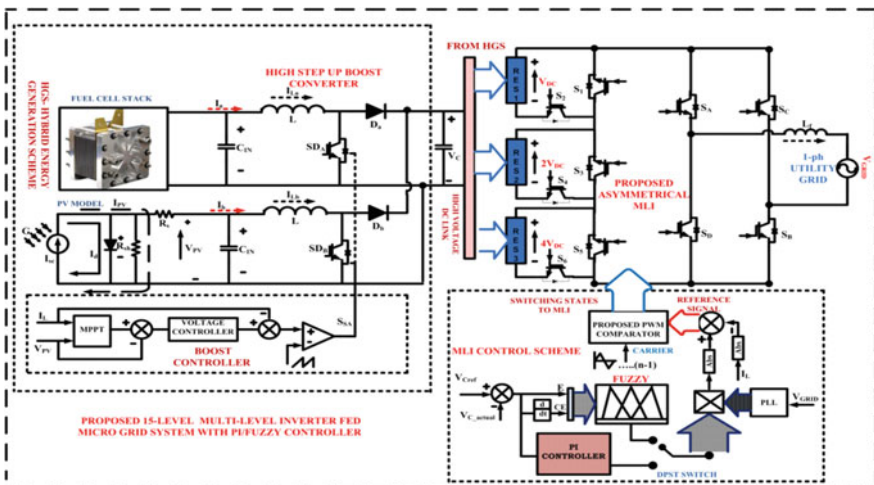


Fig. 1 Symbolic representation of intended asymmetrical 5-level MLI structure with PI/ fuzzy controller for micro-grid system with co-generation scheme

Table 1 Switching pattern selection of intended asymmetrical 15-level MLI for level generation process

V _o	S ₁	S ₂	S ₃	S ₄	S ₅	S ₆
7V _{dc}	NP	P	NP	P	NP	P
6V _{dc}	P	NP	NP	P	NP	P
5V _{dc}	NP	P	P	NP	NP	P
4V _{dc}	P	NP	P	NP	NP	P
3V _{dc}	NP	P	NP	P	P	NP
2V _{dc}	P	NP	NP	P	P	NP
V _{dc}	NP	P	P	NP	P	NP

Table 2 Switching pattern selection of intended asymmetrical 15-level MLI for polarity generation process

V _o	S _A	S _B	S _C	S _D
Zero state	NP	P	NP	P
Positive state	P	P	NP	NP
Negative state	NP	NP	P	P

Tables 1 and 2 show the switching pattern selection of both level and polarity generation of proposed asymmetrical 15-level inverter topology. In that, “NP” highlights the switch is at “Non-Perform” state and “P” highlights the switch is at “Perform” state.

3 Proposed Switching Patterns

The improved switching performance of several inverter topologies requires highly intensifying switching patterns for developing the standard pulse width modulation (PWM). At current scenario, various inverters are functioned by high switching frequency under carrier-based PWM scheme. The single or multimodal carrier PWM techniques like level-/phase-shifted PWM techniques are regularly utilized by several scholars [13–15]. The proposed advanced PWM techniques are optimal PWM technique, variable switched frequency PWM technique, incorporated optimal switching frequency technique; it is naturally selected for both asymmetrical and symmetrical inverter topologies in many applications.

The advanced modulation techniques are extremely necessary for optimal switching patterns of proposed 15-level inverter to obtain required RMS voltage, proper harmonic shifting, and low THD profile. Combination of level- and phase-shifted PWM technique is called as optimal PWM technique to trounce the phase unsymmetry condition. Therefore, all the followed multicarriers have

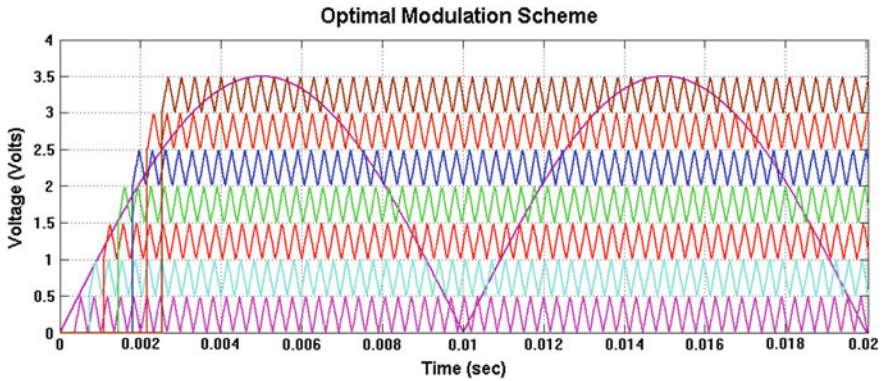


Fig. 2 Switching pattern of optimal PWM technique

uniform frequencies with a slight difference in peak amplitudes which are disposed vertically. The resultant waveform of optimal PWM technique is depicted in Fig. 2.

$$M_{\text{index}} = \frac{V_r}{V_{c(q-1)}} \tag{1}$$

$$\vartheta_d = \frac{360^\circ}{4(m-1)} \tag{2}$$

where $(m - 1)$ is the prerequisite number of carriers; the number of carriers is decided by specified levels and those are disposed essentially vertical nature by followed phase angle. V_r is reference signal, V_c is the carrier signal; M_{index} is the modulation index, and ϑ_d is the operating phase angle.

The other advanced technique is variable switching frequency technique; it is usually same as regular PWM techniques. In regular PWM techniques, all carriers have equal switching frequency and this technique has diverse range of carrier frequency with respect to certain multiple steps. In this technique, carrier frequencies are in the range of 3050, 5050, 7050 Hz; these are formed as a multicarrier modulation scheme and interacted with reference signal to generate switching patterns of the 15-level inverter topology. The resultant waveform of the variable switching frequency PWM technique is depicted in Fig. 3. The proposed hybrid PWM technique is defined based on above modulation techniques; it is a combined

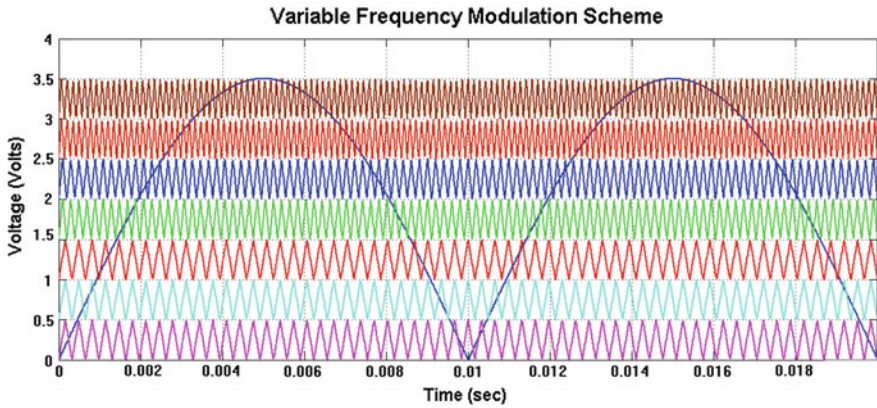


Fig. 3 Switching pattern of variable switching frequency PWM technique

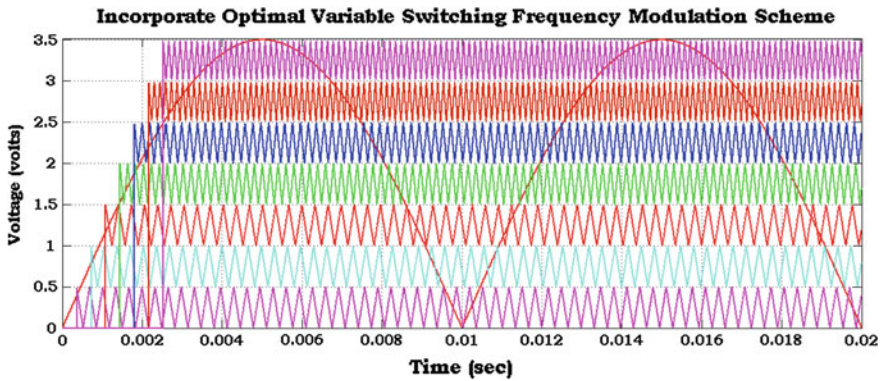


Fig. 4 Switching pattern of incorporated optimal switching frequency PWM technique

level operation of optimal modulation technique and variable switching technique. The resultant waveform of the proposed incorporated optimal switching frequency PWM technique is depicted in Fig. 4.

4 Fuzzy Control Objective

The control objective explores the attractive performance in power electronic devices which are operated under nonlinear characteristics because of several disturbances. In this work, superior control objective is functioned for reference signal generation which is based on grid voltage and capacitor voltage at DC link. At first grid voltage is detected by recognized circuitry which is supported under the unified amplitude sequence via PLL (phase-locked loop) by the sine reference frame.

However, capacitor voltage at DC link is contrasted over the actual DC link voltage to establish the error, i.e., drive to the effective controller. Both error-free terms coming from controller and PLL reference are multiplied to provide the proper reference signal to the proposed PWM technique. The reference and carrier signals are compared to produce multicarrier PWM technique for generation of 15 levels which accorded with the illustrated switching sequence. A closed-loop PI controller is usually elected to regulate DC link voltage at distinct value and to regulate the quality voltage with a good harmonic profile. Several approaches have been used for selection of PI parameters, but this parameter selection leads to peak overshoots in transient response, making it to minimize the stability index and have poor operating performances. On the other side, the fuzzy logic controller has incredible operating performances over classical controllers [16].

The term “FUZZY” bears the various facts which are related to involved logics which can deal the concept of true–false cases. It is more amiable for specific problem definition and can be casted-off based on nature of human operators which are easily administered by proper membership functions and rules [17]. The proposed PI/fuzzy operation is controlled by double pole single through (DPST) switch based on the requirement of operation. The attracted membership functions of fuzzy

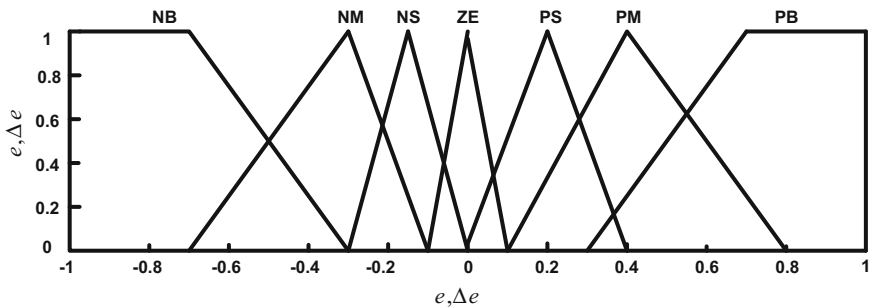


Fig. 5 Membership functions

Table 3 Rule base

Δe	e						
	NB	NM	NS	ZE	PS	PM	PB
NB	NB	NB	NB	NB	NM	NS	ZE
NM	NB	NB	NB	NM	NS	ZE	PS
NS	NB	NB	NM	NS	ZE	PS	PM
ZE	NB	NM	NS	ZE	PS	PM	PB
PS	NM	NS	ZE	PS	PM	PB	PB
PM	NS	ZE	PS	PM	PB	PB	PB
PB	NB	NM	NS	ZE	PS	PM	PB

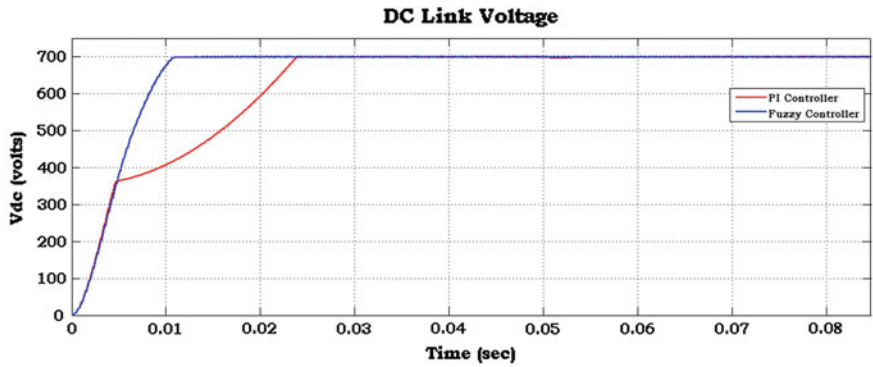
Table 4 Parameters for intended asymmetrical 15-level MLI topology

S. No	Parameters	Values
1	Photovoltaic system	50–200 V
2	Fuel cell system	50–150 V
3	Step-up inductor (L)	1 mH
4	Capacitor (C)	780 μ F
5	Filter units (Lf)	1.5 mH
6	Operated switching frequency	7050, 5050, 3050 Hz
7	PI controller	Ki-0.07, Kp-0.5,

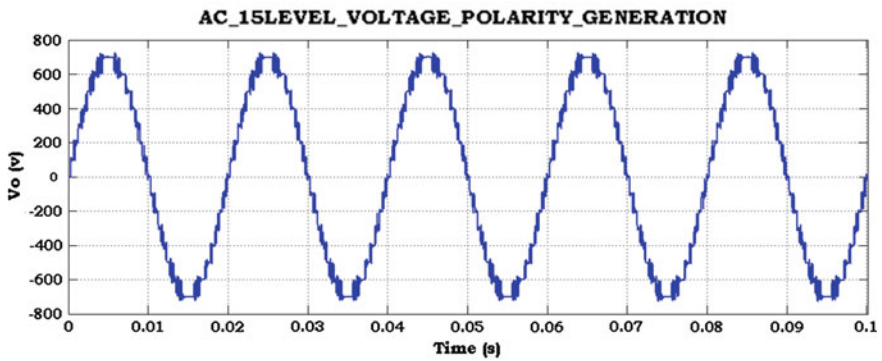
controller are illustrated in Fig. 5, and decision making as rule base is illustrated in Table 3. From the above rule base, each cross-path of every input/output variable is comprised of seven membership functions such as positive big—PB, positive medium—PM, positive small—PS, zero—ZE, negative small—NS, negative medium—NM, negative big—NB.

The performance analysis of 15-level asymmetrical MLI with intended incorporated modulation schemes is performed under both PI/fuzzy controlled objectives, which are validated by MATLAB/Simulink tool. The specific operating parameters are conferred in Table 4. It is solely applicable to single-phase, 700 V, 50-Hz micro-grid-integrated system.

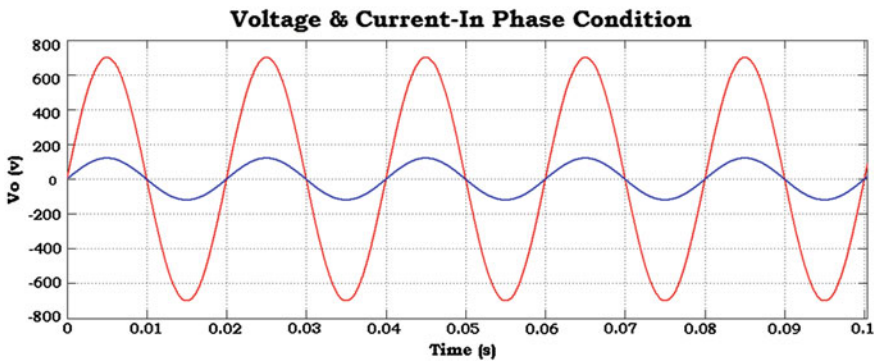
Figure 6 illustrates the various simulation outcomes of proposed asymmetrical 15-level inverter using advanced modulation schemes through PI/fuzzy controllers, which includes (a) DC link voltage of both PI/fuzzy controllers; (b) AC 15-level output voltage; (c) grid voltage and current in-phase condition; and (d) FFT of 15-Level voltage. Compared to PI controller, the proposed fuzzy controller has better features like highly recognized RMS voltage/current wave shapes, low switch stress, greater efficiency, good stability index, low THD profile which is near to



(a) DC Link Voltage of both PI-Fuzzy Controller



(b) AC 15-Level Voltage



(c) Grid Voltage & Grid Current-In phase Condition

Fig. 6 Several simulation results of proposed 15-level asymmetrical inverter using PI/fuzzy controller

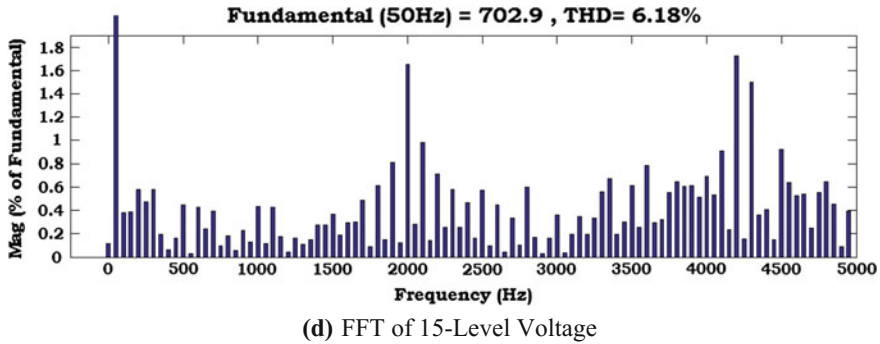


Fig. 6 (continued)

IEEE standards that makes elimination of load side filter units. The grid voltage and grid current both are in pure sine and are in-phase to each other to represent the unity power factor. The classical PI controller yields 0.024 s, and proposed fuzzy controller requires 0.011 s; it maintains the low steady-state error with better stability index under several perturbations coming from the micro-grid and DC link. Several THD comparisons are depicted in Table 5.

5 Conclusion

In this work, a new advanced modulation scheme is highly recommended for compact integrated asymmetrical inverter topology with PI fuzzy controller. The formal PI controller is virtue for providing the erupted gains to attain low peak overshoots, low THD, etc. Consequently, the benefit of utilizing intelligent approach is constituted as intensified solution to obtain the optimal modulation index. A precise modulation scheme is proposed from classical modulation techniques with the proposition of low switch stress, terrific efficiency, high comfort, low installation area, incredible power density, low cost, good stability index, low THD profile, etc. Several simulation outcomes are updated by advanced modulation techniques with PI fuzzy controllers, in which incorporating optimal switching frequency technique with fuzzy logic controller has reduced THD% profile. The outcome simulation result explores the intended MLI module with fuzzy controller which is highly suitable for micro-grid system to enhance power quality and maintain THD well within the certain IEEE standards and manage the co-energy.

Table 5 FFT analysis of asymmetric 15-level voltage using classical PI controller over proposed fuzzy controller under advanced modulation schemes

Type of controller	Regular PWM scheme			Optimal PWM scheme			Variable switching frequency PWM			Incorporated optimal switching frequency PWM scheme		
	PD	POD	APOD	PD	POD	APOD	PD	POD	APOD	PD	POD	APOD
PI controller (%)	7.75	7.76	7.76	7.65	7.67	7.67	7.68	7.70	7.7	7.29	7.32	7.31
Fuzzy controller (%)	7.22	7.35	7.36	7.39	7.43	7.44	7.28	7.31	7.29	6.28	6.18	6.20

References

1. Ashwini, K., Kapil, K., Naresh, K., Satyawati, S., Saroj, M.M.: Renewable energy in India: current status and future potentials. *Renew. Sustain. Energy Rev.* **14**, 2434–2442 (2010)
2. Jain, S., Agarwal, V.: An integrated hybrid power supply for distributed generation applications fed by nonconventional energy sources. *IEEE Trans. Energy Convers.* **23**(2), 622–631 (2008)
3. Bragard, M., Soltau, N., Thomas, S., Doncker, R.W.D.: The balance of renewable sources and user demands in grids: power electronics for modular battery energy storage systems. *IEEE Trans. Power Electron.* **25**(12), 3049–3056 (2010)
4. Liserre, M., Sauter, T., Hung, J.Y.: Future energy systems: integrating renewable energy sources into the smart power grid through industrial electronics. *IEEE Ind. Electron. Mag.* **4**(1), 18–37 (2010)
5. Kjaer, S.B., Pedersen, J.K., Blaabjerg, F.: A review of single-phase grid-connected inverters for photovoltaic modules. *IEEE Trans. Ind. Appl.* **41**(5), 1292–1306 (2005)
6. Zheng, F., Lai, J.-S., Rodriguez, J.: Multilevel inverters: a survey of topologies, controls, and applications. *Ind. Electron., IEEE Trans.* **49**(4), 724–738 (2002)
7. Rodriguez, J., Franquelo, L.G., Kouro, S., Leon, J.I., Portillo, R.C., Prats, M.A.M., Perez, M.A.: Multilevel converters: an enabling technology for high-power applications. *Proc. IEEE* **97**(11), 1786–1817 (2009)
8. Malinowski, M., Gopakumar, K., Rodriguez, J., Perez, M.: A survey on cascaded multilevel inverters. *IEEE Trans. Ind. Electron.* **57**(7), 2197–2206 (2010)
9. Choi, S., Saeedifard, M.: Capacitor voltage balancing of flying capacitor multilevel converters by space vector PWM. *IEEE Trans. Power Deliv.* **27**(3), 1154–1161 (2012)
10. Busquets Monge, S.: Multilevel diode-clamped converter for photovoltaic generators with independent voltage control of each solar array. *IEEE trans. Ind. Electron.* **55**(7), 2713–2723 (2008)
11. Hinago, Y., Koizumi, H.: A single phase multilevel inverter using switched series/parallel DC voltage sources. *IEEE Trans. Ind. Electron.* **57**(8), 2643–2650 (2010)
12. Mei, J., Xiao, B., Shen, K., Jian, L.M., Zheng, Yong: Modular multilevel inverter with new modulation method and its application to photovoltaic grid-connected generator. *IEEE Trans. Power Electron.* **28**(11), 5063–5073 (2013)
13. McGrath, B.P., Holmes, D.G.: Multicarrier PWM strategies for multilevel inverters. *IEEE Trans. Ind. Electron.* **49**(4), 858–867 (2002)
14. Bahr, S.M.E., Rama Rao, K.S.: A new multi carrier based PWM for multilevel converter. In: 2011 IEEE Applied Power Electronics Colloquium (IAPEC). 63–68, IEEE (2011)
15. Mao, X., Ayyanar, R., Krishnamurthy, H.K.: Optimal variable switching frequency scheme for reducing switching loss in single-phase inverters based on time-domain ripple analysis. *IEEE Trans. Power Electron.* **24**(4), 991–1001 (2009)
16. Cecati, C., Ciancetta, F., Siano, P.: A multilevel inverter for photovoltaic systems with fuzzy logic control. *IEEE Trans. Ind. Electron.* **57**(12), 4115–4125 (2010)
17. Premkumar, E., Rajkumar, S.: Balanced PV cascaded multilevel grid-connected inverters under level-shifted PWMs with fuzzy controller. In: 2014 International Conference on Information Communication and Embedded Systems (ICICES). 1–4 Feb 2014

Modeling of Energy Consumption in Foundries by Integrating Renewable Energy Sources: Kolhapur Foundry Sector

Dhanashri P. Patil, Nilkanth N. Shinde and Mahesh M. Wagh

Abstract Energy is a vital issue in the discussion of sustainable development. Increasing demand and scarce availability of resources with limited environmental impact are outlining aspects of developing the energy model. This paper reveals a grid–solar–wind energy system for energy modeling. Mathematical model has been developed which relies on two important factors of industrial energy consumption: energy cost and CO₂ emission. This model is validated by using data from foundry cluster, Kolhapur industrial sector. Load assessment and resource assessment in Kolhapur area have been done. Constraints required for programming are obtained from HOMER software. Genetic algorithm multi-objective optimization is carried out by using MATLAB to solve these two conflicting objectives. Pareto optimal solution gives no judgment about equality of distribution in different energy sources. But it gives a set of optimal values which satisfies the two objectives: minimization of energy cost and minimization of CO₂ emission. This developed modeling will help to do proper integration of largely available renewable sources such as solar and wind energy sources.

Keywords Energy cost · Genetic algorithm · MATLAB · Optimization Consumption

1 Introduction

In industrial sector, increasing energy demand, higher energy cost, energy supply security and CO₂ emission are some problems which need to be solved. Two main objectives arise in the modeling: One is to minimize energy consumption cost and

D.P. Patil · N.N. Shinde (✉) · M.M. Wagh (✉)
Department of Technology, Shivaji University, Kolhapur, India
e-mail: energyunishivaji@gmail.com

M.M. Wagh
e-mail: waghmahesh2006@gmail.com

D.P. Patil
e-mail: patildhanashrip@gmail.com

another is to minimize CO₂ emission. These objectives are in conflict since reducing cost increases more usage of established conventional energy sources instead of renewable energy. Therefore, energy system modeling and optimization have become important. So, it is needed to find optimal set of solution and choose most preferred solution.

For this modeling, methodology has been established. This starts with the study of Kolhapur area, assessment of resources available such as annual solar radiation, wind data and assessment of collected energy consumption load data. The mathematical model has been formulated to minimize energy cost and CO₂ emission by fixing constraints using HOMER. Genetic algorithm multi-objective optimization is carried out using MATLAB to obtain the optimal distribution of energy consumption in grid-solar-wind.

Energy modeling can help to understand the energy consumption pattern, forecasting the future of energy technologies, and for establishing energy models to a large-scale system. Kolhapur urban industrial sector is selected for case study. Different industries are dispersed across various geographical clusters of which foundry cluster is the major one. Therefore, for detailed study, foundry cluster has been selected.

2 Methodology

2.1 Objectives

- To analyze the energy consumption pattern in industrial sector.
- To check the feasibility of resources by collecting monthly average wind speed and annual solar insolation data for selected study area.
- Mathematical modeling by integrating of renewable energy sources to minimize the energy cost and the CO₂ emission.
- To study genetic algorithm and develop multi-objective optimization program by using MATLAB. Constraints for programming obtained from HOMER.

2.2 Energy Consumption

Thermal energy and electricity are important aspects in direct energy consumption. This consumption is obtained from thermal requirement, production capacity and no. of units required

Thermal energy consumption = Thermal requirement \times production capacity utilization

Production capacity utilization = Requirement/production capacity

Electrical energy consumption = No. of units required (from electricity bill)

Coal and fuel oil consumption is required to generate electricity which is the need of the industry. This indirect consumption depends on the electricity consumption of respective industry and the proportion of coal and fuel oil used for electricity generation.

$$CTGE = CPKwh \times PCIEG \times TEC$$

where

CTGE Coal consumption to generate electricity

CPKwh Coal consumption per kWh

PCIEG Proportion of coal in electricity generation

TEC Total electricity consumption

2.3 *CO₂ Emission*

The CO₂ emission from foundry includes CO₂ emission from fuel consumption, from production and from electricity generation. The fuel consumption in foundry varies as the furnace used varies. In foundry cluster, Kolhapur industrial area, fuel consumption by different types of furnaces is given below along with respective CO₂ emission per kg of respective fuel.

2.4 *Mathematical Modeling*

The objective of this study is to build a mathematical model that will form product mix by meeting annual energy consumption from foundry cluster, Kolhapur MIDC, and satisfy two conflicting objectives. Nevertheless, different approaches to minimize the energy cost and CO₂ emission develop the following mathematical model.

(a) *Objective function*

The main objective of the modeling is to minimize the cost and the CO₂ emission.

- To minimize the energy cost:

$$\text{Cost minimize : } Z_1 = f(x_1, x_2, x_3)$$

$$Z_2 = Ax_1 + Bx_2 + Cx_3$$

where

- A Rs./unit grid source
- B Rs./unit wind energy source
- C Rs./unit solar energy source
- X_1 no. of units by grid
- X_2 no. of units by wind power
- X_3 no. of units by solar

Here, for this calculation, energy cost per unit for grid, wind power and solar power is 7.01, 4.19 and 7.08 Rs./kWh values of A , B , C , respectively.

Therefore,

$$\text{Min } Z_1 = 7.01x_1 + 4.19x_2 + 7.08x_3 \quad (1)$$

- To minimize CO₂ emission

$$\text{CO}_2 \text{ emission minimize: } Z_2 = f(x_1, x_4)$$

$$Z = Dx_1 + E$$

where

- D Kg of CO₂ emission/kWh electricity
- E total CO₂ emission due to coal, oil, gas consumption

Here, for calculation, total emission due to coal, oil and gas has been calculated. From table,

$$\begin{aligned} \text{Total CO}_2 \text{ emission} &= (\text{MT of CO}_2)_{\text{coal}} + (\text{MT of CO}_2)_{\text{oil}} \\ &\quad + (\text{MT of CO}_2)_{\text{gas}} \\ &= 31052.3 + 755820 + 19790 \\ E &= 806662.3 \end{aligned}$$

$D = 0.37$ (kg of CO₂ emission per kWh electricity is 0.37) [8].

Therefore,

$$\text{Min } Z_2 = 0.37x_1 + 806662.3 \quad (2)$$

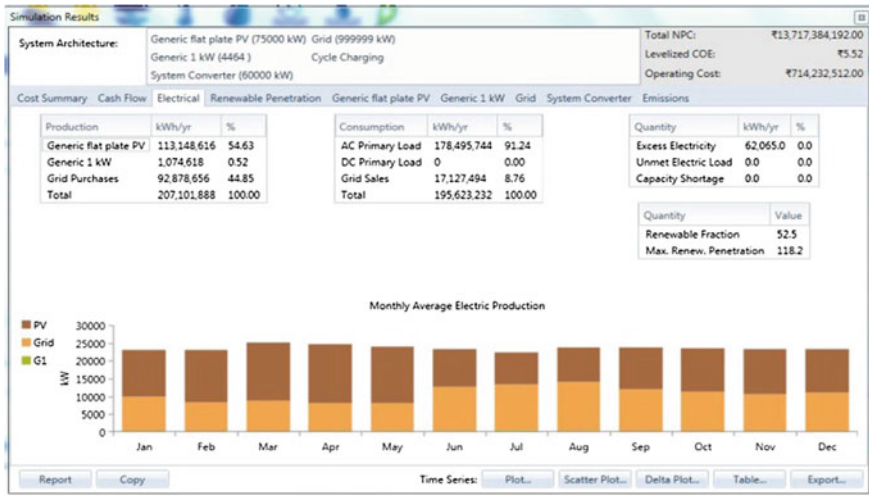


Fig. 1 Simulation result by HOMER

Objective function:
Minimize

$$Z_1 = 7.01 x_1 + 4.19 x_2 + 7.08 x_3$$

$$Z_2 = 0.37 x_1 + 806662.3$$

(b) Constraints

To find optimum values of no. of units of grid, solar power and wind power which satisfy the objectives, i.e., minimization of energy cost and CO₂ emission, we need to fix some constraints.

We have maximum values of solar power and wind power which can be generated in Kolhapur area. These values are obtained from HOMER software by using resource assessment and load assessment data (Fig. 1).

- No. of units by solar power $x_3 \leq 113, 148, 616 \text{ kWh/yr}$
- No. of units by wind power $x_4 \leq 1, 074618 \text{ kWh/yr}$

3 Case Study

3.1 Study Area

Kolhapur is situated in the southwest corner of Maharashtra (Fig. 2; Table 1).



Fig. 2 Kolhapur: selected area for study

Table 1 General information about study area

Country	India
State	Maharashtra
Name of the district	Kolhapur
Latitude	16° 41' 20.71"N
Longitude	74° 14' 41.52"E
Region	Hilly region
Elevation from mean sea level	577.33 m
Population	549,283

Fig. 3 Monthly average insolation incident on horizontal surface (kWh/m²/day)

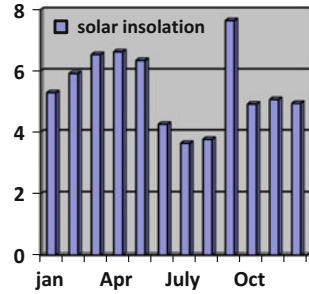
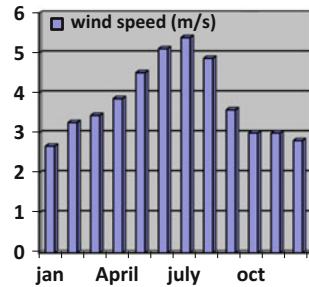


Fig. 4 Monthly average wind speed at 50 m above the surface of the earth (m/s)



3.2 Resources Assessment

Resources assessment studies the availability of solar radiation and wind in selected study area. A survey is conducted to collect information regarding availability of insolation and wind speed data. The potential assessment has been carried out (Figs. 3 and 4).

3.3 Load Assessment

Electrical energy load in foundries is categorized on the basis of furnaces use like single blast cupola, divided blast cupola and induction furnace. No. of units, annual energy consumption and annual electricity bill in lakhs are given in Tables 2, 3 and 4.

Table 2 Electricity load data in foundry cluster (Kolhapur MIDC)

S. No.	Category	No. of units	Annual electricity consumption (kWh)	Annual electricity bill (lakhs)
1.	Single blast cupola	10	15,54,136	124.33
2.	Divided blast cupola	22	8,97,546	71.8
3.	Induction furnace	33	12,51,22,440	10009.8
4.	Divided blast and induction furnace	3	35,70,672	285.6
5.	Single blast and induction furnace	2	4,73,50,000	3788
6.	Gas fired furnace	2	0	0
7.	Pit furnace	2	0	0
8.	Oil fired furnace	9	1440	0.1152
	Total	83	17,84,96,234	14279.6

Table 3 Annual consumption of fuel (foundry cluster, Kolhapur)

Category	No. of units	Annual coal consumption (MT)	Annual oil consumption (L)	Annual gas consumption (kg)
Single blast cupola	10	1842	0	0
Divided blast cupola	22	2415	0	0
Induction	33	0	1500	900
Divided blast and induction	3	520	24,000	0
Single blast and induction	2	8700	7200	288
Gas fired	2	0	0	5880
Pit furnace	2	24	0	0
Oil fired	9	0	42,000	0
Total	83	13,501	74,700	7068

Table 4 CO₂ emission/kg of fuel

Category	No. of units	CO ₂ emission/kg of coke (MT)	CO ₂ emission/L of oil (kg)	CO ₂ emission/kg of gas (kg)
Single blast cupola	10	4236.6	0	0
Divided blast cupola	22	5554.5	0	0
Induction	33	0	3900	2520
Divided blast and induction	3	0	3900	2520
Single blast and induction	2	1196	624,000	0
Gas fired	2	20,010	18,720	806.4
Pit furnace	2	55.2	0	0
Oil fired	9	0	109,200	0
Total	83	31052.3	755,820	19,790

Fig. 5 Pareto front obtained from MATLAB results

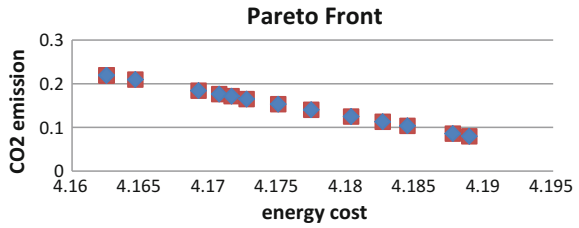


Table 5 Calculated optimal energy distribution in grid–solar–wind

Grid purchase MWh/day	Wind power MWh/day	Solar power MWh/day	Total energy cost (Rs. $\times 10^6$)
337.5275	2.9996	254.4756	4.1803
Grid purchase kWh/yr	Wind kWh/yr	Solar kWh/yr	
101,258,250	899,880	76,342,680	

Table 6 Annual CO₂ emission

CO ₂ emission from grid (tonnes of CO ₂) $\times 10^3$	CO ₂ emission in foundries (tonnes of CO ₂) $\times 10^3$	Total CO ₂ emission per day (tonnes of CO ₂) $\times 10^3$
0.1249	2.6888	2.8137
CO ₂ emission (foundry) kg/yr	Total CO ₂ emission per day (tonnes of CO ₂) $\times 10^3$	Total CO ₂ emission in kg/yr
80662.3×10^3	2.8129×10^3	843870×10^3

4 Results

MATLAB programming is used to determine optimal one to satisfy two conflicting objectives with the two renewable energy sources: solar and wind. The output of the MATLAB result gives the points on Pareto front (Fig. 5).

Following optimal solution is arbitrarily considered to calculate values from Pareto set (Tables 5, 6)

337.5275 2.9996 254.4756
4.1803 0.1249

5 Conclusion

Multi-objective optimization of energy cost using genetic algorithm in MATLAB has been successfully used. A number of points obtained on Pareto front are 16. These 16 optimal solutions satisfy information between minimization of total energy cost and CO₂ emission. Selected solution from Pareto set gives the energy required in Kolhapur foundry sector in MWh/day by grid purchase, wind power, solar power are 337.5275, 2.9996, 254.4756, and CO₂ emission from grid is 124.9 tonnes and from foundries 2688.8 tonnes. These are the optimum values to fulfill the energy consumption.

References

1. Edgeworth, F.Y., Kegan, P.: *Mathematical Psychics: An Essay on the Application of Mathematics to the Moral Sciences* vol. 10 (1881)
2. Stadler W.: *Applications of Multicriteria Optimization in Engineering and the Sciences (a survey)*. Multiple criteria (1984)
3. Stadler, W., Steuer, R.E.: *Multicriteria Optimization-Theory, Computation and Application* (1985)
4. Keirstead, J., Samsatli, N., Shah N.: SynCity—an integrated tool kit for urban energy systems modelling. *Energy efficient cities: assessment tools and benchmarking practices*. 21–42 (2010)
5. Howard, B., Saba, A., Gerrard, M., Modi, V.: Combined heat and power's potential to meet New York city's sustainability goals. *Energy Policy* **65**, 444–454 (2014)
6. Suganthi, L., Williams, A.: Renewable energy in India—a modelling study for 2020–2021. *Energy policy* **28**(15), 1095–1109 (2000)
7. Logan, D., Neil, C., Taylor, A.: *Modeling Renewable Energy Resources In Integrated Resource Planning* (No. NREL/TP-462-6436). National Renewable Energy Lab., Golden, CO (United States) (1994)
8. Thakor, N.V., Webster, J.G., Tompkins, W.J.: Design, implementation, and evaluation of a microcomputer-based portable arrhythmia monitor. *Med. Biol. Eng. Comput.* **22**, 151–159 (1984)

Analysis of Ripple Voltage at the Output of Five-Phase Converter with Five-Phase Inverter Drive for Renewable Energy Applications

Manjesh

Abstract Technological advancement in power electronic systems, renewable energy usage is tremendous applications in industries and electric vehicles. Various solar-powered systems are designed, and performances have been improved by the researchers. This proposed work will imply on power-handling capability of five-phase inverter with DC Buck-Boost converter. Power from the solar cells will be buck boosted and charged to a battery and then used to power up the adjustable speed drives and AC systems. This paper is a simulation work, proposed to study the power-handling capability of the renewable energy and used in five-phase VSI, and also output of five-phase DC converter ripple voltage is analyzed and found minimum ripple voltage for DC-powered applications.

Keywords Renewable energy · Solar energy · Buck-boost · Five phases Battery · Simulink

1 Introduction

Use of sustainable renewable energy resources is increasing as the oil, fuels sources are at risk of extension. In renewable energy sources, use of solar energy is growing enormously. Solar energy can be used in both domestic and industrial applications. Most of the industries mainly use applications of induction motors such as blowers, fans, high-voltage alternating current, industrial ASDs and intelligent automotive control. Use of induction machines is increasing in industries due to superior reliability, sturdiness or robustness, good efficiency, less maintenance while operating. Solar energy applications are either in small scale (pumping of water, home

Manjesh (✉)
Bangalore University, Bangalore, India
e-mail: manjesh1972@gmail.com

appliances and domestic lighting, electric cars, defense and aerospace applications) or in large scale (electric hybrid systems, electrical power plants). Challenge rises when designing power converter systems, which couples to load from the input source efficiently [1].

As the advancement in technology of power system and devices, multi/polyphase has become alternative to three-phase systems. Fault lenience and power divided into three phases which is the main advantages over the three-phase systems. In a conventional three-phase system if a phase is inactive, then the complete system will be inactive. In case of multi-drives, it preserves and continues toward developing rotary magnetic flux, if single or other phase is inactive or faulted. In multi-drives DC link voltage will imposes high current per phase requirements, implying the advantage in multi/polyphase drives, because of these advantages five-phase systems are suitable than the three-phase systems, and reductions in current per phase for the given input/output can be obtained.

Buck-boost DC–DC power converters are broadly utilized in solar energy applications; using this output voltage can be boosted or bucked. This type of power converter will charge battery from solar cells, freewheeling diode in the converter behaves as blocking diode, and it blocks the reverse flowing back to solar panels. This blocking criterion is not available in case of buck converter. Most of the loads are run by AC; hence, from the battery an inverter must be used to convert AC from DC. The complete proposed models' block diagram is shown in Fig. 1.

From the solar panels the converted electrical energy is connected to the Buck-boost converter, and this unit will boost or buck the voltage according to the user requirement and help to charge the battery. Therefore, the battery is connected to the five-phase inverter drive, which converts DC to AC for AC load applications. Ripple voltage is a type of signal distortion which will be harmful to the system. Reduction in these ripples is a crucial part while designing any power systems [2–7].

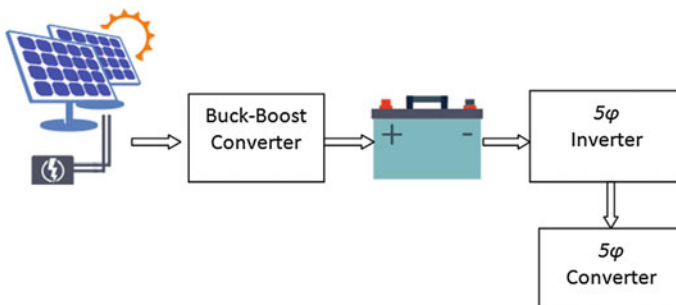


Fig. 1 Proposed model's block diagram

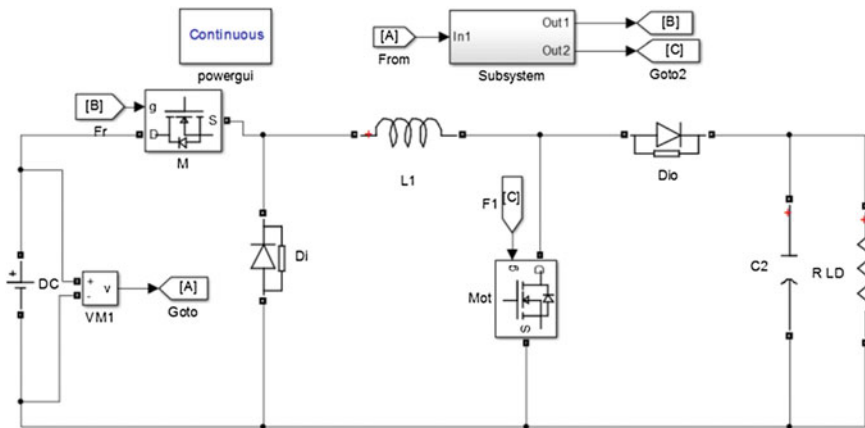


Fig. 2 Buck-boost DC-DC converter circuit diagram

2 DC-DC Buck-Boost Converter

Solar energy is converted into electrical energy and stored into a battery and used for AC or DC load applications. Solar energy is generated depending upon the intensity of sunlight; if the sunlight is less, energy generated in the solar energy is less; therefore, the energy is required to boost up, to operate the load and therefore to boost or buck the output voltage to DC-DC converter; and an inverter is employed to drive the load. A five-phase application-dependent power distribution designs have been developed based on the DC-DC and DC-AC for energy conversion system. Buck-boost converter is constructed using Matlab as shown in Fig. 2.

The Buck-Boost converter can be designed to a desired output and operated in constant conduction manner using Eq. (1).

$$V_{out} = \frac{V_{in}}{1 - D_c} \tag{1}$$

where D_c is duty cycle

$$D_c = T_{on} / (T_{on} + T_{off})$$

3 Five-Phase PWM Inverter Drive

Five-phase PWM inverter drive is constructed with Simulink/Matlab. Pulse generators P1-P10 are programmed and connected to gate terminal of switches MOSFET/IGBT S1-S10. All switches will conduct as per the designed period of

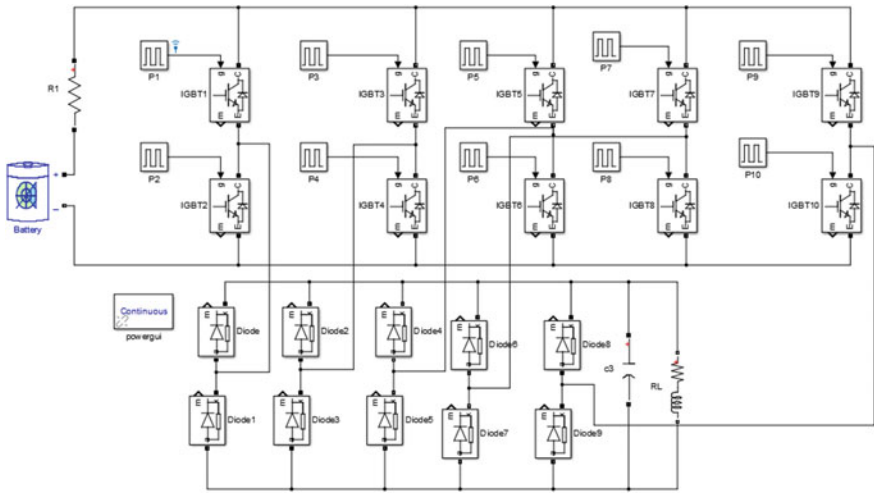


Fig. 3 Five-phase inverter with five-phase converter circuit diagram

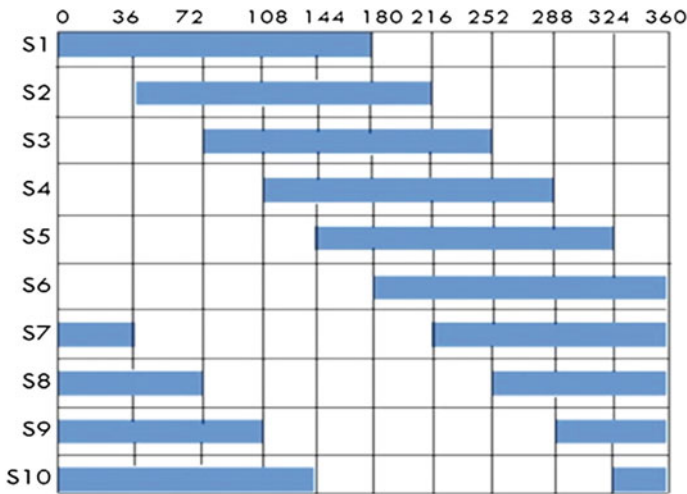


Fig. 4 Switching sequence of inverter switches

180° conduction mode, and also all phases have 72° phase difference with each other. Switches are programmed in such a manner that three from upper and two from lower will be activated and vice versa. Proposed model's diagram of five-phase inverter is shown in Fig. 3. Switching pattern of five-phase inverter is shown in Fig. 4.

Ripple factor can be calculated using the formula.

$$R_f = V_{RMS} / V_{DC}$$

where V_{RMS} = RMS of the voltage, V_{DC} = DC voltage.

4 Simulation Results

In Buck/Boost converter, DC output voltage versus time is measured using Simulink software and shown in Fig. 5. Simulation carried out by initializing input 50 Hz as frequency. Output voltage is measured and plotted for five-phase PWM inverter drive. Voltage waveforms of five-phase inverter are presented in Fig. 6. Measurement of THD and FFT analysis has been taken by using Simulink. In Simulink the individual harmonic order's percentage of harmonics is found and presented in bar graph of Fig. 7. Five-phase converter output voltage is shown in Fig. 8.

The voltage ripple is minimized in this proposed model. Ripple factor has been measured for various load values for the comparison as shown in Table 1.

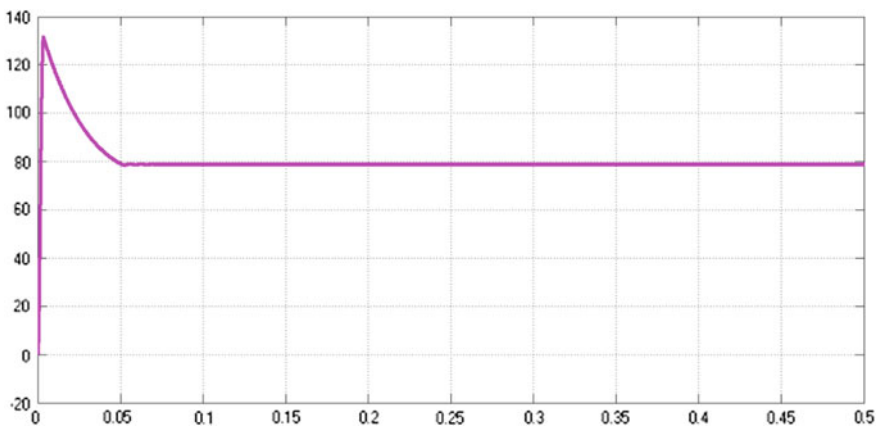


Fig. 5 Output voltage of buck-boost converter

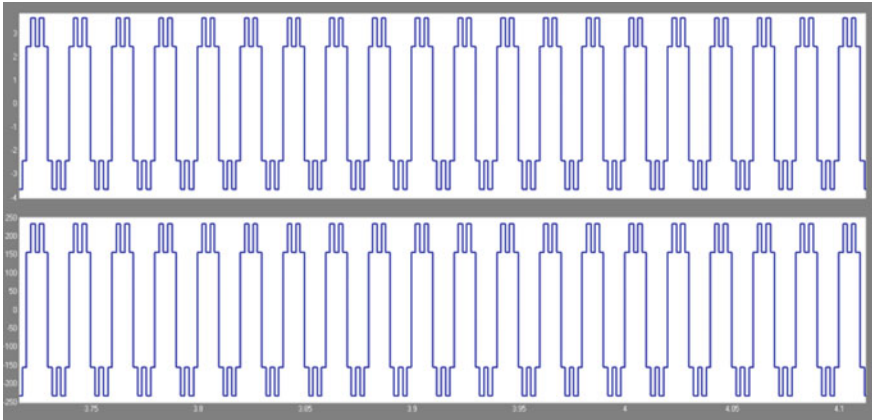


Fig. 6 Voltage and current waveforms of individual phase in normal five-phase inverter

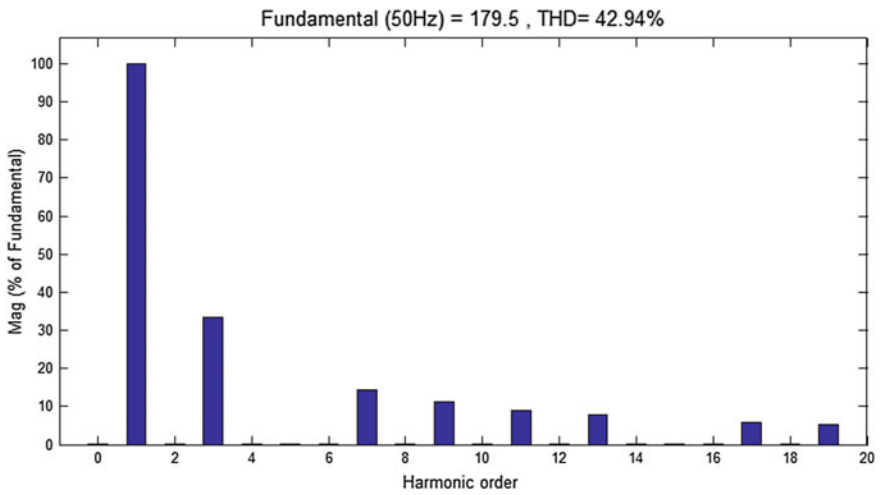


Fig. 7 FFT analysis of output voltage of the five-phase inverter

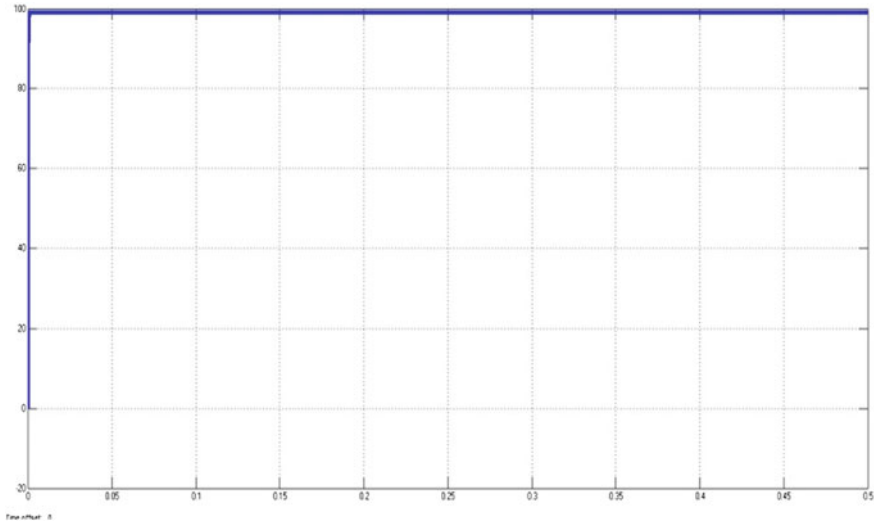


Fig. 8 Five-phase converter output voltage

Table 1 Ripple factor at various loads

Load resistance	Load inductance	Ripple factor
10	300 mH	0.77
5	1	0.707
10	10	0.707
0.1	–	0.717
1 k	–	0.740
1 k	10 mH	0.747
0.1	1 mH	0.710

5 Conclusion

A five-phase converter and inverter drive have been constructed for renewable energy applications, the total harmonic distortion and buck boost analysis of five-phase inverter drive are studied, and analysis of ripple voltage at the output of the converter is also studied and minimized the content of the ripple voltage using five-phase inverter drive. This work can be proposed to drive ripple-free DC drives.

References

1. Levi, E.: Multiphase electric machine for variable speed applications. *IEEE Trans. Ind. Electron.* **55**(5), 1893–1909 (2008)

2. Brunelli, D., Moser, C., Thiele, L., Benini, L.: Design of a Solar-Harvesting Circuit for Batteryless Embedded Systems, *IEEE Trans. Circ. Syst. I Reg. Pap.* **56**(11), 2519–2528 (2009)
3. Chini, A., Soci, F.: Boost-converter based solar harvester for low power applications. *Electron. Lett.* **46**(4), 1–2 (2010)
4. Crespi, A.M., Somdahl, S.K., Schmidt, C.L., Skarstad, P.M.: Evolution of power sources for implantable cardioverter defibrillator. *J Power Sour.* **96**, 33–38 (2001)
5. Bhende, C.N., Malla, S.G.: Novel control of photovoltaic based water pumping system without energy storage. *Int. J. Emerg. Electr. Power Syst.* **13**(5) (2012)
6. Levi, E., Bojoi, R., Profumo, F., Toliyat, H.A., Williamson, S.: Multiphase induction motor drives—A technology status review. *IET Elect. Power. Appl.*, **1**(4), 489–516 (2007)
7. Husna, A.W., Siraj, S.F, AbMuin, M.Z.: Modeling of DC-DC converter for solar energy system applications. In: *IEEE Symposium on Computers and Informatics*, pp. 125–129, (2012)

A Novel Six-Switch Power Converter for Single-Phase Wind Energy System Applications

K. Kumar, K.R. Prabhu, N. Ramesh Babu and P. Sanjeevikumar

Abstract In this paper, a six-switch AC/DC/AC converter is proposed for single-phase wind energy system application. The proposed converter consists of two arms with three switches in each, where the top layer switches are used for the rectification mode and lower layer switches are used for the inversion mode of operation. The middle layer switches are shared by the both rectification and inversion mode operation based on the modified PWM scheme. A small rated DC link capacitor is chosen by providing suitable coordination control and EX-OR gate logic between the rectification and inversion mode of operation. The proposed single-phase six-switch converter has the advantage of both reduced number of switches and small DC link capacitor size. To validate the effectiveness of the proposed converter, simulation results are presented for 1 kW wind system.

Keywords AC/DC/AC converter · Wind energy system · Modified PWM
Reduced switch count topology

K. Kumar · K.R. Prabhu · N. Ramesh Babu (✉)
School of Electrical Engineering, Vellore Institute Technology (VIT) University,
Vellore, India
e-mail: nrameshbabu@vit.ac.in

K. Kumar
e-mail: Kumar3kk@gmail.com

K.R. Prabhu
e-mail: Prabhu.kr@vit.ac.in

P. Sanjeevikumar
Department of Electrical and Electronics Engineering, University of Johannesburg,
Auckland, Johannesburg, South Africa
e-mail: sanjeevi_12@yahoo.co.in

1 Introduction

The nonlinearity of renewable energy sources leads to intermittent and uncertain voltage with frequency fluctuations [1]. To overcome these fluctuations, different power electronic converters are used like AC/DC/AC back-to-back converter found in wind system [2–4] and DC/DC boost converter with inverter in the PV system applications [5]. Among all available renewable energies, wind energy source becomes more popular due to its abundant availability in nature [6], and its cumulative installed capacity in India has reached 27151.40 MW as of July 30, 2016 [7].

Single-phase AC/DC/AC power conversion without change in frequency is found in different applications like line voltage restorer during faults, uninterruptible power supply system in domestic applications, adjustable speed drive system, power quality enhancement devices and low rating wind turbine systems [8–13].

Figure 1 shows the traditional converter topology available for single-phase wind energy system of type back-to-back converter, which consists of totally eight switches (S_1 – S_8). The first four switches S_1 – S_4 are used for converting input AC supply into DC by rectification action and store the DC voltage in DC link capacitor, and C_{dc} and the remaining four switches S_5 – S_8 are used for inversion action to convert DC link capacitor voltage into AC voltage for single-phase AC voltage applications [14].

The single-phase AC/DC/AC conversion can be obtained by placing capacitor between the source and load for different applications. The traditional converter requires an eight active switches and a high DC link capacitor, which causes limited life span and increased cost. In order to reduce the switch count, cost and size of the DC link capacitor, different converter configuration topologies are investigated in [15–18].

A new topology for power converter is proposed for single-phase wind energy system in this paper. The conventional topology is replaced by a proposed

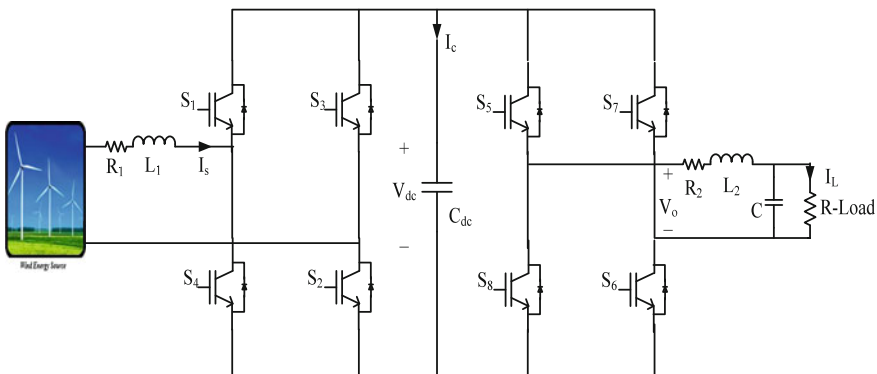


Fig. 1 Conventional topology for single-phase AC/DC/AC conversion

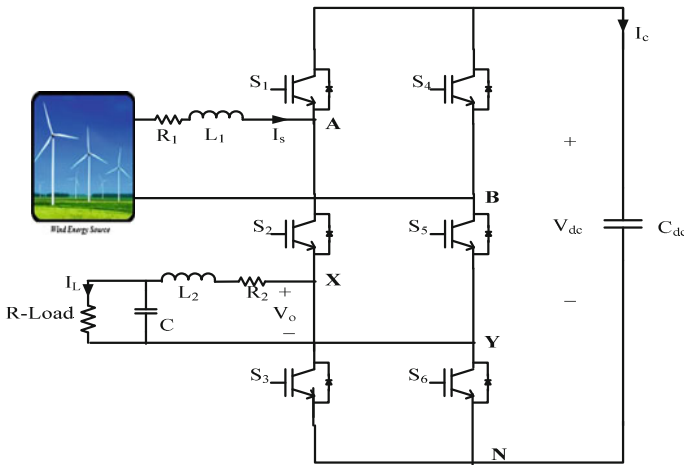


Fig. 2 Proposed topology for single-phase AC/DC/AC conversion

Table 1 Switching states of the proposed converter

Switching state	S ₁	S ₂	S ₃	V _{AN}	V _{XN}
1	1	1	0	V _{dc}	V _{dc}
2	0	1	1	0	0
3	1	0	1	V _{dc}	0

six-switch converter as shown in Fig. 2. The modified carrier-based PWM scheme and EX-OR gate logic are used to eliminate the switching constraints of the proposed converter. It provides the sinusoidal input and output voltage and currents, maintains unity power factor and reduces the cost of the converter by reducing the switch count.

2 Design and Modulation Scheme for the Proposed Converter

The proposed converter consists of two arms with three switches in each as shown in Fig. 2. The top layer switches S₁ and S₄ are used for the rectification mode of operation, and lower layer S₃ and S₆ are for the inversion mode of operation. The middle layer switches S₂ and S₅ are shared by the both top layer and lower switches to operate in AC/DC rectification and DC/AC inversion modes. The switching states of the proposed topology are described in Table 1.

Even the middle layer switches in the proposed converter are shared by the rectification and inversion modes, and the converter input and output voltages can be controlled independently. Let us consider the first leg of the proposed converter, when S₁ is ON and S₃ is OFF then S₂ will turn ON through EX-OR gate logic, then

$V_{AN} = V_{XN} = V_{dc}$. Similarly, S_1 is OFF and S_3 is ON then S_2 will ON, then $V_{AN} = V_{XN} = 0$. When S_1 and S_3 are ON then S_2 will turn OFF, then $V_{AN} = V_{dc}$ and $V_{XN} = 0$ as clearly shown in Table 1.

Where V_{AN} and V_{XN} are the node voltages at nodes A and X with respect to negative DC bus node N, respectively.

To meet the switching constraint of the proposed converter, the modified carrier-based PWM technique is implemented. The upper rectifier and lower inverter modulation references are compared with a triangular carrier wave as shown in Fig. 3, where instantaneous value of upper rectifier reference is always greater than the lower inverter reference wave. PWM signals of S_1 and S_3 are obtained when the reference and carrier signals are compared as shown in Eqs. (1) and (2)

$$S_1 = \begin{cases} 1, & V_{rA} \geq V_{tri} \\ 0, & V_{rA} < V_{tri} \end{cases} \tag{1}$$

$$S_3 = \begin{cases} 1, & V_{rX} \leq V_{tri} \\ 0, & V_{rX} > V_{tri} \end{cases} \tag{2}$$

where

V_{rA} is upper modulation reference signal

V_{rX} is lower modulation reference signal

V_{tri} is triangular carrier signal

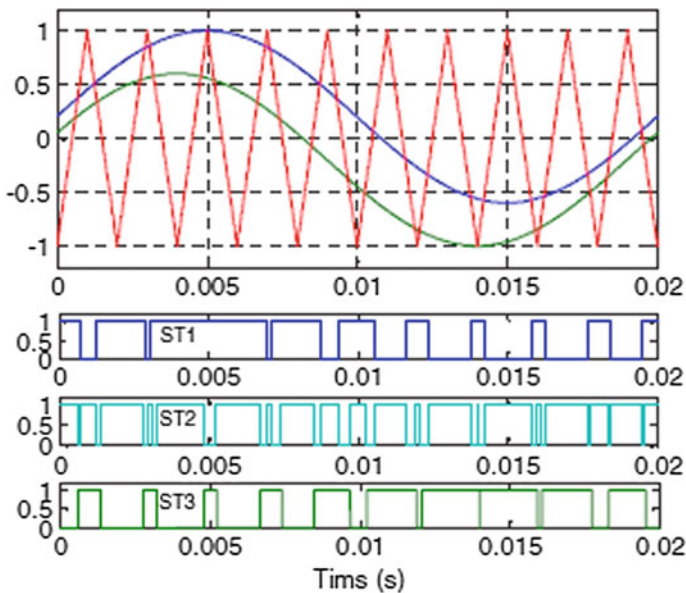


Fig. 3 Modulation scheme for the proposed converter

The PWM pulses for S_2 and S_5 are obtained by EX-OR gate logic operation and are expressed in Eqs. (3) and (4)

$$S_2 = S_1 \oplus S_3 \tag{3}$$

Similarly,

$$S_5 = S_4 \oplus S_6 \tag{4}$$

To eliminate the second-ordered power variations in DC link capacitor and for obtaining the sinusoidal input and output voltages, the phase angle must be tuned between rectifier and inverter appropriately. The fluctuations in the DC link capacitor are proposed by the current flowing through it as shown in Eq. (5).

$$V_{dc} = \frac{1}{C_{dc}} \int i_c(t) dt + V_{dc} \tag{5}$$

where

C_{dc} is the DC link capacitor

V_{dc} is the DC link capacitor voltage

$i_c(t)$ is the current flowing through the DC link capacitor

The current flowing through the DC link capacitor in proposed converter is shown in Eq. (6)

$$i_c(t) = i_1(t) - i_4(t) \tag{6}$$

where $i_1(t)$ and $i_4(t)$ are the currents flowing through the switches S_1 and S_4 .

The average values of currents $i_1(t)$ and $i_4(t)$ are calculated from the switching states, and its equivalent circuit of the proposed topology as shown in Fig. 4 is given in Eqs. (7) and (8).

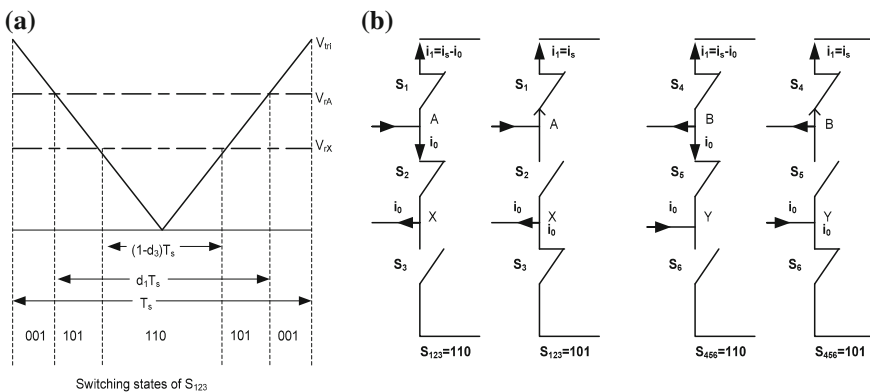


Fig. 4 a Switching states, b equivalent circuit of the proposed topology

$$i_1(t) = (1 - d_3)(i_s(t) - i_L(t)) + (d_1 + d_3 - 1)i_s(t) \quad (7)$$

$$i_4(t) = (1 - d_6)(i_s(t) - i_L(t)) + (d_4 + d_6 - 1)i_s(t) \quad (8)$$

By substituting Eqs. (7) and (8) in Eq. (6), we get the total instantaneous current flowing through the DC link as shown in Eq. (9)

$$i_c(t) = (d_1 - d_4)i_s(t) - (d_6 - d_3)i_L(t) \quad (9)$$

where

$i_s(t)$ is the source input current

$i_L(t)$ is the load output current

$$d_1 = \frac{1 + m_r \sin(\omega t + \theta_2)}{2} + d_{\text{off}1} \quad (10)$$

$$d_4 = \frac{1 - m_r \sin(\omega t + \theta_2)}{2} + d_{\text{off}1} \quad (11)$$

$$d_3 = \frac{1 - m_i \sin(\omega t + \theta_2 + \varphi)}{2} - d_{\text{off}2} \quad (12)$$

$$d_6 = \frac{1 + m_i \sin(\omega t + \theta_2 + \varphi)}{2} - d_{\text{off}2} \quad (13)$$

Equations (10)–(13) give the duty ratios of the proposed converter to achieve the coordination control between the rectifier and inversion mode of operation.

Where d_1 , d_4 , d_3 and d_6 are the duty cycle ratios of the proposed converter, m_r is the rectifier modulation index, m_i is the inverter modulation index, θ and φ are the phase angles of the rectifier/inverter modulation reference and $d_{\text{off}1}$ and $d_{\text{off}2}$ are the offset values for moving up/down modulation references of rectifier/inverter.

3 Numerical Simulation Results and Discussion

A single-phase six-switch AC/DC/AC power converter for a 1 kW wind energy system has been simulated by using the control logic analyzed in this paper. The ratings of the overall system are shown in Table 2.

Table 2 Ratings of the proposed system

Components	Ratings
Wind power rating, P	1 kW
Voltage, V	230 V
Current, A	5 A
Input filter, L1	3 mH
Input filter, R1	0.1 Ω
Output filter, L2	0.43 mH
Output filter, R2	0.3 Ω
DC link capacitor, Cdc	470 μF
Load resistance, RL	45 Ω

Figure 5 shows the input voltage and current to the proposed converter from the wind energy system, and its magnitude of input voltage is 230 V and current is 5 A. The output of the wind energy source is given as input to the developed converter in between top and the middle layer, which converts input AC voltage into DC voltage and stores in the DC link capacitor.

Figure 6 shows the DC link voltage varies from 80 to 230 V. The DC link capacitor voltage is connect to the resistive load of $R_L = 45 \Omega$. The lower switch layer converts DC link voltage into AC by operating the developed converter in inversion mode. Figure 7 shows the load voltage and current waveforms with the magnitude of 230 V and 5 A. Thus, the developed converter effectively converts the output of the wind energy source to the load by sharing the switches of the converter.

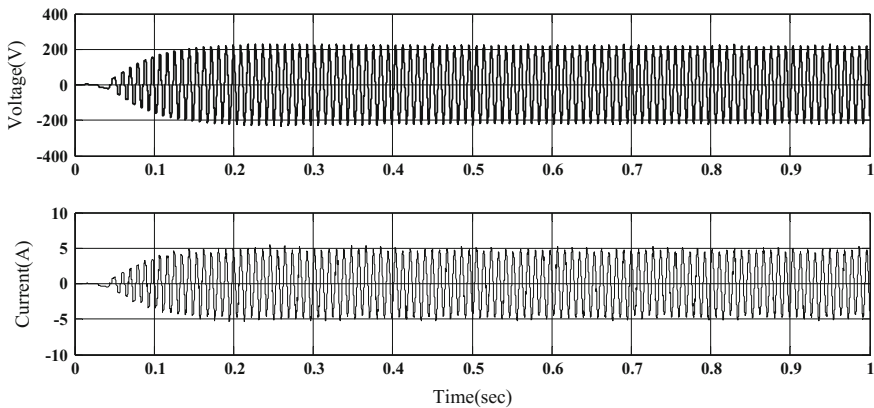


Fig. 5 Simulated wind input voltage and current waveforms

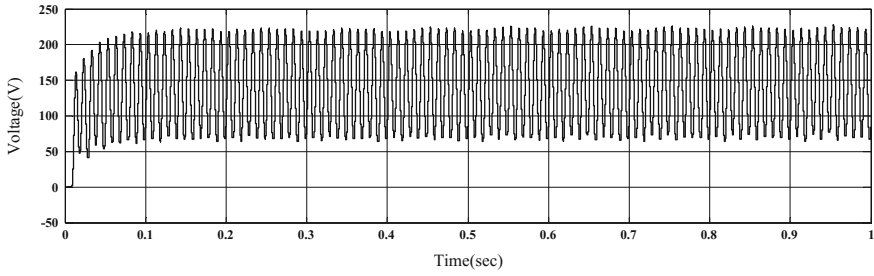


Fig. 6 Simulated DC link capacitor voltage waveforms

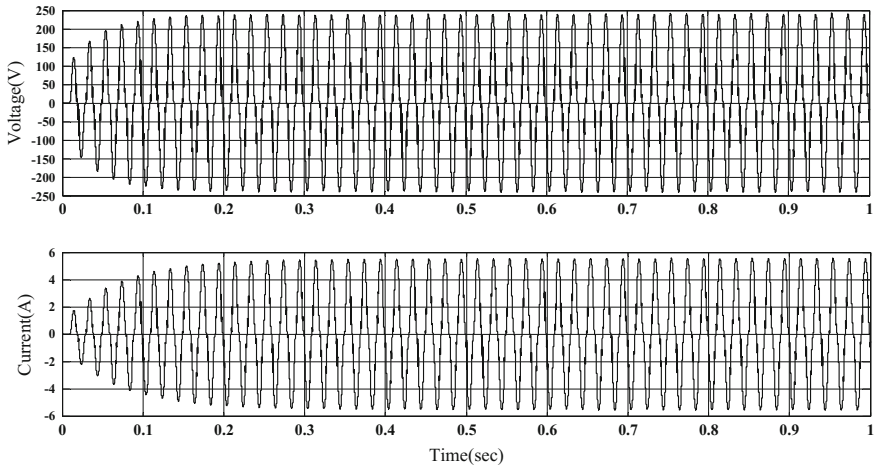


Fig. 7 Simulated output voltage and current waveforms

4 Conclusions

The novel single-phase AC/DC/AC converter with six switches has been introduced in this paper for single-phase wind energy system application. The modified PWM scheme and EX-OR gate logic provide the coordination control between rectifier and inverter modes of operation by sharing the middle layer switches. The developed converter provides near sinusoidal input and output voltage/current. The developed model has reduced cost due to the reduced switch count converter topology and with low rated DC link capacitor. The simulation results obtained show the effectiveness of the proposed converter topology.

References

1. Liu, X., Loh, P.C., Wang, P., Blaabjerg, F.: A direct power conversion topology for grid integration of hybrid AC/DC energy resources. *IEEE Trans. Ind. Electron.* **60**(12), 5696–5707 (2013)
2. Tiwari, R., Saravanan, S., Ramesh Babu, N., Kumar, G., Siwach, V.: Design and development of a high step-up DC-DC converter for non-conventional energy applications. In: Biennial International Conference on Power and Energy Systems: Towards Sustainable Energy (PESTSE), Bengaluru, India, 1–4 (2016)
3. Sanjeevikumar, P., Geethalakshmi, B., Dananjayan, P.: Performance analysis of AC-DC-AC converter as a matrix converter. In: Conference Proceedings IEEE India International. Conference on Power Engineering, IEEE-IICPE'06, Chennai, (India). 57–61 (2006)
4. Ramji, T., Ramesh Babu, N.: Recent developments of control strategies for wind energy conversion system. *Renew. Sustain. Energy Rev.* **66** 268–285 (2016)
5. Saravanan, S., Ramesh Babu, N.: RBFN based MPPT algorithm for PV system with high step up converter. *Energy Convers. Manag.* **122**, 239–251 (2016)
6. Ramji, T., Ramesh Babu, N.: Fuzzy logic based MPPT for permanent magnet synchronous generator in wind energy conversion system. *IFAC-PapersOnLine* **49**(1), 462–467 (2016)
7. Cumulative development of various renewable energy system/devices in country. Retrieved from <http://mnre.gov.in/mission-and-vision-2/achievements>
8. Jung, H.S., Chee, S.J., Sul, S.K., Park, Y.J., Park, H.S., Kim, W.K.: Control of three-phase inverter for AC motor drive with small DC-link capacitor fed by single-phase AC source. *IEEE Trans. Ind. Appl.* **50**(2), 1074–1081 (2014)
9. Dos Santos, E.C., Rocha, N., Jacobina, C.B.: Suitable single-phase to three-phase AC–DC–AC power conversion system. *IEEE Trans. Power Electron.* **30**(2), 860–870 (2015)
10. Jacobina, C.B., Oliveira, A.C.: Single-phase AC–AC double-star chopper cells (DSCC) converter without common DC-link capacitor. *IEEE Trans. Ind. Appl.* **51**(6), 4642–4652 (2015)
11. Choi, J.H., Kwon, J.M., Jung, J.H., Kwon, B.H.: High-performance online UPS using three-leg-type converter. *IEEE Trans. Ind. Electron.* **52**(3), 889–897 (2005)
12. Park, J.K., Kwon, J.M., Kim, E.H., Kwon, B.H.: High-performance transformerless online UPS. *IEEE Trans. Ind. Electron.* **55**(8), 2943–2953 (2008)
13. Kolhatkar, Y.Y., Das, S.P.: Experimental investigation of a single-phase UPQC with minimum VA loading. *IEEE Trans. Power Del.* **22**(1), 373–380 (2007)
14. Portillo, R.C., Prats, M.M., Leon, J.I., Sanchez, J.A., Carrasco, J.M., Galvan, E., Franquelo, L.G.: Modeling strategy for back-to-back three-level converters applied to high-power wind turbines. *IEEE Trans. Ind. Electron.* **53**(5), 1483–1491 (2006)
15. Lin, B.R., Huang, C.H.: Single-phase AC/DC/AC converter based on capacitor clamped topology. *IEEE Proc. Electr. Power Appl.* **152**(3), 464–472 (2005)
16. Jacobina, C.B., Oliveira, T.M., da Silva, E.R.C.: Control of the single-phase three-leg AC/AC converter. *IEEE Trans. on Ind. Electron.* **53**(2), 467–476 (2006)
17. De Freitas, I.S., Jacobina, C.B., da Silva, E.R.C., Oliveira, T.M.: Single-phase AC–DC–AC three-level three-leg converter. *IEEE Trans. Ind. Electron.* **57**(12), 4075–4084 (2010)
18. Jacobina C.B., Rocha, N., Marinus, N.S., Santos E.C.: Ac-ac single-phase dc-link converter with four controlled switches. In: Twenty-Seventh Annual IEEE Applied Power Electron Conference and Exposition (APEC). 1927–1932 (2012)

Fuzzy Logic-Based Pitch Angle Controller for PMSG-Based Wind Energy Conversion System

Ramji Tiwari, N. Ramesh Babu and P. Sanjeevikumar

Abstract A comparative analysis of different types pitch angle controller is designed in this paper to achieve a steady output torque for stable wind turbine operation. The control techniques are implemented and developed to provide a uniform constant torque to the permanent magnet synchronous generator (PMSG). The wind system consists of a wind turbine, a pitch actuator and PMSG. The control strategy used are proportional-integral (PI) and fuzzy logic controller (FLC). The performance of the control strategies is investigated in terms of aerodynamic torque, generator speed and the generator power. The complete wind energy conversion system (WECS) is developed and tested using MATLAB/Simulink. The performance of the control strategies is evaluated under varying wind-speed condition. The performance of the pitch angle controllers is found satisfactory, but the strategy with fuzzy logic-based controller shows better performance as compared to PI controller.

Keywords Wind energy conversion system · PMSG · Pitch angle controller
PI controller · Fuzzy controller

1 Introduction

Motivated by the issue of global warming and depletion of fossil fuel, the focus on renewable energy-based power generation is gaining interest rapidly. Due to environmental impact of fossil fuel-based generation, there is a need for alternative

R. Tiwari · N. Ramesh Babu (✉)
School of Electrical Engineering, VIT University, Vellore, India
e-mail: nrameshbabu@vit.ac.in

R. Tiwari
e-mail: ramji.tiwari2015@vit.ac.in

P. Sanjeevikumar
Department of Electrical and Electronics Engineering, University of Johannesburg,
Auckland, Johannesburg, South Africa
e-mail: sanjeevi_12@yahoo.co.in

source which is cleaner and economically cost-effective [1]. Among the renewable energy source, wind power is the fastest growing sustainable source [2]. Massive development is carried out in field of wind power generation in recent years. Wind energy has an advantage of reduced power loss, grid connection and stabilized voltage profile. Technical development of WECS is the current major research area. Power rating of wind energy is increased to MW range, which is significant for grid integration [3].

Variable-speed wind turbine (VSWT) is most preferred wind-based power generation system for its efficiency and controllability. Variable pitch control strategy is implemented in VSWT to achieve efficient and reliable power conversion [4]. Based on the wind speed, the modes of operation of wind turbine are classified into two typical regions as shown in Fig. 1. In Region 1, where the wind speed is below the rated one, the turbine speed is controlled to obtain the maximum power from the available wind. In Region 2 where the wind speed is greater than that of rated wind speed, the power is limited at the rated value to protect the generator and the power electronic converter associated with it. The pitch angle controller is implemented in the Region 2 to limit the turbine speed by controlling the blade angle and during Region 1, pitch controller can be used for power smoothening.

The controlled and reliable operation of WECS is mainly depending upon the type of controller applied in the wind turbine in different regions. Pitch angle controller is mainly applied to reduce the aerodynamic torque caused due to increase in wind speed above the rated wind speed. The pitch angle is mainly used in high-power wind turbine [5]. In small WECS, pitch angle is employed to smoothen the power output. Numerous pitch-based control strategy is designed for wind power generation based on the parameters such as generator used, power capacity, average wind speed [6].

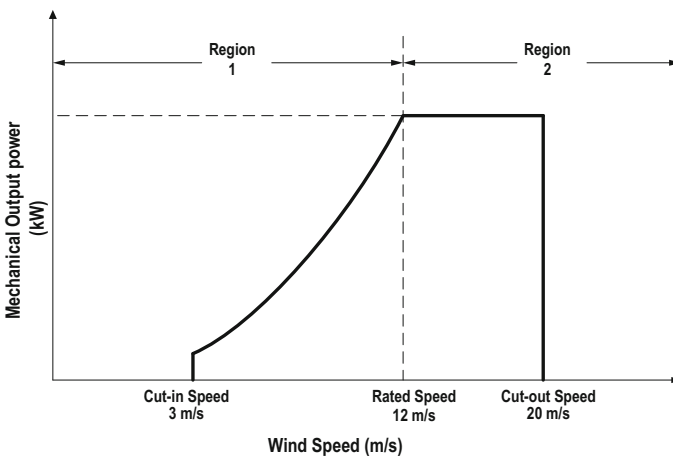


Fig. 1 Regions based on wind speed

In this paper, a comparative analysis of PI- and fuzzy-based pitch angle controller for WECS is carried out. The performance of PI and fuzzy logic controller is evaluated in varying wind condition. The ability of the controllers to track the nonlinearity is analyzed and compared using MATLAB/Simulink software. The main focus of the proposed controller is to limit the aerodynamic torque during high-wind-speed region and optimize the power during low-wind-speed region.

2 Modeling of Wind Energy Conversion System

(A) Modeling of Wind Turbine

Wind turbine is an important mechanical aspect of WECS. The kinetic energy of the wind is converted to mechanical energy as aerodynamic torque. The magnitude of the torque produced by wind turbine is associated with the wind velocity/speed and the air density. The torque obtained by the turbine can be expressed as [7]

$$T_m = \frac{1}{2} \frac{C_p(\beta, \lambda)}{\lambda} \rho \pi R^3 V_{wind}^2 \tag{1}$$

where the rotor coefficient is expressed as C_p which defines the amount of wind power that can be transformed into mechanical power, the ρ represents the air density, the radius of wind turbine blade is denoted as R , and V_{wind} is the wind speed. The coefficient constants β and λ are represented as blade pitch angle and tip-speed ratio (TSR), respectively.

The rotor power conversion coefficient C_p is expressed as,

$$C_p(\lambda, \beta) = c_1 * \left(c_2 \frac{1}{\eta} - c_3 \beta - c_4 \beta^x - c_5 \right) * \exp\left(-c_6 \frac{1}{\eta} \right) \tag{2}$$

where $\frac{1}{\eta} = \left(\frac{1}{\lambda + 0.08\beta} \right) - \left(\frac{0.035}{1 + \beta^3} \right)$ and $c_1 = 0.5, c_2 = 116, c_3 = 0.4, c_4 = 0, c_5 = 5, c_6 = 21$ and $x = 0$. The above analysis is implemented for the proposed system.

(B) Pitch actuator

The pitch angle control is generally implemented to limit torque in wind turbine during high wind speed. The pitch actuator adjusts the blade angle around the longitudinal axes for altering the turbine speed according to the wind speed [8]. The pitch actuators are basically of two types electric pitch actuator and an hydraulic pitch actuator [9]. The later actuator is in the verge of diminish as they require frequent maintenance, high implementation cost and less accuracy. The electric actuator is widely preferred for its simplicity, efficiency and high response rate.

The dynamic behavior of pitch actuator is modeled as integrator with the time constant (τ_c). The pitch actuator is expressed as:

$$\frac{d\beta}{dt} = -\frac{1}{\tau_c}\beta + \frac{1}{\tau_c}\beta_{\text{ref}} \quad (3)$$

which is limited between the pitch angle minimum (β_{min}) and pitch angle maximum (β_{max}), $\beta_{\text{min}} \leq \beta \leq \beta_{\text{max}}$.

Equation 3 states that the time constant of the pitch actuator determines the response time of pitch control, which is normally in the range 0.2–0.25. The rate limiter in the pitch actuator system shows the realistic response to the variability of the system. The accuracy and efficiency of pitch angle controller depend on the response time of the pitch rate ($d\beta/dt$). The typical range of pitch angle lies between -2 and 30° . Thus, the performance of the power regulation of wind turbine is related to the rate of change of pitch angle [10].

3 Pitch Angle Control

In this section, PI- and fuzzy-based pitch angle control has been described.

(A) *Proportional-Integral (PI) Controller*

The conventional pitch control system uses PI controller for power regulation of the wind turbine. The PI-based pitch control is used to optimize the rotor speed or the power of the generator. In Region 1, PI controller cannot be applied. Hence, MPPT control strategy is applied to regulate the power. The PI controller is activated in Region 2 to stabilize the rotor speed or the generator output power using the error value generated by the reference value and the actual value obtained [11]. The block diagram of PI-based pitch angle controller is shown in Fig. 2, where the variable (X_g) is either the rotor speed (ω_r) or the generator output power (P_g). K_{sys} is set as 1 for PI controller.

The PI controller can generate the pitch angle value using electric and mechanical value as an input variable. The electrical input values are generator power, the mechanical input variables are mechanical power or the generator speed. The input variable for PI controller is chosen depending upon the wind speed [12].

The input gains of the PI controller should be reframed to sustain the stability and dynamic response of the system. This technique is simple and provides robustness to the controller system. However, when the wind speed is varied with sudden changes the PI controller fails to track the gain and chattering phenomena are increased [13]. Thus, the stress of the system is increased.

(B) *Fuzzy logic controller*

The fuzzy logic controller (FLC) is designed based on the human knowledge about the system. In general there are three stages in FLC, namely fuzzification, rule base lookup table and defuzzification. The rules are framed based on the prior knowledge of the system [14]. The control block diagram of FLC is shown in

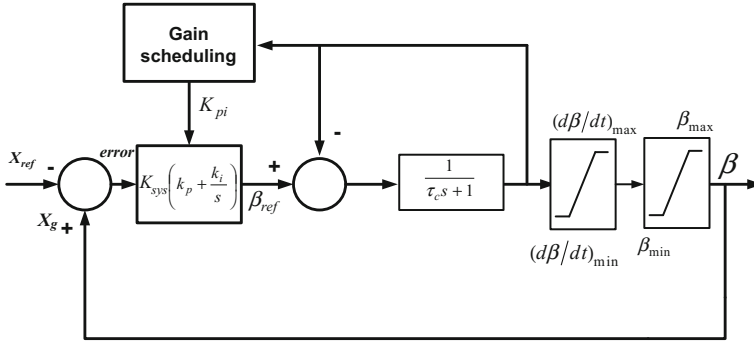


Fig. 2 Block diagram of PI-based pitch angle controller

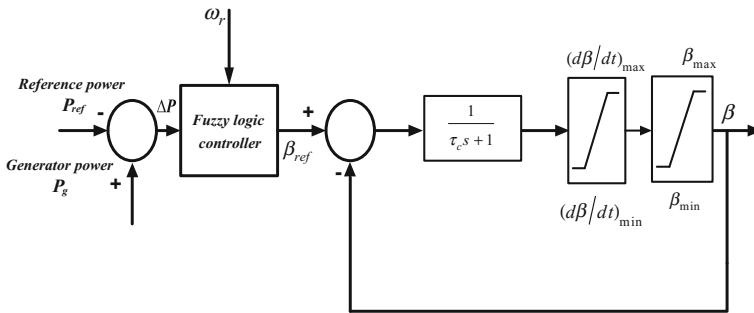


Fig. 3 FLC-based pitch angle controller

Fig. 3. The inputs of the FLC are the generator output power and rotor speed. The output of FLC is pitch angle [15].

In proposed controller, the error of generator power ΔP and change in power error $\delta(\Delta P)$ are the input variables. The output of the FLC-based controller is pitch angle reference [16, 17]. The ΔP and $\delta(\Delta P)$ are defined as,

$$\Delta P(k) = P_g - P_{ref}(k) \tag{4}$$

$$\delta(\Delta P) = \Delta P(k) - \Delta P(k - 1) \tag{5}$$

The membership functions of the fuzzy sets for the proposed system are represented by the linguistic variables. The variables are represented by Negative Large (NL), Negative Small (NS), Zero (ZE), Positive Small (PS), and Positive Large (PL).

The control rules are derived from the experience and knowledge on the control system. Table 1 shows the rules for mapping of input and output variables of FLC. In this paper, fuzzy uses Mamdani-type inference system. The input and output variables

Table 1 Rules for fuzzy logic controller

E/CE	NL	NS	ZE	PS	PL
NL	PS	PL	NL	NS	ZE
NS	PL	NL	NS	ZE	PS
ZE	NL	NS	ZE	PS	PL
PS	NS	ZE	PS	PL	NL
PL	ZE	PS	PL	NL	NS

Table 2 Wind turbine and PMSG parameters

Parameters of wind turbine		Parameters of PMSG	
Rated power	20 kW	Rated power	20 kW
Blade radius	3.86 m	Stator resistance	3.1052 Ω
Air density	1.225 kg/m ³	Stator inductance	3.75 mH
Max. power coefficient	0.411	Friction factor	0.001189 Nms
Cut-in speed	3 m/s	Pole pair	32
Cut-out speed	20 m/s	Generator inertia	48,000 kg.m ²
Rated wind speed	12 m/s		
Blade inertia	6.3 × 10 ⁶ kg.m ²		

are generated using triangular membership function. Minimum (min) method is used for the implication, whereas the maximum (max) for aggregation. The centroid method is preferred for defuzzification processing.

4 Numerical Simulation Results

The detailed modeling of 20 kW PMSG-based wind turbine system is implemented in MATLAB/Simulink to validate the system for FLC-based pitch angle controller. The parameter of wind turbine and PMSG generator is listed in Table 2. The obtained FLC sampling time is 2 ms. Pitch angle is specified within limit of ±10°/s.

The wind speed used for the system is shown in Fig. 4. The variation in torque and generated power are shown in Figs. 5 and 6. The pitch angle generated is shown in Fig. 7. These parameters are fed into the system to control and stabilize the generator speed in the rated value.

Figures 8, 9 and 10 show the performance comparison of both the strategies PI- and FLC-based pitch angle controller. The generator speed for both the control strategy is shown in Fig. 8. For PI-based controller, the generator speed is not stable at the rated value and has a high ripple component. Whereas, in FLC-based controller speed is almost kept constant at rated value. The generator power obtained in PI and FLC is compared in Fig. 9.

The nonlinearity of the wind system is not sustained using the PI controller as it fails to trace the sudden changes of wind speed and the output power is also minimized. In FLC-based strategy, the generator output power is higher than that of

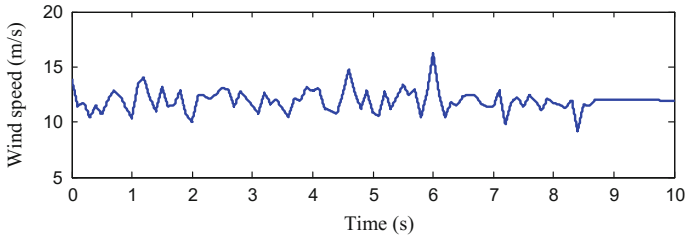


Fig. 4 Wind speed

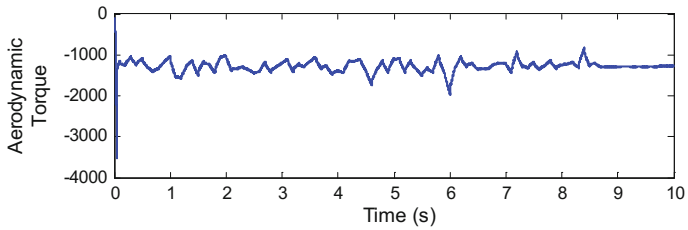


Fig. 5 Aerodynamic torque without controller

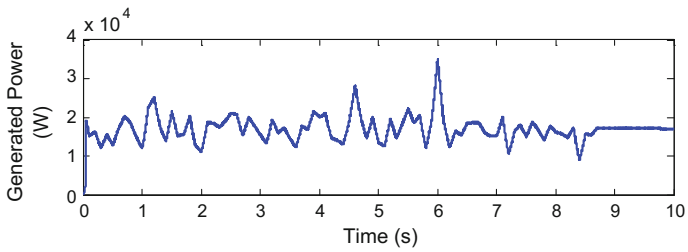


Fig. 6 Generated power without controller

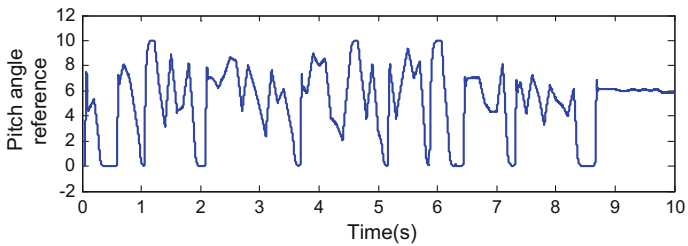


Fig. 7 Pitch angle reference

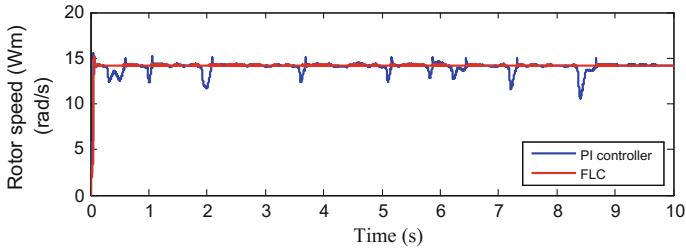


Fig. 8 Rotor speed of the PMSG generator

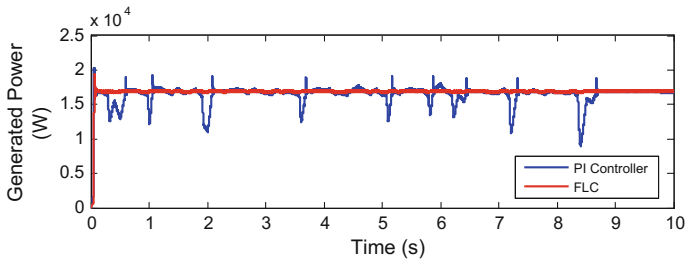


Fig. 9 Output power obtained from generator

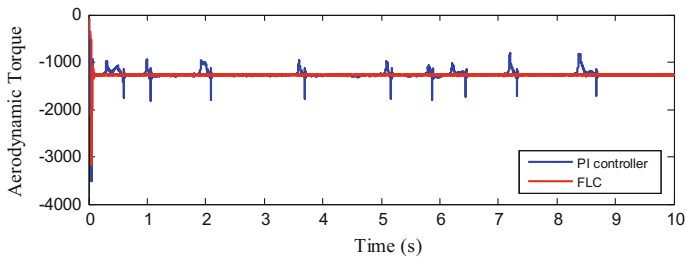


Fig. 10 Aerodynamic torque of wind turbine

Table 3 Performance analysis of pitch angle controller

Controller technique/parameter	PI controller	Fuzzy logic controller
Power	16.9 kW	17.2 kW
Generator speed	Varying	14.2 rad/s

PI-based controller. The aerodynamic torque is compared in Fig. 10. The torque contains ripple when the wind speed is shifted from Region 1 to Region 2 or vice versa in PI-based control strategy, but the ripple content is minimized to the extent in FLC-based pitch angle controller. The performance comparison of pitch angle controllers is defined in Table 3.

5 Conclusion

In this paper, a comparative analysis and implementation of PI and fuzzy logic controller-based pitch angle is designed for PMSG wind turbine system. The control strategy is implemented to limit the turbine output power and aerodynamic torque to the rated value. The performance of both the control strategy is assessed under varying wind speed. The control strategy is implemented in MATLAB/Simulink software for validation of results. From the analysis it is stated that FLC-based pitch angle controller is more reliable, efficient and consistent control strategy for stable operation. Since, PI controller fails to overcome the nonlinearity and ripple in the torque increases the stress of the system and may damage the turbine. FLC strategy requires no wind-speed data to perform task and has fast response to generate variable pitch angle. Thus, it is most suitable technique which can be applied to WECS for optimal operation.

References

1. Uehara, A., et al.: A coordinated control method to smooth wind power fluctuations of a PMSG-based WECS. *IEEE Trans. Energy Convers.* **26**(2), 550–558 (2011)
2. Lee, J., Kim, Y.S.: Sensorless fuzzy-logic-based maximum power point tracking control for a small-scale wind power generation systems with a switched-mode rectifier. *IET Renew. Power Gener.* **10**(2), 194–202 (2016)
3. Tiwari, R., Ramesh Babu, N.: Recent developments of control strategies for wind energy conversion system. *Renew. Sustain. Energy Rev.* **66**, 268–285 (2016)
4. Babu, N.R., Arulmozhivarman, P.: Wind energy conversion system—A technical review. *J. Eng. Sci. Tech.* **8**, 493–507 (2013)
5. Han, B., Zhou, L., Yang, F., Xiang, Z.: Individual pitch controller based on fuzzy logic control for wind turbine load mitigation. *IET Renew. Power Gener.* **10**(5), 687–693 (2016)
6. Zhang, J., Cheng, M., Chen, Z., Fu, X.: Pitch angle control for variable speed wind turbines, In: *Electric Utility Deregulation and Restructuring and Power Technologies, DRPT Third International Conference Nanjing*, 2691–2696 (2008)
7. Van, T.L., Nguyen, T.H., Lee, D.C.: Advanced pitch angle control based on fuzzy logic for variable-speed wind turbine systems. *IEEE Trans. Energy Convers.* **30**(2), 578–587 (2015)
8. Jonkman, J., et al.: Definition of a 5-MW reference wind turbine for offshore system development. National Renewable Energy Laboratory, Golden, CO, Technical Report No. NREL/TP-500–38060 (2009)
9. Yin, X., Lin, Y., Li, W., Ya-jing, G., Wang, X., Lei, P.: Design, modeling and implementation of a novel pitch angle control system for wind turbine. *Renewable Energy* **81**, 599–608 (2015)
10. Soedibyo, S., Firdaus, A.A.: Design and simulation of neural network predictive controller pitch-angle in permanent magnetic synchronous generator wind turbine variable pitch system. In: *Information Technology, Computer and Electrical Engineering (ICITACEE), International Conference Semarang*. 346–350 (2014)
11. Sanjeevikumar, P., Blaabjerg, F., Siano, P., Martirano, L., Leonowicz, Z., Pandav, K.M.: PI and fuzzy control strategies for high voltage output DC-DC boost power converter—hardware implementation and analysis. In: *Conference Proceedings of 16 IEEE International Conference on Environment and Electrical Engineering, Florence (Italy)*, (2016)

12. Ren, Y., Li, L., Brindley, J., Jiang, L.: Nonlinear PI control for variable pitch wind turbine. *Control Eng. Practice*. **50**, 84–94 (2016)
13. Chedid, R., Mrad, F., Basma, M.: Intelligent control of a class of wind energy conversion systems. *IEEE Trans. Energy Convers.* **14**(4), 1597–1604 (1999)
14. Tiwari, R., Ramesh Babu, N.: Fuzzy logic based MPPT for permanent magnet synchronous generator in wind energy conversion system. *IFAC-PapersOnLine* **49**(1), 462–467 (2016)
15. Qi, Y., Meng, Q.: The application of fuzzy PID control in pitch wind turbine. *Energy Procedia*. **16**, 1635–1641 (2012)
16. Sanjeevikumar, P., Daya, F.J.L., Blaabjerg, F., Wheeler, P., Szcześniak, P., Oleschuk, V., Ertas, A.H.: Wavelet-fuzzy speed indirect field oriented controller for three-phase AC motor drive-investigation and implementation. *Int. J. Eng. Sci. Tech.* **19**(3), 1099–1107 (2016)
17. Gao, R., Gao, Z.: Pitch control for wind turbine systems using optimization, estimation and compensation. *Renew. Energy*. **91**, 501–515 (2016)

Experimental Investigation of VFD-Fed Scalar Control of Induction Motor for Pumping Application

Vishnu Kalaiselvan Arun Shankar, Subramaniam Umashankar, Shanmugam Paramasivam, Padmanaban Sanjeevikumar and K.N. Dileep Sailesh

Abstract In this proposed paper, the experimental results on variable frequency drives (VFDs)-fed pumps are taken out into considerations that are obtained from the laboratory set-up and the modelling done by the author. The simulation study of induction machine using the speed control technique V/F for pumping application is made. To survey the drive performance, VFDs manufactured by Danfoss, with their own control system is used as a special planned simulator. The aim of this paper is to compare and evaluate the results taken out in laboratory and MATLAB/Simulink for an effective pumping system. The simulation and experimental results shown in the article are used to determine the performance of pumping system.

Keywords Squirrel cage induction motor (SCIM) · Variable frequency drives
Scalar control · Centrifugal pumps · Experimental set-up

V.K. Arun Shankar · S. Umashankar (✉) · K.N. Dileep Sailesh
Department of Energy and Power Electronics, Vellore Institute of Technology
(VIT) University, Vellore, Tamil Nadu, India
e-mail: umashankar.s@vit.ac.in

V.K. Arun Shankar
e-mail: arunshankarvk@gmail.com

K.N. Dileep Sailesh
e-mail: dileepsailesh94@gmail.com

S. Paramasivam
Danfoss Industries Private Limited, Chennai, Tamil Nadu, India
e-mail: paramsathya@yahoo.com

P. Sanjeevikumar
Department of Electrical and Electronics Engineering, University of Johannesburg,
Auckland Park, Johannesburg, South Africa
e-mail: sanjeevi_12@yahoo.co.in

1 Introduction

The centrifugal pumps are normally preferred in commercial as well as industrial applications for pumping the fluids. They contribute for around 73% of the total pumps installed throughout the world for various pumping applications [1]. The flow rate of the fluid pumped by centrifugal pump is continuous, and the torque exhibited by centrifugal pump on the electric motors is proportional to square of the motor speed [2].

2 Modelling of Pumping System

The centrifugal pump driven by induction motor using VFD is modelled in MATLAB/Simulink as shown in Fig. 1. The pumps are characterised through flow rate Q (m^3/s), definite rotational speed [3]. The relation between pump flow rate, pressure developed and speed of the motor is given by affinity laws.

$$\frac{Q_1}{Q_2} = \frac{N_1}{N_2} \tag{1}$$

$$\frac{H_1}{H_2} = \left(\frac{N_1}{N_2}\right)^2 \tag{2}$$

Performance curves describe the relationship between the flow and head at different speeds [4]. The hydraulic power of the pump is given by Eq. 3.

$$P_h = \rho \cdot g \cdot Q \cdot H \tag{3}$$

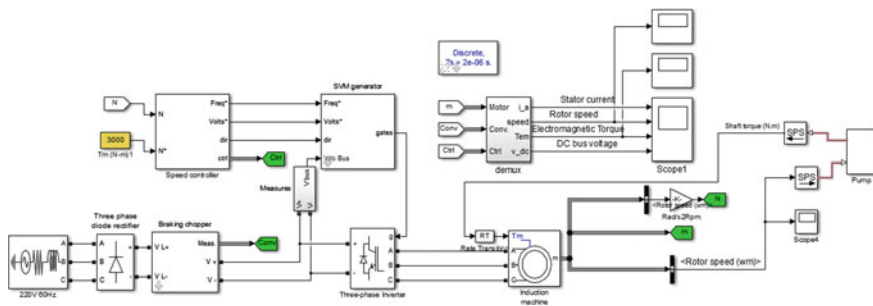


Fig. 1 Modelling of induction motor for pumping application

Since 3-phase induction motor is widely used in industries because of its attractive speed regulation, robust construction and high power factor [5]. The advantage of taking V/F technique is that it improves both dynamic as well as static characteristics of a machine [6].

3 Simulation Results

The proposed model of induction motor-fed pumping system is analysed for different operating conditions and approved in terms of DC bus voltage, torque, stator current and speed.

We can see from Fig. 2 that the time of DC bus voltage is reaching the settling value in less than 60 ms with dc bus voltage as 530 V.

In Fig. 3, the torque oscillates and on further variation, it reaches to 19 N m and gets stable. As, $T \propto V^2$, the torque at a given slip decreases with decrease in input voltage.

Figure 4 indicates the stator current of the induction motor, and Fig. 5 indicates that the speed is within the stable operation and reached to 2900 rpm. At low speeds, difference in load torque and motor torque accelerates the machine.

$$T_{\text{motor}} - T_{\text{load}} = J \frac{dw_m}{dt} \tag{4}$$

Figures 6 and 7 show the system performance of the pump [7]. When selecting the pumps, the rated operating or discharge pressure of the pump must be greater than the required pressure for the system at desired flow rate [8].

Fig. 2 DC bus voltage versus time curve

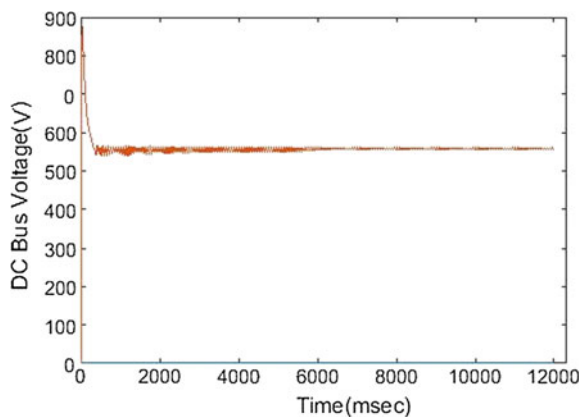


Fig. 3 Torque versus time curve

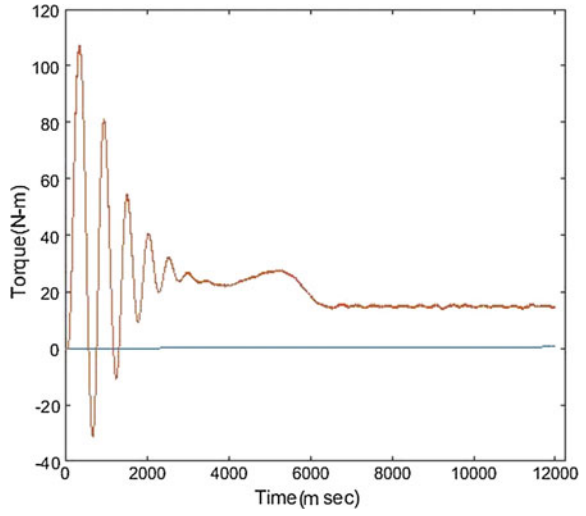
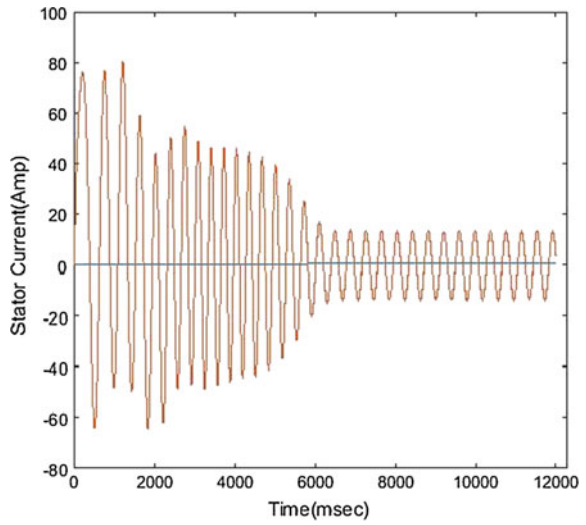


Fig. 4 Stator current versus time curve



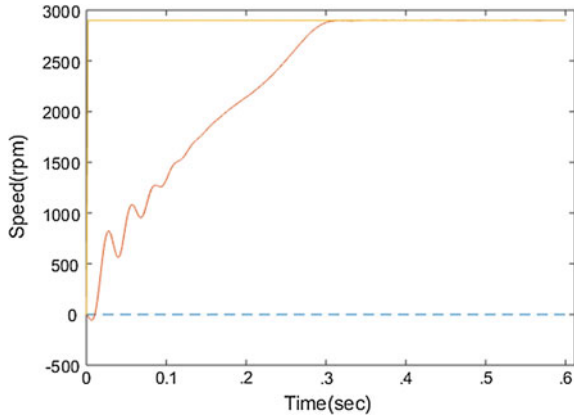


Fig. 5 Speed versus time curve

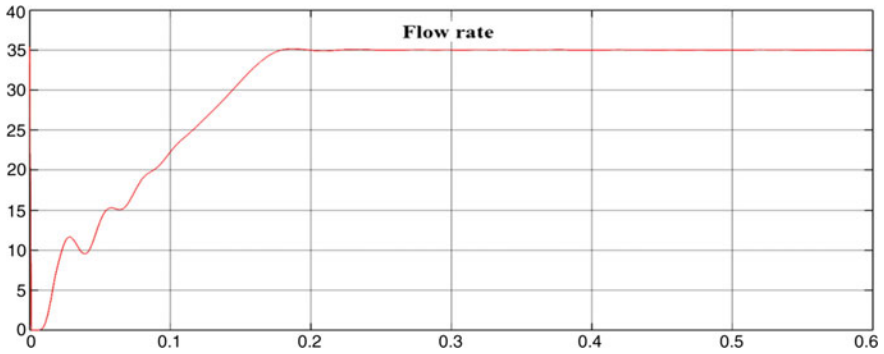


Fig. 6 Flow rate of centrifugal pumps

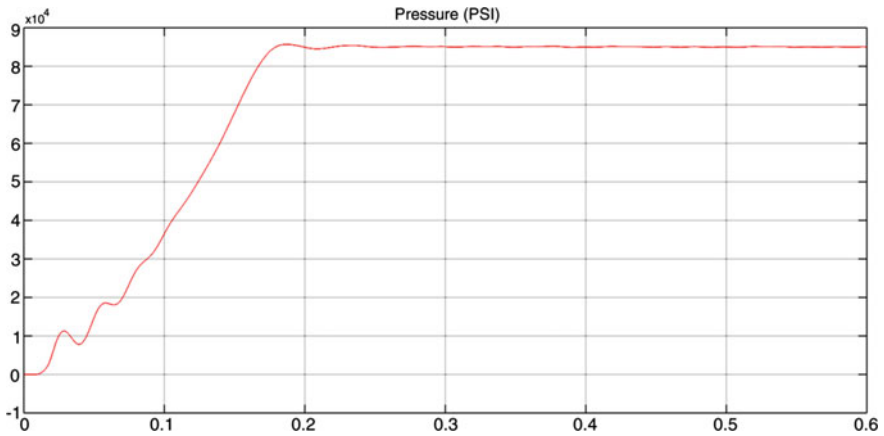


Fig. 7 Pressure in PSI

Table 1 Induction motor parameters

Specification		Values	Units
Phases		3	
Rated power	P	2.2	kW
Line voltage	V	400	V_{rms}
Line current	I	7	A_{rms}
Poles	P	2	
Magnetising inductance	L_m	0.1722	H

**Fig. 8** Laboratory set-up

4 Experimental Results

The test set-up in comprising of electric drive, motor and PC is shown in Fig. 8. The load drive and the testing drive of induction motors, VLT FC-302 series controlling panel, cabinet, cabling equipment. These machines are coupled to each other mechanically through clutch which provides them the joint rotation. Machine nominal power is 2.2 kW, voltage is 400 V, and current is 7 A, respectively as shown in Table 1.

In braking region of the drive, the energy proceeds back to the delivered line through the line side rectifier [9]. The hardware results shown below induction motor which gives the desired data to the drive and further it is put in the form of excel sheet where those data are taken to form these curves. The vertical line on the curve shows the value at that particular instant [10].

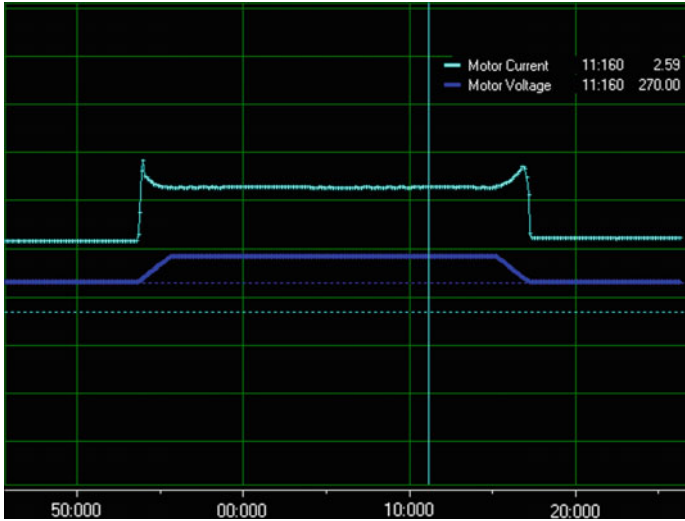


Fig. 9 Motor current and motor voltage

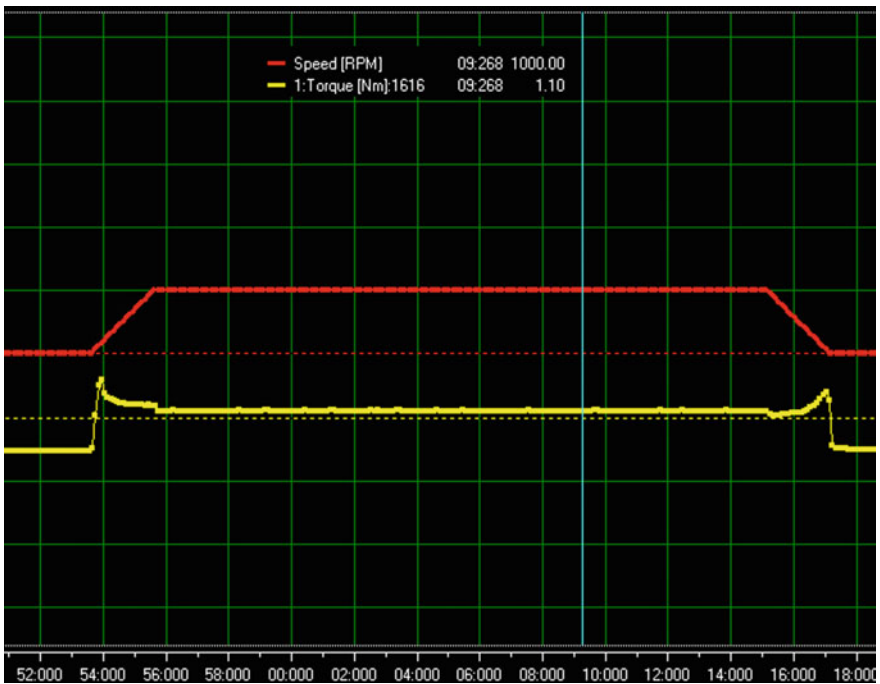


Fig. 10 Speed and torque

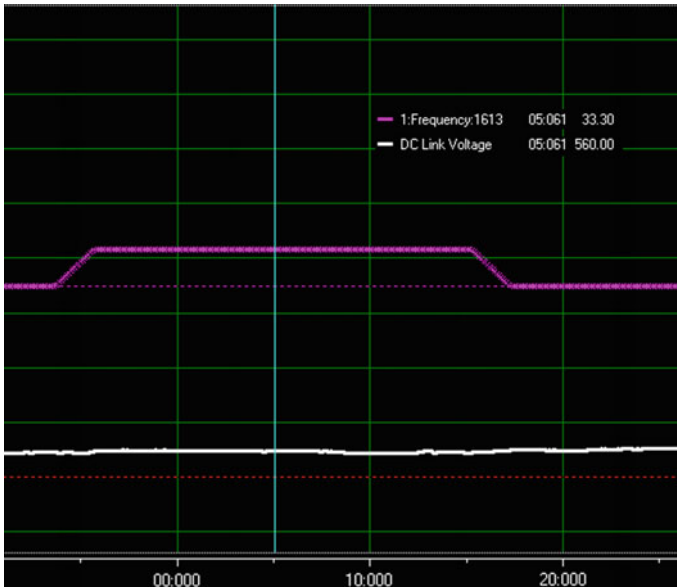


Fig. 11 Frequency and dc link voltage

Waveform shown in Fig. 9 shows output voltage and current variation where motor voltage increases to 270 V and motor current to 2.59 A. As the motor voltage and current are significantly increasing that means motor is running under variable power and constant torque.

The waveform in Fig. 10 represents the speed and torque variation where the speed decreases with constant load torque. Here the speed is 1000 rpm where torque comes to 1.10 N m.

The speed is 1000 rpm, the frequency is 33 Hz where the DC link voltage is 560 V, shown in Fig. 11.

5 Conclusion

In this paper, the simulation and experimental verification of Variable frequency drives (VFDs)-fed centrifugal pumps are made. The simulation study of induction machine using the speed control technique V/F for pumping application is made. The performance of the VFDs with their own control algorithm is studied using the experimental set-up. The proposed hardware results with MATLAB simulation investigate the pumping system performance, with different operating speeds. Information about the drive performance at normal operating condition is explained along with Simulink results.

References

1. Kioskesidis, I., Margaris, N.: Loss minimization in scalar controlled induction motor drives with search controller. *IEEE Trans. Power Electron.* **11**(2), 213–220 (1996)
2. Kioskesidis, I., Margaris, N.: Loss minimization in induction motor adjustable speed drives. *IEEE Trans. Ind. Elect.* **43**(1), 226–231 (1996)
3. Thanga Raj, C.: Improving energy efficiency in partial loaded induction motor-using power electronic controllers. *J Eng. Technol.* **1**(2), 13–17 (2006)
4. Muravlev, O., Muravleva, O., Vekhter, E.: Energetic parameters of induction motors as the basis of energy saving in a variable speed drive. *Electr. Power Qual. Utilization* **9**(2) (2005)
5. Kim, J.W., Kim, B.T., Kwon, B.I.: Optimal stator slot design of inverter-fed induction motor in consideration of harmonic losses. *IEEE Trans. Magn.* **41**(5) (2005)
6. Cacciato, M., Concoli, A., Scarcella, G., Seelba, G., Testa, A.: Efficiency optimization technique via constant optimal slip control of induction motor drives. In: *Proceedings IEEE Power Electronics, Electric Drives, automation, and Motion*, pp. 32–42 (2006)
7. Femia, N., Petrone, G., spagnuolo, G., Vitelli, M.: Optimizing of perturb and observe maximum power point tracking. *IEEE Trans Power Electron.* **20**(4), 963–73 (2005)
8. Abdin, E.S., Ghoneem, G.A., Diab, H.M.M., Deraz, S.A.: Efficiency optimization of vector controlled induction motor drive using an artificial neural network. In: *Proceedings of IEEE Conference IECON*, pp. 2543–2548 (2003)
9. Eram, T., Chapman, P.I.: Comparison of photovoltaic array maximum power point tracking techniques. *IEEE Trans. Energy Convers.* **22**, 439–449 (2006)
10. Zenginobuz, G., Cadirci, I., Ermis, M., Barlak, C.: Performance optimization of induction motors during voltage-controlled soft starting. *IEEE Trans. Energy Conv.* **19**(2), 278–288 (2004)

Comparison Between PI Controller and Fuzzy Logic-Based Control Strategies for Harmonic Reduction in Grid-Integrated Wind Energy Conversion System

Ramji Tiwari, N. Ramesh Babu, R. Arunkrishna
and P. Sanjeevikumar

Abstract In this paper, a novel fuzzy logic-based control (FLC) strategy is developed to perform multi-function strategy for smooth and controlled operation of three-phase renewable energy system (RES)-based wind energy conversion system (WECS) with grid integration. The inverter acts as a converter to infuse the power obtained from the wind energy and as a active power filter to compensate reactive power demand and load current harmonics. The control strategies in accordance with 3-phase 4-wire unbalanced load tend to appear as a balanced linear load system at grid. The control strategy is developed and validated using MATLAB/Simulink. The proposed controller is compared with PI-based controller and validate that the proposed FLC provide better efficiency by reducing harmonics.

Keywords WECS · Distributed generation · PMSG · Proportional–integral controller · Fuzzy logic controller · Harmonic reduction

R. Tiwari · N. Ramesh Babu (✉) · R. Arunkrishna
School of Electrical Engineering, Vellore Institute of Technology (VIT) University,
Vellore, India
e-mail: nrameshbabu@vit.ac.in

R. Tiwari
e-mail: ramji.tiwari2015@vit.ac.in

R. Arunkrishna
e-mail: r.arunkrishna10@gmail.com

P. Sanjeevikumar
Department of Electrical and Electronics Engineering, University of Johannesburg,
Auckland, Johannesburg, South Africa
e-mail: sanjeevi_12@yahoo.co.in

1 Introduction

The constant development of electric utilities and depletion of fossil fuel are becoming major concern of maintaining energy demand. Currently, fossil fuel-based generation shares a large portion of global energy demand, but simultaneously increasing the air pollution and global warming concern. Thus, to overcome the all above major concern, renewable energy-based power generation is gaining more interest in all countries. To promote renewable energy and to accelerate the interest among private institute, government is providing many incentives [1].

The distributed generation (DG) should follow a grid code to integrate the renewable energy source (RES) at distribution level. RES such as solar, wind, tidal are the major sources of renewable energy. Among RES, wind-based energy generation is the most preferred energy source for its cost-effective production. The major threat of RES is the stability, nonlinearity, voltage regulation and power quality issue. Thus, an advance control strategy is required to overcome the issue and enhance the system operation for grid integration. However, power electronics converter and the nonlinear load create the harmonic current which causes issue in power stability [2].

A considerable amount of harmonic current is being injected into power system by the nonlinear load. Thus, the harmonic current in the power system causes voltage distortions which increases the loss in line and decrease the power factor. The current harmonic in the system add up arithmetically at the neutral bus till 1.73 times of the phase magnitude thus causes heating of the transformers and cables. This may reduce the energy efficiency and damage the electronic equipment [3].

The LC filter is the traditional method to reduce the current harmonics because of the simplicity and reduced cost. But, they have an disadvantage of large size, inductor turns ratio and risk of resonance [4, 5]. So in order to remove the harmonic from the power network, an active filter is developed which has dynamic response for the power quality problem. [6]

In this paper, author compares the control strategy based on PI and fuzzy logic which incorporates the features of active power filters for interfacing the renewable to the grid. The control strategy can mitigate the unbalance voltage disturbance caused due to injection of harmonic current into the grid. The active power filter is used to compensate the current imbalance and reactive power demand. The neutral current compensation of 3-phase 4-wire system is performed using the control strategy implemented for grid-interfacing inverter.

2 System Description

The proposed system consists of wind energy conversion system interconnected with DC-link and the grid through inverter. The voltage source inverter (VSI) is the key element of the distributed generation (DG) as it interfaces the WECS to grid

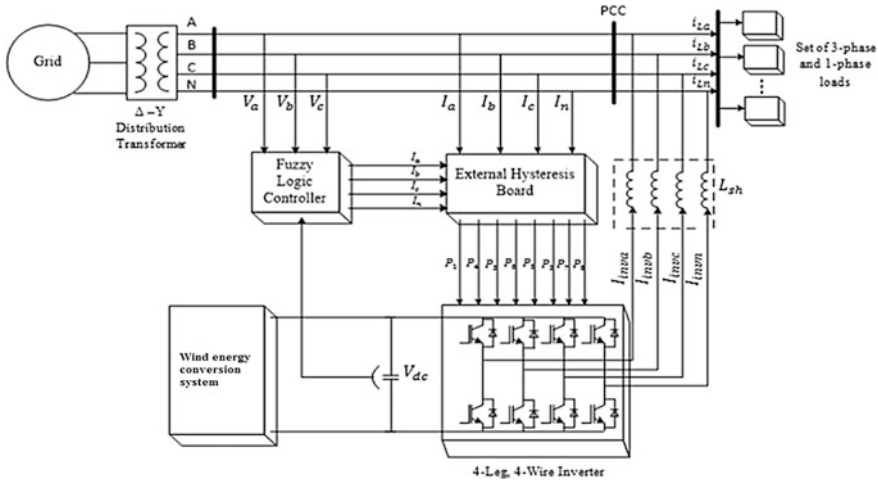


Fig. 1 Schematic of WECS-based distributed generation system

and supplies the generated power to the utility [7]. As shown in Fig. 1, 3-phase 4-wire inverter is used in this paper for interfacing the WECS to the grid. The proposed system consists of a diode rectifier followed by the boost converter before interfacing with the grid. The variable speed wind turbine is highly nonlinear in nature. Thus, the power obtained from the WECS needs to be smoothened before connected to the DC-link. The dc capacitor is connected to decouple the WECS from the grid to perform independent control on the either side.

3 Analysis of Wind Energy-Based Conversion System

The WECS system comprises of wind turbine and permanent magnet-based synchronous generator (PMSG). The wind turbine produces the torque which is converted into electric power by the PMSG. The power and torque equation of WECS is determined by the following equation,

$$P_m = \frac{1}{2} C_p(\beta, \lambda) \rho \pi R^2 V_{wind}^3 \tag{1}$$

$$T_m = \frac{P_m}{\lambda} \tag{2}$$

where β (blade pitch angle) and λ (tip speed ratio) are the variables of C_p (rotor power coefficient), ρ implies the air density, R refers to the radius of wind turbine blade, and wind speed is represented as V_{wind} [8].

The electromagnetic torque generated from the rotor of PMSG is given by the equations

$$T_e = 1.5 \frac{P}{2} \left[\psi_p i_{sq} + i_{sd} i_{sq} (L_{sd} - L_{sq}) \right] \tag{3}$$

where the dq axis current and voltages are represented as i_{sd} , i_{sq} , u_{sd} and u_{sq} , respectively, and angular frequency of the generator is defined by ω_s . Inductances of the generator are denoted as L_{sd} and L_{sq} . ψ_p is the permanent flux, R_{sa} refers to the resistance of the stator, and P refers to number of poles [9].

4 Control Strategy

Figure 2 shows the control diagram of grid interconnected with 3-phase 4-wire system. The neutral current of the load is stabilised using the fourth leg of the inverter. The main aim of the proposed topology is to stabilise the power transferred to the grid. The inverter supplies the fundamental active power to the grid by reducing the harmonics and the neutral current [10].

This control strategy is used to generate the duty ratio for the inverter using injected power and DC voltage as the input parameter. The DC-link voltage provides the data of the injected power to the grid from the WECS. The multiplication of active current (I_m) component with unit grid vector (U_a, U_b, U_c) constitutes to

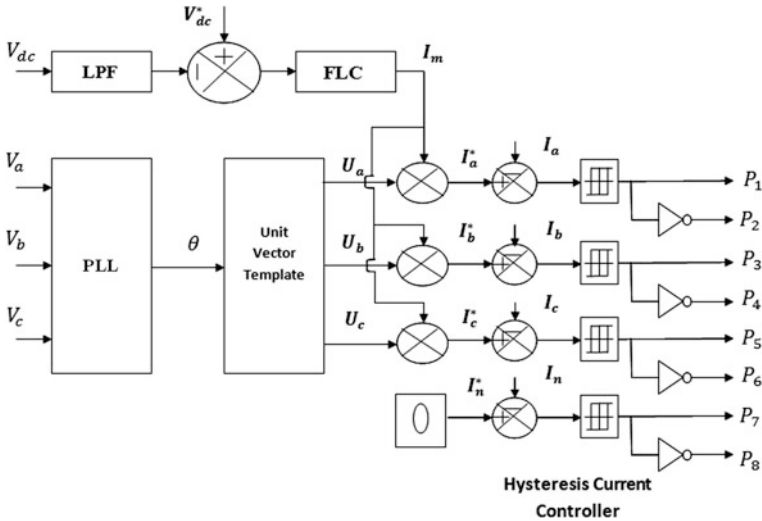


Fig. 2 Control technique for generating pulses

reference grid currents (I_a^* , I_b^* , I_c^*), and the neutral reference is set to null. The unit vectors of the grid can be given as follows

$$U_a = \sin(\theta) \quad (4)$$

$$U_b = \sin\left(\theta - \frac{2\pi}{3}\right) \quad (5)$$

$$U_c = \sin\left(\theta + \frac{2\pi}{3}\right) \quad (6)$$

The instantaneous values of grid current reference are given as

$$I_a^* = I_m * U_a \quad (7)$$

$$I_b^* = I_m * U_b \quad (8)$$

$$I_c^* = I_m * U_c \quad (9)$$

The neutral conductor connected to load generates the neutral current. Neutral current is compensated using the fourth leg of the grid-interfacing inverter. The reference neutral current (I_n^*) is considered to be zero as shown in Eq. 10. Neutral current should not be drawn from the grid.

$$I_n^* = 0 \quad (10)$$

The above analysis is given to the controller in order to obtain the switching pulses for the gate drivers for the grid-interfacing inverters.

(A) *PI controller*

In PI-based control technique, the reference voltage and the DC voltage across the converter are analysed to generate an error signal. The obtained error signal is then fetched to the PI controller in order to generate the output signal [11]. The obtained PI output signal is then fed to the PWM generator where the signal is compared with the triangular wave to deliver the pulses in form of duty cycle which controls the inverter switch in such a way that the DC-link is maintained constant under rapid variation of wind speed. [12]. The equation used for PI controller is

$$D(s) = (K_p + K_i / s) * E(s) \quad (11)$$

where K_p and K_i are the proportional and integral parameter of PI controller. $E(s)$ is the error signal of obtained voltage and desired voltage, and $D(s)$ represents the duty cycle generated by the PI controller. The DC-link voltage error is given by Eq. 12.

$$E(s) = V_{dc}^* - V_{dc} \tag{12}$$

The output of PI controller is expressed as

$$I_m = I_m^* + K_p(V_{dc}^* - V_{dc}) + K_i E(s) \tag{13}$$

where, value of K_p is calculated as 10 and K_i as 0.05.

(B) Fuzzy logic controller

PI controller fails to determine the change in rise and fall of the error and only capable to react to the instantaneous value of error. Thus, they are not suitable for nonlinear system like wind energy. To overcome this problem, FLC is implemented which has an advantage of overcoming the nonlinearity of system, fast convergence. FLC works on the principle of three steps in order; they are Fuzzification, inference system and Defuzzification [13]. The rules are framed from the former knowledge of the system. The error signal obtained from the difference between the obtained with respect to desired value and change in error signal are considered as the input for the FLC. The output of the controller is the duty cycle for inverted. The efficiency of FLC is purely depending upon the user’s knowledge about the system and the framing right computation error.

Table 1 presents rules set used for FLC used in this topology. The rules are framed in seven levels, namely Negative large (NL), Negative medium (NM), Negative small (NS), Zero (ZE), Positive small (PS), Positive medium (PM) and Positive large (PL). Inference mechanism is basically defined by membership functions which show the relevance of rules from Table 1. Methods, Minimum (min) and Maximum (max), are defined for the implication and aggregation, respectively, whereas, centroid is used for the Defuzzification processing.

(C) Switching control

The switching pattern of the proposed topology is determined using hysteresis current controller technique as shown in Fig. 2. The significance of the pattern of switch is determined using the error generated using the FLC or PI controller. The hysteresis strategy is the major cause for the high harmonic band in the switching frequency though they are preferred for nonlinear system as they provide better response and robust for sudden variation [14, 15].

Table 1 Fuzzy logic table

E/CE	NL	NM	NS	ZE	PS	PM	PL
NL	PS	PM	PL	NL	NM	NS	ZE
NM	PM	PL	NL	NM	NS	ZE	PS
NS	PL	NL	NM	NS	ZE	PS	PM
ZE	NL	NM	NS	ZE	PS	PM	PL
PS	NM	NS	ZE	PS	PM	PL	NL
PM	NS	ZE	PS	PM	PL	NL	NM
PL	ZE	PS	PM	PL	NL	NM	NS

5 Simulation Results

The proposed control topology is verified by interfacing the WECS to the 3-phase 4-wire inverter connecting to the grid. An simulation study is analysed using MATLAB/Simulink. The inverter is controlled actively to achieve balanced sinusoidal grid voltage despite of varying wind speed. Capacitor at DC-link is used to connect the inverter with the WECS. The harmonics and reactive power of the 3-phase 4-wire system need to compensate using the suitable control strategy to follow the grid regulations.

The grid side voltage is set as 360 V as shown in Fig. 3. The grid current, unbalanced load current and inverter current for the PI-based controller are shown in Figs. 4, 5 and 6, respectively. At $t = 0.1$, the inverter tends to inject active power to the grid. It can be clearly seen that in Fig. 6 load current takes time to settle when PI controller used.

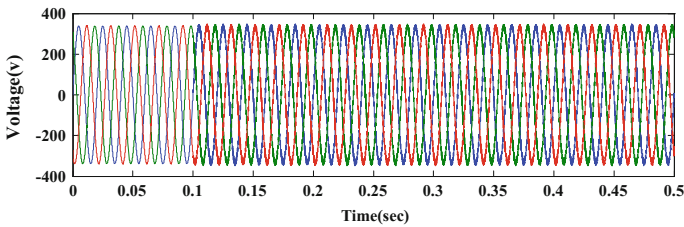


Fig. 3 Grid voltage

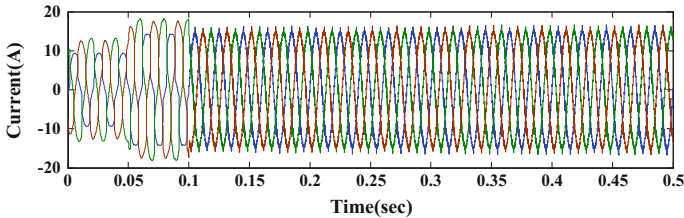


Fig. 4 Grid current (PI-based control strategy)

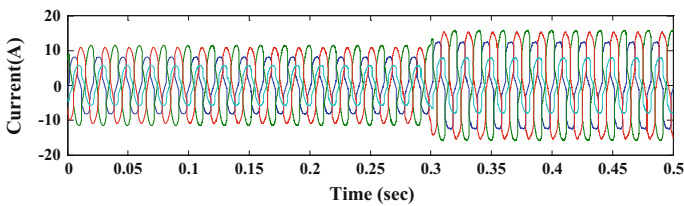


Fig. 5 Load current (PI-based control strategy)

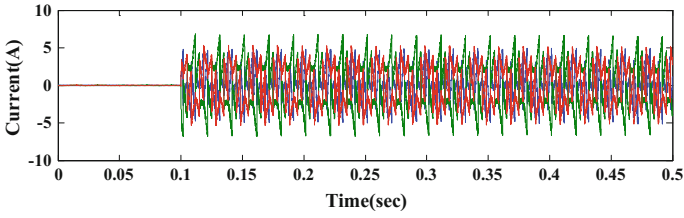


Fig. 6 Inverter current (PI-based control strategy)

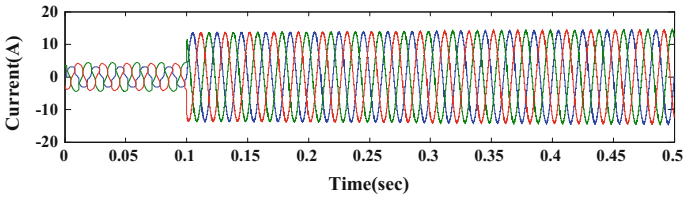


Fig. 7 Grid current (FLC-based control strategy)

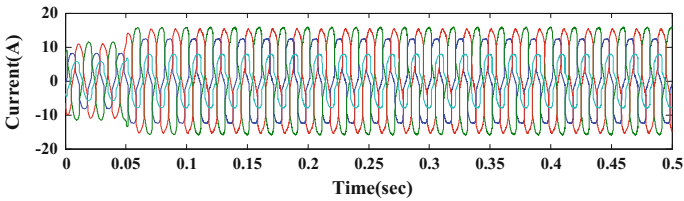


Fig. 8 Load current (FLC-based control strategy)

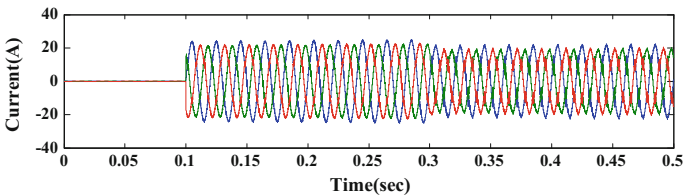


Fig. 9 Inverter current (FLC-based control strategy)

The waveforms for grid current, unbalanced load current and the inverter current for FLC-based control strategy are shown in Figs. 7, 8 and 9. The FLC requires only few times when compared to PI controller to compensate the load current. The harmonics induced by the PI controller is high when compared to the FLC-based controller.

Form the results, it can analysed that FLC-based control strategy provide better stabilisation of the load current and elimination of harmonics when compared with the PI-based control strategy.

6 Conclusion

The paper presents a comparative analysis of PI- and FLC-based control strategies for active grid-interfacing inverter to compensate the harmonic produced by non-linear system. A 3-phase 4-wire-based DG system is interfaced with the grid inverter which is utilised effectively without disturbing the normal operation of active power transfer. The inverter can be used for multi-objective function, such as to inject active power generated from wind energy to the grid and to compensate the harmonics and the current distortion produced due to nonlinearity of the system.

Thus, this will eliminate the need of separate filter used for power condition operation. The neutral current is prevented to flow into grid by the fourth leg of the inverter thus by reducing the damage. The quality of power is increased reducing the harmonic content from the load current.

The comparison between two control strategies is analysed and it is clear that FLC-based control system provides dynamic response and has higher efficiency than the PI-based control technique. FLC-based system provides robustness toward the nonlinearity of the system. The current harmonics, unbalance current and the load reactive power are compensated effectively using the combination of FLC control strategy for 3-phase 4-wire grid-integrated inverter.

References

1. Tiwari, R., Ramesh Babu, N.: Recent developments of control strategies for wind energy conversion system. *Renew. Sustain. Energy Rev.* **66**, 268–285 (2016)
2. Peças Lopes, J.A., Hatziargyriou, N., Mutale, J., Djapic, P., Jenkins, N.: Integrating distributed generation into electric power systems: a review of drivers, challenges and opportunities. *Electr. Power Sys. Res.* **77**(9), 1189–1203 (2007)
3. Sanjeevikumar, P., Geethalakshmi, B., Dananjayan, P., Performance analysis of AC-DC-AC converter as a matrix converter, In: Conference Proceedings IEEE India International Conference on Power Engineering, IEEE-IICPE'06, Chennai (India), pp. 57–61, 19–21 (2006)
4. Sanjeevikumar, P., Geethalakshmi, B., Dananjayan, P.: A PWM current source rectifier with leading power factor”, Conference Proceedings IEEE International Conference on Power Electron., Drives and Energy Systems for Industrial Growth, IEEE-PEDES'06, pp. 1–5, 12–15 Dec. 2006, Delhi (India) (2006)
5. Enslin, J.H.R., Heskes, P.J.M.: Harmonic interaction between a large number of distributed power inverters and the distribution network. *IEEE Trans. Power Electron.* **19**(6), 1586–1593 (2004)
6. Steink, J.K.: Use of an LC filter to achieve a motor-friendly performance of the PWM voltage source inverter. *IEEE Trans. Energy Convers.* **14**(3), 649–654 (1999)

7. Singh, M., Khadkikar, V., Chandra, A., Varma, R.K.: Grid interconnection of renewable energy sources at the distribution level with power-quality improvement features. *IEEE Trans. Power Del* **26**(1), 307–315 (2011)
8. Ramesh Babu, N., Arulmozhivarman, P.: Wind energy conversion systems—a technical review. *J. Eng Sci. Technol.* **8**, 493–507 (2013)
9. Alizadeh, M., Kojori, S.S.: Augmenting effectiveness of control loop of a PMSG (permanent magnet synchronous generator) based wind energy conversion system by a virtually adaptive PI (proportional integral) controller. *Energy* **91**, 610–629 (2015)
10. Dong, S., Li, Y., Wang, A., Xi, W.: Control of PMSG wind turbines based on reduced order resonant controllers under unbalanced grid voltage conditions. In: *IEEE 11th International Conference on Power Electronics and Drive Systems, Sydney*, pp. 326–329 (2015)
11. Tripathi, S.M., Tiwari, A.N., Singh, D.: Optimum design of proportional-integral controllers in grid-integrated PMSG based wind energy conversion system. *Int. Trans. Elect. Energy Sys.* **26**(5), pp. 1006–1031 (2016)
12. Simoes, M.G., Bose, B.K., Spiegel, R.J.: Design and performance evaluation of fuzzy-logic-based variable-speed wind generation system. *IEEE Trans. Ind. Appl.* **33**, 956–965 (1997)
13. Tiwari, R., Ramesh Babu, N.: Fuzzy logic based MPPT for permanent magnet synchronous generator in wind energy conversion system. *IFAC-PapersOnLine* **49**(1), 462–467 (2016)
14. Tiwari, R., Saravanan, S., Ramesh Babu, N., Kumar, G., Siwach, V.: Design and development of a high step-up DC-DC Converter for non-conventional energy applications. In: *Biennial International Conference on Power and Energy Systems: Towards Sustainable Energy (PESTSE), Bengaluru, India*, pp. 1–4 (2016)
15. Natarajan, Prabakaran, Palanisamy, K.: Investigation of single phase reduced switch count asymmetric multilevel inverter using advanced pulse width modulation technique. *Int. J. Renew. Energy Res.* **5**(3), 879–890 (2015)

Direct-Coupled Permanent Magnet DC Motor-Driven Solar Photovoltaic Water Pumping System—A Literature Review

R. Sivapriyan, S. Umashankar, P. Sanjeevikumar and Atif Iqbal

Abstract This paper presents different controlling techniques of the converter used for the solar photovoltaic water pumping system (SPVWPS) driven by permanent magnet DC (PMDC) motor. The direct-coupled PMDC motor-driven solar water pumping systems have many advantages like high efficiency, longer life cycle and less cost due to the absence of energy storage element such as batteries. This direct coupled PMDC-driven SPVWPS is easy to control when we compare with inverter circuit-fed AC motor-driven water pumping systems (WPS). In this literature review, DC–DC converter controlling techniques and maximum power point tracking (MPPT) methods adopted in direct coupled PMDC motor-driven SPVWPS have been discussed. This literature review will serve as a complete reference to identify the advantages and the scope for future work in direct-coupled PMDC motor-driven solar PV water pumping systems.

Keywords DC–DC power converter · Maximum power point tracking (MPPT) Photovoltaic (PV) · PMDC motor · Water pumping system (WPS)

R. Sivapriyan · S. Umashankar (✉)
School of Electrical Engineering, Vellore Institute of Technology (VIT) University,
Vellore, Tamil Nadu, India
e-mail: umashankar.s@vit.ac.in

R. Sivapriyan
e-mail: sivapriyan@gmail.com

P. Sanjeevikumar
Department of Electrical and Electronics Engineering, University of Johannesburg,
Auckland, Johannesburg, South Africa
e-mail: sanjeevi_12@yahoo.co.in

P. Sanjeevikumar
Research and Development, Power Electronics Division, Ohm Technologies,
Chennai, India

A. Iqbal
Department of Electrical Engineering, Qatar University, Doha, Qatar

1 Introduction

The solar PV water pumping system (SPVWPS) gains more importance nowadays due to the depletion of oil reserve and increase in the grid electricity cost. This solar water pumping technology can be implemented from a small-scale residential water pumping systems to large-scale irrigation purpose. The SPVWPS consists of different components such as electrical, electronic and mechanical components. Therefore, it gives lot of opportunities and challenges in integration of the various components to achieve the maximum performance of the overall system. The direct-coupled SPVWPS consists of solar photovoltaic array, DC–DC converter with MPPT controller and a PMDC motor-driven water pump.

This direct-coupled PMDC motor-driven SPVWPS avoids the energy storage element such as batteries. Due to the absence of electrochemical energy storage element, this SPVWPS life cycle and the efficiency will be improved marginally. Also, the direct-coupled PMDC motor-driven SPVWPS is easy to control since only one DC–DC converter is present, whereas the AC motor-driven SPVWPS will be controlled by an inverter which increases the complexity in controlling the WPS (Fig. 1).

The advantage of using this drive is small in construction, and to excite the field winding, no additional DC supply is required. The cost of PMDC motor is less when we compare with AC motor. Also the PMDC motor is rugged in construction. The brief outline of the literature review is as follows: In Sect. 2, the literature review of direct-coupled PMDC motor-driven SPVWPS is discussed, and in Sect. 3, the scope for improvement is discussed. The main outcome of the literature review is to find the scope for improvement.

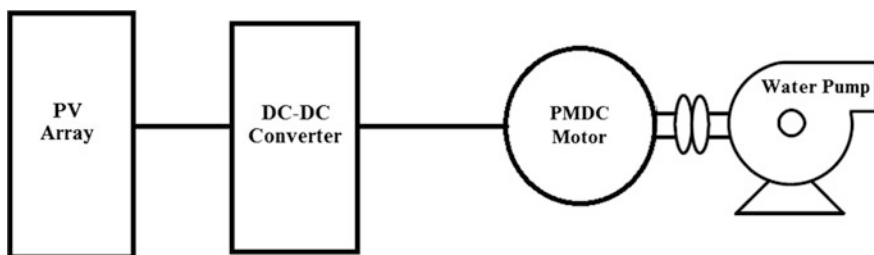


Fig. 1 Block diagram of direct-coupled PMDC-driven SPVWPS

2 Classification of Literature on Direct-Coupled PMDC Motor-Driven SPVWPS

This literature review intends to give a broad overview about the direct coupled PMDC-driven SPVWPS and the scope for research in this field. For this purpose, more detailed analysis of need of PMDC motor for SPVWPS, control technique of the DC converter and different MPPT methods were discussed in this review. This literature review is sectioned into three parts. First section discusses about the importance and advantages of PMDC motor for SPVWPS. Second section analyzes about the DC–DC converter and its controlling techniques to control the PMDC motor and also discusses the various converter topologies used for PMDC motor-driven SPVWPS. In third section, the detailed analysis and comparison of the various MPPT techniques implemented in the PMDC-driven SPVWPS are presented. Also this section compares the various MPPT techniques to find the suitability of the particular MPPT technique to improve the overall efficiency and to reduce the cost.

2.1 PMDC Motor for SPVWPS

For low-power application, the PMDC motor is the most suitable motor than the AC induction motor for SPVWPS [1, 2]. Also the number of components, power stages and switches required for a PMDC motor drive is lesser than the induction motor drive. In the same article, Chandrasekaran proves that the efficiency of the PMDC motor-driven SPVWPS is more than that of the AC motor-driven SPVWPS.

Mokeddem [3] tested the performance of direct-coupled SPVWPS without MPPT. The overall system delivers the efficiency of less than 30%, which is higher than the other SPVWPS without MPPT. And the author suggests that this kind of system is suitable for low-head irrigation.

The pump similarity law [4] is used to assess the performance of the centrifugal pump under different speed variations. By combining the motor–pump equation with solar array model, the author links the flow rate of the pump with solar radiation.

To select the suitable electromechanical system for SPVWPS, Mohanlal Kolhe analyzed the performance of direct coupled SPVWPS at different irradiance and temperature [5]. From this analysis, if the average solar intensity is known, then the system component can be selected to give higher efficiency.

Hsiao and Blevins conclude that the efficiency of the SPVWPS was improved by matching the ratio between the speed of motor and pump [6]. For better utilization of the solar array, they also suggested the implementation of any MPPT method.

Advantages of PMDC drive/motor are as follows:

- Less number of power components
- Less number of power stages
- Less number of switches
- Overall system efficiency is high
- Ease of control
- PMDC motor is rugged in construction

2.2 Converters and Controllers for PMDC Motor-Driven SPVWPS

To choose the suitable DC–DC converter for solar-powered PMDC motor, Jesus Gonzalez suggested a mathematical model to get the relationship between duty cycle and MPP [14] as well as duty cycle and motor speed.

For the MPP of the solar photovoltaic array, Sharaf et al. suggested a dynamic multi-loop driven proportional–integral–derivative (PID) controller [7]. In this method, the motor current, motor terminal voltage and speed with change in the irradiation, temperature and load are taken into account. Using this method, they achieved 10% more output from the PV array.

An error-driven self-adjusting control (SAC) [8] has been suggested by Sharaf and Yang. In this method, the solar panel current, voltage and PMDC motor speed, and current signals are used to generate PWM pulses. This system consists of three loops to generate a global error signal which in turn controls the controlling pulses for a four-quadrant PWM converter. The motor speed loop, motor current limiter loop and the MPPT loop are the three loops present in this technique. These three signals will be multiplied with respective loop weighting factors and added together to produce a global error signal. This signal will be further processed to get the PWM pulses for the DC–DC converter. In this method, the selection of loop weighting factor is very important.

A novel proportional–integral–derivative (PID) dual-loop controller [9] was suggested by Sharaf. In this method, a speed-limiting loop and current controller loop are present. This method continuously tracks the MPP while following required speed level.

Akbaba shows that the maximization in utilization of energy and good ratio of cost to performance can be achieved by selecting the duty ratio of the converter at particular value and varying it with respect to irradiance [10]. This system is simpler to implement and delivers an efficiency of around 85%.

To increase the efficiency of the SPVWPS, Smrithi and Jayapal suggest a linear current booster (LCB) [11]. The LCB is a DC–DC controller integrated with MPPT. The LCB is used to find MPP as well as used to match the source with load.

2.3 MPPT Techniques in PMDC Motor-Driven SPVWPS

Implementation of the MPPT technique is necessary to utilize the solar power from the panel under different irradiance conditions. The MPPT will improve the overall system efficiency by observing maximum possible power from the solar panel. Elgendy compared the reference voltage P&O method and direct duty ratio of perturb and observe method for the photovoltaic pumping applications [12]. The reference voltage P&O method is suitable for fast change in the weather conditions. But this method leads to loss in stability due to high rate of perturbation. The direct duty ratio gives better utilization of solar energy and good stability for slow change in the weather conditions. But this method is not suitable for fast change in the environment conditions. Elgendy also suggested a constant voltage MPPT scheme at low cell temperature [13]. This scheme delivers better energy utilization under slow or fast irradiance changing environment. In this method, voltage measured at standard test condition will be considered as reference to the control loop. This feedback control loop consists of a PI controller to get optimum duty cycle to control the converter. This method is simple in circuit to implement in analog as well as digital circuits. Jesus Gonzalez suggested a linear reoriented coordinate method (LRCM) to track the maximum power under different irradiance conditions [14]. In this method, the open-circuit voltage is taken into consideration to get MPP in spite of any change in the temperature and irradiance. To minimize the swing around MPP and to avoid the failure during fast changes, genetic algorithm (GA) optimization for MPPT is used [15]. In this method, Mohamed explains optimization of control parameters for PMDC motors used in SPV applications. Also this scheme modifies the control algorithm to provide better voltage regulation in the motor drive circuit. The performance comparison of perturb and observe method and INC method has been discussed by the various authors by taking various points into consideration. Oi et al. compared the P&O and INC MPPT algorithm and concluded that P&O technique will be easy to realize in circuit, but INC MPPT algorithm gives better performance under cloudy weather conditions [16]. Elgendy concludes that the P&O algorithm results in chaotic behavior pattern and INC algorithm results in quasiperiodic pattern [17]. He also finds that the PWM of the MPPT converter induces the ripple in the current and voltage waveform. Under constant irradiation and temperature condition, Jayakumar and Rajini found that the INC MPPT algorithm gives better performance [18]. A meaningful comparison of P&O and INC MPPT methods is realized by Jaziri, and the author concludes that INC MPPT is excellent in performance due to high accuracy in tracking the MPP [19]. By using only DC motor speed, Gonzalez designed a control law that purely depends on DC motor model and model of the controller with MPP under different values of irradiance [20]. This control law was implemented by a simple analog circuit.

Fuzzy logic controller (FLC) to extract maximum power from the panel for SPVWPS was suggested by Aashoor [21]. By using the solar array voltage, current and motor speed, this FLC generates PWM pulses to control the DC–DC converter.

Table 1 MPPT comparison

	MPPT	Advantage	Disadvantages
1	P&O	Easy to implement [12]	Swing around MPP and not efficient [12, 22]
2	INC	Good accuracy in tracking [16, 18, 19]	Swing around MPP
3	Constant voltage MPP	Better energy utilization under slow and fast irradiance change [13]	Feedback control loop is necessary [13]
4	LRCM	Good for different irradiance condition [14]	Relatively difficult
5	GA	Better voltage regulation [15]	Difficult to implement
6	FLC	Efficient tracking [21]	Relatively difficult to implement
7	SMC	Power oscillation is eliminated [22]	Difficult to implement

The sliding mode control scheme suggested by Alsumiri achieves optimal operating point in a better way [22]. This method overcomes the power oscillation around the maximum point or the operating point (Table 1).

3 Scope for Improvement

The amount of reliable water pumping of the direct-coupled PMDC-driven SPVWPS system is low, due to the absence of energy storage system. But it decreases the complexity and cost of the overall system. During rainy season and winter season, the system will not be able to pump the required amount of water. Also in the morning (6–9 AM) and in the afternoon (5–6 PM), the amount of pumped water level is negligible, which decreases the system efficiency. Since it is a direct-coupled system, the water head level is very low and normally it will be under 15 ft. Therefore, the challenges and scope for improvement of the direct-coupled SPVWPS involve in improving the system reliability by ensuring the water pumping during low sunny days and also in the MPPT side. Simple and effective tracking mechanism is needed to fix the MPP with minimum swing around that point during fast climate-changing conditions. Nowadays, ease in implementation of MPPT techniques in analog or digital circuits is also gaining the popularity.

4 Conclusion

The direct-coupled PMDC motor-driven SPVWPS lacks reliable water pumping during less sunny days. Therefore, the challenge lies in improving the water pumping level during less sunny days by improving the converter topologies to operate the PMDC motor to pump the water. In this review, efforts are taken

carefully to analyze the existing technology and its advantages and disadvantages. This review will be helpful to the researchers to understand and identify the problem and opportunities associated with the direct-coupled solar water pumping systems.

References

1. Chandrasekaran, N., Thyagarajah, K.: Comparative study of photovoltaic pumping system using a DC motor and PMDC motor. In: 2012 IEEE International Conference on Advances in Engineering, Science and Management, pp. 129–132 (2012)
2. Chandrasekaran, N., Thyagarajah, K.: Simulation and experimental validation of AC motor and PMDC motor pumping system fed by photovoltaic cell. *Indian J. Eng. Mater. Sci.* **21**(1), 93–103 (2014)
3. Mokeddem, A., Midoun, A., Ziani, N., Kadri, D., Hiadsi, S.: Test and analysis of a photovoltaic DC-motor pumping system. In: 2007 IEEE ICTON Mediterranean Winter Conference, pp. 1–7 (2007)
4. Suehrcke, H., Appelbaum, J., Breshef, B.: Modelling a permanent magnet DC motor/centrifugal pump assembly in a photovoltaic energy system. *Sol. Energy* **59**(1), 37–42 (1997)
5. Kolhe, M., Joshi, J.C., Kothari, D.P.: Performance analysis of a directly coupled photovoltaic water-pumping system. *IEEE Trans. Energy Convers.* **19**(3), 613–618 (2004)
6. Hsiao, Y.R., Blevins, B.A.: Direct coupling of photovoltaic power source to water pumping system. *Sol. Energy* **32**(4), 489–498 (1984)
7. Sharaf, A.M., Elbakush, E., Altas, I.H.: An error driven pid controller for maximum utilization of photovoltaic powered pmdc motor drives. In: IEEE Canadian Conference on Electrical and Computer Engineering, pp. 129–132 (2007)
8. Sharaf, A.M., Yang, L.: A novel maximum power tracking controller for a stand-alone photovoltaic dc motor drive. In: 2006 IEEE Canadian Conference on Electrical and Computer Engineering, pp. 450–453 (2006)
9. Sharaf, A.M., Elbakush, E., Altas, I.H.: Novel control strategies for photovoltaic powered PMDC motor drives. In: 2007 IEEE Electrical Power Conference, pp. 461–466 (2007)
10. Akbaba, M.: Optimization of the performance of solar powered permanent magnet dc motor drives. In: 2007 IEEE International Aegean Conference on Electrical Machines and Power Electronics, pp. 725–729 (2007)
11. Radhakrishnan, S., Jayapal, R.: Linear current booster for solar FED DC pumps. In: 2015 IEEE International Conference on Circuit, Power and Computing Technologies, pp. 1–6 (2015)
12. Elgendy, M.A., Zahawi, B., Atkinson, D.J.: Assessment of perturb and observe MPPT algorithm implementation techniques for PV pumping applications. *IEEE Trans. Sustain. Energy* **3**(1), 21–33 (2012)
13. Elgendy, M.A., Zahawi, B., Atkinson, D.J.: Comparison of directly connected and constant voltage controlled photovoltaic pumping systems. *IEEE Trans. Sustain. Energy* **1**(3), 184–192 (2010)
14. Gonzalez-Llorente, J., Ortiz-Rivera, E.I., Salazar-Llinas, A., Jimenez-Brea, E.: Analyzing the optimal matching of dc motors to photovoltaic modules via dc-dc converters. In: Twenty-Fifth Annual IEEE Applied Power Electronics Conference and Exposition, pp. 1062–1068 (2010)
15. Mohamed, A.A., Berzoy, A., Mohammed, O.: Optimized-fuzzy MPPT controller using GA for stand-alone photovoltaic water pumping system. In: 40th Annual Conference of the IEEE Industrial Electronics Society, pp. 2213–2218 (2014)

16. Oi, A., Anwari, M., Taufik, M.: Modeling and simulation of photovoltaic water pumping system. In: 2009 Third Asia International Conference on Modelling & Simulation, p. 497 (2009)
17. Elgendy, M.A., Zahawi, B., Atkinson, D.J., Giaouris, D.: Dynamic behaviour of DC motor-based photovoltaic pumping systems under searching MPPT algorithms. In: 2009 IEEE International Conference on Power Engineering, Energy and Electrical Drives, pp. 413–418 (2009)
18. Jayakumar, M., Rajini, V.: Investigation of photovoltaic water pumping system. In: 2013 IEEE International Conference on Circuits, Power and Computing Technologies, pp. 275–282 (2013)
19. Jaziri, S., Jemli, K.: Optimization of a photovoltaic powered water pumping system. In: 2013 IEEE International Conference on Control, Decision and Information Technologies, pp. 422–428 (2013)
20. Gonzalez-Llorente, J., Ortiz-Rivera, E.I., Diaz, A.: A maximum power point tracker using positive feed forward control based on the dc motor dynamics and pvm mathematical model. In: 2009 IEEE International Electric Machines and Drives Conference, pp. 259–264 (2009)
21. Aashoor, F.A.O., Robinson, F.V.P.: Maximum power point tracking of photovoltaic water pumping system using fuzzy logic controller. In: 2013 IEEE 48th International Universities Power Engineering Conference, pp. 1–5 (2013)
22. Alsumiri, M.A., Jiang, L., Tang, W.H.: Maximum Power Point Tracking controller for photovoltaic system using sliding mode control. In: 3rd IET Renewable Power Generation Conference, pp. 1–5 (2014)

Decoupled Active and Reactive Power Control of Cascaded H-Bridge PV Inverter for Grid-Connected Applications

V. Sridhar, S. Umashankar and P. Sanjeevikumar

Abstract In a conventional solar power plant, DC input voltage to the inverter is fed from the multiple solar panels with series parallel combination. So the maximum power point tracking (MPPT) is possible only on the series parallel combination of all the arrays together, which is not so efficient. Independent maximum power point tracking (MPPT) is needed to improve the system efficiency. Independent control of the voltage is possible through the cascaded inverters. Hence, independent MPPT control can be obtained by using cascaded H-Bridge-based inverters for PV applications. In this paper, decoupled control of active and reactive powers for a CHB inverter in PV applications is explained and the simulation results are presented. System operation with equal and unequal irradiances on PV arrays is also explained.

Keywords Multilevel inverter · Cascaded H-bridge · Maximum power point tracking · Photovoltaic, power control

V. Sridhar · S. Umashankar (✉)
School of Electrical Engineering, Vellore Institute of Technology (VIT) University,
Vellore, Tamil Nadu, India
e-mail: umashankar.s@vit.ac.in

V. Sridhar
e-mail: sridhar.spark@gmail.com

P. Sanjeevikumar
Department of Electrical and Electronics Engineering, University of Johannesburg,
Auckland, Johannesburg, South Africa
e-mail: sanjeevi_12@yahoo.co.in

P. Sanjeevikumar
Research and Development, Power Electronics Division, Ohm Technologies,
Chennai, India

1 Introduction

In a conventional grid-connected PV system, multiple solar modules connected in series parallel combination provide the DC input to the PV inverter. Single-stage converter, i.e., DC to AC converter or chopper-based two-stage converter is used to transfer the power from PV array to the grid. With single-stage and two-stage inverters, maximum power point tracking can be done only on the entire PV array, which is not so efficient.

Independent MPPT control is required to improve the efficiency, which is possible through string inverters or through cascaded inverters [1, 2]. Since cascaded inverters can give multilevel output on the AC side, there is an improvement in the voltage THD. Hence, cascaded inverters are preferred over string inverters for high power applications. A review on CHB-based multilevel inverter topologies was discussed in [3–5]. CHB-based multilevel inverter has the following advantages (a) modular in construction (b) low dv/dt (c) low output THD (d) small filter size (e) suitable for high power applications [6].

A grid-connected cascaded H-Bridge-based PV inverter consists of PV arrays, CHB inverter, transformer, LCL filter, AC and DC breakers is shown in Fig. 1. Transformer provides the isolation between grid and the PV array. Transformer is also required to match the inverter and grid voltages. An L-C or an L-C-L filter is used to get sinusoidal output.

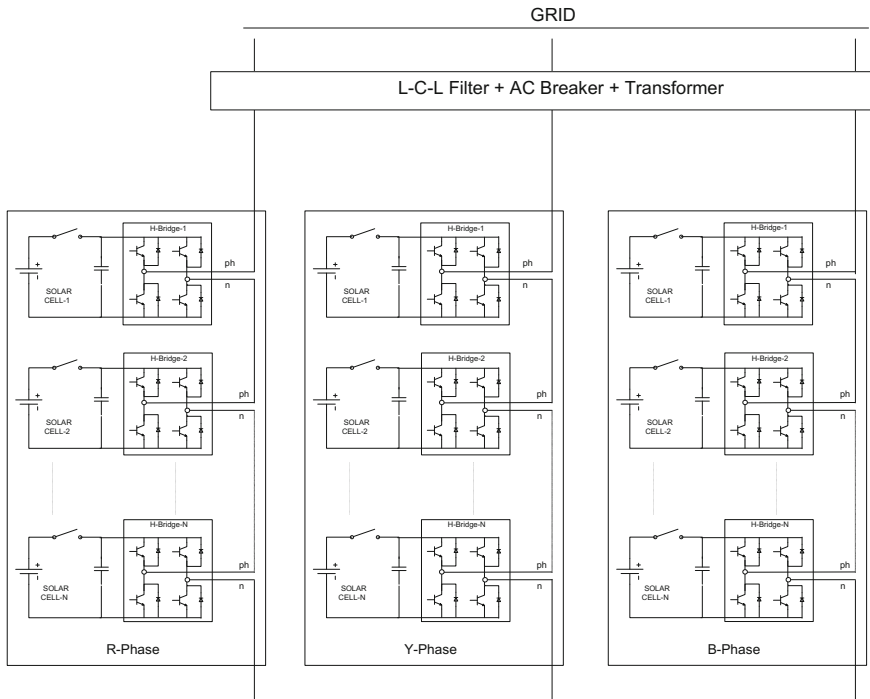


Fig. 1 Block diagram a CHB MLI-based grid-connected PV inverter

2 Active and Reactive Power Control of CHB-Based Multilevel Inverters in PV Applications

PV inverter transfers the DC power received from PV modules into the AC power for utilization during day time and will be in idle state when the irradiation is weak. To improve the utilization of PV inverter, it is preferred to operate as a PV-STATCOM, i.e., PV inverter along with the feature of reactive power control.

The concept of PV-STATCOM is operating a PV inverter as an active power source as well as a reactive power compensator [7, 8].

In this section, a CHB MLI-based PV inverter along with reactive power compensation capability is explained briefly. Figure 2 shows a control structure for a CHB MLI-based PV inverter for grid applications. Grid voltage is monitored for determining the angle ωt through phase locked loop (PLL). Voltage and currents of each PV array are monitored for independent MPP tracking. Based on MPP of each

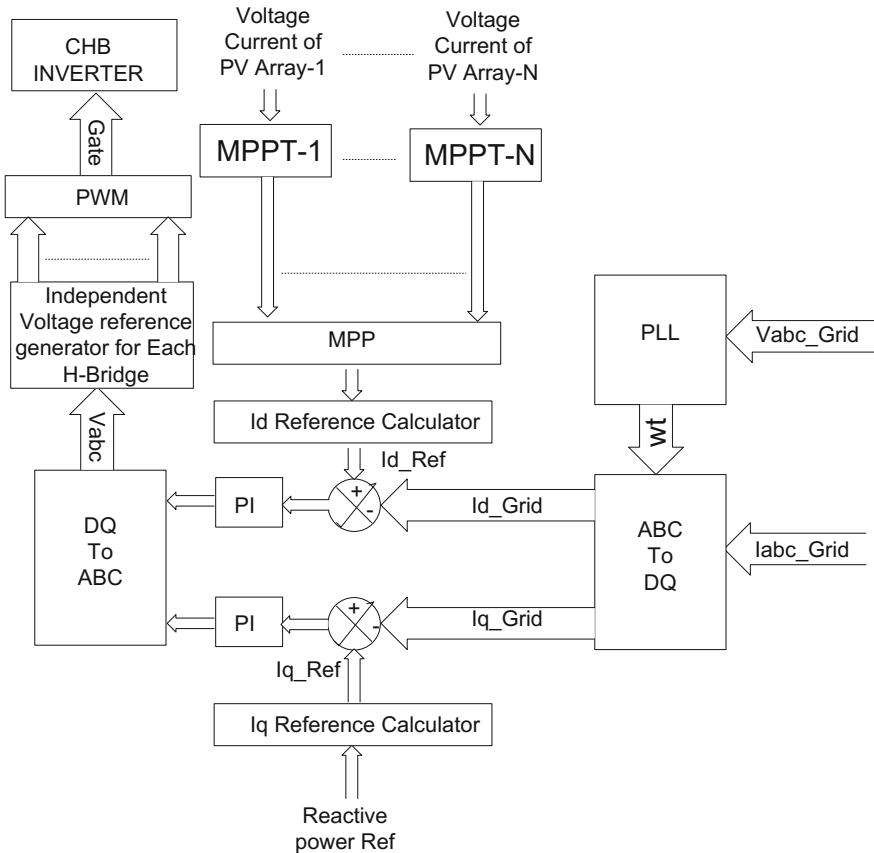


Fig. 2 Block diagram for current control of a CHB MLI-based grid-connected PV inverter

array, the MPP of three phases is obtained. MPP of the overall system is obtained based on the minimum MPP value among the three phases to avoid unbalancing.

Direct current reference (I_{d_Ref}) to the inverter is obtained from overall MPP, and w_t . I_{q_Ref} is generated based on the reactive power to be supplied. The power control is carried out through PI controller by comparing the dq components of reference grid current with dq components of actual grid current. Output of PI controller gives the reference output voltage. Based on individual MPP of PV array, voltage reference for each H-Bridge is obtained and pulse generator generates the gate pulses for each H-bridge of the CHB inverter.

3 Results and Discussions

Simulation studies are carried out to check the performance of the system by considering a grid-connected CHB inverter with nine number of H-Bridges, i.e., three H-Bridges per phase connected to a separate PV array. Level shifted PWM is applied for generating gate pulses. System operation with equal irradiance and unequal irradiances on PV arrays is explained in next subsections.

3.1 Case1: PV Arrays with Equal Irradiance

When the irradiance on all the nine PV arrays is equal, i.e., during the ideal state of the system, the MPP of each PV array will be equal; hence, the overall MPP is the

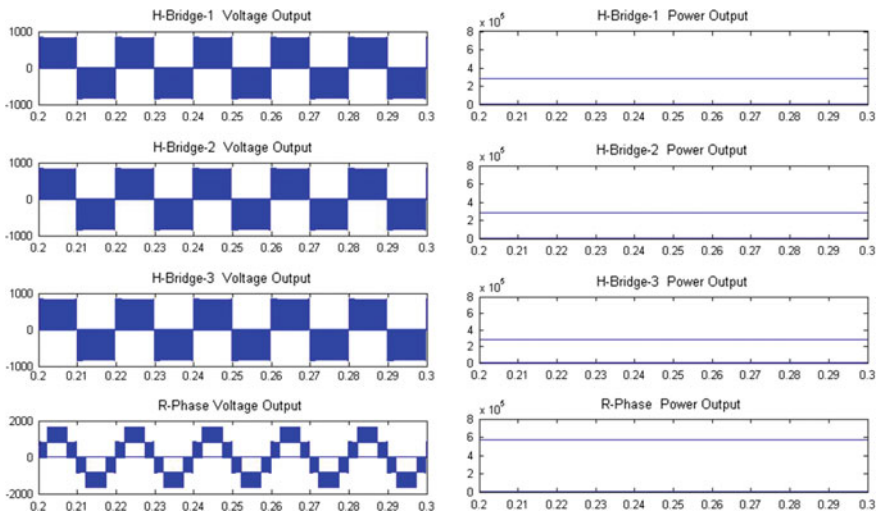


Fig. 3 Voltage and power output of R-phase of CHB inverter with equal irradiance

sum of MPPs of all nine PV arrays. The voltage and the power output of all the PV arrays are equal since the irradiance is equal. When irradiance value is simulated at 700 W/m^2 for all the PV arrays, since the system is at ideal state, the output voltage and power of all the three H-Bridges of R-phase are equal as shown in Fig. 3.

3.2 Case 2: PV Arrays with Unequal Irradiance

Practically, the irradiance on all the PV arrays will not be equal due to mounting arrangement, partial clouding, etc.

Figure 4 shows the voltage and output power of each H-Bridge of R-phase. Irradiance value is simulated at 1000 W/m^2 for PV array 1, 400 W/m^2 for PV array 2 and 700 W/m^2 for PV array 3.

By comparing Figs. 3 and 4, it is observed that the power output of H-Bridge 3 of R-phase is same since there is no change in the irradiance value.

Output power of H-Bridge 1 is more in Case 2 since the irradiance is increased, and similarly the output power of H-Bridge 2 is reduced in Case 2 due to reduction in the irradiance. However, the R-phase output voltage and power are same in both the cases, since the MPP of R-phase is same.

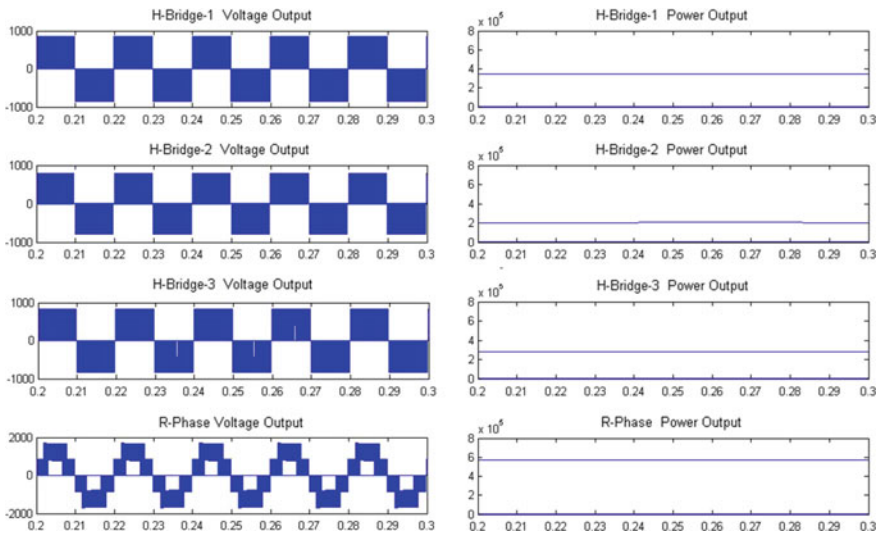


Fig. 4 Voltage and power output of R-phase of CHB inverter with unequal irradiance

3.3 Decoupled Active, Reactive Power Control

Consider an R-L load equal to the capacity of PV inverter connected on the grid.

When the reference active and reactive powers (P_{Ref} and Q_{Ref}) of the CHB inverter are zero, then the total load current is supplied only from grid and the CHB inverter current is zero as shown in Fig. 5.

When the P_{Ref} of CHB inverter is 1 P.U., then the total active power required for load is fed from CHB inverter. The reactive power required for load is supplied from the grid. Since the CHB inverter is feeding only the active component of the power, voltage and currents are in phase. Similarly since grid is supplying only the reactive component of power, the grid current is lagging the grid voltage by 90° as shown in Fig. 6.

Similarly when the Q_{Ref} of PV inverter is 1 P.U., CHB inverter supplies the reactive power requirement of the load, since the P_{ref} of inverter is zero and the active power is supplied by the grid. From Fig. 7, it is observed that since the grid is feeding the only the active component of the power, voltage and currents are in phase. Inverter current is lagging the voltage by 90° since inverter is supplying only the reactive component of power.

In Fig. 8, when the P_{Ref} and Q_{Ref} are 1 P.U. for CHB inverter, then the total power is supplied only from the CHB inverter and the current drawn from grid is zero. From the above results, it is observed that decoupled active and reactive power control enables the CHB inverter to operate as a multilevel PV-STATCOM which improves the utilization factor of the system.

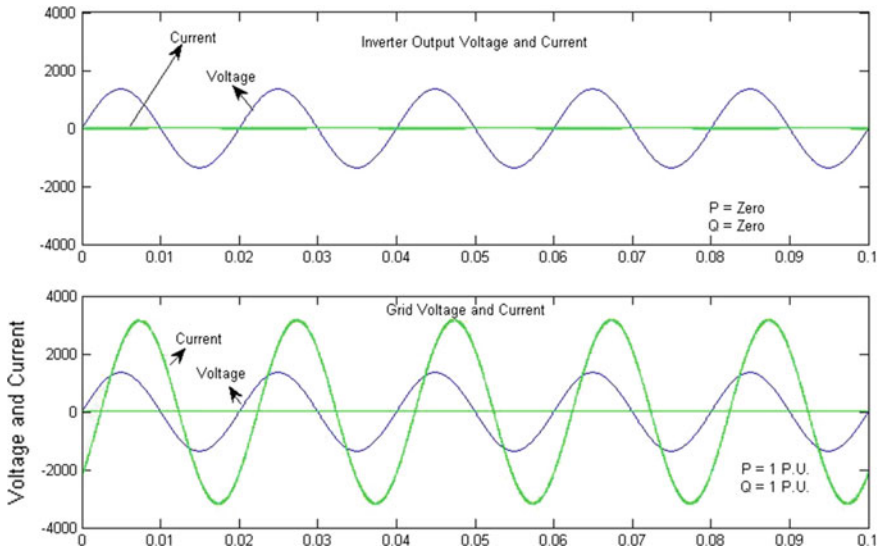


Fig. 5 Phase voltage and currents of CHB inverter and grid when $P_{Ref} = 0$ and $Q_{Ref} = 0$

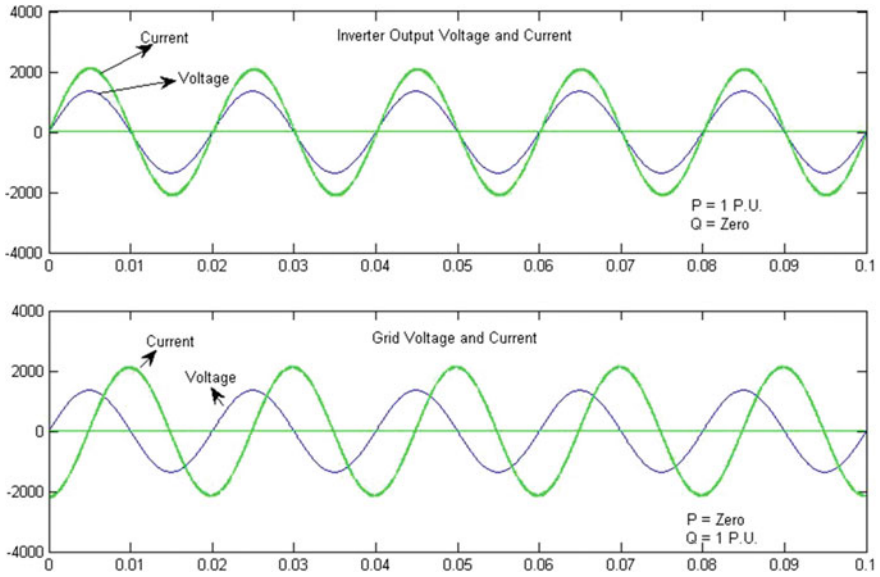


Fig. 6 Phase voltage and currents of CHB inverter when $P_{Ref} = 1$ P.U. and $Q_{Ref} = 0$

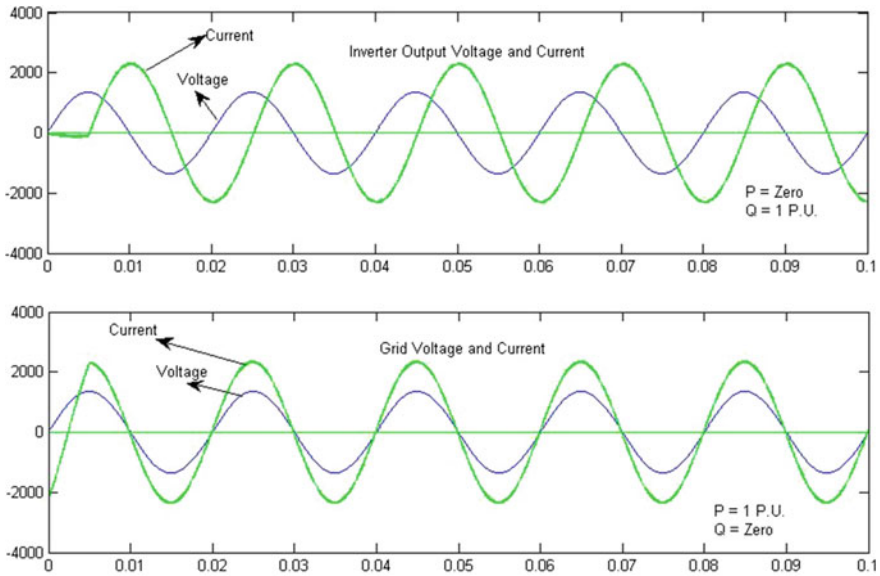


Fig. 7 Phase voltage and currents of CHB inverter and grid when $P_{Ref} = 0$ and $Q_{Ref} = 1$

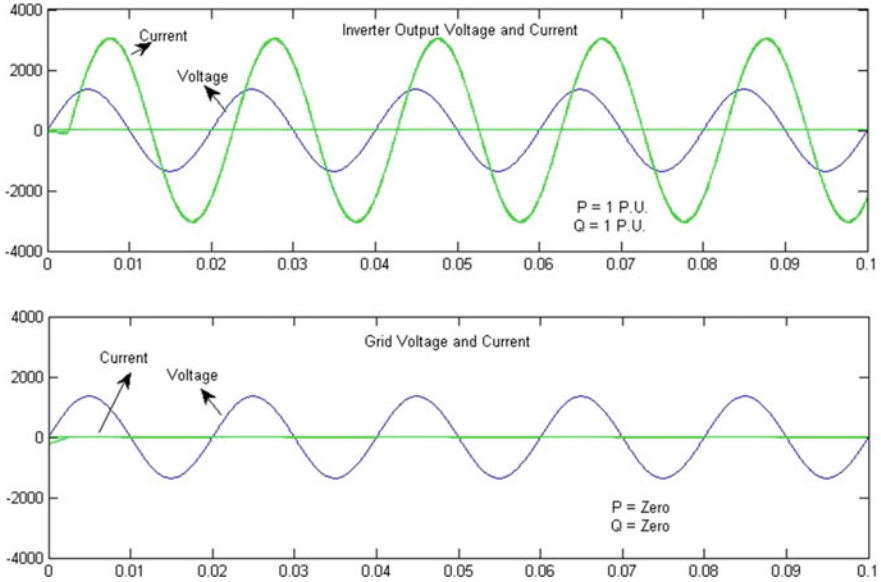


Fig. 8 Phase voltage and currents of CHB inverter when $P_{\text{Ref}} = 1$ P.U. and $Q_{\text{Ref}} = 1$ P.U.

4 Conclusions

CHB configuration is most suitable for independent MPPT control in PV applications as independent voltage control is possible in a CHB inverter. Independent MPPT tracking of each PV array explained in Sect. 3 improves or maximizes the efficiency of the system. Decoupled control of active and reactive power with CHB MLI gives a better performance since the CHB is ideal for photovoltaic systems where isolated input DC source is available and for STATCOM applications where there is no DC source requirement. In this paper, decoupled active, reactive power control for the CHB inverter is explained. From the presented results, it can be concluded that the CHB MLI-based PV inverter along with the features of independent MPPT and decoupled active, reactive power control acts like a multilevel PV-STATCOM which improves the efficiency and the utilization factor of the system.

References

1. Huang, Q., Yu, W., Huang, A.Q.: Independent DC link voltage control of cascaded multilevel PV inverter. In: IEEE Applied Power Electronics Conference and Exposition (APEC), Long Beach, CA, pp. 2727–2734 (2016)
2. Metry, M., Bayhan, S., Balog, R.S., Rub, H.A.: Model predictive control for PV maximum power point tracking of single-phase sub multilevel inverter. In: IEEE Power and Energy Conference at Illinois (PECI), Urbana, IL, pp. 1–8 (2016)

3. Krishna, R.A., Suresh, L.P.: A brief review on multi level inverter topologies. In: International Conference on Circuit, Power and Computing Technologies (ICCPCT), Nagercoil, pp. 1–6 (2016)
4. Shehadeh, S.H., Aly, H.H., El-Hawary, M.E.: Photovoltaic multi-level inverters technology. In: IEEE 28th Canadian Conference on Electrical and Computer Engineering (CCECE), Halifax, NS, pp. 648–655 (2015)
5. Sankar, D., Babu, C.A.: Cascaded H bridge multilevel inverter topologies for PV application: a comparison. In: International Conference on Circuit, Power and Computing Technologies (ICCPCT), Nagercoil, pp. 1–5 (2016)
6. Wu, B.: High-Power Converters and AC Drives (Ch-7), pp. 119–142
7. Selwa, F., Djamel, L., Imen, L., Hassiba, S.: Impact of PSS and STATCOM on transient stability of multi-machine power system connected to PV generation. In: International Conference on Renewable Energy Research and Applications (ICRERA), Palermo, pp. 1416–1421 (2015)
8. Abdel-Aziz, E.Z., Ishaq, L., Al-Khulayfi, A.M., Fawzy, Y.T.: Voltage stability improvement in transmission network embedded with photovoltaic systems. In: IEEE International Energy Conference (ENERGYCON), Leuven, 2016, pp. 1–7 (2015)

Fuzzy-Based Microgrid Energy Management System Using Interleaved Boost Converter and Three-Level NPC Inverter with Improved Grid Voltage Quality

Swaminathan Ganesan, V. Ramesh, S. Umashankar
and P. Sanjeevikumar

Abstract This paper demonstrates a novel method to integrate and control PV source and Battery storage in to a microgrid system to attain reduction in total harmonic distortion at the output. The closed-loop control of inverter has been achieved through using proportional integral controller (PI) and fuzzy logic controller. The results of output harmonics contents are compared for simple open-loop control and proposed closed-loop controls, and it clearly indicates that the closed-loop results far superior in terms of harmonic contents at the inverter output voltage. The control of battery energy storage system (BESS) has been presented, with the aid of a DC–DC bidirectional buck–boost converter for the different modes of operation, such as hold state, charging state and discharging state. With the intention of tracking the maximum power point from PV array, P&O MPPT technique has been used by which duty cycle of converter is controlled. Various operating conditions, such as photovoltaic source alone supplying to the entire load requirement and supplying to battery for its charging, PV source supplying to load requirement only, battery storage unit supplying to load requirement and lastly PV source and battery storage unit jointly supplying to the load requirement, have been analyzed extensively. Detailed analysis has been carried out on the output voltage,

S. Ganesan · V. Ramesh · S. Umashankar (✉)
School of Electrical Engineering, VIT University, Vellore, Tamil Nadu, India
e-mail: umashankar.s@vit.ac.in

S. Ganesan
e-mail: swaminathan.ganesan@schneider-electric.com

V. Ramesh
e-mail: vramesh@vit.ac.in

P. Sanjeevikumar
Department of Electrical and Electronics Engineering, University of Johannesburg,
Auckland Park, Johannesburg, South Africa
e-mail: sanjeevi_12@yahoo.co.in

output current and output power waveforms for different operating conditions as discussed above, and the output results are analyzed for achieving more beneficial performance of the system. The suggested microgrid energy management system has been modeled and analyzed using MATLAB/Simulink tool.

Keywords Microgrid · Photovoltaic inverter · Battery · Maximum power point tracking (MPPT) · Fuzzy logic · Energy management system (EMS) Closed-loop control

1 Introduction

Sustainable energy sources such as solar, wind and fuel cells are abundantly available and have benefit of reducing global warming problems. Majority of the global population depends on conventional energy sources such as coal, oil and natural gas. Due to the consistent increase in per capita energy consumption over many years, the traditional energy reserves are depleted, thus prompting the necessity for integration of sustainable sources of energy into the regular energy network. In this paper, PV inverter and lead–acid-based battery storage system have been integrated to form a microgrid [1]. As the solar irradiation is highly intermittent in nature due to passing clouds, it is necessary to have storage energy system connected in the network to compensate intermittency in the microgrid network. Power electronic converters are used to transform the PV array's DC input to AC or DC at another level. The output AC power produced at the inverter terminal is connected to the connected loads locally or to the mains. During off-peak load conditions, the available PV energy is used to charge batteries. Transformer-based isolation converters are high priced in addition to higher loss of power, as a large number of switches are used. Lead–acid batteries are taken in to consideration in this paper for analysis due to its cost-effectiveness and longer life.

Normal and interleaved boost converters are deployed to boost the PV output to the required DC-link voltage level [2]. The battery is charged and discharged using a bidirectional DC–DC converter. IGBT switches are employed since they have the advantage of less output impedance and high switching speeds [3]. Detailed analysis has been carried out for various operating conditions as stated above by combining PV source and battery energy storage system. In this work, a non-conventional source of energy consisting of solar PV arrays and energy storage system connected with different types of loads within a microgrid network are considered in various operating modes [4]. These different operating modes are influenced by the PV output, the battery SOC and dissimilar loads. Figure 1 illustrates the interconnections between components of the microgrid network under consideration.

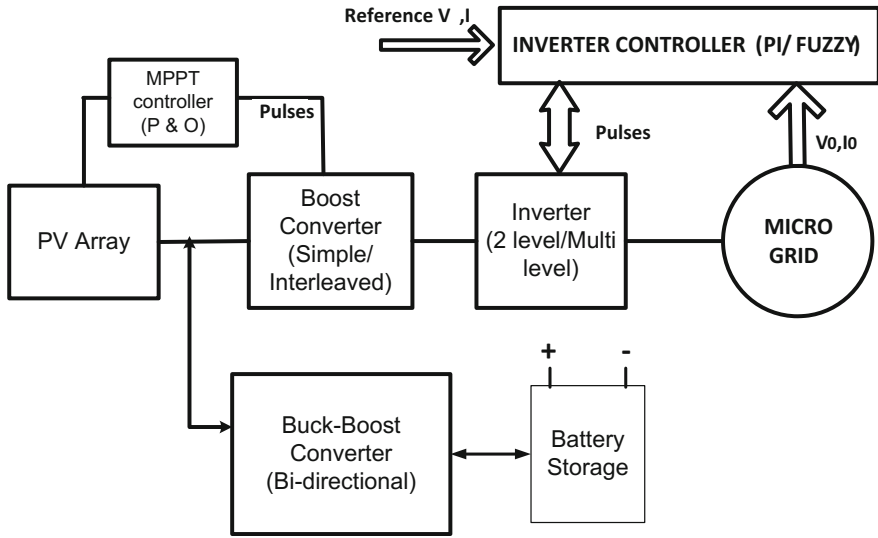


Fig. 1 Interconnection scheme of proposed system

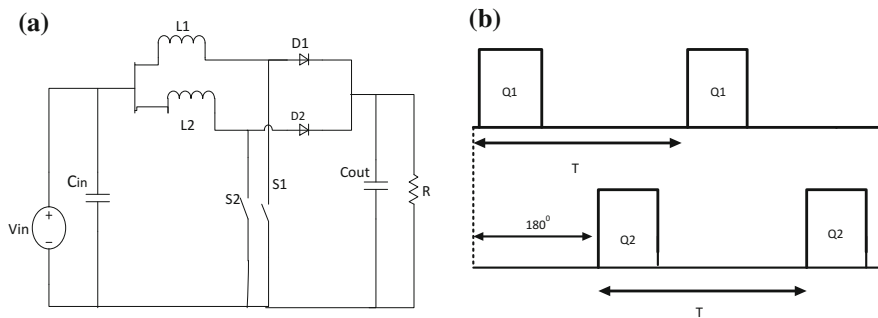


Fig. 2 a Schematic diagram of interleaved boost converter; **b** timing signals for IBC

2 Microgrid Network Configuration

2.1 DC-DC Interleaved Boost Converter

In general, to maintain or to step up the DC voltage of a PV array, the boost converters are employed with the capability to track MPP. Figure 2a shows schematic representation of a normal boost converter. The analysis of steady-state operating conditions of continuous operating mode is given below for both the intervals, in terms of volt-second balance for inductor and charge balance for capacitor. Thereafter, the required converter is premeditated with the help of a small ripple approximation [5].

2.2 Design of Interleaved Boost Converter (IBC)

The value of inductance is obtained from Eq. (1)

$$L = \frac{V_{in} \times m}{f_s \times \Delta I_L} \tag{1}$$

where f_s is frequency of switching, V_{in} voltage at input, m modulation index and ΔI_L inductor current ripples.

Capacitor value is obtained from Eq. (2)

$$C = \frac{I_0 \times m}{f_s \times \Delta V_c} \tag{2}$$

where f_s is frequency of switching, I_0 current at output, m modulation index and ΔV_c capacitor voltage ripples.

2.3 Controlling of Inverter

2.3.1 PI Control

Figure 3 shows the PI control block diagram. In PI, control loop error is detected, which is the difference between output and given reference signal. It minimizes error by controlling inputs to the system.

The gate pulses to the inverter switches are derived from PI controller output [6].

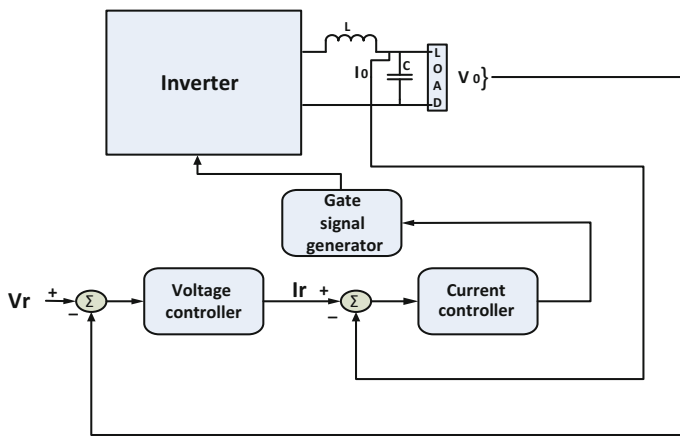


Fig. 3 PI controller block diagram

2.3.2 Fuzzy Logic Controller (FLC)

To abbreviate the harmonic distortions, fuzzy logic controllers (FLC) are casted off. Fuzzy logic controllers will contain easy mathematical algorithm involving linguistic variables. FLC is carried out in three different stages.

2.3.3 Fuzzification

Method of converting variable which is in numerical form to linguistic form is fuzzification. Fuzzy rules for the proposed system are given in Table 2. Input variables that are considered are change in voltage which is the alteration between original voltage (V_0) and voltage of reference and change in error (Δe) which is the change in current of sample interval. Output membership function is the PWM generator reference signal [7–9].

2.3.4 Inference

Fuzzy interference is dependable on fuzzy rule-based system. Within the inference block, fuzzy rules will be framed. Behavior of the control surface which is led by set of rules connects the output and input variables.

2.3.5 Defuzzification

Crisp value is transformed in to fuzzy with the help of defuzzification. It is the inverse of fuzzification. Centroid method is used in general for defuzzification

which is given as $\int \frac{x \times \mu(x)dx}{\mu(x)dx}$ (Table 1; Fig. 4)

Table 1 Fuzzy rules

ΔI	Input voltage (Vs)						
	V0	V1	V2	V3	V4	V5	V6
PL	P1	P0	P2	P4	P5	P6	P8
PA	P0	P1	P2	P4	P5	P7	P8
PS	P0	P1	P3	P4	P5	P7	P8
PZ	P0	P1	P3	P4	P6	P7	P9
Z0	P0	P2	P3	P4	P6	P7	P9
NZ	P0	P2	P3	P5	P6	P8	P9
NS	P0	P2	P3	P5	P6	P8	P9
NA	P1	P2	P4	P5	P7	P8	P10
NL	P1	P2	P4	P5	P7	P8	P10

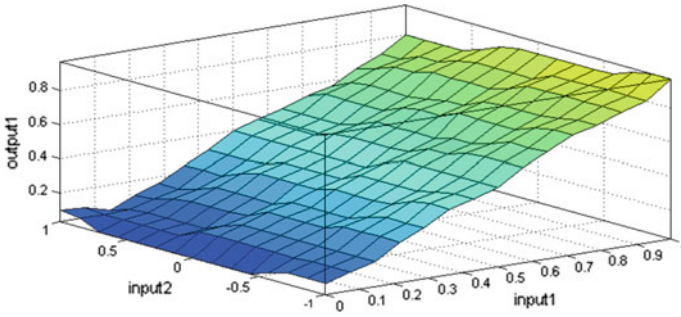


Fig. 4 Fuzzy surface

Table 2 Factors considered for bidirectional buck–boost converter

Factor	Value
Inductance	6.46 e–6 H
Pulse width of IGBT 1	21%
Capacitance	7.8 e–1 F
Pulse width IGBT 2	79

2.4 Bidirectional DC–DC Buck–Boost Converter

A non-isolated bidirectional DC–DC buck–boost converter has been employed in order to increase output voltage of PV system to the required level during charging as well as discharging modes of operation of the battery and also reduces the battery output voltage to suit the load demand [10]. The essential parameters are designed in continuous mode of operation as follows for the buck mode converter, and the duty cycle is quantified by

$$\frac{V_O}{V_{in}} = \frac{1}{1 - D_{boost}} \tag{3}$$

The current at the discontinuous–continuous periphery is specified by

$$I = \frac{DT_s}{2L} (V_{out} - V_{inp}) \tag{4}$$

$$L = \frac{(2 \times 10^{-5}) \times 0.209 \times (110 - 23)}{2 \times 30} = 6.46 \times 10^{-6} \tag{5}$$

Factors considered for bidirectional converter in this paper are presented in Table 2.

2.4.1 Battery Model

In this paper, a lead–acid battery which has 100 V rated voltage and 6.5 Ah capacity has been taken into consideration. Default state of charge (SOC) value can be allocated as per the simulation requirement.

2.4.2 Load

The authors compared the performance of a two-level inverter with a three-level inverter which is connected to 220 V resistive load of 10 Ω with capacity of 4.65 kW power. The power available from PV array or from the storage battery is converted into AC voltage to a RMS value of 310 V as per the operating mode of microgrid network.

2.4.3 Controller Logic

To scrutinize PV irradiation and fluctuation in load demand, comparative operators are incorporated in the control logic. Multiport switches were used to control the IGBT switches in bidirectional converter. [11–13]. [A] go-to block takes care of boost mode and [B] go-to block takes care of buck mode of operation. The battery unit is connected to main structure with ideal switches which is taken care by [C] go-to block. Equally, the photovoltaic modules are connected to the scheme using ideal switch which is handled by block [D] go-to. The control logic gives digital pulse train with 0 or 1 states for all go-to blocks to distinguish the different operating modes of the structure. Table 3 reveals the sum of outputs created for each go-to block for the diverse modes of operation.

Table 3 Controller logic scheme

Insolation (W/m ²)	Working modes	[A]	[B]	[C]	[D]
1000	Mode I—PV source to load and battery	0	1	1	1
700	Mode II—PV source only to load	NA	NA	0	1
300	Mode III—battery source only to load	1	0	1	0
1000	Mode IV—PV and battery sources to load	1	0	1	1

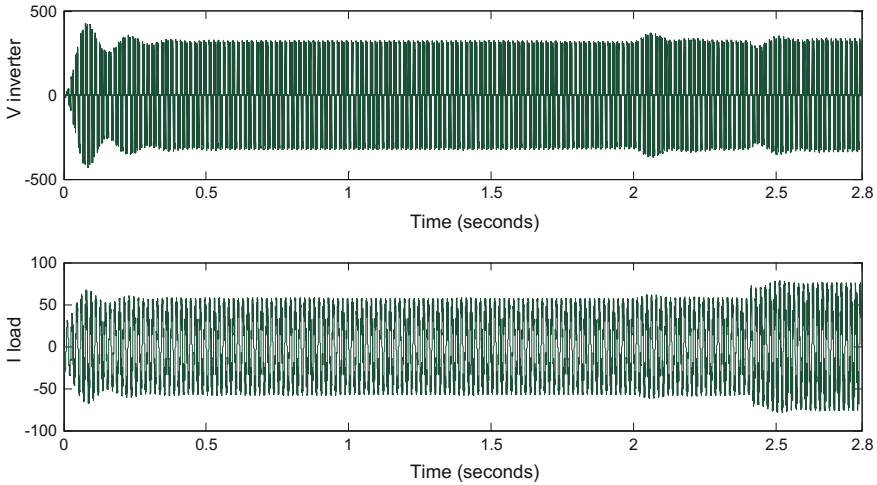


Fig. 5 Output load voltage and current

2.5 Simulation Results and Discussion

For mode I: Mode I runs from 0 to 1.3 s with insolation level of 1000 W/m^2 , only PV operates in this mode. The PV array delivers to load besides charging the battery. In Fig. 5, voltage and current outputs are displayed. The predefined value of state of charge (SOC) of battery is taken as 50% while simulation are presented in Fig. 6.

For mode II: Simulation time of mode II is from 1.3 to 2.0 s with insolation level of 700 Wm^{-2} . Since insolation level decreases, PV array output also reduces and it would not be able to supply for both load and charge battery. Resulting disconnection of the battery and the remaining load is supplied by the PV array alone. In Fig. 7, currents and voltages are displayed.

For mode III: Insolation level in mode III is further reduced to 300 Wm^{-2} and simulation running time is from 2.0 to 2.4 s; because of very less insolation level, output of PV array reduces below the working conditions results disconnection of PV scheme. Battery alone will supply load throughout this mode. In Fig. 6, output current and output voltage are displayed.

For mode IV: Running time of this last mode is from 2.4 to 2.8 s at insolation level of 1000 Wm^{-2} . Sudden increase in insolation level results in load variation as

Table 4 Comparison of boost and interleaved boost converters

Sl. No	Parameter	Boost converter	IBC
1	Input voltage	23.19 V	23.19 V
2	Output voltage	317.2 V	337.1 V
3	Inductor current ripple	3.32%	2.04%
4	Output voltage ripple	2.83%	1.63%

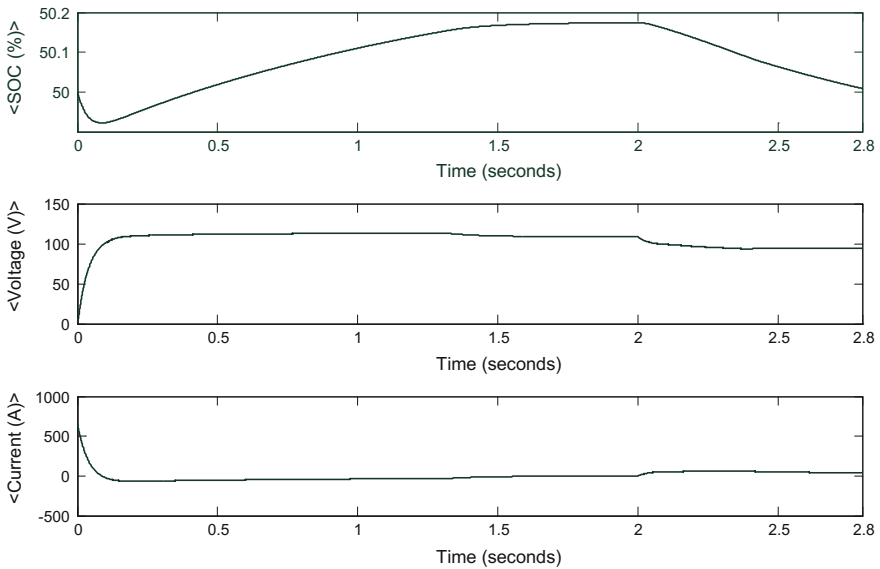


Fig. 6 Output SOC, voltage and current waveforms of battery

rise in resistance is practiced. In order to balance the system to the enhanced load demand, both PV source and battery unit will deliver to the load throughout this mode. In Fig. 5, output of voltage and current for each configuration are displayed.

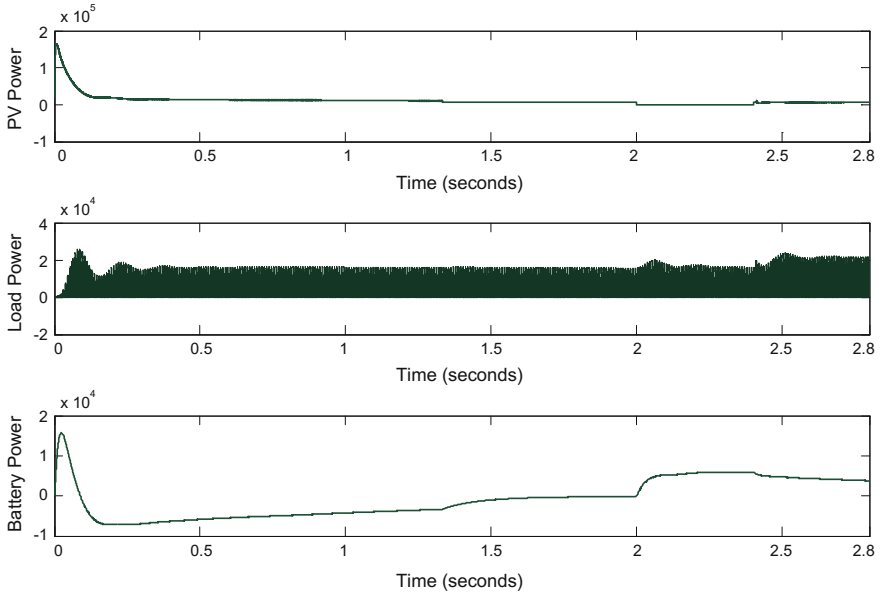


Fig. 7 Output of PV power, load power and battery power

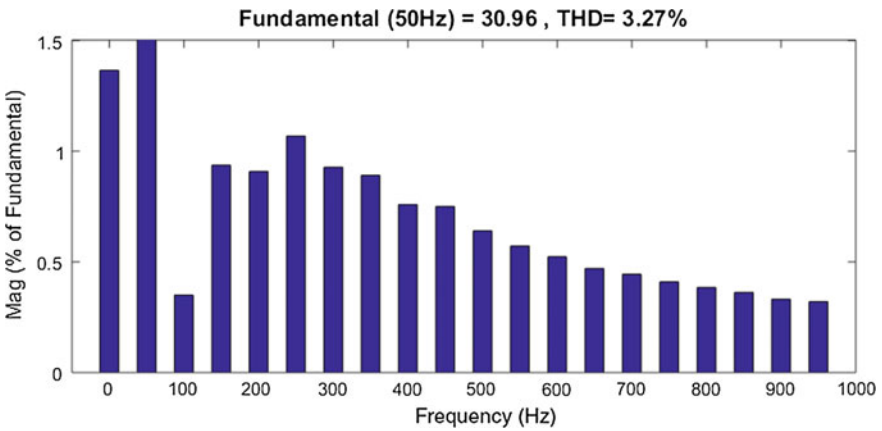


Fig. 8 THD in closed-loop control with FLC (3.27%)

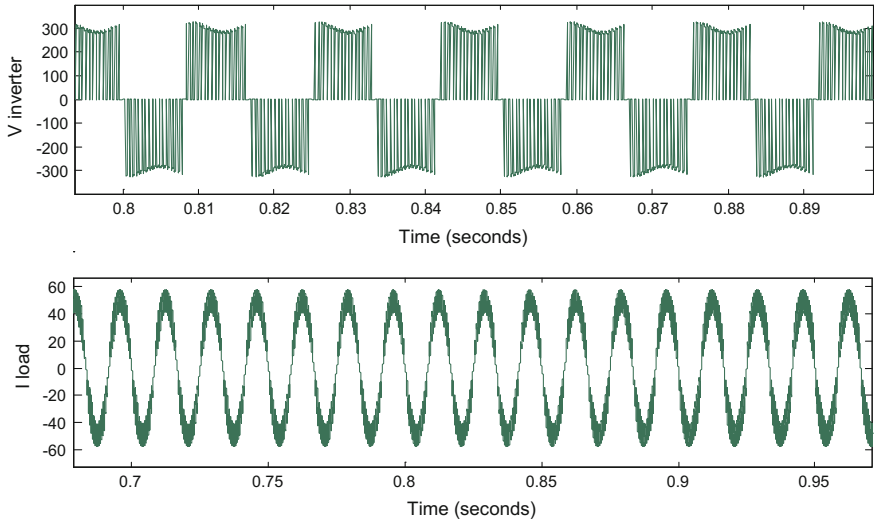


Fig. 9 Output voltage and current in open loop

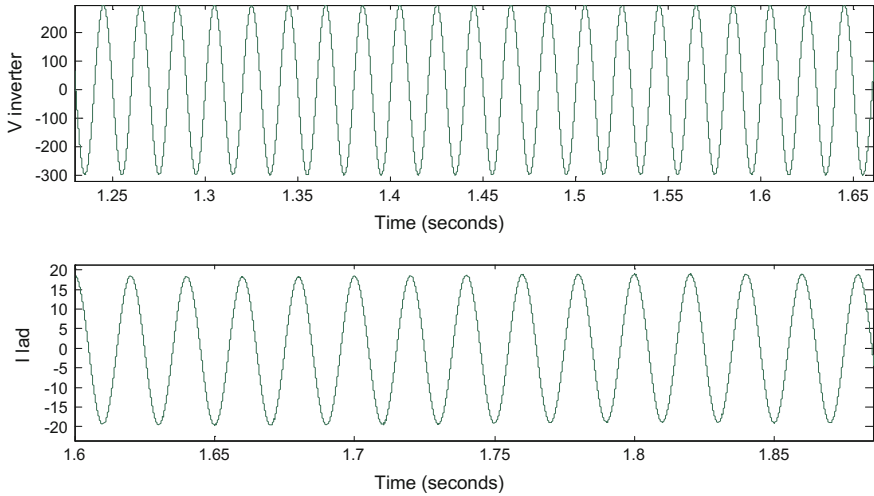


Fig. 10 Output voltage and current with PI control

2.5.1 Comparison of Inverter Controls

See Figs. 9, 10 and 11.

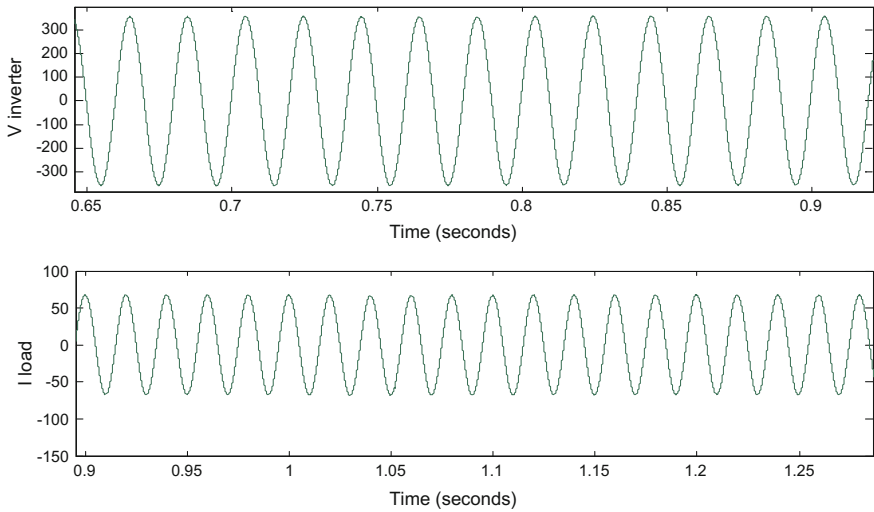


Fig. 11 Output voltage and current with fuzzy logic control

Table 5 Comparison of total harmonic distortion (THD)

	Open-loop control	PI control	Fuzzy logic control
THD	24.88%	7.72%	3.27%

3 Conclusions

The voltage and current output waveforms for battery and load plotted from simulation analysis for all the modes describe the functioning of the system based on particular precondition of charge and discharge of the battery. The Table 4 compares the critical parameters of Boost converter and IBC. During mode I which is from time 0 to 1.3 s, PV output is optimum and will deliver to load, and the lead-acid battery gets charged. Mode II is from 1.3 to 2 s; during this period, only PV source delivers to load demand. Mode III is from 2.0 to 2.4 s, and here, battery alone delivers to load. Mode IV starts from 2.4 to 2.8 s, because of the load demand; both PV source and battery together will supply to the load. The output of the current and voltage attained defines clearly the tractability of microgrid with proposed closed-loop control with PI and fuzzy logic controller in various modes of operation. Resulting output state of charge (SOC), voltage and current of different operating modes are shown in Fig. 6. Power at the terminals of PV source, load and battery are shown in Fig. 7. Total harmonic distortion at output as shown in Fig. 8 has been compared with the aid of PI controller and fuzzy logic controls, and comparison table is shown in Table 5 which shows that by using fuzzy logic-based control, the current harmonic distortion is very less, i.e., 3.27% in comparison with open-loop system and a conventional PI controller. This further improves the

efficiency of the overall microgrid system. Lastly the complete arrangement represents how a renewable energy source such as PV system which is employed with MPPT can be utilized with battery in microgrid to distribute power to the local loads in an efficient manner. It is observed that while transitioning from one operating mode to the other mode was found to be seamless and no traces of any disturbance at system level and also this solution is very much suitable for sporadic nature of the solar insolation and clouding effects.

References

1. Sonal, G., Birla, C., Lamba, A., Umashankar, S., Ganesan, S.: Energy management of PV–battery based microgrid system. *Procedia Technol.* **21**, 103–111 (2015)
2. Ganesan, S., Ramesh., V, Umashankar, S.: Performance improvement of micro grid energy management system using interleaved boost converter and P&O MPPT technique. *Int. J. Renew. Energy Res.* **6**(2), (2016)
3. Wu, B., Kouro, S., Mariusz, M., Pou, J., Franquelo, LG., Gopakumar, K., Rodriguez, J.: Recent advancement in industrial application of multilevel converter. *IEEE Trans. Indus. Electron.* **57**(8), 2553–2580 (2010)
4. Kim, S.K., Jeon, J.H., Cho, C.H., Kon, S.H.: Dynamic modeling and controls of a grid-connected hybrid generation system for versatile power transfers. *IEEE Trans. Indus. Electron.* **55**(4), 1677–1688 (2008)
5. Sanjeevikumar, P., Grandi, G., Blaabjerg, F., Wheeler, P., Ojo, O., Siano, P.: A Comprehensive analysis and hardware implementation of control strategies for high output voltage DC-DC boost power converter. *Int. J. Comput. Intell. Syst. (IJCIS)* (Accepted for publication)
6. Rech, C., et al.: Analysis and design of a repetitive predictive-PID controller for PWM inverters. In: *Power Electronics Specialists Conference, 2001. PESC. 2001 IEEE 32nd Annual. vol. 2*, IEEE (2001)
7. Cecati, C., Ciancetta, F., Siano, P.: A multilevel inverter for photovoltaic systems with fuzzy logic control. *IEEE Trans. Indus. Electro.* **57**(12), 4115–4125(2010)
8. Sanjeevikumar, P., Blaabjerg, F., Siano, P., Martirano, L., Leonowicz, Z., Maroti, K.P.: PI and fuzzy control strategies for high voltage output dc-dc boost power converter—hardware implementation and analysis. In: *Conference Proceedings. of 16 IEEE International. Conference on Environment and Electrical Engineering. Florence (Italy), 7–10* (2016)
9. Sanjeevikumar, P., Thiagarajan, Y., Sivakumaran, T.S.: Design of fuzzy logic controller for a DC-AC converter for a grid connected system using PV cell. In: *Conference Proceedings IEEE International. Conference on Computing, Communication and Networking, IEEE-ICCCNET'08, 1–6. Tamilnadu (India), 18–20* (2008)
10. Chang, L., Hu, B., Xue, Y.: Studying of buck-boost converter in photovoltaic system (PV). In: *For Electrical Machine and System, 2008. ICEMS 2008. 2602–2606. IEEE* (2008)
11. Cecati, C., Ciancetta, F.: A multi-level inverter for photo-voltaic systems with fuzzy-logic control. *IEEE Trans. Indus. Electron.* **57**(12), 4115–4125 (2010)
12. Yuvaraja, S., Shob, J.: A fast and accurate maximum power point tracker for PV system. In *Applied Power Electronics Conference, 2008. APEC 2008. Twenty-Third Annual IEEE, 167–172* (2008)
13. Hamrouni, N., Jraidi, M., Chrif, A.: New control strategy in 2-stage grid-connected photovoltaic power system. *Renew. Energy* **33**(10), 2212–2221 (2008)

Impact of Power Quality Disturbances on Grid-Connected Double Fed Induction Generator

Karthik Tamvada, S. Umashankar and P. Sanjeevikumar

Abstract Wind power integration in the electric grid causes power quality (PQ) disturbances. This would result in system instability and other related issues. This work tries to emulate different power quality (PQ) disturbances on a grid-connected DFIG and assess them according to their severity. This is done in order to assess the different generator operating variables for the PQ disturbances at their instant of occurrence.

Keywords Doubly fed induction generator · Power quality · Transients
Voltage sag · Voltage unbalance

1 Introduction

Wind energy due to its economics and policies, environmental benefits, modularity, scalability, relative ease of installation, mature technology and penetration in modern power systems [1–3] is the most preferred form of renewable energy. DFIG is a preferred choice in high-power grid-connected wind energy conversion systems, due to the huge economic gains resulting from reduced sizes of power converters and filters [4]. Proportionate to the amount of wind energy connected, power quality problems persist, acting detrimental to electric grid performance [5]. IEEE standard 1159–1995 [6] underlines various the PQ disturbances in a wide range including transient to steady-state variations for a time-scale ranging from tens of nanoseconds to steady state. This article attempts to provide an overview on

K. Tamvada · S. Umashankar
School of Electrical Engineering, Vellore Institute of Technology (VIT), Vellore,
Tamil Nadu, India
e-mail: umashankar.s@vit.ac.in

P. Sanjeevikumar (✉)
Department of Electrical and Electronics Engineering, University of Johannesburg,
Auckland Park, Johannesburg, South Africa
e-mail: sanjeevi_12@yahoo.co.in

different power quality issues related to interconnection of DFIG to the electric grid and categorize them for DFIG power quality improvement to attain increased wind power penetration in the electric grid. The paper organization is as follows, Sect. 2 discusses the DFIG converters, Sect. 3 discusses their associated control, Sect. 4 provides the numerical simulation results and discussion for response of DFIG to different power quality (PQ) disturbances and Sect. 5 provides the conclusion of the paper.

2 DFIG Converter

Decoupled power control is easily achieved by implementing vector control on the DFIG [5] fractional rated power converters. Doubly fed induction generator utilizes variable frequency voltage source converters that feed rotor winding in a back-to-back (B2B) configuration. The partial-scale power converters take between 25 and 30% of the nominal power output from the generator significantly reducing the rating and cost of power converters.

2.1 Rotor Side Converter (RSC)

It controls active and reactive power by control of the rotor circuit for stator terminal voltage. However, due to the small ratings, the large amount of currents induced in the rotor windings of the generator during disturbances cause reduced stator voltage to exceed safe limits [7].

2.2 Grid Side Converter (GSC)

It provides dc link voltage control and also warrants higher power factor for DFIG operation. This converter is capable of achieving slight active and reactive power processing. Direct grid connection of GSC makes it unnecessary for limited voltage issues to be considered. Three-phase to two-phase coordinate transformation is enabled by aligning the d-axis vector of the electric grid voltage. Main operating concerns for GSC might be torque and total active power oscillations, depending on working condition of the DFIG.

3 Converter Control

Vector control (VC) uses conventional proportional–integral controllers for ensuring control of flow of active and reactive power flow between DFIG and electric grid in an independent manner. This is implemented through control of rotor currents in SRF (synchronous reference frame) [8], where stator flux vector has d-axis alignment. For grid-connected operation, it is feasible to align reference frame to the stator voltage vector. Vector control advantages include improved steady-state performance, low power ripple and lesser converter switching frequency. But, slow transient performance occurs as a result of complex decoupling and coordinate transformation, tuning of the PI regulators and sensitivity to the machine parameter variation. It also necessitates positive and negative sequence current extraction, deteriorating performance of the system.

4 Numerical Simulation Results

The response of a 1.5 MW grid-connected DFIG in the presence of power quality disturbances is presented in this section, and the severity of different power quality (PQ) disturbances is assessed accordingly. The power quality (PQ) disturbances that were accounted for include: (a) transients (due to lightning) (b) voltage sag (due to L-L-G fault) (c) voltage swell (d) voltage unbalance (single phasing condition) and (e) harmonics. Also the operation of the DFIG was analyzed for fluctuating wind speed conditions. The different operating parameters of DFIG that were assessed are dc link voltage (V_{dc}), DFIG rotor speed (ω_r), total real power generated (P), total reactive power (Q), DFIG stator voltages (V_{abc}) and DFIG stator currents (I_{abc}). All the parameters are considered in per unit (p.u.) values.

Figure 1a shows the behavioral response of dc link voltage (V_{dc}) for different PQ disturbances. In terms of magnitude, transients and voltage sag result in the maximum fluctuation, followed by voltage unbalance and voltage swell, with voltage swell causing sustained deviation from desired value of V_{dc} for a longer time duration. A constant V_{dc} is maintained even in the presence of harmonics. Figure 1b depicts the behavioral response of DFIG rotor speed (ω_r) with respect to the different PQ disturbances. It is clearly noticed that the DFIG rotor speed fluctuates for all the PQ disturbances with respect to magnitude and decreases gradually. It fluctuates greatly for voltage swell and to a lesser extent to voltage sag disturbances. Voltage unbalance and transients cause the DFIG rotor speed to slightly deviate with lesser fluctuations, while harmonics contribute the least to the variation in the DFIG rotor speed. Figure 1c illustrates the behavioral response of total real power generated (P) by the DFIG with respect to the different PQ disturbances. There is a decrease in real power

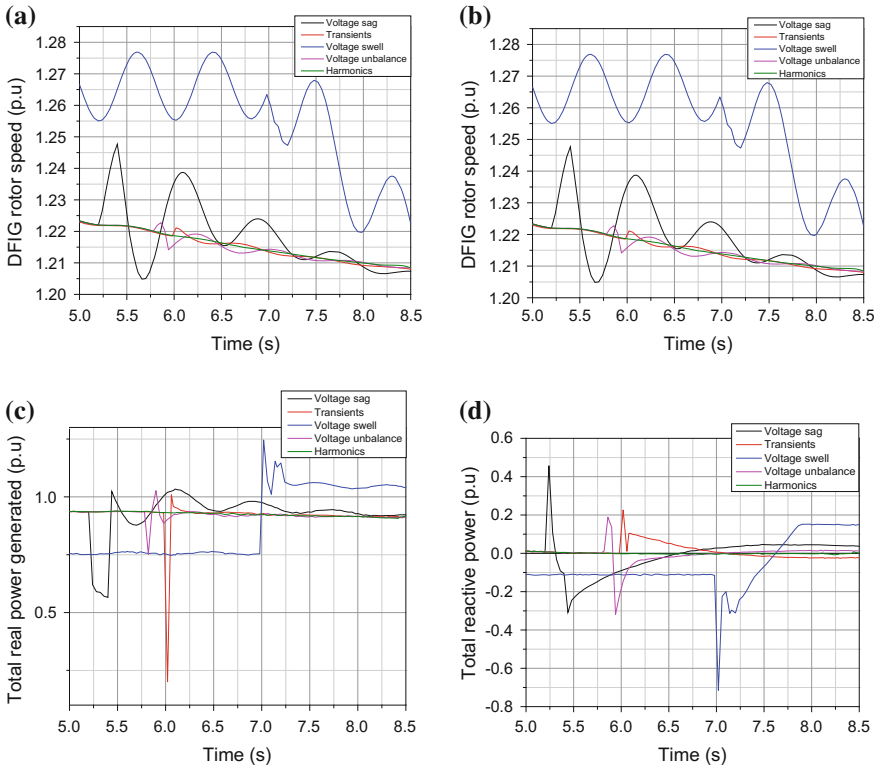


Fig. 1 a Effect of PQ disturbances on dc link voltage. b Effect of PQ disturbances on DFIG rotor speed. c Effect of PQ disturbances on total active power generated. d Effect of PQ disturbances on total reactive power

generation output for all PQ disturbances apart from fluctuations. Transients cause a steep fluctuation followed by voltage swell. Fluctuations persist for a longer time duration. Voltage swell causes fluctuation only at its instant of occurrence. Harmonics result in reduced real power generation output comparable to other PQ disturbances devoid of any fluctuations. Figure 1d portrays the behavioral response of total reactive power (Q) of DFIG with respect to the different PQ disturbances. Voltage swell and voltage sag followed by transients inject the maximum reactive power with respect to magnitude. Voltage unbalance along with voltage sag and swell supplies and consumes reactive power to and from the electric grid. Transients consume reactive power at the instant of occurrence. Harmonics neither consume nor

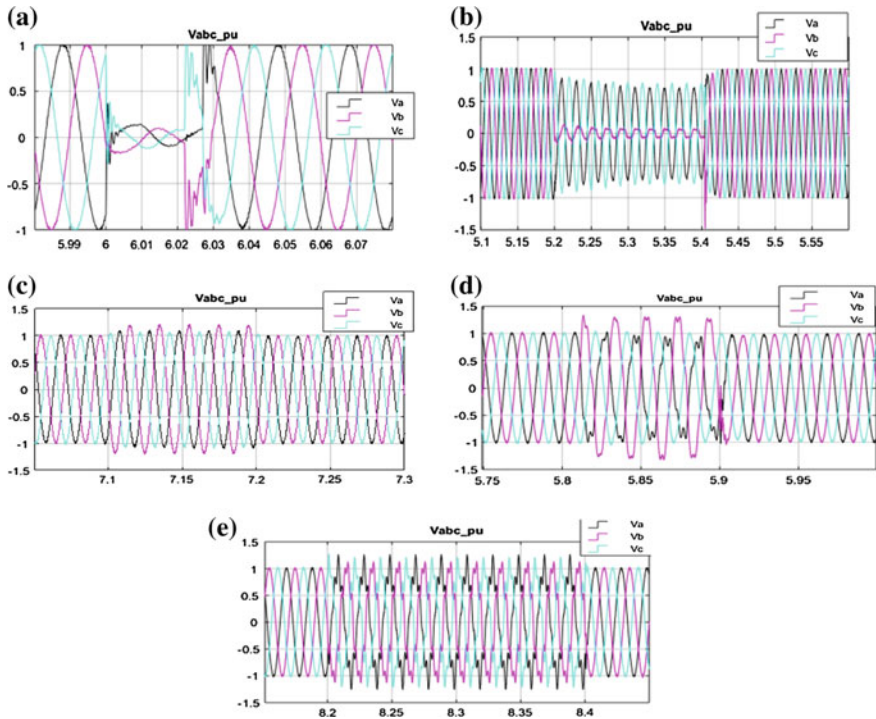


Fig. 2 **a** DFIG stator voltages in presence of transients. **b** DFIG stator voltages in presence of voltage sag. **c** DFIG stator voltages in presence of voltage swell. **d** DFIG stator voltages in presence of voltage unbalance. **e** DFIG stator voltages in presence of harmonics

inject reactive power with respect to the electric grid. To enable a clear understanding, the individual responses of DFIG stator voltages and stator currents to the different PQ disturbances are shown in Figs. 2a–e and 3a–e. Performance of operating variables of grid-connected DFIG studied under PQ disturbances considered shows that the PQ disturbances that act severely with respect to all the operating variables are sag, swell and unbalance, with sag being the most prominent among the three. The effect of transients is most severe in the case of dc link voltage and DFIG stator voltages and currents. Harmonics show least effect on dc link voltage, real power generation and the reactive power but cause slight disturbances in rotor speed of DFIG and stator voltages and currents.

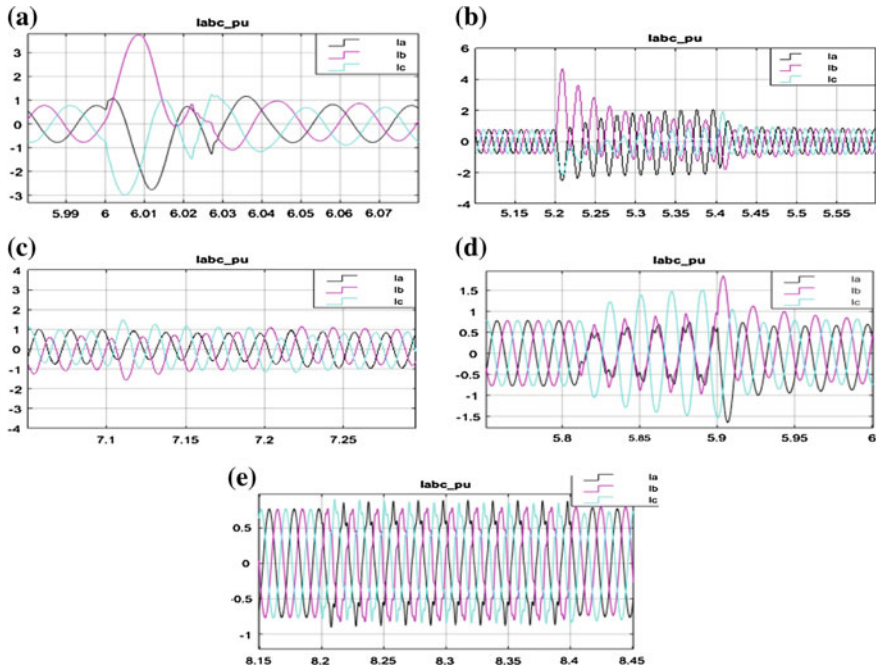


Fig. 3 **a** DFIG stator currents in presence of transients. **b** DFIG stator currents in presence of voltage sag. **c** DFIG stator currents in presence of voltage swell. **d** DFIG stator currents in presence of voltage unbalance. **e** DFIG stator currents in presence of harmonics

5 Conclusion

In this article, an overview on different power quality issues related to interconnection of DFIG wind energy system in the electric grid has been simulated, and an attempt is made to categorize their severity for DFIG power quality in order to attain increased wind power penetration in the electric grid. The future of DFIG wind energy systems is to benefit both utility systems and individual consumers of energy in a safe and reliable manner and achieve optimum performance and resiliency to power quality issues.

References

1. Cheng, M., Zhu, Y.: The state of the art of wind energy conversion systems and technologies: a review. *Energy Convers. Manag.* **88**, 332–347 (2014)
2. Leung, D.Y.C., Dennis, Y.C., Yang, Y.: Wind energy development and its environmental impact: a review. *Renew. Sustain. Energy Rev.* **16**(1), 1031–1039 (2012)

3. Saqib, M.A., Saleem, A.Z.: Power-quality issues and the need for reactive-power compensation in the grid integration of wind power. *Renew. Sustain. Energy Rev.* **43**, 51–64 (2015)
4. Carrasco, J.M., et al.: Power-electronic systems for the grid integration of renewable energy sources: a survey. *IEEE Trans. Industr. Electron.* **53**(4), 1002–1016 (2006)
5. Tazil, M., et al.: Three-phase doubly fed induction generators: an overview. *IET Electric Power Appl.* **4**(2), 75–89 (2010)
6. Hossain, M.M., et al.: Future research directions for the wind turbine generator system. *Renew. Sustain. Energy Rev.* **49**, 481–489 (2015)
7. IEEE Standard 1159–1995: Recommended Practice for Monitoring Electric Power Quality, The Institute of Electrical and Electronics Engineers (1995)
8. Colak, I., et al.: Critical aspects of wind energy systems in smart grid applications. *Renew. Sustain. Energy Rev.* **52**, 155–171 (2015)

Health Monitoring System of Solar Photovoltaic Panel: An Internet of Things Application

Prutha M. Badave, B. Karthikeyan, S. M. Badave, S.B. Mahajan,
P. Sanjeevikumar and Gurjit Singh Gill

Abstract A wireless remote monitoring system for solar photovoltaic (PV) plant is proposed in this paper. It is an Internet of Things (IoT) application implemented with an objective to offer a cost-effective solution of monitoring system, which continuously presents remote energy yields and its performance either on computer or on handheld gadgets such as smart phones. A system for proof of concept is developed with eight solar panels to monitor string voltage, string current, temperature and humidity. System is controlled by CC3200 microcontroller with ARM Cortex-M4 as core. On board Wi-Fi, wireless communication enhances the system performance with reduced area and facilitates to monitor system parameters after every 30 s.

Keywords Remote monitoring system · Data acquisition system
Internet of Things · Parameter measurement · Solar photovoltaic

P.M. Badave (✉) · B. Karthikeyan
School of Electronics Engineering, Vellore Institute of Technology, Vellore, India
e-mail: pruthabadave11@gmail.com

B. Karthikeyan
e-mail: bkarthikeyan@vit.ac.in

S.M. Badave · S.B. Mahajan
Department of Electrical and Electronics Engineering,
Marathwada Institute of Technology, Aurangabad, India
e-mail: smb.eed@gmail.com

S.B. Mahajan
e-mail: sagar25.mahajan@gmail.com

P. Sanjeevikumar
Department of Electrical & Electronics Engineering,
University of Johannesburg, Auckland Park, South Africa
e-mail: sanjeevi_12@yahoo.co.in

G.S. Gill
Gill Instruments Private Limited, Bengaluru, India
e-mail: contact@gill-instruments.com

1 Introduction

In last few years, the development of sustainable energy has strongly constrained due to the depletion of fossil fuel and contamination of environmental issues. The demands of sustainable energy generation systems can progressively replace conventional supply system. Nowadays, solar photovoltaic (PV) generation is gaining importance because of foremost advantages is that, it is clean and free energy source. Apart from that, it also offers the benefit includes ease of installation, low economic viability, noise-free generation, more resilient and more affordable to grid connected systems. Furthermore, efficiency of PV panels is increasing day-by-day due to technological advancement.

Solar systems are essentially installed over the wide range of capacity from less than kW as roof top installation to few tens of MW as solar farming system. For better performance and ease of maintenance, the performances of the solar PV systems need to be monitored continuously, especially when installations are in rural areas or spread over huge land, at reduced operational cost. Remote monitoring system mainly divided in three parts (i) a sensing unit, (ii) processing unit and (iii) display unit. Sensing unit basically includes various sensors and signal conditioning units. Obviously, this unit is located in close proximity with PV system. Information given by sensing unit is conveyed to processing unit either with wired or wireless network, which further given to display unit. Many times, sensing unit is equipped with smart sensors, to handle the PV system signals effectively before transmitting it to central processing unit. A case study of solar PV plant in UiTM Pulau Pinang, Malaysia is an automated data acquisition systems used to monitor small-scale solar PV plant by collecting all the data regarding the installed system [1]. National Instruments (NI) software LabView along with its data acquisition modules is used for real-time data collection of PV plant parameters on regular intervals. In this case sensing system, processing and monitoring system are in close proximity. PV voltage and current connect are mainly monitored as measure of performance parameters [2, 3]. GSM voice channel is used as communication media. Analog transmission is preferred for communication by work on various communication protocols is also carried out thoroughly in [4]. An improved wireless remote monitoring and control system of a solar photovoltaic distributed generator (PV-DG) for micro-grids applications is implemented with full-duplex wireless communication using the ZigBee protocol [4, 5]. The supervisory control system is implemented on a digital signal processor (DSP) and a Human–Machine Interface (HMI) software is developed to measure PV parameters such as current, voltage and humidity along with solar tracking. Sensing unit is operated with intelligence of digital signal processor; however, ARM-based microcontroller LPC2148 is used for central control system. Though this kind of systems is offering efficient monitoring and control appeared to be costly solution due to smart sensors at each node. The electrical and physical parameters such as voltage, current, temperature and humidity [6, 7] are monitored with Programmable Logic Controller (PLC) and Supervisory Control and Data Acquisition (SCADA)

system. It is a system implemented with basic programming and with relevant peripherals, which offers operational simplicity; however, it is suitable for industrial environment where existing infrastructure of PLC and SCADA is readily available.

A cost-effective, Internet of Things (IoT)-based health monitoring system is proposed here for solar PV plant, where sensors are embedded in solar PV system and are linked to the Internet through wireless networks, using the Internet Protocol, MQ Telemetry Transport (MQTT).

2 Proposed Solar Photovoltaic System

The proposed solar photovoltaic PV monitoring system, shown in Fig. 1, consists of PV array, storage battery banks, operational control unit of battery and an electrical load.

2.1 Photovoltaic Array

A prototype photovoltaic (PV) system of 2.5 kW is implemented using an assembly of polycrystalline PV modules, each is capable of yielding short-circuit current (I_{SC}) of 8.7 A and open-circuit voltage (V_{OC}) of 37.25 V. PV array is of such eight panels, arranged in form of two strings. Charge controller is a vital part of a system, which controls the power flow of battery thereby maximizing the battery life. Inverter is also essential to power AC load. In proposed work, instead of using charge controller and inverter as a separate entity, a power conditioning unit is installed to serve the purpose. Sensors placed at different locations are used to monitor system operation.

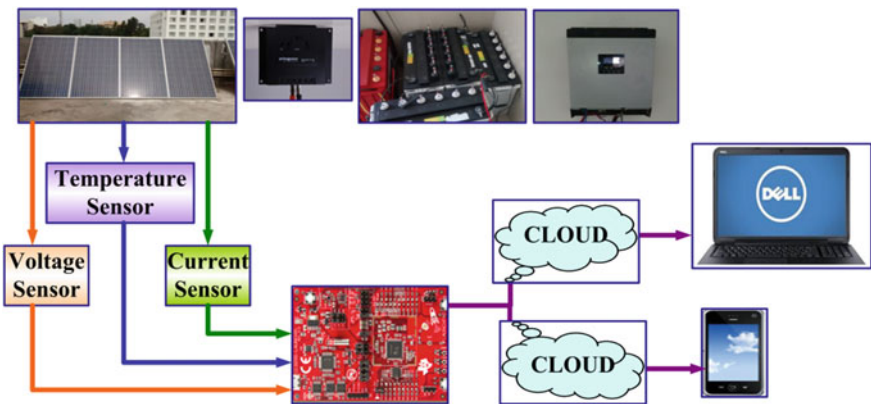


Fig. 1 Proposed solar photovoltaic system

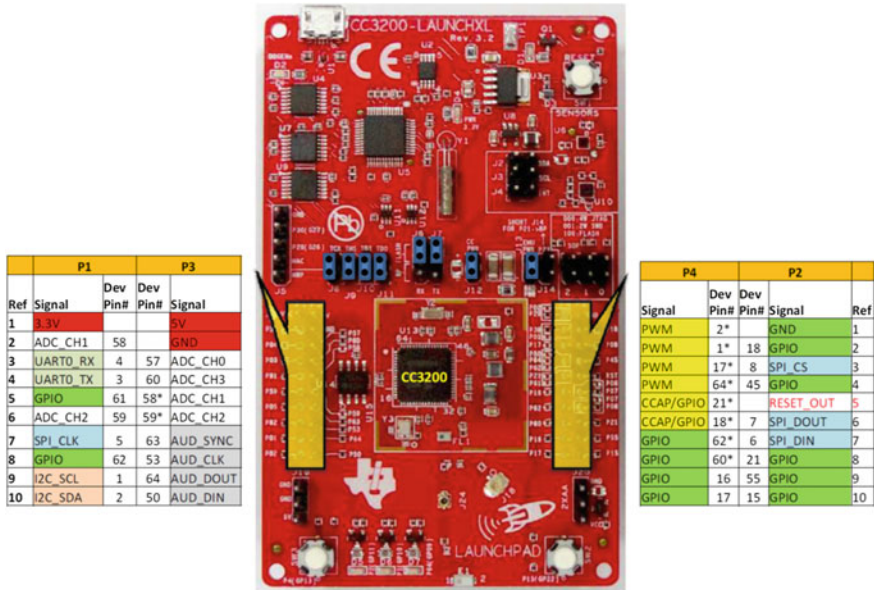


Fig. 2 CC3200 launch pad

2.2 Processing Unit

Processing unit comprised with CC3200 launch pad (shown in Fig. 2) used to control complete solar PV panel health monitoring system. It is a low-cost evaluation platform integrated with high-performance ARM® Cortex®-M4 and built-in Wi-Fi connectivity. It is also featured with ADC operating on 1.5 V.

2.3 Battery Storage

Another essential element of solar array photovoltaic system (SAPV) is the storage battery. These batteries are necessary in order to avoid fluctuating nature of the output delivered by PV array. Batteries are designed to capture surplus electricity generated by solar PV system by permitting to store solar electricity for use later in the day. The energy obtained during day time directly feeds to load and unutilized energy can be stored in a battery to meet the demand during lack of solar energy. During the night, or during a period with low solar irradiation, energy is supplied to the load from the battery.

2.4 Monitoring System

Solar PV panel monitoring system comprises with three major units, sensing unit, processing unit and display unit. An Internet of Things (IoT)-based system is developed to monitor system parameters such as solar panel voltage, current, temperature and humidity.

2.5 Display Unit

Continuous monitoring is facilitated by display unit, which includes smart phones and remote terminal on Internet connected by MQTT protocol. ThingSpeak is an open source Internet of Things (IoT) application. It is an application programming interface (API) to store and retrieve data from sensors. ThingSpeak enables the creation of sensor logging applications, location tracking applications and a social network of things with status updates. It allows user to collect, store, analyze, visualize and act on data from sensors. Sensor unit comprised with voltage and current sensor is connected to analog inputs of 12 bit ADC section of controller CC3200; however, humidity and temperature sensor to Inter-Integrated circuit I²C bus section. The Wi-Fi network processor subsystem features a Wi-Fi Internet-on-a-chip and contains an additional dedicated ARM MCU that completely offloads the applications MCU. An 802.11 protocol is used for system with a powerful crypto engine for fast, secure Internet connections with 256-bit encryption. CC32XX network processor and MCU Block arrangement is shown in Fig. 3.

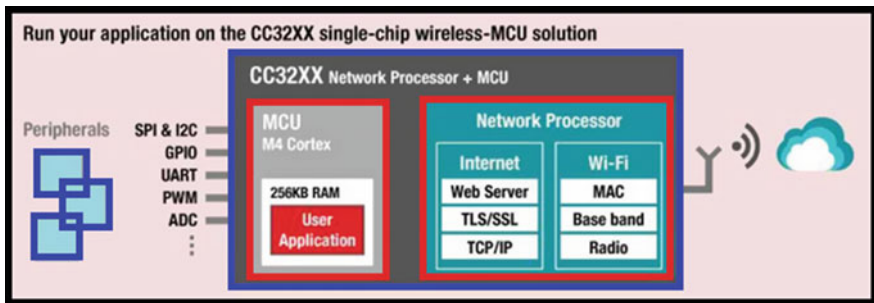


Fig. 3 CC32XX network processor and MCU

3 Sensing Units of Proposed System

Function of sensing unit is to sense system parameters and to act as an interface to processing unit. In proposed work, system operation is controlled by CC3200 launch pad, which is equipped with inbuilt ADC and accepts analog as well as digital inputs within the range of 0–1.5 V.

3.1 Voltage and Current Sensor

A desired level of string voltage is obtained from voltage divider circuitry, comprised with linear resistive elements and is as shown in Fig. 4. Commonly available linear potentiometer also can serve the purpose. A Hall effect sensor, 9350 CSLA2CD, is an inductive analog current sensor (shown in Fig. 5), works on AC or DC current up to 72 A and operating temperature is from -25 to 85 °C, which varies its output voltage in response to a magnetic field. Desired level of voltage is obtained by adjusting input number of terms.

Fig. 4 Voltage sensing unit

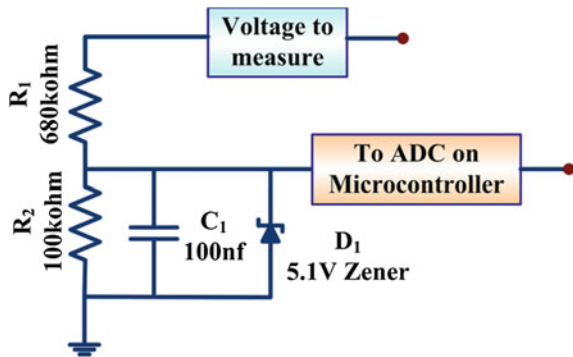
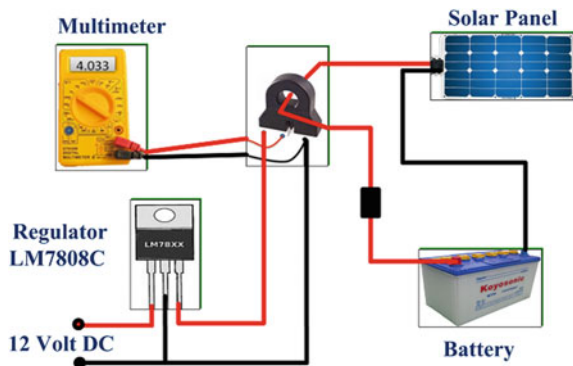


Fig. 5 Current sensing unit



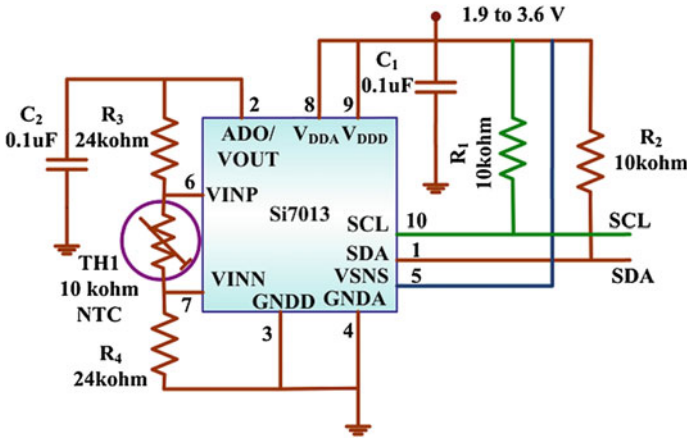


Fig. 6 Humidity and temperature sensor

3.2 Humidity and Temperature Sensor

For an Internet of Things (IoT) application, the humidity measurement using large footprint is no longer suitable. A Single-Chip Relative Humidity and Temperature Sensors, SI7013, with fully calibrated sensing elements, on chip analog to digital converter with signal conditioning circuitry is used in proposed system. It also provides an Inter-Integrated circuit (I²C) interface with processing unit for operating range from 0 to 80% relative humidity (RH) of humidity sensor and from -10 to 85 °C temperature range for temperature sensor. A thermistor is used to measure the temperature at remote location with the help of the auxiliary analog pins as shown in Fig. 6.

4 Performance Evaluation

Remote monitoring of PV panel is achieved through machine-to-machine ‘Internet of Things’ connectivity protocol MQTT, which is used to transport message at remote location. Launch Pad has two analog inputs, which are used to capture solar system performance parameters directly connected to sensor. On chip 10 bit ADC convert these inputs in digital form for further processing. During normal operating conditions, system sends the message to smart phone as well as publishes on cloud as shown in Fig. 7. Input received from temperature and humidity sensor is directly logged to memory, as it is I²C compatible and further it is sent on Internet.

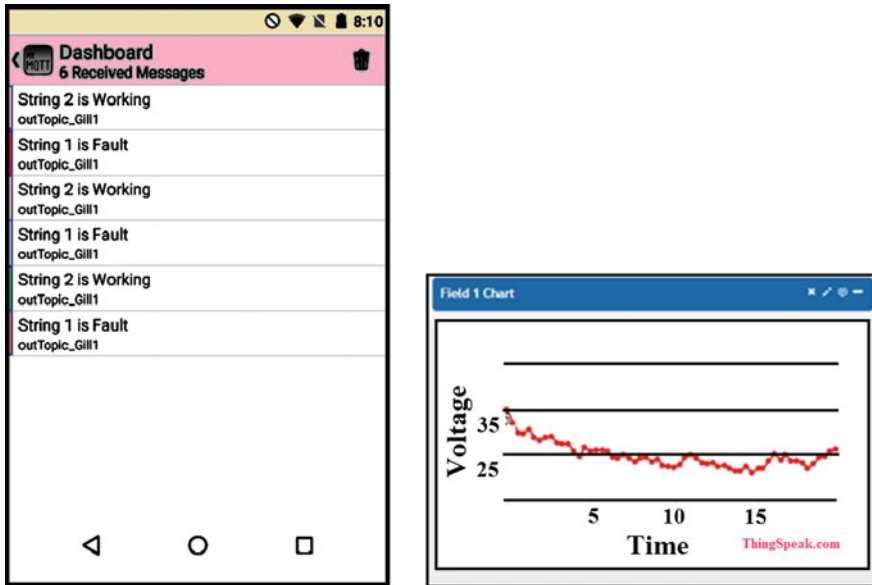


Fig. 7 Performance result (received by smart phone and cloud)

5 Conclusions

In this work, a wireless remote monitoring system for solar photovoltaic (PV) plant is proposed. Proposed wireless remote monitoring system is offering an automated cost-effective solution for measurement of solar PV parameters on real time. It is flexible system and can easily be expanded with more number of strings at ultra-low-power consumption. On chip facilities, such as ADC of high resolution and Wi-Fi connectivity reduces system size to a great extent.

References

1. Othman, N.A., Damanhuri, N.S., Ibrahim, I.R., Radzali, R., Mohd, M.N.: Automated monitoring system for small scale dual-tariff solar PV plant in UiTM Pulau Pinang. In: Proceedings of the World Congress on Engineering, Vol. II, London, UK (2010)
2. Zahran, M., Atia, Y., Abdullah A., El-Sayed I.: Wired and wireless remote control of PV system. WSEAS Trans. Syst. Control **5**(8), 656–666 (2010)
3. López, M.E.A., Mantiñan, F.J.G., Molina, M.G.: Implementation of wireless remote monitoring and control of solar photovoltaic (PV) system. Transmission and Distribution: Latin America Conference and Exposition, pp. 1–6 (2012)
4. Tejwani, R., Kumar, G., Solanki, C.: Remote monitoring for solar photovoltaic systems in rural application using GSM voice channel. ISES Sol. World Congr. 1526–1535 (2013)

5. Al-Dahoud, A., Fezari, M., Belhouchet, F.Z.: Remote monitoring system using WSN for solar power panels. *First International Conference on Systems Informatics, Modelling and Simulation*, pp. 120–125 (2014)
6. Nagalakshmi, R., Babu, B.K., Prashanth, D.: Design and development of a remote monitoring and maintenance of solar plant supervisory system. *Int. J. Eng. and Comput. Sci.* **3**(12), 9382–9385 (2014)
7. Narayan L.P., Anshika: Data acquisition of solar power plant using scada system. *Int. J. Eng. Trends and Technol.*, **23**(4), 189–194 (2015)

Design and Implementation of Solar-Powered Low-Cost Model for Greenhouse System

Shrivardhan Suryawanshi, Sudha Ramasamy, S. Umashankar and P. Sanjeevikumar

Abstract In the recent scenario, monitoring the greenhouse automatically with solar energy is the need of the hour due to power constraints and climatic change. The proposed system introduces a new technique for monitoring and controlling the greenhouse environment. This paper focuses on low-cost sensor modules for Arduino microcontroller. We are measuring three sensing parameters like humidity, temperature and soil moisture and displaying the current environment scenario on the LCD screen. These physical parameters are continuously monitored, based on the requirement the actuators are controlled like natural heating unit, cooler and sprinkler. These actuators are driven by microcontrollers through a relay. We have implemented an effective power management unit which is driven by solar power. Proposed system has an extra feature of detecting animal intrusion system, and its implementation is done in small scale.

Keywords Animal intrusion system · Farmland · Greenhouse · Solar Low-cost sensors

S. Suryawanshi · S. Ramasamy (✉) · S. Umashankar
School of Electrical Engineering, Vellore Institute of Technology (VIT) University,
Vellore, Tamil Nadu, India
e-mail: sudha.r@vit.ac.in

S. Suryawanshi
e-mail: shrieducation1@gmail.com

S. Umashankar
e-mail: umashankar.s@vit.ac.in

P. Sanjeevikumar
Department of Electrical and Electronics Engineering, University of Johannesburg,
Auckland Park, Johannesburg, South Africa
e-mail: sanjeevi_12@yahoo.co.in

1 Introduction

Due to high growth of population, there is a huge gap between production of grain and demand. In India, many states are facing scarcity of food. Farmers are not getting proper returns of their investments. Each farm land has different types of soil moisture, humidity and temperature. According to these conditions, soil productivity differs from every part of the country. Greenhouse system is basically a system with the ability to control conditions affecting the surrounding area of crops. Automation plays an important role in agriculture sector. Application of automation in farm field will be useful to farmers. It will surely reduce the headache of the farmer. This proposed system is controlling uncertain conditions of weather. Farmers will have to monitor the system with some threshold conditions they require. In our algorithm, we have made a small model of greenhouse. In this model, we have controlled relay of an actuator with a microcontroller. We are considering here mainly three relays for small-scale application. That are sprinkler, heater and cooler. Using solar energy for power management will reduce dependency of farmers on conventional electricity. In this system, we have just introduced prototype for solar energy usage in an efficient manner. The proposed system is cost-effective and easy to implement in farm land. We also touched on the topic of damage reduction in the farmland. Most of the time animals are damaging green areas. This paper introduces a method to avoid animal intrusion in farmland [1]. There are many strategies to implement the control system for greenhouse environment. It explains about the design and implementation of control with sensors and actuators. It includes data collection from sensors and uses that data to implement control using the Arduino platform. The same control can also be implemented for home automation. One of the papers explains about implementing wireless sensor networking using ZigBee for precision in agriculture. They implemented two identical setups: one is exposed to the natural environment, and the other one is under control environment. The sensor temperature, humidity and soil moisture provide the data to the Arduino Mega controller. Using wireless networking, the data from the sensors are collected wirelessly using the ZigBee module. Other paper explains about an automated control system for Arduino and Android-based greenhouse. It explains about control of the greenhouse and two-way communication between greenhouse and Android. For the wireless communication, Wi-Fi module is used. Some paper even introduces the concept of neural network in the database of soil moisture and humidity. Most of the algorithm depends on technical agendas which are very hard to apply to systems in village areas [3].

2 Implementation System Block Diagram

Heart of the proposed system is microcontroller. Controlling parameter is the main aim of greenhouse algorithm. Figure 1 shows the block diagram of proposed system which contains Greenhouse soil, Signal Conditioning Circuit, Microcontroller, Actuators, LCD Screen, Solar panel and Power management unit.

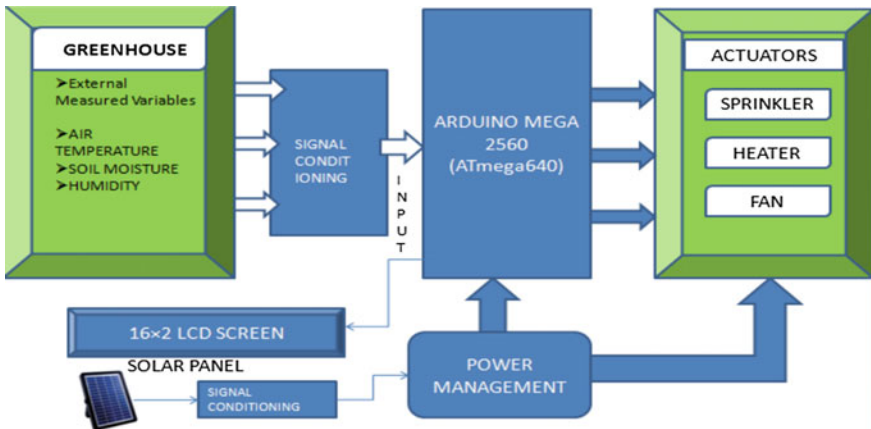


Fig. 1 Block diagram of greenhouse monitoring system

Field sensors are reading analog inputs from the greenhouse and sending it to the signal conditioning circuits. The signal conditioning module will convert signals from analog to digital. Temperature and humidity are sensed by a special purpose module called DHT11. It contains small electrode on which moisture of air will get deposited. Another task for a greenhouse is to measure soil moisture and quality, and soil moisture content can be measured by two electrodes placed in soil. These electrodes are transmitting values in analog format [4].

There are totally 3 input signals to the microcontroller. All input signals are merged together in the controller. Microcontroller is taking corrective action in a greenhouse environment. Proposed system uses an Arduino mega microcontroller. This controller is very efficient and easy to program. Arduino is advantageous as it can control not only greenhouse, but also water management system, natural heating and cooling system. In our case, for the sake of simplicity, we have considered three actuators. Sprinkler, natural heating element and cooler are the actuators taken into consideration. For each threshold, we will energize the relay to control greenhouse environment. The relay is an intermediate stage between supply and actuator device. Energizing the relay will change its contacts from ground to supply voltage [5]. Conventional system does not have the facility to continuously monitor and display it on screen. In our algorithm, we are using normal 16×2 LCD screen to display the current condition of the system. Closed-loop system will increase the accuracy of controlling parameter. The user gives feedback to microcontroller, in terms of parameters related to the sensing element. According to set point of microcontroller, it will take approximate 5 s to control the environment in the greenhouse. This step will definitely ensure higher productivity of crops. Three actuators and sensors will require effective power management. Keeping in mind about low-cost implementation, we can implement whole power unit with the help of renewable energy. In this proposed algorithm, we have implemented a prototype of solar energy. In India, almost every part of the country is having very good solar

energy radiations. A developing power management system based on solar energy will reduce dependency on conventional electricity distribution board [1]. When user wants maximum results out of his greenhouse, he should also consider the damage to the greenhouse system. In India, farmers are facing a very bad situation due to animal intrusion to the farmland. The proposed paper explains implementation of intrusion detection system in small scale. That will enhance farmland productivity [6].

3 Comparison of Conventional and New Algorithm

This section discusses about comparison of newly proposed algorithm with conventional algorithm. After rigorous supervision of the literature survey, it can be easily inferred as a new algorithm is more efficient and productive. Let us start with vegetation quality, vegetable quality will definitely improve because of supervised farming (Table 1).

The farmer is having all types of access to his greenhouse so that he can set the threshold values. There is a 5 s time lag between setting thresholds and taking particular actions. Conventional system is totally based on systems with non-renewable energies. Actuators like sprinklers, fan, and heater are usually taking lots more power from electricity board. This increases load on conventional electricity board. Newly proposed algorithm introduces prototype to control all these things in renewable energy. Solar energy with advanced technology is used in this algorithm to reduce dependency on conventional fuel. After implication of this system, we can note that productivity of land is increasing. This prototype takes some time to adapt to natural conditions. Conventional system requires a lot of manual work, such as switching ON/OFF sprinkler, turning ON/OFF temperature control unit. Proposed system is automated version of conventional systems. Many algorithms focus on desired output with a different technique. This algorithm will focus on cost optimization with damage reduction [7].

Table 1 Response time of the system

Comparison		
Parameters	Conventional	Proposed system
Vegetation quality	Lower	Will be improved
Fuel cost	Higher	Will be lower
Productivity	Lower	Will increase
Manual work	Require	Won't require

Fig. 3 Soil moisture sensor implementation

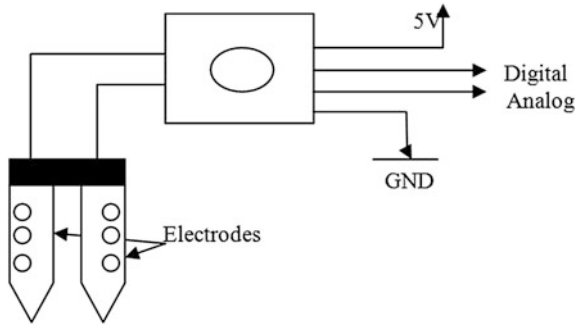
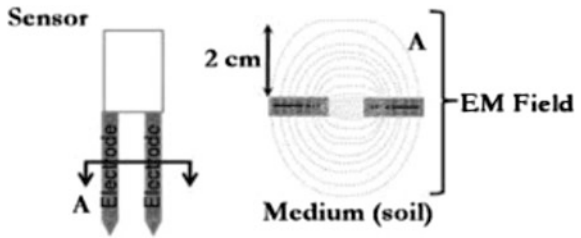


Fig. 4 Working of soil moisture sensor



immediately respond to host. When we are using single bus sequence, we can access a single device. The device will not respond to any problematic sequence [10] (Figs. 3 and 4).

4.2 Soil Moisture Sensor

Soil moisture sensors will measure capacitance, and it will find permittivity of the surrounding medium. In soil, dielectric permittivity is proportional to content of water. This project uses sensors which create a voltage proportional to the dielectric permittivity. As per the construction given in the figure, sensor averages the water content over the entire length of the sensors. There are around 3-cm sensitive areas around flat sensing element. The edges of this sensor are most sensitive to soil content. We regularly use soil sensors to: (1) measure the loss of moisture; (2) monitor soil moisture requirement for each crop. The sensor can be calibrated when we require more accuracy. If standard soil moisture content is known to us, we will get accurately calibrated results [11].

4.3 Animal Intrusion System

There is another issue for the greenhouse that animals can enter and eat the crops or damage the system. In India, it happens usually that animals enter into farmland and destroy all the crops and this costs a lot for the farmers. Authors are proposing a low-cost approach for detection of animal intrusion. Here, we use LDR with a laser system as shown in Fig. 6. We are using two LDRs and two lasers to detect whether animals enter the greenhouse. This system will detect only animals and not human. Animals can be detected at night with the help of laser and LDR technology. We are using XOR logic gates to implement this system in a simpler way. In the proposed system, we have considered a 6-feet-taller wall with a laser mounted on it. Only two lasers are enough for detection purpose. The EXOR gate will give output when only one laser is working and the other is intruded by the animal. The output of EXOR gate is given to buzzer. When human passes through that same area, it will avoid

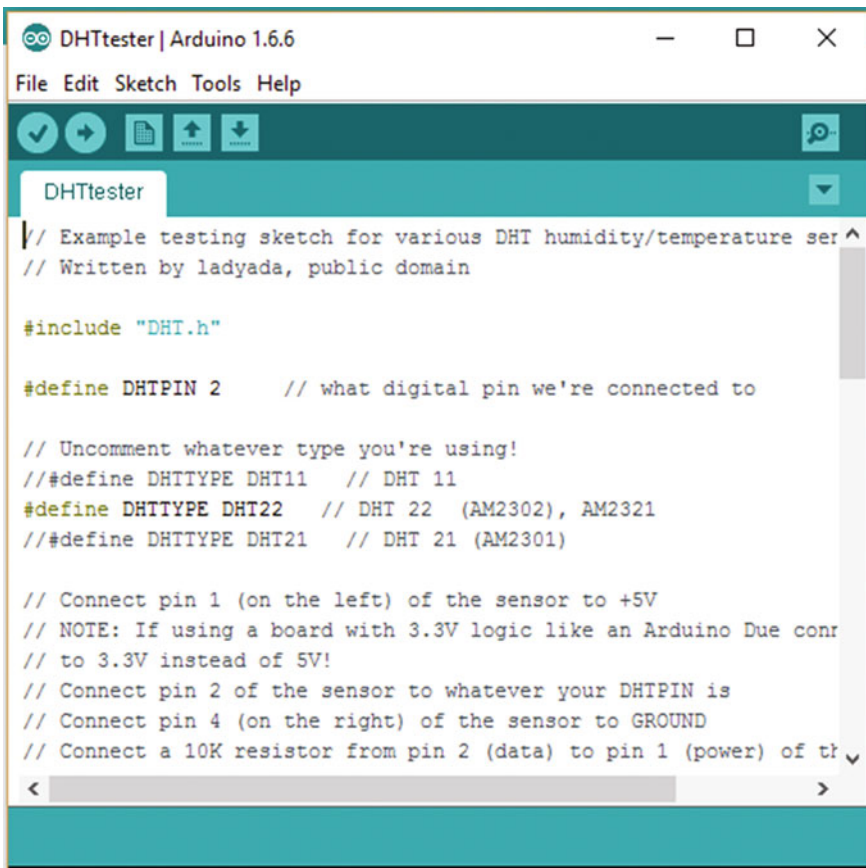
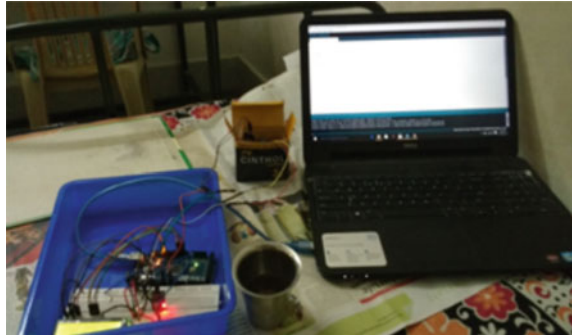


Fig. 5 Software implementation

Fig. 6 Hardware implementation of real-time system



buzzing because lasers are aligned in such a way that human will block light coming from both the lasers. In this way, the animal intrusion system is designed and implemented. Low-cost implementation is the main agenda of our algorithm, and we can adapt the technology of renewable energy 96% of solar energy still unused [8] (Fig. 5).

In India, almost all farmland is having very good sunlight. The solar panel is most probably used where all types of energies are less accessible. Most of the village areas can be converted into solar utility sectors. Using three types of actuators with the controller will require more amount of energy. That energy can be taken from either conventional electricity or solar-generated energy [9]. Software used in this proposed system is Arduino IDE 1.6.6. This software is well known for its simplicity. SETUP and LOOP can be programmed as per user's convenience. As per the name is stating about starting up and setting up something, in this section of programming, we have initialized all I/O pins for a microcontroller. Resembling features of C, here we have the declaration of variables they are mostly global variable. Then, it comes to initialization of hardware peripherals. We initialize ultrasonic sensor pump relay, infrared sensor and other required components. LOOP part contains a cyclic programming of algorithm [1].

5 Results and Discussion

The algorithm proposed in this paper is implemented in small model. It will replicate in large manner with high success rate. Sensors like humidity, temperature and moisture are designed in such a way that it will give optimum results. In our algorithm, we have implemented three actuators that are sprinkler, cooler, heater. Threshold for each actuator control signal is given by farmers. Now, if we consider that the farmer has set the parameters at time t , then that parameters will take action at $t + 5$ s to whole plant. There is only a 5 s delay possible between actual and desired results. Considering software requirement and programming this algorithm is a comparatively easy algorithm. Another part is the animal intrusion system,

where we have implemented XOR logic with LDR and laser. This intrusion system is most effective and implemented in less cost [9].

6 Conclusions

This paper is the basic idea of smart farmland. If smart cities can be developed, then smart farms can also be developed. We can add wireless technology to this prototype using XBee, Bluetooth or Wi-Fi. The farmer can actually control all parameters by sitting at home. There is much more to do with automation when it comes to farmhouse. We need to give more attention to make our country again independent of food.

References

1. Lukas, B., Ondrej, K.: Design and realization of low cost control for greenhouse environment with remote control. *IFAC-PapersOnLine* **48**(4), 368–373 (2015)
2. Teslyuk, T., Denysyuk, P., Kernysky, A., Teslyuk, V.: Automated control system for arduino and android based intelligent greenhouse. In: *The XI International Conference on Perspectives Technologies. and Methods in MEMS Design (MEMSTECH'15)*, Lviv, pp. 7–10 (2015)
3. Eldhose, K.A., Antony, R., Mini, P.K., Krishnapriya, M.N., Neenu, M.S.: Automated greenhouse monitoring system. *Int. J. Engg. Innov. Technol.* **3**(10), (2014)
4. Bhuvaneswari, T., Yao, J.T.H.: Automated greenhouse. In: *IEEE International Symposium Robotics and Manufacturing Automation*, Kuala Lumpur, pp. 194–199 (2014)
5. Asolkar, P.S., Bhadade, U.S.: An effective method of controlling the greenhouse and crop monitoring using GSM. In: *International Conference on Computing Communication Control and Automation (ICCUBEA'15)*, Pune, India, pp. 214–219 (2015)
6. Baviskar, J., Mulla, A., Baviskar, A., Ashtekar, S., Chintawar, A.: Real time monitoring and control system for green house based on 802.15.4 Wireless Sensor Network. In: *4th International Conference on Communication Systems and Network Technologies (CSNT'14)*, Bhopal, India, pp. 98–103 (2014)
7. Hanggoro, A., Putra, M.A., Reynaldo, R., Sari, R.F.: Green house monitoring and controlling using android mobile application. In: *International Conference on Quality in Research (QiR'13)*, Yogyakarta, pp. 79–85 (2013)
8. Lee, J., Kang, H., Bang, H., Kang, S.: Dynamic greenhouse supplemental light source control with wireless sensor network. In: *International Conference on ICT Convergence*, Jeju Island, pp. 23–27 (2012)
9. Jafar, I.B., Raihana, K., Bhowmik, S., Shakil, S.R.: Wireless monitoring system and controlling software for smart greenhouse management. In: *International Conference on Informatics, Electronics and Vision (ICIEV'14)*, Dhaka, Bangladesh, pp. 1–5 (2014)
10. <http://www.datasheetspdf.com/datasheet/DHT11.html>
11. <http://www.vernier.com/files/manuals/sms-bta.pdf>

Sustainable Organic Farming in Sikkim: An Inclusive Perspective

Jitendra Kumar, Meghan Pradhan and Niti Singh

Abstract The study explores the current trends of organic farming in the Sikkim where almost 80% people still depend upon agriculture and allied activities. State has become the first organic state with adoption of 100% organic farming by preserving its rich natural resources with abundant flora and fauna, vibrant ecosystem and soil fertility with high organic matter content. It has become the major exporter for fruits, flowers, spices and vegetable in recent years. This case study illustrates the various phases of organic farming in Sikkim, India, associated stakeholders and constraints in terms of infrastructure particularly irrigation, transportation and electricity, and financial and marketing constraints for higher output and income realization.

Keywords Organic farming · National Program of Organic Production (NPOP) Sustainable development · Sikkim · India

1 Introduction

With the advent of the Green Revolution, use of machinery, improved irrigation and synthetic agrochemicals particularly fertilizers and insecticides became integral part for enhancing agricultural production and productivity at a national level for food security. However, excessive and unplanned use of such chemicals and irrigation facilities has adversely affected the soil fertility (through land degradation, soil salinization and genetic erosion) and resulted in decline in ground water level,

J. Kumar (✉) · M. Pradhan · N. Singh
Department of Management Studies, Sikkim Manipal Institute of Technology,
Sikkim, India
e-mail: jitendra1_smit@yahoo.co.in

M. Pradhan
e-mail: pmegen@yahoo.com

N. Singh
e-mail: nitisingh85@gmail.com

distress in marginal and small farmers due to high input costs, and total replacement of local indigenous farm practices in the last four decades. Thus, outcome of this revolution has compelled the nation to rework towards sustainable and a more balanced approach. Organic farming is a technique of cultivating the land and raising crops with only organic inputs such as crop, animal and aquatic wastes, farm wastes and other biological materials along with beneficial microbes to retain the soil fertility and increase the nutrients level of the land, thus providing sustainable production in an eco-friendly manner for further consumption.

Based on the literature reviews performed on the issue, study finds the some India centric study. Organic in organic agriculture signifies products that have been manufactured with certain standards during production, processing, handling and marketing stages. The produced items are certified by a constituted certification authority [1]. The organic label is a process claim rather than a product claim. The implementation of soil and water management is the important element of rain-fed farming. That is why these two are considered as the important pillars of organic farming. Protecting the soil to conserve moisture and increase the nutrition level of the soil by mulching, cover cropping, green leaf manuring and residue management are some other vital approaches of organic production methods [2]. The enormous benefits of organic and conventional agriculture in order to attain sustainable food safety; organic, conventional, and 'hybrid' structure nutrition to be produce at reasonable prices, to guarantee livelihoods for the growers, and decrease the environmental expenses in cultivation [3]. The implementation of organic farming in Sikkim and examined its cascading impact on other non-farm activities development with reference to governmental policies related to organic farming. Organic farming does not only promotes only agricultural sector but also promotes the entire economy having direct impact on improving socio-economic condition of the people in general and for the farmers in particular [4]. Conventionalization, regulations and agri-business are major threat for the organic farms to attain resilience-building potential [5]. The soil health measured by pH, soil organic matter and phosphorus, input, labour, marketing strategies, organizational factors like inter-farm competitive and cooperative relations are some important attributes for organic farm profitability [6]. Traditional farming systems approach of Sikkim state presents sustainable solution for ongoing climate problems by acting as perennial carbon sinks [7]. Land management practices intending to promote biodiversity and soil quality are significant drivers of sustainable organic agriculture [8]. Study suggests that farm productivity in organic and conventional farming remains same in three Indian states namely Madhya Pradesh, Uttarakhand and Tamil Nadu. Further, input cost declines in organic farming than that in conventional farming system [9]. The rest part of the paper is organized as follows. Section 2 deals with scope of organic farming in India followed by current trends of organic farming in particular Sikkim. Section 4 concludes the study.

2 Scope of Organic Farming in India

Having diverse geographical and climatic conditions across nation provides suitable environment for different kinds of agricultural farming particularly in terms of type (food crops including cereals, pulses and oilseeds, horticulture, floriculture, medicinal and aromatic plants, apiculture and sericulture) and its variety. With people becoming more health aware and nature friendly and due to its rising demand in domestic and international levels, Government at federal and state level initiated focusing on organic farming for sustainable farming practices by further updating technology, quality and agro-infrastructure.

It has an added advantage as several states still continue the traditional way of farming. Nowadays, high demand for organic products has been felt, and it encourages the organic growers to produce more. The premium export marketplace is significantly growing at the average rate of 15–25% annually. Presently, in world, India ranks 33rd position as per the total cultivated land area under organic farming. India is the net exporter of over 300 organic products under 19 types, such as cotton and textiles, basmati and non-basmati rice, oil crops, tea and coffee, spices, dry fruits, cereals, spices, medicinal and herbal plants, vegetables, aromatic oil and pulses to the Europe, Canada, USA and Asian countries (Fig. 1).

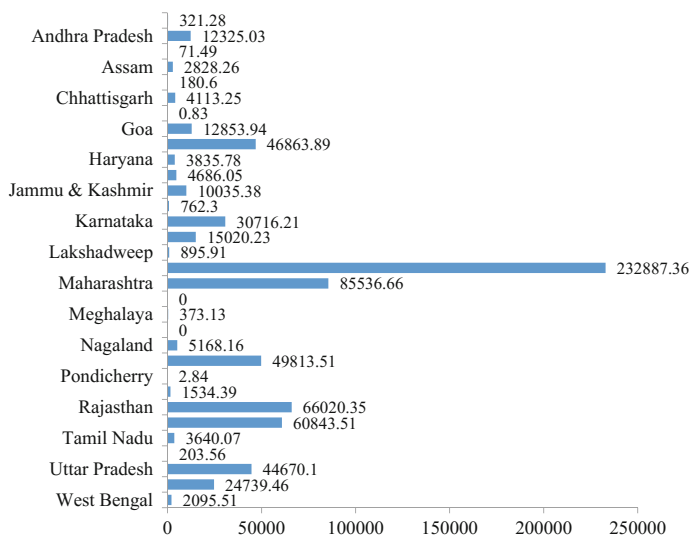


Fig. 1 State-wise farm area in hectare (excluding forest area) under organic certification during 2013–14

3 Organic Farming in Sikkim

Sikkim is the 22nd state of the Republic of India integrated in 1975 with just 7096 km² (709,600 ha) of territorial area and 6 lakhs population (Census 2011). However, only 10.47% area is being used for the farming activities, and the remaining areas consist of uncultivable area, cultural waste, permanent pastures, forest area and barren land. Almost 85% of population in the North, South and West Sikkim still lives in the rural area against the average of 75%. More than 60% state population depend upon agriculture and allied activities for their livelihood with a mere contribution of 8% in state economy. Thus, understanding the future potential of the agriculture for more inclusive and faster development, Sikkim Legislative Assembly passed a resolution to adopt organic farming in early 2003. This pace could not move fast until Sikkim Organic Mission was started on 15 August 2010. About 74,000 ha of agricultural land covering the whole state has been certified as organic. Sikkim is the first state in the country to officially adopt and become a totally organic farming state in the end of December 2015. The farming system practiced since ancient time is an integrated farming system where crops and animals are grown together and are codependent. Farming is done under rain-fed condition due to lack of assured irrigation infrastructure facility and geographical hilly location. Thus, emphasis is given to high-value low-volume crops which give good economic return. The varied agro-climatic condition of the state gives scope for cultivation of crops suitable in subtropical-to-temperate climate. Since the climate is humid with good vegetation, the soil is rich in organic carbon leading to good nitrogen availability. Honourable Prime Minister also commended the initiative of Government of Sikkim to make Sikkim an organic state during his address in a joint session of parliament, New Delhi, in April 2014.

3.1 *Benefits of Organic Farming for Sikkim*

- Sikkim's soil contains 2–7% organic carbons indicating its richness in organic matter contents, thus requiring very low consumption of pesticides and chemical fertilizer. Average limited fertilizer (7 kg/ha) and negligible pesticide use prior to 2003 do not any adverse effect on yield per hectare even after gradual adoption of organic farming.
- More emphasis on bio-fertilizers, organic manures and pesticides thus reduces the dependence on external inputs up to certain extent.
- Only 11% of total geographical area is under agricultural activities. However, remaining 89% geographical area had not been affected by the influence of pesticides, fertilizers and other agrochemicals.
- Based on rain-fed farming system due to lack of proper irrigation infrastructure and hilly geography thus contributing to water conservation.

- Improves agro-biodiversity (both varieties and crops) conservation and environmental protection in long run.
- With the adoption of locally suitable methods and inputs for agriculture further reduces the cost of production by approximately 25–30%.
- Organic farming enhances and protects traditional knowledge of farming, agricultural processing and new seed improvement for the betterment of future generation.
- About 10,000 ha area under large cardamom¹ farming with zero fertilizer use can be easily brought under organic farming.
- Potential for environmentally sustainable tourism development based on organic farms.
- Premium price in the domestic and international markets due to rising demands from health- and environment-conscious people.

3.2 Area Covered for Organic Farming in Sikkim

Sikkim Organic Mission prepared a three-phase execution plan to make Sikkim an organic state in line with National Programme of Organic Production (NPOP) guidelines. Table 1 provides a snapshot of phase-wise organic farming area targets and achievements. The state total area under organic farm achieved was 56777.59 ha against the target of 50,000 ha. Thus, state has always excelled against its targets in all three phases with an average of 113.55%.

Table 2 shows the district-wise and phase-wise organic farming area targets and achievements (in hectares). During phase 1, South Sikkim performed best followed by West Sikkim, East Sikkim and North Sikkim as second, third and fourth, respectively. However, East and North Sikkim were having maximum and minimum area covered under organic farming during phases 2 and 3, respectively.

The average land holding for organic farming among four districts is maximum in North Sikkim (1.96 ha), but minimum in East Sikkim due to higher population concentration in the district in phase 1. Almost 43% of Sikkim population lives in East Sikkim. These areas have achieved organic certification by NPOP. Similar trends were also found in remaining two phases. During phase 2, organic certification particularly for Internal Control System (ICS²) development involved the participation of the more numbers of service providers like SIMFED, IPL, Sresta and Moraka. Against a target of converting 50,000 ha, a land of 56,771 ha has been certified at the end of phase 3. Certifying agencies like OneCert Asia, Lacon, IMO control, Moraka, Ecocert, Justrop and SGS were more active in the state.

¹Sikkim is the largest producer of large cardamom in the India with annual production of 4500 MT (more than 88% of total production).

²Internal Control System (ICS) is the process taken by various service providers to inspect and certify that the process of organic farming is maintained as per the NPOP.

Table 1 Sikkim Organic Mission phase-wise targets and achievements

S. No.	Phase	Financial year	Proposed area (in ha)	Achieved area (in ha)	Achieved %
1	<i>Phase 1</i>	2010–11	18,000	18234.33	101.31
2	<i>Phase 2</i>	2011–12	18,000	19255.11	106.17
3	<i>Phase 3</i>	2012–13	14,000	19283.15	137.73
Total			50,000	56777.59	113.55

Source Sikkim Organic Mission—journey of a fully organic farming state (2015)

Table 2 District-wise and phase-wise targets and its achievements (in ha) and number of farmers involved

Particulars	Districts	Phase 1	Phase 2	Phase 3
District-wise and phase-wise area of achievement in Sikkim	East	4900	6019	7613
	South	5466	4573	4486
	West	5118	5301	6390
	North	2755	3361	791
Project-wise number of farmer involved in Sikkim	East	4455	5364	4227
	South	4524	5259	4227
	West	3850	4923	5263
	North	1403	2268	627
District-wise and phase-wise area holding (in ha per farmer) in Sikkim	East	1.10	1.12	1.045
	South	1.20	0.86	1.06
	West	1.33	1.07	1.06
	North	1.96	1.48	1.26

Source Sikkim Organic Mission—Journey of a fully organic farming state (2015)

The total number farmers involved in organic farming cultivation are 14,232, 17,814 and 17,333 during phase 1, 2 and 3, respectively. The farmers are benefitted as organic farming helps to retain and sustain the nutrients of the soil as well as higher financial return on their investment. Thus, it helps them to maintain the complex agro-ecosystem, decreases the risk of health ailments and contributes to ample scope for farming by fetching premium price for the organic products. East Sikkim has seen maximum participation of the farmers during the three phases, whereas North Sikkim has minimum number of farmer's participation. Though, South Sikkim has seen maximum involvement of organic farmers during phase 1.

3.3 Production and Productivity of Crops in Sikkim

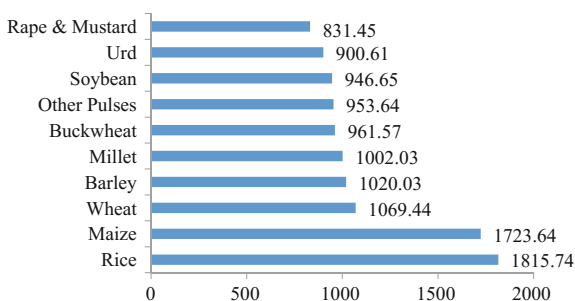
The climate is humid with good vegetation; the soil is rich in organic carbon leading to good nitrogen availability. The use of fertilizers and pesticides is curbed by the government by reducing the subsidy by 10% every year to make the fertilizers and pesticides more expensive. Thus, high cost of fertilizers and pesticides and state ban on transporting of these chemicals from outside state discourage the farmers for its uses in farming. About 11% of the total area is under agriculture, and 89% of the area has not been affected by the use of chemicals. The government has taken various measures such as initiating vermin culture hatcheries, government farms, bio-fertilizer, rural compost pit, organic manure, effective microorganism (EM) technology, seed processing unit, integrated pest management and establishment of organic school on organic farming. The main crops of Sikkim are maize and rice among cereals; soybean and mustard among oilseed; urd and rice bean among pulses, respectively. Ginger, cardamom, turmeric and cherry pepper are important spices. Figure 2 provides the crop productivity of major crops in the state during the year 2013–14. Crop productivity is maximum in rice, followed by maize, wheat, barley, millet and buckwheat.

Figure 2 provides some details regarding fruits and vegetables productivity in the state. Maximum productivity is in case of tomato, followed by bitter gourd and carrot. The state remains net exporter for the organic fruit and vegetables in the domestic as well as international markets due to its premium price advantages (Fig. 3).

Figure 4 suggests that productivity is maximum in case of ginger followed by Rabi potato, other roots and tuber, Kharif potato and turmeric, and least in case of large cardamom.

Sikkim has maximum production of the Gladiolus, followed by Lilium, Cymbidium, Roses, Calla Lily, Gerbera, Alstroemeria Eria, etc., as shown in Fig. 5. These expensive flowers have very good demand in developed cities particularly metros and international markets.

Fig. 2 Productivity (kg/ha) of field crop in Sikkim (2013–14)



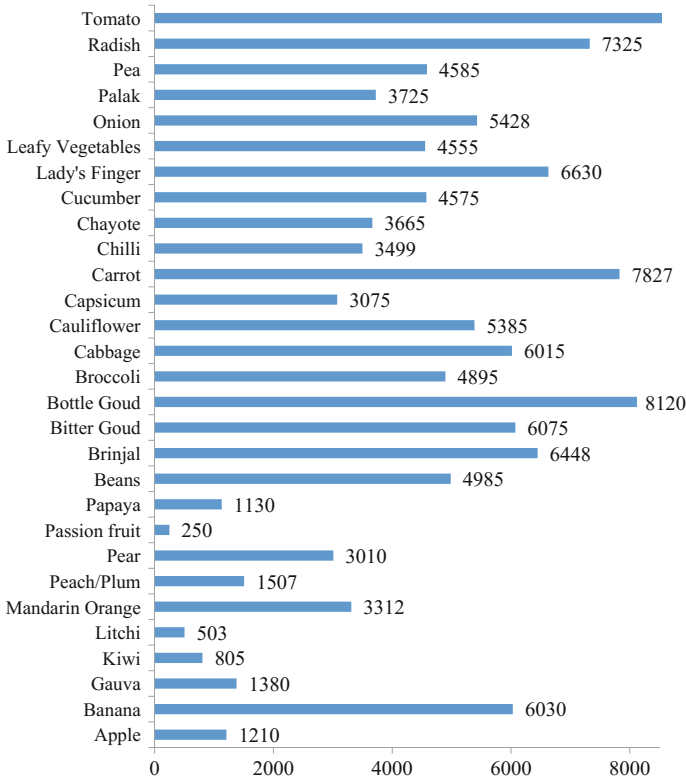
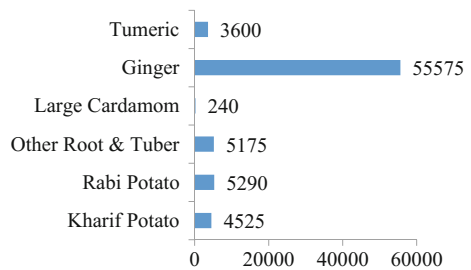


Fig. 3 Productivity (kg/ha) of fruits and vegetables in the Sikkim (2013–14)

Fig. 4 Productivity (kg/ha) of roots and spices in the Sikkim (2013–14)



3.4 Service Providers in Sikkim

The torch of the organic mission was carried forward by various service providers. Sikkim State Cooperative Supply and Marketing Federation Limited and International Panaacea Limited provide basic organic goods for bulk marketing to the consumers and remedy for healthy agricultural practices, respectively. Sresta

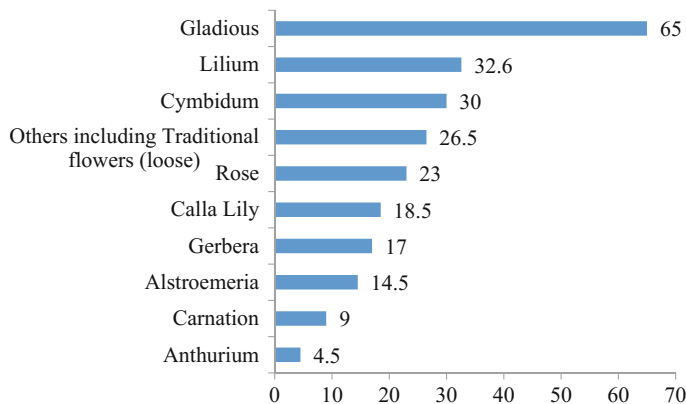
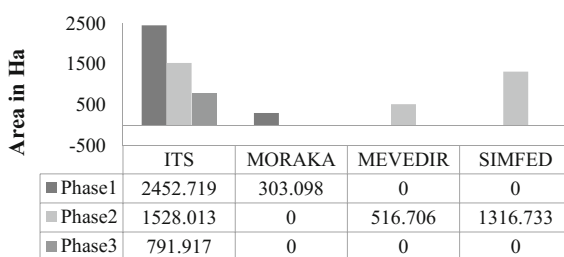


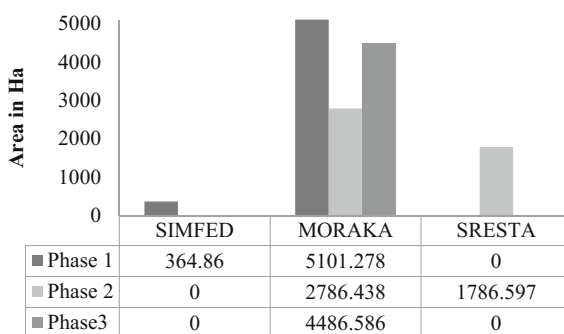
Fig. 5 Productivity (in lakhs) of flowers in Sikkim (2013–14)

Fig. 6 Active service providers in the North Sikkim region



focuses on creating better livelihood for the organic growers across state for better price realization of their products. Moraka provider plays a vital role in improving productivity of ginger, whereas Sheel Biotech Limited takes care for floriculture and agro-management practices. Mevedir provides complete agricultural practices solution related with specifically crop post-harvest. ITS, SIMFED, MEVEDIR and Moraka are the four major active service provider in the northern region of the state for organic cultivation. ITS has the highest area coverage during all the phase, followed by SIMFED and Mevedir in phase 2 (Figs. 6 and 7).

Fig. 7 Active service providers in the South Sikkim



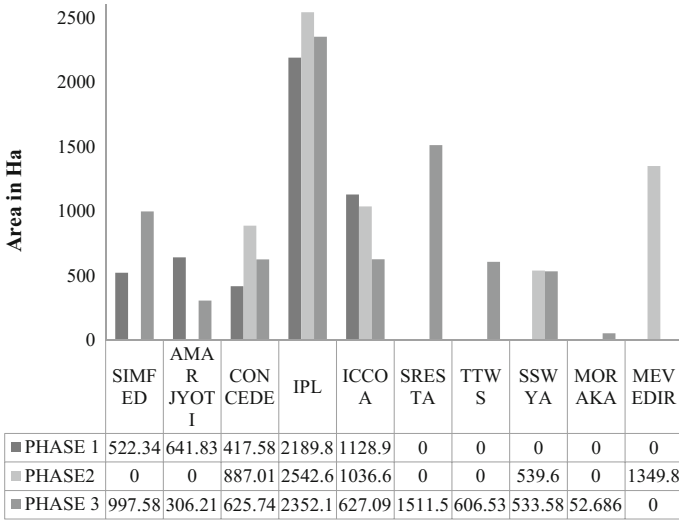


Fig. 8 Active service providers in the east region during the three phases

Moraka, Sresta and SIMFED are three most active service providers in the South Sikkim with maximum coverage by Moraka (Fig. 8).

East Sikkim has found very high amount of active service providers comprising of SIMFED, AMAR JYOTI, CONCEDE, IPL, ICCOA, SRESTA, TTWS, SSWYA, MORAKA, and MEVEDIR. IPL lead as active service provider in the district. However, Sheel Biotech followed by Mevedir and Justrup Organic Sikkim is the most active West Sikkim (Fig. 9).

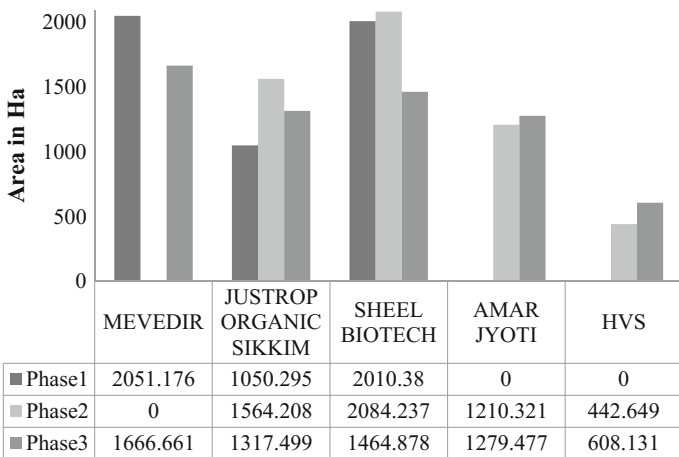


Fig. 9 Active service providers in the West Sikkim

3.5 Marketing of Organic Products

To have a structured organic market, the Government of Sikkim has recognized 187 grower groups and functioned for certification for about 300–450 farmers as per the APEDA rules. The certification process and expenditure have been fully funded by the state government due to high cost involvement. Thus, group certification is conducted in order to encourage the growers with respect to production preparation, post-harvest management and marketing of their products.

Organic farming has brought in a lot of scope and development in the state of Sikkim, but the marginal farmers are still deprived of their beneficial aspects. Thus, study proposes Gujarat-based cooperative model with the active involvement of various stakeholders with minimum government interference in currently operational SIMFED. Cooperative like Amalsad, Amul, Gambheera or Mulkanoor are still relevant and economically successful in their respective initiatives. Here, cooperation collects the raw products from the farmers and then makes it available in the market for the consumers bringing economy of scale in the process with collective interest. Better price realization needs effective marketing and supply chain management due to product-specific requirement. These activities cannot be taken by the individual marginal farmers due to capital investment and efforts needed. SIMFED Cooperative (at the village or block or even district level) model can be further strengthened where marginal farmers producing the same products can come together as collective and can access to the common facilities of resources leading to higher productivity. The growers can then avail a chance of direct interaction with the buyers to sell their products with no interference of intermediaries as recently introduced in Maharashtra. Farmers should use government buildings and places for direct selling of their crops or vegetables with some token payment to the government for sharing the basic facilities. In this way, the growers may get sufficient profit and motivated for further improving productivity. Thus, government should frame some mutual beneficial law for further empowering SIMFED for international exports for better price realization and minimizing the overall wastage.

4 Conclusion

The continuous upgradation of the organic farming should remain the focus area for the state as nearly 85% population in the North, South and West Sikkim are still rural. Their livelihoods remain agriculture and its allied activities. Organic farming brings balances among the complex agro-ecosystem minimizing environmental, soil-related problems, other biological problems in long run. Its return in term of money as well as glory will be adequate enough for the state for uplifting its socio-economic conditions. Any hindrance particularly agricultural and transportation infrastructure with adequate supplies of the inputs need for organic

farming needs to handle with great care. Any supply-side failure will need to rework whole process leading to delayed fulfilment of state objectives with very high cost. As a matter of time, organic farming has taken a new shape and direction towards the development of agriculture, health and market.

References

1. Ramesh, P., Singh, M., Rao, S.A.: Organic farming: its relevance to the Indian context. *Curr. Sci.* **88**, 561–568 (2005)
2. Venkateswarlu, B.: Organic farming in rainfed agriculture: prospects and limitations. *Organic farming in rainfed agriculture. Opportunities Constraints* **7**, (2008)
3. Hazarika, S., Manoj, K., Thakuria, D., Bordoloi, L.J.: Organic farming: reality and concerns. *Indian J. Hill Farming* **26**, 88–97 (2013)
4. Chettri, B.: Organic farming in Sikkim: implication for livelihood diversification and community development. Doctoral dissertation, Sikkim University (2015)
5. Milestad, R., Darnhofer, I.: Building farm resilience: the prospects and challenges of organic farming. *J. Sustain. Agric.* **22**(3), 81–97 (2003)
6. Sheahan, C.M., Bray, D.B., Bhat, M.G., Jayachandran, K.: Ecological, economic, and organizational dimensions of organic farming in Miami-Dade County. *J. Sustain. Agric.* **36**, 83–105 (2012)
7. Sharma G., Dhakal T.: Opportunities and challenges of the globally important traditional agriculture heritage systems of the Sikkim Himalaya. *Biodiversity of Sikkim: exploring and conserving a global hotspot*. IPR Department, Government of Sikkim, Gangtok, pp. 411–440 (2011)
8. Underwood, T., McCullum-Gomez, C., Harmon, A., Roberts, S.: Organic agriculture supports biodiversity and sustainable food production. *J. Hunger Environ. Nutr.* **6**, 398–423 (2011)
9. Panneerselvam, P., Hermansen, J.E., Halberg, N.: Food security of small holding farmers: comparing organic and conventional systems in India. *J. Sustain. Agric.* **35**, 48–68 (2010)

Investigations of Microgrid Stability and Optimum Power Sharing Using Robust Control of Grid Tie PV Inverter

G. Swaminathan, V. Ramesh, S. Umashankar and P. Sanjeevikumar

Abstract This paper demonstrates a novel method to establish robust control and stability of microgrid connected with photovoltaic (PV) grid tie inverter, battery storage with bidirectional inverter, and diesel generator. The proposed control scheme enables optimum power sharing among the sources based on the changes in generation due to intermittent nature of PV source and level of energy stored in battery. Power flow control has been achieved by varying the active power generated by the PV inverter as a function of the system frequency in the islanded mode of operation. Detailed analysis has been carried out in MATLAB/Simulink tool and the captured results are found to effective and same has been confirmed with hardware prototype setup with PV inverter and bidirectional battery charger.

Keywords Microgrid · Photovoltaic inverter · Battery · Active power control
Phase locked loop (PLL)

G. Swaminathan · V. Ramesh · S. Umashankar (✉)
School of Electrical Engineering, Vellore Institute of Technology (VIT),
Vellore, Tamil Nadu, India
e-mail: umashankar.s@vit.ac.in

G. Swaminathan
e-mail: cg.swaminathan@gmail.com

V. Ramesh
e-mail: vramesh@vit.ac.in

P. Sanjeevikumar
Department of Electrical and Electronics Engineering,
University of Johannesburg, Auckland Park, Johannesburg, South Africa
e-mail: sanjeevi_12@yahoo.co.in

1 Introduction

Microgrid constituted by aggregation of renewable energy sources like solar, wind, fuel cells and battery energy storage devices, traditional diesel generator and utility grid. The penetration of renewable sources helps in reducing carbon foot print and in turn reduces global warming. In today’s scenario, the larger amount of world population completely rely upon traditional source of energy, such as coal-fired thermal power plant, oil and natural gas powered plants. Day by day, the conventional energy sources reserves are getting depleted, but the energy demand and per capita energy consumption are growing rapidly. This situation necessitates the integration of sustainable sources of energy into the regular energy network. The initiatives like introduction of federal tax incentives, feed in tariffs are the main driving factors for rapid increase in penetration of PV source. As the PV source is highly intermittent in nature, nonavailability of PV during night time has resulted in need for the integration of energy storage to ensure the system stability. In this paper PV inverter, battery storage system with bidirectional inverter and a diesel generator has been integrated to form a microgrid [1]. The power electronic converters are used to convert the PV source of energy to AC energy at different level [2]. Figure 1 shows the schematic diagram of microgrid system under consideration. The output AC power produced at the PV inverter, bidirectional converter of

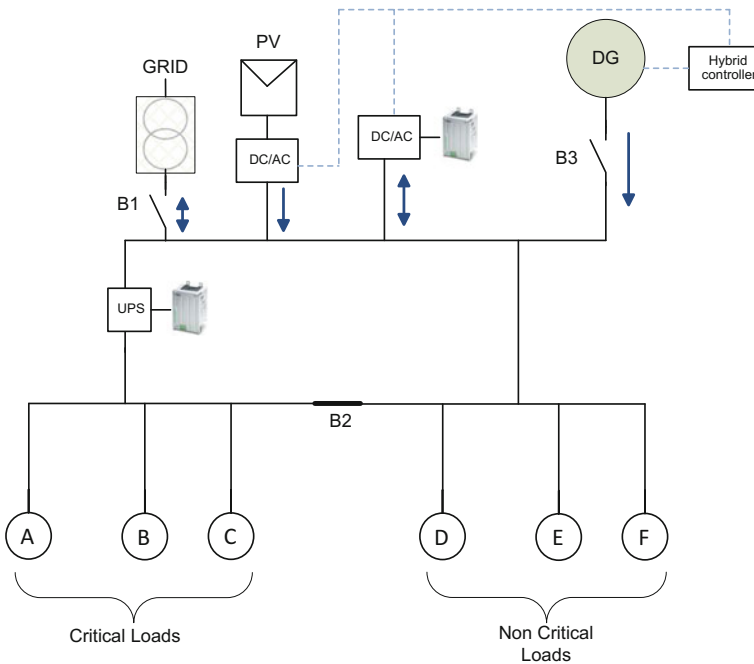


Fig. 1 Microgrid network schematic diagram

battery storage unit and diesel generator terminals is connected to the local loads and to the mains [3]. The connected loads are classified into two categories, critical loads and noncritical loads (shed-able). In the absence of utility grid, bidirectional converter will act as a voltage source reference for PV grid tie inverter to continue power generation to the microgrid. If diesel generator is present in the system, then voltage reference will be provided by the generator. PV inverter will detect the presence of voltage reference and start generating power [4, 5]. During off-peak load conditions, the available PV energy is used to charge batteries.

2 Problem Definition

In the event of utility grid outage and during islanded mode of operation of microgrid, the PV inverter to AC couple with the AC outputs of off-grid energy sources like non-grid tied bidirectional converter coupled with battery storage. PV inverters are typically designed to operate on highly stable grids and required to aggressively protect from destabilizing the grid under dynamic load conditions or when utility generation (grid formers) exhibits over or under excitation. During such scenarios, PV inverters are required to coexist with DC coupled charge controllers and participate in load and battery management [6]. This requires all energy sources and sinks in a system to communicate demand and constraints effectively. This can be achieved in a number of ways, and the authors present a control algorithm to achieve this through is modulation of frequency at a common point of coupling.

3 System Configuration

The system configuration details presented in Table 1 were used as the basis for modeling and simulation analysis. All noncritical (shed-able) loads are disconnected when the grid is not present and hence, they are not considered in the off-grid (islanded mode) scenario. To serve all critical loads, a separate UPS is

Table 1 Microgrid system configuration

Microgrid system capacity	25 kVA, 400 V—3PH + N, TT grounding
PV generation	20 kVA, 400 V, 3 PH, 4 wire transformerless
Battery storage	1200 Ah, 5 kW
Diesel generator	10 kVA, 400 V—3PH, 4 wire
UPS—online	10 kVA, 400 V, 3PH, 4 wire
Critical loads (3-ph)	400 V—3PH + N: 8 kVA, PF 0.93
Noncritical loads (1-Ph)	Ph 1-N 230 V, lighting, 7 kVA, PF 0.7
Noncritical loads (1-Ph)	Ph 2-N 230 V, air condition: 7 kVA, PF 0.7
Noncritical loads (1-Ph)	Ph 3-N 230 V, lighting: 7 kVA, PF 0.7

provided during grid outage and thus, they are also not included during the off-grid condition when battery storage is feeding the network. After grid loss, the time taken by the battery storage unit to ramp up and to be able to feed these loads is 0.8–1 s. Modeling of various blocks and the methodology used to generate reference currents for the PV inverter is explained in following sections.

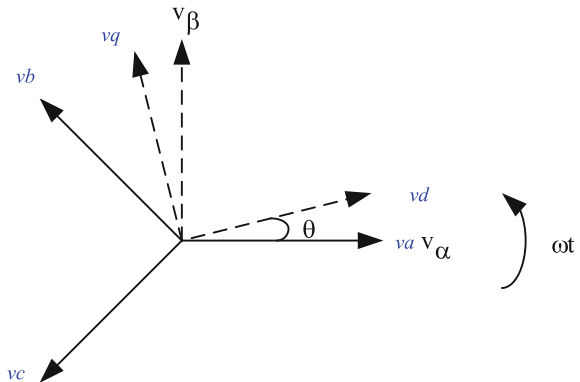
4 Control System Design

4.1 Phase Locked Loop (PLL) Control System Design for PV Inverter Synchronization with Reference Voltage

The objective of PLL is to lock the inverter phase to the grid or reference voltage that is present in the network [7]. A space vector comprising V_q and V_d can be derived from a three-phase source using Clarke–Park transforms. If the voltage space vector of reference voltage (V_d) is aligned to d axis, then corresponding space vector component for q axis (V_q) will be zero (Fig. 2). Following equations represent three-phase grid voltage vectors (a, b, c) and their ab and d–q axis transformation voltages. To achieve successful synchronization, the $\theta = \omega t$ in Eq. (3).

$$\begin{aligned}
 v_a &= V_m \cos(\omega t) \\
 v_b &= V_m \cos\left(\omega t - \frac{2\pi}{3}\right) \\
 v_c &= V_m \cos\left(\omega t - \frac{4\pi}{3}\right) \\
 \theta &= \omega t
 \end{aligned}
 \tag{1}$$

Fig. 2 Three-phase vector representation in d – q axis



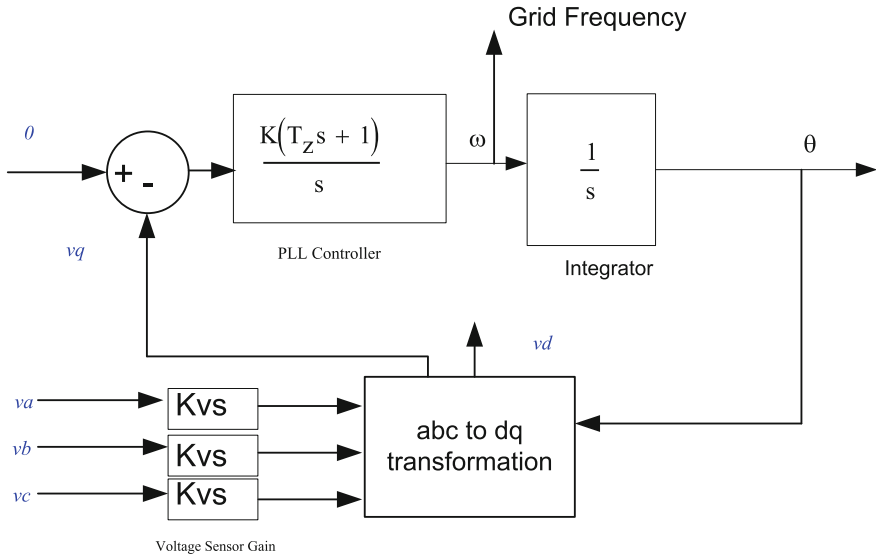


Fig. 3 PLL block diagram

$$\begin{aligned}
 v_\alpha &= v_a \\
 v_\beta &= \frac{(v_b - v_c)}{\sqrt{3}}
 \end{aligned}
 \tag{2}$$

$$\begin{aligned}
 v_d &= v_\alpha \cos \theta + v_\beta \sin \theta \\
 v_q &= -v_\alpha \sin \theta + v_\beta \cos \theta \\
 v_d &= V_m \cos(\omega t - \theta) \\
 v_q &= V_m \sin(\omega t - \theta)
 \end{aligned}
 \tag{3}$$

Figure 3 represents block diagram of PLL control implementation. The simulation results for voltage waveforms in abc frame and ab frame are shown in Fig. 4. From 0 to 0.3 S, no disturbances were created; from 0.3 to 0.4 S, one-phase voltage magnitude reduced to create unbalance. From 0.4 to 0.5 S, the voltage magnitude for all the three phases reduced equally; from 0.5 to 0.55 S, huge unbalance has been created. From the resultant waveform, the response time of PLL control is fast and also the synchronization with the reference voltage is achieved.

4.2 System Stability Control in Off-Grid Mode

When the grid voltage disconnects from the network, the PV inverters will cease power generation immediately, and this will prevent any back feeding of power

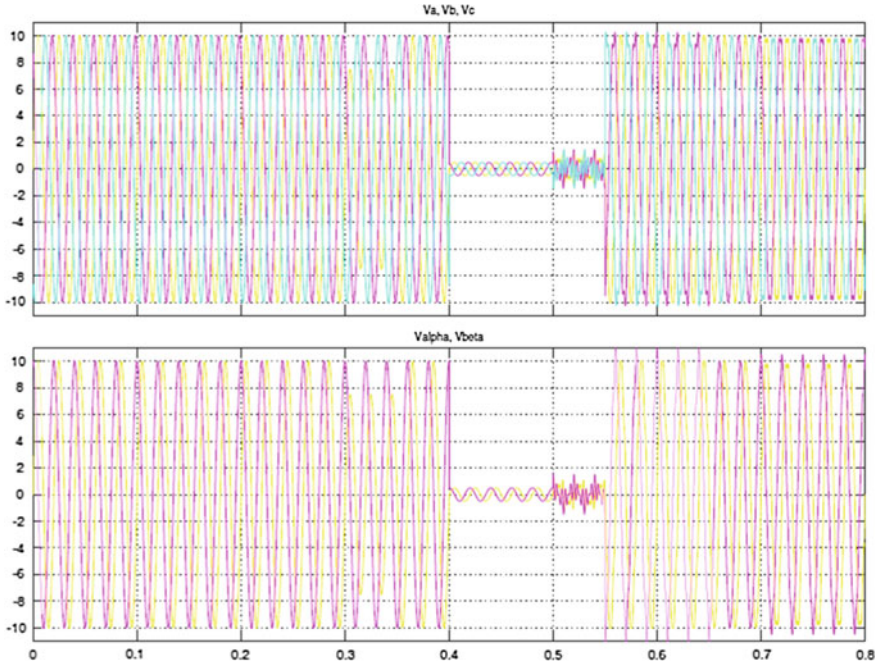


Fig. 4 PLL controller output voltage waveforms for balanced and unbalanced reference voltage inputs

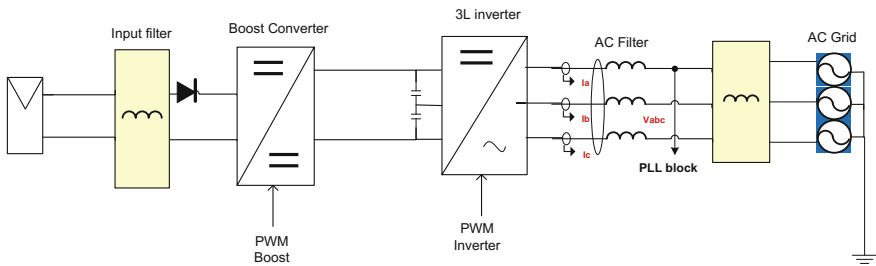


Fig. 5 PV inverter block diagram

from PV generator to diesel generator in the same network [8]. The Fig. 5 shows the block diagram of PV inverter. During utility grid outage, the PV inverters control to be designed for taking voltage reference from bidirectional inverters connected with battery storage. Typically the PV inverters will have anti-islanding capability by checking grid impedance. For grid forming, the PV inverter takes the voltage reference from battery inverter output and PLL block will synchronize PV inverter output to the bidirectional inverter output and thus emulate the grid condition for sustained operation. Once the voltage synchronization is achieved, it is important to

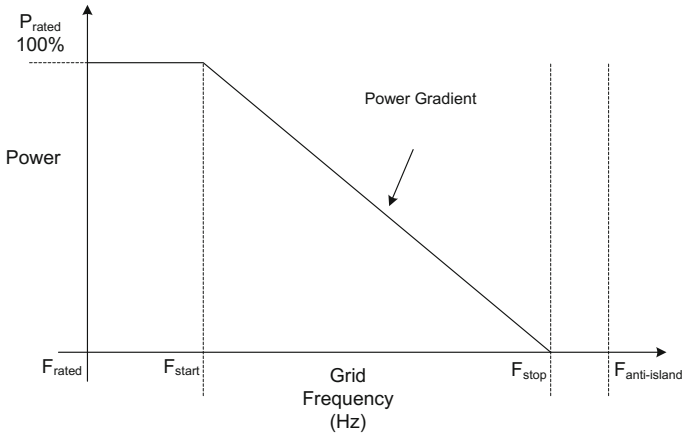


Fig. 6 Power gradient diagram for active power (P) versus frequency (F) control function

ensure the stability of the system by controlling active power as a function of frequency. Figure 6 depicts the gradient curve for power as a function of frequency. At F_{start} , the PV inverter will start to derate active power. At $F_{anti-island}$ frequency, the PV inverter will disconnect from the network. The slope will define the derating as % power reduction with regard to frequency. At F_{stop} frequency, active power derating will reach 0%.

4.3 Power Sharing Control Between Battery and Loads from PV Source

Considering the operation microgrid network in the absence of utility grid, and as per Fig. 1, the breaker B1 is open and connected load is lesser than the power available at PV inverter output terminals. Under this condition, the generated power from PV source will be injected into the bidirectional inverter, and control loop of battery inverter will switch the power flow direction as it detects the increased power availability at its output terminals. Now the batteries will start charging from the PV generation. Once the battery attains sufficient charge level, the bidirectional inverter will increase the AC output frequency and thus forcing PV inverter to follow the gradient control of active power reduction as per the increase in frequency values. If the battery voltage drops, then frequency will reduce and hence active power generation will ramp up. The proposed control system has been implemented in digital signal processor TMS320F28335 and tested with hardware setup as shown in Fig. 7. The captured test results are plotted in Fig. 8.

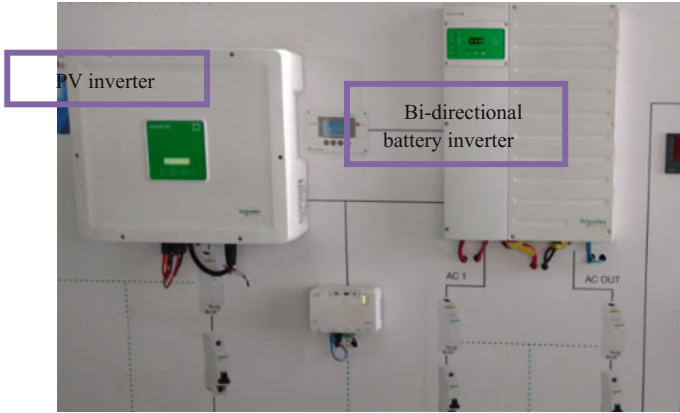
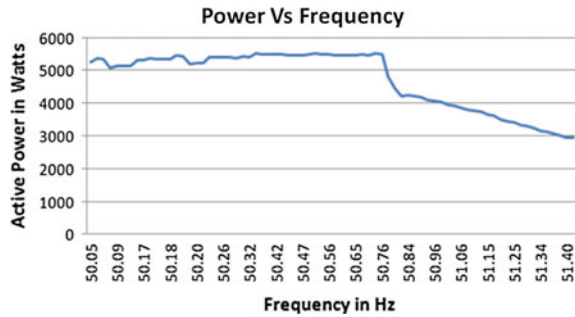


Fig. 7 Prototype test set up

Fig. 8 Test results of PV inverter control of active power output as a function of versus Frequency in off-grid mode of operation in microgrid system



5 Conclusion

The proposed control blocks have been simulated using MATLAB/Simulink, and the results are evident that the PV inverter disconnects from the microgrid network soon after the utility grid disappears. The bidirectional inverter with battery storage unit supplies the reference voltage to PV inverter for grid forming. Once the PV inverter detects reference voltage, automatically synchronizes with battery inverter and start generating power, during this mode of operation, the PV energy can be utilized for serving load and charging the battery. The diesel generator can also be integrated to the microgrid network to serve the load during higher load demand and in the absence of PV source in the night times. The proposed control logic proves that the PV inverter stays connected in the microgrid system during utility grid outage and forms AC grid with battery inverter. With the implementation of active power control as a function of frequency, the stability of off-grid mode of operation is ensured.

References

1. Gaurav, S., Birla, C., Lamba, A., Umashankar, S., Ganesan, S.: Energy management of PV–battery based microgrid system. *Procedia Technol.* **21**, 103–111 (2015)
2. Ganesan, S., Ramesh, V., Umashankar, S.: Performance improvement of micro grid energy management system using interleaved boost converter and P&O MPPT technique. *Int. J. Renew. Energy Res.* **6**(2), (2016)
3. Wu, B., Kouro, S., Malinowski, M., Pou, J., Franquelo, L.G., Gopakumar, K., Rodriguez, J.: Recent advancement in industrial application of multilevel converter. *IEEE Trans. Ind. Electron.* **57**(8), 2553–2580 (2010)
4. Kim, S.K., Jeon, J.H., Cho, C.H., Kon, S.H.: Dynamic modeling and controls of a grid-connected hybrid generation system for versatile power transfers. *IEEE Trans. Ind. Electron.* **55**(4), 1677–88 (2008)
5. Padmanaban, S., Grandi, G., Blaabjerg, F., Wheeler, P.W., Siano, P., Hammami, M.: A comprehensive analysis and hardware implementation of control strategies for high output voltage DC–DC boost power converter. *Int. J. Comput. Intell. Syst.* **10**(1), (2017)
6. Pota, H.R., Hossain, M.J., Mahmud, M.A., Gadh, R.: Control for microgrids with inverter connected renewable energy resources. *IEEE PES General Meeting, Washington DC*, 27–31 July 2014
7. Adhikari, S., Li, F.: Coordinated V-f and P-Q control of solar photovoltaic generators with MPPT and battery storage in microgrids. *IEEE Trans. Smart Grid* **5**(3) (2014)
8. Lin, R., Yang, M., Li, H.: Analysis of parallel photovoltaic inverters with improved droop control method. *International Conference on Modeling and Applied Mathematics (MSAM 2015)* The authors—Published by Atlantis Press

Design and Graphical Analysis of 8-kW Off-Grid Solar Photovoltaic Power System

Nikhil Kumar Yadav and Dharmendra Kumar Singh

Abstract In this paper, a 8-kW off-grid photovoltaic system is presented for Korba Collectorate Office which is situated in mid-Korba District, Chhattisgarh. This off-grid system comprises 30 solar photovoltaic panels, battery bank, solar power conditioning unit, lightning arrester, distribution panels and important electrical components such as MCCB and conductors. The rating of all these equipments is mathematically calculated and presented. The expected energy of this system is obtained by the System Advisor Model (SAM) Software designed by National Renewable Energy Laboratory (NREL). Finally, the simulation result of the system is presented and compared with the actual output measured from the system. This off-grid system reduces the dependency on grid and promotes power system security, and it also offers financial saving up to 16,000 rupees every month.

Keywords Grid · SAM · MCCB · NREL · Lightning arrester

1 Introduction

The Korba Collectorate Office Latitude is 22.367750° north and the longitude is 82.734607° east. Its elevation is 316 m above sea level. The 8-kW solar photovoltaic system is installed by Chhattisgarh Renewable Energy Development Agency. Solar electrical power system reduces the monthly electricity bill up to 16,000 Indian Rupees per month. This system provides green energy which helps in maintaining the ecological balance of the city. The data are collected with the help of various electrical equipments and software like SAM, RET Screen Plus and

N.K. Yadav (✉)

Institute of Technology Korba, Korba, Chhattisgarh, India
e-mail: nikhil14.nikhil@gmail.com

D.K. Singh

Department of Electrical and Electronics Engineering, Dr. C.V. Raman University,
Bilaspur Kargi Road Kota, Bilaspur, Chhattisgarh, India
e-mail: dmsingh2001@rediffmail.com

MATLAB. This system promotes power system security and reduces the power dependency on coal and fossil fuel.

2 Methodology

The Korba is industrial power hub and surrounded by thermal power stations from all sides. The monthly average wind speed of Korba is 3.2575 km/h. The wind speed is maximum, i.e., 3.86 km/h in the month of March, and the speed of wind is minimum in the month of October. The solar insolation plays a vital role in the production of electricity. The voltage and current are directly dependent on the solar radiation incident on the panel. There is increase in sunlight radiation from morning to afternoon; then, from afternoon to evening there is decrease in radiation. The Korba receives monthly solar radiation of 4.9291 kWh/month. The area covered by solar panels is 59.2 m² [1, 2] (Figs. 1 and 2).

Fig. 1 Solar panels at installed site. *Source* CREDA



Fig. 2 Satellite map of site. *Source* Google Map

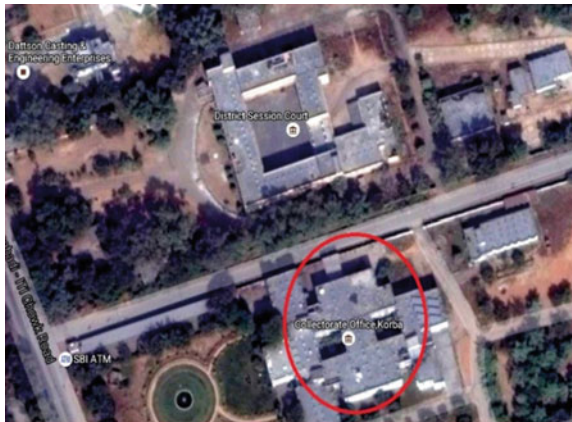


Table 1 Load consumption of various electrical equipments

Name of equipment	Quantity	Power consumption (W)	Usage in hours	Total electrical energy consumed (Wh)
A.C.	2	1800	7	25,200
Tube light	4	40	6	960
Fan	4	60	7	1680
Computer	2	150	6	1800
Printer	2	30	6	360
LED TV	1	70	2	140
CFL	8	20	10	1600
Biometric scanner	1	20	7	140
Miscellaneous	1	120	1	120
Total units = 32 kWh				

Table 2 Battery parameters chart

Average daily WH requirement	Days of autonomy	Battery temp. multiplier	Nominal supply from PV system	Discharge limit
32,000 (max. load in 24 h)	2	1.19 (for 25 °C)	120 V	50%

2.1 First Step: Load Estimation

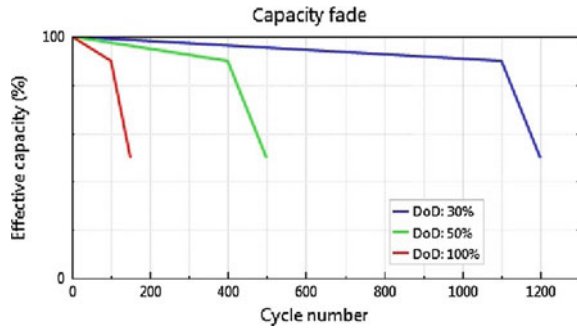
The maximum load that can be supplied from solar off-grid system is 32 units. The equipment-wise power consumption is given in Table 1.

2.2 Second Step: Battery Sizing

The sizing of battery is done as per the nominal supply voltage of PV system, days of autonomy, maximum load in 24 h and battery temperature multiplier. The battery temperature multiplier is taken 1.19 for 25 °C as per IEC [3, 4] (Table 2).

The days of autonomy decides the duration to provide continuous power to load in the absence of sunlight with the help of battery. Each cell of 2 V has capacity equal to 20 Ah. So, 60 cells are connected in series and strings in parallel are 20.

Fig. 3 Effective capacity versus no. of cycles curve



2.3 Calculation

$$32,000 \times 2 \times 1.19 \times 0.5 = 38,080$$

$$38,080 \div 120 = 317.33.$$

So, the battery of 120 V 400 Ah is selected for our system. If battery draining is 50%, it lasts for 500 cycles and if draining is 30%, it lasts for 1200 cycles (Fig. 3).

2.4 Third Step: Charge Controller Rating

Charge controller manages charging of battery, prevents overcharging and controls the rate of charging; nowadays, some charge controller provides automatic load disconnect function and it also prevents flow of charges from battery to panels at night. The maximum power point tracker (MPPT) charge controller is used in our system, and it tracks solar insolation and adjusts itself in such a way to get maximum output. Array and battery voltage mismatching can be easily managed with this controller [5].

2.5 Calculation

$$\text{MPPT Charge Controller Rating} = \text{Wattage of Panels} \times \text{No. of Panels} \div \text{System Nominal Voltage} \times 1.25.$$

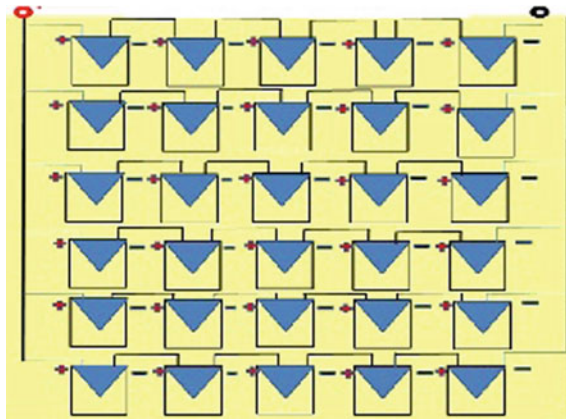
$$275 \times 30 \div 120 \times 1.25 = 55 \text{ A.}$$

So, 60-A MPPT charge controllers are used for the above configuration [3, 6–8].

Table 3 Watt solar module parameters

Parameters	Description	Parameters	Description	Parameters	Description
Manufacturer	HHV Solar	Isc.	8.21A	Frame	Anodized aluminum
Model number	HSTBF24275P	P_{max}	275 W	Junction box	IP67/4t/3Diodes
Maximum power (P_m)	275 W	Weight	22 kg	Warranty	15 years limited warranty
V_m	36.5 V	Type of cell	Mono crystalline silicon	Nominal voltage	24 V
I_m	7.53 A	Front face	Tempered glass	Vo.c.	44.3 V

Fig. 4 275 Wp solar module series-parallel connection



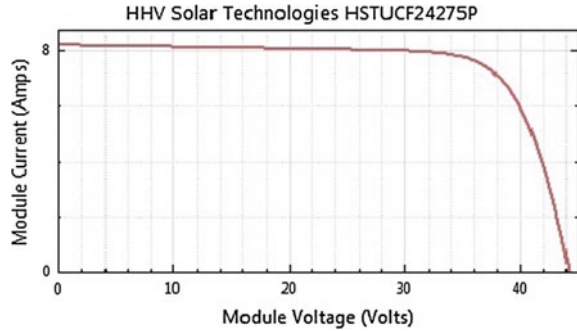
2.6 Fourth Step: Solar Array Configuration

Solar array is the device that converts the solar radiation into electricity without any intermediate steps. Modules have power rating from 1.5 to 300 W and are available nowadays, and several megawatt range can be easily generated by the formation of solar arrays with number of modules in series and parallel as per requirement [9].

In 8-kW off-grid system, solar panel of 275 Wp is used. It has following parameters (Table 3).

The 8-kW solar photovoltaic system has 5 modules connected in series, and these series strings are connected in parallel. The connection diagram is in Figs. 4 and 5.

Fig. 5 I–V characteristics of 275 Wp HHV solar module



2.7 Calculation

Number of modules in series = $V_{\max} \div V_m = 182.5 \div (36.5) = 5$

Number of modules in parallel = $I_{\max} \div I_m = 45.187 \div 7.53 = 6$

Maximum power of PV array = $P_m \times N_s \times N_p = 274.8 \times 5 \times 6 = 8244 \text{ W}$.

2.8 Fifth Step: Cables Rating

Here, 4, 10 and 25 mm² cables are used. 4 mm² cables are used for panel connections. Array junction box is connected to main junction box with the help of 10 mm² cable. After main junction box, the complete connections are made with 25 mm² cable [2, 9].

2.9 Sixth Step: Protection Equipment

The complete system has 2 lightning arrestors of 3000 mm mounted on walls both sides. The array junction box provides surge protection at 150 V earthing voltage. To avoid hot spot formation due to partial shading, bypass diodes are used, and to avoid flow of charge from battery to solar panel side, blocking diodes are used [2] (Figs. 6 and 7).

2.10 Software Analysis Report

The System Advisor Model software is used to perform the simulation task of 8-kW solar photovoltaic systems. The SAM is developed by National Renewable Energy Laboratory, and 2016 version is used. It offers simulations of entire renewable

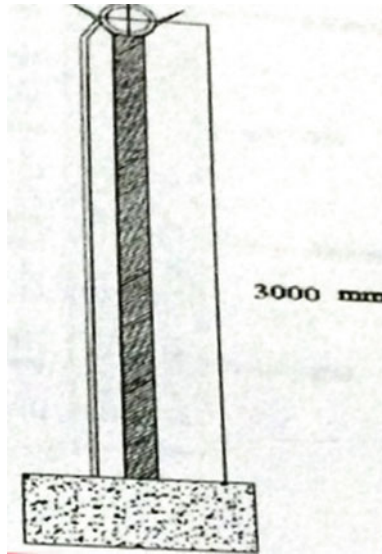


Fig. 6 Lightning arrester. Source CREDA

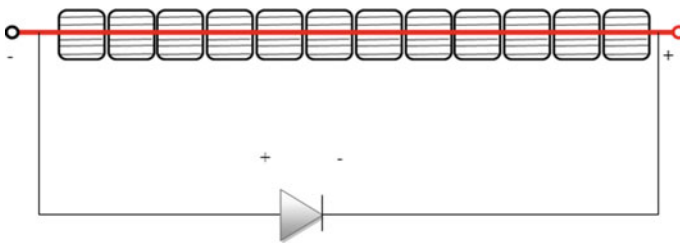


Fig. 7 Series connection of 12 solar cells with 1 bypass diode

energy sources and planning and detailed graphical results. The monthly curves for the system include wind data from SAM weather file, power to/from battery curve, power to load from photovoltaic system, power to load from grid, losses curve, estimated power output for coming 25 year and irradiance curves. One by one each graph is represented [1].

2.10.1 Wind Curve and Power Curve

The wind speed in m/s of the installed location is represented by the curve in Fig. 8.

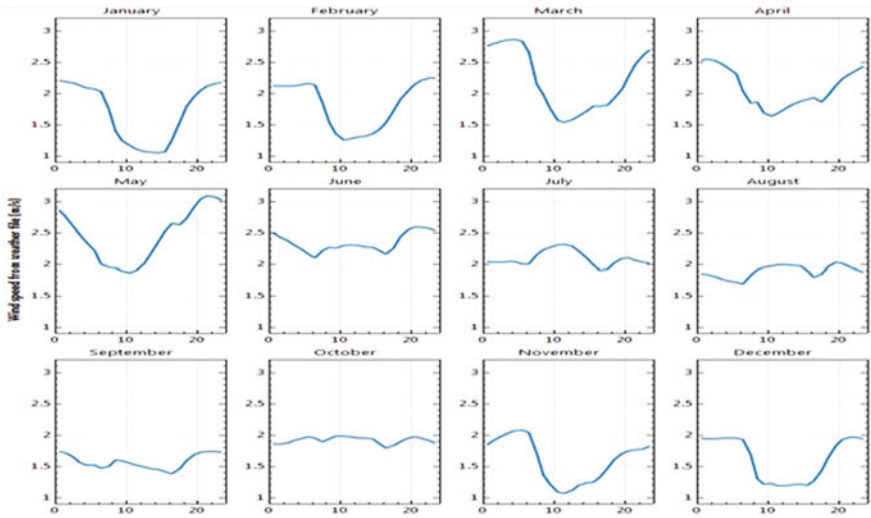


Fig. 8 Wind curve. Source SAM

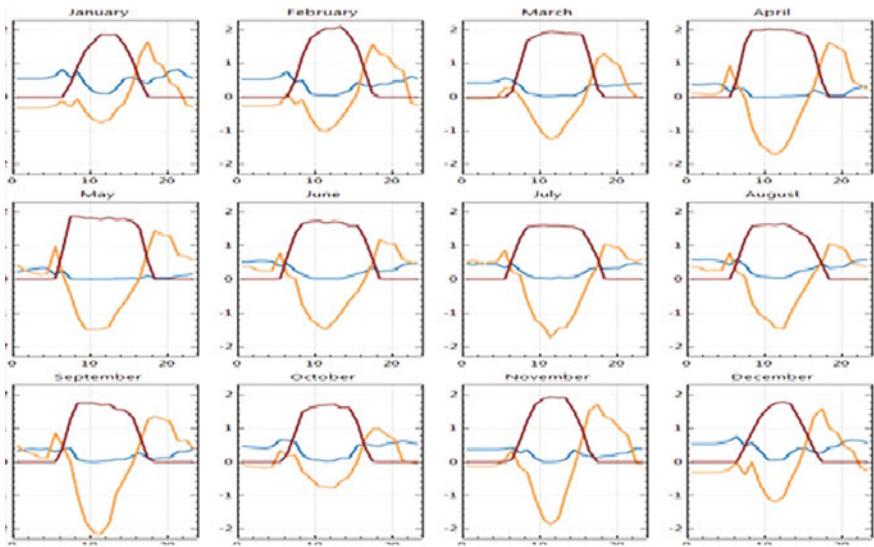





Fig. 9 Power graphs in kW

The power to/from battery in kW , power from grid in kW  and power from photovoltaic system in kW  are represented by the graph in Fig. 9.

2.10.2 Irradiance Curve

See Fig. 10.

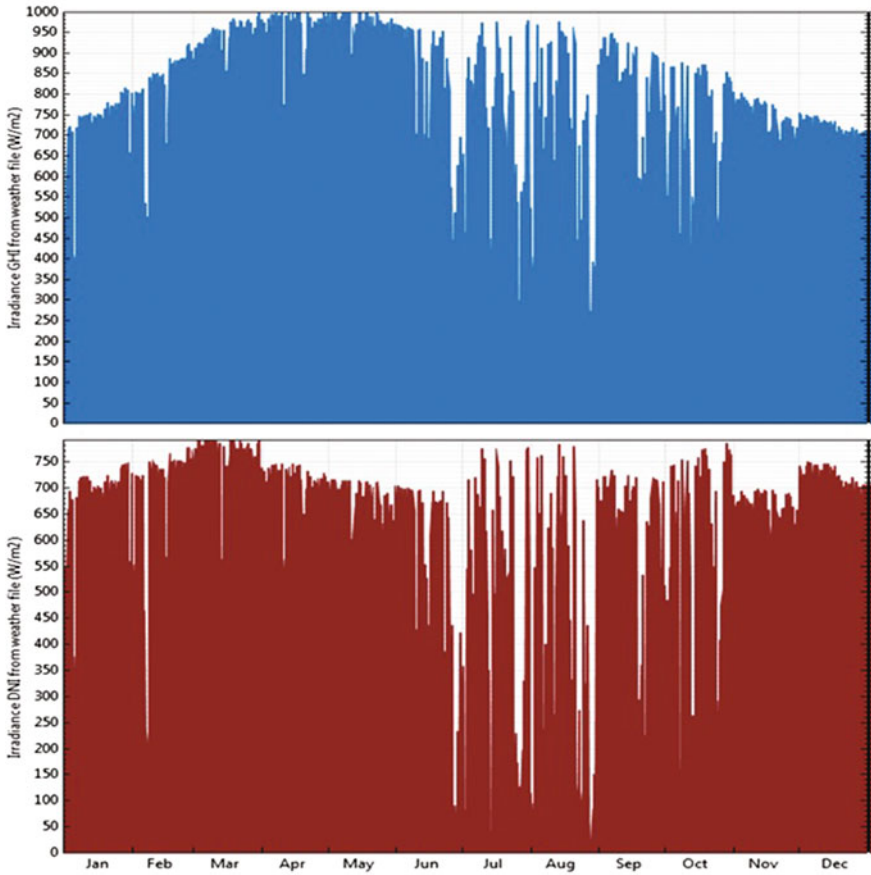


Fig. 10 Irradiance curve. *Source* SAM

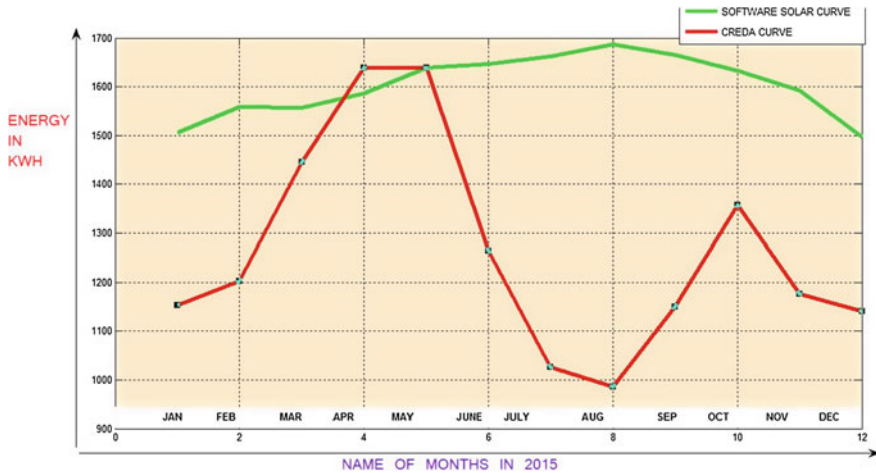


Fig. 11 Comparative measured versus software graph

3 Conclusion

In this way, design analysis of 8-kW systems is completed with all important parameters. This system promotes power system security; as I am using 400 Ah battery for this system, so we can run our load without sunlight and grid power for two days without any outage. This system is designed for Korba Collectorate Office by Chhattisgarh Renewable Energy Development Agency. Nowadays, the cost per watt power generation from solar has come down to Rs. 40. With an increase in per capita energy consumption, solar power can be the best alternative. It also requires less maintenance than any other power generation. The energy payback period of solar energy is 4.5 years. So, one can easily get the invested amount back in coming 4.5 years after installation but power from that system lasts for 15 years, so an installer can take free power after 5 years without any cause to environment. In the coming journal, concept of string inverter will be presented with 50-kW battery-less system. Finally, the complete system software output is compared with actual output. And measured output from CREDA is far better than software output. So, for this location hardware implementation is better than the software implementation. The designing parameters of 8-kW solar photovoltaic systems are studied, and with the help of data provided by CREDA department, Korba, software simulation has been performed with the help of SAM. The solar irradiance curves are drawn with the help of RET SCREEN PLUS which provides weather data from NASA. The 8-kW solar PV grid connected system is presented and simulated with the help of various curves. Here, grid is only used for taking power in the absence of solar and battery. In future, a better system model with enhanced capacity will be presented with online grid charging. As the system wattage will be higher, the extra generated solar power will be sent to the grid with the help of power conditioning

unit of larger capacity. The concept of string inverter will be presented in future with the help of its complete characteristics and curve. Another recommendation of the future model will be of 50 kW on grid PV system without battery backup. The designing, operating as well as simulating parameters will be considered in detail (Fig. 11).

References

1. Yadav, N.K., Singh, D.K., Agrawal, A.: Graphical and mathematical designing analysis of 8 kW solar photo-voltaic system. *IOSR J. Electr. Electron. Eng. (IOSR-JEEE)* **11**(3), 46–61 (2016)
2. CREDA (Chhattisgarh Renewable Energy Development Agency) is a only agency which performs renewable energy installation and maintenance tasks as per MNRE
3. Rai, G.D.: *Non conventional energy sources*. Khanna Publisher, New Delhi (2004)
4. Brown, E.W.: *An introduction to solar energy* (1988)
5. Solanki, C.S.: *A solar PV manual*. PHI Publication, New Delhi
6. Rai, G.D.: Data from world weather information service website and solar radiation data from non conventional energy sources
7. www.mnre.gov.in/file-manger/annual-report/20142015/EN/Chapter%204/Chapter_4.html/. Accessed on Apr 2016
8. Theologitis, I.T.: *Comparison of existing PV models and possible integration under EU grid specifications* (2011)
9. *Solar Energy International: Photovoltaic design and installation manual* (2004)

An Internet of Things to Maximum Power Point Tracking Approach of Solar PV Array

Himanshu Manghani, J. Prasanth Ram and N. Rajasekar

Abstract Internet of Things (IoT) is one of the emerging trends and has great potential to bring advances in electrical engineering and renewable energy. It is estimated that by 2020, IoT will be a \$20 trillion industry. Hence, this paper proposes the method of incorporating IoT in solar energy and photovoltaic research at the laboratory level. The proposed method includes IoT's diverse application in (a) MPPT tracking; (b) partial shading; (c) security switch for turning ON Arduino's serial monitor; and finally, (d) building up the direct communication between professor (sitting in the cabin) and the research scholar performing experiment (in the laboratory which is at some particular distance from the professor's cabin). The whole setup is based on the newly developed Indian microcontroller-BOLT (An Internet of Things platform) launched on 21 February 2016.

Keywords Internet of Things · Partial shading · Maximum power point tracking

1 Introduction

In accordance with the challenges like increasing population and standard of living, demand of energy is increasing drastically. Contemporary researches show that the population will increase up to 9 billion in 2040 with reference to 7 billion people living in the world today. Current scenario for fulfilling electricity demand of our people includes the use of fossil fuels extremely. Extreme use of fossil fuels is a

H. Manghani · J. Prasanth Ram · N. Rajasekar (✉)
Solar Energy Research Cell, School of Electrical Engineering, VIT University,
Vellore, India
e-mail: nrjasekar@vit.ac.in

H. Manghani
e-mail: h.manghani2014@vit.ac.in

J. Prasanth Ram
e-mail: jkprasanthram@gmail.com

threat in itself because of its slow rate of formation and threatening environmental hazards. The rate of formation of fossil fuels is very low with respect to their high consumption. Moreover, their excessive consumption results in an increase in the amount of carbon dioxide (and other harmful gases) which eventually get trapped in ocean and atmosphere leading to greenhouse effect and global warming [1, 2]. Going to the basic, we know that energy is neither created nor destroyed; it can only be transformed from one state to the other. And going even deeper, we know that fossil fuels are the compound which has converted, years of trapped solar energy into chemical energy. To conclude, sun is an ultimate source of energy. Therefore, for the safe future of our mother earth fulfilling our electricity demands from renewable energies like solar, wind (caused by temperature differences between different earth's regions) can mitigate the current challenges of electrical engineering [3].

The advancements which have been seen in electrical engineering and renewable energy over the past decades are superlative, for example, study of partial shading and maximum power point tracking (MPPT) in the field of solar photovoltaics [4, 5]. These techniques play an imperative role in increasing the efficiency of solar photovoltaic system with the special application of the subject—power electronics. To aid the research, authors have introduced IoT in photovoltaic's domain. It is also important to give a note that recent works involving IoT are gaining recognition where self-cleaning solar power system in [6] and controller design of street lamps using ZigBee protocol in [7] are found in the literature.

2 Description About IoT

In order to understand the history, theory behind IoT, structure of Internet of Things and data flow components are discussed in this section. For better understanding of readers, the following discussion is made. Internet of Things is especially the application of the two subjects, namely embedded system and computer networking, resulting in the connection of physical devices over internet to collect and exchange data with the help of sensors, actuators, WiFi module, etc. In addition, the term Internet of Things was first coined by Kevin Ashton, who cofounded the auto-ID center at the Massachusetts Institute of Technology (MIT) [8]. Universally on a basic level an IoT-based system can be shown in Fig. 1.

Segmentation and implementation follows a control structure where the applications and server get interfaced. Different stages followed in interfacing the user interface to the server are shown in Fig. 2. Also various components involved in construction of an IoT application to a user interface are presented in Table 1.

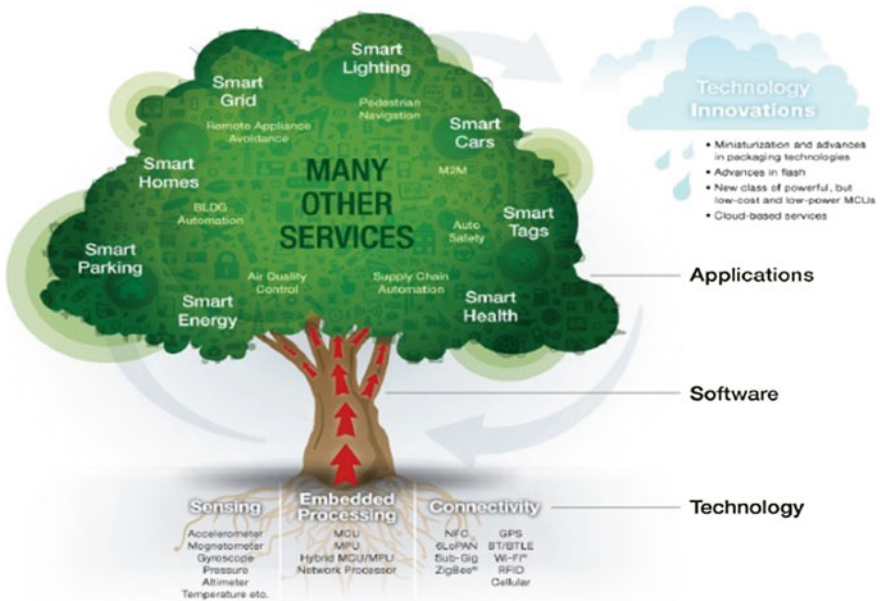


Fig. 1 Representation of basic IoT structure



Fig. 2 Stages in UI interface to server

Table 1 Description of components used in constructing IoT system

S. No.	Data flow components	Examples	Remarks
1	User interface (UI) application	Mobile apps, web apps, etc.	Allows user to control or monitor IoT-enabled device over local network or internet
2	Network components	Routers, WiFi, etc.	Helps transferring information to and from the UI application and IoT-enabled devices
3	Server	Google Chrome	Computing machine which host the UI application
4	Hardware control script	CSS, HTML, JavaScript, etc.	Programming language used to communicate between server and IoT-enabled devices
5	The thing	Bulb, buzzer, etc.	IoT-enabled device which the end user can control or monitor

2.1 Maximum Power Point Tracking in Solar PV System

Solar cells have an efficiency of less than 20%. Hence, to perpetually get optimum power from the solar cells (irrespective of low irradiance and other contradictions), some intelligent algorithms are required to propel the PV curve of solar cell to MPP. This process is called maximum power point tracking or MPPT, and the devices that perform this process are called MPP trackers. Among the different MPPT techniques followed in the literature, the most commonly used MPPT methods are Perturb and Observe, Incremental Conductance and Hill Climbing algorithm [4, 5]. In this paper, authors used P&O-based control structure to appreciate simplicity. The control logic behind MPP tracking is explained in the following. Voltage and current at MPP are measured via sensor circuitry and given back to the Arduino controller. This controller will effectively alter the duty ratio to find the maximum PV power irrespective of shading. The hardware model comprising of a boost converter and PV simulator developed in the laboratory is shown in Fig. 3a.

3 Experimentation

In order to achieve IoT implemented to MPPT, experiment is carried out carefully with the use of components presented in Table 2. The major component in the whole experiment is BOLT. BOLT is a microcontroller which is not only one of the most influential boards out there for the price, but also one of the most versatile controllers preferred for IoT applications. When it comes to what this board is capable of, the options are almost incalculable. Further any of the programming can be made by utilizing HTML, CSS and JavaScript. The schematic layout of BOLT is presented in Fig. 3b.

4 Experimentation and Methodology

Firstly the code has been written in Notepad editor using HTML and JavaScript languages to develop a web page for controlling the experiment. This is the first thing to be followed to start with IoT. For the ideation proposed in this paper, four options or buttons are built, namely (i) partial shading, (ii) communication, (iii) serial monitor turn ON and (iv) MPPT data. All the four mentioned options (Fig. 5) can be used to get the respective results by just a touch of finger (in this case, smart screen). After the development of our page, the code is uploaded. The code can be uploaded to web browser by using the cloud service of BOLT and BOLT device's IP address. It should be noticed that the BOLT device and the phone should be connected to the same network to see the results.

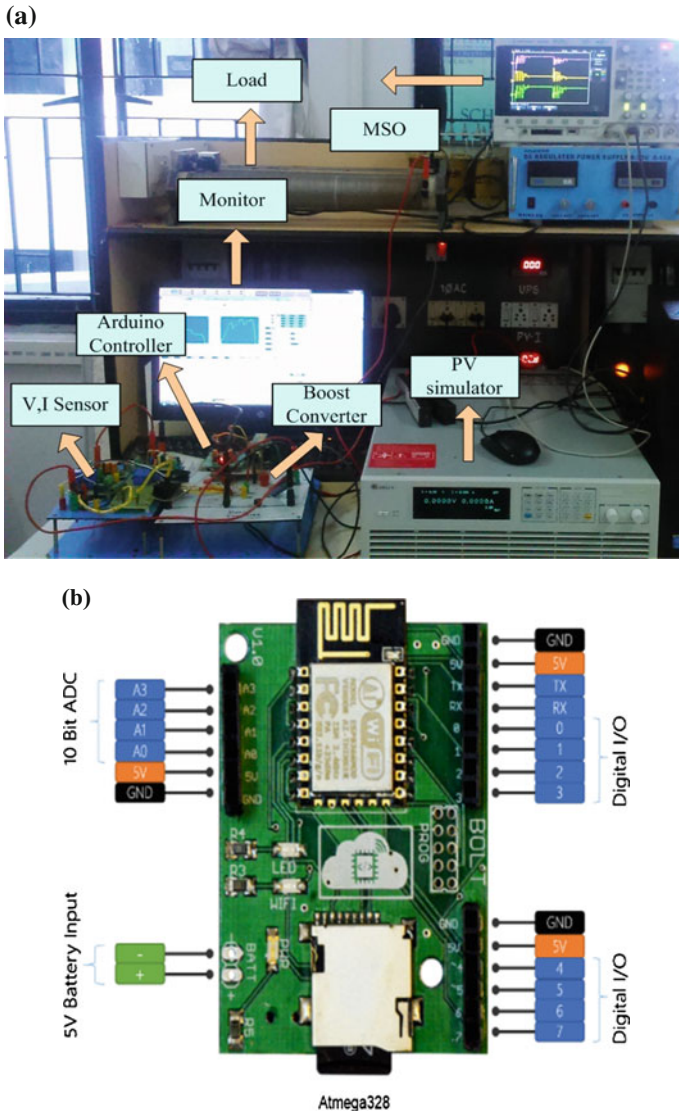


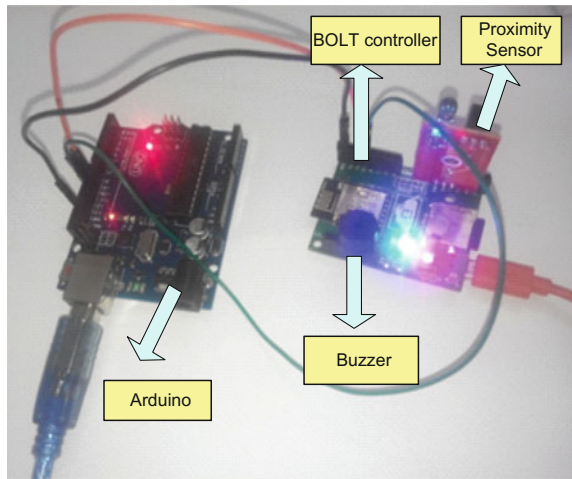
Fig. 3 a Hardware model for MPPT system. b Schematic of BOLT

Secondly, sensor is attached to the GPIO pins of BOLT. Proximity sensor is connected by putting its Vcc pin to 5 V pin of BOLT, output pin to BOLT pin number 4 and ground pin (GND) to ground pin (GND) of Bolt. Subsequently, connection with Buzzer is made. Negative pin of Buzzer is grounded, and positive pin is connected to pin A1 of BOLT. Buzzer is used to get a notification (or hear an

Table 2 Components used in constructing IoT-based laboratory system

S. No.	Name of component	Quantity	Purpose
1	BOLT microcontroller	1	For IoT (connecting devices over internet)
2	Smart screen (mobile phone, laptop, etc.)	1	For communication and observing the end results
3	MPPT device	1	For tracking MPPT (should have inbuilt Arduino)
4	Proximity sensor and buzzer	1 each	For partial shading

Fig. 4 Arduino interfaced to BOLT

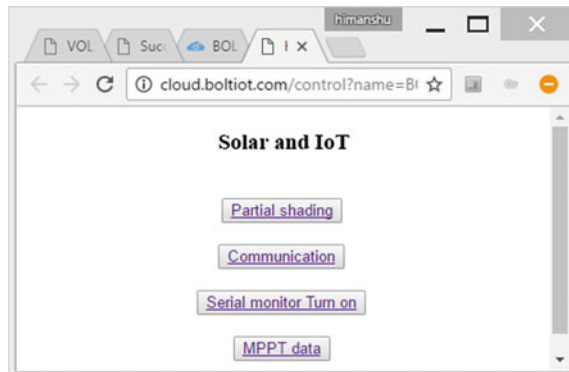


alarming sound) that the panel is facing an obstacle or hindrance in irradiance either by bird droppings or some kind of undesirable shadows.

Finally, connection of the Arduino is done with BOLT. It is hereby mentioned that the Arduino board which is used for MPPT tracking should be connected to BOLT. Rx pin and Tx pin are used for connections. Rx pin of BOLT is connected to Tx pin of Arduino (using Software Serial library, pin 10 has been made Tx pin of Arduino) and Tx pin of BOLT is connected to Rx pin of Arduino (i.e., pin 9, with the help of Software Serial library again).

Furthermore, changes in the Arduino’s MPPT code have been done to an extent that incorporates the control of serial monitor of Arduino by smart screen as a switch and communication protocol. In this context, communication means providing messages from professor to student over serial monitor with the help of web service. Web service can be used by Google Chrome browser only (as BOLT supports Google Chrome only as of now). The browser can be accessed by any means such as phone and laptop. The hardware realization of Arduino interfacing to BOLT microcontroller is shown in Fig. 4. It is essential to give a note that the connected Arduino to BOLT is the controller used to generate duty cycle for MPPT.

Fig. 5 Welcome page for BOLT and PV interface in web browser window



5 Results and Discussion

After the successful completion of hardware interfacing and uploading of our notepad file (HTML file) to browser, we have seen our first desired result in a window as shown in Fig. 5. Further results are observed by clicking (one by one) the four buttons (options) which have been developed using Notepad editor. Description of each button is discussed as follows:

Option 1: Partial Shading

This is the first option that we see on the page. After clicking the button, another web page window opens (Fig. 6a) which gives real-time dynamic graph of obstacle present in front of panel with respect to time. It is observed that whenever an obstacle is detected by the proximity sensor, the value at y axis steps down to 0 and the buzzer starts alarming to indicate that there is an obstacle in front of the solar panel. On the other side, when the path of light is not hindered by any obstacle the, value of y axis remains at one and buzzer goes in OFF condition (giving no sound). This gives an idea that there are no undesired particles (like bird dropping, dust) blocking the path of sunlight falling on the panel. With the use of such recorded data, it becomes easy to identify when the panel requires cleaning, maintenance or change of its direction. This saves our time by reducing our possibilities of going to panels and understanding their state of functioning. Hence, partial shading condition can be seen directly just by the click of our finger to smart screen. As a result, this can prove to be one of the emerging trends with MPPT in the study of renewable energy.

Option 2: Communication

Suppose a condition when a student is taking reading of MPPT experiment with the help of Arduino serial monitor, and the professor wants to convey him/her the message to stop the experiment and come in the laboratory. So, this button will help the professor in completing his task. In practical, when we click “communication” button by sitting in the cabin (which is situated away from the laboratory), a text message is sent directly to Arduino serial monitor (seen in Fig. 6b) and as a

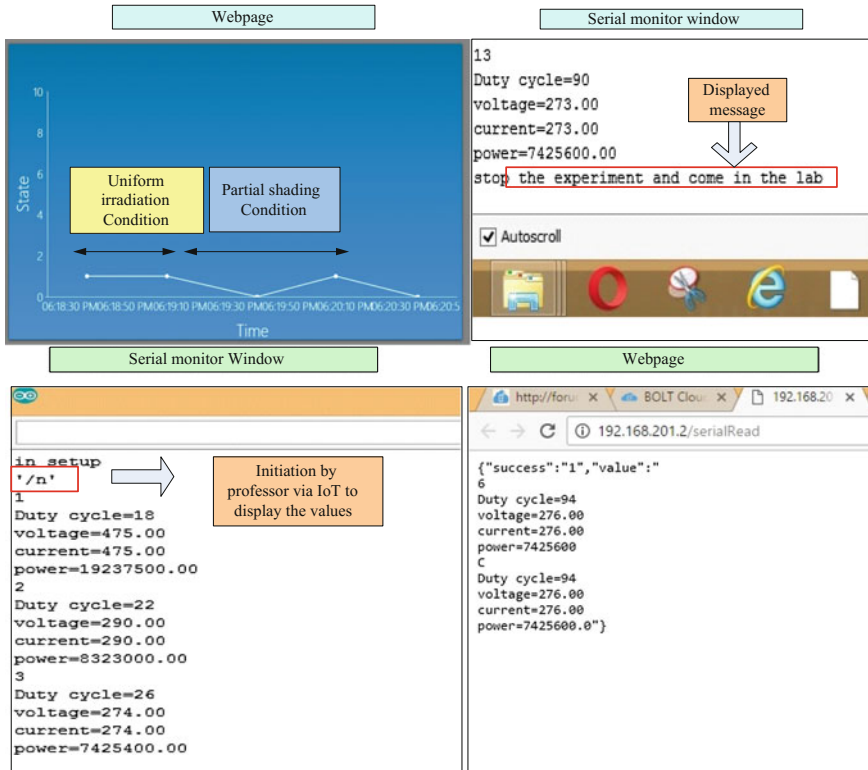


Fig. 6 a Graph displayed in web browser window after clicking partial shading option, b message displayed in serial monitor after clicking communication option, c serial monitor window after clicking serial monitor turn ON option, d MPP data representation in web browser window after clicking MPPT data option

consequence, we are able to develop a direct communication which can help in the better working of laboratory and interactions within and outside the laboratory. Therefore, we would like to propose this method for test conditions which has a potential to emerge as a trend in electrical and renewable engineering.

Option 3: Serial Monitor Turn ON

This button ensures security. The experiment values in serial monitor are displayed only when professor initializes the experiment via IoT (i.e., by clicking serial monitor turn on option shown in Fig. 6c) The values like duty cycle, voltage, current and power are spread out only when the professor commands to display the results (as shown in Fig. 6b). This gives an advance feature of adding security in the laboratory experimentation of MPPT.

Option 4: MPPT Data

When this button on the web page using smart screen is clicked, then the MPPT data can be retrieved from any place (i.e., even outside the laboratory) as shown in

Fig. 6d. Hence, with the help of this proposed method, experiments related to MPPT tracking can be made more versatile and accessible.

Note: (i) The features (options) mentioned from 1 to 3 can be incorporated in any of the laboratory experiments (irrespective of MPPT). Hence, the authors have proposed a universal way of making the laboratory smarter. (ii) However, some of the garbage values are encountered while pushing MPP data to cloud, authors are confident to mitigate this effect in near future by working on the code.

6 Summary/Conclusion

In this paper, the authors have amalgamated the subjects like renewable energy and IoT to envisage the emerging trend in solar energy. The work proposes intelligent handling of partial shading occurrence in MPPT conditions by getting a dynamic graph of shading patterns. Pushing the MPPT data to a cloud gives automatic control to the server that can be accessed from any part of the world. In addition, the protocol for direct communication between researchers has also been introduced. Future scope of this paper is to mitigate some garbage values, delays occurring in pushing the MPPT data to cloud and other area is to extend the study of partial shading conditions with orientations of various sensors. However, the research at present is on preliminary level but has a great motivation to enhance the domain of photovoltaic engineering by the proposed innovation and creation.

References

1. Prasad, S.S., Kumar, C.: A green and reliable internet of things. *Commun. Netw.* **5**(01), 44–48 (2013)
2. Nandyala, C.S., Kim, H.K.: Green IoT agriculture and healthcare application (GAHA). *Int. J. Smart Home* **10**(4), 289–300 (2016)
3. Yao, L., Lai, C.C., Lim, W.H.: Home energy management system based on photovoltaic system. In: 2015 IEEE International Conference on Data Science and Data Intensive Systems, pp. 644–650 (2015)
4. Sudhakar, Babu T., Rajasekar, N., Sangeetha, K.: Modified particle swarm optimization technique based maximum power point tracking for uniform and under partial shading condition. *Appl. Soft Comput.* **34**, 613–624 (2015)
5. Babu, T.S., Sangeetha, K., Rajasekar, N.: Voltage band based improved particle swarm optimization technique for maximum power point tracking in solar photovoltaic system. *J. Renew. Sustain. Energy*, **8**(1) (2016)
6. Zhang, W., Zhang, Z.: High power solar street lamps controller design based on ZigBee. In: *Industrial Electronics and Applications (ICIEA)*, 2015 IEEE 10th Conference on IEEE (2015)
7. Guannan, D., Zhang, X., Wei, S., Ji, Q., Wei, H., Du, G.: Based on the internet of things a self-cleaning solar power system of the household micro-grid. In: 2016 Chinese Control and Decision Conference (CCDC), IEEE (2016)
8. McFarlane, D., Sarma, S., Chirn, J.L., Wong, C., Ashton, K.: Auto ID systems and intelligent manufacturing control. *Eng. Appl. Artif. Intell.* **16**(4), 365–376 (2003)

Energy Storage Considerations for High Renewable Power Penetration: A Case Study

James R. Doyle and Hannah Johlas

Abstract A simple model for high penetration wind and solar for the MISO region of North America is used to study the effects of geographical diversity, source diversity, and over-generation on storage capacity requirements. Combining wind and solar generation over a wide geographical region significantly reduces the storage requirements. Further substantial reduction occurs using over-generation of wind and solar and allowing a modest energy deficit to be made up by dispatchable sources. Based on a simple model we found that for 95% of the load energy supplied by wind and solar (with the other 5% supplied by other dispatchable sources) with approximately 10% over-generation approximately 1 day of storage of the average load energy per year of storage is required for energy balance. A simple model to estimate total capital costs is minimized for approximately 15–20% over-generation.

Keywords Solar energy · Wind energy · Grid storage

1 Introduction

Wind and solar energy (mainly photovoltaics) is currently the most promising as well as highly developed sources of low-carbon energy. However, including large amounts of wind and solar generated electricity on the grid is problematic due to their intermittent and unpredictable nature. It is generally believed that some kind of energy storage will be required to smooth out or “balance” the load if wind and solar dominate our energy portfolio. A number of possible energy storage technologies are being considered, and electrochemical battery storage is likely to play a dominant role

J.R. Doyle (✉) · H. Johlas
Department of Physics and Astronomy, Macalester College, St. Paul,
MN 55105, USA
e-mail: doyle@macalester.edu

H. Johlas
e-mail: hjohlas@gmail.com

at least in the near future [1]. However, all kinds of storage, including battery technology, are currently very expensive, and implementing large amounts of storage capacity would significantly raise the cost of electricity even as wind and solar costs approach grid parity. Thus, it is important to implement strategies that will minimize the amount of energy storage capacity required to balance the grid load.

Methods to reduce the storage capacity include mixing wind and solar generation in the appropriate ratio (source diversity), having wind and solar sources widely distributed over a large area (geographical diversity), and various “smart grid” proposals. Another way to reduce storage capacity is “over-generation,” that is, the combined wind and solar generation exceeds the total load energy over a given time. Of course this means that energy at least equal to the over-generated amount will be “spilled” and not utilized, (or equivalently, the generation sources will have to be shut down during times when they could be producing power). This will reduce the return on investment in these sources since it will take longer to recoup the initial capital investment of implementing the generators. On the other hand, if the cost of over-generation is cheaper than the cost of implementing more storage, the overall costs could be reduced. Indeed, this is precisely what Budischak et al. [2] found in their modeling of the eastern US electricity grid.

In this work we look at the effects of geographical and source diversity as well as over-generation on energy storage requirements the region of the USA that is part of the Midcontinent Independent System Operator (MISO) energy market. We also propose a simple model to estimate the effects of over-generation on the total capital costs of combining wind, solar, and energy storage.

2 Methods

The simulation is based on a simple conservation of energy condition. Given wind and solar power $P_W(t)$ and $P_S(t)$ generation at time t , the energy generated during time Δt at t , given by $E_{\text{gen}} = [P_W(t) + P_S(t)] \times \Delta t$, is compared to the load energy E_L during Δt at t . If E_L exceeds E_{gen} , then energy is drawn from storage. If the storage is completely depleted, a deficit energy E_d is recorded. If instead E_{gen} exceeds E_L , the surplus energy is transferred to storage, up to a maximum storage capacity E_{storemax} . If the energy storage is already maximized at E_{storemax} , the surplus energy is spilled. At $t = 0$ the storage is assumed to be at E_{storemax} . The time resolution of the simulation is $\Delta t = 15$ min.

We have chosen to parameterize the simulation as follows. The total load energy consumed over a given year was normalized to 1.0. The total wind energy and solar energy produced over a given year was scaled to be a fraction of the total load energy, denoted wind fraction f_W and solar fraction f_S , respectively. Thus, if $f_W + f_S = 1.0$, the total energy produced by wind and solar over the year is equal to the load energy. The deficit energy is also given as a fraction of the total annual load energy. Finally, the storage capacity E_{storemax} is given in units of average daily load consumed. That is, one day of storage capacity is equal to the average load per day for that year (i.e., $1.0/365$).

Historical load data for the MISO region for the years 2007, 2008, 2009, and 2010 were taken from the Energy Online database [3]. Wind production data were taken from the National Renewable Energy Laboratory's Wind Integration Data Sets [4] for the years 2007, 2008, 2009, and 2010. The distribution of wind sites among states was chosen according to the current distribution of wind farms in the MISO region, which also corresponds approximately to the optimal wind resource distribution. For a total of 23 sites this resulted in 6 sites in the state of Iowa, 4 sites in Illinois, 3 sites in Minnesota, 2 sites each in Indiana, Michigan, and North Dakota, and 1 site each in Missouri, Montana, South Dakota, and Wisconsin.

Solar energy production data were taken from the National Renewable Energy Laboratory's Solar Integration Data Sets [5]. Data are only available for the year 2006, and these data were used for all years simulated. Since solar PV accounts for less than 1% of US electricity, the vast majority of which is outside the MISO region, it is more difficult to assign a geographical distribution of solar power that would anticipate the future distribution at high penetration. For the purposes of this study we adopted a simplified approach where the solar power distribution was approximately allocated according to the respective populations of the states in MISO, adjusted for the fraction of the state that is included in the MISO network. Using this approach we choose four sites for Michigan, three sites in each of Illinois, Wisconsin, Indiana, and Minnesota, two sites in Missouri and Iowa, and one site each in South Dakota and Montana (no NREL data were available for North Dakota). The sites themselves were chosen to favor the large population centers of the respective states. However, an alternative set of sites, chosen randomly within a given state, was also simulated and gave negligible difference in the results.

It should be emphasized that the current study does not claim to provide an accurate map of future wind and solar power resources for the MISO region at high renewable penetration levels. This distribution will depend on future local and national policy decisions and future economic conditions that are very difficult to predict. Nor does our model address power requirements or grid energy quality. Our goal is instead to utilize realistic load and power generation profiles with simple models to explore global energy storage capacity requirements as a function of geographical diversity, source diversity, and over-generation.

2.1 Wind-Only Generation

Figure 1 shows the deficit energy as a function of storage capacity using only for $f_W = 1.0$ and $f_S = 0.0$ for the years 2007–2010. With no storage, the deficit energy fraction is about 0.25. That is, other non-wind sources would need to supply about 25% of the total load energy in order to balance load and production, even when the total wind energy produced is equal to the total load energy consumed for the year. The amount of storage capacity needed to achieve zero deficit energy is about 40 days, or about 11% of total load energy for the year.

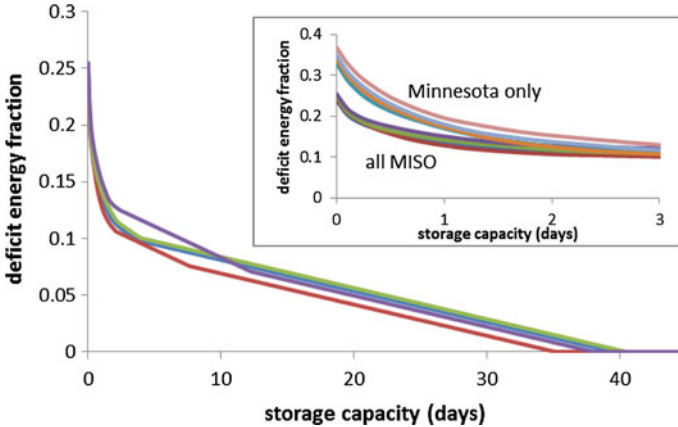


Fig. 1 Wind-only deficit energy as a function of storage capacity

The effect of geographical diversity on wind energy production is shown in the inset of Fig. 1. Upper curves assume all of the wind generation occurs in the state of Minnesota, and the lower curves include all of the MISO region sites. Geographical diversity has a large effect in reducing deficit energy for a given storage capacity requirements at low storage capacities. Even with no storage the deficit energy is reduced by almost 30% when sources from a larger geographical region are included. Other studies have also found a significant leveling effect with geographical diversity [2, 6]. However, as storage capacity increases, the effect of geographical diversity becomes less important. The spilled wind energy for all of these cases is very close to the deficit energy at low storage capacities, as expected since the total wind energy production is set equal to the total load energy for the year.

2.2 Addition of Solar Energy

Including solar energy in the generation portfolio improves the situation considerably, as shown in Fig. 2. The wind fraction that minimized the storage capacity for zero deficit energy was in the range 50–60% varying slightly with year. In Fig. 2 we use a 60% wind and 40% solar mix. The amount of storage needed for zero deficit energy drops from 35 to 0 days for the wind-only case down to about 12–22 days by adding solar, roughly a factor of two decrease. Others have noted the leveling effect that a mix of solar and wind provides in load matching compared to wind or solar alone [2, 6].

However, the requirement that the energy deficit drops to zero is probably too restrictive for assessing storage requirements, and allowing for a small percentage of deficit energy is more realistic. For example, in a completely renewable scenario,

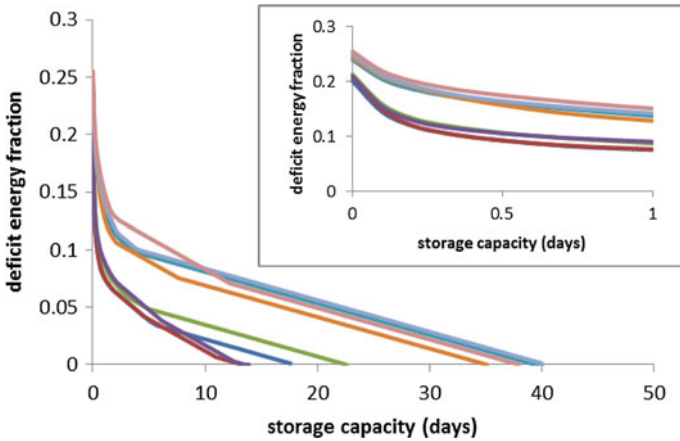


Fig. 2 Combined wind and solar generation energy deficit as a function of storage days. *Upper curves* wind only; *lower curves* wind plus solar. *Inset* detail at low storage

a small energy deficit could be supplied by hydroelectric or possibly even biofuels. Even a small amount of electricity generated by natural gas might be tolerable. Allowing for some deficit energy also helps to mitigate the yearly variations in storage requirements. The main requirement for deficit power sources is that they are fully dispatchable, that is, are capable of providing peaking power. From Fig. 2 we find that if for example a 5% energy deficit is allowed, the storage requirement averaged over the four years simulated drops from 20.1 days for the wind-only case to 4.2 days when solar is added, nearly a factor of 5. The 4.2 days of storage capacity represents a little over 1% of the total load energy for the year.

2.3 Effect of Over-Generation

The results presented above apply to a scenario where the total wind+solar energy is matched to the total load energy for the year (i.e., $f_w + f_s = 1.0$). It is important to keep in mind that even 4 days of storage represents an enormous capacity. For example, in 2010 the net energy load for the MISO region was 585,274,000 MWh [7]. Storage capacity equivalent to 4.2 days would be about 6,700,000 MWh. If Li-ion storage batteries were used for the energy storage, at current estimates of approximately \$400/kWh [8] the capital cost for storage alone would be about \$2.3 trillion (10^{12}) US dollars. Over-generation of wind and solar can be used to reduce the total storage capacity required. The main question then becomes one of economics, i.e., whether it is less expensive to add more generation capacity or storage capacity.

Figure 3 shows the storage capacity needed for a 0 and a 5% energy deficit as a function of the over-generation. Above 10% over-generation a 5% energy deficit

reduces the storage required by about an order of magnitude, to below 1 days worth of storage, or <0.3% of the total load energy for the year.

An accurate economic model of trade-off between over-generation and storage is a complicated and depends on unknown future costs of the relevant technologies. However, a rough estimate of this trade-off can be made using the following very simplified model. We assume that the costs are dominated by initial capital costs. The capital cost of wind and solar is approximately

$$CC_{gen} = \frac{f_s E_L (1 + OG) C_S}{CF_S \times 8670} + \frac{f_w E_L (1 + OG) C_W}{CF_W \times 8670} \tag{1}$$

where CC_{gen} is the total generation capital cost, $f_s = 0.4$ and $f_w = 0.6$ are the fractions of wind and solar generation, respectively, E_L is the total load energy in kWh, OG is the over-generation fraction, C_S and C_W are the capital costs per kW for solar and wind, respectively, CF_S and CF_W are the respective capacity factors for solar and wind, and 8670 is the number of hours in a year. The capital cost of the energy storage is assumed to be

$$CC_s = \frac{D_s}{365} E_L C_B \tag{2}$$

where CC_s is the total capital cost for storage, C_B is the capital costs per kWh for storage, and D_s is the number of days of storage required for a 5% deficit energy (Fig. 4). In Fig. 4 we show the results of this model for several values of C_B (see below) as a function of OG , using $C_S = 2$ \$/W, $C_W = 1.33$ \$/W and assuming capacity factors of $CF_S = 0.20$ and $CF_W = 0.35$. The total cost has been normalized to the cost corresponding to 0% over-generation.

According to this model, over-generation of wind and solar results in lower total capital costs for any capital cost of storage that exceeds \$5/kWh. It is very unrealistic to assume that energy storage costs could reach such low prices based on any current technology. Current lithium-ion battery costs (at present the least expensive option) are about \$400/kWh, but a more applicable number is probably the industry goal of \$120/kWh thought to be achievable within the next decade or so [8].

Fig. 3 Storage capacity required for 0 and 5% deficit energy as a function of over-generation for $f_w = 0.6$ and $f_s = 0.4$

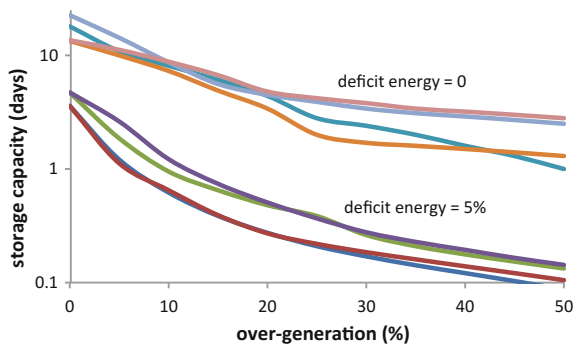
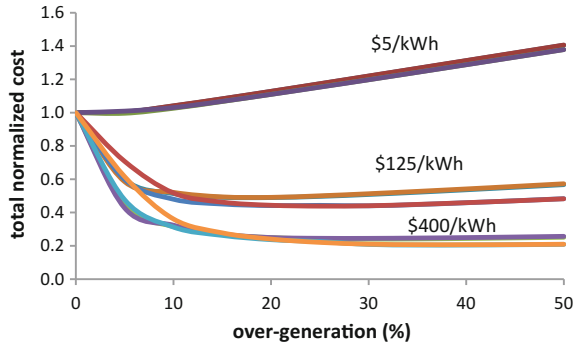


Fig. 4 Total capital cost as a function of over-generation for different storage capital costs



At this cost it appears that the lowest total capital costs occurs for about 15–20% over-generation, corresponding to a storage capacity of less than 1 day, and a ratio of storage to generation capital costs of 0.1 to 0.2.

3 Conclusions

The role of source diversity, geographical diversity, and over-generation on reducing energy storage requirements is explored using a simple energy balance model for realistic load and generation profiles for the Midcontinent Independent System Operator (MISO) region of the USA. These strategies result in a dramatic reduction in required storage capacity. Furthermore, allowing for a modest deficit energy, to be made up by other dispatchable sources, reduces the storage even more dramatically. A simple cost model indicates that the economics of trading over-generation for storage capacity could be very favorable. Despite the simplicity of our model, these strategies should be considered for reducing the storage capacity should be considered in any renewable energy scenario.

References

1. Luo, X., Wang, J., Donner, M., Clarke, J.: Overview of current development in electrical energy storage technologies and the application potential in power system operation. *Appl. Energy* **137**, 511–536 (2015)
2. Budischak, C., Sewell, D., Thomson, H., Mach, L., Veron, D.E., Kempton, W.: Cost-minimized combinations of wind power, solar power and electrochemical storage, powering the grid up to 99.9% of the time. *J. Power Sour.* **225**, 60–74 (2013)
3. EnergyOnline: MISO actual load. Available at http://www.energyonline.com/Data/GenericData.aspx?DataId=10&MISOActual_load
4. National Renewable Energy Laboratory: Wind Integration Data Sets. <http://www.nrel.gov/grid/wind-integration-data.html>

5. National Renewable Energy Laboratory: Solar Integration Data Sets. Available at <http://www.nrel.gov/grid/solar-integration-data.html>
6. Tarroja, B., Mueller, F., Eichman, J.D., Samuelsen, S.: Metrics for evaluating the impacts of intermittent renewable generation on utility load-balancing. *Energy* **42**, 546–562 (2012)
7. National Renewable Energy Laboratory: 2014 Renewable Energy Data Book. Available at <http://www.nrel.gov/docs/fy16osti/64720.pdf>
8. Wood, D.L., Li, J., Daniel, C.: Prospects for reducing the processing cost of lithium ion batteries. *J. Power Sour.* **275**, 234–242 (2015)

Development and Implementation of Renewable Energy Potential Geospatial Database Mapping in India for Cloud SDI Using Open Source GIS

Rabindra K. Barik, K. Muruga Perumal, P. Ajay-D-Vimal Raj and S. Rajasekar

Abstract India is owing to the substantial gaps amongst the established energy demand and mounted power capacity, with the conclusion that the per capita energy consumption in India is one of the lowermost in the world. The opportunity for development in India's energy system is huge. Renewable energy presently makes up a slight share (0.36%) of total main commercial energy supply, whereas 96.9% of such supplies come from fossil energies and 2.76% from hydro and atomic resources in India. The present research paper primarily proposed the renewable energy potential scenario in each and every state of India by taking different aspects with the clarification to the developed energy demand in future of India. Secondly, it has also developed the renewable energy potential geospatial database in India with the help of open-source GIS software further implementation in cloud SDI (Spatial Data Infrastructure) Model for better visualization and mapping of potential sites. Present paper has used Quantum GIS 2.14.3 open-source GIS software for the geospatial database creation. The developed geospatial database has been successfully viewed and implemented with Quantum GIS 2.14.3 as thick client environment for sharing of various factors, i.e. wind, small hydropower, biomass power and solar which are associated with the renewable energy potential scenario in India.

Keywords Renewable energy · GIS · Open-source · Geospatial database

R.K. Barik (✉)

School of Computer Application, KIIT University, Bhubaneswar, India
e-mail: rabindra.mnnit@gmail.com

K. Muruga Perumal · P. Ajay-D-Vimal Raj

Department of Electrical & Electronic Engineering,
Pondicherry Engineering College, Pondicherry University, Puducherry, India
e-mail: murugae@gmail.com

P. Ajay-D-Vimal Raj

e-mail: ajayvimal@pec.edu

S. Rajasekar

Researcher of NEC Laboratories, NEC Asia Pacific Pte. Ltd., Singapore, Singapore
e-mail: rajasekarsmvec@gmail.com

1 Introduction

A large amount of electrical energy consumption in a country indicates increased activities in this power sector providing high relaxation in modern industrial and residential power applications. On the another side, the conventional method of power generation leads to increasing environmental pollutions and carbon footprints in our nation; at present, the main objective of any significant country is to increase power generation to meet pollution-free developed energy demand.

India is known as the fourth biggest electricity-using country after the orders of China, USA and Russia, respectively [1, 2]. And also it is noted as one of the fast-growing economics to meet the following major encounters of (a) fulfilling global warming mitigation through international protocols, (b) demanding the eradication of the un-electrified villages and (c) secured energy supply which is independent of fuel imports instability [3, 4].

As per statement of International Energy Agency (IEAD), India will be the second top country to rise in the global electrical energy demand by 2035 [1]. The major electricity production in India was obtained from fossil fuels such as coal (201,360 MW), natural gas (24,509 MW), nuclear power (5780 MW) and small quantities of crude oil (994 MW). India has the installed power of 288 GW as on 29 February 2016. Out of installed power, the 13% was only from various renewable energy resources such as solar, wind, mini hydro and biomasses. Figure 1 shows the installed electricity in India as on 29 February 2016.

2 Development of Renewable Power Group in India

The welfares of organizing renewable resources are providing uncontaminated energy, whereas dropping trust on fossil energies, thereby dipping CO₂ productions. Using renewable energy to complement the energy desires and to shrink

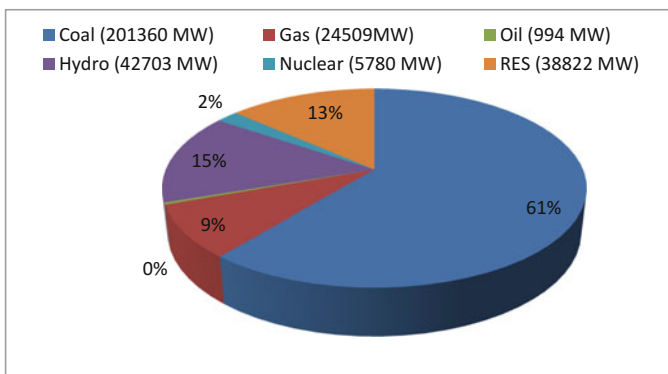


Fig. 1 Installed electricity in India as of 29 February 2016

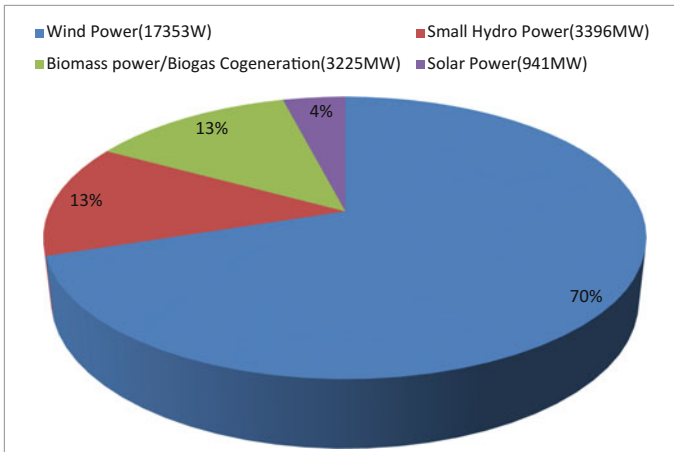


Fig. 2 Installed renewable electricity in India as of 29 February 2016

eco-friendly impact is an important goal of several nations round the ecosphere. Technical developments compact cost, and administrative inducements have complete some renewable resource such as solar and wind, additional economical in the market. Figure 2 shows the classification of renewable resource-based electrical power (counting off grid and on grid). Agreeing to the Ministry of Renewable Energy department, grid-connected renewable resources consist of solar, wind, minor hydro, industrial waste and bagasse cogeneration biomass power, etc. Amongst these, the major portion is 17 GW from wind mill, next 3.39 GW from mini hydro plant, 0.94 GW from sun energy and 3.22 GW from grid-connected bagasse and biomass [1–3, 5, 6]. The main objective of the present research work in renewable energy scenario of India is recommending suitable best configuration of hybrid renewable models for each renewable resource-rich regions of India and giving the solution to developed energy demand in future of our country [7, 8].

It has been observed that the sharing of suitable best configuration of hybrid renewable models' information for the analyst or decision-makers can be possible with the help of spatial technology with cloud computing environment for achievement of the main aim of development of Spatial Data Infrastructure (SDI) model.

3 Need of SDI Model for Renewable Energy Scenario in India

With the combination of mobile, Web and spatial technologies, it has been a greater potential for numerous functionality in terms of geospatial data allotment over Internet. It can offer a real-time and dynamic way to denote information through

maps. So there is an urgent need to launch a well-organized SDI Model which is a geoportal where each and every participant can use, exchange and access spatial data for economic, social and ecological application [9]. Geospatial Web service is one of the key technologies required for development and application of SDI [10]. Design and implementation of SDI is used in cloud computing technology which is used for sharing the information about the renewable energy potential in India [11]. It enables the end user or data analyst to quickly look into the problem and get the information according to their need. Thus, the next section describes the details of related works which have been done with the Cloud SDI Model.

4 Cloud SDI Model

Cloud SDI Model delivers a platform in which organizations interrelate with technologies, tools and expertise to nurture deeds for producing, handling and using geographical statistics and data. SDI also defines the cumulative of technology, standards, strategies, policies and manpower required to attain, allot, sustain, process, use and reserve spatial data. The basic constituents of SDI have been observed as data, networking, public, policy and standards [12]. Further, SDI Model can be implemented through service-oriented architecture (SOA) or cloud computing technologies for better and efficient use. The SOA tries to construct dynamic, distributed and flexible facility system over the Web in order to see data and required services for development of SDI. Components in the service-oriented architecture-based spatial data infrastructure are geospatial Web services, i.e. structured collections of activities which are stateless, self-confined and independent upon the state of other services [13–15].

Likewise, Cloud SDI Model deploys a unique-instance, multitenant design and permits more than one client to contribute assets without disrupting each other. This integrated hosted service method helps installing patches and application advancements for user's transparency. Geospatial cloud is another characteristic embrace of Web services and SOA, a wholly established architectural methodology in the engineering [16]. Many cloud platforms uncover the applications statistics and functionalities via Web service. This permits a client to query/update different types of cloud services and applications data programmatically, along with the provision of a standard mechanism to assimilate different cloud applications in the software cloud with enterprise SOA infrastructure [17–19, 22]. Figure 3 illustrates the system architecture for Cloud SDI Model [20].

It has been shown from the system architecture of Cloud SDI Model where geospatial databases are a vital module in data layer in Cloud SDI Model. Thus, next section has been emphasized on the geospatial database creation.

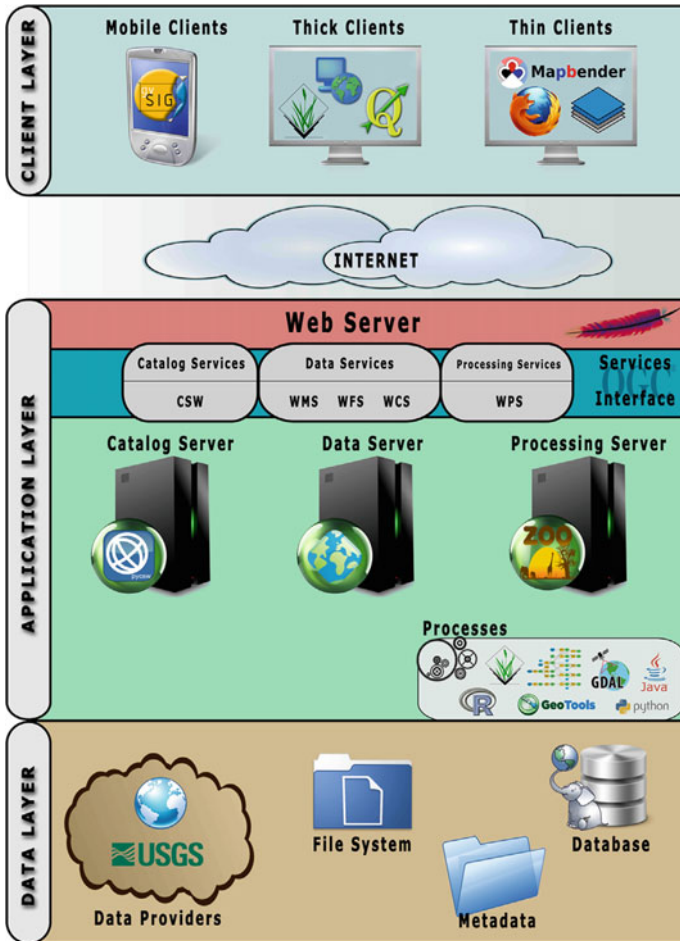


Fig. 3 System architecture for cloud SDI Model

5 Geospatial Database Creation for Renewable Energy Potential

The creation of geospatial databases for renewable energy potential in India is significant and tedious assignment where efficacy in geospatial related project depends upon. Integrated geospatial database creations include stages such as inputs of data on spatial and non-spatial attributes, and its authentication by connecting with same set of data. Geospatial database delivers a platform in which organizations interrelate with technologies to nurture actions for handling, spending and generating geographical data [20]. The development of geospatial database supports

in various administrative and political levels through these decision-making functions. Quantum GIS 2.14.3 has been selected for creation of geospatial database.

6 Objective of the Present Research Work

The aim of the present research work is to use Quantum GIS 2.14.3 which has been utilized for geospatial database creation and also broadly used for development of geospatial database for renewable energy potential in India. It has also proposed a robust software engineering methodology approach for the development of geospatial database with the help of Quantum GIS 2.14.3. Thus, the next section describes about the methodology adopted for the geospatial database creation for renewable energy potential in India.

7 Methodology Adopted for Geospatial Database Creation for Renewable Energy Potential in India

For creation of geospatial database, the prime emphasis has been on the real-world approach to discover and spread the thought of geospatial database creation for renewable energy potential in India. The established geospatial database has to provide a proficient means of allocation of geospatial and non-spatial data in Cloud SDI Model. The prototype is based on object-oriented software engineering (OOSE) proposed by Jacobson’s method to combine the time-critical nature and strong user focus [21, 22]. Figure 4 represents the fully win–win procedure model for creation of geospatial database creation.

The procedure model of geospatial database creation is recurring or frequent in nature, and each operation improves the study and strategy steps through assessment and testing of a completed component. In complete component, Quantum GIS 2.14.3 open-source GIS software has set up geospatial database for renewable energy potential in India with the help of political map of India. Quantum GIS 2.14.3 is also used for integrated geospatial database creation. The geospatial

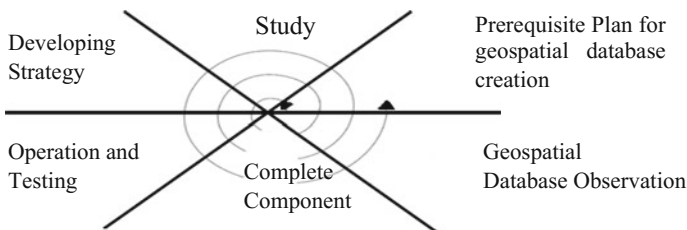


Fig. 4 Spiral model for geospatial database creation renewable energy potential in India

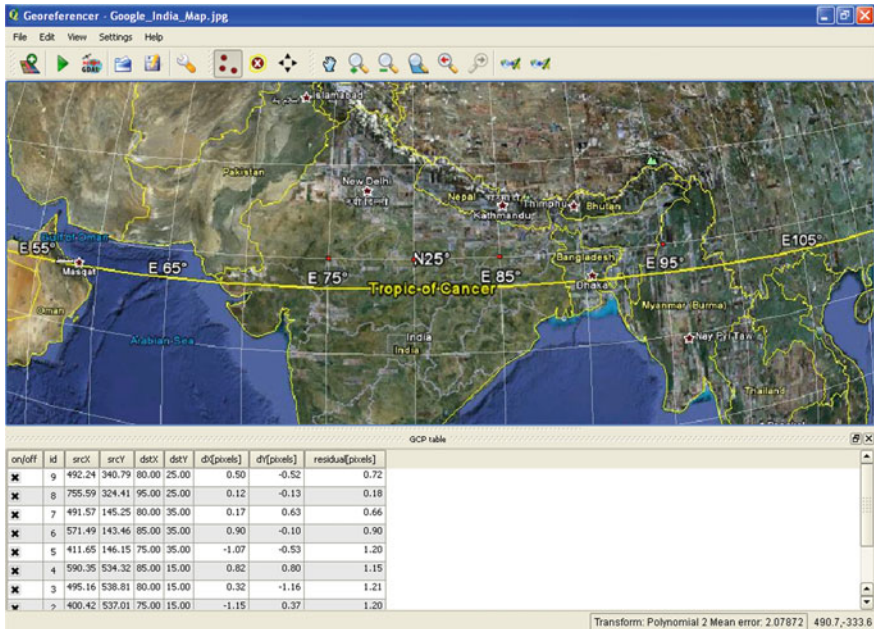


Fig. 5 Georeferencing: map of India

database for renewable energy potential in India has been nominated to illustrate the capabilities of developed framework. Geospatial database for renewable energy potential in India has been prepared by Quantum GIS Ver. 2.13.4. Initially, the base image of India has been downloaded from the Google Earth. The downloaded image is georeferenced with the help of Georeferencer Tool in Quantum GIS Ver. 2.14.3. For georeferencing the base map of India, 10 numbers of GCPs have been taken. The GCPs have been selected at the intersection of latitudinal and longitudinal lines. For universal coordinate system, WGS-84 with EPSG: 4326 coordinate reference system has been chosen. Now, the image is ready for georeferencing. After georeferencing, the generated image is used to extract the thematic maps. Figure 5 shows the snapshot of georeferencing of Indian map in Georeferencer Tool from Quantum GIS Ver. 2.14.3.

In the present application case study, the entire renewable energy potential in India has been taken. These have been categorized into the different layers with schema definition. Figures 6 and 7 show the layer name with respect to schema definition and instant of the database.

After schema definition, two thematic layers have been created. First layer has been developed as renewable energy potential in India and second layer has been created which indicates the whole India State Boundary. For these two layers, WGS-84 with EPSG: 4326 coordinates reference system has been chosen. The Indian state boundary has been created by on-screen digitization process in

Renewable energy potential in India

Sl. No	State s/ UTs	Wind Power	Small Hydro Power	Biomass Power	Bagasse Co-Gen.	Waste to Energy	Solar	Total	Chance to Hybrid system
--------	--------------	------------	-------------------	---------------	-----------------	-----------------	-------	-------	-------------------------

India State Boundary

UID	State Name	State Capital Name
-----	------------	--------------------

Fig. 6 Schema definitions for renewable energy potential in India

ID_1	NAME_1	ENGYE_1	Wind Power	S_Hydro_P	Bio_P	Bagasse Co	Waste_Emg	Solar	Total	C_Hybrid_S
0	Andaman and Nic.	Union Territory	365	8	0	0	0	0	373	No
1	2 Andhra Pradesh	State	14487	978	578	300	123	38440	54916	Yes
2	3 Arunachal Pradesh	State	236	1341	8	0	0	8650	10236	No
3	4 Assam	State	112	239	212	0	8	13790	14330	No
4	5 Bihar	State	144	223	419	300	73	11200	12559	No
5	6 Chandigarh	Union Territory	0	0	0	0	4	0	4	No
6	7 Chhattisgarh	State	314	1187	236	0	24	38370	39951	No
7	8 Dadra and Nagar.	Union Territory	0	0	0	0	0	0	0	No
8	9 Daman and Diu	Union Territory	4	0	0	0	0	0	4	No
9	10 Goa	State	0	7	26	0	0	880	912	No
10	11 Gujarat	State	10071	202	1221	350	112	39770	72726	Yes
11	12 Haryana	State	93	110	1333	350	24	4560	6470	No
12	13 Jharkhand Pradesh	State	64	238	142	0	2	33840	36446	No
13	14 Jammu and Kash.	State	5685	1431	43	0	0	113050	130208	Yes
14	15 Jharkhand	State	91	209	90	0	10	18380	18580	No
15	16 Karnataka	State	13583	4141	1131	450	0	24200	44015	Yes
16	17 Kerala	State	837	304	1044	0	36	6130	8732	No
17	18 Lakshadweep	Union Territory	0	0	0	0	0	0	0	No
18	19 Madhya Pradesh	State	2931	820	1364	0	78	63660	66553	Yes
19	20 Maharashtra	State	5861	794	1887	1250	287	64320	74000	Yes

Fig. 7 Instance of the database for renewable energy potential in India

Quantum GIS 2.14.3 in ESRI shape file format. From the Spatial Converter Tool, two thematic layers, i.e. renewable energy potential in India and India State Boundary, have been generated.

It has been observed that overlaying analysis of various vector data and raster data of particular area has been performed. Initially, the developed geospatial databases have been opened with Quantum GIS 2.14.3 and performed some join operations. The desired overlay operation has been done with stand-alone application and is known as thick client operation. Finally, these layers have been overviewed with India State Boundary. Figure 8 shows the snapshot of two layers in Quantum GIS 2.14.3.

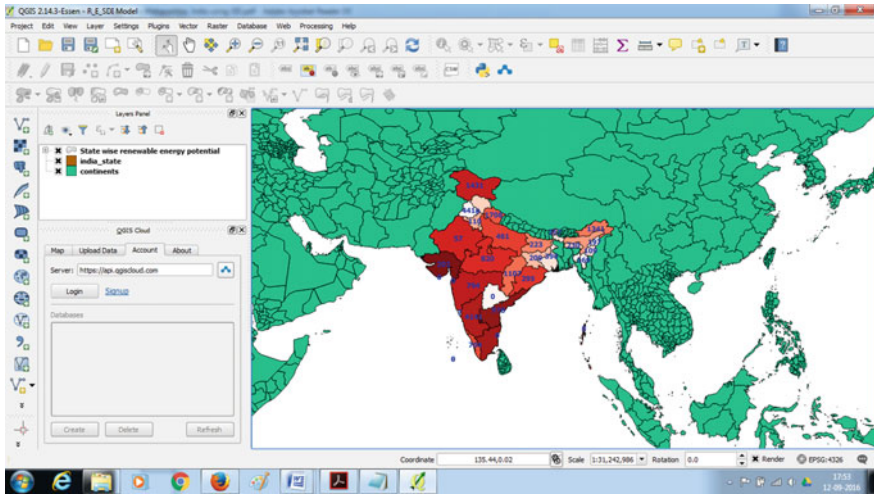


Fig. 8 Integration of renewable energy potential geospatial database

8 Concluding Remarks

The present research endeavours to link the information between the real merits and demerits of open-source GIS software via comprehensive exploration and evaluation of particular aspects correlated with functionality and complete execution. It is recognized as competent for delivering vigorous proficiencies to form the geospatial database creation for renewable energy potential in India. In regard to the creation of geospatial database, Quantum GIS 2.13.4 software invented as appropriate. However, the core emphasis of the current research is to cultivate the renewable energy potential geospatial database particularly at national level and further it will implement for Cloud SDI Model. Therefore, the database which has been established is analytical and does not include complete structures. This geospatial database may be made more ample in forthcoming studies. Currently, it has been planned to extend for other national level, and the equivalent may be deployed on the cloud environment in imminent studies.

References

1. Bhattacharya, S.C., Jana, C.: Renewable energy in India: historical developments and prospects. *Energy* **34**, 981–991 (2009)
2. Garg, P.: Energy scenario and vision 2020 in India. *J. Sustain. Energ. Environ.* **3**, 7–17 (2012)
3. Nagamani, C., Saravana Ilango, G., Reddy, M.J.B.: Renewable power generation Indian scenario—a review. *Electric power components and system*. Taylor and Francis, UK (2015)
4. Yep, E.: India's widening energy deficit, *The India Real Time Daily*, March (2011)

5. Schmid, G.: The development of renewable energy power in India: which policies have been effective? *Energy Policy* **45**, 317–326 (2012)
6. Tamil Nadu Energy Development Agency (TEDA) under the aid of Ministry of Non-conventional Energy Sources (MNES), Government of India, available at: <http://teda.in>, as on 10.02.2016
7. Kapoor, K., Pandey, K.K., Jain, A.K., Nandan, A.: Evolution of solar energy in India: a review. *Renew. Sustain. Energy Rev.* **40**, 475–487 (2014)
8. Jawaharlal Nehru National Solar Mission, Ministry of New and Renewable Energy (MNRE), Annual report 2013–2014, March 2014, available at: <http://mnre.gov.in>, as on 10.02.2016
9. Barik, R.K., Samaddar, A.B.: Service oriented architecture based SDI model for mineral resources management in India. *Univers. J. Geosci.* **2**(1), 1–6 (2014)
10. He, L., Yue, P., Di, L., Zhang, M., Hu, L.: Adding geospatial data provenance into SDI—a service-oriented approach. *IEEE J. Sel. Top. Appl. Earth Observ. Remote Sens.* **8**(2), 926–936 (2015)
11. Kulkarni, S., Banerjee, R.: Renewable energy mapping in Maharashtra; India using GIS. In: *World Renewable Energy Congress-Sweden*; Link A ping; Sweden, No. 057, pp. 3177–3184 (2011)
12. Mansourian, A., Rajabifard, A., Mansourian, M.J., Valadan Zoej, A., Williamson, I.: Using SDI and web-based system to facilitate disaster management. *Int. J. Comput. Geosci.* **32**, 303–315 (2005)
13. Barik, R.K., Samaddar, A.B., Samaddar, S.G.: Service oriented architecture based SDI model for geographical indication web services. *Int. J. Comput. Appl.* **25**, 42–49 (2011)
14. Vaccari, L., Shvaiko, P., Marchese, M.: A geo-service semantic integration in spatial data infrastructure. *Int. J. Spat. Data Infrastruct. Res.* **4**, 24–51 (2009)
15. Leidig, M., Teeuw, R.: Free software: a review, in the context of disaster management. *Int. J. Appl. Earth Obs. Geoinf.* **42**, 49–56 (2015)
16. Yang, C., Raskin, R., Goodchild, M., Gahegan, M.: Geospatial cyberinfrastructure: past, present and future. *Comput. Environ. Urban Syst.* **34**(4), 264–277 (2010)
17. Wu, B., Wu, X., Huang, J.: Geospatial data services within cloud computing environment. In: *IEEE International Conference on Audio Language and Image Processing (ICALIP)*, pp. 1577–1584 (2010)
18. Evangelidis, K., Ntouros, K., Makridis, S., Papatheodorou, C.: Geospatial services in the cloud. *Comput. Geosci.* **63**, 116–122 (2014)
19. Schäffer, B., Baranski, B., Foerster, T.: Towards spatial data infrastructures in the clouds. *Geospatial Thinking Lect. Notes Geoinf. Cartography* **0**, 399–418 (2010)
20. Yang, C., Goodchild, M., Huang, Q., Nebert, D., Raskin, R., Xu, Y., Bambacus, M., Fay, D.: Spatial cloud computing: how can the geospatial sciences use and help shape cloud computing? *Int. J. Digit. Earth* **4**(4), 305–329 (2011)
21. Smith, J., Mackaness, W., Kealy, A., Williamson, I.: Spatial data infrastructure requirements for mobile location based journey planning. *Trans. GIS* **8**(1), 23–44 (2004)
22. Barik, R. K., Dubey, H., Samaddar, A. B., Gupta, R. D., Ray, P. K.: FogGIS: Fog Computing for Geospatial Big Data Analytics. arXiv preprint [arXiv:1701.02601](https://arxiv.org/abs/1701.02601). (2016)

A Robust Controller Design for Standalone Microgrid System Feeding Composite Loads

Md. Asif Hasan, Raj Kumar Mishra and Md. Ashique Hassan

Abstract Microgrid is one of the popular architectures to accommodate renewable-based distributed energy resources (DER's). A microgrid may be operating in grid-tied mode or it may be in standalone mode feeding local loads of different natures. In this paper, design of a robust controller is presented for a standalone microgrid system which is feeding a composite load consisting of a linear load and a constant power-type load. Performance of standalone microgrid system with and without controller has been compared. Results are indicative that microgrid has stable operation with controller while feeding composite loads.

Keywords Microgrid · Composite loads · Controller · Stability · Standalone

1 Introduction

Microgrid has emerged as a potential solution to the problem of accommodation of various renewable energy sources into convention grid structure [1]. Unlike conventional synchronous generators, renewable energy sources like solar, wind, tidal are of intermittent nature. Availability of energy from these sources is very much of variable in nature, and the exact magnitude of availability at any specific time is very much unpredictable [2]. Due to intermittent nature, the load management becomes a difficult task in case of energy generation from renewable energy sources. A varying gap between active power generation and load causes unstable operation which results in frequency and voltage variation [3]. To maintain the frequency of supply and voltage magnitude, such renewable energy sources are

Md.A. Hasan (✉) · R.K. Mishra
Department of Electrical and Electronics, Birla Institute of Technology,
Mesra, Patna Campus, Patna, Bihar 800014, India
e-mail: hasan.asif6@gmail.com

Md.A. Hassan
Department of Mechanical, Birla Institute of Technology,
Mesra, Patna Campus, Patna, Bihar 800014, India

connected to conventional grid. This is called grid-tied mode of operation of microgrid [4]. In grid-tied mode, infinite bus bar or main grid maintains the frequency and terminal voltage stable [5]. The point of connection at which microgrid and main grid are attached is called point of common coupling (PCC) [6].

When any transient fault takes place anywhere in the conventional grid network, the current drawn at the PCC from distributed sources consisting microgrid may shoot very high. This high current may be dangerous for the various small-sized energy sources in microgrid. For the safeguard of renewable energy sources, the microgrid separates itself from the main grid. This is called islanding or standalone mode of microgrid operation [7]. In standalone operation mode, a microgrid system is supposed to supply the local loads at the PCC uninterruptible. The responsibility to maintain the load terminal voltage and frequency of the supply constant now lies with the microgrid alone. So a controller is necessary for stable operation of standalone microgrid.

This paper presents the mathematical modeling of a standalone microgrid feeding a combination of different types of loads. The composite load includes linear R - L load and a constant power-type load. Based on the mathematical modeling, a state-space model and transfer function of standalone microgrid have been prepared. Stability analysis has been performed over uncontrolled microgrid. Based on the stability analysis, a controller has been designed for stable operation of microgrid system even when operating in standalone mode.

2 Mathematical Modeling of Microgrid

Figure 1 presents the microgrid architecture in standalone mode. Under occurrence of transient fault, the circuit breaker CB operates and isolates the microgrid structure from main grid. A renewable energy source that is producing dc voltage output V_{dc} , feeds a current I_{dc} to a DC/AC converter. DC/AC converter is connected to PCC through distribution line consisting resistance R_{s1} and line inductance L_{L1} . Voltage at the point of common coupling is maintained at V_{m1} with the help of main grid supply. However, under transient fault condition, CB operates and dissociates the microgrid from main grid. Under isolated mode of operation, microgrid alone feeds a composite load connected at PCC. The composite load consists of a linear load (R_{L1} and L_{L1}) and a constant power-type load (P_1 , Q_1).

The dynamic equation of the microgrid system under standalone mode of operation in abc frame of reference consists of equations representing transmission line, inverter and the composite loads. The equations that present the transmission line dynamics are given below (1–3),

$$V_{s1a} = V_{m1a} + L_{s1}pI_{s1a} + R_{s1}I_{s1a} \quad (1)$$

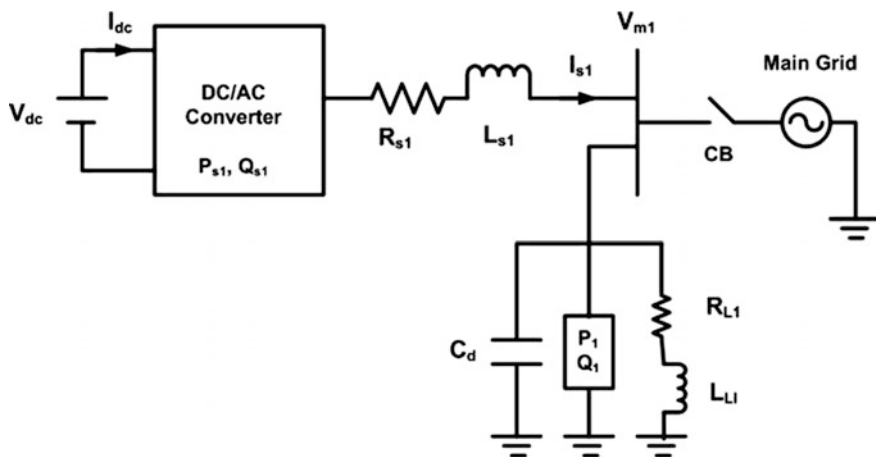


Fig. 1 Equivalent circuit of microgrid

$$V_{s1b} = V_{m1b} + L_{s1}pI_{s1b} + R_{s1}I_{s1b} \tag{2}$$

$$V_{s1c} = V_{m1c} + L_{s1}pI_{s1c} + R_{s1}I_{s1c} \tag{3}$$

The three-phase inverter equation is given as (4–6),

$$V_{s1a} = \frac{V_{dc}}{2} (2S_{ap} - 1) \tag{4}$$

$$V_{s1b} = \frac{V_{dc}}{2} (2S_{bp} - 1) \tag{5}$$

$$V_{s1c} = \frac{V_{dc}}{2} (2S_{cp} - 1) \tag{6}$$

Where S_{abc} is the switching function of inverter switches. Switching functions are generated using the modulation index value for a certain desired output from DC/AC converter. Linear loads that are represented by a simple R – L load are represented through following Eqs. (7–9),

$$V_{m1a} = R_{L1}I_{L1a} + L_{L1}pI_{L1a} \tag{7}$$

$$V_{m1b} = R_{L1}I_{L1b} + L_{L1}pI_{L1b} \tag{8}$$

$$V_{m1c} = R_{L1}I_{L1c} + L_{L1}pI_{L1c} \tag{9}$$

where I_{L1abc} is the three-phase current flowing into R – L load branch. A capacitor has been connected in parallel to the loads at PCC so as to absorb the voltage fluctuations. The dynamic equation for capacitor at PCC is given as (10–12),

$$C_d pV_{m1a} = I_{s1a} - I_{L1a} - I_{1a} \quad (10)$$

$$C_d pV_{m1b} = I_{s1b} - I_{L1b} - I_{1b} \quad (11)$$

$$C_d pV_{m1c} = I_{s1c} - I_{L1c} - I_{1c} \quad (12)$$

where I_{s1a} is the net current coming from PCC toward the load and I_{L1abc} and I_{1abc} are the currents entering into linear load and constant power-type load, respectively.

Since the abc frame equations are time dependent, and hence involve complexity in solving set of equations presenting the dynamics of microgrid system, so the set of dynamic equations are transformed into d - q frame. Using the following transformation matrix in (13), abc frame equations have been converted into d - q frame of reference.

$$k_s = \begin{bmatrix} \cos \theta & \cos(\theta - \frac{2\pi}{3}) & \cos(\theta + \frac{2\pi}{3}) \\ \sin \theta & \sin(\theta - \frac{2\pi}{3}) & \sin(\theta + \frac{2\pi}{3}) \\ 1/2 & 1/2 & 1/2 \end{bmatrix} \quad (13)$$

After d - q transformation over the dynamic equation set of microgrid with $\omega_s t = \theta$, we obtain following equations for linear loads (14–15),

$$pI_{L1q} = \frac{1}{L_{L1}} (V_{qmi} - R_{L1}I_{L1q} - L_{L1}\omega_s I_{L1d}) \quad (14)$$

$$pI_{L1d} = \frac{1}{L_{L1}} (V_{dmi} - R_{L1}I_{L1d} - L_{L1}\omega_s I_{L1q}) \quad (15)$$

Dynamic equation of capacitor in d - q frame is given as (16–17),

$$pV_{qm1} = \frac{1}{C_d} (I_{s1q} - I_{L1q} - I_{1q} - C_d\omega_s V_{dm1}) \quad (16)$$

$$pV_{dm1} = \frac{1}{C_d} (I_{s1d} - I_{L1d} - I_{1d} - C_d\omega_s V_{qm1}) \quad (17)$$

Current of the constant power-type load is given as follows (18–19),

$$I_{1d} = \frac{2P_1V_{qm1} - Q_1V_{dm1}}{3(V_{qm1}^2 + V_{dm1}^2)} \quad (18)$$

$$I_{1q} = \frac{2P_1V_{dm1} - Q_1V_{qm1}}{3(V_{qm1}^2 + V_{dm1}^2)} \quad (19)$$

Dynamic equation of the transmission line presents the behavior of load and generation both, as it connects the two segments of the system. To include the effect of DC/AC converter, which give a desired output corresponding to a control parameter modulation index (M), dynamic equation is prepared as follows (20–21),

$$pI_{s1q} = \frac{1}{L_{s1}} \left(M_q \frac{V_{dc}}{2} - R_{s1}I_{s1q} - L_{s1}\omega_s I_{s1d} \right) \tag{20}$$

$$pI_{s1d} = \frac{1}{L_{s1}} \left(M_d \frac{V_{dc}}{2} - V_{md1} - R_{s1}I_{s1d} + L_{s1}\omega_s I_{s1q} \right) \tag{21}$$

Since the constant power-type loads will carry a constant current so far the load voltage is maintained constant, so prior to the transient fault, the constant power-type load current is assumed to be constant. With transmission line current, load current and load terminal voltage as state variables, state-space model equations for islanded microgrid are represented as (22–24),

$$\dot{X}(t) = AX(t) + bu(t) \tag{22}$$

$$y(t) = cX(t) \tag{23}$$

$$u(t) = V_{dc} \tag{24}$$

where

$$A = \begin{bmatrix} \frac{-R_{s1}}{L_{s1}} & \omega_s & 0 & \frac{-1}{L_{s1}} \\ -\omega_s & \frac{-R_{s1}}{L_{s1}} & 0 & 0 \\ 0 & 0 & \frac{-R_{L1}}{L_{L1}} & \frac{1}{L_{L1}} \\ \frac{1}{C_d} & 0 & \frac{-1}{C_d} & 0 \end{bmatrix}$$

$$b^T = \left[\frac{M_d}{2L_{s1}} \quad \frac{M_q}{2L_{s1}} \quad 0 \quad 0 \right]$$

$$c = [0 \quad 0 \quad 0 \quad 1]$$

$$X^T = [I_{s1d} \quad I_{s1q} \quad I_{L1d} \quad V_{m1d}]$$

Now, considering isolated microgrid as a Single Input Single Output (SISO) system, transfer function of the overall system with V_{s1d} as input and V_{m1d} as output can be written as (25),

$$g(s) = c(sI - A)^{-1}b \tag{25}$$

Table 1 Data of the open-loop microgrid system

Parameter	Value
Transmission line resistance R_{s1}	3.2 m Ω
Transmission line inductance L_{s1}	550 μ H
Load resistance R_{L1}	85 Ω
Load inductance L_{L1}	125 mH
Load capacitance C_d	80 μ F
Reference source voltage V_{dc}	1200 V
D axis modulation index M_d	0.75
Q axis modulation index M_q	0.27
Rated frequency w_s	377 rad/s

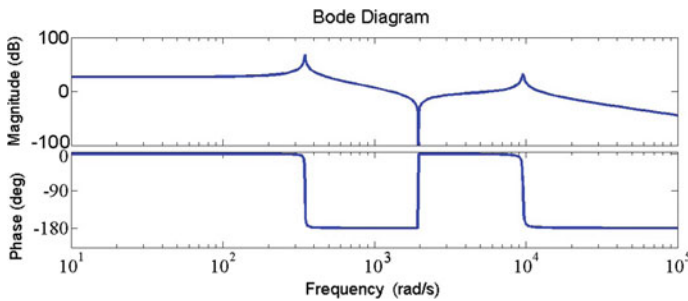


Fig. 2 Bode plot of uncontrolled isolated microgrid system

3 Simulation and Results

A microgrid system consisting of a DC source, a DC/AC converter, a transmission line and a composite load as presented in Fig. 1. has been considered for simulation. The data related to the microgrid system components are given in Table 1. Based on the transfer function equation developed for isolated microgrid, the complete transfer function based on data taken in Table 1 for specific microgrid model considered in this paper is given below (26),

$$g(s) = \frac{6.328e7s^2 + 1.8e6s + 2.4e14}{s^4 + 151.3s^3 + 9.1e7s^2 + 2.7e8s + 1.1e13} \tag{26}$$

As presented in Figs. 2 and 3, the phase margin of the system is -0.0641° and gain margin is -4.13 dB which indicates that system is unstable. To drag the system into a stable region, a PI controller has been designed using Empirical Ziegler–Nichols tuning formula. The method yields a value of $K_p = 494$ and $K_i = 9.6$. The step response for closed-loop microgrid system along with PI controller is given in Fig. 4.

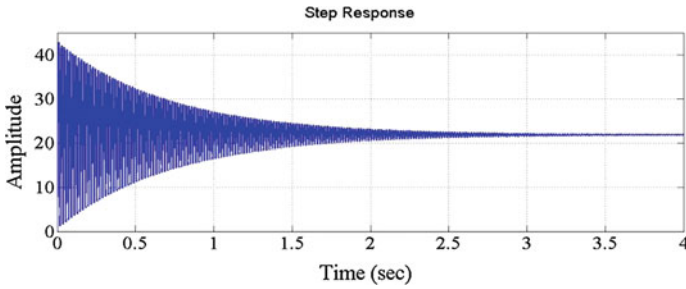


Fig. 3 Step response of the uncontrolled microgrid system

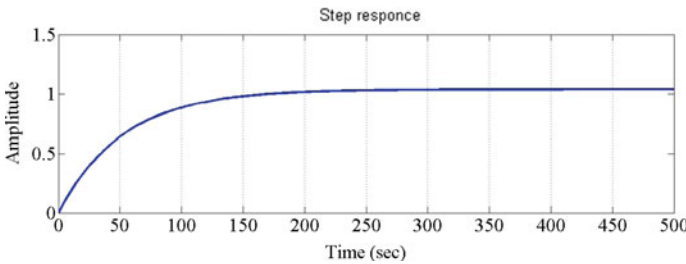


Fig. 4 Step response of closed-loop system

As the step response clearly indicates, the system has become a stable system. For disturbances occurring in dc source connected at input end, the load terminal voltage is now made constant and hence it can absorb the disturbances occurring in renewable-based energy source.

4 Conclusion

This paper investigates the stability of a standalone microgrid system feeding a composite load connected through DC-AC converter. Considering load terminal voltage as desired output, system is found to be unstable when operating under disturbances from source side. Occurrence of such disturbances is a common phenomenon in case of renewable energy sources. A PI controller designed for the microgrid system shows the ability to absorb the disturbances occurring at the source end and maintains the terminal voltage constant.

References

1. Kahrobaeian, A., Mohamed, Y.A.R.I.: Analysis and mitigation of low-frequency instabilities in autonomous medium-voltage converter-based microgrids with dynamic loads. *J. IEEE Trans. Ind. Electron.* **61**(4), 1643–1658 (2014)
2. Jiayi, H., Chuanwen, J., Rong, X.: A review on distributed energy resources and microgrid. *J. Renew. Sustain. Energy Rev.* **12**(9), 2472–2483 (2008)
3. Basak, P., Chowdhury, S., et al.: A literature review on integration of distributed energy resources in the perspective of control, protection and stability of microgrid. *J. Renew. Sustain. Energy Rev.* **16**(8), 5545–5556 (2012)
4. Planas, E., Gil-de-Muro, A., et al.: General aspects, hierarchical controls and droop methods in microgrids: a review. *J. Renew. Sustain. Energy Rev.* **17**(1), 147–159 (2013)
5. Jackson, J.J., Mwasilu, F., et al.: AC-microgrids versus DC-microgrids with distributed energy resources: a review. *J. Renew. Sustain. Energy Rev.* **24**(1), 387–405 (2013)
6. Liu, X., Wang, P., et al.: A hybrid AC/DC microgrid and its coordination control. *J. IEEE Trans. Smart Grid* **2**(2), 278–286 (2011)
7. Lu, X., Guerrero, J.M., et al.: Hierarchical control of parallel AC–DC converter interfaces for hybrid microgrids. *J. IEEE Trans. Smart Grid* **5**(2), 683–692 (2014)

Maximum Power Point Tracking of Direct-Drive PMSG with High-Efficiency Boost Converter

J. Barsana Banu, M. Balasingh Moses and S. Ganapathy

Abstract This chapter describes the variable speed stand-alone wind power supply system that incorporates permanent magnet synchronous generator, three-phase diode rectifier, and improved dc–dc boost converter with resistive load. Improved dc–dc boost converter controls to concentrate the most extreme power from the accessible wind. In the wind generation system, the power converter efficiency is one of the important considerations realizing the system performance. In those systems, dc–dc step-up converter is broadly utilized for high-conversion system. Considering the converter's expense and efficiency, this chapter mostly concentrates on the outline of an enhanced topology of the boost converter received for high-power stand-alone wind power system. It describes the perturbation and observation maximum power point tracking algorithm. The MPPT algorithm in addition to the dc–dc step-up converter is simulated by MATLAB/Simulink software. The outcomes demonstrate that the dc–dc converter topology can understand the most extreme power point tracking control of the wind turbine.

Keywords DC–DC boost converter · Efficiency · MPPT · Perturb and observe algorithm · WECS

1 Introduction

These days, renewable energy sources are turning into a vital choice to take care of the developing demand of energy such as contamination-free environment and all the while prevent the production of green gas from conventional fossil fuels.

J. Barsana Banu (✉) · M. Balasingh Moses · S. Ganapathy
Electrical and Electronics Engineering, Anna University, Trichy, India
e-mail: barsanajamal@gmail.com

M. Balasingh Moses
e-mail: mosesaut@gmail.com

S. Ganapathy
e-mail: mail2ganapathy@gmail.com

Depending upon the requirements, stand-alone or grid-connected operation is possible also the added advantage of renewable energy sources. Among different sorts of renewable energy sources, wind energy conversion systems have rapidly evolved around the world [1, 2]. Wind turbine, power electronics converter, and controllers are the key factors that are incorporated within the WECS. The wind turbine has the ability to extract power from the wind, which depends upon available wind power. There are two distinct categories based on the rotation axis of wind turbine: horizontal axis wind turbines (HAWTs) and vertical axis wind turbines (VAWTs).

In horizontal axis, the revolution of wind turbine is parallel to the ground, and in vertical axis, the revolution of wind turbines (VAWTs) is opposite to the wind, that is, vertical, and thus dissimilar to the horizontal wind turbines. They can catch winds from any heading beyond the requirement of rotor relocation as the wind bearing alters (Without a special yaw control).

Vertical axis wind turbines were, likewise, utilized as a part of a few applications as they have the favorable position that they don't rely on upon the heading into the wind. It is conceivable to concentrate on control generally less demanding. In any case, there are a few disservices, for example, no self-starting and minimum power coefficient than HAWT. Contrasted with VAWT, HAWT provides maximum efficiency, which is generally connected in the wind energy industry. The HAWT further splits into constant- and variable-speed wind turbines. The fixed-speed wind turbines achieve high efficiency at rated wind speed and possess the benefits that they are uncomplicated and long-lasting, and need lesser development and support cost. In any case, their operation speed is fixed and cannot be controlled by the variation in the wind speed, which outcomes minimum transformation efficiency contrasted with the variable-speed wind turbines.

These days, the vast majority of the wind turbines connected in industry are variable-speed wind turbines to build its energy capture at different wind speeds. Among various types of variable speed WECSs, three sorts are most generally connected to industries: DFIG (double-fed induction generator), SCIG (squirrel-cage induction generator), and WRSG (wound rotor synchronous generator) with geared or gearless or PMSG (permanent magnet synchronous generator) WECSs with full-capacity power converters.

The performances of different topologies of generator-converter combinations of WECS with distinct control algorithms are compared in [3]. With the approach of high-power thickness permanent magnets, the generator is manufactured with a most extreme power thickness contrasted with wound rotor sort bringing about the disposal of extra dc supply for outside excitation, brushes and slip rings gathering. Contrasted with induction generator (IG), PMSG does not require capacitors for excitation and voltage builds up. For small-scale installations, the use of PMSG is more useful on account of its minimized size and high-power density, not a requirement for gearbox.

WECS based on the permanent magnet synchronous generator was investigated in recent researches [4, 5]. Another major benefit of WECS has made an effective move from small stand-alone areas to satisfy consumer demand to high

grid-connected networks. Depending upon the requirement, the grid provides real power to the loads or absorbs the abundance power from the site when accessible. However, significant literature is available on stand-alone power generation with PMSG [6, 7]. The stand-alone system should, consequently, have few methods of reserving energy. It can be utilized afterward to contribute the demand for the period of low or nil output power. Several control strategies and algorithm for stand-alone WECS are developed for variable wind speed, and the load is described in [8, 9]. Most of WECS are projected for grid-connected systems [10]. In [11], an effortless control method is presented for finest extraction of power from grid-tied PMSG-VS wind energy conversion. It utilizes sensor less maximum power point tracking algorithm but with lagging power factor.

In [12], sliding mode (SM) evaluation of DTC is investigated to maximize the extracted power at unity power factor. The execution of WECS has been shown under fluctuating wind circumstances. At that point, the networks not only obtain the most extreme power but also keep up the unity power factor output voltage at fixed frequency. MPPT procedure is employed for obtaining the most extreme power available in the wind. The principal MPPT strategies are as follows: tip-speed ratio (TSR), optimum relation based (ORB) (power vs. speed and power vs. torque), and perturb and observe (P&O) strategies.

Various MPPT techniques are described in [13]. The power electronic converter integration plays a vital role in understanding the maximum power point tracking (MPPT) process [14]. The methodology of a converter in view of a 3 Φ rectifier with the boost converter is more appropriate for small wind energy system requirements in view of its minimum price and high consistency [15], and MPPT estimation with modified perturb and observe algorithm is projected to fulfill an optimization of the MPPT in the quickly changing wind speed.

This chapter focuses the stand-alone wind power supply system with improved power electronic boost converter control to track the most extreme power from the accessible wind in all directions as shown in Fig. 1. The detailed modeling of wind turbine and permanent magnet synchronous generator is described in Sects. 2 and 3. Uncontrolled rectifier and proposed boost converter are explained in Sects. 4 and 5. MPPT algorithm and its implementation are described in Sect. 6. Simulation analyses are carried out in Sect. 7. Finally, conclusions are drawn in Sect. 8.

2 Modeling of Wind Turbine

The power obtained from the wind has the accompanying expression:

$$P_w = \frac{1}{2} \rho \pi R^2 V_w^3 C_p \quad (1)$$

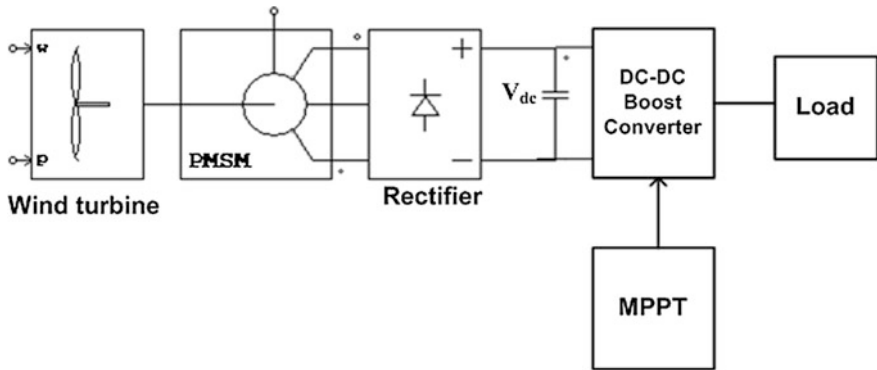


Fig. 1 Proposed system arrangement

- R Turbine sweep (radius) (m)
- q Thickness of the air (kg/m^3)
- V_w Velocity of the wind (m/s)
- C_p Turbine power coefficient

The wind turbine torque can be expressed as follows:

$$T_w = \frac{P_w}{\Omega_m} = \frac{1}{2} \rho \pi R^2 \frac{V_w}{\Omega_m} C_p \tag{2}$$

Ω_m Pivot velocity of the turbine (rad/s). The power coefficient can be communicated as follows:

$$C_p = 0.5176 \left(\frac{116}{\lambda_i} - 0.4\beta - 5 \right) e^{-\frac{21}{\lambda_i}} + 0.0068\lambda \tag{3}$$

$$\frac{1}{\lambda_i} = \frac{1}{\lambda + 0.08\beta} - \frac{0.055}{\beta^3 + 1} \tag{4}$$

where β is the angle of the blades (rad) and λ is the tip-speed ratio (TSR) which is represented by:

$$\lambda = \frac{R\Omega_m}{V_w} \tag{5}$$

It is observed that the TSR is optimum ($K\Omega_{mopt}$) at maximum power coefficient C_{Pmax} . Hence, the wind power extraction is higher. At this condition, optimum power is attained by applying λ in (1)

$$P_{w\max} = K\Omega_{\text{mopt}}^3 \quad (6)$$

Equation (6) should be utilized to understand the MPPT examination.

$$K = \frac{\frac{1}{2}\rho\pi R^5 C_{p\max}}{\lambda_{\text{opt}}^3} \quad (7)$$

where K is the power gain at maximum power and Ω_{mopt} is an ideal turn speed compared to a particular wind speed.

3 PMSG Modeling

The modeling of PMSG is represented by d - q reference frame by the following:

$$V_d = R_s i_d + L_d \frac{di_d}{dt} - \omega_e L_q i_q \quad (8)$$

$$V_q = R_s i_q + L_q \frac{di_q}{dt} - \omega_e L_d i_d + \omega_e \Phi_m \quad (9)$$

where V_d and V_q are d and q components of stator voltages (V); i_d and i_q are stator current (A) of the d and q components; R_s is the resistance in the stator (ohms); L_d and L_q are the d - and q -axis machine inductances (H); ω_e is the electric speed (rad/s); and Φ_m is the flux (wb).

The electrical torque is obtained from the accompanied equation:

$$T_e = \frac{3}{2}p \{ \Phi_m i_q + (L_d - L_q) i_d i_q \} \quad (10)$$

where p is the pole pairs. The dynamics of the machine rotor is given as follows:

$$T_m - T_e = B\omega_r + J \frac{d\omega_r}{dt} \quad (11)$$

where B is the rotor friction (kg m²/s), J is the rotor inertia (kg m²), ω_r is rotor speed (rad/s), and T_m is the mechanical torque created by wind (Nm).

For simplification, assume ($L_d = L_q = 0$), the d reference current is zero ($i_d^* = 0$), and hence, the product term ($L_d - L_q$) $i_d i_q$ is negligible.

4 Diode Rectifier

The 3Φ full-wave bridge rectifier can be connected directly to the three-phase source to convert the ac output voltage from the PMSG to the rectified dc. The average dc output voltage across the rectifier is as follows:

$$V_{dc} = \left(3\sqrt{2}/\pi\right)V_L \quad (12)$$

where V_{dc} is dc or average output voltage across the rectifier, and V_L is the ac line voltage from PMSG.

5 DC–DC Boost Converter

The unregulated dc voltage from the diode rectifier is given as input to the improved boost converter. The rectifier output voltage will fluctuate due to variations in wind speed. Improved step-up converter is needed to obtain the regulated dc output voltage and also to understand the MPPT process. A single-control switch S is desirable due to its low expense and robust control. The resistive burden R_L associated with step-up converter is expected to acquire the power from WECS. The boost converter output voltage is obtained as follows:

$$\frac{V_0}{V_{dc}} = \frac{1}{1 - K} = \frac{I_0}{I_{dc}} \quad (13)$$

The MPPT computation utilizes the dc voltage and current acquired from the rectifier to regulate the duty cycle K .

6 MPPT Algorithm

The MPPT computation processes the optimum speed for the most extreme power point utilizing data on direction and magnitude of output power variation owing to the variation in grasp speed. The stream diagram for MPPT is shown in Fig. 2. It depicts the step-by-step execution of proposed MPPT procedure. The controller operation is clarified underneath. The active power $P_0(k)$ is calculated, and if the distinction between its values at present and past examining moment, $\Delta P_0(k)$ is within a predefined minimum and maximum power limits P_{\min} and P_{\max} correspondingly; then, no action is made; still, if the distinction is outside this extent, at that point, certain important control move is made. The control activity made relies on the direction and magnitude of power variation because of the adjustment to the grasp speed.

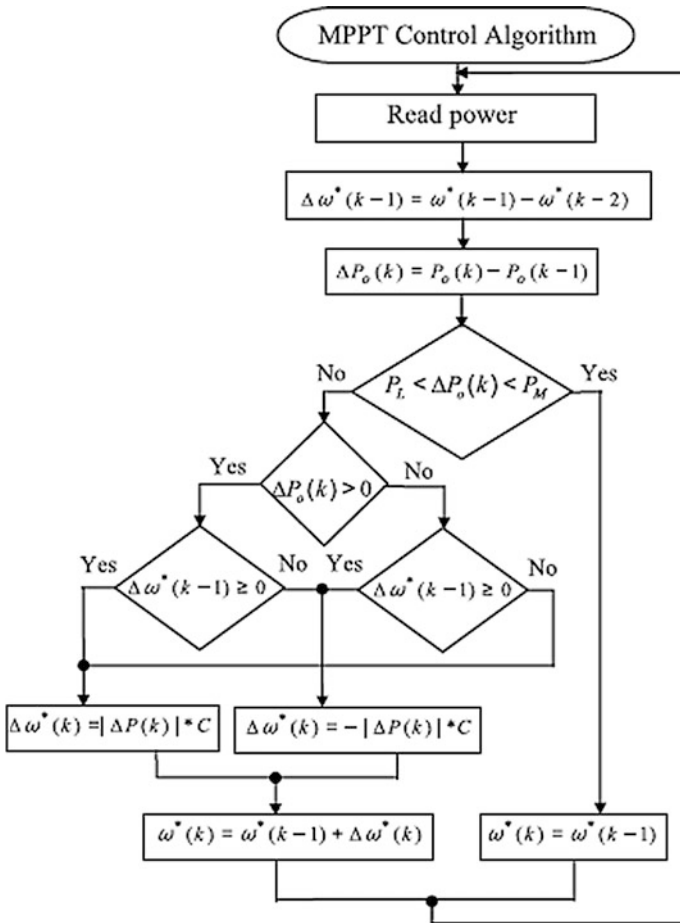


Fig. 2 Flowchart for the proposed MPPT algorithm

- (i) On the off chance that the power in the present testing moment is observed to be higher, i.e., $\Delta P_o(k) > 0$ either because of an expansion in grasp speed or grasp speed staying unaltered in the past examining moment, i.e. $\Delta\omega^*(k-1) \geq 0$, after that the grasp speed is increased.
- (ii) If the power in current testing moment is observed to be higher, i.e., $\Delta P_o(k) > 0$, because of diminution in the grasp speed over the past examining moment, i.e., $\Delta\omega^*(k-1) < 0$, after that the reference speed is reduced.
- (iii) In addition, if the power diminishing in the current inspecting moment is observed, i.e., either because of a steady or expanded grasp speed over the past examining moment, i.e., $\Delta\omega^*(k-1) \geq 0$, at that moment grasp speed is minimized.

- (iv) At long last, if the power in current testing moment is observed to be diminished, i.e., $\Delta P_0(k) < 0$, because of an abatement in grasp velocity in the past examining moment, i.e. $\Delta \omega^*(k - 1) < 0$, the grasp speed is incremented.

The extent of variation, assuming any, in the reference velocity in a control sequence is chosen by the result of extent of power error $\Delta P_0(k)$ and C . The quality C is chosen by the rate as the wind speed. All along the most extreme power point tracking process handles the item said above reductions gradually lastly equivalents to zero at the crest power point.

To have the incredible following ability at all wind ranges, the estimation of C ought to fluctuate the variation at the adjustment in the wind velocity. If the wind rate is not ascertained, rotor velocity is used to set its regard. After that, at lower wind speed, power varies with speed deviation and the rate of C is higher; then, the speed increases as C decreases. In the proposed chapter, a number of simulations are carried out with distinct inputs to find out the above-mentioned values which indicate the excellent outcomes.

7 Results and Discussions

Wind turbine with MPPT control of the improved boost converter is completed utilizing MATLAB simulation software to assess the feasibility of the presented configuration. Simulink model of wind-driven PMSG step-up converter is shown in Fig. 3.

The sub-blocks of wind turbine and MPPT controller are shown in Fig. 3. The perturb and observe MPPT controller initially measures the power from the wind and compares the power in the present state and in the previous state. Based on the ratio of difference in the power, the duty ratio of the boost converter switch can be

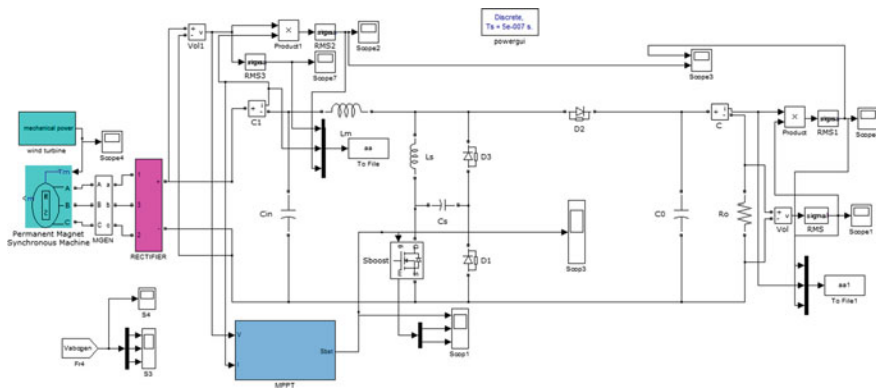


Fig. 3 Simulink model

perturbed at each second, and the different characteristics of the wind turbine are shown in Fig. 4.

The wind turbine operating for 15 and 17 m/s is considered and measures the rectifier outputs and the improved boost converter outputs. Figures 5a and 6a depict the dc waveforms of the uncontrolled bridge rectifier for 15 and 17 m/s wind speeds. Figures 5b and 6b represent the converter waveforms, respectively, by considering the wind speed at 15 and 17 m/s at the phase angle of 0°. The proposed boost converter receives input from the uncontrolled bridge rectifier then this boost converter step up this uncontrolled dc outputs in order to be controlled dc voltage, current and power, double the input given and achieves the high converter efficiency up to 97%. If the wind speed increases from 15 to 17 m/s, the output voltage and power also increased as shown in Figs. 5 and 6.

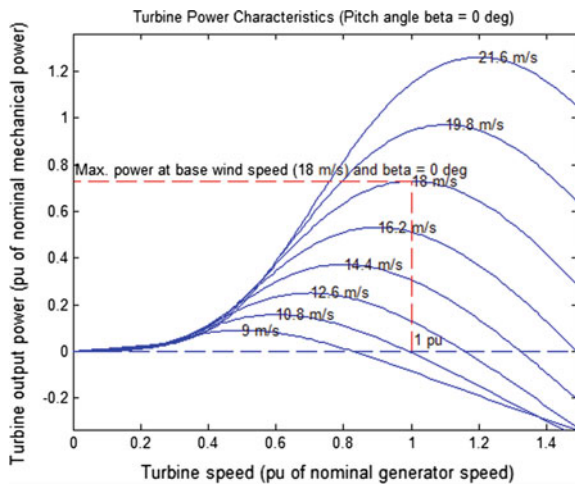


Fig. 4 Characteristics of the wind turbine

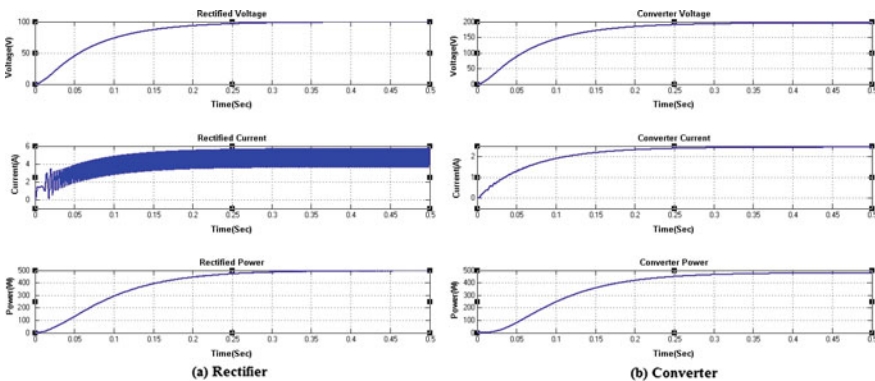


Fig. 5 O/P voltage, current, and power at 15-m/s wind speed. a Rectifier and b converter

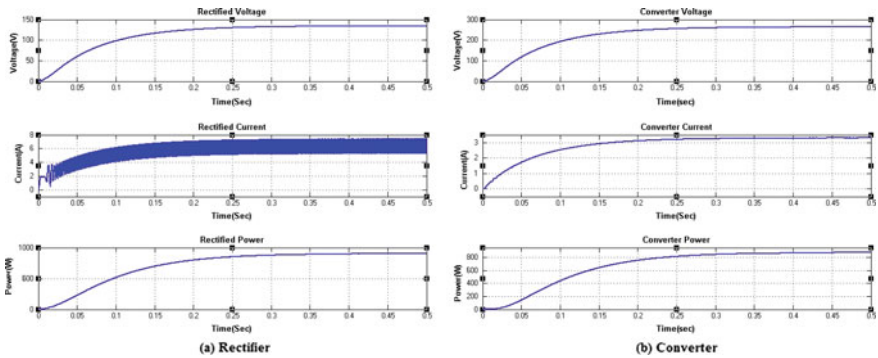


Fig. 6 O/P voltage, current, and power at 17-m/s wind speed. **a** Rectifier and **b** converter

8 Conclusion

In this chapter, the wind-driven PMSG with high-efficiency dc–dc step-up converter is described. The perturb and observe algorithm works efficiently for the proposed boost converter circuit. The simulation results for two different wind speeds are compared and show that the proposed boost converter achieves high efficiency with maximum power point tracking. The topology and control strategy of the proposed converter provide a valid solution for stand-alone wind turbine applications.

References

1. Babu, N.R., Arulmozhiarman, P.: Wind energy conversion systems-a technical review. *J. Eng. Sci. Technol.* **8**(4), 493–507 (2013)
2. Kekezoglu, B., Tanrioven, M., Erduman, A.: A new wind turbine concept: design and implementation. *Acta Polytech. Hung.* **12**(3), 199–211 (2015)
3. Baroudi, J.A., Dinavahi, V., Knight, A.M.: A review of power converter topologies for wind generators. *Renewable Energy.* **32**(14), 2369–2385 (2007)
4. Messaoud, M., Abdessamed, R.: Modeling and optimization of wind turbine driving permanent magnet synchronous generator. *Jordan J. Mech. Ind. Eng.* **5**(6), 489–494 (2011)
5. Wu, Z., Dou, X., Chu, J., Hu, M.: Operation and control of a direct-driven PMSG-based wind turbine system with an auxiliary parallel grid-side converter. *Energies* **6**(7), 3405–3421 (2013)
6. Vlad, C., Bratcu, A.: Munteanu, I., Epure, S.: Real-time replication of a stand-alone wind energy conversion system: error analysis. *Int. J. Electr. Power Energy Syst.* **55**, 562–571 (2014)
7. Singh, B., Sharma, S.: Stand-alone wind energy conversion system with an asynchronous generator. *J. Power Electron.* **10**(5), 538–554 (2010)
8. Hussein, M.M., Senjyu, T., Orabi, M., Wahab, M.A., Hamada, M.M.: Control of a stand-alone variable speed wind energy supply system. *Applied Sciences.* **3**(2), 437–456 (2013)

9. Lopez, M., Vannier, J.C.: Stand-alone wind energy conversion system with maximum power transfer control. *Ingeniare. Revistachilena de ingenieria* **17**(3), 329–336 (2009)
10. Linus, R.M., Damodharan, P.: Maximum power point tracking method using a modified perturb and observe algorithm for grid connected wind energy conversion systems. *IET Renew. Power Gener.* **9**(6), 682–689 (2015)
11. Linus, R.M., Damodharan, P.: Wind Velocity Sensorless Maximum Power Point Tracking Algorithm in Grid-connected Wind Energy Conversion System. *Electric Power Compon. Systems.* **43**(15), 1761–1770 (2015)
12. Errami, Y., Maaroufi, M., Ouassaid, M.: Maximum power point tracking of a wind power system based on the PMSG using sliding mode direct torque control, In: *International Renewable and Sustainable Energy Conference (IRSEC)*, Ouarzazate, pp. 218–223 (2013)
13. Abdullah, M.A., Yatim, A.H.M., Tan, C.W., Saidur, R.: A review of maximum power point tracking algorithms for wind energy systems. *Renew. Sustain. Energy Rev.* **16**(5), 3220–3227 (2012)
14. Li, P., Li, D.Y., Wang, L., Cai, W.C., Song, Y.D.: Maximum power point tracking for wind power systems with an improved control and extremum seeking strategy. *Int. trans. electr. energy syst.* **24**(5), 623–637 (2014)
15. Daili, Y., Gaubert, J.P., Rahmani, L.: Implementation of a new maximum power point tracking control strategy for small wind energy conversion systems without mechanical sensors. *Energy Convers. Manag.* **97**, 298–306 (2015)

PEM Fuel Cell System Identification and Control

Pinagapani Arun Kumar, Mani Geetha, K.R. Chandran
and P. Sanjeevikumar

Abstract A model is an input–output mapping that suitably explains the behavior of a system. Model helps to analyze the functionality of the system and to design suitable controllers. System identification builds model from experimental data obtained by exciting the process with an input and observing its response at regular interval (Wibowo et al. in System identification of an interacting series process for real-time model predictive control, American Control Conference, pp. 4384–4389, 2009). Fuel cells (FC) systems are a potentially good clean energy conversion technology, and they have wide range of power generation applications. Classification of fuel cells is based on the fuel and the electrolyte type used. The proton exchange membrane fuel cells (PEMFC) are portable devices with superior performance and longer life. They act as a good source for ground vehicle applications. They also possess high power density and fast start-up time. In this work, mathematical model of a real-time PEMFC is obtained and its quality is assessed using various validation techniques. The model is obtained using system identification tool in MATLAB, and validation procedures like recursive least square algorithm, ARX and ARMAX were employed to assess the model. Controllers such as PI and PID were employed in order to achieve the desired load current by controlling the hydrogen flow rate. The values of the gain constant,

P. Arun Kumar (✉)

Department of Instrumentation & Control Systems Engineering,
PSG College of Technology, Coimbatore, Tamil Nadu, India
e-mail: arunkumarakshai@gmail.com

M. Geetha

School of Electrical Engineering, Vellore Institute of Technology (VIT) University,
Vellore, Tamil Nadu, India
e-mail: geethamani@gmail.com

K.R. Chandran

Department of Information Technology, PSG College of Technology,
Coimbatore, Tamil Nadu, India
e-mail: chandran_k_r@yahoo.co.in

P. Sanjeevikumar

Department of Electrical and Electronics Engineering, University of Johannesburg,
Auckland Park, Johannesburg, South Africa
e-mail: sanjeevi_12@yahoo.co.in

integral time and derivative time were obtained using Cohen-Coon method. PI and PID control schemes were implemented using SIMULINK in MATLAB environment, and the system response was observed.

Keywords Proton exchange membrane fuel cell (PEMFC) · Recursive least square algorithm · ARX · ARMAX · Cohen-Coon · PI · PID

1 Introduction

The utilization of fossil fuels has become the need of the hour due to increased concentration of greenhouse gases such as CO, CO₂, NO and SO. Renewable energy sources have become alternative energy sources, as the available non-renewable energy sources are becoming scarce and expensive. Also, the need for cleaner energy sources is on the rise. So a trade-off between cleaner energy and their efficiency has become mandatory. Among the various cleaner alternative energy sources like wind power, hydropower, photovoltaic power, the fuel cells have been critically acclaimed in the recent years due to their superior performance, better efficiency than other clean energy sources, less or nil pollution to the environment, longer life and excellent dynamic response. Due to its manifold advantages, fuel cells have become the focus of research.

Various FC models are available, and the proton exchange membrane fuel cell (PEMFC) is one of the models. PEMFC has good characteristics that make it suitable for use in small- and large-scale distributed generation systems, residences and industries.

2 Proton Exchange Membrane Fuel Cell

Proton exchange membrane fuel cells (PEMFC) are electrochemical devices, and traditionally they use hydrogen as the fuel. PEMFC requires pure hydrogen as the input, and hence, these fuels can either be directly fed into the fuel cell, or sent to a reformer to extract pure hydrogen, which is then directly fed to the fuel cell. Other fuel options range from methanol, ethanol bio-derived materials.

A fuel cell shown in Fig. 1 [2] consists of a negatively charged electrode (anode), a positively charged electrode (cathode) and an electrolyte membrane.

3 Modeling and Control of PEMFC System

System identification algorithm was implemented and validated for the benchmark process shown in Fig. 2. An empirical model for the process is developed from the experimental data using system identification toolbox in MATLAB.

Fig. 1 A single PEMFC configuration

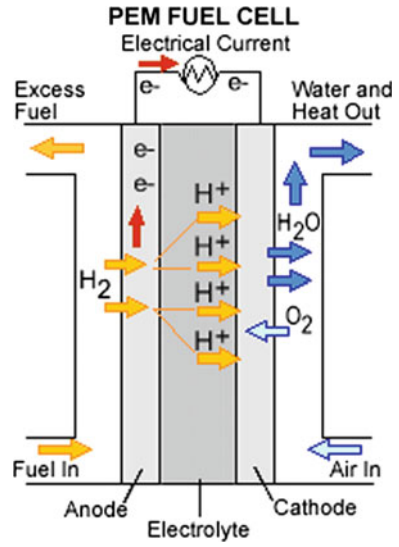


Fig. 2 Fuel cell system



Fuel cell testers (FCT) is a complete station for electrochemical testing of proton exchange membrane fuel cell (PEMFC). The FCT is made to study single cells.

3.1 PEMFC System Specifications

The input flow data, cell voltage data and output cell current data are obtained from the FC-lab[®] software. Two sets of data have been acquired from the FC-lab software among which first set is used for modeling the PEMFC and the second set is used for validation of PEMFC. It is considered as a single-input and single-output (SISO) process with input as hydrogen flow rate and the output as current.

The inflow was maintained constantly at 500 ml/min. The cell current data and flow data were collected till the steady state is achieved. In this case, constant cell current at 12.5 A and the system specifications are given in Table 1.

3.2 Open-Loop Response of the System

One of the several ways to determine what values to use for the proportional, integral and differential parameters in the controller is Cohen-Coon method.

By looking at the system's open-loop response, the values for the controller parameters are determined. The system's response (G) is modeled to a first-order response plus dead time. K is the system gain which is obtained by dividing the output steady state divided by the input step change, τ is the effective time constant of the response, and t_d is the dead time

$$G(s) = \frac{Ke^{-t_d s}}{1 + \tau s} \quad (1.1) \quad G(s) = \frac{0.028865}{935.14s + 1} \quad (1)$$

Using the open-loop response shown in Fig. 3, it was found that

$$K = 0.028865, \tau = 935.14 \text{ and } \tau_d = 100 \text{ s.}$$

Table 1 Fuel cell system specifications

Description	Value
Cell size	25 cm ²
Cell temperature	35 °C
Purge flow	100 ml/min
Flow of H ₂	500 ml/min
Flow of O ₂	300 ml/min
H ₂ /O ₂ ratio	100:21
Humidifier temp. of H ₂	70 °C
Line temp. of H ₂	70 °C
Humidifier temp. of O ₂	60 °C
Line temp. of O ₂	60 °C

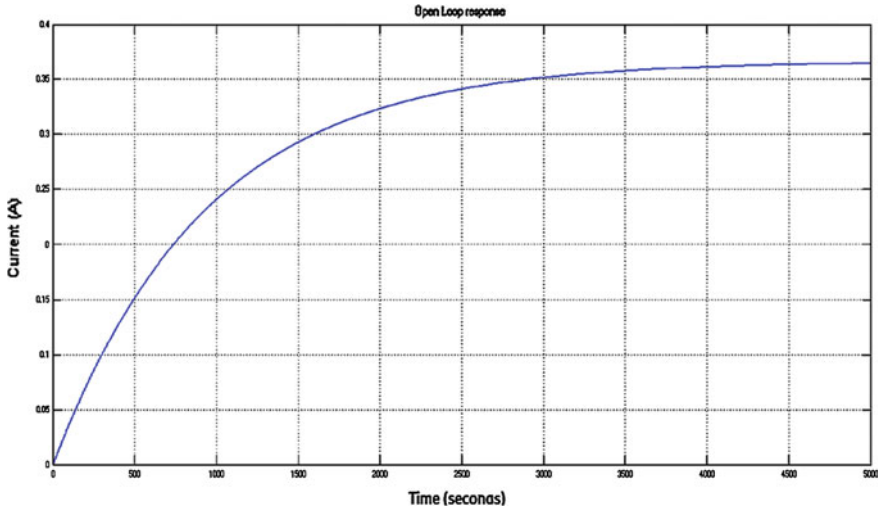


Fig. 3 Open-loop response of PEMFC system

The discrete transfer function is

$$G(z) = \frac{0.02167}{z - 0.9847} \tag{2}$$

3.3 Model Validation

Case 1: Model Performance versus Actual System Performance

A second set of data (test data) was obtained by maintaining the inflow constantly at 500 ml/min as that for the model. The cell current data and flow data were collected till the steady state is achieved. In this case, constant cell current is 12.77 A.

The response of the actual system in comparison with that of the model for the given data is shown in Fig. 4. It is inferred that both the responses almost have the same magnitude. A fit of 77.19% is observed between the actual system and the model.

Case 2: RLS Algorithm

RLS, an adaptive algorithm is implemented in MATLAB for estimating the parameters of the system. The obtained discrete-time transfer function model for first region is

Fig. 4 Validation response by changing process dynamics

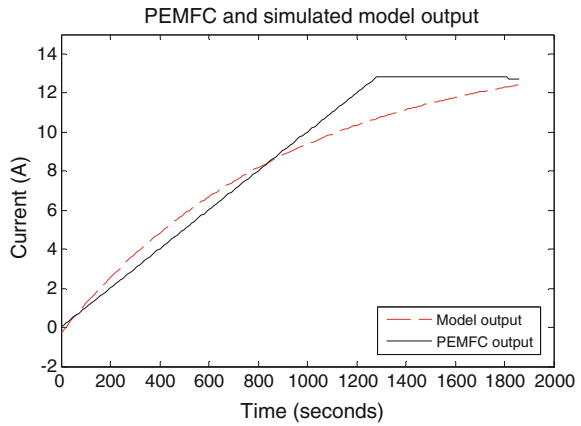
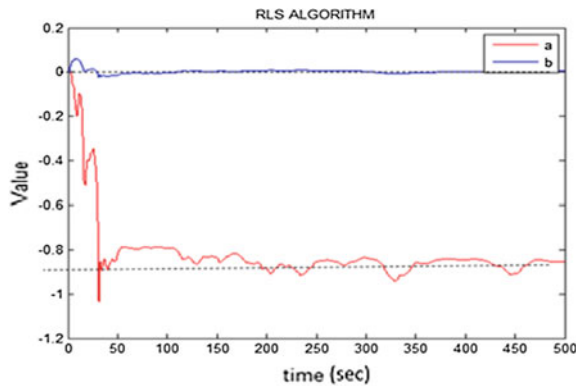


Fig. 5 Parameter estimation by RLS algorithm



$$y(t) = \frac{0.02167}{z - 0.9847} u(t) + e(t) \tag{3}$$

It can be noted that from the above equation, $a = -0.9894$ and $b = 0.000307$.

It can be inferred from Fig. 5 that the process parameters estimated by RLS algorithm are being converged to that of the process parameters a and b obtained from the model, and hence, the model tends to be the best approximated model.

Case 3: ARX method

In the system identification tool box, select estimate > polynomial models to open the polynomial models dialog box. From the structure list, select ARX: $[n_a \ n_b \ n_k]$. Edit the orders field to try all combinations of poles, zeros and delays, where each value is from 1 to 10: [1:10 1:10 1:10]. Click estimate to open the ARX model structure selection window, which displays the model performance for each combination of model parameters. The best fit model is $n_a = 5, n_b = 10, n_k = 1$,

Fig. 6 ARX model response

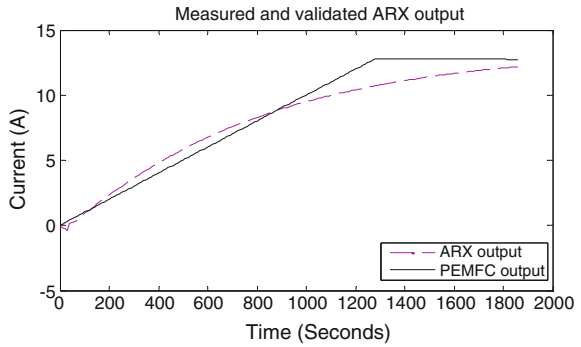
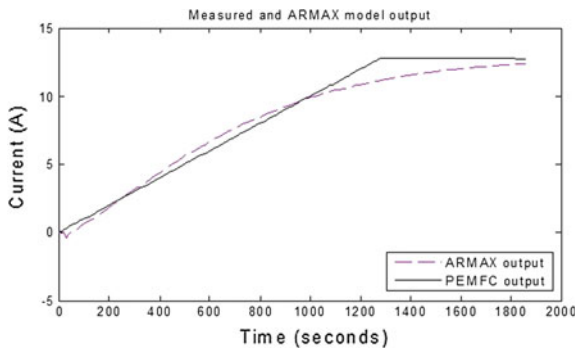


Fig. 7 ARMAX model response



but the lower-order models fit the same way; hence, the model is of order $n_a = 5, n_b = 1, n_k = 1$. Figure 6 shows the ARX model response.

Case 4: ARMAX method

In the system identification tool box, select estimate > polynomial models to open the polynomial models dialog box from the structure list, and select ARMAX: $[n_a n_b n_c n_k]$. Set the orders n_a, n_b, n_c and n_k to the following values: $[5 1 1 1]$ in the orders field. Click estimate to add the ARMAX model to the system identification app. The ARX model output is taken as same as the values of ARX parameters along with the disturbance parameter n_k as 1. Figure 7 is a graph showing the response of the model in comparison with the one obtained using ARMAX method.

The comparison of the first-order process model, actual system performance, ARX and ARMAX model gives a better understanding about the validation procedures. It is shown in Fig. 8. The percentage of the output variations with respect to the PEMFC output that is reproduced by the model is given by percentage fit. A higher number means a better model. From Fig. 8, it is inferred that the validated ARX model tracks the same output as that of the actual system versus model, i.e., fit is almost the same.

3.4 Controller Design and Implementation

The controller gains are found out by using the Cohen-Coon method.

For PI controller, $K_p = 294.4601$, $T_i = 997.81$ s.

For PID controller, $K_p = 440.621$, $T_i = 235.586$ s and $T_d = 35.67$.

The response of the system with PI and PID controller is shown in Fig. 9. It can be inferred from Table 2 that the rise time is lesser in PID controller than in PI controller. But PI controller settles faster than the PID controller since there is no overshoot in the PI controller.

Fig. 8 Validated model outputs

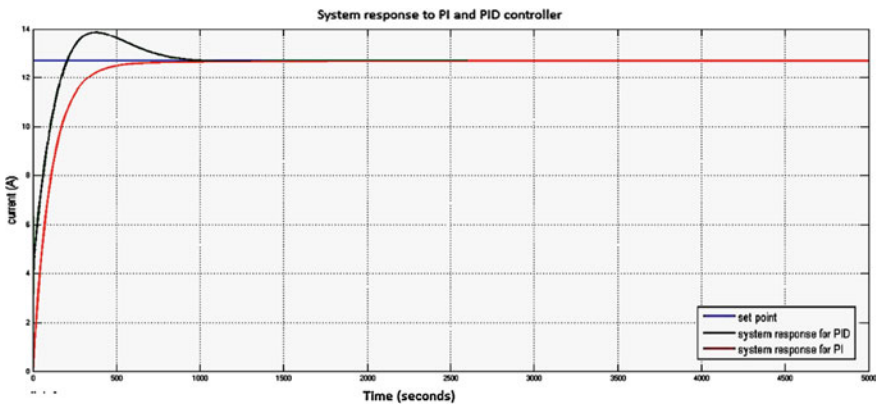
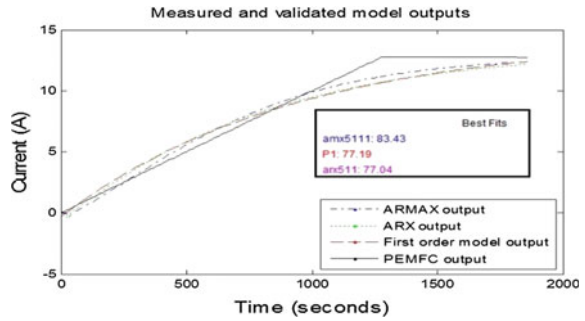


Fig. 9 System response with PI and PID controller

Table 2 Comparison of performance for PI and PID controller

Controller	Rise time (s)	Settling time (s)	Overshoot (A)	Peak(A)
PID	146.43	757.43	9.18	13.86
PI	245.63	462.55	0	12.69

4 Conclusion

A model for a single PEM fuel cell is built from experimental data obtained by exciting the process with an input and observing its response at regular interval, using system identification technique. The model is validated by changing the dynamics of the inflow to the system. Models are able to adapt to the change in dynamics, and hence, the obtained model is found to be the best approximated model. An adaptive algorithm, i.e., RLS algorithm, is used to estimate the parameters of the process. From the response, it can be inferred that the process parameters are tracked, and hence, the model is valid. ARX and ARMAX methods are also employed, and from the response, it can be inferred that the model is valid. PI and PID control strategies are implemented to obtain the desired cell current. It was found that the PID controller had a rise time which was less than that of PI controller; however, the settling time was found to be the same.

References

1. Wibowo, T.C.S., Saad, N., Karsiti, M.N.: System identification of an interacting series process for real-time model predictive control, American Control Conference, pp. 4384–4389 (2009)
2. Spiegel, C.: PEM fuel cell modeling and simulation using MATLAB. Academic Press, London (2011)
3. Ljung, L.: System identification—theory for the user, 2nd edn. Prentice-Hall, New Jersey (1999)
4. Astrom, K.J., Wittenmark, B.: Adaptive control, 2nd edn. Dover Publications, New York (2008)

Lightweight Microwave Absorber from Industrial Waste Fly Ash Cenosphere

Pritom J. Bora, K.J. Vinoy, Kishore, Praveen C. Ramamurthy
and Giridhar Madras

Abstract The present investigation demonstrates the microwave absorption property of magnetic alloy nanoparticle-coated solid industrial waste fly ash cenosphere (FAC). Here, cobalt iron (CoFe) alloy nanoparticles were chemically coated over FAC, and a composite matrix was made from these particles using epoxy resin. Surface morphology of both CoFe-FAC and epoxy/CoFe-FAC composites was studied. The dielectric loss and reflection loss (RL) of this polymer composite were studied by rectangular waveguide transmission line method. A 10 wt% CoFe-FAC-loaded epoxy composite shows an excellent microwave absorption property in the X-band (8.2–12.4 GHz). The most effective RL value -29 dB was obtained for epoxy/CoFe-FAC composite, whereas a pristine epoxy/FAC composite combination exhibits -12 dB RL under same condition. The thickness dependency of RL was also studied, and it indicates that the standard -10 dB RL can be obtained

P.J. Bora · G. Madras
Interdisciplinary Centre for Energy Research (ICER), Indian Institute of Science,
Bangalore 560012, India
e-mail: jyotipritom09@gmail.com

G. Madras
e-mail: giridharmadras@gmail.com

K.J. Vinoy
Department of Electrical and Communication Engineering,
Indian Institute of Science, Bangalore 560012, India
e-mail: vinoykj@gmail.com

Kishore
Department of Material Engineering, Indian Institute of Science,
Bangalore 560012, India
e-mail: balkis@materials.iisc.ernet.in

P.C. Ramamurthy (✉)
Department of Material Engineering, Interdisciplinary Centre for Energy
Research (ICER), Indian Institute of Science, Bangalore 560012, India
e-mail: onegroupb203@gmail.com

for epoxy/CoFe-FAC composite at a minimum thickness of 2 mm. The enhancement of dielectric loss, EM attenuation constant and loss factor with frequency was found to be responsible for the obtained RL.

Keywords Fly ash cenosphere (FAC) · Polymer composite · Reflection loss (RL) · Dielectric loss · Loss factor

1 Introduction

The microwave-absorbing materials, especially polymer-based composites, are one of the most attractive materials in the recent times due to its many advantages such as flexible, lightweight, corrosion protective and inexpensive [1–3]. Magnetic conducting core–shell materials such as Ag@Ni, Ni–Cu and CoNi have been well studied for microwave absorption. However, magneto-dielectric core–shell structure such as Fe/SiO₂, Fe₃O₄–ZnO, Co–MnO₂ and Fe–MnO₂ also shows promising microwave absorption property with an appreciable thickness [3–8]. The hollow microsphere-based microwave absorber is lightweight and has high reflection loss [6, 8, 9]. The fly ash cenosphere (FAC), a by-product and a waste material from thermal power plants, is a typically hollow microsphere and is rich in alumina and silica along with small constituents of other metal oxides (K, Fe, C) and exhibits some unique properties such as chemical inertness, high thermal stability and low density [9–13]. Moreover, the mechanical strength of a polymer matrix can be increased by loading FAC, e.g. the FAC-loaded epoxy (epoxy/FAC composite) shows excellent mechanical strength [14]. The magnetic nanoparticle-coated FAC can be believed as a good microwave absorber due to magnetic loss and dielectric loss over the FAC surfaces [6, 8, 9]. The objective of the present work is to investigate the microwave-absorbing property of cobalt iron (CoFe) alloy nanoparticle-coated FAC (CoFe-FAC)-loaded epoxy composite.

2 Experimental

The FAC was obtained from National Thermal Power Corporation (NTPC), Karnataka (particle size 50–80 μm). The obtained FAC particles were cleaned by conventional acidic and followed by alkali treatment. The CoFe alloy nanoparticles were coated over FAC chemically according to the procedure described in the literature [15]. In brief, a 10 wt% of the as-prepared CoFe-FAC was mixed with epoxy (Atul Pvt. Ltd., Gujarat) by mechanical stirring and poured into a rectangular silver sample holder (22.86 × 10.16 × 3 mm³) and kept for drying in open air (24 h). In a similar way, the pristine epoxy/FAC composite was also prepared.

The complex *S*-parameter (S_{11} , S_{21} , S_{12} , S_{22}) measurements were taken for the as-prepared samples using the vector network analyser (VNA, Agilent NS201). A full two-port calibration (thru-reflect-line or TRL) was performed in the *X*-band (8.2–12.4 GHz) before the measurements. From the obtained *S* parameters, the complex permittivity ($\epsilon_r = \epsilon' - i\epsilon''$) and permeability ($\mu_r = \mu' - i\mu''$) were calculated by using Nicolson–Ross–Weir (NRW) algorithm [16].

3 Results and Discussion

Surface morphology of the cleaned FAC and CoFe-FAC is shown in Fig. 1. Figure 1a, b shows cleaned FAC as low and high resolution, respectively. As shown in Fig. 1c, d, the uniform coating of CoFe over FAC was observed. However, the non-uniform coating was also observed in some regions. The CoFe-FAC was focused ion beam (FIB) cut to determine the coating thickness (Fig. 1e). The CoFe coating thickness was found to be ~ 250 nm over FAC, whereas the porous shell thickness of FAC was observed to be ~ 2.5 – 3 μm . Figure 2 shows the cross-sectional surface morphology of epoxy/CoFe-FAC composite. The measured real (ϵ') and imaginary (ϵ'') parts of complex permittivity of epoxy/FAC and epoxy/CoFe-FAC composite are shown in Fig. 3a, b, respectively. In the presence of CoFe, both ϵ' and ϵ'' values of FAC increase, and hence, epoxy/CoFe-FAC composite was found higher than epoxy/FAC composite. In the *X*-band, the ϵ' value of epoxy/FAC was found to be 2.2–2.4 which was increased to 3.8–3.6 for epoxy/CoFe-FAC composite. Figure 3c shows the variation of μ' and μ'' of epoxy/CoFe-FAC composite. The electrical loss ($\tan \delta_e = \epsilon''/\epsilon'$) and magnetic

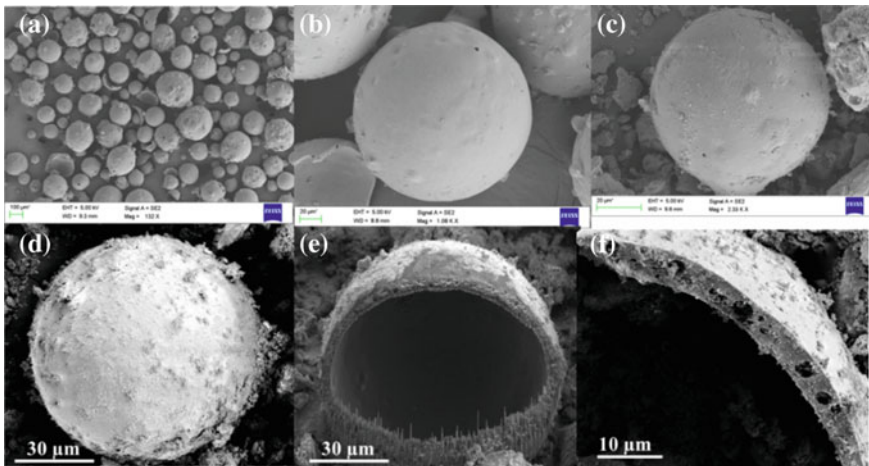


Fig. 1 a, b Cleaned fly ash cenosphere (FAC), c, d CoFe-coated FAC (CoFe-FAC), e FIB cut of a CoFe-FAC and f broken edge of CoFe-FAC

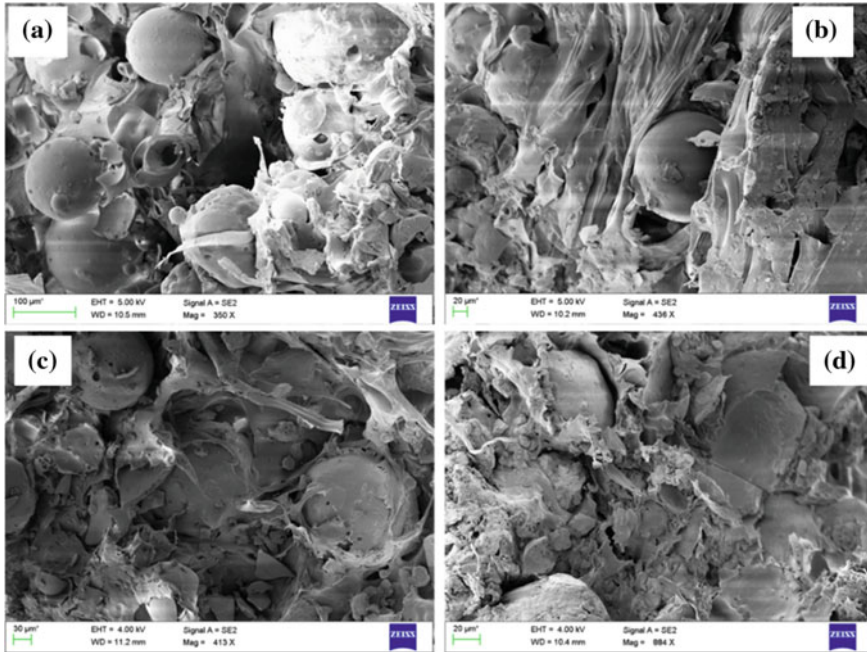


Fig. 2 a–d Cross-sectional surface morphology of epoxy/CoFe-FAC composite

loss ($\tan \delta_m = \mu''/\mu'$) are the two major factors of microwave absorption. The variation of total dielectric loss ($\tan \delta_e + \tan \delta_m$) of epoxy/FAC and epoxy/CoFe-FAC composite is shown in Fig. 3d.

The maximum dielectric loss was obtained in 10.5–12 GHz; the dielectric loss value of epoxy/CoFe-FAC composite (~ 0.3) was found to be two times higher than epoxy/FAC composite (~ 0.15).

The microwave absorption property of a material is generally studied in terms of reflection loss (RL). According to the transmission line theory, the RL of a composite material is given by the following equation [5, 6],

$$RL(\text{dB}) = 20 \log \left| \frac{Z_{\text{in}} - Z_0}{Z_{\text{in}} + Z_0} \right| \quad (1)$$

where Z_0 is the intrinsic impedance of free space ($Z_0 = 377$) and Z_{in} is the input impedance of the composite material, and it can be calculated by using the following equation:

$$Z_{\text{in}} = Z_0 \sqrt{\frac{\mu_r}{\epsilon_r}} \tanh[j(2\pi fd/c)] \sqrt{\epsilon_r \mu_r} \quad (2)$$

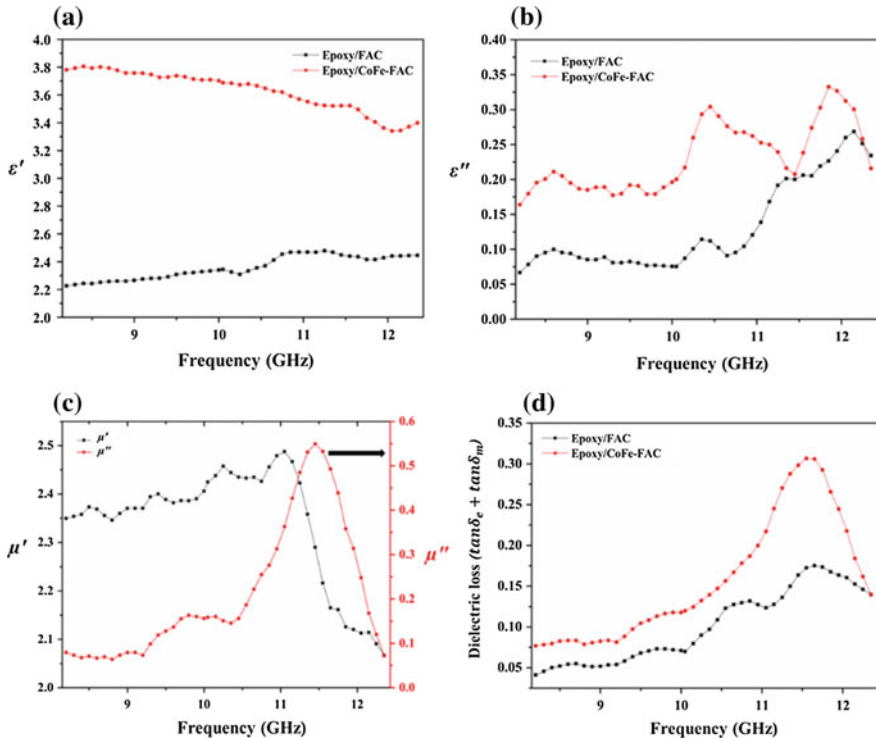


Fig. 3 Variation of **a** real (ϵ') and **b** imaginary parts (ϵ'') of complex permittivity of epoxy/FAC and epoxy/CoFe-FAC composite, **c** real (μ') and imaginary (μ'') parts of complex permeability of epoxy/CoFe-FAC composite and **d** dielectric loss ($\tan \delta_e + \tan \delta_m$) of epoxy/FAC and epoxy/CoFe-FAC composite in the X-band

where f is the frequency and d is the thickness of the material. The obtained RL of the epoxy/FAC and epoxy/CoFe-FAC composites for different thicknesses in the X-band is shown in Fig. 4a, b, respectively. The two distinct nature of RL of epoxy/FAC and epoxy/CoFe-FAC composite was observed. The latter one (epoxy/CoFe-FAC) shows most promising and thus suggests that the CoFe-FAC is more effective for microwave absorption. The most efficient RL value -29 dB (~ 11.5 GHz) was obtained for 6 mm-thick epoxy/Co-FAC composite, whereas pristine epoxy/FAC composite shows -12 dB RL (12.4 GHz). The standard RL value required for most of the applications is -10 dB. The epoxy/CoFe-FAC composite shows -10 dB RL at a minimum thickness of 2 mm. A comparison of RL is shown in Table 1. This excellent behaviour of epoxy/CoFe-FAC composite also can be understood in a better way in terms of EM attenuation loss (EM attenuation constant) and loss factor. The real part of propagation constant is the EM attenuation constant (α) and its equation is [2, 7]:

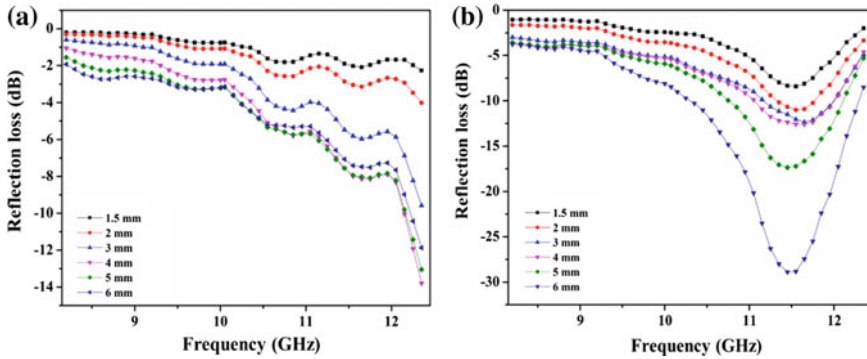


Fig. 4 The reflection loss (RL) of **a** epoxy/FAC and **b** epoxy/CoFe-FAC composite in various thicknesses

Table 1 Optimum reflection loss (dB) of various reported materials with the present work

Material	Frequency (GHz)	RL (dB)	Thickness (mm)	Ref
Paraffin/Fe/C	15	~ -10	1.4	[4]
Epoxy/Fe ₂ O ₃ nanoflowers	10	-15	3	[17]
Epoxy/Fe-CMK3	9.5	-12	1.6	[18]
Paraffin/MnO ₂ -Fe-graphene	12	-12	2	[3]
Epoxy/Fe micron fibre	7.5	-11	1.5	[2]
Paraffin/MnO ₂ nanorod	5	-8	2.5	[3]
Paraffin/MnO ₂ -Fe nanorod	15	~ -10	2.5	[3]
Epoxy/CoFe-FAC	11.5 11.3	-11 -29	2 6	This work

$$\alpha = \frac{\sqrt{2}\pi f}{c} \times \left[(\mu''\epsilon'' - \mu'\epsilon') + \left\{ (\mu''\epsilon'' - \mu'\epsilon')^2 + (\mu'\epsilon'' + \mu''\epsilon')^2 \right\}^{\frac{1}{2}} \right]^{\frac{1}{2}} \quad (3)$$

Figure 5a shows the variation of α value of epoxy/FAC and epoxy/CoFe-FAC composites in the X-band. The α value of epoxy/FAC composite was found to be 9–30. In case of epoxy/CoFe-FAC composite, α increased exponentially from 20 to 105 in the frequency range of 8.2–11.5 GHz and then decreased to 20. Thus, maximum EM attenuation loss was found in the middle of 11–12 GHz. The loss factor (LF) of the composite material can be calculated by using the following relations:

$$LF(\%) = 100 \times (1 - |S_{11}|^2 - |S_{21}|^2) \quad (4)$$

The variation of LF of epoxy/FAC and epoxy/CoFe-FAC composites is shown in Fig. 5b. The LF of epoxy/FAC composite was found to be 46–60%, whereas it is increased to 53–70% for epoxy/CoFe-FAC composite. Thus, it suggests the excellent microwave absorption property of epoxy/CoFe-FAC composite in the X-band.

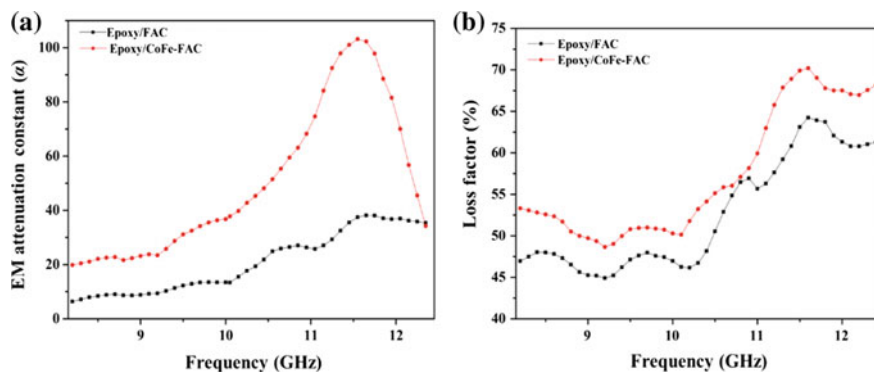


Fig. 5 Variation of **a** EM attenuation constant (α) and **b** loss factor (LF) of epoxy/FAC and epoxy/CoFe-FAC composites in the X-band

4 Conclusion

The CoFe alloy-coated FAC was prepared by chemical heterogeneous thermal reduction process. The epoxy/CoFe-FAC composite was prepared by simple mechanical stirring. The observed morphology suggests uniform coating of CoFe over FAC. The epoxy/CoFe-FAC composite shows -29 dB reflection loss (RL), whereas epoxy/FAC composite shows -12 dB RL in the X-band (8.2–12.4 GHz) frequency. The thickness dependency of RL was also studied, and it indicates that the standard -10 dB RL can be obtained for this composite at a minimum thickness of 2 mm. The factors such as the enhancement of dielectric loss, EM attenuation constant and loss factor with frequency were found to be responsible for the obtained RL.

Acknowledgements Authors gratefully acknowledge the Department of Science and Technology (SB/S3/ME/51/2012) for financial support. This work is technically supported by IISc advanced characterization centre and CeNSE.

References

1. Vinoy, K.J., Jha, R.M.: Radar Absorbing Materials: From Theory to Design and Characterization. Springer, US (2011)
2. Wu, M., He, H., Zhao, Z., Yao, X.: Electromagnetic and microwave absorbing properties of iron fibre-epoxy resin composites. *J. Phys. Appl. Phys.* **33**, 2398 (2000)
3. Lv, H., Ji, G., Liu, W., Zhang, H., Du, Y.: Achieving hierarchical hollow carbon@Fe@Fe₃O₄ nanospheres with superior microwave absorption properties and lightweight features. *J. Mater. Chem. C* **3**, 10232–10241 (2015)
4. Khani, O., Shoushtari, M.Z., Farbod, M.: Excellent improvement in the static and dynamic magnetic properties of carbon coated iron nanoparticles for microwave absorption. *Phys. B Condens. Matter.* **477**, 33–39 (2015)

5. Lv, H., Liang, X., Cheng, Y., Zhang, H., Tang, D., Zhang, B., Ji, G., Du, Y.: Coin-like α -Fe₂O₃@CoFe₂O₄ core-shell composites with excellent electromagnetic absorption performance. *ACS Appl. Mater. Interfaces* **7**, 4744–4750 (2015)
6. Du, Y., Liu, W., Qiang, R., Wang, Y., Han, X., Ma, J., Xu, P.: Shell thickness-dependent microwave absorption of core-shell Fe₃O₄@C composites. *ACS Appl. Mater. Interfaces* **6**, 12997–13006 (2014)
7. Bora, P.J., Porwal, M., Ramamurthy, P.C., Madras, G.: Influence of MnO₂ decorated Fe nano cauliflowerers on microwave absorption and impedance matching of polyvinylbutyral (PVB) matrix. *Mater. Res. Express*. **3**, 095003 (2016)
8. Fu, W., Liu, S., Fan, W., Yang, H., Pang, X., Xu, J., Zou, G.: Hollow glass microspheres coated with CoFe₂O₄ and its microwave absorption property. *J. Magn. Magn. Mater.* **316**, 54–58 (2007)
9. Li, Q., Pang, J., Wang, B., Tao, D., Xu, X., Sun, L., Zhai, J.: Preparation, characterization and microwave absorption properties of barium-ferrite-coated fly-ash cenospheres. *Adv. Powder Technol.* **24**, 288–294 (2013)
10. Kolay, P., Singh, D.: Physical, chemical, mineralogical, and thermal properties of cenospheres from an ash lagoon. *Cem. Concr. Res.* **31**, 539–542 (2001)
11. Kumar, A.: *Industrial Pollution: Problems and Solutions*. Daya Publishing House (2006)
12. Bora, P.J., Vinoy, K.J., Ramamurthy, P.C., Kishore, Madras, G.: Lightweight polyaniline-cobalt coated fly ash cenosphere composite film for electromagnetic interference shielding. *Electron. Mater. Lett.* 1–7 (2016)
13. Bora, P.J., Mallik, N., Ramamurthy, P.C., Kishore, Madras, G.: Poly(vinyl butyral)-polyaniline-magnetically functionalized fly ash cenosphere composite film for electromagnetic interference shielding. *Compos. Part B Eng.* **106**, 224–233 (2016)
14. Kulkarni, S.M.: Studies on fly ash-filled epoxy-cast slabs under compression. *J. Appl. Polym. Sci.* **84**, 2404–2410 (2002)
15. Meng, X., Shen, X.: Preparation of FeCo-, FeNi- and NiCo-alloy coated cenosphere composites by heterogeneous precipitation. *Particuology* **10**, 334–338 (2012)
16. Chen, L.F., Ong, C.K., Neo, C.P., Varadan, V.V., Varadan, V.K.: *Microwave electronics: measurement and materials characterization*. Wiley, New York (2004)
17. Guo, C., Xia, F., Wang, Z., Zhang, L., Xi, L., Zuo, Y.: Flowerlike iron oxide nanostructures and their application in microwave absorption. *J. Alloys Compd.* **631**, 183–191 (2015)
18. Wang, J., Zhou, H., Zhuang, J., Liu, Q.: Magnetic γ -Fe₂O₃, Fe₃O₄, and Fe nanoparticles confined within ordered mesoporous carbons as efficient microwave absorbers. *Phys. Chem. Chem. Phys.* *PCCP* **17**, 3802–3812 (2015)

Concrete Solar Collector

Pratik M. Waghmare, Shrishail B. Sollapur and Shweta M. Wange

Abstract Concrete solar collector is an attempt to create an effective alternative for conventional solar collectors. Concrete has high heat storage capacity. Also, the problem of corrosion automatically gets eliminated due to the alkaline characteristic of cement. Cement concrete plays the role of heat absorber while the flow tubes are made up of copper. For the enhancement of heat transfer, dimpled surface copper flow tubes are used. Dimples improve the heat transfer rate with very little pressure drop. The project consists of a 2 m × 1 m setup and it deals with analyzing its performance under various conditions. For testing, we use pyranometer for measuring solar radiation, thermocouples for measuring the temperature of inlet and outlet water and digital temperature indicator for temperature indication.

Keywords Concrete collector · Dimple surface · Digital temperature indicator
Pyranometer · Thermocouple

1 Introduction

Concrete solar collector is an attempt to create an alternative for conventional solar collectors. The use of copper absorber plates and copper flow tubes leads to the elevated cost of conventional solar water heater. It aims at reducing this cost without negatively affecting the performance of the collector. Experiment used polyvinyl chloride pipes embedded into concrete supported with wire mesh. Priority was given to identify tube-to-tube spacing as a measure and according to it the pitch was defined. The drop in the water pressure while flowing through the tubes was also noted [1]. Experimental study using aluminum tubes embedded in concrete was also done. Here, parallel pattern was considered for laying of flow tubes in the

P.M. Waghmare (✉) · S.B. Sollapur · S.M. Wange
Mechanical Engineering Department, Savitribai Phule Pune University, Pune, India
e-mail: pratiik.waghmare@gmail.com

S.B. Sollapur
e-mail: shrishail.sollapur@gmail.com

structure. The flow tubes are embedded in the concrete in such a way that 30% of the tube surface remains exposed the sun while the remaining portion is buried in the concrete [2]. Use of dimpled surface further elevates the heat transfer rates. Dimples can increase the outlet temperature as they create disturbance in the water passage, thus enhancing the heat transfer rate which increases in temperature [3].

2 Use of Concrete as Absorber

The performance of the absorber component partially depends on two properties of the material used for the surface finish of the absorber—absorptivity and emissivity. Concrete can absorb 65% of light incident upon it. Blackening its surface can further increase this percentage up to 96%. It offers high emissivity of 0.87. Where concrete is used both to absorb and to store solar energy, the surface exposed to solar radiation should be as dark as possible.

3 Components of Concrete Collector

A concrete solar collector consists of the following parts.

3.1 Water Flow Tubes

The arrangement of the flow tube grid is manufactured by pipe bending machine. The distance between two risers is 8 cm.

Dimple dimensions: Three dimples at an angle of 120° and two dimples at an angle of 180° are alternately placed at a pitch of 1.5 cm and of depth.

Procedure: Dimpled surfaces on the copper tubes are fabricated using a punch tool whose edge is made spherical with the help of a grinding machine. And then these are punched using a hammer (Figs. 1 and 2).

3.2 Wooden Cabinet

The inner dimensions of the enclosure box are $100 \times 200 \times 10$ cm. Wooden plank of thickness 18 mm is used to make sides and base of the box. It is open at the top. The provisions are there to accommodate inlet and outlet flow pipes.



Fig. 1 Arrangement of copper flow tubes for water flow



Fig. 2 Dimpled protrusions on the copper tube

3.3 Stand

It is made up of *L* angles of mild steel. These are selected with thickness of 3 cm in order to bear the weight of the collector. The collector is mounted on it and is inclined at an angle of latitude of that place with respect to horizontal.

3.4 Transparent Cover

A transparent glass cover is placed on the top of the enclosure box. The purpose of this is to trap the solar energy within the enclosure box. Due to use of cement instead of copper cells, the cost of the collector reduces significantly.



Fig. 3 Actual setup of concrete solar collector

4 Experimental Setup of Concrete Collector

The sand and cement are mixed in adequate proportions and accommodated in an enclosure box up to a thickness of 6 mm. Wire mesh is placed on this. Flow tubes are mounted over this wire mesh along with some metal scrap. Over this, concrete is poured up to the thickness of 20 mm from the base of the enclosure box. Copper flow tubes are embedded into the concrete in such a way that their upper half portion remains exposed. The collector is kept for curing with a layer of 3 mm of water for ten days. After that, absorber plate is painted with black color.

Experimental setup consists of an enclosure box of dimensions $100 \times 200 \times 10$ cm. Concrete is poured in this box up to a height of 15 cm from the bottom of the box. Over this, a metal wire mesh is placed. Further, the serpentine copper flow tubes are placed over this. Then, concrete is poured over this arrangement in such a way that the upper surface of the flow tubes remains exposed. This arrangement is kept for curing for a day. Later, a transparent glass cover is mounted on the box. This panel is now mounted at an angle equal to the latitude of the experimental place with the horizontal facing toward south.

Figure 3 shows the actual setup of the concrete solar collector on the roof of the building.

5 Energy Balance of Concrete Solar Collector

A concrete solar collector is built up from a concrete absorber with a black surface coating and an integral duct system, together with a glazed cover and a wooden case.

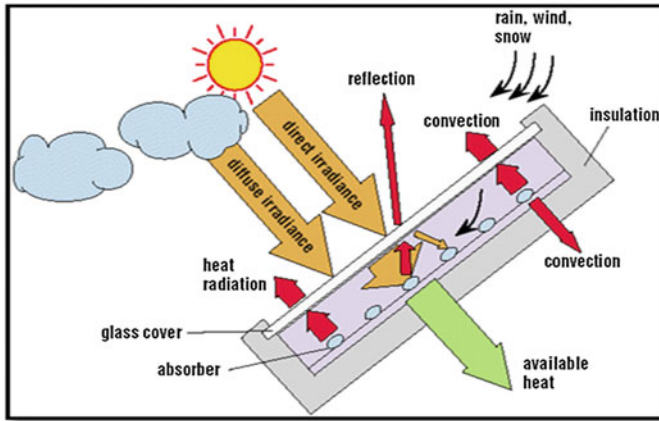


Fig. 4 Energy flow in concrete solar collector

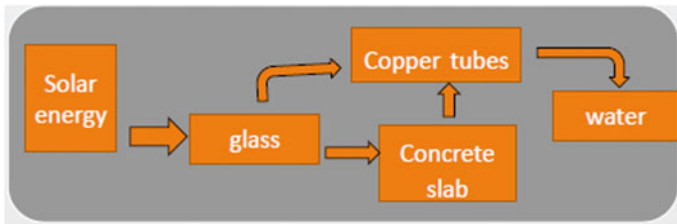


Fig. 5 Heat flow in concrete solar collector

Water flows through the duct system (metal grid). The solar collector receives a varying radiation flux $\phi(w)$ of which one part is converted to heat and is carried away by heat absorbing medium, another part is lost to the surroundings and the remainder is stored as heat in the solar collector. The energy balance can be expressed as (Fig. 4):

$$dQ_c/dt = \phi - (Q_{out} - Q_{in}) - QL$$

$$Q = m C_p dt$$

where (dQ_c/dt) = the change in the heat content of the solar collector and the enclosed heat carrying medium.

The term (dQ_c/dt) for a given solar collector is affected not only by the radiant flux ϕ , but also by the change in the temperature of the water at the inlet by its flow velocity.

The heat flow takes place in concrete solar collector is shown in Fig. 5.



Fig. 6 Positioning of thermocouples at the inlet and outlet of collector

6 Equipments Used for Testing

The equipments used for testing of concrete collectors are

1. Thermocouple
2. Pyranometer
3. Digital temperature indicator.

6.1 Thermocouple

Thermocouples are used to measure water temperatures at the incoming and outgoing nodes of the solar collector. For this purpose, thermocouples of *K* type are utilized. Its one end is kept in water and other end is connected to the digital temperature indicator (Fig. 6).

6.2 Pyranometer

It is used to measure solar radiation intensity from a field of view 360°. It displays the reading in digital format in W/m^2 (Fig. 7).

6.3 Digital Temperature Indicator

It indicates the temperature of inlet and outlet water in °C in digital format. It is a 12-channel indicator (Fig. 8).

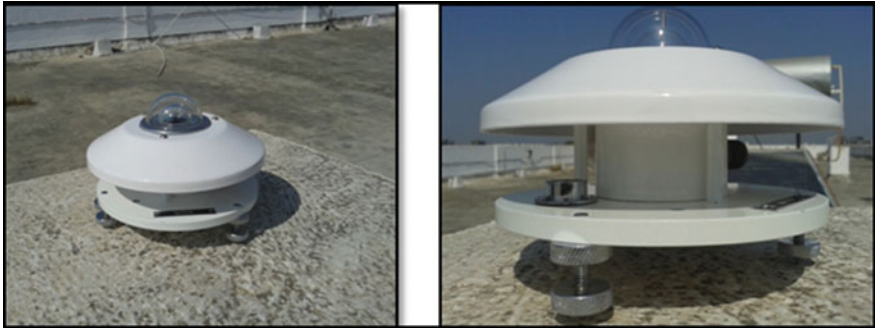


Fig. 7 Pyranometer



Fig. 8 Digital temperature indicator

7 Observations

We had taken the readings in every month of each season. A total of five observations would be taken on each day for a flow of 30 L per hour. These observations would be recorded between 12:00 pm and 4:00 pm. After completion of observation procedure, the readings would be analyzed and the standard of the collector would be found out.

Table 1 gives the readings of rainy season.

Here we can draw the graph from above table (Graphs 1 and 2).

- Incident solar energy, $W = \text{Solar Intensity (W/m}^2) * \text{Area of flat plate collector (m}^2)$
- Useful heat gain = heat absorbed by the water =

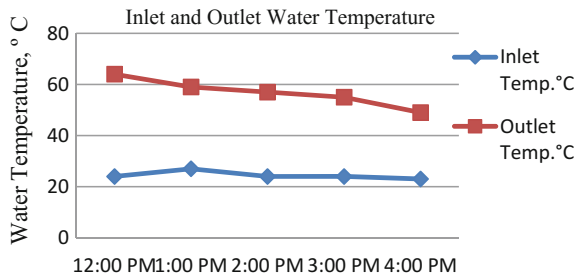
$$Q = m * Cp * dT$$

Table 1 Readings of rainy season

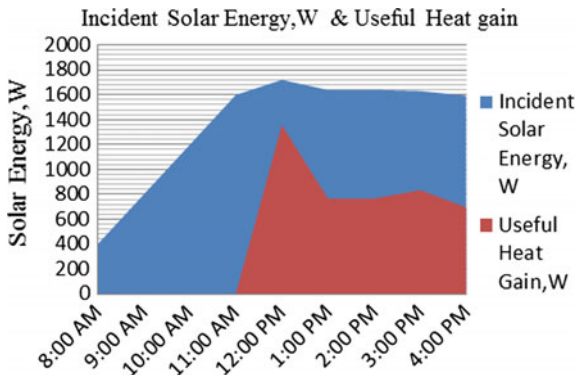
Time	Inlet temp. (°C)	Outlet temp. (°C)	Solar intensity (W/m ²)
12 pm	22	61	860.50
1 pm	23	45	820.37
2 pm	22	44	828.55
3 pm	22	46	815.50
4 pm	21	41	797.60

Average outlet temperature = 42 °C
 Water storage temp. on the next morning = 47 °C

Graph 1 Inlet and outlet temperature of rainy season



Graph 2 Useful heat gain from solar radiation



where

- dT Change in temperature of water
- m kg of water flowing per s through the tubes
- C_p specific heat of water = 4.18 kJ/kgK.

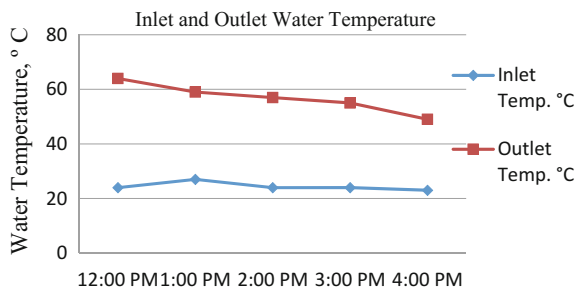
Now, Table 2 gives the readings of Winter Season (Graphs 3 and 4).

Table 2 Readings of winter season

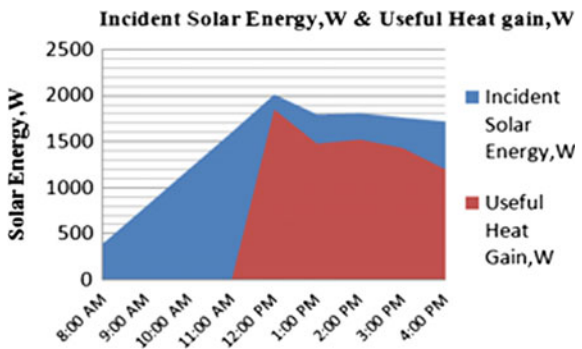
Time	Inlet temp. (°C)	Outlet temp. (°C)	Solar intensity (W/m ²)
12 pm	24	64	855.63
01 pm	27	59	897.90
02 pm	24	57	904.67
03 pm	24	55	880.90
04 pm	23	49	809.80

Average outlet temperature = 56.80 °C
 Water storage temp. on the next morning = 49 °C

Graph 3 Inlet and outlet temperature of winter season



Graph 4 Useful heat gain from solar radiation



8 Conclusion

The concrete collector gives satisfactory performance in the rainy and winter seasons during which there is a great need of hot water. In the summer season, the concrete solar collector can be used in low temperature solar thermal power plants. By testing our solar concrete collector, we can conclude that we can get hot water in the temperature range of 40–65 °C. Overall cost of conventional solar collector is about Rs. 26,000, whereas the price of concrete solar collector is about Rs. 15,000 and it can be further reduced. Thus, a concrete solar collector performance is fair enough.

References

1. Bopshetty, S.V., Nayak, J.K., Sukatme, S.P.: Performance analysis of solar concrete collector. *Energy Convers. Manage.* **33**, 1007–1016 (1992)
2. Chaurasia, P.B.: Solar water heaters based on concrete collectors. *Energy* **25**, 703–716 (2000)
3. Kore, S.S., Sane, N.K.: Experimental investigations of heat transfer enhancement from dimpled surface in a channel. *Int. J. Eng. Sci. Technol.* 6227–6334 (2012)

Power Quality Improvement of Microgrid with Cascaded Controller-Based PMSG Used in Wind Turbines

W.J. Praiselin and J. Belwin Edward

Abstract Due to increasing power demand and environmental aspects, power generation from renewable energy sources that have been assumed to be a different source of energy can bring new challenges. Globally, an increasing number of wind energy generation systems are integrated into the electrical power network. In the wind turbine the reduction of various negative impacts of power quality issues such as voltage sag, swell, power variation, voltage and current harmonics are noticeable. In this paper, permanent magnet synchronous generator is operated as a parallel connection of reactive power compensator. Also, the cascaded controller technique is analyzed with the performance of compensator. The whole system is simulated through the MATLAB/SIMULINK using Simpower system library. The simulations give the improvement of inverter phase and load voltage profile, reduce the voltage harmonics in the inverter voltage control and compensate the current-injected active/reactive power operation in grid-connected wind energy system.

Keywords Power quality • Microgrid • Wind generation system
Cascaded controller • Permanent magnet synchronous generator

1 Introduction

In everyday life, human being needs electricity which is the easy going form of electrical energy. Distributed energy resources (DERs) and interconnect with loads are the form of renewable energy resources (RES) that form microgrids. In the general terms, microgrids are the small-scale power systems of macrogrid [1]. Microgrids are the recent development with the potential to bring distributed generation into the mainstream. In the microgrid operation, power quality is the

W.J. Praiselin (✉) · J. Belwin Edward
School of Electrical Engineering, VIT University, Vellore 632014, India
e-mail: praiselin1@gmail.com

J. Belwin Edward
e-mail: belwinedward@yahoo.com

serious problem that affected the system. Disturbances to the supplied power, which are related to the voltage, frequency, harmonic distortion, active and reactive power, can be performed by both the islanding and grid-connected modes [2]. Comparing these RES such as wind energy, solar energy, hydro power, wind energy is an important source because of its benefits like lower cost per MW as compared to other energy sources. The power quality issues of grid-connected renewable energy sources into the transmission and distribution operation of the network is classified into customer and utility related problems [3, 4]. Reactive power demand, unbalanced load and total harmonic distortion (THD) are the customer-side problems; among all these PQ problems, harmonic distortion is the severe PQ distortion in the customer side. These should reduce the life time of the equipments and reduce the ability of the overall electrical power system [5]. In the earlier days, squirrel cage induction generators are utilized because of the generators operated under the range of limits of wind speed. Recently used wind turbines (WT) are not produced to supply power, but it also maintains the grid during unbalance and faulty condition. Therefore, this type of wind turbine capability is called as ride-through capability. Induction generator, synchronous generator (SCIG) and doubly fed induction generator (DFIG) are commercially used in the wind turbines with power electronics devices [6, 7]. This paper presents the power quality improvement of microgrid operation with PMSG-based wind turbines. Cascaded current control scheme is deployed for the PMSG control. Thus, the proposed control method which is used to attain the IEEE standards improves the power quality of point of common coupling (PCC). The simulation results using MATLAB/SIMULINK of PMSG-based grid-connected wind energy system to control the reactive power and improve the voltage profile is shown to validate the results.

2 System Description

The wind turbine generator considered under a PMSG is utilized in a variable or adjustable speed wind turbine which consists of two converters which is connected with a common dc link [8]. The general structure of the adjustable speed wind turbine is illustrated in Fig. 1.

2.1 Wind Turbine

Wind turbine absorbs the energy from the wind, and the power is delivers to the dc bus. The system consists of a mechanical parts and electrical parts [9]. Voltage, frequency and harmonic levels are not determined within the limits when the wind turbine is operated under an abnormal condition. The issues of wind turbine in the

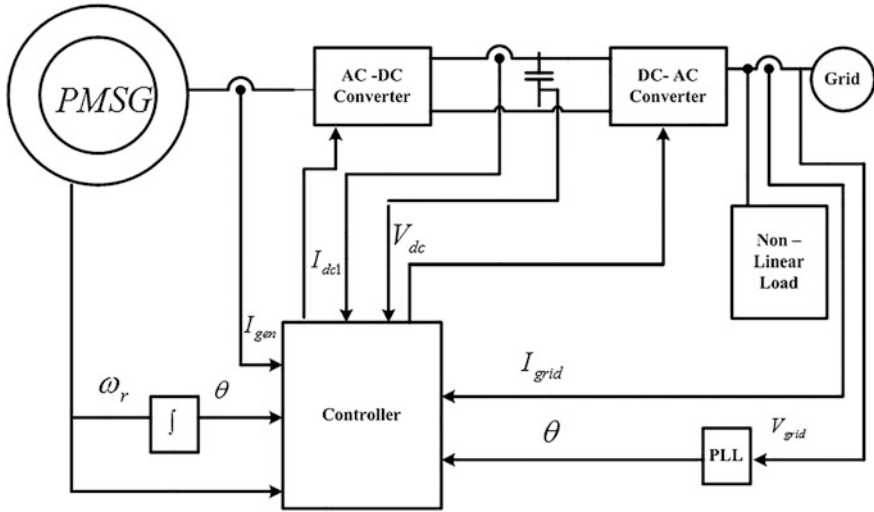


Fig. 1 General block diagram of adjustable speed wind turbines with PMSG [8]

grid depend on the characteristics of wind turbine and grid at the connection of PCC [10].

The captured mechanical power by the wind is given by,

$$P_t = \frac{1}{2} \rho A_t u^3 C_p \tag{1}$$

where,

- ρ air density
- C_p power coefficient
- A_t area covered by the rotor blades.

Also, the ratio of tip speed (λ) is expressed by Eq. (2),

$$\lambda = \frac{\omega_r R}{v} \tag{2}$$

where

- R radius of the rotor
- ω_r angular velocity of the rotor.

In the above equations, coefficient of power C_p is not constant and depends on the tip speed ratio and pitch angle. When C_p value reaches to high level, only wind turbine captures the output power.

2.2 Cascaded Control Technique

Cascaded control technique is an inner loop control technique which controls the inverter load voltage and the grid current. This controller technique consists of two loops. First loop represents the inner voltage loop which has to regulate the load voltage of the inverter u_0 , and the second loop determines the outer current loop which is used to control the grid current i_2 [11, 12]. The improvement of the PQ in the inverter local load voltage under nonlinear condition and the inverter load has to be adjusted with the grid. PLL used the transfer the signals of the grid voltage, and it can produce the reference current i_{ref} .

3 Simulation Results

The simulation result of the PMSG-based grid-connected wind energy system is explained here. This section includes inverter control output of the phase and load voltage, wind power output and inverter reactive power of the proposed system. Table 1 gives the simulation parameters done in MATLAB/SIMULINK (Fig. 2).

Table 1 Parameters used for simulation

Simulation parameters	Values
Frequency	50 Hz
Nominal mechanical power output	8.5×10^3 W
Base wind speed	12 m/s
Sample time	$2e-6$

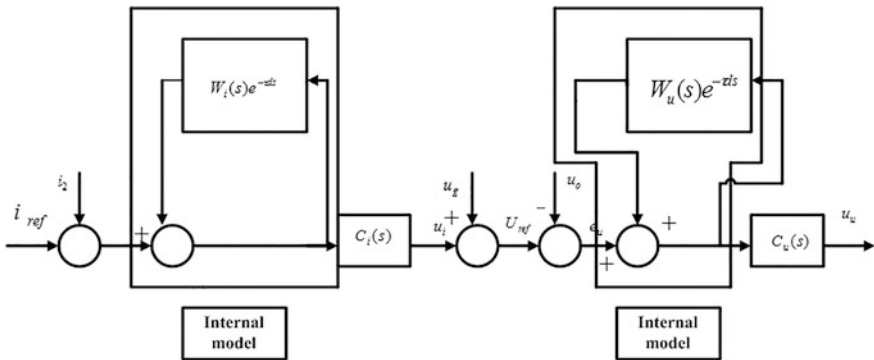


Fig. 2 Design of cascaded control technique [11]

3.1 Results and Discussion

The inverter control output of the PMSG-based grid-connected wind energy system is shown in Fig. 3. After using the grid side controls, the variation of load voltage and phase voltage satisfies the reactive power and harmonic components of the load. It helps to reduce the harmonics in the grid.

Figure 4 shows the output of the wind power which follows the speed of the generator when the output of the power is maximum.

In the wind energy system, injected current into the grid with cascaded current controller technique is shown in Fig. 5.

Figure 6 shows that the inverter output voltage which determines the pure sinusoidal waveform. The grid-connected inverter side voltage harmonics should be reduced by using the proposed controller.

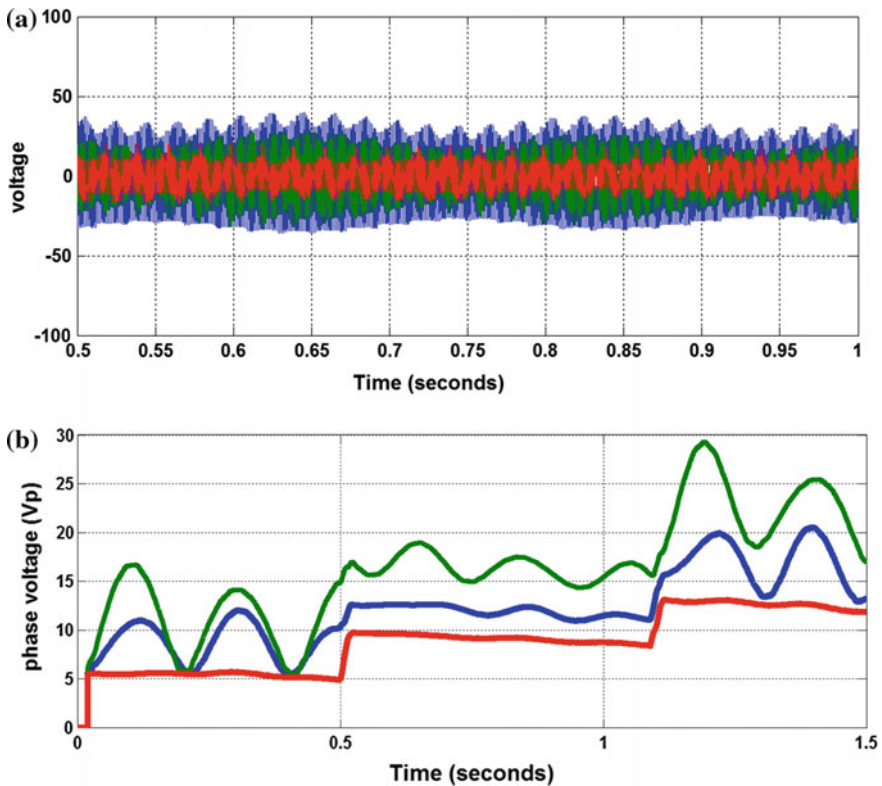


Fig. 3 Inverter control output of a load voltage, b phase voltage

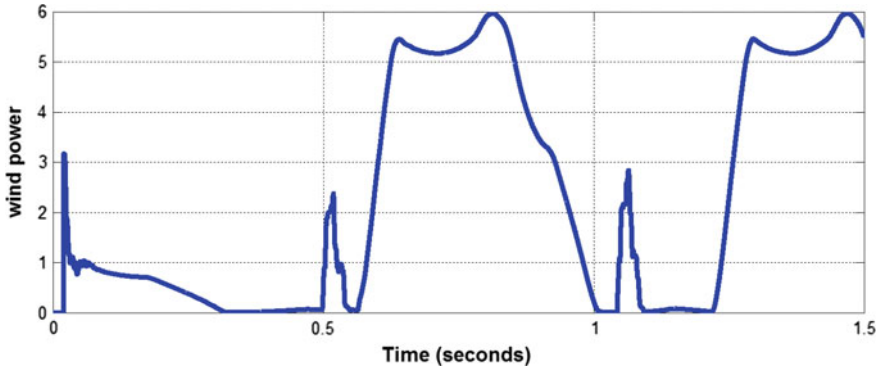


Fig. 4 Wind power output

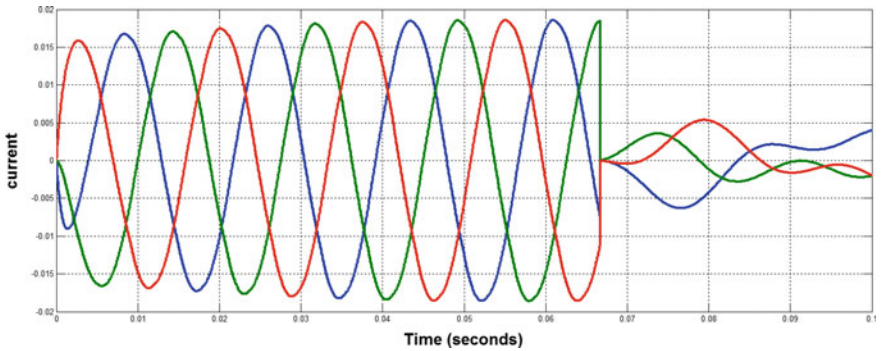


Fig. 5 Current injected into the grid

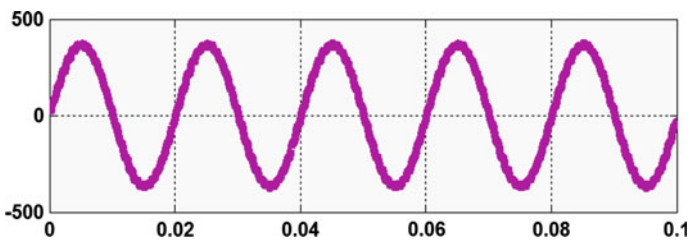


Fig. 6 Inverter voltage control

4 Conclusion

The power quality improvement of microgrid using PMSG-based wind generation system is considered. Cascaded controller of the inverter local load voltage performance is explored in this paper. The MATLAB simulation results explore the

nonlinear load in the grid-connected mode, and load voltage of the inverter was controlled by using cascaded controller. Hence, the PQ could improve the grid-connected PMSG-based wind energy system. As a result, the nonlinear voltage harmonics do not affect the grid.

References

1. Parhizi, S., Lotfi, H., Khodaei, A., Bahramirad, S.: State of the art in research on microgrids: a review. *IEEE Access* **3**, 890–925 (2015)
2. Mwinyiwiwa, B.M.M., Manyahi, M.J., Gregory, N., Kyaruzi, A.L.: Conceptual synthesis of multi-source renewable energy based microgrid. *Int. Sch. Sci. Res. Innov.* **7**, 1687–1692 (2013)
3. Jamshidi, A., Ghahderijani, M.M., Barakati, S.M.: Power quality improvement in stand-alone microgrid including fixed-speed wind farm. In: 11th International Conference on Environment and Electrical Engineering, pp. 206–211 (2012)
4. Mahela, O.P., Shaik, A.G.: Topological aspects of power quality improvement techniques: a comprehensive overview. *Renew. Sustain. Energy Rev.* **58**, 1129–1142 (2016)
5. SenthilKumar, A., Rajasekar, S., Ajay-D-Vimal Raj, P.: Power quality profile enhancement of utility connected microgrid system using ANFIS-UPQC. *SMART GRID Tech. Energy Procedia* **21**, 112–119 (2015)
6. Singh, M., Khadkikar, V., Chandra, A.: Grid synchronisation with harmonics and reactive power compensation capability of a permanent magnet synchronous generator-based variable speed wind energy conversion system. *IET Power Electr.* **4**, 122–130 (2011)
7. Jena, N.K., Pradhan, H., Mohanty, K.B., Sanyal, S.K.: A comparison between PI & SMC used for decoupled control of PMSG in a variable speed wind energy system. In: International Conference on Energy Power and Environment: Towards Sustainable Growth (ICEPE), pp. 1–6 (2015)
8. Ansa Fathima, A., Babu, C.M.B.: Power quality improvement of a grid connected with hybrid energy system using fuzzy logic controller. *Adv. Res. J. Sci. Eng. Tech.* **3**, 341–345 (2016)
9. Nguyen, T.H., Lee, D.C., Song, S.H., Kim, E.H.: Improvement of power quality for PMSG wind turbine systems. In: Energy Conversion Congress and Exposition (ECCE), pp. 2763–2770, IEEE (2010)
10. Tripathi, S.M., Tiwari, A.N., Singh, D.: Grid-integrated permanent magnet synchronous generator based wind energy conversion systems: a technology review. *Renew. Sustain. Energy Rev.* **51**, 1288–1305 (2015)
11. Zhong, Q.-C., Hornik, T.: Cascaded current–voltage control to improve the power quality for a grid-connected inverter with a local load. *IEEE Trans. Ind. Elec.* **60**, 1344–1355 (2013)
12. Bouzid, A.M., Cheriti, A., Sicard, P.: H-infinity loop shaping controller design of micro-source inverters to improve the power quality. In: IEEE 23rd International Symposium (ISIE), pp. 2371–2378 (2014)

Experimental Investigation and Fabrication of Biogas Digester

Jeetendra Bhandari, Premendra Mani Pradhan
and Rohit Kumar Choudhary

Abstract In the present day scenario, the non-renewable source of energy is the matter of serious concern either in terms of availability or in terms of cost concern. Considering the future prospective, there is a serious need for the alternate energy which has the ability of satisfying the need for energy quest. Energy is vital to living beings as well as nature. Everything that happens is the result of flow of energy in its different forms. With increased use, depletion of fossil fuel and its negative impact of conventional fuel on environment, alternative fuel will become more common in the coming decades. The objective of this paper is to analyze composition of the biogas obtained from the combined mixture of waste from kitchen (uncooked vegetable waste and food) and cow dung in self-fabricated 200 l biogas digester which is portable and economical.

Keywords Biogas · Chromatography · Methane · Calorific value

1 Introduction

Biogas consists of about 60% methane, 35% carbon dioxide and some impurities like H_2 , H_2S and some N_2 . It is the result of decomposition of plant and animal waste. Biogas is a clean source of energy, but it is a burning gas and usually its calorific value ranges from 5000 to 5500 kcal/kg (20,934 to 23,027 kJ/kg). There are few

J. Bhandari (✉) · P.M. Pradhan · R.K. Choudhary
Department of Mechanical Engineering, Sikkim Manipal Institute of Technology,
Majitar, Sikkim, India
e-mail: je10b1994@gmail.com

P.M. Pradhan
e-mail: premendramani@gmail.com

R.K. Choudhary
e-mail: rohitchoudary3307@gmail.com

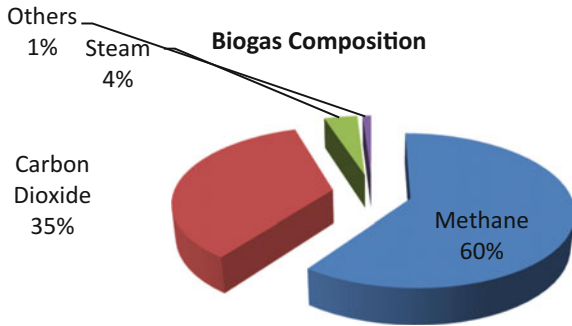
R.K. Choudhary
Tata Consultancy Services, Majitar, India

stages in which a decomposing mass has to pass through, which are digestion, pyrolysis and hydrogasification. Digestion being the biological process and taking place in the absence of oxygen and due to the presence of anaerobic organisms at temperature of 35–70 °C and ambient pressure results in the formation of biogas.

Appropriate Rural Technology of India, ARTI [1], has developed a biogas plant which was compact in nature and was used for generation of biogas using feed stock as waste food. The main advantage of this plant is that it is sufficiently compact and can be used in both urban as well as in rural areas. In their second experiment using sugary feedstock, they were able to generate 500 g of methane in just 24 h from 2 kg of it. The conventional systems produce same quantity of gas with 40 kg of feedstock (cattle dung), and it took around 40 days to complete the reaction. The system so developed is 20 times efficient than conventional one, and from reaction point of view it takes roughly 40 time less time as compare to old one. Cheng-qiu et al. [2] proved that biogas compression is possible and this could facilitate the expansion of biogas benefits even in the field of automobile fields as a fuel for dual-fuel diesel–biogas engines. Mahanta et al. [3] had discussed about the various factors affecting the production of biogas. Though there are several factors which can affect the production of biogas, they concerned about the temperature, pH value, loading rate, retention time and carbon and nitrogen ratio (i.e., C/N ratio). According to them, best temperature for efficient production of biogas is between 30 and 45 °C, with decrease in temperature below 30° and increase in temperature above 40 °C will adversely affect the production of biogas. They said that neutral or mildly alkaline environment is best for efficient gas production. Loading rate also affects gas production. We have to feed digester properly and in regular basis. If feed rate is increase, then the concentration of acid will increase and inhibit the methane formation, and at the same time if the feeding rate is decrease, then the production of gas will be low because of alkalinity. According to them, 16 kg of volatile solid per m³ of digester is optimum value of loading rate. Higher loading rate is possible in those places where ambient temperature is higher. Hydraulic retention time (HRT) depends upon the design and operating temperature of digester; in India HRT is usually taken as 40–60 days. Carbon/nitrogen ratio is also an important factor affecting the gas production. During the digestion process, bacteria utilize carbon 20–30 times higher than nitrogen. Hence to meet this requirement, feedstock constituent is chosen in a way to ensure a C/N ratio of 25:10 to 30:10. Yadvika et al. [4] have presented a comprehensive view of the different methods for enhancing the production of the biogas. They have found that the generation of biogas is low during winter season due to which it resulted in some problem during the practical application of biogas technology. Taleghani et al. [5] in their study have enumerated few economic benefits of biogas production which are;

1. Solid waste treatment resulting in low follow-up costs
2. Good quality fertilizer could be generated which results in reduction in the dependence of chemical fertilizers.
3. Income generation through compost and energy sales (like biogas, electricity, and heat) (Fig. 1).

Fig. 1 Composition of biogas [1]



1.1 Benefits of Biogas

The importance of biogas is well known because it has proved itself in terms of smoke and ash free, sustainable source of energy spared from the burden of collecting firewood. The by-product of biogas could be used as a good source of fertilizer for the agricultural purpose, which could result in protection of forest. As stated above, even a sludge yielded after digestion is rich in valuable nutrients and can be used as a quality fertilizer. Some other usefulness of this alternate source of energy is that it can be used for diverse field few could be generation of electricity, alternate to LPG, room heating, boiling of water, process heating and many more.

1.2 Anaerobic Way of Digestion

Biogas generation is a function of microorganisms, and possibly there are different types of them. Bacteria, fungi and viruses are few of them. Bacteria are divided in two measure groups based on the requirement of oxygen. The one which survive in oxygen presence is aerobic, while the others which flourish in the absence of oxygen are anaerobic. The fermentation of organic matter (chemical change in organic matter by the activity living organisms) in anaerobic condition results in the generation of gas, and this gas is known as biogas.

Organic matter from animal or any plant could be possibly used for the conversion into biogas through anaerobic digestion. Generally, feed used in biogas generation is sewage from sewage, human waste, waste food, cow and pig manure and residues of agriculture. Methane content associated with some feedstock is given in Table 1.

Table 1 Methane content of few waste substrates [6]

Feedstocks	Methane content
Pig waste	00.250–00.500 m ³ /kg
Cow waste	00.200–00.300 m ³ /kg
Chicken food waste	00.350–00.600 m ³ /kg
Human waste	00.030 m ³ /person
Vegetable waste	00.250–00.500 m ³ /kg
Food waste	00.500–00.600 m ³ /kg
Plant leaves	00.100–00.300 m ³ /kg

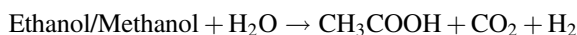
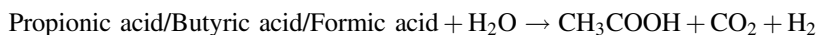
1.3 Stages of Anaerobic Digestion

This anaerobic digestion or biochemical energy conversion process consists broadly of four phases—hydrolysis, acidogenesis, acetogenesis and methanogenesis. The details of each stage have been described in the following paragraph.

During hydrolysis, the complex polymers such as fats, carbohydrate, proteins of biomass are broken down into simpler compounds. The hydrolysis process is carried out by exoenzymes excreted by bacteria. The hydrolysis results in the conversion of carbohydrate to sugar, alcohol; cellulose converted to glucose; proteins converted to amino acids, peptides; and fats converted to fatty acids and glycerol.

In acidogenesis stage, acidogenic bacteria transform the products of hydrolysis into a short-chain ketones, volatile acids and aldehydes, H₂ and CO₂. In this stage, amino acids are converted to fatty acid; sugar to fatty acid, CO₂, H₂; glycerol to acetic acid, CO₂; alcohol to fatty acid, CO₂. Main product of acidogenesis is propionic acid, butyric acid, formic acid, acetic acid, ethanol, methanol, CO₂ and H₂.

In the acetogenesis stage, the acetogenic bacteria produce acetic acid (CH₃COOH), H₂ and CO₂ from the acidogenesis products. Some of the important chemical reactions taking in this stage are shown in the following:



In the methanogenesis stage, methanogenic bacteria convert products of acetogenesis (mainly acetic acid) to methane and carbon dioxide.

2 Development of Digester

2.1 Materials Used for Construction of Digester

Based on the availability of the materials in the local market, the capacity of the digester was conceived. The digester was made of plastic water tank of 200 l capacity, and the following process was done.

2.2 Method of Fabrication

The following steps will be adopted for making of digester for biogas generation using kitchen waste and cow dung:

- Inlet and outlet of feed stock and slurry, respectively, were marked on the surface of water tank.
- A 50-mm hot GI pipe was penetrated through the marks made on the surface of tank.
- Then, PVC pipe of 63 mm diameter is cut into the length of 20 cm to make inlet and outlet channel.
- The PVC pipe is inserted into the hole which is quite smaller than the diameter of pipe; this is because to make tight fitting between hole and pipe.
- Now m-seal is applied around the joint to make it leak proof.
- Once the m-seal is applied, the digester is filled with water to check any leakage from fabricated point and we used soap solution to test the air leakage.

If there is no leakage, then we can use the digester for digestion process. Final digester is shown in Fig. 2.



Fig. 2 A 200 l digester and gas collector

3 Production of Biogas

As the digester was developed and fabricated successfully, the next step was to generate biogas from the feedstock. To accomplish this, two tests were carried out using different feedstocks. The particular has been shown in Table 2.

In the first test, feedstock was collected from waste food of kitchen. It was crushed into very small size and mixed with water. It was then fed into the digester. After feeding, the inlet point was closed tightly. In the second test, same procedure was followed, except the feedstock was the mixture of food waste, cow dung and water.

4 Results and Discussions

The result and discussion for the test mentioned in Table 2 are as follows:

4.1 Test No. 1

In the first test, a large amount of gas was produced in the first week, after feeding the digester. After that there was no sign of production. The presence of biogas was tested by putting burning candle near the gas discharge point every day for one month. But there was no indication of the presence of biogas during these periods. This could be the absence of acid-forming bacteria in kitchen food waste, excess loading rate and uneven loading interval.

4.2 Test No. 2

In this test, the presence of biogas was detected on 18th day after feeding. The produced gas was burned with blue flame. Which is nothing, but a biogas produced from the feedstock. Then, the produced gas was collected in 0.8 m³ capacity balloon for demonstration and analysis of composition.

Table 2 Particulars of test

Particulars	Test No. 1	Test No. 2
Feedstock	Food waste	Food waste and cow dung
Ratio of feedstock and water	1:1	1:1
Temperature range (°C)	23–29	23–32

4.3 Composition Analysis

The composition of biogas was analyzed using gas chromatography. This facility is available in IIT Guwahati. The samples were collected in the balloons, and they were analyzed in gas chromatography. The result so obtain of gas chromatography has been shown in Fig. 3 and in Table 3. The analysis indicates the methane composition of 31% and nitrogen of 69% and fails to detect the presence of component like carbon dioxide and other gases.

4.4 Calorific Value

In order to find the calorific value of produced biogas, we used a standard formula as given in Eq. (1). It is based on the volume of constituent present in the gas. The formula requires the percentage of carbon monoxide, hydrogen and methane by volume present in the so-produced gas. However, in our case, the gas chromatograph that we use was only meant for detecting percentage of methane and nitrogen present in the sample by volume. So considering the above situation, we took only the percentage of methane present in the sample to calculate the calorific value. And the rest parameters required in the formula were set to zero [6].

$$\text{Calorific value} = \frac{[(\text{CO}_{\text{vol}} \times \text{CO}_{\text{cv}}) + (\text{H}_{2\text{vol}} \times \text{H}_{2\text{cv}}) + (\text{CH}_{4\text{vol}} \times \text{CH}_{4\text{cv}})]}{100} \text{ MJ/kg} \tag{1}$$

Therefore, as the calorific value of methane is 23 MJ/kg, the calorific value of biogas was found to be 7.13 MJ/kg.

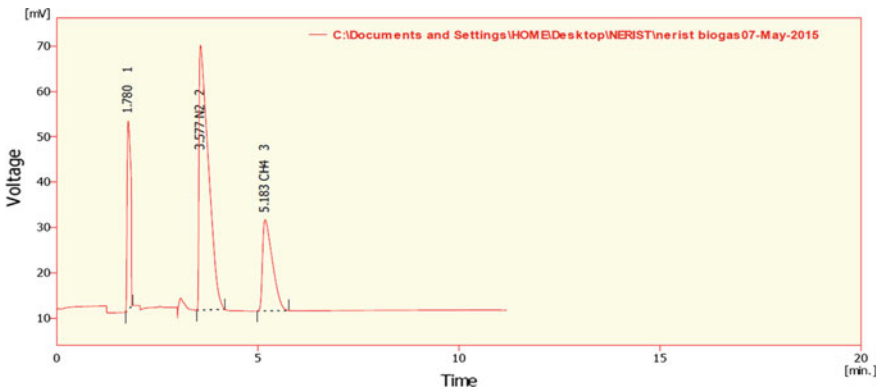


Fig. 3 Detection of various gases at different time and voltage

Table 3 Compositions of biogas

	Reten. time (min)	Response	RB	Amount (mg)	Amount (%)	Peak type	Compound name
1	1.780	251.044	A	0.000	0.0		
2	3.577	946.619	A	35.674	69.0	Ordnr	N ₂
3	5.183	341.810	A	16.033	31.0	Ordnr	CH ₄
	Total			51.707	100.0		

4.5 Conclusion and Future Work

The objective was to produce gas and to check its composition. As we know that biogas can be produce from various biomasses, we used cow dung and kitchen food waste to produce biogas in our case. Since there are different types of biogas plant designs, we preferred the close-dome-type digester because of its portability and economic advantages. A 200 l biogas digester was constructed, and our work was initiated. When we read about the production of biogas, it seems quite easy to produce but as there are always some differences between theory and practical work, in real case when we were practically producing it, we faced lots of problem. Weather condition was one of them, as the production of biogas depends upon the atmospheric condition. Fortunately, the weather condition became suitable and we performed our experiment. We feed the digester regularly, and finally we achieved our objective of producing biogas using self-fabricated digester. The biogas had composition of 31% methane and nitrogen of 69%. And the calorific value of biogas was 7.13 MJ/kg. Though our project work does not include sophisticated equipment's and formulas, we have gained lots of knowledge regarding biogas. In the future, the following works can be done on our developed digester.

- Study the quantity of gas produced in different extend of time.
- Effect of different feedstock on gas production rate.
- Effect of thermodynamic properties like pressure and temperature on the production of biogas.

References

1. ARTI: Appropriate Rural Technology Institute. NGO based organization, Maharashtra, India (2003)
2. Cheng-qi, J., Tian, W.L., Jian Li, Z.: A study on compressed biogas and its application to the compression ignition dual-fuel engine. *Biomass* **20**(1–2), 53–59 (1989)
3. Mahanta, P., Saha, U.K., Dewan, A., Kalita, P., Buragohain, B.: Biogas digester: a discussion on factors affecting biogas production and field investigation of a novel duplex digester. *SESI* **15**(2), 1–12 (2005)

4. Yadvika, S., Sreekrishnan, T.R., Kohli S., Vineet, R.: Enhancement of biogas production from solid substrates using different techniques—a review. *Bioresour. Technol.* **95**, 1–10 (2004)
5. Gebrezgabher, S.A., Meuwissena, M.P.M., Prins, B.A.M., Oude Lansinka, A.G.J.M.: Economic analysis of anaerobic digestion—a case of green power biogas plant in The Netherlands. *NJAS Wageningen J. Life Sci.* **57**(2), 109–115 (2010)
6. Schwarz, W.H.: The cellulosome and cellulose degradation by anaerobic bacteria. *Appl. Microbiol. Biotechnol.* **56**, 634–649 (2001)

Validation of an Inverter Topology for Transformerless Grid-Connected Photovoltaic System

Asim Datta, Rishiraj Sarker, Sanjay Debbarma and Amit Kumar

Abstract Solar photovoltaic (PV) systems are getting more and more widespread due to the recent price reduction in modules and technological developments of power electronics devices to be used in designing power conditioning unit. Generally, a strong affinity in grid-connected PV inverter topology is to use transformer in the grid interface. However, due to transformer, systems become bulky and involve additional losses. The elimination of the transformer abolishes galvanic isolation between the PV system and the utility grid, thus treating from the danger of direct current (dc) injection into the grid. Therefore, the choice of a proper topology for transformerless grid-connected application is crucial to avoid undesirable operational effects. This paper provides a detailed performance study of an IGBT-based modified full-bridge inverter topology from the aspect of single-phase transformerless grid-connected PV system application. Detailed simulation results under different environmental conditions are presented to validate suitability in the transformerless grid-connected application.

Keywords Photovoltaic · Grid-connected system · Transformerless Ground leakage current

1 Introduction

Among the various renewable energy sources, solar energy has always been in the forefront to substitute major percentage of fossil fuel dominance in the energy sector. Especially in a country like India, where availability of solar is in abundance,

A. Datta (✉) · R. Sarker

Department of Electrical Engineering, Mizoram University, Aizawl, India
e-mail: asimdatta2012@gmail.com

R. Sarker

e-mail: sarker.rishiraj88@gmail.com

S. Debbarma · A. Kumar

Department of Electrical Engineering, National Institute of Technology Meghalaya, Shillong, India

government must give more traction towards improvement of technologies for photovoltaic (PV) power conditioning and integration with the electric grid [1].

Nowadays, the rising directions of PV technology comprise the increase in photovoltaic conversion efficiency and in power conditioning efficiency. The power processing deals fundamentally with power electronics interface optimization while in the photovoltaic conversion includes the PV current generation process and maximum power point tracking (MPPT) [2]. The power electronics interfacing is usually a two-stage process with conversion of dc–dc followed by dc–ac power or a single power electronic stage with dc–ac power conversion followed by a transformer [3]. This is done to achieve a regulated voltage and frequency which is good enough to be synchronized with the ac voltage grid. But the introduction of more power electronic switches introduces more losses in the overall system. The incorporation of a transformer makes the system more bulky if it is a line frequency transformer or introduces noise in the system if it is a high-frequency transformer [4]. Transformerless grid interface for PV system is, therefore, getting more and more attention by the research community to make the whole system, starting from PV panels to the synchronization process with the power grid, more efficient and feasible [5]. However, such a system can generate high leakage current in the absence of an isolation transformer between the dc PV generator and the ac grid [6]. This leakage current can produce electromagnetic interference in other nearby systems and can also cause dc offset in the inverter output current flowing into the load and the connected grid.

Technological advancement can make feasible the use of an inverter avoiding transformer and has no impact on the system characteristics relating to grid interfacing and personal safety. For transformerless application, it is essential to develop new inverter topology that avoids the ground leakage current by making constant common-mode voltage of the inverter.

Thus, the main challenge to make a transformerless grid-tied PV system realizable comes in the control strategy and the injection of leakage current in the system [7, 8]. Control strategy poses an issue in the fact that both the MPPT and the current control scheme need to be regulated by tuning the power electronic switches of the converter [9]. Thus, balancing the two controls may be somewhat difficult [10]. The issue of leakage current can be prominent if the inverter switches are modulated using unipolar pulse width modulation (PWM) scheme [5, 10]. The bipolar PWM scheme has an inherent capability to minimize the leakage current. Nonetheless, unipolar PWM is more suitable than bipolar PWM because the dominant high-frequency component in unipolar PWM is half the switching frequency of bipolar PWM [11]. This helps in lower filter requirements as compared to bipolar PWM.

The conventional H-bridge inverter, when modulated using a unipolar modulation scheme, generates excessive leakage current in the system in the absence of an isolation transformer between the PV system and the utility grid [6]. In this study, a modified H-bridge topology of ac/dc inverter is considered for transformerless grid-connected system applications. Thus, emphasis has been given to

study the leakage current elimination performance of the topology, i.e. whether can reduce or completely eliminate the ground leakage current. A detailed simulation-based study validates performance of the inverter.

2 Inverter Topology for Grid-Connected Systems

A single-phase H-bridge inverter topology, which is applied quite often in grid-connected PV system, is a H-bridge inverter as shown in Fig. 1. Different modulation schemes could be adopted to this topology. Based on the output waveform shape, they are categorized into two classes, namely unipolar [6, 10, 12] and bipolar PWMs [10, 13]. During positive half cycle of the inverter output voltage, switches $S1$ and $S2$ are commutated at the modulation frequency, while switch $S4$ is on. For the negative half cycle, $S3$ and $S4$ commutate at the switching frequency and $S2$ is on. In the inverter topology, two switches are on simultaneously, and one diode and one switch only conduct at the modulating frequency under imposed rated input voltage. Generation of a pulsating common-mode voltage with magnitude $V_{PV}/2$ at the triggering frequency is the primary disadvantage of the scheme. Thus, when the full bridge is part of a conversion stage without a transformer, unipolar modulation techniques cannot be adopted.

With a bipolar PWM scheme, the crosswise pairs of switches $S1-S4$ and $S2-S3$ are triggered at the modulating frequency, therefore,

$$V_{cm} = V_{PV}/2 \tag{1}$$

The switching losses become twice with the scheme as two diodes and two switches are triggered at the modulating frequency with the imposed rated input voltage. Furthermore, current ripples become double compared to the unipolar modulation switching scheme as the output voltage varies between $+V_{PV}$ and $-V_{PV}$. Therefore, bipolar PWM technique is to be avoided.

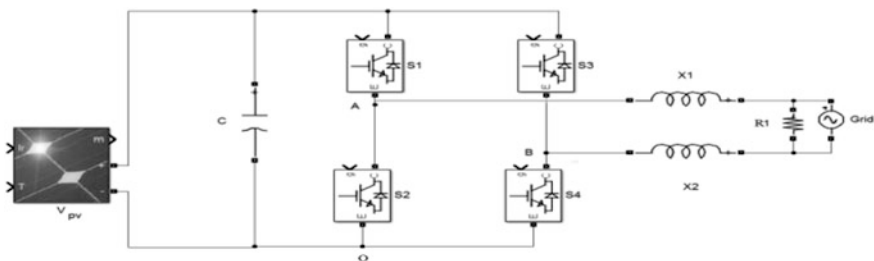


Fig. 1 Full-bridge inverter

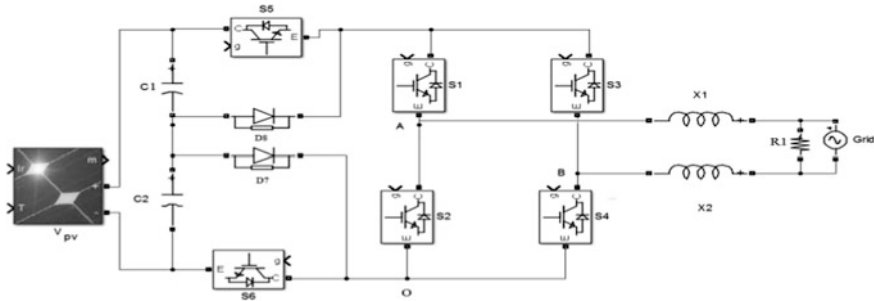


Fig. 2 H6 topology of inverter for grid-tied application without transformer

A modified topology (H6) for transformerless application is shown in Fig. 2 [10]. This topology comprises two diodes and six switches. There are two modes of operation for the H6 topology:

Mode 1: When S1 and S4 are ON: For modulating the input voltage, switches S5–S6 conduct at the modulating frequency. S2 and S3 also commutate at modulating frequency, but complementarily with S5 and S6.

Case 1: When S5 and S6 ON: In this case the output current increases flowing through the path S5, S1, S4, and S6.

During the time, the value of common-mode voltage can be calculated as:

$$V_{CM} = (V_{AO} + V_{BO})/2 = \frac{V_{PV} + 0}{2} = V_{PV}/2 \tag{2}$$

Case 2: When S2 and S3 ON: The output current splits into two routes. One is through S1, the grid circuit and the freewheeling path of S3. Another part follows through S4, the grid circuit and the freewheeling path of S2.

Now voltage V_{AB} tends to zero and due to diodes D7 and D8, the voltages V_{AO} and V_{BO} are maintained at $V_{PV}/2$. Hence, common-mode voltage can be calculated as:

$$V_{CM} = (V_{AO} + V_{BO})/2 = (V_{PV}/2 + V_{PV}/2)/2 = V_{PV}/2 \tag{3}$$

Mode 2: When S2 and S3 ON: For modulating the input voltage, switches S5–S6 conduct at the modulating frequency. S1 and S4 also commutates at the modulating frequency, but complementarily with S5 and S6.

Case 1: When S5 and S6 ON: In this case the output current decreases flowing through S5, S3, grid circuit, S2, and S6. The common-mode voltage value is:

$$V_{CM} = (V_{AO} + V_{BO})/2 = \frac{0 + V_{PV}}{2} = V_{PV}/2 \tag{4}$$

Case 2: When S1 and S4 ON: The output current follows two routes: the first one is through S3, grid circuit and the freewheeling diode of S1; the second one is through

S_2 , grid circuit and the freewheeling diode of S_4 . Now also voltage V_{AB} tends to zero and the voltages V_{AO} and V_{BO} are maintained at $V_{PV}/2$ through diodes D_7 and D_8 . Hence, common-mode voltage can be calculated as:

$$V_{CM} = (V_{AO} + V_{BO})/2 = \left(\frac{V_{PV}}{2} + \frac{V_{PV}}{2} \right) = V_{PV}/2 \quad (5)$$

As the common-mode voltage of the inverter is invariable during all the switches states, leakage current could be limited to nearly zero.

3 Validation of Transformerless Inverter Topology

A MATLAB/SIMULINK model (shown in Fig. 2) is developed to simulate the topology, and the results are presented. Parameter values used in the MATLAB/SIMULINK model are presented in Table 1. X_1 and X_2 are reactances due to split filter inductances L_1 and L_2 .

3.1 Simulation Results

In the case of unipolar sinusoidal PWM, for half cycle (positive or negative) of the inverter output voltage, the crosswise switches S_1 – S_4 (or S_2 – S_3) are triggered at modulating frequency (F_{sw}). Output voltage (V_{AB}) of the inverter and the common-mode voltage (V_{cm}) with unipolar PWM scheme are shown in Fig. 3a, b, respectively. During positive half cycle, $V_{AO} = V_{PV}$ (i.e. 400 V), and $V_{BO} = 0$. Whereas, in the negative half cycle, $V_{AO} = 0$, and $V_{BO} = V_{PV}$ (i.e. 400 V) (shown in Fig. 3a). Henceforth, it causes varying V_{CM} of amplitude $V_{PV}/2$ (i.e. 200 V) at the modulating frequency which is presented in Fig. 3b.

In the case of bipolar sinusoidal PWM, S_1 – S_4 and S_2 – S_3 are triggered alternately at modulating frequency. Output voltage of the inverter, V_{AB} , and the common-mode voltage, V_{CM} , with bipolar PWM scheme are shown in Fig. 4a, b, respectively. At any instant of triggering either ($V_{AO} = 0$, $V_{BO} = V_{PV}$) or ($V_{AO} = V_{PV}$, $V_{BO} = 0$) (as presented in Fig. 4a). Hence, V_{CM} is constant at $V_{PV}/2$ (i.e. 200 V)

Table 1 Parameters used in simulation model

Parameter	Value
Switching frequency	$F_{sw} = 10$ kHz
PV voltage	$V_{PV} = 400$ V
Filter capacitance	$C = 3$ μ F
Filter inductance	$L_1 = L_2 = 30$ mH
Grid voltage	220 V
Grid frequency	50 Hz

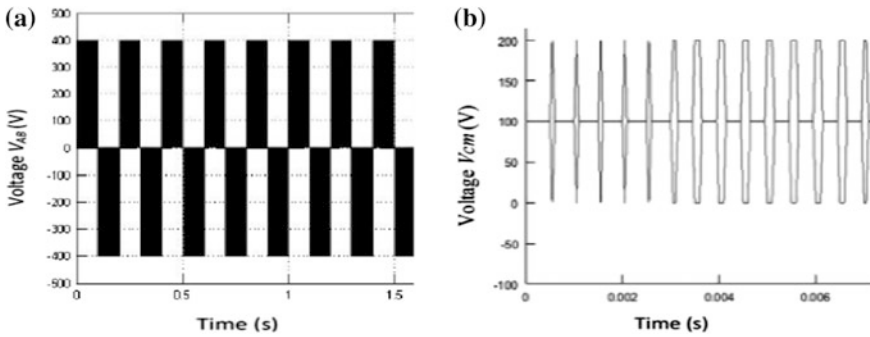


Fig. 3 **a** Output voltage (V_{AB}) of the inverter with unipolar scheme, **b** common-mode voltage (V_{CM}) of the inverter with unipolar scheme

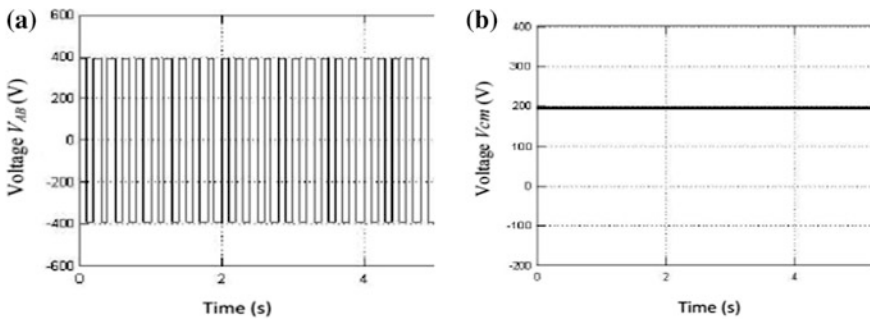


Fig. 4 **a** Output voltage (V_{AB}) of the inverter using bipolar scheme, **b** common-mode voltage (V_{CM}) for bipolar scheme

(as presented in Fig. 4b). The simulation shows that common-mode voltage is constant in bipolar mode, whereas in case of unipolar mode, it is fluctuating.

3.2 Performance Study Under Different Ambient Conditions

PV array always poses an intricate relationship among output voltage, current, and power producing a nonlinear output [8]. Frequent changes in environmental conditions (i.e. solar insolation and temperature) exhibit frequent shifts of the current–voltage ($I-V$) characteristic curve. As temperature raises output voltage of solar array increases and vice versa, but has smaller effect on the output current. Changes in solar insolation have proportional effect on output current of PV array. In order to achieve maximum power, MPPT is a regular adjustment of PV array output under variable ambient conditions.

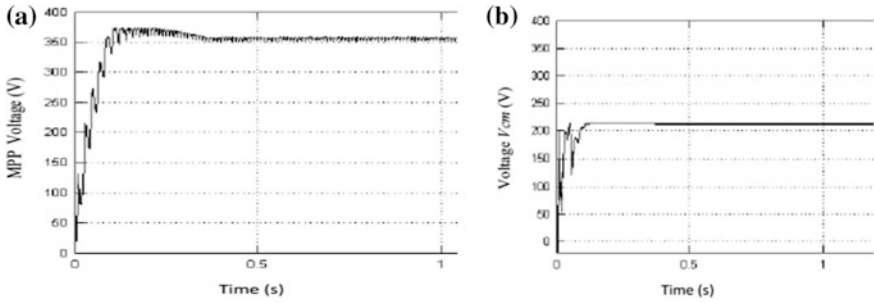


Fig. 5 a MPP voltage of the system, b common-mode voltage (V_{CM}) of the H6 topology

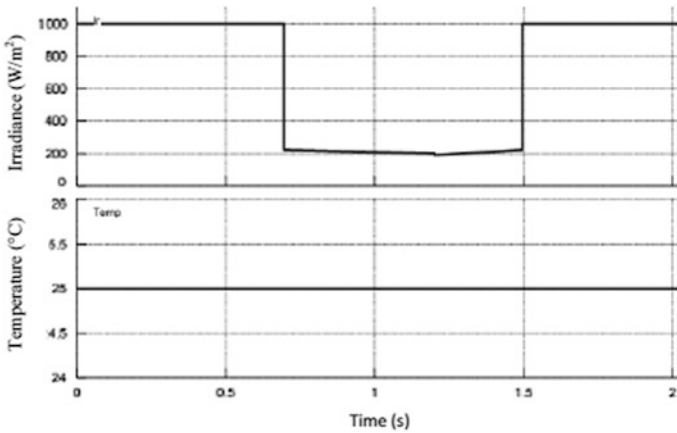


Fig. 6 Variation of irradiation (W/m^2) at constant temperature ($25\text{ }^\circ\text{C}$)

Maximum power point (MPP) voltage and corresponding V_{CM} of the inverter under $1000\text{ }W/m^2$ illumination and $25\text{ }^\circ\text{C}$ ambient temperature are shown in Fig. 5a, b, respectively. The common-mode voltage, shown in Fig. 5b, obtained for the improved inverter topology is a constant one under steady condition.

A variation in irradiation (W/m^2) at constant temperature ($25\text{ }^\circ\text{C}$), as shown in Fig. 6, is applied. It can be observed in Fig. 7 that during the period of $0.7\text{--}1.5\text{ }\mu\text{s}$, the MPP voltage has reduced due to the decreased value in irradiance. Figure 8 shows the corresponding change in common-mode voltage V_{CM} of the inverter. In a particular ambient condition, V_{CM} remains constant.

3.3 Discussion

Using the circuit parameters given by the theoretically analysis and simulation adjustments, the system converges to MPPs stably with acceptable accuracy as

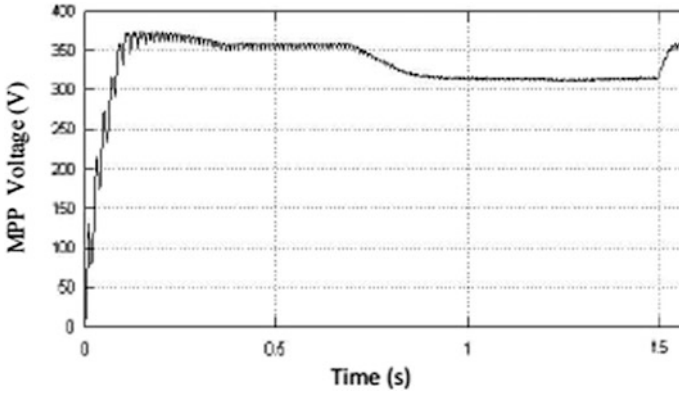


Fig. 7 Variation of MPP voltage

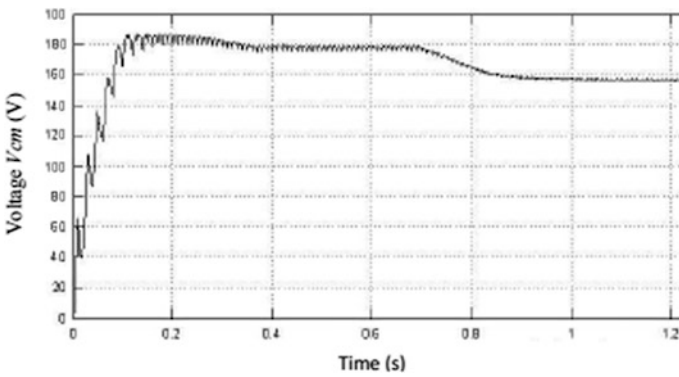


Fig. 8 Variation of common-mode voltage (V_{CM})

demonstrated by the simulation results. The modified topology under validation can be a reliable and efficient one for connecting photovoltaic system to the grid. The simulation result shows that the system inherently converges to the operating point around the MPP. As the common-mode voltage value is constant during all commutation states, ground leakage current can be limited to almost zero.

4 Conclusion

The work involves the validation of single-phase PV converter topology with six switches and two diodes for a transformerless grid-connected PV application. With the converter, PV system is also simulated to verify the ground leakage current issue of the transformerless system. The system produces no pulsating

common-mode voltage, thus supporting the ground leakage current suppression ability. MPPT has been used for boosting the voltage of the PV array. The effect of changing irradiance is seen in the output power of the converter.

Acknowledgements The work is supported by DietY under project grant no. 25(5)/2015-ESDA.

References

1. Myrzik, J.M.A., Calais, M.: String and module integrated inverters for single-phase grid connected photovoltaic systems—a review. In: IEEE Bologna Powertech Conference, Italy (2003)
2. Kadri, R., Gaubert, J.P., Champenois, G.: An improved maximum power point tracking for photovoltaic grid-connected inverter based on voltage-oriented control. *IEEE Trans. Industr. Electron.* **58**, 66–75 (2011)
3. Datta, A., Bhattacharya, G., Mukherjee, D., Saha, H.: Ground leakage current elimination in a transformerless unipolar modulation based single phase grid-connected photovoltaic system. In: Hong Kong Proceedings. 5th IEEE PES Asia-Pacific Power and Energy Engineering Conference (2013)
4. Kjaer, S.B., Pedersen, J.K., Blaabjerg, F.: A review of single-phase grid-connected inverters for photovoltaic modules. *IEEE Trans. Ind. Appl.* **41**, 1292–1306 (2005)
5. Yang, B., Li, W., Gu, Y., Cui, W., He, X.: Improved transformerless inverter with common-mode leakage current elimination for a photovoltaic grid-connected power system. *IEEE Trans. Power Electron.* **27**, 752–762 (2012)
6. Hu, S., Li, C., Li, W., He, X., Cao, F.: Enhanced HERIC based transformerless inverter with hybrid clamping cell for leakage current elimination. In: Energy Conversion Congress and Exposition (ECCE), pp. 5337–5341. IEEE (2015)
7. Calais, M., Agelidis, V.G.: Multilevel converters for single-phase grid connected photovoltaic systems—an overview. In: IEEE International Symposium (1998)
8. Calais, M., Myrzik, J., Spooner, T., Agelidis, V.G.: Inverters for single-phase grid connected photovoltaic systems—an overview. In: IEEE PESC Record (2002)
9. Mei, Q., Shan, M., Liu, L., Guerrero, J.M.: A novel improved variable step-size incremental-resistance MPPT method for PV systems. *IEEE Trans. Industr. Electron.* **58**, 2427–2434 (2011)
10. González, R., López, J., Sanchis, P., Marroyo, L.: Transformerless inverter for single-phase photovoltaic systems. *IEEE Trans. Power Electron.* **22**, 693–697 (2007)
11. Datta, A., Bhattacharya, G., Mukherjee, D., Saha, H.: Modeling and simulation based performance study of a single-stage transformerless grid-connected PV system in Indian ambient conditions. *Int. J. Ambient Energy* **37**, 172–183 (2016)
12. Anand, S., Gundlapalli, S.K., Fernandes, B.G.: Transformer-less grid feeding current source inverter for solar photovoltaic system. *IEEE Trans. Ind. Electron.* **61**, 5334–5344 (2014)
13. Eltawil, M.A., Zhengming, Z.: Grid-connected photovoltaic power systems: technical and potential problems—a review. *Renew. Sustain. Energy Rev.* **14**, 112–129 (2010)

Harvesting Insolation Using Mo–W–Sulfide Compound Nanoparticle Semiconductor as Photocatalyst: A Pollution Controlling Material

Debabrat Kalita, Lakhi Chetia and Gazi A. Ahmed

Abstract In this report, nanoparticles of Mo–W–sulfide compound, confirmed by XRD, SEM and EDX spectra, have been successfully synthesized using solid-state reactions. The as-synthesized material is found to be an efficient photocatalyst that can utilize a broad range of the solar spectra due to the presence of multiple optical band gaps (BG) that have been observed by analyzing UV–Visible spectra. The compound semiconductor nanoparticles show better photocatalytic activity than MoS₂ nanoparticles because of the combined effect of Mo and W leading to greater exciton pair generation. It is observed that the as-synthesized compound nanoparticles degrade dye methyl orange and rhodamine B very efficiently with 97% degradation in just 90 min. The as-synthesized compound can be a promising material to control dye-pollution through photocatalysis using the higher-intensity part of the solar spectrum, and thus providing an advantageous, eco-friendly and low-cost process.

Keywords Compound semiconductor · Multiple BG · Photocatalysis
Rate constant · Energy harvesting

1 Introduction

Solar energy harvesting is one kind of technique to solve present-day environmental problems. The development of such eco-friendly approaches is one of the crucial demands of the current time as well as for the future. Use of solar radiation, or insolation, in controlling pollution in ecosystems is a very optimistic step toward

D. Kalita (✉) · L. Chetia · G.A. Ahmed
Department of Physics, Tezpur University, Tezpur 784028, Assam, India
e-mail: kalitadeb@gmail.com

L. Chetia
e-mail: moon444.in@gmail.com

G.A. Ahmed
e-mail: gaziaahmed@yahoo.com

healthy environment. Photocatalysis is one such effective way of minimizing pollution due to polluting materials by using naturally available solar radiation. It has been observed that in many applications several dye materials are used in different industries like textile, paper, rubber industries, some of which are very toxic and harmful to the environment [1–3]. Because of such hazardous dyes, growth of plants and living organisms is severely effected. Wrong waste disposal methods and faulty drainage systems of many industries directly or indirectly expose these kinds of polluting dyes into the water bodies of the ecosystem from which they spread outwards. In order to reduce their harmful effects, they must be decomposed or degraded before releasing them into the ecosystem. Existing studies reveal that semiconductor (SC) nanomaterials can act as potential catalysts to degrade such dyes into benign substances. MoS_2 and WS_2 are nontoxic highly stable graphene analogous and layered SC members of the transition metal dichalcogenides (TMD) family and which have exciting electronic and optical properties due to their finite band gap (BG) energy lying in the visible light spectrum. However, the BG is small (approx. 1.3 eV) in the bulk form but increases (up to approx. 1.9 eV) when thickness is reduced to monolayer [4–9]. The BG may again increase further due to quantum confinement effect when the dimensions are reduced to nanoscale. There are reports of photocatalysis using MoS_2 - and WS_2 -sensitized TiO_2 catalyst. Again, H_2 gas evolution using MoS_2/CdS composite has also been reported. Also, photocatalysis using composite of TiO_2 and MoS_2 /graphene cocatalyst has been reported [10, 11]. Due to slight difference in BG and similar structure of MoS_2 and WS_2 their compound materials may act as efficient photocatalysts, a possibility that has not been explored till date. In this work, synthesis of compound Mo–W–Sulfide nanoparticles has been done to investigate their photocatalytic behavior. It has been observed that the compound nanoparticles, being a semiconductor having multiple BG, degrade polluting dyes with improved efficiency, compared to MoS_2 nanoparticles, within few hours. In this work, methyl orange (MO) and rhodamine B (RB), both being harmful, are used as model dye. The as-synthesized compound material is found to have mixed phases with multiple BG which provide efficient utilization of a wide spectral range of the visible solar radiation. Also the reusability of the catalyst provides a cheaper and advantageous way to control pollution due to dyes.

2 Experimental Details

2.1 Material Synthesis and Characterization

The materials are synthesized using solid-state reaction between molybdic/tungstic acid and excess thiourea (1:48 molar ratio) at 500 °C in N_2 gas environment [12, 13]. After synthesis, the material is cleaned using warm distilled water to

remove soluble impurities followed by centrifugation and filtration. After drying, the material is further grinded gently into fine powder form by mortar and pestle. The morphology of the materials is characterized by X-ray diffractometer (XRD) (make: RIGAKU MINIFLEX) with Cu-K α radiation ($\lambda = 1.5405 \text{ \AA}$) and Scanning Electron Microscope (SEM) (make: make: JEOL JSM-6390LV). Composition of the material is analyzed using energy dispersive X-ray spectroscopy (EDX). The photocatalytic activity under a xenon arc lamp (make: Xenon Lamp Zolix SLH-X500 Xenon Arc Light Source) acting as visible light source is observed using a UV–Visible spectrometer (make: UV 2450, SHIMADZU CORPORATION).

2.2 Evaluation of Photocatalytic Degradation

In order to measure the photocatalytic activity of the as-synthesized material, 10 μM solution of MO and RB is prepared. The as-synthesized MoS₂ and Mo–W–Sulfide compound nanoparticles are then added into the solution in the proportion of 1 mg/ml and stirred for few hours to attain absorption–desorption equilibrium in the dark. After that the solution mixture is kept in a wide surface beaker and exposed to visible light radiation. For irradiation, a 500 W xenon arc lamp with an output intensity of 12,000 lx is used. Ten milliliters of the sample is taken out at regular intervals of half an hour and centrifuged at 7000 rpm for 12 min. Four milliliters of the aliquot from each sample is taken out and is then analyzed by UV–Vis absorption spectroscopy (Fig. 1).

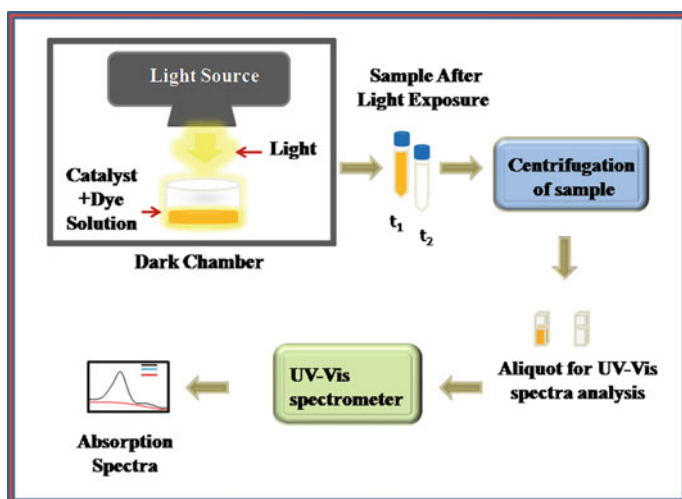


Fig. 1 Schematic of photocatalytic measurement setup

3 Results and Discussion

The XRD pattern of the as-synthesized nanoparticles is shown in Fig. 2a, b. Plot 2a confirms the formation of MoS₂ nanoparticles when compared with JCPDS software (card no. 1999 JCPDS No. 75-1539), while Plot 2b reveals the formation of compound material of Mo, W and S. From the SEM micrographs, the particles are found to be in the nanoscale dimension having different size in the range between 100 and 1 μm; however, most of them get agglomerated. It is found from EDX spectra, given in Fig. 2e, that the as-synthesized material is mainly composed of Mo and S, S being most abundant and spectra Plot 2f reveal that the compound is composed of mainly Mo, W and S. Multiple optical BG lying in the range of visible light energy are formed in both the samples as is evident from the analysis of UV–Visible spectra of the powdered sample (Fig. 3a, b) [14]. The higher value of BG in the compound is probably due to the combined effect of ligands S and W which leads to splitted d-orbitals that raises the energy levels. Multiple BG which occurred due to the presence of defect states and mixed phases of the material provide a better way to utilize broad spectrum of the solar radiation during photocatalysis, generating more number of electron–hole (e[−]–h⁺) pairs that accelerates the reaction mechanism.

The photocatalytic activity measurement is evaluated by observing the degradation of UV–Vis absorption peak of model dye MO and RB after irradiation using MoS₂ and Mo–W–Sulfide compound nanoparticles. The percentage degradation of the dye samples can be calculated using relation (1) [14, 15].

$$\%D = \left(\frac{A_0 - A_t}{A_0} \right) \times 100\% \quad (1)$$

where A_0 is the absorbance before radiation and A_t is the absorbance after radiation time ' t '.

The kinetic analysis of the catalytic reaction can be obtained using the first-order reaction equation (considering the photocatalytic reaction to obey first-order kinetics)

$$\ln(C_0/C_t) = kt \quad (2)$$

where C_0 and C represent reactant concentration before radiation and after radiation at time t , k is the reaction rate constant (RC).

From Beer–Lambert's law for the attenuation of light during propagation through a absorbing material we have,

$$\text{Absorbance, } A = a(\lambda)bc \quad (3)$$

where $a(\lambda)$ is a wavelength-dependent absorptivity constant, b is the length through which light propagates, and C represents the analyte concentration. During the

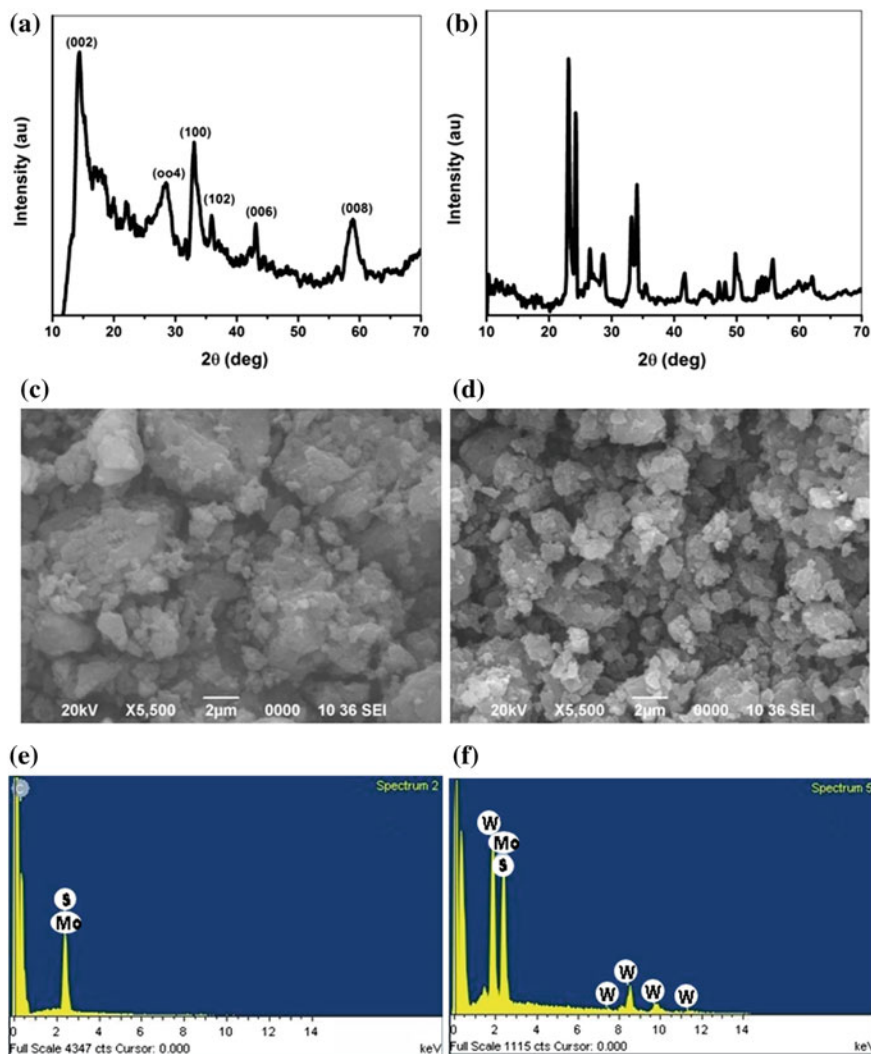


Fig. 2 a, b XRD plot, c, d SEM micrograph, e, f EDX spectrum of the as-synthesized MoS₂ and Mo–W–Sulfide compound nanoparticles respectively

UV–Vis spectroscopic analysis $a(\lambda)$ and b remains constant. Therefore, A is directly proportional to C and C can be replaced by A in Eq. (2) to obtain the relation (4).

$$\ln(A_0/A_t) = kt \quad (4)$$

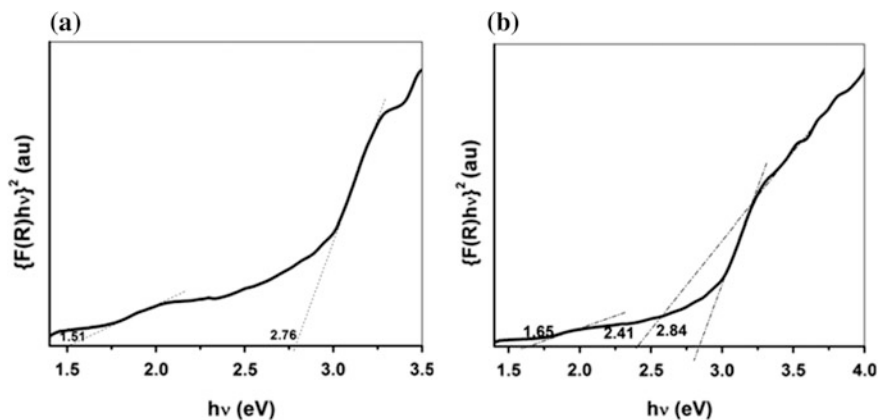
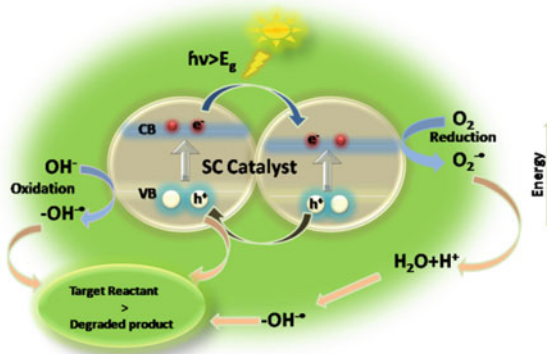


Fig. 3 Kubelka Munk plot of **a** MoS₂ and **b** Mo–W–Sulfide compound nanoparticles

Fig. 4 Schematic of photocatalysis mechanism using SC catalyst having multiple BG



where A_0 and A_t represent the absorbance before radiation and after radiation at time t , respectively. The slope of the plot $\ln(A_0/A_t)$ vs t determines the value of the reaction RC. RC represents a measure of how fast or slow the reaction proceeds. Larger the value of RC faster the reaction. It is observed from Fig. 5a–d that the degradation of the UV–Vis peaks of MO and RB due to the effect of catalyst Mo–W–Sulfide compound nanoparticles is faster than that due to MoS₂ nanoparticles. The compound material degrades the dyes almost above 97% in 90 min. This is probably due to the presence of W atoms that raises the BG value of the material in the compound, corresponding to a BG energy required for absorption of the most intense part of the solar visible light spectrum with larger photon density, leading to more number of exciton pair generation during photocatalytic process. These

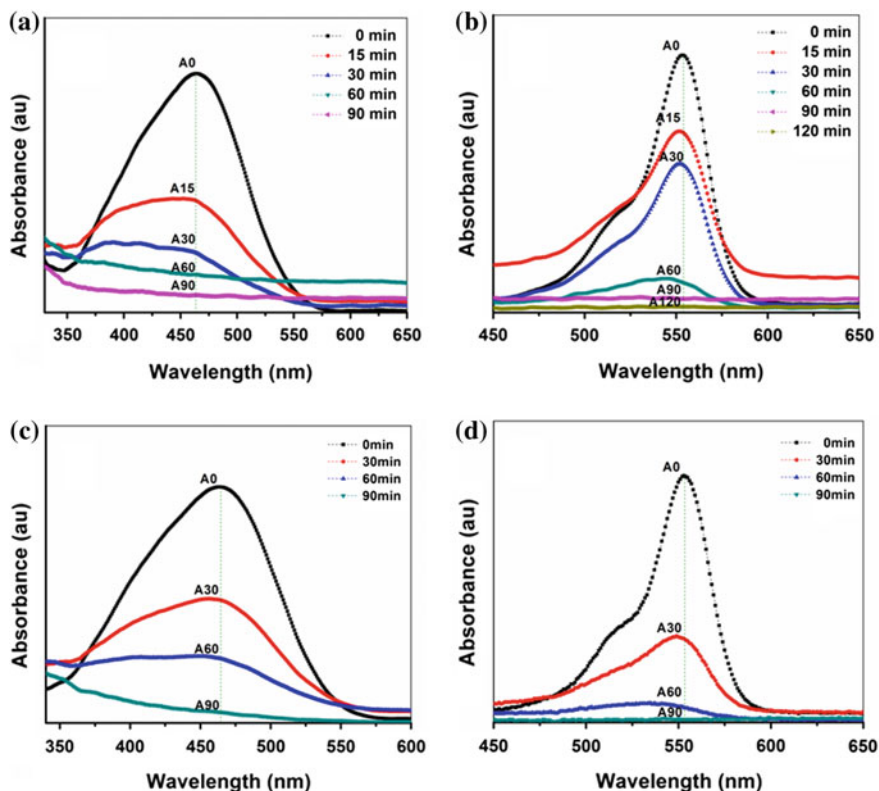


Fig. 5 a, b Represent degradation of MO and RB by catalyst MoS₂ nanoparticles and c, d represent degradation of MO and RB by catalyst Mo–W–Sulfide compound nanoparticles, respectively

exciton pairs before recombination react with water and oxygen molecule absorbed in water to produce hyperactive hydroxyl ($-\text{OH}^{\cdot-}$) ions. These $-\text{OH}^{\cdot-}$ and h^+ agents further react with the target dye molecules and degrade them. The mechanism can be understood from Fig. 4.

The amount of %D is shown in Fig. 6a, b for both the catalysts. Also the RCs of different reactions, determined from the plots in Fig. 7, reveal that the photocatalytic activity becomes faster in case of the as-synthesized compound material. Thus, it has been found that both the catalysts used for degradation of the model dyes act efficiently. The Mo–W–Sulfide compound nanoparticles are more efficient to degrade such kind of hazardous dyes and can be used as pollution controlling material.

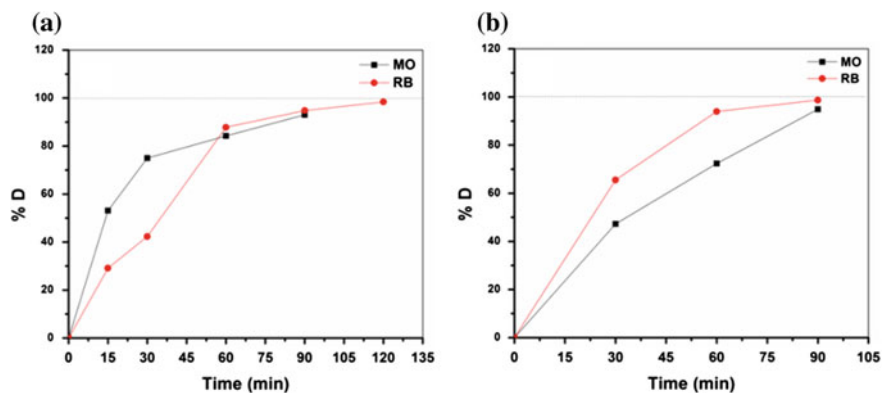


Fig. 6 Shows the percentage degradation of MO and RB using catalyst. **a** MoS₂ nanoparticles and **b** Mo-W-Sulfide compound nanoparticles

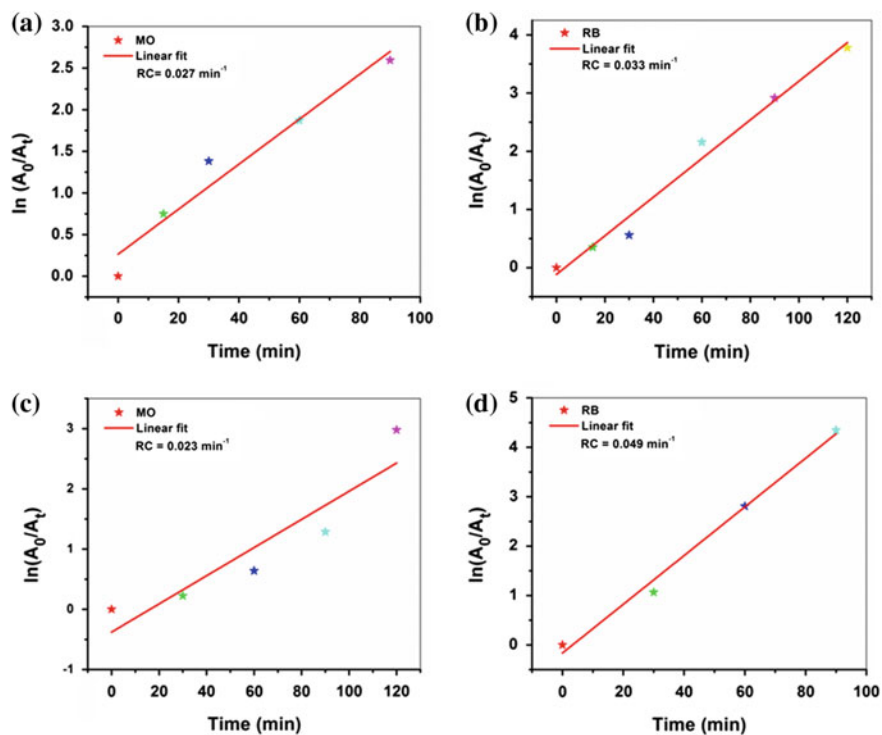


Fig. 7 Shows the plot to determine the reaction RC using catalyst. **a** MoS₂ nanoparticles and **b** Mo-W-Sulfide compound nanoparticles

4 Conclusion

In this report, synthesis of MoS₂ and Mo–W–Sulfide compound nanoparticles is successfully achieved. From photocatalytic activity, it is observed that though MoS₂ and as-synthesized compound nanoparticles act as good photocatalyst, the latter shows better efficiency and can be used as dye-pollution controlling material in future. As the catalyst is insoluble in water and dilute acids, it can be easily removed from the solution mixture and being solid, nontoxic and stable can be reused. Because of its reusability it reduces the overall cost of synthesis process. The multiple BG of the material provide utilization of the intense (nearly 45%) part of solar radiation. Thus, the as-synthesized compound nanoparticles are found to be very good photocatalysts which can degrade polluting dyes within few hours in cheaper way with great efficiency.

References

1. Kaur, J., Bansal, S., Singhal, S.: Photocatalytic degradation of methyl orange using ZnO nanopowders synthesized via thermal decomposition of oxalate precursor method. *Phys. B* **416**, 33–38 (2013). doi:[10.1016/j.physb.2013.02.005](https://doi.org/10.1016/j.physb.2013.02.005)
2. Chen, T., Zheng, Y., Lin, J.M., Chena, G.: Study on the photocatalytic degradation of methyl orange in water using Ag/ZnO as catalyst by liquid chromatography electrospray ionization ion-trap mass spectrometry. *J. Am. Soc. Mass Spectrom.* **19**, 997–1003 (2008). doi:[10.1016/j.jasms.2008.03.008](https://doi.org/10.1016/j.jasms.2008.03.008)
3. Carmen, Z., Daniela, S.: Textile organic dyes—characteristics, polluting effects and separation/elimination procedures from industrial effluents—a critical overview. In: Puzyn, T. (ed.) *Organic Pollutants Ten Years After the Stockholm Convention—Environmental and Analytical Update*. ISBN: 978-953-307-917-2 (2012). InTech, Available from: <http://www.intechopen.com/books/organic-pollutants-ten-years-after-the-stockholm-convention-environmental-and-analytical-update/textile-organic-dyes-characteristics-polluting-effects-and-separation-elimination-procedures-from-in>. Accessed 05 Aug 2016 (General Internet site)
4. Mak, K.F., Lee, C., Hone, J., Shan, J., Heinz, T.F.: Atomically thin MoS₂: a new direct-gap semiconductor. *Phys. Rev. Lett.* **105**(13), 136805 (2010). doi:[10.1103/PhysRevLett.105.136805](https://doi.org/10.1103/PhysRevLett.105.136805)
5. Tang, Q., Zhou, Z.: Graphene-analogous low-dimensional materials. *Prog. Mater. Sci.* **58**, 1244–1315 (2013). doi:[10.1016/j.pmatsci.2013](https://doi.org/10.1016/j.pmatsci.2013)
6. Radisavljevic, B., Radenovic, A., Brivio, J., Giacometti, V., Kis, A.: Single-layer MoS₂ transistors. *Nat. Nanotechnol.* **6**, 147–150 (2011). doi:[10.1038/NNANO.2010.279](https://doi.org/10.1038/NNANO.2010.279)
7. Chang, K., Chen, W.: L-cysteine-assisted synthesis of layered MoS₂/graphene composites with excellent electrochemical performances for lithium ion batteries. *ACS Nano* **5**(6), 4720–4728 (2011). doi:[10.1021/mn200659w](https://doi.org/10.1021/mn200659w)
8. Shanmugam, M., Bansal, T., Durcan, C.A., Yu, B.: MoS₂/TiO₂ nanoparticle composite bulk heterojunction solar cell. In *Proceedings of 12th IEEE International Conference on Nanotechnology (IEEE-NANO)* (2012)
9. Jin, W., Yeh, P.C., Zaki, N., Zhang, D., Sadowski, J.T., Al-Mahboob, A., Zande, A.M., Chenet, D.A., Dadap, J.I., Herman, I.P., Sutter, P., Hone, J., Osgood, R.M.: Direct measurement of the thickness-dependent electronic band structure of MoS₂ using angle-resolved photoemission spectroscopy. *Phys. Rev. Lett.* **111**, 10680 (2013). doi:[10.1103/PhysRevLett.111.10680](https://doi.org/10.1103/PhysRevLett.111.10680)

10. Xiang, Q., Yu, J., Jaroniec, M.: Synergetic effect of MoS₂ and graphene as cocatalysts for enhanced photocatalytic H₂ production activity of TiO₂ nanoparticles. *J. Am. Chem. Soc.* **134**, 6575–6578 (2012). doi:[10.1021/ja302846n](https://doi.org/10.1021/ja302846n)
11. Zong, X., Wu, G., Yan, H., Ma, G., Shi, J., Wen, F., Wang, L., Li, C.: Photocatalytic H₂ evolution on MoS₂/CdS catalysts under visible light irradiation. *J. Phys. Chem. C* **114**, 1963–1968 (2010). doi:[10.1021/jp904350e](https://doi.org/10.1021/jp904350e)
12. Rao, C.N.R., Nag, A.: Inorganic analogues of graphene. *Eur. J. Inorg. Chem.* **2010**(27), 4244–4250 (2010). doi:[10.1002/ejic.201000408](https://doi.org/10.1002/ejic.201000408)
13. Matte, H.S.S.R., Gomathi, A., Manna, A.K., Late, D.J., Datta, R., Pati, S.K., Rao, C.N.R.: MoS₂ and WS₂ analogues of graphene. *Angew. Chem.* **122**(24), 4153–4156, (2010). doi:[10.1002/ange.201000009](https://doi.org/10.1002/ange.201000009)
14. Chetri, P., Basyach, P., Choudhury, A.: Structural, optical and photocatalytic properties of TiO₂/SnO₂ and SnO₂/TiO₂ core–shell nanocomposites: an experimental and DFT investigation. *Chem. Phys.* **434**, 1–10 (2014). doi:[10.1016/j.chemphys.2014.02.007](https://doi.org/10.1016/j.chemphys.2014.02.007)
15. Paul, S., Choudhury, A.: Investigation of the optical property and photocatalytic activity of mixed phase nanocrystalline titania. *Appl. Nanosci.* **4**, 839–847 (2014). doi:[10.1007/s13204-013-0264-3](https://doi.org/10.1007/s13204-013-0264-3)

Visible Light Harvesting Titania-Coated Diatom Frustules with Superior Photocatalytic Activity

Lakhi Chetia, Debabrat Kalita and Gazi A. Ahmed

Abstract Porous silica frustules of diatoms are naturally occurring microcellular, solar light harvesting hierarchical structures. In this work, titania-deposited diatom frustule is presented as a heterogeneous catalyst having high efficiency for photodegradation of major pollutants under visible light irradiation. The heterogeneous catalyst is synthesized by depositing titania nanoparticles in the pores and surface of diatom frustules by solgel method and is characterized by XRD, UV–visible absorption spectroscopy, SEM, and TEM. Increase in crystallite size with the transformation of titania phase at high-temperature synthesis is confirmed by XRD. UV–visible spectra reveal that synthesized catalysts exhibit absorption in the visible light range and are able to perform catalytic activity for the degradation of azo-dyes. The effect of photocatalyst on dye concentration in aqueous solution and presence of anatase–rutile titania phases are also presented. As-prepared catalysts responsive to visible light could be a promising candidate in application of environment remediation by harvesting solar energy with the use of the morphology of diatom frustules and presence of nano titania phases in it.

Keywords Diatom frustule · Mixed phase · Band gap · Rate constant Degradation

1 Introduction

Textile and color industries make the whole world colorful by producing various kinds of dyes. Industries such as leather, rubber, plastic, wools, food, cosmetics, drugs, inks, papers, art, and craft use many synthetic dyes for coloring. Such

L. Chetia (✉) · D. Kalita · G.A. Ahmed
Department of Physics, Tezpur University, Tezpur 784028, Assam, India
e-mail: moon444.in@gmail.com

D. Kalita
e-mail: kalitadeb@gmail.com

G.A. Ahmed
e-mail: gaziaahmed@yahoo.com

industries discharge large amount of wastewater into the environment without proper purification. World Bank reported that nearly 20% water pollution is caused by textile industries [1]. Most of the dyes are highly toxic, carcinogenic, non-self-degradable, and their complex structures give them thermal and photostability. Aromatic-structured azo group dyes are obstinate to degradation [2] and ever-growing emission of dyes to the environment and ecosystem that contribute significantly to water pollution. There exist lots of conventional techniques such as filtration, absorption, coagulation/flocculation, solvent extraction, electrochemical techniques, and reverse osmosis to remove persistent dyes released into aquatic environment [3, 4]. But these methods are highly expensive and require high power consumption with some of them releasing harmful products, while some are incapable of completely removing color. Therefore, in transferring harmful organic dyes into eco-friendly benign products, more efficient and cost-effective methods are needed. Prior studies reveal that semiconductor photocatalysis is a potentially strong complex multi-step process for complete degradation of dyes to benign substances with high cost-effectiveness [5]. But single semiconductor has high electron-hole (e^- - h^+) recombination rate, low capability of harvesting solar energy, and poor selective adsorption [6]. Therefore, to improve and exploit the advantageous photocatalytic activity of semiconductors, hybrid of two or more semiconductor systems has been developed to utilize solar radiation [7]. Pristine TiO_2 is the benchmark in the field of photocatalysis due to its high photoreactivity, good time stability, low cost including its environment-friendly nature. It is photoreactive to light of wavelength $\lambda \leq 3875 \text{ \AA}$ that lies in the UV range (about 3–5% of solar energy) due to its large band gap (BG) [5]. Because of the potential increase of light utilization over wide range of visible light spectra (about 45% of solar spectra) by harvesting natural organisms, improved photocatalytic activity can be expected in this manner [8].

In this study, a potent photocatalyst was developed to increase the photoactivity in the visible light range by using diatoms as template; naturally available unicellular microscopic algae possessing amorphous porous silica skeleton, called frustules, for coating titania phases were used. Periodic nanopores contained in the frustules of diatoms are efficient light collectors, capitalize on solar energy, can interact effectively with light photons, and have high photosynthesis efficiency due to their internally located chloroplast [9, 10]. Calcined diatom frustules can absorb light from ultraviolet to a broad visible range [8]. Synthesis of photocatalyst using diatom frustules and titania, that become hetero-semiconducting-system, permits more efficient use of solar energy and thus becomes sustainable solution to environmental problem. We have considered methylene blue (MB) as model dye in this study as MB is an azo dye having undesirable consequences on environment. It is used in various industries. Smelling of this dye can even cause problems in the respiratory system and is also harmful for the eyes. It can create nausea and vomiting, burning of the skin, and also can cause mental disorders [4]. A lot of work has been reported on photocatalytic degradation of MB under UV light. It is also observed that the time period required for MB degradation is also very high.

In this present work, our aim is to minimize the required time for complete degradation of MB dye not only by UV light but by the visible solar spectrum (about 45%) also, using our as-prepared titania-coated diatom frustules as catalyst with different dye concentrations.

2 Experimental Work

2.1 *Synthesis of Anatase and Anatase–Rutile Mixed Phase-Coated Diatom Template*

Diatom species from freshwater bodies were collected and cultured using WC media [11]. After one month, the diatoms were cleaned with distilled water. The diatoms were then treated with glutaraldehyde solution. Titania coating was carried out by the sol-gel method [8]. 5% TTIP (titanium tetra isopropoxide) in isopropanol was prepared. Cleaned diatom frustules were added in the slowly stirred TTIP solution. Next, the samples were filtered, dried in air, and thereafter calcined at 500 and 800 °C. The final products were labeled as TDA and TDAR corresponding to synthesis temperature 500 and 800 °C, respectively.

Photocatalytic degradation of MB is done by adding 20 mg of prepared photocatalyst (TDA and TDAR) in 100 ml of 20 and 50 µM MB solution and stirred in the dark for 3 h. Thereafter, the solution mixture was exposed under visible light irradiation. After every 10 min during the photodegradation process, 10 ml of MB suspension is taken out and centrifuged for 10 min at 7000 rpm to remove the catalyst particles from the dye solution. From this, we take 3 ml of the aliquot for further analysis.

2.2 *Characterization Details*

The morphology, identification, and classification of microbiological organisms are done using scanning electron microscopy (SEM) (JEOL JSM-6390LV scanning electron microscope) and TEM (TECNAI G2 20 S-TWIN (200 kV), FEI COMPANY, USA) instrument. The XRD patterns of the samples were collected using a diffractometer (RIGAKU MINIFLEX diffractometer) with Cu-K α radiation ($\lambda = 1.5405 \text{ \AA}$) for structural analysis. Full scan (2θ , 20°–70°) is performed with step size of 0.05° and scan rate of 1.0 $2\theta/\text{min}$. The optical absorption spectra of diatom samples were obtained using a UV–visible absorption spectrophotometer (UV 2450, Shimadzu Corporation).

A 500 W visible light source is used for irradiating (Xenon Lamp Zolix SLH-X500 Xenon Arc Light Source) MB solution for photocatalytic degradation.

3 Results and Discussions

A detailed analysis of the morphology of raw diatom frustules is performed using SEM. The frustules contain nanoscale-ranged areolae, a slightly wider central and narrow axial area. With these observations and also comparing with diatom identification guides and ecological resource databases [12], the diatom species is confirmed to be freshwater *Cosmioneis Reimeri* species. Figure 1a shows the SEM micrograph of the *Cosmioneis Reimeri* frustules of diatoms cleaned by acid-base treatment. The total length, thickness of the cell, and average diameter of pores are found to be around 16.34 μm , 2.38 μm , and 165 nm, respectively.

The morphology and size of TiO_2 nanoparticles coated on diatom frustules are confirmed by TEM analysis (Fig. 1), which illustrated that nanoparticles are polycrystalline in nature. From the TEM micrographs, the lattice spacing of 0.35 and 0.32 \AA corresponding to the inter-planar distance between adjacent (101)A and

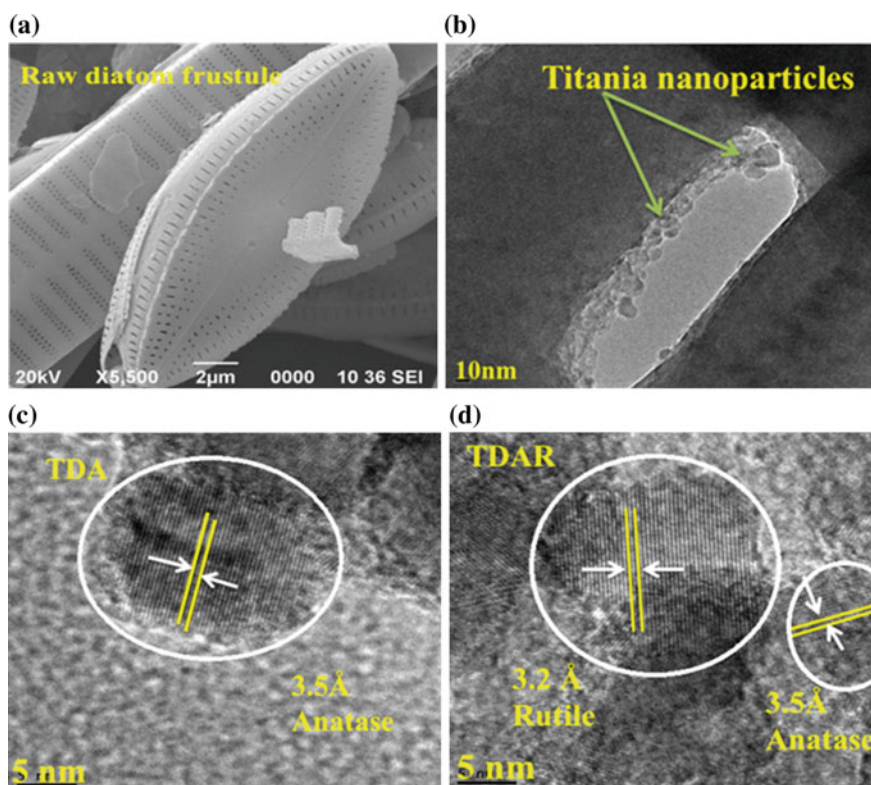


Fig. 1 a SEM micrograph of diatom species *Cosmioneis Reimeri*, TEM micrographs of b titania nanoparticles coated in the pores, c anatase phase, and d anatase–rutile mixed phase

(110)R crystallographic planes of anatase and rutile TiO_2 , respectively, is obtained (Fig. 1c, d).

The phases contained in the prepared samples are determined using the XRD pattern shown in Fig. 2a. The XRD peaks at 25.2° , 27.3° , 36.0° , 37.1° , 41.2° , 47.9° , 54.2° , 56.5° , and 62.6° of the sample TDAR correspond to diffractions at the planes (101)A, (110)R, (101)R, (004)A, (111)R, (200)A, (211)R, (220)R, and (002)R when compared with JCPDS no. 71.1167 and JCPDS no. 89-4920 (A-anatase, R-rutile). The peaks at 25.2° , 37.9° , 48.1° , 53.9° , 55.2° , and 62.8° of the sample TDA correspond to diffraction at the planes (101)A, (004)A, (200)A, (105)A, (211)A, and (204)A when compared with JCPDS no. 71.1167. TDAR contains both rutile and anatase phases confirmed by the presence of peaks corresponding to both the phases. Contradictory to the amorphous nature of raw diatom frustules (Fig. 2a), sharp and intense peaks indicate that prepared samples are highly crystalline in nature. Using Debye–Scherrer formula, the average crystallite sizes of the samples are found to be 35 and 16 nm for TDA and TDAR, respectively.

The UV–visible absorption spectra of TDA and TDAR are shown in Fig. 2b. TDAR sample shows significant increase of broad range visible light absorption due to the band to band transition from 3d levels of Ti to 2p levels of O [13] and marginally broader as compared to TDA sample. TDAR sample also shows redshift relative to TDA. Kubelka–Munk (KM) plot method is used for calculating the BG value for TDA and TDAR [14]. The calculated BG value for TDA and TDAR is 3.08 and 2.87 eV, respectively, from the KM plot in Fig. 2c.

3.1 Photocatalytic Activity Measurement

The photocatalytic activity of the as-synthesized materials is studied by observing the degradation of absorption peaks under visible light irradiation in the UV–Vis spectra of MB. The absorption spectra of MB in the presence of TDA and TDAR with 20 and 50 μM dye concentrations under visible light irradiation are shown

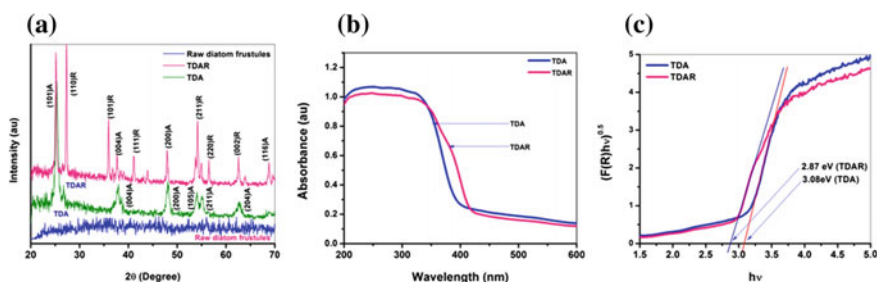


Fig. 2 a X-ray diffraction pattern of raw diatom frustules, TDA, and TDAR; b UV–visible absorption spectra, and c KM plot showing the BG value of TDA and TDAR

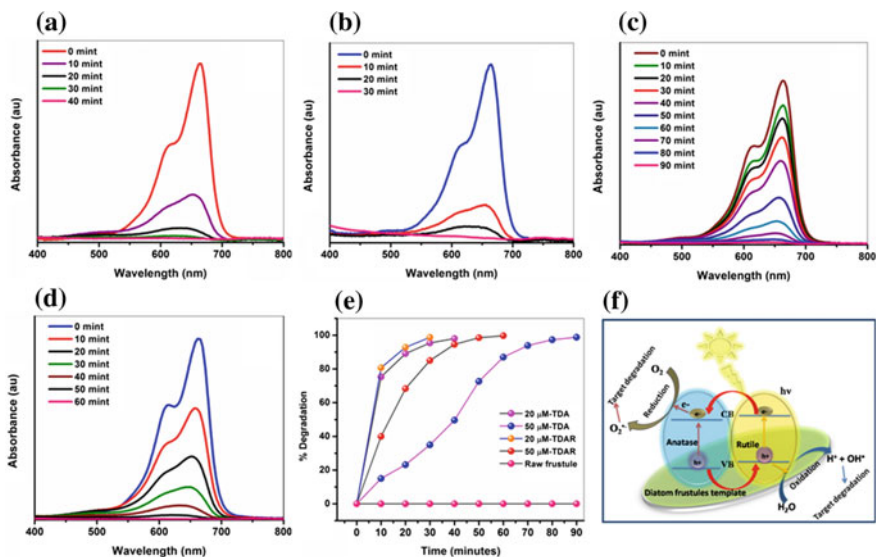


Fig. 3 Absorption spectra of 20 μM dye conc. **a** TDA, **b** TDAR as catalyst, 50 μM dye conc. **c** TDA and **d** TDAR as catalyst under visible light irradiation at different photodegradation time, **e** degradation curve of MB under visible light irradiation, **f** schematic of photocatalytic mechanism due to mixed phase TiO_2 -coated diatom frustules

in Fig. 3a–d. The spectrum ranges from 400 to 800 nm with maximum absorption at 664 nm wavelength. The characteristic absorption peak intensity of MB decreases with the increase of irradiation time. Catalyst TDA degrades MB up to 98% in 40 min of irradiation while catalyst TDAR degrades MB up to 98% in just 30 min of irradiation for 20 μM dye concentration. With the increase in dye concentration, same amount of catalyst degrades the dye in more time. In this case also, TDAR is seen to be more efficient. For 50 μM MB solution, using catalyst TDA, 98.75% degradation needed 90 min and TDAR took 60 min for 99.68% degradation, after which the absorption peak became flat. The photocatalytic behavior using raw diatom frustules as catalyst under same conditions shows no degradation.

Photocatalytic degradation of MB using catalysts TDA and TDAR with two different dye concentrations is shown in Fig. 3e. The degradation efficiencies of the samples are calculated using Formula 1:

$$\%D = \left(\frac{A_0 - A_t}{A_0} \right) \times 100\% \quad (1)$$

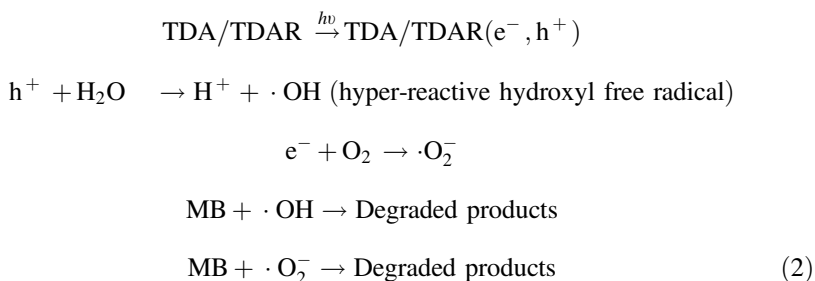
where A_0 is the initial absorbance and A_t is the absorbance at time t .

From the plot 1.3.3(e), TDAR exhibits more efficiency compared to TDA as photocatalyst for different dye concentrations. Morphology of diatom frustules and

phases of the nanoparticles are the important factors affecting photocatalytic activity. In the photocatalytic process, dye molecules get trapped in the reactive site of porous chambers of frustules, where titania nanoparticles already exist. Light focusing and light transmission capacity of diatom frustules make the heterogeneous catalysts more efficient with the advantageous property of using broad spectrum of solar radiation [9, 10] compared to free single titania nanoparticles capable of using only UV light. Moreover, composites having two phases of the same compound are more efficient in reducing recombination rate of the photo-generated e^-h^+ pairs, leading to higher photocatalytic efficiency [15]. TDAR contains both anatase and rutile phases and thus shows better degradation in the different concentrations of dyes than TDA with solitary anatase phase only.

In the photocatalytic process, due to the absorption of light by titania nanophasse, e^-h^+ pairs are generated and they combine with water and oxygen dissolved in water to form hydroxyl radicals and superoxide anions. These hydroxyl radicals and superoxide anions act as the key functionals in the photodegradation process, adsorbed on different active sites of the photocatalysts namely TDA and TDAR [13].

The mechanism of heterogeneous photocatalysis is elaborated in Eq. 2 (Fig. 3f):



3.2 Photocatalytic Reaction Rate Constant (RC) Measurement

The rate constants of the photocatalytic reactions are also obtained using the relation

$$\ln \frac{A_0}{A_t} = kt \tag{3}$$

where A_0 is the initial absorbance, A_t is the absorbance at time t , k is the rate constant (min^{-1}), and t is the time.

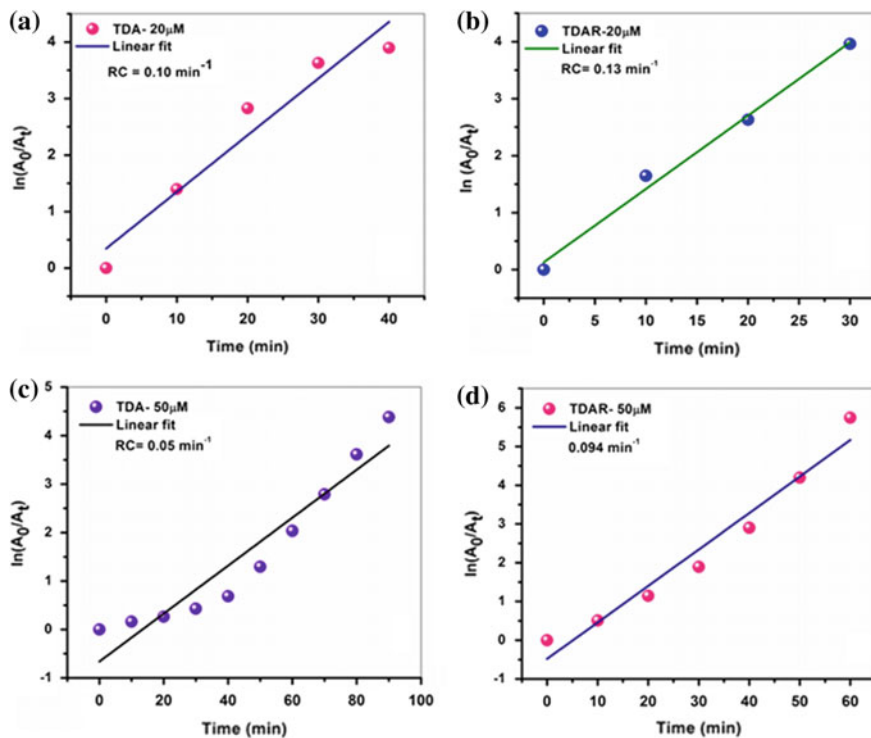


Fig. 4 Plot to determine RC value for 20 μM dye concentration using **a** TDA and **b** TDAR as catalyst, respectively, and for 50 μM dye concentration using **c** TDA and **d** TDAR as catalyst, respectively

Table 1 RC values for different photocatalytic reactions

Catalyst-dye concentration	Rate constant (min^{-1})	R^2
TDA-20 μM	0.10	0.92
TDAR-20 μM	0.13	0.98
TDA-50 μM	0.05	0.90
TDAR-50 μM	0.09	0.95

From the plot in Fig. 4, the RC values in different photocatalytic reactions using TDA and TDAR catalysts are listed in Table 1.

From Table 1, it is observed that the RC value is more for the reaction using TDAR catalyst in the case of both 20 and 50 μM dye concentrations than that using TDA catalyst. This confirms that TDAR catalyst speeds up the reaction faster than TDA catalyst.

4 Conclusion

We have successfully developed an environment-friendly, low-cost catalyst using diatom frustules as biotemplates coated by titania nanophases using simple solgel method that can not only harvest the intense part of solar energy spectrum effectively, but also make use of a wide range of visible light wavelengths. Thermal treatment leads to the transformation of anatase to rutile phase with increase in crystallite size and crystallinity in TDAR catalyst. Mixed phase TDAR catalyst shows improved photocatalytic activity compared to solitary phase TDA with higher reaction rate constant. Unique morphology of the diatom frustules, solar light harvesting properties of diatom frustules, and formation of titania nanophases are the main factors of the developed photocatalysts to show efficient photocatalytic process under visible light irradiation.

References

1. Molla, A., Sahu, M., Hussain, S.: Synthesis of tunable band semiconductor nickel sulphide nanoparticles: rapid and round the clock degradation of organic dyes. *Sci. Rep.* **6**, 26034 (2016)
2. Qin, X.D., Zhu, Z.W., Liu, G., Fu, H.M., Zhang, H.W., Wang, A.M., Li, H., Zhang, H.F.: Ultrafast degradation of azo dyes catalyzed by cobalt-based metallic glass. *Sci. Rep.* **5**, 18226 (2015)
3. Yang, X., Chen, W., Huang, J., Zhou, Y., Zhu, Y., Li, C.: Rapid degradation of methylene blue in a novel heterogeneous $\text{Fe}_3\text{O}_4@\text{rGO}@\text{TiO}_2$ -catalyzed photo-Fenton system. *Sci. Rep.* **5**, 10632 (2015)
4. Dariani, R.S., Esmaeili, A., Mortezaali, A., Dehghanpour, S.: Photocatalytic reaction and degradation of methylene blue on TiO_2 nano-sized particles. *Optik* **127**, 7143–7154 (2016)
5. Makama, A.B., Salmiaton, A., Saion, E.B., Choong, T.S.Y., Abdullah, N.: Synthesis of CdS sensitized TiO_2 photocatalysts: methylene blue adsorption and enhanced photocatalytic activities. *Int. J. Photoenergy* **2016**, 2947510 (2016)
6. Abbasi, A., Ghanbari, D., Salavati-Niasari, M., Hamadani, M.: Photo-degradation of methylene blue: photocatalyst and magnetic investigation of $\text{Fe}_2\text{O}_3\text{-TiO}_2$ nanoparticles and nanocomposites. *J. Mater. Sci. Mater. Electron.* **27**, 4800–4809 (2016)
7. Ibhaddon, A.O., Fitzpatrick, P.: Heterogeneous photocatalysis: recent advances and applications. *Catalysts* **3**, 189–218 (2013)
8. He, J., Chen, D., Li, Y., Shao, J., Xie, J., Sun, Y., Yan, Z., Wang, J.: Diatom-templated TiO_2 with enhanced photocatalytic activity: biomimetics of photonic crystals. *Appl. Phys. A* **113**, 327–332 (2013)
9. De Tommasi, E., Rea, I., De Stefano, L., Dardano, P., Di Caprio, G., Ferrara, M.A., Coppola, G.: Optics with diatoms: towards efficient, bioinspired photonic devices at the micro-scale. *SPIE Proc* **8792**, 879200-1 (2014)
10. Noyes, J., Sumper, M., Vukusic, P.: Light manipulation in a marine diatom. *J. Mater. Res.* **23**, 3229–3235 (2008)
11. Gogoi, A., Buragohain, A.K., Choudhury, A., Ahmed, G.A.: Laboratory measurements of light scattering by tropical fresh water diatoms. *J. Quant. Spectrosc. Radiat. Transfer* **110**, 1566–1578 (2009)

12. Available at: http://westerndiatoms.colorado.edu/taxa/species/cosmioneis_reimeri. Accessed 14th Sep 2016
13. Paul, S., Choudhury, A.: Investigation of the optical property and photocatalytic activity of mixed phase nanocrystalline titania. *Appl. Nanosci.* **4**, 839–847 (2014)
14. Lopez, R., Gomez, R.: Band-gap energy estimation from diffuse reflectance measurements on sol–gel and commercial TiO₂: a comparative study. *J. Sol-Gel. Sci. Technol.* **61**, 1–7 (2012)
15. Mao, L., Liu, J., Zhu, S., Zhang, D., Chen, Z., Chen, C.: Sonochemical fabrication of mesoporous TiO₂ inside diatom frustules for photocatalyst. *Ultrason. Sonochem.* **21**, 527–534 (2014)

A Review on Grid Codes and Reactive Power Management in Power Grids with WECS

K.V. Ramana Reddy, N. Ramesh Babu and P. Sanjeevikumar

Abstract Nowadays, electrical energy has become one of the important daily needs in human life. It is not only used in the household appliances but it is also used in the industrial applications such as transportation purposes, industries. Now, the total entire world power sale corporations look at the free cost of fuel power like wind energy which is available at all the times comparatively with all the remaining sources. The conversion of wind energy into electrical energy has instable voltage due to short distortions and long distortions in the availability of winds which addresses the increasing of the demand of reactive power to the power grid. This paper presents a Grid code that decides cheap cost of coordinated reactive power management scheme with TCR+FC-based excitation framework for doubly fed induction generator (DFIG) utilized as a part of wind energy. The grid converter (GSC), the rotor converter (RSC), the DC link capacitor and TCR+FC devices which can deal with the dynamic currents exchange with the rotor of DFIG and the voltage network freely. Using the normal for high-productive vitality stockpiling and speedy reaction of dynamic VAR devices can be used to level the wind power variance, mitigate the impact on voltage quality and enhance fault ride-through capability and current issues in the reactive power management.

Keywords Doubly fed induction generator • Progressive energy management
Fixed capacitor static VAR compensator • WECS

K.V. Ramana Reddy · N. Ramesh Babu (✉)
School of Electrical Engineering, VIT University, Vellore, Tamil Nadu, India
e-mail: nrameshbabu@vit.ac.in

K.V. Ramana Reddy
e-mail: kv.ramanareddy2015@vit.ac.in

P. Sanjeevikumar
Department of Electrical and Electronics Engineering, University of Johannesburg,
Auckland, Johannesburg, South Africa
e-mail: sanjeevi_12@yahoo.co.in

1 Introduction

Due to the deficiency of the coal supply and the pollution brought by the fossil energy, countries around the world have put forward many strategic objectives with regard to energy efficiency, emissions reduction and environmental protection in order to develop a low-carbon economy and increase energy security of supply [1]. Total wind energy installed 369,597 MW capacity globally (until December 2014). Total wind energy installed in India is 24,677 MW. India ranks 4th in total installed power (as of 31 Oct 2015).

Similarly, the European Union is focusing of generation of 20% of the power from renewable energy by 2020, in which wind energy has been recognized as a main contributor. China has also published its goals to control greenhouse emissions and focus on the reduction of carbon foot prints by the end of 2020 relatively with the economic growth of the country by 40%.

Similarly, China plans to build seven large wind farms that will generate tens of giga watts of wind energy across the Hexi Corridor in Gansu, the plains of East Inner Mongolia, the plains of West Inner Mongolia, Hami in Xinjiang, Jilin province, Hebei Province and in the coastal area of northern Jiangsu.

For transmitting of the power obtained from the wind source situated in remote locations, the developers and the producers are facing a challenge to overcome it [2]. These include the issues of large wind power transmission technologies, management of wind generation intermittency and uncertainties for transmission systems with high influence of wind power, and maintenance of grid reliability and availability. This paper is trying to tackling to these issues and is organized as follows:

The various technical solutions based on the advanced FACTS and HVDC technologies for large wind farm connections are introduced and compared (Fig. 1).

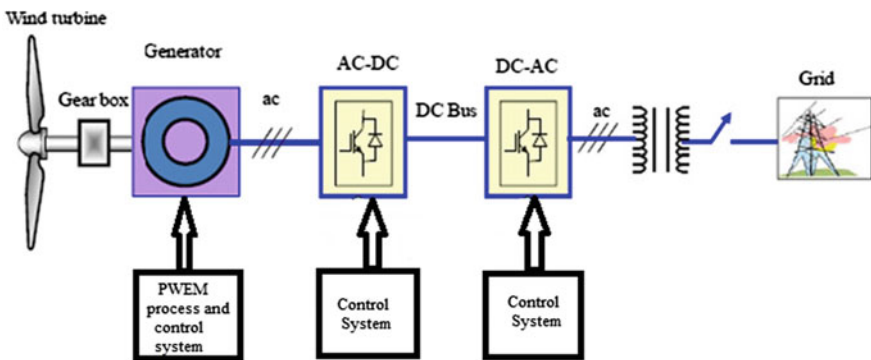


Fig. 1 Grid-integrated wind energy system with PWEM system

2 Technical Gestes

2.1 Issues

Wind is a natural source which is renewable and eco-friendly, but wind is intermittent and uncontrollable. Wind farms are not only interfaced with the medium-voltage grid, also there is a trend that more and more wind farms are integrated into high-voltage grid or EHV (extra high voltage) or UHV (ultra-high voltage) grid. However due to intermittence and fluctuation of wind energy, increasing wind power penetration levels to power grid has given rise to many technical issues that need to be overcome to make sure the operation security and reliability of grid.

These include the following:

- Wind climate assessment methodologies,
- Modelling for wind energy and resource assessment,
- Wind energy transmission by long-distance transmission lines and
- Operation and management for transmission grid with high penetration of wind power.

2.2 Grid Code Review

There are many constraints specified by the Grid codes for integrating the wind farm in the grid as specified earlier. The Grid codes may also be different from every country [2–6]. Table 1 provides an outline of the Grid codes concerned by countries. In many papers, the Grid codes are presented from various countries [2–4]. But in this paper, the Indian Grid codes are mainly focused to maintain the standards in the means of maintaining the economics of power quality.

Table 1 Grid codes from different countries

Grid code	Institute	Year issued	Constraints
Germany Grid code	E.ON	2006	380, 220 and 110 kV
GB Grid code	National Grid	2008	400, 275 and 132 kV
China Grid code (Revision)	CEPRI	2009	Transmission network
Nordic Grid code	NORDEL	2006	Higher than 110 kV
Danish Grid code	Eltra and Eikraft	2004	Below 110 kV
Canadian Grid code	Hydro-Quebec	2006	49–240 kV
USA Grid code	FERC	2005	Transmission network
Indian Wind Grid code	CWET	2009	Transmission network
Indian Electrical Grid code	CERC	2010	Transmission network
Indian Grid code	CWET	2015	Transmission network

3 Progressive Wind Energy Management System

The growth of progressive wind system management in wind resource, leads to rapid changes occurring at the transmission system. To eliminate the impacts of high penetrations of wind energy, such a wind energy management should be able to deal effectively. Wind energy short durations, long durations and interruptions are need to be identified from the control, monitoring and recorded information data from wind plant grid onwards. Provide operational experience and advanced wind resource monitoring and control with advanced user interface, including wind production observability for grid operators in order that wind production can be injected from distribution feeders into subtransmission grids depending on the grid configuration. Integrate into a real-time environment of the wind resource production, cope with uncertainties and inaccuracies, provide advanced alarm trending and look-ahead functions to anticipate developing conditions. Retain stability of transmission grid. Provide reserve management and generation control, from the ability to optimize reserve calculation and minimize generation control required to compensate for the intermittent characteristics of wind energy production. Generation control also encompasses wind energy production curtailment capabilities with a full audit trail to support grid operation in unsecured grid conditions. Conduct wind production scenario simulation, allowing dispatcher training using realistic and/or already experienced wind production scenarios, driven by wind production forecasts and related uncertainties.

The basic layout and architecture of progressive wind system management is shown in Fig. 2.

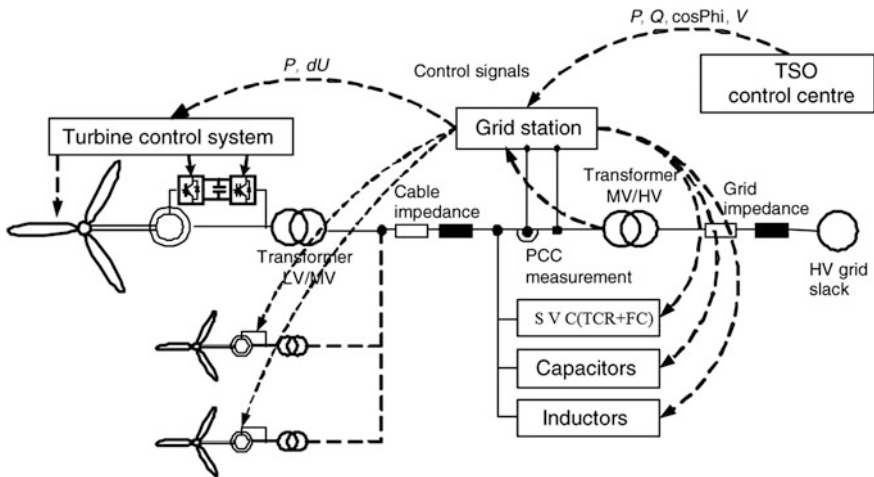


Fig. 2 Basic layout of progressive wind energy management system wind power plant and control signals

4 Alternative Links

The remotely located wind farms are connected with the grid using HVDC and HVAC transmission systems. In general, AC connection is used for “small” wind farm with “short” connection distance, while HVDC is preferred when huge wind farm is connected over a long-distance grid (Fig. 3).

4.1 AC Link

HVAC connection is most simplest and economical-based connection method, and it is very attractive for “small” wind farm with a short connection. But the line losses are increased as by increasing the p.u length of transmission line. The number of conductors required to transmit the power is more in HVAC comparatively with HVDC. Sometimes, to satisfy the link agreement it requires a substation for every 40 km distance, AC tap-changing transformers, electronic tap-changing transformers or power electronics-based FACTS devices are required to be installed such as static VAR compensator (SVC) or static synchronous compensator (STATCOM) which increases the overall system cost increases, except mechanically operated tap-changing transformers remain all devices increases reactive power management accuracy in the power system (Fig. 4).

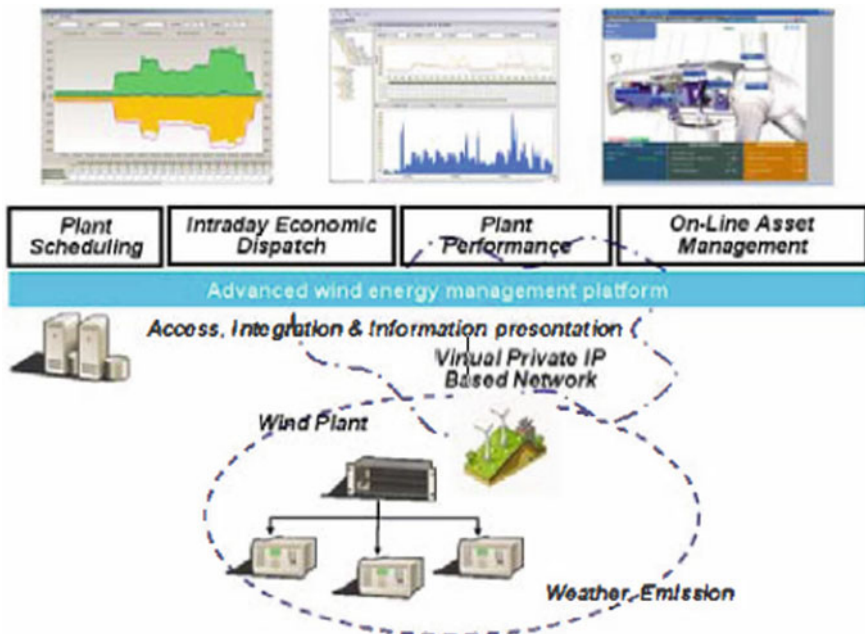


Fig. 3 Architecture of a progressive wind energy management

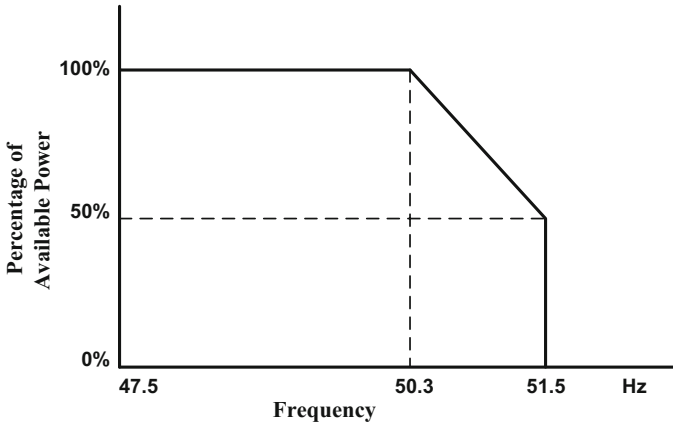


Fig. 4 Active power output versus frequency

Thyristor-controlled reactor (TCR) and thyristor-switched capacitor (TSC) are subsets of SVC [2]. The reactive control and AC voltage control are implemented by controlling the equivalent shunt impedance in SVC. Majority of the loads are inductive type, so to provide the reactive power management, the economical solution is framed with TCR+FC.

The operation principle of a STATCOM is based on controlling the AC voltage amplitude generated by the converter to control the generated reactive current. This indicates that STATCOM has better capability for providing reactive power compensation during low AC voltage compared to SVC.

4.2 DC Link

HVDC transmission is very attractive, especially for interconnection of large wind farm with significant long distance.

The following advantages are provided by HVDC transmission:

- The number of conductors in HVDC is low comparatively with HVAC;
- Power flow is fully defined and controlled;
- The cable charging current has no effect on the DC transmission;
- AC cable system has lower cable power loss.

Voltage source converter (VSC) and line-commutated converter (LCC) are the two types of HVDC transmission. The advantages of VSC transmission over HVDC and LCC are as follows:

- They do not require any external voltage source.
- They are self-commutation.

- The control features of reactive power is possible at each AC networks.
- Active and reactive power controls are independent.

The above features make VSC as the most preferred HVDC transmission from offshore wind farm [3, 4].

4.3 Grid Behaviour of Wind Turbines

- Induction generators are mostly preferred to the asynchronous generator in past.
- Capacitor banks are used to provide the VAR support to the induction generator.
- The reactive power drawn from the grid affects voltage profile of system.
- The synchronous generator-based wind turbine has an advantage of absence of reactive power control, but they have overcome the harmonic content.
- The generator configuration of the wind turbine has its own grid profile which has to be followed from grid integration.
- The wind system should be cut off from grid when install position as it may draw the power from the grid.
- During fault condition, the wind turbine must require an additional reactive power support else it should be removed from the grid.
- Since wind is nonlinear in nature, the power generated cannot be scheduled.

4.4 Centre for Wind Energy Technology (Indian and World Scenario)

Countries such as USA, India, Germany, Denmark, China and Spain, which are major producers of wind-based energy, have their own Grid code which should be followed while interconnecting the wind system to central grid. The basic parameters which should be focused for Grid code are as follows:

- Active power control,
- Frequency,
- Voltage and reactive power issues,
- Fault ride-through capability,
- Protection and
- Power quality issues such as flicker and harmonics.

MNRE, an Indian government-based organization issues a five-year plan for development of the renewable-based generation and their need based on the supply–demand ratio.

Table 2 Specified voltage profile of wind energy in India for grid integration

Voltage (kV)			
Nominal	% Limit of variation	Maximum	Minimum
400	+5 to -10	420	360
220	+11 to -9	245	200
132	+10 to -9	145	120
110	+10 to -12.5	121	96.25
66	+10 to -9	72.5	60
33	+5 to -10	34.65	29.7

4.5 Grid Code Requirements

Table 2 summarizes the criteria for grid integration of wind energy.

4.6 Grid Code Frequency Standards

In India, the standard frequency of 50 Hz with $\pm 2\%$ variations is allowed at necessary conditions. The frequency variation of wind farm can be withstood until 0.5 Hz/s. The transmission line grid frequency is most important one as by increasing the line frequency the currents in the line also increases up to its resonance condition after the resonance condition the currents get decreases.

$$F = PN/120 \quad (1)$$

The speed of the DFIG is directly proportional to frequency. In wind mills, the wind energy is not available as constant at all the times; it changes accordingly change of climatic conditions. Thus, reactive power demand of grid changes with respect to change in climate. In many of the papers, they concentrated that the total demand of reactive power is delivered to grid without any suitable compensation devices, but in this paper with help of progressive wind energy management, we can reduce the demand of the reactive power to the grid up to certain limits. The remaining required reactive power is supported by the economics of reactive power compensation device TCR+FC.

4.7 Grid Code-Required Power Factor Standards

The minimum power factor specified for wind farm is 0.95 lagging to 0.95 leading which gives the better operating voltage stability in wind farms comparatively with the remaining power factors. Figure 5 shows the rectangular, whose sides of power factor offer at the grid voltages [7–10].

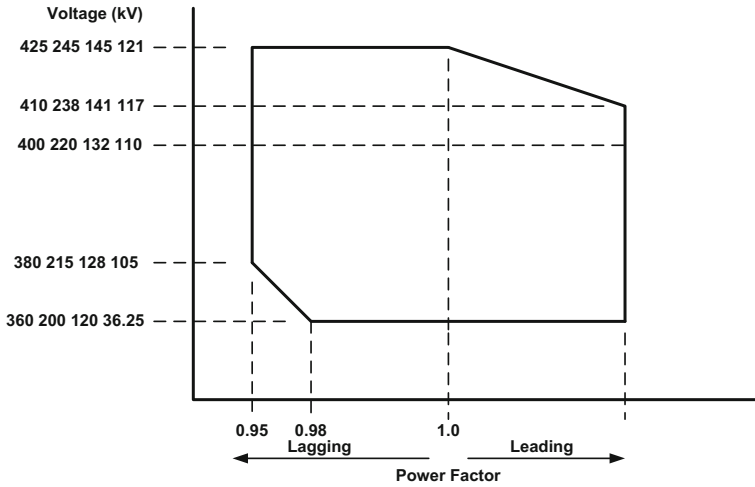


Fig. 5 Power factor characteristic of wind farm above 66 kV

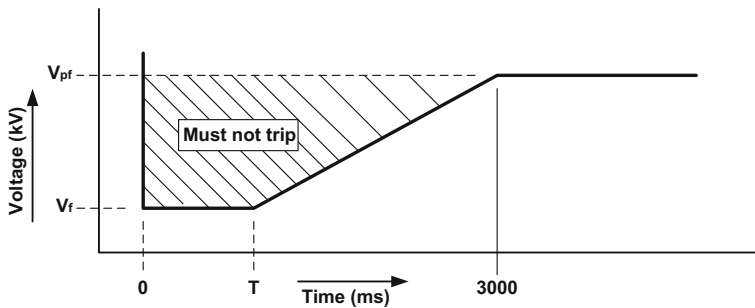


Fig. 6 Fault/low-voltage ride through. V_f : Nominal voltage, V_{pf} : voltage required for wind turbine operation

For the wind farms connected above 66-kV grid transmission system every operated grid voltage operates at subsynchronous resonance condition therefore whose operating power factor is near to unity power factor, but near to 15 papers they mentioned about various types of reactive power compensation methods, its dynamic operating accuracy, its operative optimizing methods through various algorithms but in this paper proposed and discussed about progressive wind energy management scheme along with optimized TCR+FC economics of reactive power compensation method. The appreciated current issues are concluded from this method. The fault ride-through capability is reduced, and it becomes as low-voltage ride-through capability can be identified from the following graph (Fig. 6; Table 3).

Table 3 Constraints of fault time and voltage of Indian grid standard

Nominal voltage (kV)	Fault clearing time, T (ms)	V_{pf} (kV)	V_f (kV)
400	100	360	60.0
220	160	200	33.0
132	160	120	19.8
110	160	96.25	16.5
66	300	60	9.9

5 Harmonics

Variable pitch wind turbine in accordance with power converters is the source of the harmonics like DFIG. The harmonics measurement for variable speed turbines is recommended as per IEC61400-21. But in this paper, the Indian Grid code also maintains the same standards issued by international electro-technical commission.

$$V_{\text{THD}} = \sqrt{\sum_{n=2}^{n=50} \frac{V_n^2}{V_i^2}} \quad (2)$$

where

V_n : n th harmonic of voltage and

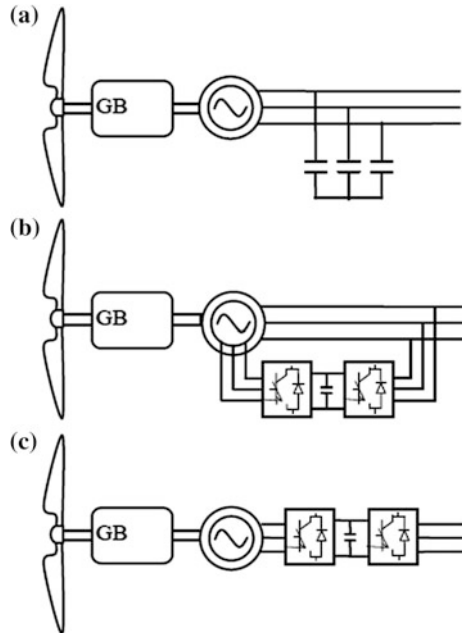
V_i : fundamental frequency voltage.

Therefore, from above statistics the Indian Grid code transmission system restricted and appreciated THD values between 1.5 and 2.5% given by CWET in the year of 2015, the Indian wind power plants which operates at this allowable THD value through progressive wind energy management system which turns into economics of reactive power compensation is required and it is economical for current issues.

5.1 Wind Turbine—Fault Ride-Through, Reactive Power Control

Power quality issue like voltage dips is the major problem faced by the WECS. Transmission system operators (TSO) require an additional energy support for the system during voltage sag condition as there is large penetration of wind energy in the grid [11–16]. This leads to high investment in the strategy for supporting the grid in voltage sag condition.

Fig. 7 Topology of wind turbine



The wind system has a different performance during constant mode or in voltage sag mode. Figure 7a shows the squirrel cage induction generator (SCIG) which is integrated to the grid through transformer, so they are fixed speed type. Figure 7b shows that wound rotor generator with partial converter which provides a limited variable speed control. Figure 7c represents the generator connected to full-scale converter configuration which provides a stable and full control of variable speed wind turbine. The active and reactive power control of wind system is controlled using rotor of the generator which is integrated to grid through power converter, whereas stator is integrated with grid directly. The voltage dip across the grid causes high injection of rotor current which is supplied to the power converter; thus, a high rotor voltage is required to overcome the rotor current [16–20]. When the voltage is increased further, the control of rotor current is no longer possible. This large amount of current will flow through the converter which will damage the converter. To overcome the drawbacks, crowbar system is associated with rotor circuit. The converter is disconnected from the system when the rotor current is too high. The rotor current is then passed through the crowbar resistance; then, the generator acts as an induction machine. Thus using this topology, the wind turbine will maintain during voltage dip and also follow the grid requirement. SCIG is a fixed speed wind turbine and has an advantage of rugged nature, low cost, brushless and simplicity. However, they require a more reactive power to overcome the air

Table 4 Indian voltage harmonic limits for wind power plants

Voltage (kV)	Total harmonic distortion (%)	Individual harmonic (%)
765	1.5	1.0
400	2.0	1.5
220	2.5	2.0
132	3.0	2.0

gap flux when the power system is under short circuit. Otherwise, they are tended to be unstable in nature (Table 4).

5.2 *Fault Ride-Through Solutions*

Flexible AC transmission systems (FACTS) are rapidly replacing the capacitor- and reactor-based control technique. Recent wind turbines installed have superlative controllers to reduce voltage dips, whereas the old wind turbines are associated with the FACTS devices for the same. The installation of FACTS devices is either at PCC or at individual. The FACTS devices implemented for wind turbine are categorized as follows:

- Dynamic voltage restorer (DVR),
- Static voltage compensator and static compensator (STATCOM) and
- Unified power quality conditioner (UPQC).

5.3 *Static Voltage Compensator*

The capacitive or inductive current of the system is controlled using the static VAR compensator, which shunts with the wind system as shown in Fig. 8. They are generally interconnected with the system in between the utility and generator. The reactive power is generally between 0 and 1 p.u. They are low cost when compared with the STATCOM, but the efficiency of the latter is superior than that the SVC as shown in Fig. 9. The SVC is basically an electronic switch connected in association with thyristor.

Static VAR compensator subsets are TCR and TSC. The operating characteristics of these two subsets are different, and its demand is also required at different load operating conditions, and also they supply or draw different amounts of low reactive power from the existed transmission line. STATCOM, BESS, SMES, UPFC, etc, are the preferred devices for higher demand of reactive power, which are described in [20–28] papers.

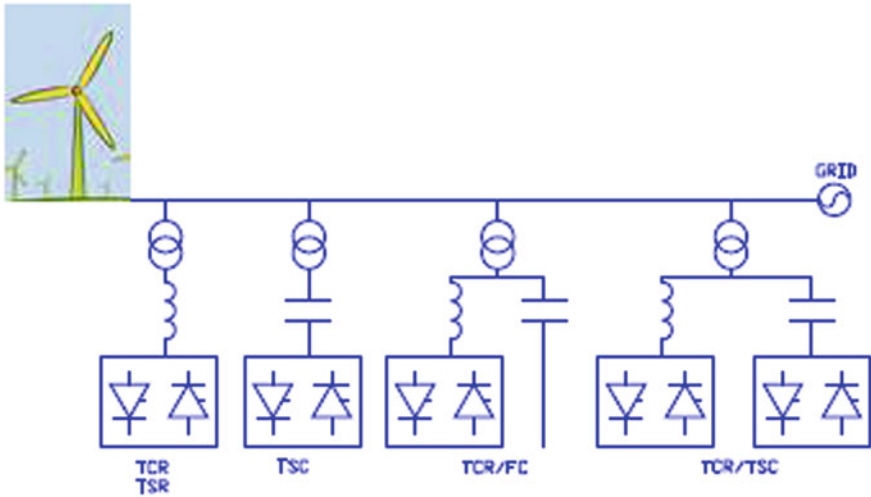


Fig. 8 Different topologies of SVC

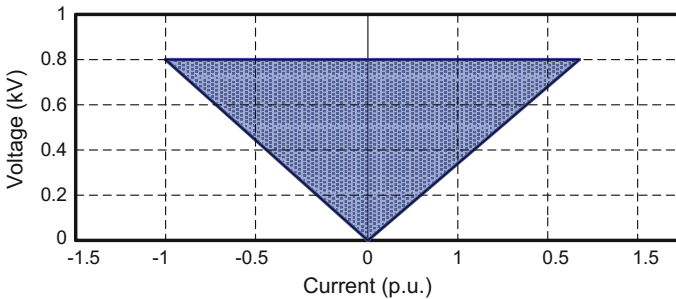


Fig. 9 V-I characteristics of TCR+FC

6 Summary

Progressive energy management scheme controls the distortions while the generation of wind power and maintains good power quality for very low short-duration variations such as instantaneous, momentary and temporary variations and interruptions whose distortion time period is less than 1 min at steady-state condition. These short-duration-type problems are occurred more number of times comparatively with long-duration variations whose time duration is greater than 1 min. So in this paper, an economical reactive power compensation is proposed to mitigate low-voltage fault ride-through problems due to short-duration variations in the wind speed are overcome by TCR+FC a subset of SVC.

The overall Grid code requirement of wind energy is summarized in this paper. The requirement of the small wind system is suggested in this paper. The condition like fault ride through is analysed, and the suitable suggestions are made on the control techniques. Thus, this paper tends to support the overall issue of WECS at grid side of the system.

References

1. Tiwari, R., Babu, N.R.: Recent developments of control strategies for wind energy conversion system. *Renew. Sustain. Energy Rev.* **66**, 268–285 (2016)
2. Singh, B., Singh, S.N.: Wind power interconnection into the power system: a review of Grid code requirements. *Elec. J.* **22**, 54–63 (2009)
3. Eminoglu, U., Alcinoz, T., Herdem, S.: Location of FACTS devices on power system for voltage control. *IEEE Power Eng. Conf.* **1**, 338–342 (2008)
4. Xu, L., Yao, L., Sasse, C.: Comparison of using SVC and STATCOM for wind farm integration. In: *IEEE International Conference on Power System Technology*, pp. 1–7 (2006)
5. Xu, L., Yao, L., Sasse, C.: Grid integration of large DFIG based wind farms using VSC transmission. *IEEE Trans. Power Syst.* **22**, 976–984 (2007)
6. Erlich, I., Winter, W., Dittrich, A.: Advanced grid requirements for the integration of wind turbines into the German transmission system. In: *Proceedings of IEEE Power Engineering Society General Meeting*, Montreal, pp. 1–7 (2006)
7. Rueda, J.L., Shewarega, F.: Small signal stability of power systems with large scale wind power integration. *ERIAC Reg. Iberoamericano DE CIGRE*, Puerto de Iguaçu, Argentina, pp. 1–8, (2009)
8. Cai, L.-J., Erlich, I.: Dynamic voltage stability analysis in multimachine power system. In: *Power System Computational Conference*, vol. 15, pp. 1–6 (2005)
9. Cai, L.-J., Fortmann, J., Erlich, I.: Power system dynamic voltage stability analysis for integration of large scale wind parks. *Workshop on Large-Scale Integration of Wind Power into Power System Transmission Networks for Offshore Wind Power Plants*, pp. 1–7 (2010)
10. Tamura, J., Yonaga, S., Matsumura, Y., Kubo, H.: A consideration on the voltage stability of wind generators. *Trans. IEE Jpn.* **122**, 1129–1130 (2002)
11. Heier, S.: *Grid Integration of Wind Energy Conversion System*. Wiley, New York (1998)
12. Teodorescu, R., Liserre, M., Rodriguez, P.: *Grid Converters for Photovoltaic and Wind Power Systems*. IEEE Press/Wiley (2011)
13. Holger, B.: *Transmission Code 2007—Network and System Rules of the German Transmission System Operators*. VDN Pub. (2007)
14. Network code for requirements for grid connection applicable to all generators. <http://www.entsoe.eu/major-projects/network-code-development/requirements-for-generators/Pages/default.aspx> (2012)
15. Conroy, J.F., Watson, R.: Low-voltage ride-through of a full converter wind turbine with permanent magnet generator. *IET Renew. Power Gen.* **1**, 182–189 (2007)
16. Ullah, N.R., Thiringer, T., Karlsson, D.: Voltage and transient stability support by wind farms complying with the E. ON Netz Grid code. *IEEE Trans. Power Syst.* **22**, 1647–1656 (2007)
17. Ullah, N.R., Thiringer, T.: Variable speed wind turbines for power system stability enhancement. *IEEE Trans. Energy Convers.* **22**, 52–60 (2007)
18. Kayikci, M., Milanovic, J.V.: Reactive power control strategies for DFIG-based plants. *IEEE Trans. Energy Convers.* **22**, 389–396 (2007)
19. Garcia, J.M., Kjaer, P.C., Rodriguez, P., Teodorescu, R.: Active current control in wind power plants during grid faults. *Wind Energy* **13**(8) (2010)
20. Sulla, F.: *Fault Behavior of Wind Turbines*. Ph.D. dissertation, Lund University, Lund (2012)

21. Jauch, C.: Transient and dynamic control of a variable speed wind turbine with synchronous generator. *Wind Energy* **10**, 247–269 (2007)
22. Mullane, A., Lightbody, G., Yacamini, R.: Wind-turbine fault ride through enhancement. *IEEE Trans. Power Syst.* **20**, 1929–1937 (2005)
23. Rodriguez, P., Luna, A., Candela, I., Mujal, R., Teodorescu, R., Blaabjerg, F.: Multiresonant frequency-locked loop for grid synchronization of power converters under distorted grid conditions. *IEEE Trans. Ind. Electron.* **58**, 127–138 (2011)
24. Babu, N.R., Arulmozhiarman, P.: Wind energy conversion system—a technical review. *J. Eng. Sci. Tech.* **8**, 493–507 (2013)
25. Tiwari, R., Babu, N.R.: Fuzzy logic based MPPT for permanent magnet synchronous generator in wind energy conversion system. *IFAC-PapersOnLine* **49**(1), 462–467 (2016)
26. Sanjeevikumar, P., Thiagarajan, Y., Sivakumaran, T.S.: Design of fuzzy logic controller for a DC-AC converter for a grid connected system using PV cell. In: Conference proceedings. Proceedings of IEEE International Conference on Computing, Communication and Networking. *IEEE-ICCCNET'08*, pp. 1–6 (2008)
27. Sanjeevikumar, P., Geethalakshmi, B., Dananjayan, P.: Performance analysis of AC-DC-AC converter as a matrix converter. Conference Proceedings. *IEEE India International Conference on Power Engineering, IEEE-IICPE'06*, Chennai, India, pp. 57–61 (2006)
28. Sanjeevikumar, P., Geethalakshmi, B., Dananjayan, P.: A PWM current source rectifier with leading power factor. In: Conference Proceedings of IEEE International Conference on Power Electronics, Drives and Energy Systems for Industrial Growth, *IEEE-PEDES'06*, pp. 1–5, 12–15 (2006)

PEM Fuel Cell Modeling Using Genetic Algorithm—A Novel Approach

K. Priya, Sashang Roy Choudhury, K. Sathish Kumar
and N. Rajasekar

Abstract In order to analyze, model, and control of power generation, precise models of proton exchange membrane fuel cells (PEMFCs) are very important. As we know, there has been a lot of research on nanofluid coolants and how they improve the heat transfer properties of the base fluid. Hence, a PEM fuel cell modeling using genetic algorithm (GA) is presented in this paper that exactly tries to estimate the output of the fuel cell performance when Al_2O_3 nanofluid coolant is used. In this paper, we determine the thermal conductivity of Al_2O_3 nanofluid coolant with different concentrations of ethylene glycol and water and simulate the PEMFC performance by means of the data generated using GA.

Keywords Nano fluids · PEMFC · Modeling of PEMFC

1 Introduction

Researchers around the world are urging to contribute to reduce global warming, in particular the air pollution. The proton exchange fuel cell (PEMFC) is an electro-chemical device that operates at low temperature is to be the best alternative renewable energy source to replace with current conventional generation of energy sources. Among the different types of fuel cells, PEMFCs have several physio-chemical advantages.

K. Priya (✉) · S.R. Choudhury · K. Sathish Kumar · N. Rajasekar
School of Electrical Engineering, VIT University, Vellore, Tamil Nadu, India
e-mail: priya.k2013@vit.ac.in

S.R. Choudhury
e-mail: shashankrc94@hotmail.com

K. Sathish Kumar
e-mail: ksathishkumar@vit.ac.in

N. Rajasekar
e-mail: nrajasekar@vit.ac.in

They can be used in application which requires low temperature and high current densities. PEMFCs are smaller, lighter, durable, and most tolerant to shock and vibration than any other kind of fuel cells. They have long stack life due the use of solid electrolyte and have fast startup due to thin structures, high energy efficiency, and ability to be used under conditions which require discontinuous operation (tolerant to many cycles of starts and stops) [1–5]. Furthermore, PEMFCs do not emit any kind of air pollutants such as NO_x or CO. Utilizing hydrogen as a fuel, PEMFC only releases water as the chemical by-product. This is why many experts consider PEMFCs as the source of energy for an ideal zero emission vehicle (ZEV). All these qualities of PEMFCs make it a perfect alternative having a wide range of applications in a series of power applications ranging from watt levels of portable micro power to kilowatts level of transportation and megawatt levels for stationary power sources for residential and distributed power system [5–8]. A PEMFC works at its maximum efficiency when it is operated within its temperature limits. As we know the electrochemical process of producing water from hydrogen and oxygen is an exothermic reaction, some heat is always produced from the fuel cell which needs to be dissipated to keep the operating temperature of the fuel cell within limits. Thus, the need of coolants arises here to dissipate the excess heat produced. A lot of research has been done to improve the coolants' heat transfer properties by preparing nanofluid coolants. Thus, thermal management is a very important factor in the overall PEMFC performance. Thermal management is defined as the dissipation of heat, generated within the fuel cell during the electrochemical process, to the surrounding environment [9]. The heat generated from the electrochemical reaction, if not dissipated properly might hamper the PEMFC operation. As a result, this excess heat might dry out the membrane. Drying out of the membrane reduces its overall ionic conductivity. In such conditions, if the thermal stress is not handled properly, it can lead to destruction of the membrane. In addition, at extreme operating conditions, the temperature can also affect the fuel cell performance [10]. Thus, when there is increase in temperature as a result voltage decreases and also low temperatures reduce the overall fuel cell reaction, subsequently increasing the losses. Therefore, it is very important to keep the fuel cell under very small temperature changes and optimal operating conditions by letting the additional heat to exit the PEMFC. To operate a PEMFC under optimal conditions, it essential to remove the heat at the same rate as it is produced; thus, a heat removal system is unavoidable.

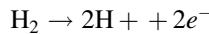
In order to improve the heat transfer of the fuel cell, several attempts have been carried out such as increasing heat transfer area, heat transfer coefficient, and temperature difference that result in heat flow. Though miniaturizing the size of heat transfer mechanism is very important, this has been made possible with the use of nanoparticle added to coolant liquids to increase their thermal conductivity. In this paper, we have produced a model of PEMFC by generating the parameters using genetic algorithm, simulating the data with different values of thermal conductivity of Al₂O₃ nanofluid with different base fluids, and considering the case where there is no forced heat transfer. The input values for thermal conductivity of coolant were kept close to the actual calculated values of 0.5% Al₂O₃ nanofluid as measured in

the laboratory. Considering the effect of temperature change due to the use of nanofluid coolant on the humidity and water content of membrane, the simulation is conducted to estimate the PEMFC performance curve when operated with coolants.

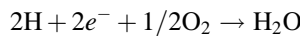
2 PEMFC Model

The electrochemical model of fuel cell is widely accepted by the engineers to evaluate fuel cell performance. In this work, popular electrochemical model proposed by Amphlett et al. [11] is used. The equivalent output voltage proposed by Amphlett is described as the sum of the Nernst equation E_{nernst} and all the losses, activation loss (V_{act}), ohmic loss (V_{ohm}), and concentration loss (V_{conc}). Fuel cell is an electrochemical device that converts the stored energy of fuel directly into electricity with the help of an oxidant. It consists of a cathode and an anode with a proton-conducting membrane which serves as the electrolyte. The electrochemical equations occurring in electrodes of a PEMFC can be described as follows:

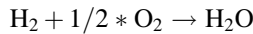
At anode



At cathode



Overall Equation



The overall output voltage that governs a fuel cell is as follows:

$$V_{\text{oc}} = E_{\text{nernst}} - V_{\text{act}} - V_{\text{ohm}} - V_{\text{conc}} \tag{1}$$

The Nernst reversible equation is as follows [12]

$$E_{\text{nernst}} = 1.22 - 8.5 * e^{-3}(T - 298.15) + 4.3085 * e^{-5} * T(\ln[P_{\text{H}_2} + 0.5P_{\text{O}_2}]) \tag{2}$$

where P_{H_2} and P_{O_2} are the partial pressures of hydrogen and water, respectively. T is the temperature in Kelvin.

The overall activation potential can be written as follows:

$$V_{\text{act}} = \varepsilon_1 + \varepsilon_2 T + \varepsilon_3 T \ln(C_{\text{O}_2}) + \varepsilon_4 T \ln(i) \tag{3}$$

where ε_i are the semi-empirical coefficients, i is the cell current and CO_2 is the concentration of oxygen in catalytic interface of the cathode (mol cm^{-3}).

$$C_{O_2} = \frac{P_{O_2}}{5.08e^{-6} * \theta^{\frac{-498}{T}}} \quad (4)$$

The ohmic loss can be expressed as the sum of resistance offered by the path of flow of electrons and the resistance offered to the flow of ions through membrane.

$$V_{ohm} = i(R_m + R_c) \quad (5)$$

$$R_m = \rho_m \left(\frac{L}{A} \right) \quad (6)$$

$$\rho_m = \frac{181.6 \left[1 + 0.03 \left(\frac{i}{A} \right) + 0.062 \left(\frac{T}{303} \right)^2 \left(\frac{i}{A} \right)^{2.5} \right]}{\left[\lambda - 0.634 - 3 \left(\frac{i}{A} \right) \right] \exp \left[4.18 \left(\frac{T-303}{T} \right) \right]} \quad (7)$$

R_c is the ohmic loss is related to the proton conductivity of the membrane. This ionic resistance is highly dependent on the water content of the semipermeable membrane, which may be controlled through external humidification of the inlet supply of hydrogen or oxygen. The semipermeable membrane keeps losing water because of the movement of hydrogen ions across the membrane. Every hydrogen ion that crosses the membrane takes some water molecules with itself and some water is lost through evaporation. Thus, the humidity must be above 80%, otherwise the membrane would dry up, but at the same time, it must not be above 100%, otherwise water would collect in the electrodes [13].

The following equations relating water content of the membrane and ionic resistance.

$$R_c = \frac{L_m}{A\sigma_m} \quad (8)$$

where L_m and σ_m are the thickness and conductivity, respectively. The membrane conductivity has been related to water content as follows [14].

$$\sigma_m = a\lambda m - b \quad (9)$$

where

$$a = 0.005193 \exp \left[1268 \left(\frac{1}{303} - \frac{1}{T} \right) e^{-2} \right] \text{ Sm}^{-1} \quad (10)$$

$$b = 0.00326 \exp \left[1268 \left(\frac{1}{303} - \frac{1}{T} \right) e^{-2} \right] \text{ Sm}^{-1} \quad (11)$$

Now, the relation between water content relative humidity is defined as follows [15]:

$$\lambda = 0.043 + 17.18\Phi - 39.85\Phi^2 + 36\Phi^3; \quad 0 < \Phi < 1 \tag{12}$$

$$\lambda = 14 + 1.4(\Phi - 1); \quad \Phi > 1 \tag{13}$$

where Φ is relative humidity and,

$$\phi = \frac{P_w}{P_{sat}} \tag{14}$$

where P_w is the partial pressure of water vapor and P_{sat} is the saturation pressure of air. The saturation pressure of air is dependent on temperature. This relation is described by Antoine equation [16].

$$\log_{10} P_{sat} = A - \frac{B}{C + T} \tag{15}$$

The temperature is in Celsius and A , B , and C are constants. The pressure (P_{sat}) is measured in mm of H_g .

Apart from these losses, there is concentration loss also. The concentration loss can be explained through the following equation.

$$V_{conc} = -b \ln\left(1 - \frac{I}{I_{max}}\right) \tag{16}$$

3 Problem Statement

In order to demonstrate the overall improvement in performance of the fuel cell, we need to incorporate the convective heat transfer equation in the simulation. In this simulation, we have considered only natural convection as a means of heat transfer through the coolant and radiator fins. The case of forced convection is not considered here. Thus, the convective heat transfer equation is as follows.

$$q = \frac{k}{l} A (T_a - T_b) \tag{17}$$

where K is the thermal conductivity of the coolant, A and l are the area of radiator fins and thickness of pipes, respectively, q is the heat produced and T_a , T_b are the temperatures inside the fuel cell and room temperature, which is set to 27 °C.

Now, from this equation, we need to calculate the T_a , since we have q , A , l , T_b^{-1} , and K . The value of K will be generated using genetic algorithm. Thus, due to the effect of K , we will notice a decrease in the temperature of the fuel cell which will lead to an enhanced performance.

The objective function in this case is the sum of the error of obtained between the reference voltages (from data sheet) and calculated voltage. This sum of error is then added with one and the whole term is inversed. Thus, the objective function is aimed toward maximization of the output voltage.

$$\text{error} = V_{\text{ref}} - V$$

$$\text{Obj_function} = \frac{1}{1 + \sum \text{error}}$$

3.1 Nano Fluid Preparation and Thermal Conductivity Measurements

Two step preparation processes has been used to prepare the sample nanofluid coolants without any surfactants. Alumina is one of the most cost effective and widely used materials. Al_2O_3 nanoparticles were obtained from external means. Three different base fluid mixtures were prepared with the ratio of water: EG as 60:40, 70:80, and 80:20. The volume fraction of Al_2O_3 nanoparticles added was fixed to 0.5%. No kind of dispersant was used.

The Al_2O_3 /water/EG nanofluid was prepared by mixing the particle to the base fluid using an electromagnetic agitator operating at 600 rpm. The solution was then kept in an ultrasonic vibration for 2 h at 36 kHz and 100 W. Studies according to [17] have shown us that stability can be obtained using sonication.

Thermal conductivity measurements were taken using KD2 Pro thermal property analyzer of Decagon Devices, Inc., USA, at a constant temperature of 50 °C. The KD2 Pro uses the transient line heat source to measure the thermal properties of solids and liquids. The apparatus meets the standards of both ASTM D5334 and IEEE 442-1981. The following table shows the measured values of the nanofluid coolant samples (Table 1).

Table 1 Parameters

Particles	Base fluid (water:EG)	Thermal conductivity (w/mk)
Al_2O_3	60:40	0.592
Al_2O_3	70:30	0.697
Al_2O_3	80:20	0.751

3.2 Mathematical Model for Thermal Conductivity

Hamilton and Crosser [18] had developed an extension, of measuring the thermal conductivity developed by Maxwell [19], to measure the effective thermal conductivity of two components mixtures as a function of conductivity of pure materials, the composition mixture, and the shape of the dispersed particles. The conductivity of two components mixtures can be defined as Eq. 18

$$K_{\text{eff}} = \frac{K_p + (n - 1)Kbf - (n - 1)\phi(Kbf - Kp)}{K_p + (n - 1)Kbf + \phi(Kbf - Kp)} \tag{18}$$

4 Results and Discussions

Since the GA parameters have a significant influence on algorithm performance, the parameters were evaluated with different compositions for 20 independent trials and the best combination was selected. It was concluded that the population size of 20–30 is most appropriate to arrive an optimal solution satisfying the objective function. However, on the contrary, increasing the size of population does not reduce the number of iterations significantly. While selecting the probability of crossover and mutation, suggestions were taken from [20], i.e., the crossover probability was in the range of 0.75–0.95, and this value is adjusted till the best solution set is attained. Thus, from the computations, it was found that the value of 0.8 for crossover probability suited best. The value of mutation probability was fixed to 0.3.

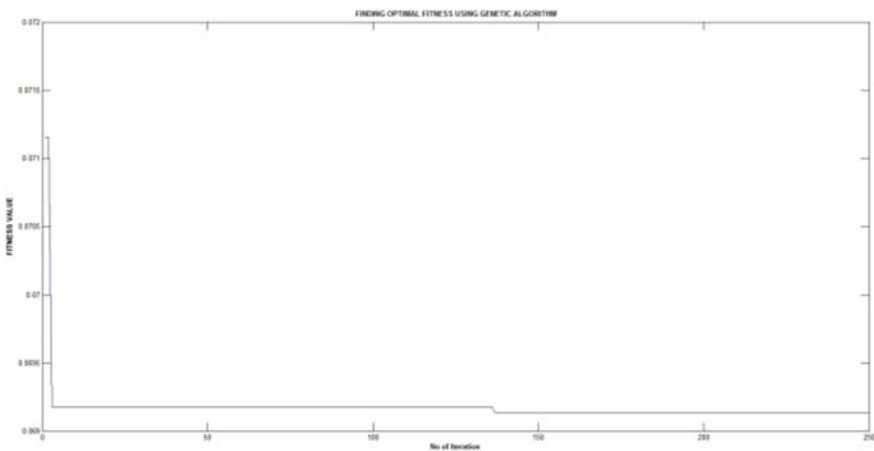


Fig. 1 Fitness curve

Thus, after several runs, the best convergence characteristic that depicted the objective function values versus number of iterations for the GA method is shown in Fig. 1.

Now, these obtained values of parameters, which are mentioned in the table, are fed to a model of PEMFC that was designed in SIMULINK. After feeding all the parameter values (ξ_1 ; ξ_2 ; ξ_3 ; ξ_4 ; b ; λ ; R_h and K_t) to the model, the value of K_t was changed to see the influence of the coolant on PEMFC operation. There was a considerable drop in the operating temperature that was noticed when a value of 0.974 W/Km was used as the thermal conductivity of coolant. Similarly, increasing

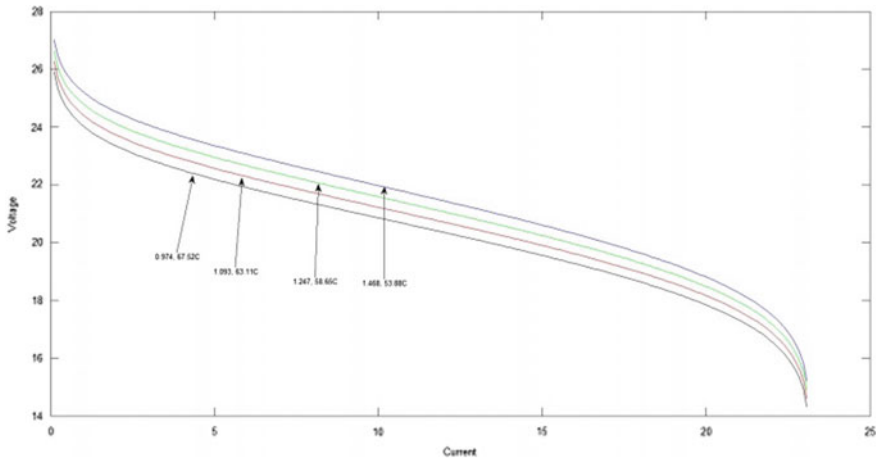


Fig. 2 V-I curve

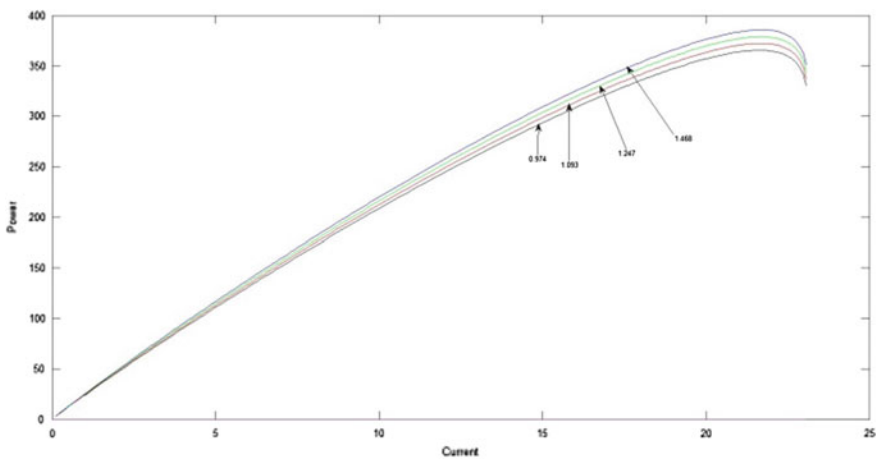


Fig. 3 P-I curve

the thermal conductivity of the coolant has significant performance enhancements of the fuel cell. The $V-I$ and $P-I$ curves for the proposed model are presented in Figs. 2 and 3, respectively.

5 Conclusion

In this work, we were able to accurately plot the output performance enhancement by simulating the data generated through GA and adding thermal conductivity of coolant as another parameter. The observed performance enhancement was for the condition where we did not consider any kind of forced heat transfer. Thus, the performance should improve further if forced heat transfer method accompanied with nanofluid coolant was implemented. Approximately 3% rise in output voltage was observed with respect to increasing value of thermal conductivity of coolant. Output voltage could be further increased with the use of a coolant which has even more thermal conductivity value than that of Al_2O_3 nanofluid.

References

1. Zhang, J., Xie, Z., Zhang, J., Tang, Y., Song, C., Navessin, T., Shi, Z., et al.: High temperature PEM fuel cells. *J. Power Sources* **160**(2), 872–891 (2006)
2. O'hayre, R., Cha, S.W., Prinz, F.B., Colella, W.: *Fuel Cell Fundamentals*. Wiley, New York (2016)
3. Lee, J.Y., Yoo, M., Cha, K., Lim, T.W., Hur, T.: Life cycle cost analysis to examine the economical feasibility of hydrogen as an alternative fuel. *Int. J. Hydrogen Energy* **34**(10), 4243–4255 (2009)
4. Peighambaroust, S.J., Rowshanzamir, S., Amjadi, M.: Review of the proton exchange membranes for fuel cell applications. *Int. J. Hydrogen Energy* **35**(17), 9349–9384 (2010)
5. Appleby, A.J.: *Fuel Cell Handbook* (1988)
6. Wee, J.H.: Applications of proton exchange membrane fuel cell systems. *Renew. Sustain. Energy Rev.* **11**(8), 1720–1738 (2007)
7. Chandan, A., Hattenberger, M., El-Kharouf, A., Du, S., Dhir, A., Self, V., Pollet, B.G., Ingram, A., Bujalski, W.: High temperature (HT) polymer electrolyte membrane fuel cells (PEMFC)—a review. *J. Power Sources* **231**, 264–278 (2013)
8. Rayment, C., Sherwin, S.: *Introduction to Fuel Cell Technology*. Department of Aerospace and Mechanical Engineering, University of Notre Dame, Notre Dame, IN 46556, pp. 11–12 (2003)
9. Matian, M., Marquis, A.J., Brandon, N.P.: Application of thermal imaging to validate a heat transfer model for polymer electrolyte fuel cells. *Int. J. Hydrogen Energy* **35**(22), 12308–12316 (2010)
10. Shahsavari, S., Desouza, A., Bahrami, M., Kjeang, E.: Thermal analysis of air-cooled PEM fuel cells. *Int. J. Hydrogen Energy* **37**(23), 18261–18271 (2012)
11. Amphlett, J.C., Baumert, R.M., Mann, R.F., Peppley, B.A., Roberge, P.R., Harris, T.J.: Performance modeling of the Ballard Mark IV solid polymer electrolyte fuel cell I. Mechanistic model development. *J. Electrochem. Soc.* **142**(1), 1–8 (1995)

12. Ye, M., Wang, X., Xu, Y.: Parameter identification for proton exchange membrane fuel cell model using particle swarm optimization. *Int. J. Hydrogen Energy* **34**(2), 981–989 (2009)
13. Larminie, J., Dicks, A., McDonald, M.S.: *Fuel Cell Systems Explained*, vol. 2. Wiley, Chichester (2003)
14. Niya, S.M.R., Hoorfar, M.: Process modeling of the ohmic loss in proton exchange membrane fuel cells. *Electrochim. Acta* **120**, 193–203 (2014)
15. Jeon, S.W., Cha, D., Kim, H.S., Kim, Y.: Analysis of the system efficiency of an intermediate temperature proton exchange membrane fuel cell at elevated temperature and relative humidity conditions. *Appl. Energy* **166**, 165–173 (2016)
16. Thomson, G.W.: The Antoine equation for vapor-pressure data. *Chem. Rev.* **38**(1), 1–39 (1946)
17. Haddad, Z., Abid, C., Oztop, H.F., Mataoui, A.: A review on how the researchers prepare their nanofluids. *Int. J. Thermal Sci.* **76**, 168–189 (2014)
18. Hamilton, R.L., Crosser, O.K.: Thermal conductivity of heterogeneous two-component systems. *Ind. Eng. Chem. Fundam.* **1**(3), 187–191 (1962)
19. Maxwell, J.C.: *A Treatise on Electricity and Magnetism*, vol. 1. Clarendon Press (1881)
20. Priya, K., Sudhakar Babu, T., Balasubramanian, K., Sathish Kumar, K., Rajasekar, N.: A novel approach for fuel cell parameter estimation using simple genetic algorithm. *Sustain. Energy Technol. Assess.* **12**, 46–52 (2015)

Renewable Energy Capacity Estimation for Indian Energy Sector Using Energy Demand Forecasting Through Fuzzy Time Series

Shibabrata Choudhury, Aswini Kumar Patra, Adikanda Parida and Saibal Chatterjee

Abstract Rapid industrialization, change in lifestyle, population growth, etc., influence the demand for energy exponentially. Till date, fossil fuel constitutes the major component of energy mix of developing countries. The declined availability of fossil fuel is a cause of concern for developing countries like India. In this paper, the probable future energy demand trend has been depicted based on the combination of k -means clustering, and the two-factor and three-order fuzzy time series techniques considering the three decade energy scenario of India in particular. Further, the paper has outlined the need and significance of renewable energy as it compensates the energy deficit in a comparative cost-effective and environmental friendly manner.

Keywords Energy demand · Renewable energy · Clustering
Fuzzy time series · India

S. Choudhury (✉)

Centre for Management Studies, North Eastern Regional Institute of Science and Technology, Nirjuli, Arunachal Pradesh, India
e-mail: shibabrata.choudhury@gmail.com

A.K. Patra

Department of Computer Science and Engineering, North Eastern Regional Institute of Science and Technology, Nirjuli, Arunachal Pradesh, India
e-mail: aswinipatra@gmail.com

A. Parida · S. Chatterjee

Department of Electrical Engineering, North Eastern Regional Institute of Science and Technology, Nirjuli, Arunachal Pradesh, India
e-mail: adikanda_2003@yahoo.co.in

S. Chatterjee

e-mail: sc@nerist.ac.in

1 Introduction

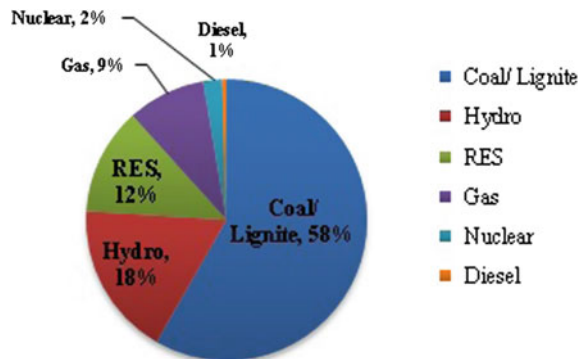
Industrialization, urbanization, and the population growth in India is the main cause for the exponential growth of the energy demand in the country. Various measures, such as energy efficiency techniques and policies adopted by different governments time to time, have insignificant impacts over energy demand reduction [1]. Researchers have highlighted a strong correlation between well-being and energy consumption. The well-being measure should not be an aggregate average; rather it is related to individuals [2]. There has been a noticeable country wide disparity in individual energy access. Moreover, whole of the rural and urban poor are deprived of energy access in developing countries [3]. However, global climatic change and environmental issues restrict the capacity addition from the nonrenewable energy sources. Besides, renewable energy assures energy security, economic competitiveness, and better human livelihood [4].

2 Status of the Indian Energy Sector

Postindependence India has shown an equal energy contribution from both hydro and thermal sources. In post 1980s, the country was unable to maintain the green supply of energy in a balanced manner to move along with the demand of energy. By the end of XII plan there was 708,427 GWh of thermal source of energy as compared to 130,511 GWh of hydro source of energy.

From IV plan onward, nuclear source of energy was introduced, whereas the cost-effective renewable source of energy was introduced after 1990s. Renewable energy source has contributed a higher value as compared to nuclear source of energy [5]. Figure 1 shows that the coal lignite constitutes 58% of the total energy contribution, followed by hydropower, and renewable energies with 18, 12%, respectively.

Fig. 1 All India installed generation capacity—end of first year of 12th plan



3 Demand Forecasting Using Fuzzy Time Series

The fuzzy-based demand forecasting has been adopted for the prediction of energy requirement as proposed in [6, 7].

3.1 Fuzzy Time Series

The fuzzy time series was proposed by Song and Chissom [8], where as the values for fuzzy time series are based on fuzzy sets [9]. Fuzzy set P of the universe discourse Z , $Z = (z_1, z_2, \dots, z_n)$ has been defined as:

$$P = f_p(z_1)/z_1 + f_p(z_2)/z_2 + \dots + f_p(z_n)/z_n$$

For fuzzy set P , f_p is the membership function, $f_p: Z \rightarrow [0, 1]$, $f_p(z_i)$ signifies the membership grade of Z_i in the fuzzy set P , and $1 \leq i \leq n$. Assuming $F(s)$, a fuzzy time series, $F(n)$ is caused by $F(s-1)$, $F(s-2)$, ... and $F(s-n)$, then fuzzy logical relationship is as follows:

$$F(s-n) \dots F(s-2), F(s-1) \rightarrow F(s)$$

3.2 Proposed Forecasting Method Based on k-Means Clustering Techniques and Two-Factor and Third-Order Fuzzy Time Series

A methodology is proposed to predict the country's energy demand. The requirement and available energy data of three decade being taken to predict the energy demand. Based on the requirement of energy, various alternatives can be taken to buildup the energy capacity of the nation. The steps are as follows:

Step 1: Sort the data in ascending order, and the data points are represented as

$d_1, d_2 \dots d_n$. Compute the *average difference (AD)* = $\frac{\sum_{i=1}^{n-1} d_{i+1} - d_i}{n-1}$ for both the inputs *requirement* and *availability*. The *average difference* for *requirement* and *availability* are calculated as 30.10 and 27.36, respectively, from the three decade energy data.

Step 2: The data points are grouped using *k*-means clustering. The requirement and availability energy data from 1984–85 till 2012–13 are clustered into 10 bunches as presented [5] in Table 1.

Step 3: The boundary for clusters obtained in Step 2 is computed using two conditions. (i) If a cluster contains more than two elements, then all elements are rejected excluding the highest and lowest. (ii) In the case of

Table 1 Available and required energy of India (1984–2013)

S.No	Year	Requirement clusters	Availability clusters
1	1984–85	155.432	145.013
2	1985–86	170.746	157.262
3	1986–87	192.356	174.276
4	1987–88	210.993	187.976
5	1988–89	223.194	205.909
6	1989–90	247.762	228.151
7	1990–91	267.632	246.56
8	1991–92	288.974	266.432
9	1992–93	305.266	279.824
10	1993–94	323.252	299.494
11	1994–95	352.26	327.281
12	1995–96	389.721	354.045
13	1996–97	413.49	365.9
14	1997–98	424.505	390.33
15	1998–99	446.584	420.235
16	1999–00	480.43	450.594
17	2000–01	507.216	467.409
18	2001–02	522.537	483.35
19	2002–03	545.674	497.589
20	2003–04	559.264	519.398
21	2004–05	591.373	548.115
22	2005–06	631.757	578.819
23	2006–07	690.587	624.495
24	2007–08	739.343	660.007
25	2008–09	777.039	691.038
26	2009–10	830.594	746.644
27	2010–11	861.591	788.355
28	2011–12	937.199	857.886
29	2012–13	998.114	911.209

single element (e_s) cluster, then the boundary is calculated as $(e_s - AD), (e_s + AD)$.

The boundary for Table 1 data has been prepared as follows (Table 2):

Step 4: If cluster boundaries decided in previous step are represented as $(x, y), (a, b), (c, d)...$ then the intervals (u_i) are determined as follows: $u_i = (x, y), u_{i+1} = (y, a), u_{i+2} = (a, b), u_{i+3} = (b, c)...$ and so on.

The computed cluster boundaries for energy requirement and availability are mentioned in Table 3.

Step 5: The input data are fuzzified. For example, if energy requirement data belong to an item u_i then P_i is represented, similarly for energy available data are represented as Q_i . It has been depicted in Table 4.

Table 2 Boundary for requirement and availability of energy

Requirement			Availability		
c_1	155.43	223.19	c_1	145.01	174.28
c_2	247.76	323.25	c_2	187.98	228.15
c_3	352.26	446.58	c_3	246.56	299.49
c_4	480.43	559.26	c_4	327.28	390.33
c_5	591.37	631.76	c_5	420.24	467.41
c_6	660.49	720.68	c_6	483.35	519.40
c_7	739.34	777.04	c_7	548.12	578.82
c_8	830.59	861.59	c_8	624.50	691.04
c_9	907.10	967.29	c_9	746.64	788.36
c_{10}	968.02	998.11	c_{10}	857.89	911.21

Table 3 Intervals for requirement and availability of energy

Intervals of requirements (u_i)	Intervals of availability (v_i)
$u_1 = [155.432, 223.194]$	$v_1 = [145.013, 174.276]$
$u_2 = [223.194, 247.762]$	$v_2 = [174.276, 187.976]$
$u_3 = [247.762, 323.252]$	$v_3 = [187.976, 228.151]$
$u_4 = [323.252, 352.26]$	$v_4 = [228.151, 246.56]$
$u_5 = [352.26, 446.584]$	$v_5 = [246.56, 299.494]$
$u_6 = [446.584, 480.43]$	$v_6 = [299.494, 327.281]$
$u_7 = [480.43, 559.264]$	$v_7 = [327.281, 390.33]$
$u_8 = [559.264, 591.373]$	$v_8 = [390.33, 420.235]$
$u_9 = [591.373, 631.757]$	$v_9 = [420.235, 467.409]$
$u_{10} = [631.75, 660.491]$	$v_{10} = [467.40, 483.35]$
$u_{11} = [660.491, 720.682]$	$v_{11} = [483.35, 519.398]$
$u_{12} = [720.682, 739.343]$	$v_{12} = [519.398, 548.115]$
$u_{13} = [739.343, 777.039]$	$v_{13} = [548.115, 578.819]$
$u_{14} = [777.039, 830.594]$	$v_{14} = [578.819, 624.495]$
$u_{15} = [830.594, 861.591]$	$v_{15} = [624.495, 691.038]$
$u_{16} = [861.591, 907.103]$	$v_{16} = [691.038, 746.644]$
$u_{17} = [907.103, 967.294]$	$v_{17} = [746.644, 788.355]$
$u_{18} = [967.294, 968.018]$	$v_{18} = [788.355, 857.886]$
$u_{19} = [968.018, 998.114]$	$v_{19} = [857.886, 911.209]$

Table 4 Fuzzified inputs for requirement and availability of energy

S. No.	Requirements	Fuzzified requirement	Availability	Fuzzified availability
1	155.432	P_1	145.013	Q_1
2	170.746	P_1	157.262	Q_1
3	192.356	P_1	174.276	Q_2
4	210.993	P_1	187.976	Q_3
5	223.194	P_2	205.909	Q_3
6	247.762	P_3	228.151	Q_4
7	267.632	P_3	246.56	Q_5
8	288.974	P_3	266.432	Q_5
9	305.266	P_3	279.824	Q_5
10	323.252	P_4	299.494	Q_6
11	352.26	P_5	327.281	Q_7
12	389.721	P_5	354.045	Q_7
13	413.49	P_5	365.9	Q_7
14	424.505	P_5	390.33	Q_8
15	446.584	P_6	420.235	Q_9
16	480.43	P_7	450.594	Q_9
17	507.216	P_7	467.409	Q_{10}
18	522.537	P_7	483.35	Q_{11}
19	545.674	P_7	497.589	Q_{11}
20	559.264	P_8	519.398	Q_{12}
21	591.373	P_9	548.115	Q_{13}
22	631.757	P_{10}	578.819	Q_{14}
23	690.587	P_{11}	624.495	Q_{15}
24	739.343	P_{13}	660.007	Q_{15}
25	777.039	P_{14}	691.038	Q_{16}
26	830.594	P_{15}	746.644	Q_{17}
27	861.591	P_{16}	788.355	Q_{18}
28	937.199	P_{17}	857.886	Q_{19}
29	998.114	P_{19}	911.209	Q_{19}

Step 6: We can construct two-factor and three-order fuzzy logical relationship. For example, fourth year information could be obtained by considering year 1, year 2, and year 3. Similarly, the moving average rule is followed for subsequent years. It has been depicted in Table 5:

Step 7: Let the two-factor k th-order fuzzified historical data prior day i are $(P_{iv}, Q_{iv}) \dots (P_{i2}, Q_{i2})$, and (P_{i1}, Q_{i1}) where $2 \leq k \leq n$; P_{iv}, \dots, P_{i2} , and P_{i1} are the fuzzified values of the primary factor of fuzzy sets, similarly Q_{iv}, \dots, Q_{i2} , and Q_{i1} are the fuzzified values of the secondary factor of the fuzzy sets. Based on these, values forecasting are estimated [8]. There are three possible existence of fuzzy logical relationship groups based on which the forecasted value of day i is computed as follows:

Table 5 Fuzzified inputs for requirement and availability of energy

1. $(P_1, Q_1), (P_1, Q_1), (P_1, Q_2) \rightarrow P_1$	2. $(P_1, Q_1), (P_1, Q_2), (P_1, Q_3) \rightarrow P_2$
3. $(P_1, Q_2), (P_1, Q_3), (P_2, Q_3) \rightarrow P_3$	4. $(P_1, Q_3), (P_2, Q_3), (P_3, Q_4) \rightarrow P_3$
5. $(P_2, Q_3), (P_3, Q_4), (P_3, Q_5) \rightarrow P_3$	6. $(P_3, Q_4), (P_3, Q_5), (P_3, Q_5) \rightarrow P_3$
7. $(P_3, Q_5), (P_3, Q_5), (P_3, Q_5) \rightarrow P_4$	8. $(P_3, Q_5), (P_3, Q_5), (P_4, Q_6) \rightarrow P_5$
9. $(P_3, Q_5), (P_4, Q_6), (P_5, Q_7) \rightarrow P_5$	10. $(P_4, Q_6), (P_5, Q_7), (P_5, Q_7) \rightarrow P_5$
11. $(P_5, Q_7), (P_5, Q_7), (P_5, Q_7) \rightarrow P_5$	12. $(P_5, Q_7), (P_5, Q_7), (P_5, Q_8) \rightarrow P_6$
13. $(P_5, Q_7), (P_5, Q_8), (P_6, Q_9) \rightarrow P_7$	14. $(P_5, Q_8), (P_6, Q_9), (P_7, Q_9) \rightarrow P_7$
15. $(P_6, Q_9), (P_7, Q_9), (P_7, Q_{10}) \rightarrow P_7$	16. $(P_7, Q_9), (P_7, Q_{10}), (P_7, Q_{11}) \rightarrow P_7$
17. $(P_7, Q_{10}), (P_7, Q_{11}), (P_7, Q_{11}) \rightarrow P_8$	18. $(P_7, Q_{11}), (P_7, Q_{11}), (P_8, Q_{12}) \rightarrow P_9$
19. $(P_7, Q_{11}), (P_8, Q_{12}), (P_9, Q_{13}) \rightarrow P_{10}$	20. $(P_8, Q_{12}), (P_9, Q_{13}), (P_{10}, Q_{14}) \rightarrow P_{11}$
21. $(P_9, Q_{13}), (P_{10}, Q_{14}), (P_{11}, Q_{15}) \rightarrow P_{13}$	22. $(P_{10}, Q_{14}), (P_{11}, Q_{15}), (P_{13}, Q_{15}) \rightarrow P_{14}$
23. $(P_{11}, Q_{15}), (P_{13}, Q_{15}), (P_{14}, Q_{16}) \rightarrow P_{15}$	24. $(P_{13}, Q_{15}), (P_{14}, Q_{16}), (P_{15}, Q_{17}) \rightarrow P_{16}$
25. $(P_{14}, Q_{16}), (P_{15}, Q_{17}), (P_{16}, Q_{18}) \rightarrow P_{17}$	26. $(P_{15}, Q_{17}), (P_{16}, Q_{18}), (P_{17}, Q_{19}) \rightarrow P_{19}$
27. $(P_{16}, Q_{18}), (P_{17}, Q_{19}), (P_{19}, Q_{19}) \rightarrow \#$	

Principle 1: If $(P_{iv}, Q_{iv}) \dots, (P_{i2}, Q_{i2}), (P_{i1}, Q_{i1}) \rightarrow P_i$; then forecasted value m_i of day i is computed as the midpoint of the interval u_j .

Principle 2: If $(P_{iv}, Q_{iv}) \dots, (P_{i2}, Q_{i2}), (P_{i1}, Q_{i1}) \rightarrow P_{i1}$; $(P_{iv}, Q_{iv}) \dots, (P_{i2}, Q_{i2}), (P_{i1}, Q_{i1}) \rightarrow P_{i2} \dots (P_{iv}, Q_{iv}) \dots, (P_{i2}, Q_{i2}), (P_{i1}, Q_{i1}) \rightarrow P_{i3}$; then the forecasted value of day is computed to $(m_{i1} + m_{i2} + \dots + m_{ip})/P$; where m_{i1}, m_{i2}, \dots and m_{ip} are the midpoints of intervals u_{i1}, u_{i2}, \dots and u_{ip} , respectively.

Principle 3: If $(P_{iv}, Q_{iv}) \dots, (P_{i2}, Q_{i2}), (P_{i1}, Q_{i1}) \rightarrow \#$; where ‘#’ signifies an unknown value, then forecasted value of day i is computed as $(m_{i-v} + \dots + m_{i-2} + m_{i-1})/V$; (where $m_{i-v}, \dots, m_{i-2}, m_{i-1}$ are the midpoints of the intervals $u_{i-v}, \dots, u_{i-2}, u_{i-1}$, respectively).

Figure 2 compares the existing real requirement with the calculated requirement. The graph indicates there has been consistency in terms of the computed value through fuzzy time series. This study can, further, be extended to predict the long-term prediction of energy requirement through fuzzy time series. The work has considered the requirement of energy, as available energy has to cope as per the demand.

Based on Step 7, the last five-year values are compared in Fig. 2:

In developed countries like USA, the emphasis is on the renewable energy sources for its widespread benefits over other sources of energy, with a target of achieving 80% of demand by 2050. All sources of renewable energy are proved to be cost-effective and sustainable for a longer time with less capital investment involved. Proactive measures taken by India, may be, resulted in adding highest renewable capacity.

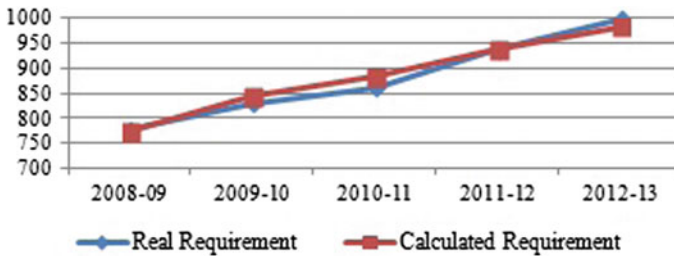


Fig. 2 Real requirement vis-à-vis calculated requirement

4 Conclusion

The work has highlighted the demand of energy considering the data of three decades. Fuzzy time series, so far, has proven utility with the real-time data prediction. This paper has attempted predicting the energy demand using fuzzy time series. The country can prepare itself to manage different regional energy demands based on the forecasted energy demand using this technique. Further, due to constraint of fossil fuel, the capacity for renewable sources of energy can be developed to meet the energy demand.

References

1. Sorrell, S.: Reducing energy demand: a review of issues challenges and approaches. *Renew. Sustain. Energy Rev.* **47**, 74–82 (2015)
2. Day, R., Walker, G., Simmock, N.: Conceptualising energy use and energy poverty using a capabilities frame work. *Energy Policy* **93**, 255–264 (2016)
3. Terrapon-Pfaff, J., Dienst, C., Koning, J., Ortiz, W.: A cross-sectional review: impacts and sustainability of small-scale renewable energy projects in developing countries. *Renew. Sustain. Energy Rev.* **40**, 1–10 (2014)
4. Lo, K.: A critical review of China's rapidly developing renewable energy and energy efficiency policies. *Renew. Sustain. Energy Rev.* **29**, 508–516 (2014)
5. Growth of electricity sector in India from 1947–2013, by Central Electricity Authority, Ministry of Power, July 2013
6. Wang, N., Chen, S.: Temperature prediction and TAIFEX forecasting based on automatic clustering techniques and two-factor high-order fuzzy time series. *Expert Syst. Appl.* **36**, 2143–2154 (2009)
7. Lee, L.W., Wang, L.H., Chen, S.M., Leu, Y.H.: Handling forecasting problem based on two-factor high-order fuzzy time series. *IEEE Trans. Fuzzy Syst.* **14**(3), 468–477 (2006)
8. Song, Q., Chissom, B.S., Fuzzy time series and its model. *Fuzzy Sets Syst.* **54**(3), 269–277 (1993)
9. Zadeh, L.A.: Fuzzy sets. *Inf. Control* **8**, 338–353 (1965)

Performance Analysis of Combined Biogas-Diesel Run Dual-Fuel Engine

Diwakar Gurung, Ankur Rajvanshi, S. Lalhriatpuia
and Premendra Mani Pradhan

Abstract The demand for the energy and power has shown stunning growth in the past decade costing drastic increase in pollution and other environmental hazards. Biogas, a new renewable source of energy has been emerged as new confidence in dealing with such problems. In this paper, an experimental investigation on the performance of combined Biogas-Diesel run Dual-fuel engine is prosecuted through several experiments conducted in a modified engine. The performance was evaluated for an equal power output of both diesel and dual-fuel engine. This type of evaluation approach can decide the feasibility of a dual-fuel engine run by using both biogas and diesel.

Keywords Biogas · Dual-fuel engine · Volumetric efficiency

1 Introduction

One of the most serious problems that the world is being confronted is the use of limited fossil fuel such as petrol, diesel, etc., which has severely harmed the environment. So, these days' alternative to this fossil fuel so-called renewable

D. Gurung (✉)

Department of Mechanical Engineering, National Institute of Technology,
Rourkela, Rourkela, Orissa, India
e-mail: diwakargurung007@gmail.com

A. Rajvanshi · P.M. Pradhan

Department of Mechanical Engineering, Sikkim Manipal Institute of Technology,
Majitar, Sikkim, India
e-mail: ankurrajvanshi.600@gmail.com

P.M. Pradhan

e-mail: premendramani@gmail.com

S. Lalhriatpuia

Department of Mechanical Engineering, Delhi Technological University,
New Delhi, India
e-mail: sactrix777@gmail.com

source of energy has been a topic of investigation for researchers. Among the various energy sources, biogas produced from animal manure waste by anaerobic digestion can be used significantly to meet the demand of environment concern [1]. Though biogas is characterized by its chemical composition and physical characteristics, the primal components include methane (CH_4) and inert carbonic gas (CO_2). On the other hand, the name “biogas” actually includes large variety of gasses produced from different organic wastes mainly animal or domestic origin waste through specific treatment process. Earlier, biogas was used for cooking in the rural household, but it can be also used for generating shaft power and electricity. The combustion and compositional characteristics of biogas are different as compared to natural gas and need a diverse prerequisite for utilizing these characteristics [2]. One of the methods for using this biogas would be dual-fueled compression ignition engine. The basic concept behind this type of engine is the use of primary fuel also known as gaseous fuel and pilot fuel. The dual-fuel engines are classified into twofolds depending on the utilization of pilot and gaseous fuel. In one category, liquid fuel such as diesel is used to burn the mixture of gaseous fuel and air. In another fold, gaseous fuel is incorporated into air suction system of conventional diesel engine. The interest of this paper lies within the second category of the dual-fueled engine. The obscurity about the feasibility of the engine is to be run by biogas and was successful in compressing the biogas and extracting the power from it [3]. The efficiency of Combined Biogas-Diesel run Dual-Fuel Engine was found superior to conventional diesel engine while investigating small biogas-diesel engine [1]. The test for biogas run engine for the extraction of energy was concluded successfully. Experimental variants were improved for utilization of biogas produced from pig manure and plant additives and establish the satisfied condition for running the heat engine properly [4]. It was also found that addition of O_2 will stabilize the combustion stability in a biogas-diesel engine by attenuating the difficulties caused by CO_2 during combustion such as reduction in mixing temperature of biogas-air and burning velocities of biogas [5].

Considering the above literature review, it is found that the researchers have done marvelous development in the context of combustion characteristics, improvement of energy utilization, quality improvement of biogas, and designing of engine parameter for power output. The present study deals with performance analysis of Combined Biogas-Diesel run Dual-Fuel Engine in which the biogas will be incorporated into the air in a fully operational diesel engine. Initially, baseline performance tests with the conventional diesel engine are executed and then with biogas. The main objective is to compare the performance of Combined Biogas-Diesel run Dual-Fuel with a normal diesel engine in the context of braking power, brake power efficiency, volumetric efficiency, exhaust temperature, and air consumption.

2 Experimental

2.1 Biogas and Pilot Fuel

Biogas which has been employed as the gaseous fuel mixed with the air is produced from cow manure through anaerobic digestion, collected from the gobar plant situated at Yupia, Naharlagun, Arunachal Pradesh, India. In our investigation, the standard diesel is used as the pilot fuel for the experimental work in Combined Biogas-Diesel run Dual-Fuel Engine. Injection pump supplies the diesel from the fuel tank through gravity.

2.2 Engine Test Rig Setup and Procedure

Petter AA1 four-stroke diesel engine is used for investigation which has single cylinder, direct injection system and is cooled through water. The maximum power rated in engine is 2.6 kW at 3600 min⁻¹, and it has a bore of 70 mm and stroke of 57 mm. The engine is loaded with a hydraulic dynamometer and standard fuel injection system. The injection nozzle consists of three holes having diameter 0.3 mm, and fuel is sprayed at maximum angle of 120°. Type K thermocouples is installed at exhaust of engine for measuring exhaust temperatures. The airflow to the engine is measured by using orifice meter and inclined tube manometer. The pressure drop is measured in millimeters of diluted ethyl alcohol and is featured in the airflow calculation from the viscous flowmeter calibration. During the dual-fuel operation, biogas is mixed with inlet air in simple T-junction mixing chamber. This chamber consists of two inlet channel for and an outlet for the mixture of both connected to the air suction manifold of the engine (Fig. 1). The flow rate of biogas was measured in the biogas flowmeter. Figure 2 shows the view of Combined Biogas-Diesel run Dual-Fuel Engine and its connected components.

Initially, Diesel engine is run idly at 1500 rpm for 20 min for smooth operation. Baseline tests carried out by using only diesel, and result will be used for further comparison. The load was varied in steps from 1.5 to 4 N in the hydraulic dynamometer. For each load, all the required parameters such as rpm, exhaust temperature, liquid level in manometer, and volume of diesel fuel consumption are noted. While operating at biogas dual-fuel mode, the opening of valve in the gas balloon releases biogas which gets mix with air in mixing chamber. The air-gas mixture from chamber enters the cylinder though carburetor, and this process further increases the engine speed an account of additional chemical energy associated with biogas. Liquid fuel cutoff valve is adjusted to maintain the supply of diesel to get speed in par with diesel mode. The data acquisition was undertaken similar to baseline tests for each step load.

To present the air consumption measured in kg h⁻¹ and volumetric efficiency, the following expression is adopted:

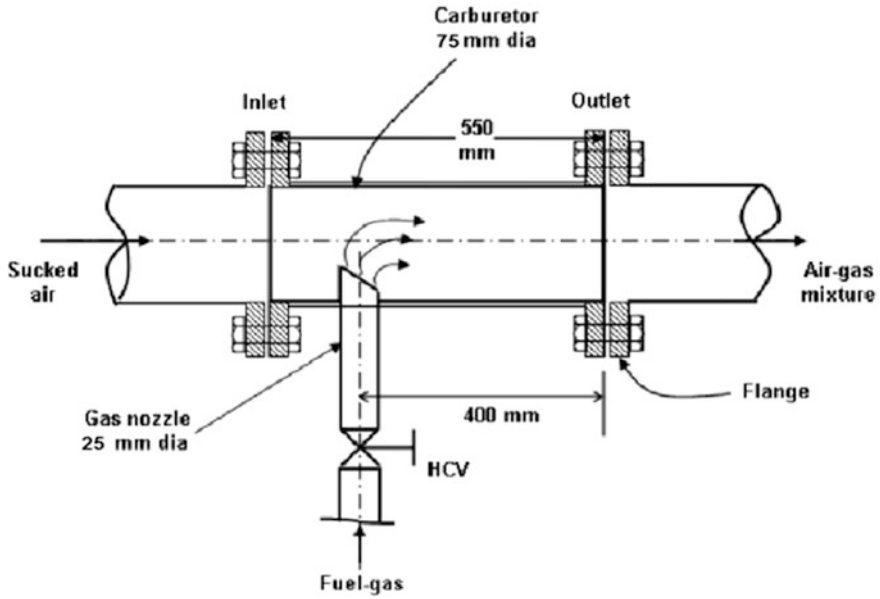


Fig. 1 T-joint mixer

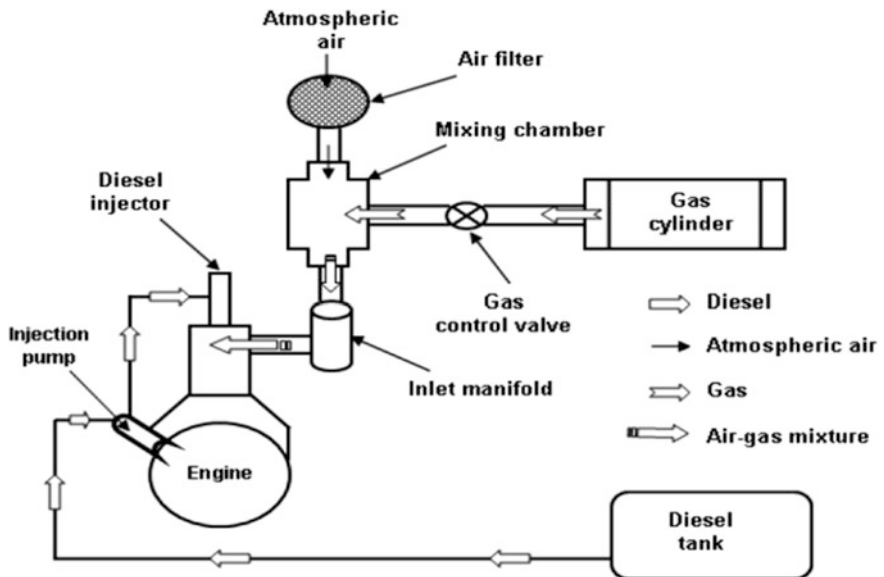


Fig. 2 Schematic view of combined biogas-diesel dual-fuel engine

Airflow rate,

$$F = C_d \times \frac{\pi}{4} \times d^2 \times \sqrt{\frac{2gh \times W_{den}}{A_{den}}} \times 3600 \times A_{den} \quad (1)$$

where C_d is discharged coefficient, d is the diameter of orifice meter in millimeter, h is the height of manometry fluid (diluted ethyl alcohol) in millimeter, and A_{den} and W_{den} is the air and manometry fluid density, respectively, in kg m^{-3} .

Volumetric efficiency,

$$\eta_v = \frac{F}{(\pi/4) \times D^2 \times L \times \frac{N}{n} \times 60 \times K \times A_{den}} \times 100 \quad (2)$$

where D is cylinder diameter in millimeter, L is the stroke length of cylinder in millimeter, N is the engine speed in revolution per minute, and K is the number of cylinder and value of $n = 2$ (four-stroke engine).

The brake power and brake thermal efficiency are calculated according to Brake Power,

$$BP = \frac{2 \times 3.142 \times N \times W \times R}{60 \times 1000} \quad (3)$$

Mass flow rate of diesel in kg hr^{-1} ,

$$m_d = (X \times 60 \times \rho_{Lf}/10^6) \quad (4)$$

where X is the cc liquid fuel consumption of engine in cc/min and ρ_{Lf} is the liquid fuel density in kg m^{-3} .

Thermal brake efficiency,

$$\eta_{bth} = \frac{BP \times 3600}{\dot{m}_d \times LHV_d} \times 100 \text{ for normal diesel operation} \quad (5)$$

$$\eta_{bth} = \frac{BP}{\dot{m}_d \times LHV_d + \dot{m}_g \times LHV_g} \times 100 \text{ for dual fuel operation} \quad (6)$$

where LHV_d is low heating value of diesel and LHV_g is low heating value of biogas in MJ kg^{-1} .

All these performance parameters were obtained from the above relation and compared the performance of Combined Biogas-Diesel run Dual-Fuel Engine and conventional diesel engine. During the process, the serious attention was given for the proper functioning of each component during the experiments.

3 Result and Discussion

The results of the experiments conducted for the comparison of Combined Biogas-Diesel run Dual-Fuel Engine are shown in Figs. 3, 4, 5, 6 and 7. The patterns of variation for each parameter are found to be almost same. Figure 3 shows the greater air consumption for diesel mode than dual mode at equal loading conditions more substitution of air takes place by fuel at higher load. Figure 4 shows lower volumetric efficiencies for dual-fuel operations than diesel mode. This is due to the preheating of the incoming fresh air by exhaust gas. Biogas displaces a greater proportion of air at higher power outputs. Figures 5 and 6 display greater braking power and thermal efficiency for conventional diesel engine than that of Combined Biogas-Diesel run Dual-Fuel Engine. Lower heating value of biogas causes significant drop in thermal efficiency (about 19–40%) in dual-fuel modes for ranges of load. This can be improved by increasing the qualities of biogas which will give higher heating value causing increase in efficiency to greater extend. Lastly, Fig. 7 shows the variation of exhaust temperature in which the temperature for dual mode was less than diesel mode.

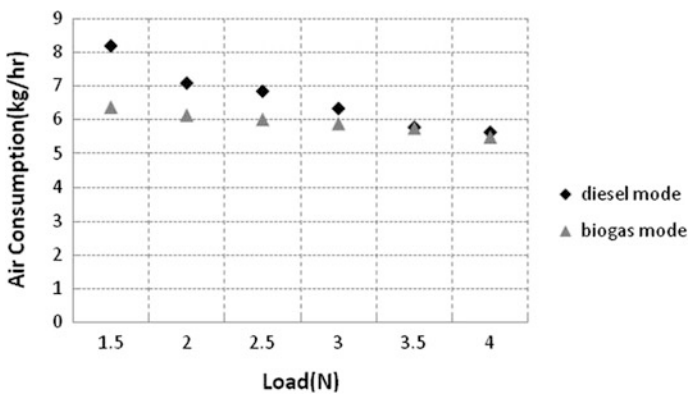


Fig. 3 Variation of air consumption rate with load from diesel and dual-fuel operation

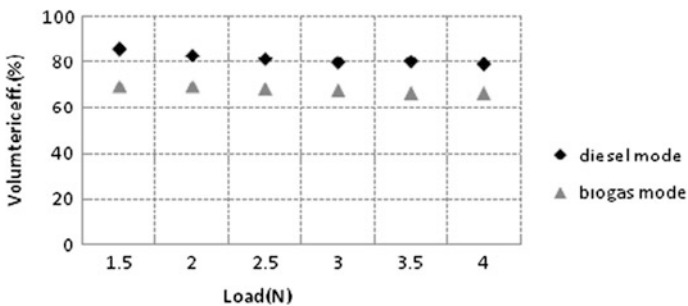


Fig. 4 Variation of volumetric efficiency with load from diesel and dual-fuel operation

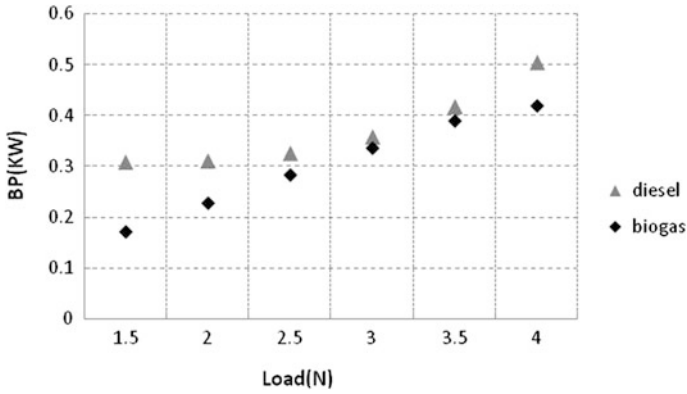


Fig. 5 Variation of brake power with load from diesel and dual-fuel operation

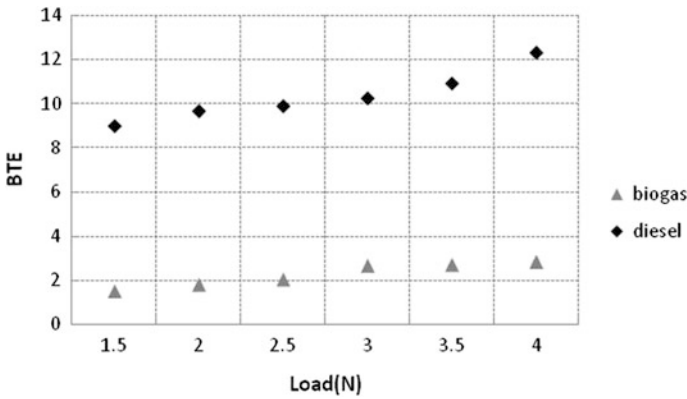


Fig. 6 Variation of brake thermal efficiency with load from diesel and dual-fuel operation

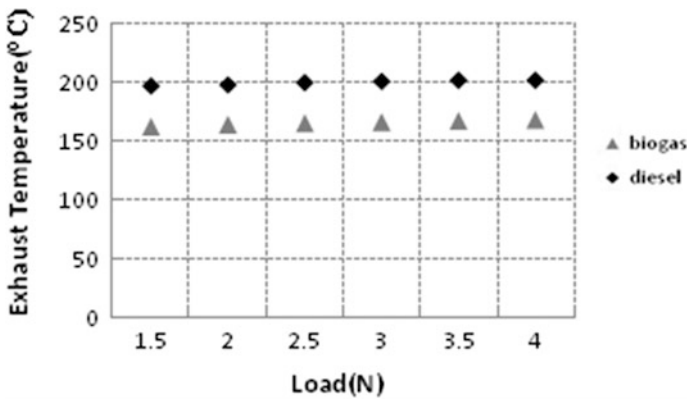


Fig. 7 Variation of exhaust temperature with load from diesel and dual-fuel operation

4 Conclusion

Diesel engines stand out greatly among all the energy utilization devices in terms of power, energy efficiency, durability, and reliability. It has largely expanded its horizon in many sectors such as transportation, farming, industries, and construction technology. But the production of greenhouse gasses such as CO and CO₂ through burning of fossil fuels has caused stern environmental hazards. Nowadays, after being concern with such insalubrious limitation of engines, people are advancing toward clean diesel technologies, viz., biogas engine, alternative fuels, and hybrid electricity. Biogas, substitute to diesel, has the great potential and can be used in clean energy technology further, reducing emission of greenhouse gas. The Combined Biogas-Diesel run Dual-Fuel Engine can be used for obtaining power from biogas. This paper has shown meticulous investigation on the performance of combined Biogas-Diesel run Dual-fuel engine, and various performance parameters are compared with the conventional diesel engine. The brake power and brake thermal efficiency for both diesel and dual-fuel mode exhibited positive increment with load. The brake power for diesel mode was greater than dual-fuel mode. The maximum brake power obtained for diesel mode was 0.50 kW at 4 N load and for dual-fuel mode was 0.41 kW at 4 N load. Thermal efficiency obtained for diesel mode was 12% at 4 N load and for dual mode was 2.82% at 4 N load. The experiment also verifies the increment in brake power and the brake thermal efficiency of the Combined Biogas-Diesel run Dual-Fuel Engine by using biogas having higher heating valve. This indicates the adoption of this biogas may reduce the diesel fuel cost which causes higher CO and CO₂ emissions. Although the power obtained through the Combined Biogas-Diesel run Dual-Fuel Engine was found to be less in the experiment conducted, this dual-fuel engine appeared to perform well producing clean energy and thus meeting the criteria of environment concern.

References

1. Tippayawong, N., Promwungkwa, A., Rerkkriangkrai, P.: Long-term operation of a small biogas/diesel dual-fuel engine for on-farm electricity generation. *Bio syst. Eng.* **98**(1), 26–32 (2007)
2. Bari, S.: Effect of carbon dioxide on the performance of biogas/diesel dual-fuel engine. *Renew. Energy* **9**(1–4), 1007–1010 (1996)
3. Jiang, C., Liu, T., Zhong, J.: A study on compressed biogas and its application to the compression ignition dual-fuel engine. *Biomass* **20**, 53–59 (1989)
4. Attila, M., Valeria, N.: Biogas and energy production by utilization of different agricultural wastes. **9**(6) (2012)
5. Sahoo, B.B., Sahoo, N., Saha, U.K.: Effect of engine parameters and type of gaseous fuel on the performance of dual-fuel gas diesel engines—a critical review. *Renew. Sustain. Energy Rev.* **13**, 1151–1184 (2009)

Photovoltaic System-Based Marx Multilevel Converter for Hybrid Modulation Strategy

Akbar Ahmad and P. Samuel

Abstract The multicarrier modulation strategy seems to be the most common thread for multilevel topologies. The harmonic observations for phase-shifted and phase disposition multicarrier strategy are different for cascaded and neutral-point-clamped topologies. The novel application of the photovoltaic implementation of self-boost capable of Marx multilevel inverter with an added feature of capacitor voltage balancing is proposed in this paper. The comparison of harmonic performance with fundamental and total harmonic distortion is shown to verify the claim. The analysis and implementation of the proposed hybrid carrier-based control strategy technique show superiority over harmonic performance on different techniques for the aforementioned topology. The exemplification of mathematical analysis and control modulation of Marx multilevel inverter for photovoltaic application are presented and discussed.

Keywords Multilevel inverters (MLI) · Field-programmable gate array (FPGA) Photovoltaic system (PVS) · Hybrid PWM (HPWM) · Total harmonic distortion (THD)

1 Introduction

With multilevel inverters, find its application majorly in DC–AC energy conversion for medium and high-power applications [1]. The term multilevel represents that the multiple levels of voltage are present in desired output waveform. As discussed in [2], the output voltage signal is obtained from the multiple voltage levels with

A. Ahmad (✉) · P. Samuel
Department of Electrical Engineering, MNNIT Allahabad, Allahabad, India
e-mail: akbar_ree0713@mnnit.ac.in

P. Samuel
e-mail: paul@mnnit.ac.in

reduced harmonic contents with the lesser rating of voltage devices producing reduced stress on each switching elements. In 1980, the neutral-point-clamped and capacitor-clamped multilevel topologies were introduced with exemplary features of handling high-power applications in renewable energy along with many other advantages creating huge interest in the recent decades among researchers and industries [3–6].

With the expanded number of levels in voltage and application in dynamic power delivering such as motor loads, these topologies twist over the capacitor voltage adjusting circuits. This, in turn, increases the leakage current in the photovoltaic applications producing various hazards to working personals. Henceforth, such multilevel inverters are not reasonable for such applications. The solution of this issue was proposed by [7] with the introduction of generalized topology for the multilevel converter with self-voltage attuning. The major deficiency with this generalized circuit is that the quantity of switching devices expands which engender complex switching states. Another topology came in existence to manage these anterior issues with economized voltage rating of the switching devices, thereby augmenting the voltage output with the step-up capability [8]. The proposed circuitry may suit its application in photovoltaic system applications with reduced leakage current. The details of proposed application, switching operation and analysis of this topology are discussed in later section.

With the increase in the energy demands with a constant reduction in the supplies of the conventional fuel and excessive emission of carbon dioxide, traces have led the foundation of the current research scenarios, majorly in the area of alternative energy resources. Among various resources, the energy from the photovoltaic cell is considered as the most suitable with least environmental impact, and its source is free and present in the abundance and distributed over the earth. A great advantage of the PV cells in the curtailment of carbon dioxide exudation targeting the year 2030, the CO₂ emission will be reduced by 1 Gton/year compared to India's equivalent emission in the year 2004, or discharge from three hundred coal plants [9].

The primary objective received with Marx topology is the determination of the most suitable switching method for the capacitors utilized as a part of the topology which must be totally charged and released amid its on–off exchanging cycles of operation. If the off states that are involved in the charging of the capacitors are not in synchronization with the output voltage, then it will create harmonics of the voltage delivering unsymmetrical operation. The computerized control calculation alongside the determination of reasonable capacitor quality is talked about in the paper. The paper discusses the real-time implementation of the carrier-based control technique on Marx multilevel inverter with a photovoltaic interface and its comparison over the other topologies like diode-clamped multilevel inverter (DCMLI) and cascaded multilevel inverter (CMLI). The significant improvement in the fundamental voltage and current with total harmonic distortion is observed and discussed in simulation section.

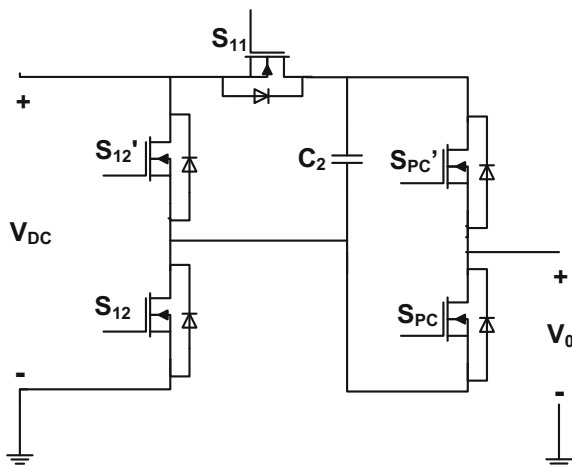
2 Topology and Control

The presented topology works on a concept of high-voltage-level circuit termed as Marx generator. The basic ideology behind the working of the proposed circuit is that it can generate high voltage level by charging a parallel capacitor bank and discharging them in a series configuration. The series connection of the capacitor is made by a switching circuit comprising of spark gaps. If we replace these spark gaps by some switching devices like MOSFET or IGBT based on the regulation of frequency, it provides ease of control to the number of capacitors in series connection with the load. Hence, this topology can generate desired voltage levels by DC bus addition (Fig. 1).

Modulation control of any multilevel inverter is a hugely challenging assignment based on the analytical and harmonic study. Carrier-based modulation maneuverings form a common thread between all the mentioned multilevel topologies with little alteration for each of them. Hence, the conventional control scheme can be adopted by the comparison of overall performance. The analytic solution and harmonics advantage for the various schemes of modulation strategies for multilevel operation are discussed in [10]. The mathematical analysis of the multicarrier modulation for Marx topology is discussed in [11]. Here for Z number of levels, Marx converter arranges $Z - 1$ high-frequency triangular carrier with identical frequency and amplitude over the range of $+V_{dc}$ and $-V_{dc}$. The comparison of these triangular carriers is done with the single low-frequency sinusoidal carrier to produce the switched voltage output of the converter. Based on the position of the carrier, these techniques can be subclassified as [11].

In phase disposition scheme, all the carrier signals are in the identical phase and amplitude. The triangular signals above the reference zero point are 180° out of phase with the below signals in phase opposition and disposition scheme. Each of the carrier signals is shifted by 180° from its adjacent signal in alternate phase

Fig. 1 Elementary single-phase Marx topology for single-phase three-level Marx inverter



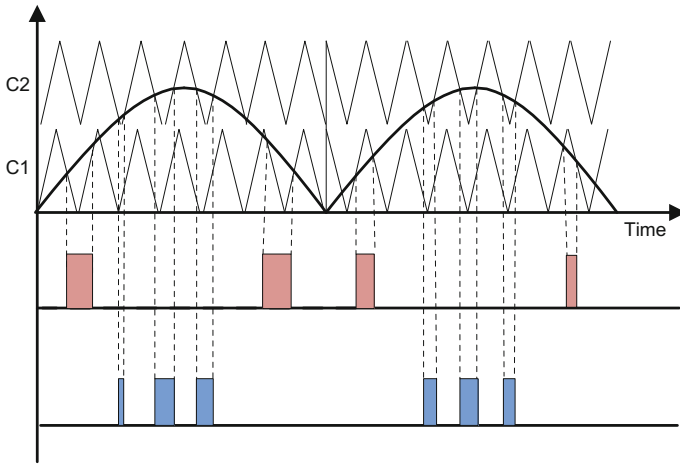


Fig. 2 The comparisons of sinusoidal low-frequency carrier and high-frequency carrier wave for proposed hybrid PWM

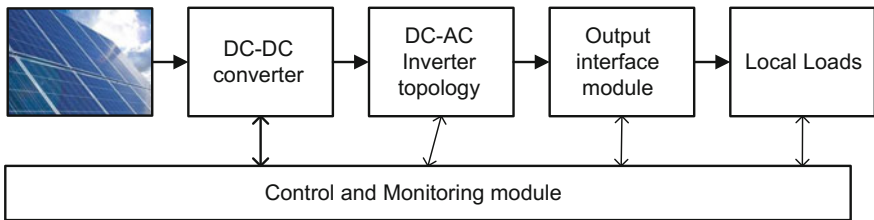


Fig. 3 General flow of the PVS with digital monitoring and control module

opposition and disposition method. The proposed algorithm for the control of this converter is shown in Fig. 2.

$$V_{an}(t) = 2V_{DC}M \cos(\omega_0t) \tag{1}$$

The time deviating swapped phase voltage $V_{an}(t)$ for this is perhaps expressed in terms of its fundamental, harmonic components and the side band components by Eq. (1). Here M represents the modulation index which varies from zero to one.

3 Simulation Studies and Discussions

The general block diagram of the photovoltaic electrical system is displayed in Fig. 3. In this, the series–parallel combination of the PV panels is connected first to generate the desired voltage and current. The regulation of the output voltage is

Table 1 Photovoltaic plant specifications

Rated power	100 kW
Output frequency	50 Hz
Boost converter frequency	5 kHz
DC-link voltage	250 V

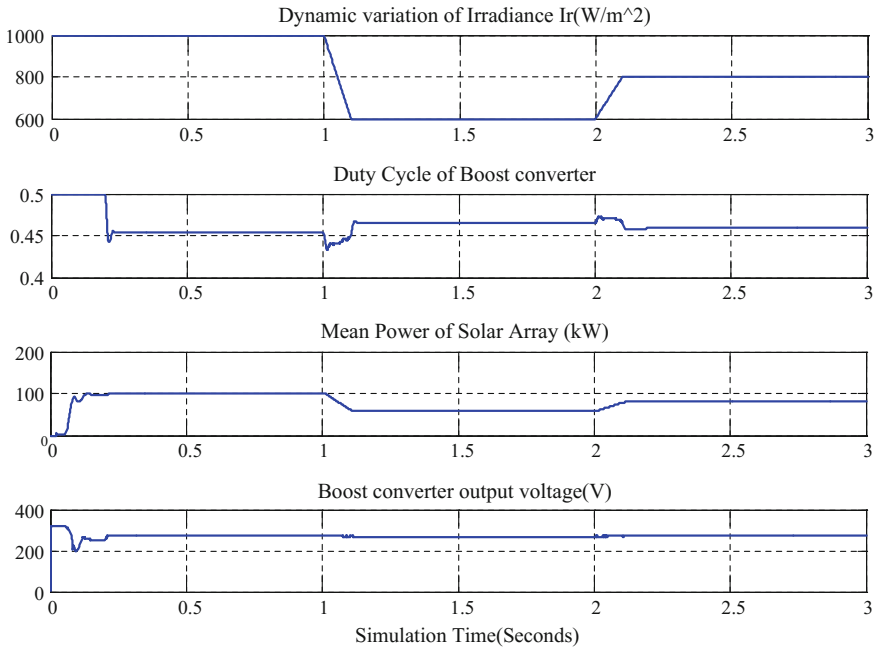


Fig. 4 Dynamic response of solar irradiance and output power

further ensured by the use of DC–DC converter such as buck–boost, single-ended primary inductor converter (SEPIC) or some other whose switching is ensured at the maximum power peak (mpp) of the PV array to achieve the maximum available power at any instant. The regulated DC voltage is then fed to the inverter topology, which converts it to the AC with suitable switching frequency. The harmonic distortion produced from this stage can be further minimized by the use of a filter in the output interface module and connected to the local loads. The use of control and monitoring is very important for the efficient operation of the overall system. Hence, choosing a fast controller with reliable and fast response may increase the system time.

The MATLAB/Simulink software has been used to simulate the five-level-based photovoltaic power plant to demonstrate the highly nonlinear behavior of the solar irradiance. The general parameters considered for the simulation are mentioned in Table 1.

Figure 4 displays the effect of the dynamic change in the solar irradiance and its effect on the average solar power output. Three case studies are discussed below to explain the various changes to regulate the DC-link voltage.

Case 1. This is the case for irradiance 1000 W/m^2 and simulation time up to the 1-time unit. It can be seen from the graph that the initial duty cycle of the boost converter is fixed to 0.5 and the maximum power tracking algorithm using incremental conductance method is initiated at the 0.2-time unit. The voltage control is done to achieve the regulated voltage of around 250 V. The duty changes to 0.45 to produce the regulated output voltage.

Case 2. During the simulation time between 1 and 2, the irradiance is dropped to 600 W/m^2 , and to compensate the voltage to be fixed, the duty is increased and the average power dips to around 60 kW. The fixed voltage can be seen from the simulated output of the boost converter. The change in the modulation index is observed in Fig. 5 to regulate the five-level output voltage around 500 V.

Case 3. In this case, the ramp rise in the irradiance is brought around 800 W/m^2 for the time duration between 2 and 3. The average power rise up to 80 kW can be observed with the variation of the boost duty cycle, and fixed five-level inverter output is achieved which is shown in Fig. 5.

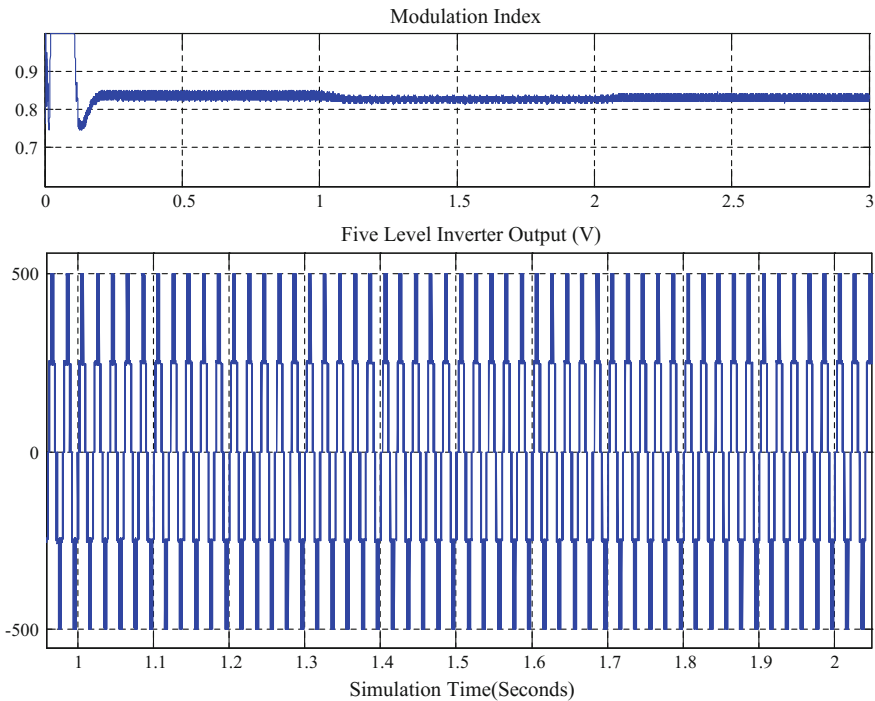


Fig. 5 Variation of modulation index with regulated five-level inverter output voltage

Table 2 Comparison of DCMLI, CMLI, and MMLI

Topology	V_{FUN} (V)	V_{THD} (%)	I_{FUN} (A)	I_{THD} (%)
DCMLI	198	27.37	1.982	10.71
CMLI	194.9	27.51	1.948	10.64
MMLI	198.5	27.09	1.984	10.51

The property of carrier-based PWM strategies (PD, APOD, and POD) for cascaded, diode-clamped, and the hybrid inverter is discussed in [11]. The carrier signal of 3 kHz with the modulation index of 1 in Table 2 shows the comparison of the hybrid phase disposition algorithms implemented on five-level topologies (DCMLI, CMLI, and MMLI) with RL load of 100 Ω and 10 mH and input voltage of 200 V. The comparison shows the improvement of around 5% in the fundamental voltage and current with the 3% reduction in the voltage total harmonic distortion by using Marx multilevel inverter.

4 Conclusion

The simulation results from perception for the usage of the single-stage five-level Marx topology for the photovoltaic application prompt the conclusion that proposed hybrid pulse width modulation a prevalence in line sense looked at over the harmonic distortion execution over different topologies for the multilevel converter. The appropriate determination of capacitor size in the circuit of the converter and a proposed PWM system will furnish symmetrical operation with allowable yield voltage THD with reasonable channel outline for improved result as indicated by different industrial standards. The balanced charging and discharging of the capacitor will lead to less leakage current, further decreasing the well-being dangers to the working personals in the area.

References

1. Rodriguez, J., Lai, J.S., Peng, F.Z.: Multilevel inverters: a survey of topologies, controls, and applications. *IEEE Trans. Ind. Electron.* **49**, 724–738 (2002)
2. Lai, J.S., Peng, F.Z.: Multilevel converters—a new breed of power converters. *IEEE Trans. Ind. App.* **32**, 509–517 (1996)
3. Bhagwat, P.M., Stefanovic, V.R.: Generalized structure of a multilevel PWM inverter. *IEEE Trans. Ind. App.* **6**, 1057–1069 (1983)
4. Nabae, A., Takahashi, I., Akagi, H.: A new neutral-point-clamped PWM inverter. *IEEE Trans. Ind. App.* **17**, 518–523 (1981)
5. Venkatesan, V.J., Subarnan, G.: Multi carrier based multilevel inverter with minimal harmonic distortion. *Int. J. Power Electron. Drive Syst.* **6**, 356–361 (2015)
6. Mohan, N., Undeland, T.M., Robbins, W.P.: *Power electronics: converters, applications, and design*. Wiley, New York (1995)

7. Peng, F.Z.: A generalized multilevel inverter topology with self voltage balancing. *IEEE Trans. Ind. App.* **37**, 611–618 (2001)
8. Rodriguez, J.I., Leeb, S.B.: A multilevel inverter topology for inductively coupled power transfer. *IEEE Trans. Power Electron.* **6**, 1607–1617 (2006)
9. Ahmad, A., Samuel, P., Amar, Y.: Solarizing India: tapping the excellent potential. *Renew. Energy* **9**, 13–17 (2015). Akshay Urja
10. Holmes, D.G., Lipo, T.A.: Pulse width modulation for power converters principles and practice. Wiley-IEEE Press, New York (2003)
11. Kant, P., Ahmad, A., Samuel, P.: Analysis and implementation of multicarrier modulation techniques for Marx multilevel inverter. In: *IEEE International Conference on Environment and Electrical Engineering*, Rome, Italy, pp. 1149–1154 (2015)

Thermal Performance Analysis of a Box-Type Solar Cooker with Finned Pot: An Experimental Approach

Jayashree Nayak, Sudhansu S. Sahoo, Ranjan K. Swain,
Antaryami Mishra and Sanju Thomas

Abstract The thermal performance of a box-type solar cooker with finned cooking pot has been investigated experimentally under local climate conditions at Talcher, Odisha, India. Box-type solar cooker with finned and un-finned cooking pots of same sizes have been used for this experimental study. Fins can be thought of as an extension of the surface which enables additional heat flow from cooker cavity to pot. The performance of the constructed solar cooker was tested using the standard procedure for testing. Testing was performed over 3-month period between May and July 2016, with 1 L water load. Furthermore, various factors affecting the cooking performance like pot type, the solar intensity, and the local time were examined. The maximum temperature in the un-finned and finned pot reached 93 and 102 °C, respectively in the clear weather condition and 70 and 76 °C in cloudy weather condition. The cooker efficiency can reach 53% for finned pot and 50% for un-finned pot in cloudy weather and 72 and 54% respectively in clear weather. The cooker temperature found to depend on the solar radiation intensity and the type of cooking pot. The present solar cooker is of low cost, fabricated locally and simple in use.

Keywords Box-type solar cooker · Finned pot · Weather · Temperature
Thermal performance

J. Nayak (✉) · A. Mishra
Department of Mechanical Engineering, IGIT Sarang, Sarang, India
e-mail: nayak.jayashree@gmail.com

A. Mishra
e-mail: antaryami_igit@yahoo.com

S.S. Sahoo
Department of Mechanical Engineering, CET Bhubaneswar, Bhubaneswar, India
e-mail: sudhansu@cet.edu.in

R.K. Swain
PMEC, Berhampur, India
e-mail: ranjanigit@yahoo.com

S. Thomas
Centre for Solar Energy, World Institute of Sustainable Energy, Pune, India
e-mail: sanju.thomas@wisein.org

1 Introduction

Indian subcontinent is blessed with sufficient amount of sunlight for most of the year, and so cooking with solar heat can be a promising alternative for fuel wood. Solar energy is a free and clean source of energy, and this can be a suitable substitute for traditional cooking fuels. Many factors like type of food, availability of conventional cooking fuels, and non-uniformity of solar heat during a day affects people's mindset about solar cooking.

The box-type solar cooker is an insulated container with a single or multiple glasses (or other transparent materials) cover at the top with or without reflectors. The principle of operation is similar to the greenhouse effect. The transparent glass cover permits passage of shorter wavelength solar radiation. Most of the longer wavelength radiation coming from relatively low temperature heated bottom surface cannot be re-radiated through the glass cover. Reflective mirrors are provided to reflect additional solar radiation into the cooking cavity. Solar box cookers cook through heating of the interior of the box using solar radiation. The bottom of a solar box cooker is selectively coated to absorb maximum solar radiation. It transfers the absorbed solar heat to anything that touches it through the process of conduction. As air at the bottom of the box is heated, it rises and is replaced by cold air from the top of the box. Then the cooker is heated and replaced in a continual circular motion [1–6].

Continuous research is still going on worldwide to optimize the performance of solar cookers. A thorough description of solar box cookers is presented by Nayak et al. [2] and Cuce and Cuce [3]. However, considering different weather condition and different types of pots inside the cooker, the performance is likely to be different. With this motivation, present analysis has been made to obtain the performance of solar cooker at varied weather condition and with different types of pots in it.

In this work, a box-type solar cooker was constructed at IGIT, Sarang, near Talcher, Odisha, India. The performance analysis of a box-type solar cooker with both finned and un-finned cooking pot of same size has been conducted experimentally under local climatic conditions at Talcher, Odisha, India.

2 Geometrical Construction

The solar cooker is constructed with a trapezoidal cavity of aluminum. The box-type solar cooker is shown in Fig. 1. Plane glass is provided at the top allows solar radiation to enter and minimizes re-radiation and convective heat losses. Glass wool insulation surrounds the cavity minimize conduction heat losses. The absorber plate which receives the most of the solar radiation is selective coated lies at the bottom [3]. Both direct and diffused solar rays enter solar cooker. The mirrors serve as reflectors. Refracted radiation from the glass cover is absorbed by the selective coated bottom absorber plate and converted to heat. Incident radiation on the mirror is reflected in the opposite direction, and it is absorbed by the glass on top of the box.



Fig. 1 Constructed box-type solar cooker with pots

Table 1 Specification of constructed solar cooker under consideration [2]

Parameters	Details
<i>Casing</i>	
Dimensions	59.6 × 59.6 × 16.5 cm ³
Thickness	1.8 cm
Material	Aluminum
<i>Absorber plate</i>	
Dimensions of bottom surface	36.6 × 36.6 cm ²
Dimension of top surface	47.5 × 47.5 cm ²
Cooker cavity shape	Trapezoidal
Material	Aluminum
<i>Glaze</i>	
Area	52.8 × 52.8 cm ²
Spacing between glazes	15 mm
Glazing material	Glass of 4 mm thickness
<i>Insulation</i>	
Thickness	2.5 cm
Material	Plywood and sawdust

Inside the box, the mirror can be slanted at an angle by slotting it into the groove made for it. Rubber gasket is provided to prevent air leakage. Finally, the cooker is equipped with four wheels to facilities its easy movement. The dimensions of the box-type solar cooker are provided in Table 1.

3 Experimentation

Experiments were conducted outdoors in IGIT, Sarang, located at 21.0863° latitude and 85.13908° longitude over 3-month period between May and July 2016, with 1-L water load. The objective was to compare the performance of the solar cooker while using a finned pot and an un-finned pot when loaded with 1 L of water at the same initial temperature. The two cooking pots were kept in solar cooker cavity. Temperature measurements were recorded at interval of 30 min during the day with K-type thermocouples.

4 Results and Analysis

Ambient temperature, pot water temperature, cooker cavity air temperature, and the solar irradiance were recorded during the experiment. Figure 2 shows temperature variation with time in clear weather condition. It was found that for clear weather condition in the month of May 2016 water in the finned cooking pot always maintained higher temperature than water in the un-finned cooking pot. In the finned pot boiling temperature of water was attained at 1.00 PM. The water in the un-finned cooking pot reached boiling temperature nearly 1 h later. The ambient temperature almost increases from 35 to 39 °C during the test period.

International Standard for Testing Solar Cooker and Reporting performance was followed for conducting tests [4]. The experimental performances of the cooker with the two cooking pots for the two different weathers are shown in Figs. 3 and 5

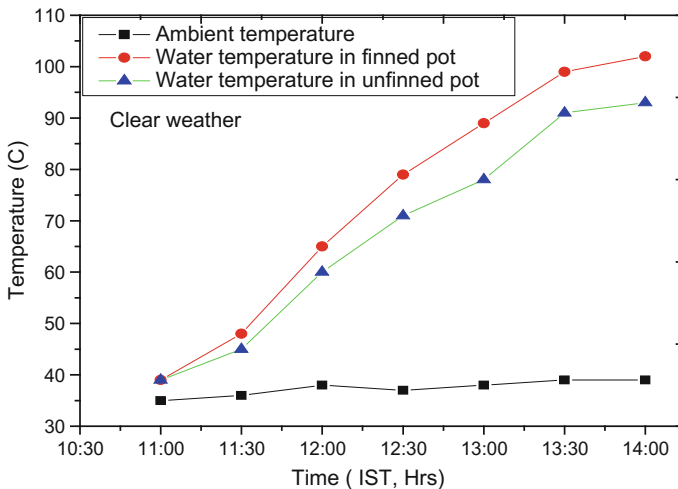


Fig. 2 Variation of temperature with time in clear weather condition

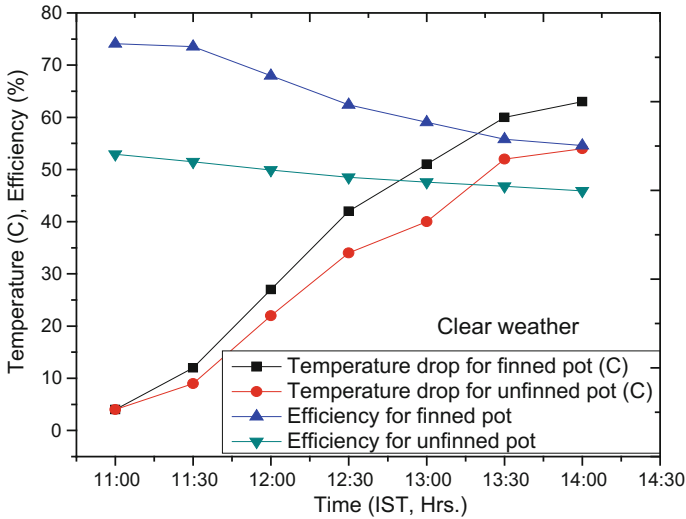


Fig. 3 Variation of temperature drop and efficiency with time in clear weather condition

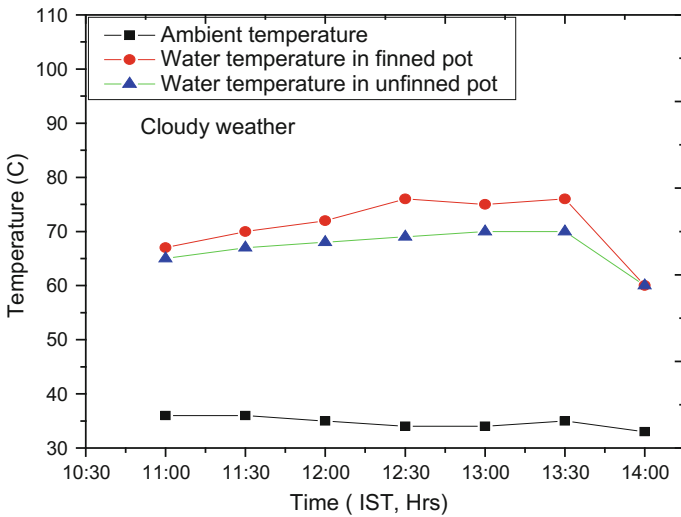


Fig. 4 Variation of temperature with time in cloudy weather condition

with 1-L water load. The temperature distribution in cooking pots, variation of ambient temperature, variation of water temperature in cooking pots and efficiencies are represented in Tables 2, 3, 4 and 5. Table 2 shows the various temperature distributions during the heating test for clear weather, and Table 4 expresses the same thing for cloudy weather condition (Fig. 4).

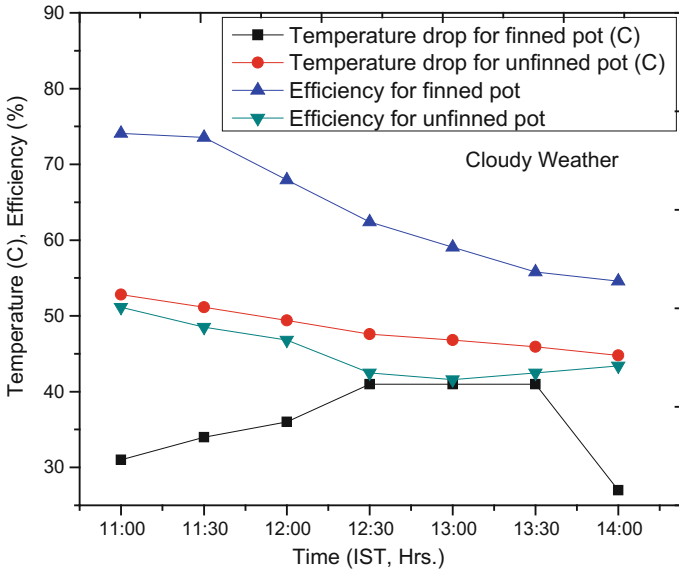


Fig. 5 Variation of temperature drop and efficiency with time in cloudy weather condition

Table 2 Temperature distribution in clear weather

Sl. No.	Time	Ambient temperature (°C)	Water in finned pot temperature (°C)	Water in un-finned pot temperature (°C)	Temperature drop (°C)		Solar radiation (W/m ²)
					For finned pot	For un-finned pot	
1	11:00 AM	35	39	39	4	4	700
2	11:30 AM	36	48	45	12	9	
3	12:00 Noon	38	65	60	27	22	
4	12:30 PM	37	79	71	42	34	
5	1:00 PM	38	89	78	51	40	
6	1:30 PM	39	99	91	60	52	
7	2:00 PM	39	102	93	63	54	

The efficiency decreases continuously with the cooking pot and the ambient temperature difference. When this difference becomes larger, the losses increase and the efficiency decreases. In addition, the efficiency for the finned pot is much higher than the water temperature increasing with time rapidly in early morning. The un-finned pot is especially at the lower values of temperature difference. The cooker efficiencies are calculated for 30-min period and assumed constant during this period. It is obvious that the efficiencies are high at early periods of the tests and decrease during afternoon. This behavior is due to the decrease in the rate of increase in ambient temperature with time.

Table 3 Temperature and efficiency in clear weather

Sl. No.	Temperature drop pot (°C)	Efficiency	Temperature drop for un-finned pot (°C)	Efficiency
1	4	74.1	4	52.9
2	12	73.54	9	51.5
3	27	67.96	22	49.9
4	42	62.4	34	48.5
5	51	59.05	40	47.6
6	60	55.79	52	46.8
7	63	54.6	54	45.9

Table 4 Temperature distribution in cloudy weather

Sl. No.	Time	Ambient temperature (°C)	Water in finned pot temperature (°C)	Water in un-finned pot temperature (°C)	Temperature drop(°C)		Solar radiation (W/m ²)
					For finned pot	For un-finned pot	
1	11:00 AM	36	67	65	31	29	700
2	11:30 AM	36	70	67	34	31	
3	12:00 Noon	35	72	68	36	33	
4	12:30 PM	34	76	69	41	35	
5	1:00 PM	34	75	70	41	36	
6	1:30 PM	35	76	70	41	37	
7	2:00 PM	33	60	60	27	54	

Table 5 Temperature and efficiency for cloudy weather

Sl. No.	Temperature drop finned pot (°C)	Efficiency	Temperature drop for un-finned pot (°C)	Efficiency
1	31	52.8	29	51.13
2	34	51.13	31	48.53
3	36	49.4	33	46.8
4	41	47.6	35	42.46
5	41	46.8	36	41.6
6	41	45.93	37	42.46
7	27	44.8	27	43.4

The heat transfer area of cooking pot is increased by addition of fins to the external surface. For this the water temperature inside the finned pot was higher than that of the un-finned counterpart. It can be seen that the water temperature reaches a maximum at about the 1.00 PM. Also, it is obvious that comparing the performance curves presented in Figs. 2 and 4 it can be seen that the water

temperature in the month of May is more than that in the month of July. This is due to higher solar intensity in May compared to July. Also, it is worth noted that the water temperature decreases during the afternoon hours.

5 Conclusion

A box-type solar cooker was constructed at IGIT, Sarang, Odisha, India. The thermal performance of the constructed cooker was investigated experimentally in local climatic conditions using both finned and un-finned cooking pots of same size. The heat transfer from cooker cavity to the pot surface was improved due to addition of fins. Fins can be considered to be extension of the pot surface which increases transfer of heat from and to the medium it is in contact depending upon the applications. The performance study of the constructed solar cooker was performed using the standard procedure for testing. The maximum temperature in the un-finned and finned pot reached 93 and 102 °C, respectively, in the clear weather condition and 70 and 76 °C in cloudy weather condition. The cooker efficiency can reach 53% for finned pot and 50% for un-finned pot in cloudy weather and 72 and 54%, respectively, in clear weather. The cooker temperature found to depend on the solar radiation intensity and the type of cooking pot it was found that, by using finned cooking pot higher temperature can be reached. The present solar cooker is of low cost, fabricated locally and simple in use. Further study is required to optimize this solar cooker. Further work can be planned to carry out similar experimentation in all the months to understand the cooking profile throughout the year.

References

1. Akoy Elamin, O.M., Ahmed Abdalla, I.A.: Design, construction and performance evaluation of solar cookers. *J. Agric. Sci. Eng.* **1**(2), 75–82 (2015)
2. Nayak, J., Sahoo, S.S., Swain, R.K., Mishra, A.: Heat loss modelling and analysis of solar cooker cavity: an analytical approach. *IEEE* (2016)
3. Cuce, E., Cuce, P.M.: A comprehensive review on solar cookers. *Appl. Energy* **102**, 1399–1421 (2013)
4. Funk, P.A.: Evaluating the international standard procedure for testing solar cookers and reporting performance. *Sol. Energy* **68**(1), 1–7 (2000)
5. Al-Azab, T.A., Al-Odat, M.Q., AlEssa, F.M.: Experimental investigation of the thermal performance of a box-type solar cooker with finned pot in Jordan. *Dirasat. Eng. Sci.* **36**(2), 145–153 (2009)
6. Sukhatme, S.P., Nayak, J.K.: *Solar energy, principles of thermal collection and storage-3e*. TMH, New Delhi (2008)

Design of Energy Efficient Voltage Multiplier Circuit for RF Energy Harvesting

Asmita Rajawat and P.K. Singhal

Abstract This paper presents the design of a voltage multiplier circuit for RF energy harvesting at 2.4 GHz. The voltage multiplier circuit designed converts the RF energy signal into DC and hence can be used to provide power to electronic devices. A voltage tripler and voltage quadrupler circuit using Schottky diode have been designed and simulated on Multisim. Simulation results reveal that the proposed passive voltage tripler circuit uses an ac input signal of $4 V_{\text{rms}}$ to produce a DC output voltage of 14.481 V, whereas voltage quadrupler circuit produced an output voltage of 19.369 V. The proposed design is applicable for commercial frequency band of 2.4 GHz.

Keywords RF energy harvesting · Schottky diode · Voltage tripler
Voltage quadrupler

1 Introduction

1.1 Related Work

Wireless technologies are in increasing use nowadays and are gaining attention by many researchers. Energy harvesting concept has come into existence to use the wireless energy as an alternative energy. Energy harvesting is the term used for capturing and storing the energy coming out from different sources. Wireless technology has become in use everywhere from satellite to cell phone. Energy radiated by the electronic devices can be utilized further by using energy harvesting devices. Wired connections are complicated, hazardous, while it is easy to transmit energy without wires and in turn the efficiency increases. The energy harvesters

A. Rajawat (✉) · P.K. Singhal
MITS, Gwalior, India
e-mail: asmitabhadoria@gmail.com

P.K. Singhal
e-mail: pks_65@yahoo.com

which are used to capture energy do not produce sufficient power to operate mechanical devices but produces sufficient power to operate low power devices. The main advantage is that we can get free electromagnetic energy from mobiles, TV broadcasting antennas, etc.

Rectenna is a device which can convert the power received from the above sources into DC power. Rectifier and antenna combine together to make rectenna. Antenna receives the microwave power, and rectifier converts it into DC power which can be used further. A low-pass filter is also connected between the antenna and rectifier to suppress the reradiation of higher harmonics from the diodes. Conversion efficiency is the microwave power that is converted into DC by rectenna [1].

To increase the efficiency, two approaches can be opted. The first approach is to increase the antenna aperture, and the second approach is to design a new rectifying circuit.

Figure 1 shows the block diagram of a basic rectenna.

The receiving antenna captures the EM waves coming from the ambient radio waves. The rectifying circuit converts it into DC power. The impedance matching circuit connects and matches the receiving antenna with the rectifying circuit. The rectifying circuit consists of a voltage multiplier, which is finally connected to the load. Much research has been done on voltage multiplier circuits. In [2], resonance circuit transformation method was used which gave an output of 0.3 V for an input power level of -26 dBm. A Cockcroft Walton multiplier circuit was presented in [3] which produced an output of 1 V DC for an input of $1 \mu\text{W}$. In [4], the design proposed produced an output of 1.04 V which was based on the Villard voltage doubler circuit. In [5], Villard voltage multiplier is designed using CMOS technology; efficiency of the circuit was found to be 22.97% at $66 \mu\text{W}$ input, and the output voltage was 1.5 V. Hong in [6] presented a 7-stage voltage multiplier which gave the output of 2.3 V. A 7-stage Schottky diode voltage doubler circuit was designed and simulated for an incident signal of 40 dBm which produced 3 mV across a $100 \text{ k}\Omega$ load [7]. In [8], 3-stage Villard voltage doubler circuit was designed for battery charging applications.

In this paper we have focused upon a simple voltage tripler and quadrupler to make the circuit compact and hence to further use it with an impedance matching circuit and output load to complete the overall energy harvesting system.

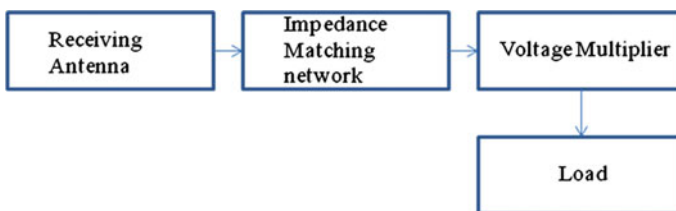


Fig. 1 Block diagram of a basic rectenna

1.2 Contribution

The research contribution of the paper is dedicated toward the study and simulation of two voltage multiplier designs to obtain a higher DC output voltage. The design concept of the paper is based on a tripler and quadrupler circuit because of its ease of fabrication, simple matching technique. Voltage tripler and quadrupler were chosen due to simple circuit without the need of cascading the stages.

1.3 Organization of Paper

The paper is organized as follows. Proposed multiplier designs and its simulation results are presented in Sects. 2 and 3 which validates the accuracy of the analysis. Section 4 concludes the paper.

2 Multiplier Design

The paper presents two multiplier designs. The software used for designing is Multisim, and the chosen value of the frequency in the task for simulation is 2.4 GHz. Schottky Diode HSMS-270B-BLKG from Avago Technologies is used for the voltage multiplier circuit. The diode can be used at high frequencies because of high switching speed and low forward voltage drop. The diode can also respond to noise spikes with rise times as fast as 1 ns because of picosecond switching. Signal degradation caused by waveshape loss is minimized by using low capacitance. Diode is not subjected to optimization. The modeling parameters are given by Agilent in their datasheet. The values of the capacitances are chosen same as the analysis of the results after prior research exhibited that the rise time and output voltage were found to be better with equal values of capacitances.

An equivalent load resistor of 1 k Ω is connected to obtain the final output across it. Without the use of load resistor, capacitor would hold the value of voltage indefinitely.

2.1 Voltage Tripler

Figure 2 shows a voltage tripler model. The newly crafted design is provided with an input voltage of 4 V_{rms} at 2.4 GHz. The tripler gives the output three times that of the input voltage. The output voltage is little less than the three times as the capacitors are partially discharged as the input moves (Table 1).

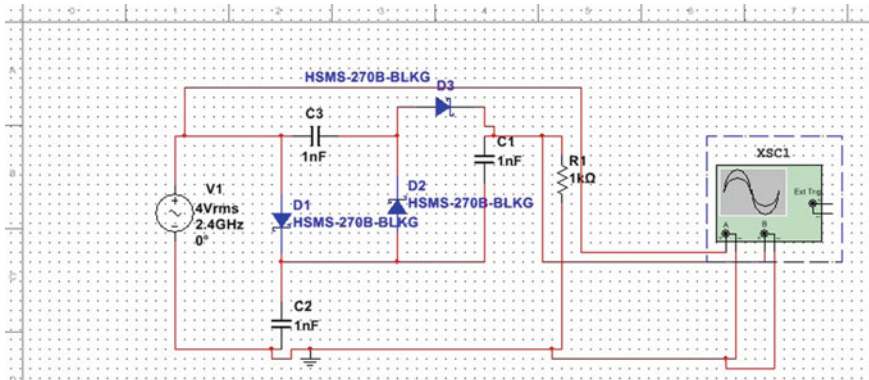


Fig. 2 Voltage tripler circuit on Multisim

Table 1 Voltage tripler parameters

Sr. No.	Components	Name in the circuit	Types	Ratings	Specifications
1	Diodes	D1, D2, D3	Schottky	HSMS-270B-BLKG	Zero biased, 2.4 GHz
2	Capacitors	C1, C2, C3	Ceramic capacitors		1 nano-farad, 10 V
3	Load resistor	R1			1 kΩ

2.2 Voltage Quadrupler

For enhancing the voltage four times, the design has been extended and a voltage quadrupler is simulated as shown in Fig. 3.

The parameters used for the quadrupler are same as that of the tripler.

3 Results and Discussion

Voltage tripler and quadrupler have been designed at 2.4 GHz after the RF signal is assumed to be incident at the input. The first design which is a tripler gave three times of the input across the load resistance. The quadrupler gave four times of the input. The results show that with increase in the stage the output DC voltage also increases. But, further increase in number of stages loading effect takes place and hence the voltage gain starts to sag considerably. So, voltage quadrupler could be a good choice for enhancing the DC output.

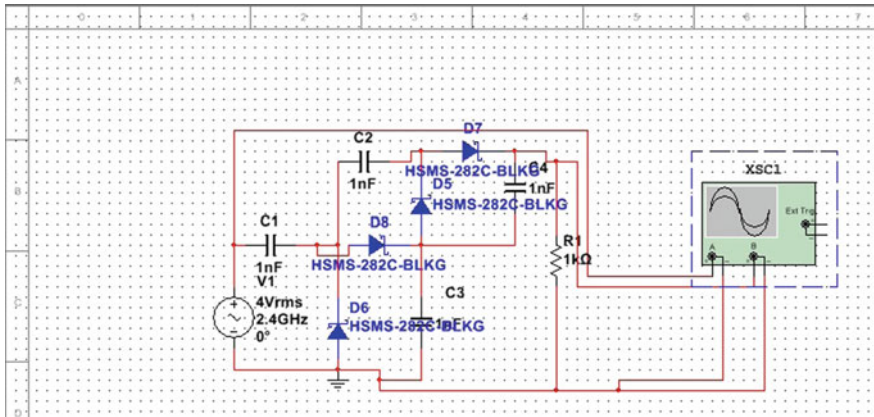


Fig. 3 Voltage quadrupler

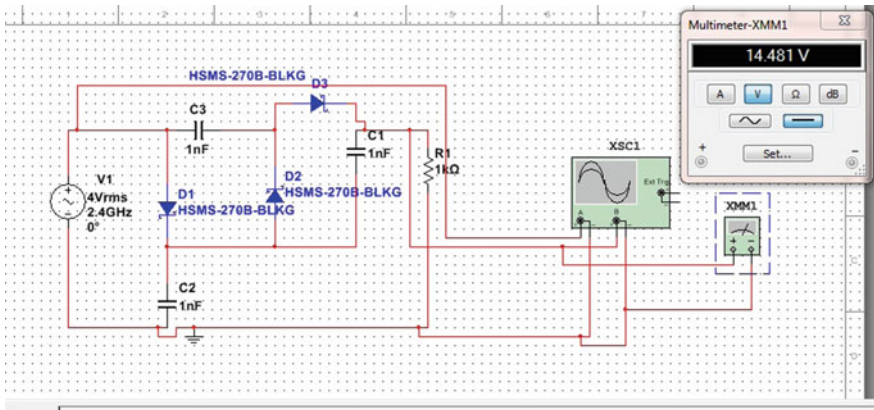


Fig. 4 Multimeter output of the voltage tripler

3.1 Results of Voltage Tripler

3.1.1 Multimeter Output of the Voltage Tripler

For the voltage tripler as shown in Fig. 4 the multimeter output depicts the value of output voltage across the load resistor which came out to be 14.481 V. The voltage is approximately three times that of the input voltage. The value is little less than exactly three times because of some losses in the capacitors.

3.1.2 Simulated Result of the Voltage Tripler

Figure 5 shows the simulated result of the voltage tripler. The result shows that the output DC voltage is 14.231 V which is in consistent with the result obtained with the multimeter.

3.1.3 Output DC Voltage Versus Rise Time of the Voltage Tripler

Figure 6 shows the graph obtained between the output DC voltage and rise time. The graph indicates that the output increases gradually and reaches approximately 10 V at 2 ns and then reaches 14 V at around 4 ns.

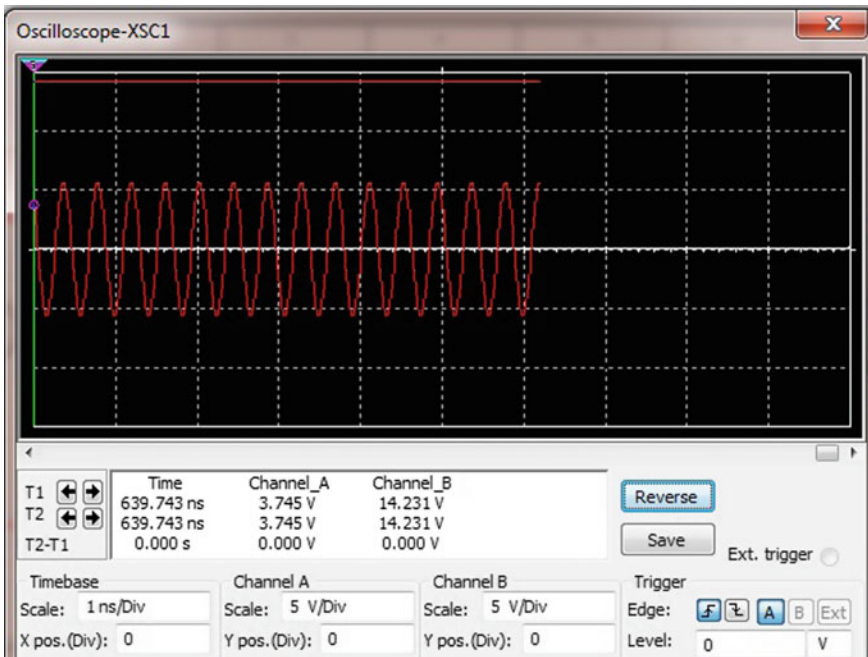


Fig. 5 Simulated result of the voltage tripler

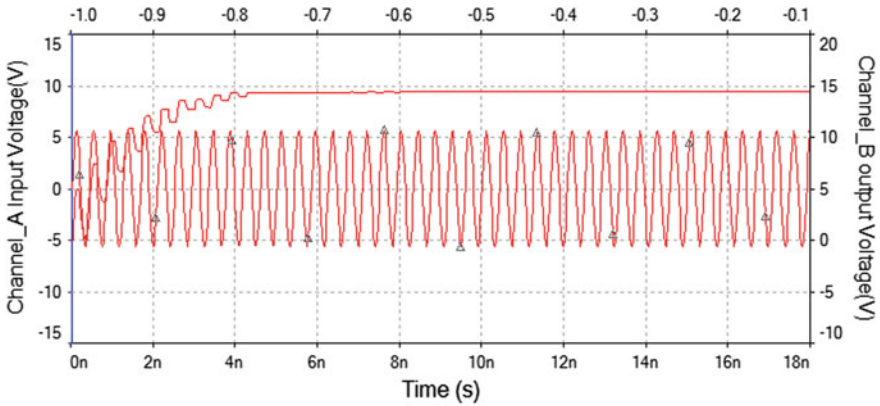


Fig. 6 Output DC voltage versus rise time of voltage tripler

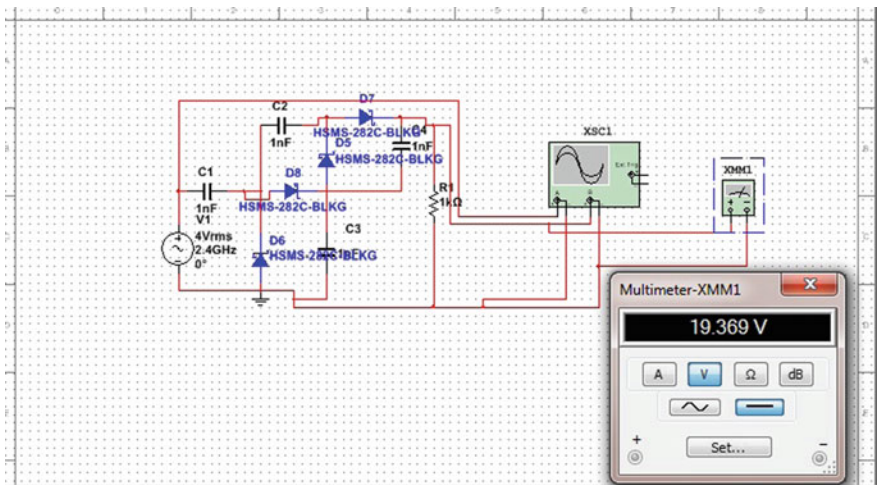


Fig. 7 Multimeter output of the voltage quadrupler

3.2 Results of Voltage Quadrupler

3.2.1 Multimeter Output of the Voltage Quadrupler

For the voltage quadrupler as shown in Fig. 7 the multimeter output depicts the value of output voltage across the load resistor which came out to be 19.361 V. The voltage is approximately four times that of the input voltage.

3.2.2 Simulated Result of the Voltage Quadrupler

Figure 8 shows the simulated result of the voltage quadrupler. The result shows that the output DC voltage is 19.361 V which is inconsistent with the result obtained with the multimeter.

3.2.3 Output DC Voltage Versus Rise Time of Voltage Quadrupler

Figure 9 shows the graph obtained between the output DC voltage and rise time. The graph indicates that the output increases gradually and reaches approximately 15 V at 4 ns and then reaches approximately 19 V at around 8 ns.

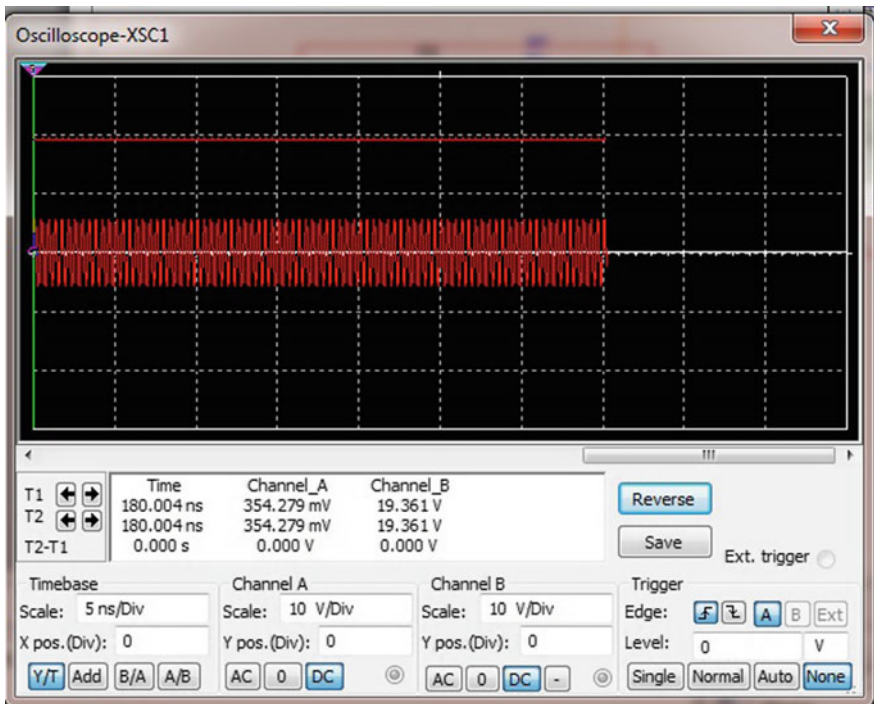


Fig. 8 Simulated result of the voltage quadrupler

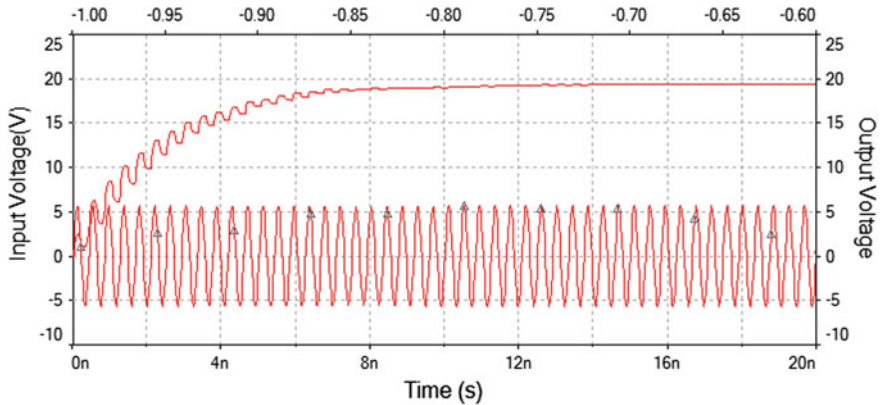


Fig. 9 Output DC voltage versus rise time of voltage quadrupler

4 Conclusion

After analyzing the simulation results it has been observed that the proposed quadrupler can be used as one of the modules in the RF–DC conversion at 2.4 GHz. The tripler gave three times the input which is 14.4 V across the 1 k Ω load resistor with input of 4 V_{rms}, and the quadrupler gave 19.3 V which is four times the input signal. The voltage multiplier circuit so designed may be the better choice to convert the RF energy signal into DC and hence can be used to energize low power electronic devices. The next phase of the research is to use this voltage quadrupler circuit at the output of a receiving antenna with appropriate matching network and a low power electronic device at the output for the complete RF energy harvesting system at 2.4 GHz.

References

1. Brown, W.C.: The receiving antenna and microwave power rectification. *J. Microw. Power* **5**, 279–292 (1970)
2. Ungan, T., Reindl, L. M.: Concept for harvesting low ambient RF-sources for microsystems. http://www.imtek.de/content/pdf/public/2007/powermems_2007_paper_ungan.pdf. Accessed 20 Mar 2010
3. Wang, J., Dong, L., Fu, Y.: Modeling of UHF voltage multiplier for radio-triggered wake-up circuit. *Int. J. Circuit Theory Appl.* (2010). doi:10.1002/cta.692
4. Arrawatia, M., Baghini, M.S., Kumar, G.: RF energy harvesting system at 2.67 and 5.8 GHz. *Proceedings of Asia Pacific Microwave Conference*, pp. 900–903 (2010)
5. Jabbar, H., Young, S.S., Taikyeong, T.J.: RF energy harvesting system and circuits for charging of mobile devices. *IEEE Trans. Consum. Electron.* **56**(1), 247–253 (2010)

6. Hong, S.S.B., Ibrahim, R., Khir, H.M.M., Zakariya, M.A., Daud, H.: WI-FI energy harvester for low power RFID application. *Prog. Electromagnet. Res. C* **40**, 69–81 (2013)
7. Ali, E.M., Yahaya, N.Z., Perumal, N., Zakariya, M.A.: Design of RF to DC rectifier at GSM band for energy harvesting applications. *J. Eng. Sci. Soc.* **10**(2), 15–22 (2014)
8. Ali, E.M., Yahaya, N.Z., Perumal, N., Zakariya, M.A.: Design and development of harvester RECTENNA at GSM band for battery charging applications. *J. Eng. Appl. Sci.* **10**(21), 10206–10212 (2015)

Integrated Model of Renewable Energy Sources Feeding Both AC and DC Load

Sisir Chettri, Suyog Pradhan, Karma Sonam Sherpa
and Saikat Chatterjee

Abstract Hybrid renewable energy system consists of two or more renewable energy sources combined together allowing improved system efficiency and reliability. Integrating this source creates a stand-alone energy source, i.e., both dependent and consistent. In this paper, an attempt has been made to integrate the power generated by renewable energy sources using programmable logic controller (PLC). Here PLC decides which source is to be connected for the given load according to the designed ladder logic program that was developed in PLC using Rx logic software. Finally, a prototype model of integrated renewable sources has been successfully implemented using PLC kit which can feed AC as well as DC load.

Keywords Hybrid renewable energy · Programmable logic controller
Rx logic · Single phase inverter · Relay

1 Introduction

The world is facing a number of challenges related to energy sustainability, continuity and security. The depletion of fossil fuel resources as well as the environment impact of burning these fuels has led to increased energy crisis, climate changes such as atmospheric temperature rise due to the increase in greenhouse

S. Chettri · S. Pradhan · K.S. Sherpa · S. Chatterjee (✉)
Department of Electrical and Electronics Engineering,
Sikkim Manipal Institute of Technology, Rangpo, Sikkim, India
e-mail: saikat.smit86@gmail.com

S. Chettri
e-mail: sisirchettri0@gmail.com

S. Pradhan
e-mail: suyogpradhan11@gmail.com

K.S. Sherpa
e-mail: karmasherpa23@gmail.com

gases emission, high oil prices which made interest in developing alternative and more sustainable energy sources [1]. The solution to above problem may be renewable energy sources. The chances leading to the depletion of fossil fuels can be prevented by using renewable energy sources. The renewable energy sources are unpredictable and inconsistency and they depend on climatic changes and the variation in the output may not match with the time distribution of load demand, so integrating different renewable energy sources using platforms like PLC can avoid such problems and creates stand-alone energy sources.

For integrating, different platforms can be used but due to simplicity and easy to control, in this paper integration using PLC is preferred [2]. Different loads and source were interfaced with input and output terminal of PLC, respectively. Ladder logic was developed in such a way that it activates different sources according to the load demand. When the load demand is low as compared to the generation, the excess power can be stored in the battery. When sources fail to supply desired power, then battery can fulfill the load demand, thus increasing the system efficiency.

2 Different Types of Renewable Energy Sources Used

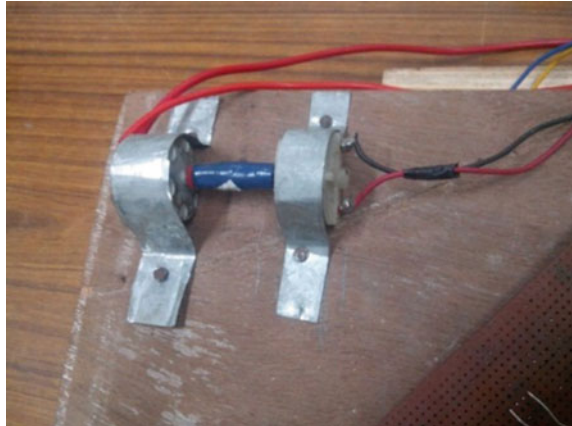
2.1 Solar Power

It is a process to harvest solar energy. Figure 1 shows a prototype of solar power used in this project.

Fig. 1 Photovoltaic (PV) cell



Fig. 2 Hydel power generation using motor coupling



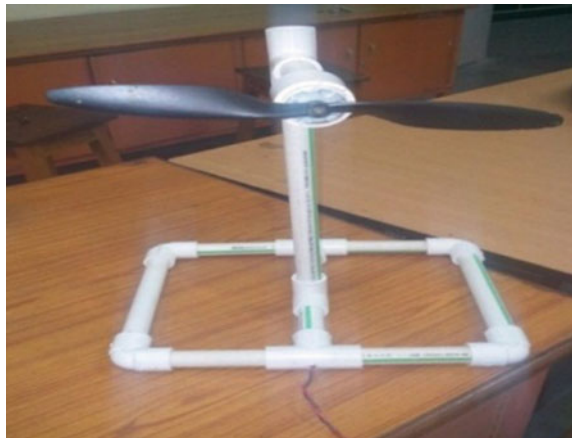
2.2 *Hydel Module*

Hydropower or water power is power derived from the energy of falling water and running water, which may be harnessed for useful purposes. Hydel module is realized using motor coupling as shown in Fig. 2.

2.3 *Wind Module*

Wind energy is the energy contained in the force of the winds. Wind energy can be converted into mechanical energy for performing work [3]. Wind generation system was worked upon, for that a small DC motor was used as a generator driven by a

Fig. 3 Wind power generation



wind through a turbine. When DC motor is driven in opposite direction at some speed, then motor acts as a generator and generates voltage across its terminals corresponding to the speed of rotation of the turbine which in turn depends upon the wind velocity. The wind model is shown in Fig. 3.

3 Methodology Project Model and Implementation

3.1 Block Diagram of Project Model

Figure 4 shows the basic block diagram of hardware model of hybrid power system considered in this project which consists of three renewable energy sources, i.e., solar, hydel and wind. Here different relays of 6 and 12 V are used which is actuated from the PLC kit. A battery bank is used which meets the load demand when all the sources fail.

This can be better understood from the working mechanism shown in Fig. 5. In Fig. 5, source is connected with the common point of the 12-V relay. The normally closed (NC) contact of a 12-V relay is connected with the battery bank and the

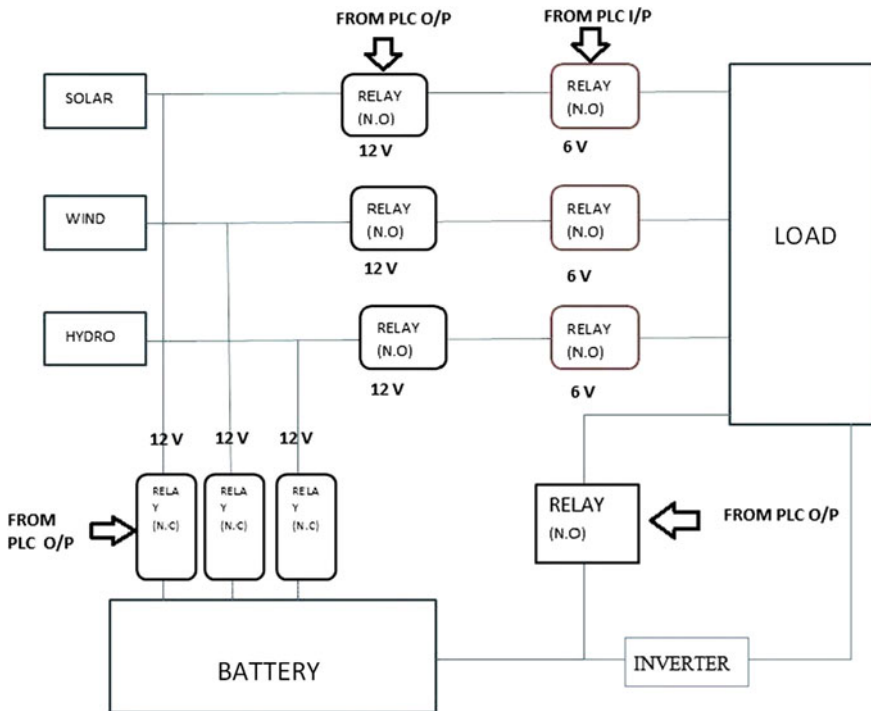


Fig. 4 Block diagram showing integration of different renewable energy sources

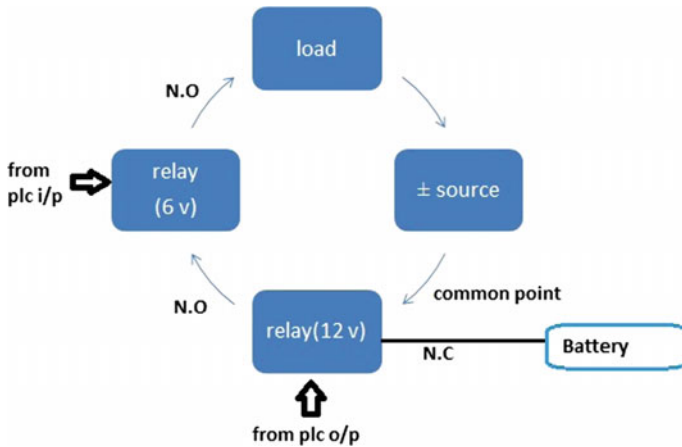


Fig. 5 Working mechanism showing integration of renewable energy sources

normally open (NO) contact with the load. When the source is ON, the battery gets charged as it is connected with the normally closed contact of the relay. When the load is connected, the PLC algorithm decides which source is to be connected and activates the 12-V relay. Now, as this relay gets activated, the common point shifts from normally closed to normally open. As a result, it gets disconnected from the battery and gets connected with the load. When any source feeds the load, the remaining sources charge the battery. When all the sources fail, then the battery meets up the load demand.

3.2 *PLC Interfacing with Hardware Module*

The hardware module is designed such that it can feed both AC and DC loads. The ladder logic executed in PLC is shown in Fig. 6.

In the ladder logic, the analog knob is varied which connects different loads at different ranges. The limit for first source, second source and third source is (1–3), (4–6), (7–10), respectively. The sources get connected according to the value stored in destination in the move instruction and not according to the value shown in the display of PLC kit. Here the move instruction was used. The value of the analog input given using the knob was moved to the register B3:0 by this move instruction. Further scaling was done using the divide instruction. The limit test was done in the range if (1–3), (4–6), (7–10) for solar, wind and hydro, respectively. This limit test checks the value stored in register B3:0 for the ranges provided and activates the corresponding output.

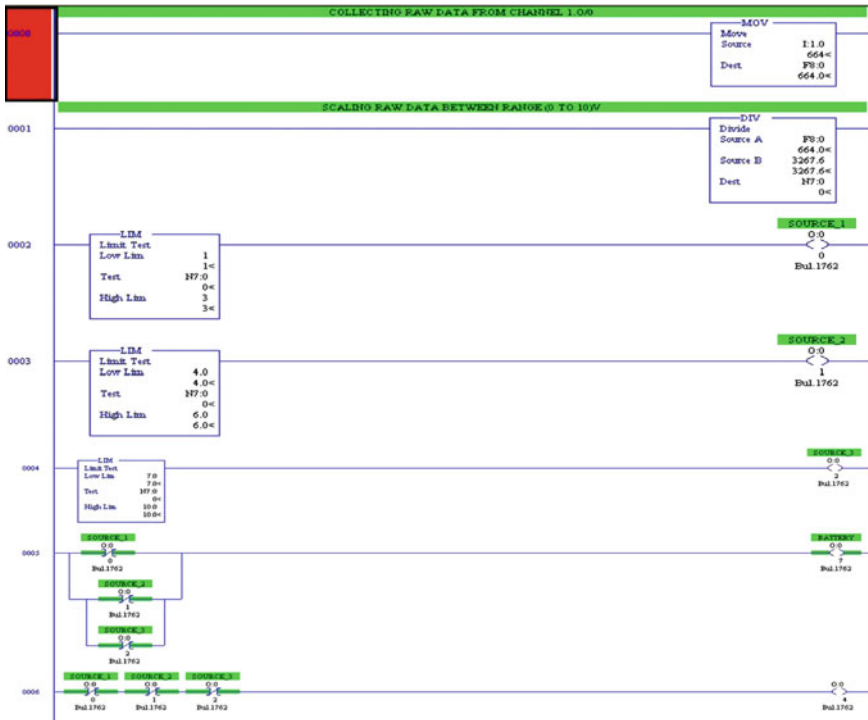


Fig. 6 PLC ladder logic

3.2.1 Feeding DC Load

Here, analog input from the PLC kit was used in the presence of external source and load. The external loads used are light-emitting diode (LED) fabricated in printed circuit board (PCB). Figure 7 shows the hardware module interfaced with PLC using external relays. Supply to the input coil of relay is tapped from PLC. When the input voltage knob is varied, the 6-V relay gets actuated, and the load gets connected. Now, according to the ladder logic particular source gets on and it feeds the load.

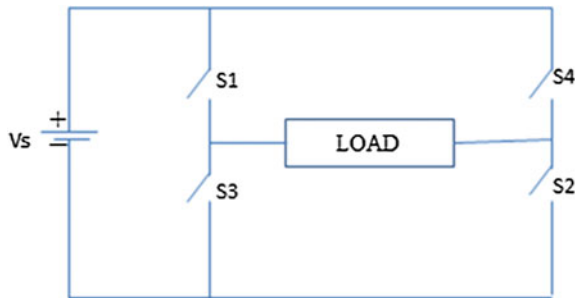
3.2.2 Feeding AC Load

In order to feed AC load, inversion of DC to AC is necessary [4]. For this single phase full-bridge inverter is designed using MOSFET IRF540 and IRF9540 as a switch. Figure 8 shows a single phase full-bridge inverter where the switches S1 and S2 are IRF540 (p-channel) and S3 and S4 are IRF9540 (n-channel). So, a common pulse is given to all the switches. Switching pulse is generated using

Fig. 7 Hardware module interfaced with PLC

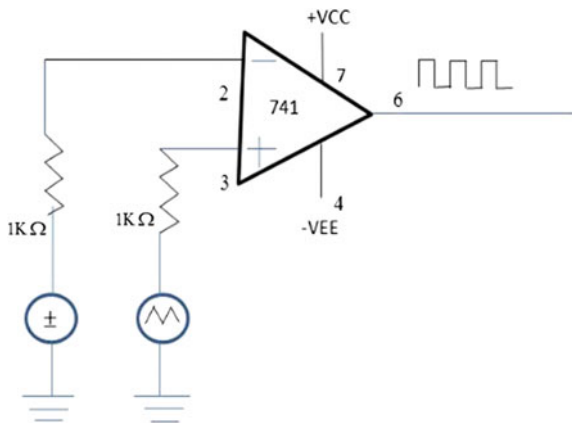


Fig. 8 Full-bridge inverter



Op-Amp IC741 used as a comparator circuit as shown in Fig. 9. Triangular wave is compared with either a DC or a sine wave.

Fig. 9 Comparator circuit



Triangular wave used in comparator circuit is generated from Fig. 10. Frequency of triangular wave can be adjusted to a desired level by adjusting the value of resistance R_b [5].

4 Result and Observation

4.1 Hardware Module Interfaced with PLC for DC Load

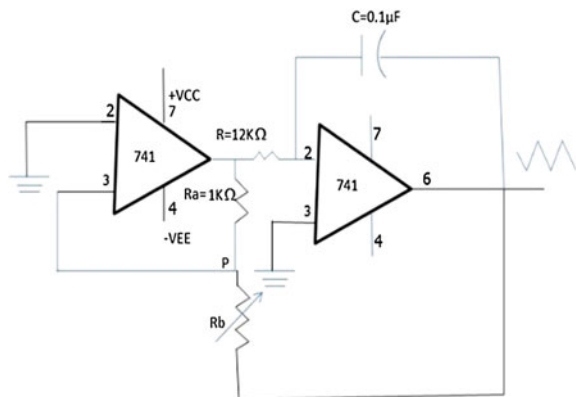
Here different loads and sources were interfaced with the PLC using analog voltage as the input. When a particular source feeds the load, remaining sources charge the battery. Figure 11 shows a condition when all the sources fail. At this situation, the battery meets the load demand.

As shown in Table 1, the source which is capable to meet the load demand at a particular time gets connected with the load and at that time other two sources which are on charges the battery. When individual sources fail to meet the load demand, at that time the battery supplies power to the load and the sources charge the battery.

4.2 Hardware Module Interfaced with PLC for AC Load

Figure 12 shows the triangular output which is compared with DC source to generate pulse as shown in Fig. 13. By comparing triangular wave with a DC source, adjusting the output frequency of the inverter to a desired value was being difficult. Figure 14 shows the inverter output when triangular wave is compared with sinusoidal wave of 50 Hz. In this method, the output frequency of inverter was obtained as 50.86 Hz as shown in Fig. 15.

Fig. 10 Ramp signal generator



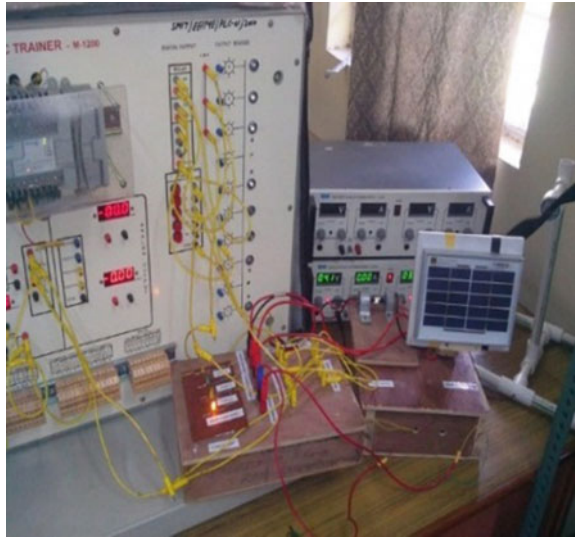


Fig. 11 Battery feeding the load

Table 1 Operating process for feeding DC load

Loads	S1	S2	S3	Battery
1	ON	OFF	OFF	S2 and S3
2	OFF	ON	OFF	S1 and S3
3	OFF	OFF	ON	S1 and S2
4	OFF	OFF	OFF	ON

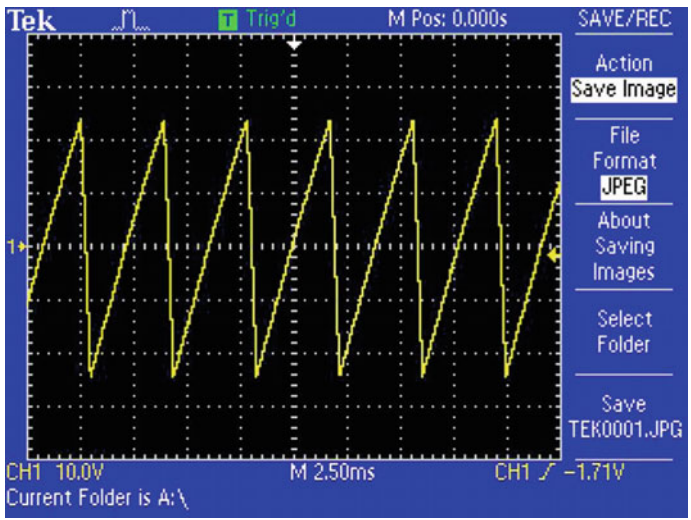


Fig. 12 Triangular wave

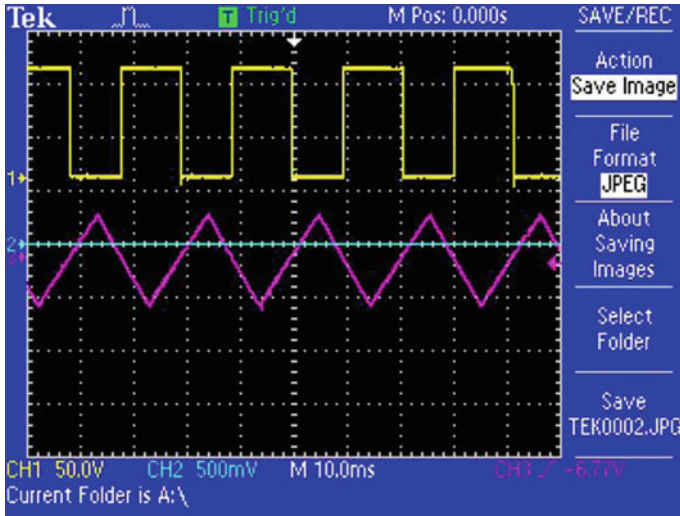
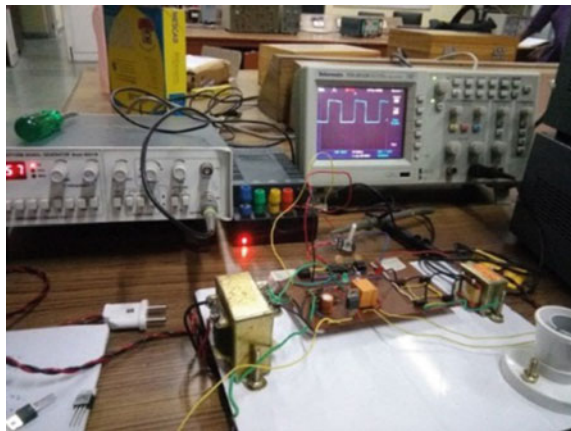


Fig. 13 Pulse output

Fig. 14 Hardware module for AC load



5 Conclusion

In this project, different renewable energy sources are combined namely solar, hydro and wind energy sources, to produce more efficient and environment friendly energy. To realize Wind and Hydro power, motor coupling is done. And for solar, photovoltaic cell (PV) is used. Programmable logic controller (PLC) decides which source is to be connected according to the designed ladder logic program that was developed in PLC using Rx logic software.

Fig. 15 Inverter output voltage



With the introduction of Integrated Power System based on renewable energy sources, rural areas can be electrified with clean, sustainable, more reliable and continuous power supply at reasonably low price [6]. Increasing environmental pollution can be controlled up to some extent, and burdens on conventional non-renewable energy sources will be eliminated. Storage system employed in this system provides back-up supply of power, i.e., when sources fail to supply desired power, then battery can fulfill the load demand, thus increasing the system efficiency. Further, an inverter was made using an analog circuit which can be used in order to feed the AC loads.

In this paper, prototype model of integrated renewable sources has been successfully implemented using PLC kit. Same concept can be implemented at higher level to meet the increasing power demand in future.

References

1. Perera, K.S., Aung, Z., Woon, W.L.: Machine learning techniques for supporting renewable energy generation and integration: a survey. *Lecture Notes in Computer Science*, vol. 8817, pp. 81–95 (2014)
2. Jaganmohan Reddy, Y., Pavan Kumar, Y.V., Padma Raju, K., Ramsesh, A.: PLC based energy management and control design for an alternative energy power system with improved power quality. *Int. J. Eng. Res. Appl.* **3**, 186–193 (2013)
3. Mamman, J., Pam, G.Y., Bala, E.J.: Design construction, simulation and testing of a 300 W wind powered battery charger. *Int. J. Eng. Sci.* **3**, 69–76 (2014)
4. Mamun, A.A., Elahi, M.F., Quamruzzaman, M., Tomal, M.U.: Design and implementation of single phase inverter. *Int. J. Sci. Res.* **2**, 163–167 (2013)
5. <http://www.circuitgallery.com/2012/04/triangular-wave-generator-using-op-amp.html>
6. Kumar, S., Garg, V.K.: A hybrid model of solar-wind power generation system. *Int. J. Adv. Res. Electr.* **2**, 4107–4116 (2013)

Investigating Effects of Shading on Performance of Solar Conversion Devices

K.J. Shruthi, P. Giridhar Kini, C. Viswanatha, Mohan Divekar and A. Amruthakala

Abstract The amount of electrical energy generation from solar photovoltaic (SPV) module depends on the range of incoming solar radiation. Generated current (as well as output power) is proportional to the amount of solar irradiance received by module. SPV module typically consists of 36 or 72 solar cells of specific area interconnected in series or parallel network to achieve required power output and in order to generate rated power, all cells should be exposed to same irradiance. In this paper, partial shading assessment on 40 W module connected in distributed network is carried out. Individual module is connected with solar parameter data logger to measure accurate instantaneous data. The data logger is based on INC MPPT method. Cell level modeling is carried out to understand the effect on module output power when individual solar cells are exposed to different irradiance levels. Experimental results show that short circuit current reduces by nearly 60% when even single solar cell in module gets partially shaded.

Keywords Solar radiation · Maximum power point tracking · Measurement Partial shading · Solar photovoltaic conversion

K.J. Shruthi (✉) · A. Amruthakala
ID, CPRI, Bengaluru, India
e-mail: shruthi.cpri@gmail.com

A. Amruthakala
e-mail: amr@cpri.in

P. Giridhar Kini
Department of EEE, MIT, Udupi, India
e-mail: giridhar.kini@manipal.edu

C. Viswanatha
DCCD, CPRI, Bengaluru, India
e-mail: c.viswanatha2013@gmail.com

M. Divekar
R & D, CPRI, Bengaluru, India
e-mail: mohandivekar@yahoo.com

1 Introduction

Current technological advances have capacitated solar energy generation as attractive alternative renewable energy generation. On geographical plane, India is located from latitude of $8^{\circ} 4'$ to $37^{\circ} 6'N$ and longitude of $68^{\circ} 7'$ to $97^{\circ} 25'E$ exposing it to abundant solar radiation throughout the year. By receiving 300 days of sunshine makes India idea for solar electrical power generation [1]. The generated electrical energy is currently used to meet the energy demands for different purposes such as agricultural, lighting, drinking, and cooking. The Jawaharlal Nehru National Solar Mission was launched by MNRE, a Government of India organization with a target of 20,000 MW solar-grid-connected energy generation by the year 2022. The current solar-grid-connected energy generation (by July 2016) is 8000 MW with 238 MW generation in Karnataka state. There are several technical issues related to grid connected solar energy generation which require critical consideration before design [2].

Different types of SPV cells have been developed which have varying performances and efficiencies. A monocrystalline silicon solar cell has conversion efficiency of 12–18%, while a polycrystalline silicon solar cell has 8–12% [3]. These conversion efficiencies stated by the manufacturers are measured under laboratory controlled conditions, and in practical installations, conversion efficiencies of the solar cells vary greatly depending upon the varying atmospheric conditions such as incoming solar irradiance, temperature, humidity, and wind speed. IEC 61215 is standard followed for measuring the conversion efficiency under standard test conditions (STC). Before solar power plant installation, site inspection is a very important as the solar radiation received is site specific and varies globally throughout the year. The data can be further used for solar energy prediction using various models. Solar radiation can be measured by instruments such as pyranometers and pyrhemometers. However, these instruments are very expensive and alternative solutions for radiation measurement developed. Maximum power point tracking (MPPT)-based solar parameter logger is designed and developed which works on sine correction factor for prediction of accurate solar irradiance on clear sky days [4].

Output power generation from same rated modules and from different manufacturers exposed to same input conditions can be different. When solar cells are connected in series or parallel interconnection to form module or modules connected in string, care should be taken that mismatch of I and V is within tolerance. For modules connected in string, mismatch in I–V can result in large power drops [5]. One common phenomenon experienced at solar installations for mismatched I and V is shading [6–12]. Shading can be caused due to several reasons such as surrounding high rise buildings, passing clouds, bird droppings, and dust accumulation over modules, trees. Partial shading is very relevant today, and different techniques have been analyzed and implemented to overcome effects of shading. One popular method to analyze partial shading is use of distributed monitoring over centralized power monitoring [6]. In distributed power monitoring, each individual

module is equipped with a power monitoring equipment which can easily measure any reduction in power output from the module and required action can be taken. In both distributed and centralized power monitoring structures different, MPPT techniques are required for accurate power measurements [9–12].

2 Modeling SPV Module and MPPT

Simple single diode electrical representation of solar photovoltaic cell is shown in Fig. 1. Mathematical modeling for single diode solar photovoltaic cell is given in Eq. (1).

Incremental conductance technique is used as MPPT technique by the solar parameter data loggers for accurate instantaneous module output power measurement. INC conductance method for MPPT is illustrated in Fig. 2 [4].

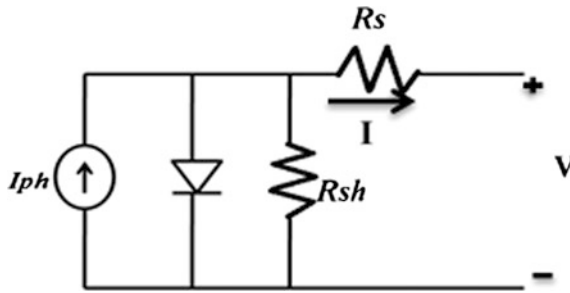


Fig. 1 Single diode SPV cell model

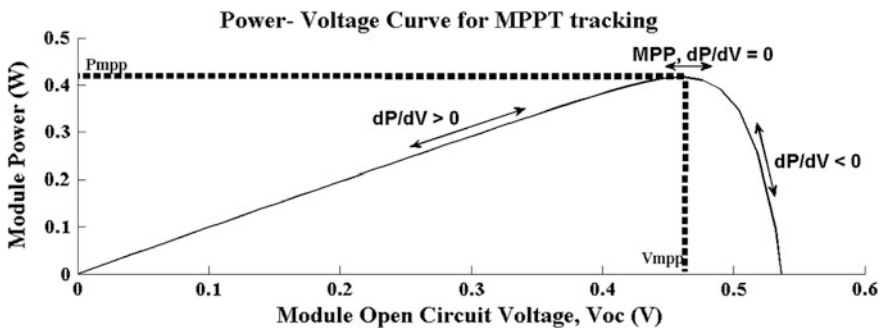


Fig. 2 INC conductance MPPT

2.1 Effects of Shading on Performance of SPV Module

In case of partial shading, only a part of module is shaded instead of complete module. Here an attempt at modeling partial shading on a module consisting of 36 solar cells in series interconnection is done. It is assumed that all the solar cells have same operating temperature since variation in temperature on power output has very low effect on its output. In order to have similar performance by solar cells of same rating, allowable tolerance limit is considered. In this analysis, tolerance limit range is selected to be from 0 to 1. Higher tolerance value reduces the short circuit current and in turn peak operating power output from the solar module. For ease, this analysis is modeled in excel. Two cases are analyzed: first when uniform irradiance falls on all the 36 solar cells and second when shading analysis involves shading on individual 36 cells exposed to different irradiance levels. This modeling gives better understanding about the effect of partial shading on the overall power output of module at cell level.

$$I = I_{ph} - \left\{ \exp\left(\frac{(V + IR_s)}{k}\right) - 1 \right\} - \left(\frac{(V + IR_s)}{R_s}\right) \tag{1}$$

where $k_0 = \frac{AkT}{q}$.

I, V —cell output current (A) and voltage (V); I_{ph} —light generated current (A); I_{sat} —cell reverse saturation current (A); A —ideality factor (=1); k —Boltzmann’s constant ($=1.3805 \times 10^{-23}$ N m/K); T —cell temperature ($^{\circ}$ C); q —electronic charge ($=1.6 \times 10^{-19}$ C); R_s —series resistance (Ω); R_{sh} —shunt resistance (Ω).

When multiple solar modules are connected in series interconnection to form a string, partial shading will reduce the string output power significantly. To understand this, MATLAB model of partial shading on string of three modules in series interconnection is developed and output characteristics are illustrated in Fig. 3. The solar modules are exposed to different illumination levels of 1000, 850 and 400 W/m². In I–V and P–V characteristics, multiple peaks can be observed as a reason for exposure to different illumination levels. The figure shows that generated

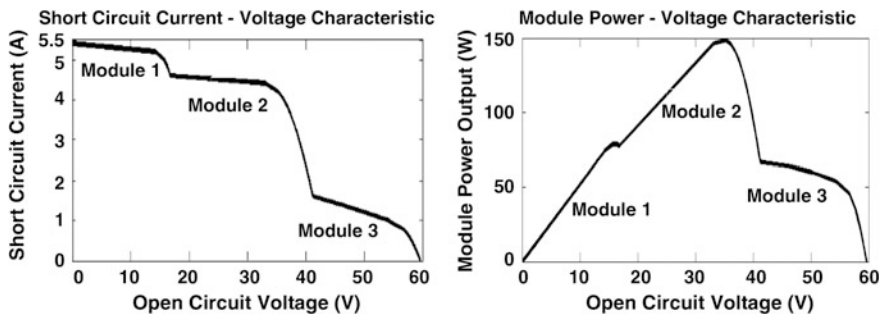


Fig. 3 I–V and P–V characteristics for partial shading on string

current in module is directly proportional to level of irradiance falling on it and correspondingly its output power varies. When modules are interconnected in series interconnection, the dominant current is the low value current generated by module exposed to low illumination level which will bring down the overall string power greatly.

3 Results and Discussion

Two types of experimental analysis are carried out using 40 W SPV module of WAREE make. Two modules are used one as reference and other as test module. Initially both the modules are cleaned from the dust/dirt accumulated on them. Both the panels are held at same optimized tilt angle of 12° as per the location of module installation. Power output from both is normalized to avoid difference in measurement. Pyranometer instrument is used to measure incoming solar irradiance. Both the modules are connected to solar parameter data logger. The test panel is the one which is shaded at different conditions, and the measured output power is compared against that of reference module which is not shaded, i.e., received irradiance without any obstruction.

In first experiment, three conditions are tested: Condition 1 (C1): single cell of module is shaded, Condition 2 (C2): two cells of module are shaded, and Condition 3 (C3): half module (18 cells) is shaded. The results are tabulated in Tables 1 and 2. The generated short circuit current is proportional to the incoming irradiance; however, with increased irradiance, the operating temperature of the module increases and brings down the power conversion efficiency. The drop in conversion efficiency increases in case of shading on module, and results are tabulated in Table 2. Figures 4 and 5 show the graphical representation of measured module output power and short circuit current comparison between reference and test modules at different conditions. From the measurements, it can be seen that when single solar cell is shaded the power output from test panel is less than 21.508% that of reference module output.

In second experimental setup, the active area of 3.76 ft² is entirely covered by mesh as shown in Fig. 6. In order to calculate the percentage irradiance of obstruction from the mesh, its dimensions were measured using high-resolution optical spectrometer. From the measurements, it is determined that the mesh results in 72.88% obstruction of incoming solar irradiance on the module. Measured results

Table 1 Power output measurements

Conditions	Reference panel (W)	Test panel (W)	Solar radiation (W/m ²)	Difference power (W)
C1	34.517	27.093	481.689	7.424
C2	33.950	24.581	499.511	9.368
C3	29.300	23.206	492.553	6.094

Table 2 Short circuit current measurements

Conditions	Reference panel (A)	Test panel (A)	Current difference (A)	Current difference (%)
C1	2.369	0.948	1.420	59.958
C2	2.405	0.227	2.178	90.561
C3	2.385	0.096	2.286	95.974

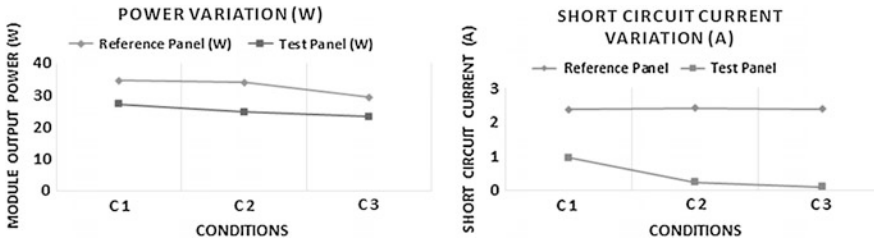


Fig. 4 Module output power and short circuit variation at different partial shading conditions

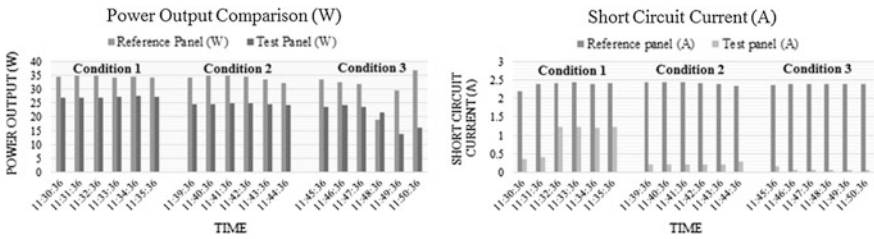
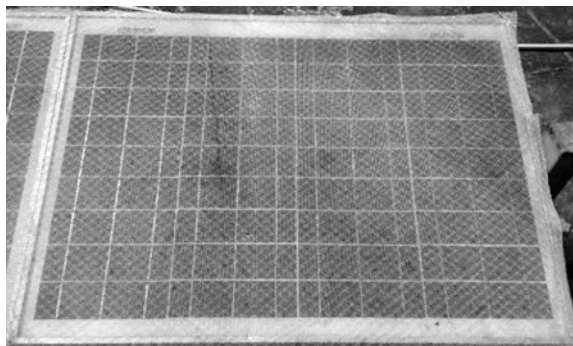


Fig. 5 Comparison between reference module and test module for output power and short circuit current at different partial shading conditions

Fig. 6 Use of mesh for partial shading experiment



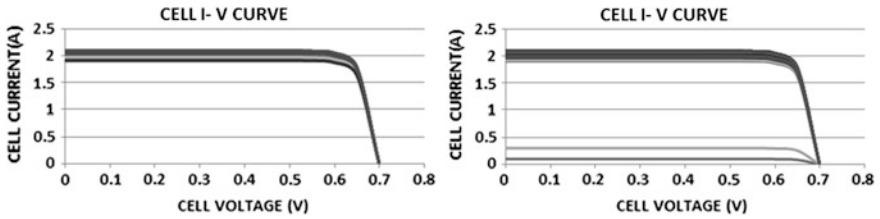


Fig. 7 Solar cell I-V curve for uniform illumination and partial shading

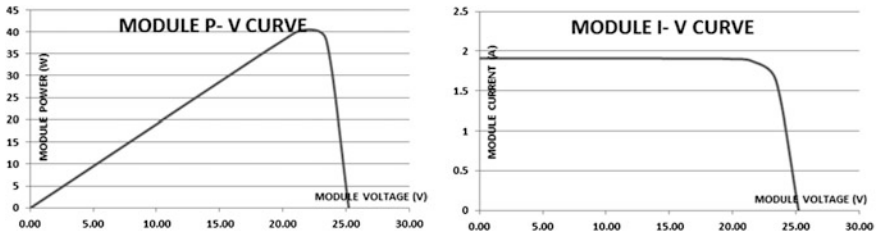


Fig. 8 40 W module P-V and I-V curve for normal illumination

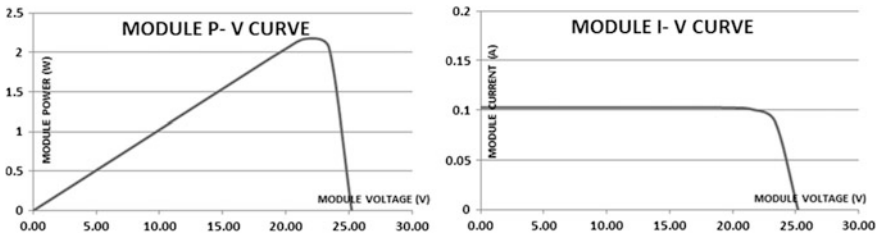


Fig. 9 40 W module P-V and I-V curve for partial shading

show that conversion efficiency of test module is reduced by 2.165% than the reference module.

As explained in previous section, the tolerance limit is set as 0.05 in excel modeling. Figure 7 illustrates individual I-V characteristic 36 solar cells of 40 W module under uniform illumination and partial shading. For analysis, two solar cells of module are exposed to lower illumination level 5 and 15% illumination where 100% illumination is equivalent to 1000 W/m^2 . Figures 8 and 9 illustrate P-V and I-V characteristics of 40 W module under uniform illumination and partial shading conditions. The excel model can be used to analyze the effect on overall module power output with individual cell shaded.

4 Conclusion

Two types of experiments were conducted to study the effects of partial shading on the power conversion efficiency of two 40 W polycrystalline solar modules. From experimental measurements, it can be concluded that the difference in power conversion efficiency of shaded module is less than 2.00% in comparison with non-shaded module. For single solar cell shading, the generated current reduces by 60%, thereby reducing the module overall power yield by 20%. Thus, shading should be avoided to optimize power yield. It is further observed that power yield reduces due to dust accumulation also, and thus, periodic cleaning of solar modules is very essential. Future work involves investigation of solar power yield optimization techniques and modeling which will be published later.

Acknowledgements The research work is carried out in Central Power Research Institute, Bangalore, under guidance of experts from organization.

References

1. Ramachandra, T.V., Jain, R., Krishnadas, G.: Hotspots of solar potential in India. *Renew. Sustain. Energy Rev.* **15**, 3178–3186 (2011)
2. Eltawil, M.A., Zhao, Z.: Grid-connected photovoltaic power systems: technical and potential problems—a review. *Renew. Sustain. Energy Rev.* **14**, 112–129 (2010)
3. Praid, B., Iniyar, S., Goic, R.: A review of solar photovoltaic technologies. *Renew. Sustain. Energy Rev.* **15**, 1625–1636 (2011)
4. Shruthi, K.J., Kini, P.G., Viswantha, C.: Unconventional and optimized measurement of solar irradiance in Bengaluru using solar photovoltaic techniques. *ICTACT J. Microelectron.* **2**, 230–236 (2016)
5. Spertino, F., Akilimali, J.S.: Are manufacturing I-V mismatch and reverse current key factors in large photovoltaic arrays. *IEEE Trans. Industr. Electron.* **56**, 4520–4531 (2009)
6. Hanson, A.J., Deline, C.A., MacAlpine, S.M., Stauth, J.T., Sullivan, C.R.: Partial shading assessment of photovoltaic installations via module-level monitoring. *IEEE J. Photovoltaics* **4**, 1618–1624 (2014)
7. Diaz-Dorado, E., Suarez-Gracia, A., Carillo, C.J., Cidras, J.: Optimal distribution for photovoltaic solar trackers to minimize power losses caused by shadows. *Renew. Energy* **36**, 1826–1835 (2011)
8. Bidram, A., Davoudi, A., Balog, R.S.: Control and circuit techniques to mitigate partial shading effects in photovoltaic arrays. *IEEE J. Photovoltaics* **2**, 532–546 (2012)
9. Patel, H., Agarwal, V.: MATLAB Based modelling to study the effects of partial shading on photovoltaic array characteristics. *IEEE Trans. Energy Convers.* **23**, 302–310 (2008)
10. Jain, S., Agarwal, V.: Comparison of the performance of maximum power point tracking schemes applied to single stage grid-connected photovoltaic systems. *IET Electr. Power Appl.* **1**, 753–765 (2007)
11. Patel, Hiren, Agarwal, V.: MPPT scheme for photovoltaic systems operating under partial shading conditions. *IEEE Trans. Ind. Electron.* **55**, 1689–1698 (2008)
12. Tey, K.S., Mekhele, S.: Modified incremental conductance algorithm for photovoltaic system under partial shading conditions and load variation. *IEEE Trans. Ind. Electron.* **61**, 5384–5392 (2014)

An Unrestricted Placement of Wind Turbines Toward Maximizing the Energy Output Using Teacher-Artificial Bee Colony Algorithm

Jaydeep Patel, Vimal Savsani, Vivek Patel and Rajesh Patel

Abstract The wind farm layout optimization (WFLO) is a problem that helps to alter the position of wind turbines and arrange in such a way that the assembly of the turbines has reduced wake effect which improves the power output and overall efficiency of a wind farm. In the present study, a novel optimization tool, Teacher-ABC (T-ABC) algorithm has been developed using the prior knowledge of artificial bee colony (ABC) algorithm and teaching–learning-based optimization (TLBO). The newly developed algorithm has been used to determine the optimized position of turbines in a wind farm to obtain maximum possible power output and improved overall efficiency for a given set of turbines. The present study considers the unrestricted placement of the turbines in a wind farm. The paper discusses the results of the algorithm for two cases; in the first case, for a given wind velocity the directions are assumed to be identical while in the second case for a given wind velocity the wind directions are assumed to be erratic. The results suggest an improved performance in view of reduced wake effect that has increased the wind velocity and thereby the power output of the wind farm. The present approach is seen to be a better alternative for the positioning of turbines in a farm compared to the conventional grid-based approach.

Keywords Wind energy · Wake effect · Wind farm layout optimization
TLBO · ABC

J. Patel (✉) · V. Savsani · V. Patel · R. Patel
Pandit Deendayal Petroleum University, Gandhinagar, India
e-mail: jaydeep Patel028@gmail.com

V. Savsani
e-mail: vimal.savsani@gmail.com

V. Patel
e-mail: viveksaparia@gmail.com

R. Patel
e-mail: rajesh.patel@sot.pdpu.ac.in

1 Introduction

Nowadays, fossil fuel is on the verge of ends and creates several environmental issues, such as emission of greenhouse gasses and global warming, when used for power generation [1]. So, the discovery of new energy sources such as the wind and solar is imperative. Among these available sources, the wind energy is a readily available source of energy and has notable growth in the form of power production. The power is extracted from wind energy using wind turbines. In early decades, where the demand of energy is less, few turbines are installed at a farm site to extract the wind energy. Because of noteworthy growth for demands of energy, a cluster of wind turbines are currently installed at wind farm site. When the turbines are placed in close proximity to a farm site, the performance of turbines is exaggerated by the wakes developed by the upstream turbine [2]. This interaction of wakes lowers the wind speeds at the downstream turbine which leads to reducing in total performance of a farm. Thus, the layout optimization of a wind farm, where wake interaction can be minimized, is the prime interest of researchers, designers and consultants.

Most research articles use a genetic algorithm (GA) with discrete solution space (i.e., 10×10) [3–7] to determine the optimized positioning of the turbine in a wind farm to minimize the wake losses. The approach for the design of optimal layout was first addressed by the Mosetti et al. [3] using the GA and Jensen wake decay model [8]. Apart from genetic algorithm, other researchers have also suggested the heuristic approaches, such as mixed-integer nonlinear discrete combinatorial optimization algorithm [9], particle swarm optimization [10], greedy randomized adaptive search procedure (GRASP) [11], teaching–learning-based optimization [1], simulated annealing [12], Monte Carlo simulation [13] and quadratic optimization (OQ) and mixed-integer linear (MIL) method [14] for solving the WFLO problem with discrete solution space. The discrete solution space does not effectively utilize the available wind farm area for turbine positioning. The critical aspect of the optimal design of the wind farm about the unrestricted positioning of the turbine was addressed by Chowdhury et al. [10]. Wan et al. [7] also solve the WFLO problem with continuous space. The critical aspect in continuous space is to maintain the safe distance between two neighboring turbines. According to Patel [15], the optimum positioning of a wind turbine is 3–6 rotor radius in a traverse wind direction and 16–24 rotor radius apart in wind direction to reduce the wake effect on each other and safe operation.

The present study considers the unrestricted placement of wind turbines for the cost minimization per energy unit. In unrestricted placement, the turbines are free to place at any available location. The present study introduces a novel optimization tool, Teacher-ABC (T-ABC) algorithm using the prior knowledge of artificial bee colony (ABC) algorithm and teaching–learning-based optimization (TLBO) for solving the WFLO problem. The results of Teacher-ABC (T-ABC) are compared with the results available in the literature with grid-based system and unrestricted placement of turbines.

2 Wake Modeling

The present study considers the analytical wake decay model proposed by Jensen [8]. This wake decay model uses the law of conservation of mass to calculate the consequence of wake of the upstream turbine on the downstream turbine. This wake effect leads to lower the velocity of the downstream turbine and can be estimated by a linearly increasing wake decay model as visualized in Fig. 1. The velocity at the downstream turbines can be calculated by applying the continuity equation and the Betz theory. The velocity at the downstream turbine is given as:

$$u_d = u_0 \left[1 - \left[\frac{2a}{\left(1 + \alpha \left(\frac{d}{2D_w}\right)^2\right)} \right] \right], \tag{1}$$

where u_d is wind velocity at downstream turbine under wake, u_0 is ambient wind velocity, α is the wake spreading constant given as $0.5 / \ln(h/h_0)$, and D_w is the diameter of the wake zone at distance d , as visualized in Fig. 1.

For multi-megawatt power generation, a cluster of wind turbines were set up at wind farm site. When turbines are placed in close proximity, the downstream turbines are affected by many wakes. Hence, the wind velocity of the downstream wind turbine under many wakes is computed using Eq. (2).

$$u_i = u_0 \left[1 - \sqrt{\sum_{i=1}^N \left(1 - \left(\frac{u}{u_0}\right) \right)^2} \right], \tag{2}$$

where u_i is wind velocity at downstream turbine under multiple wakes of N turbines. The details stepwise derivation of Jensen wake decay model was described in Ref. [1].

The power produced by the turbine is affected by velocity, intensity and direction of the wind. The total power produced by the wind farm ($P_{\text{wind farm}}$) with Nt turbines can be estimated by [3],

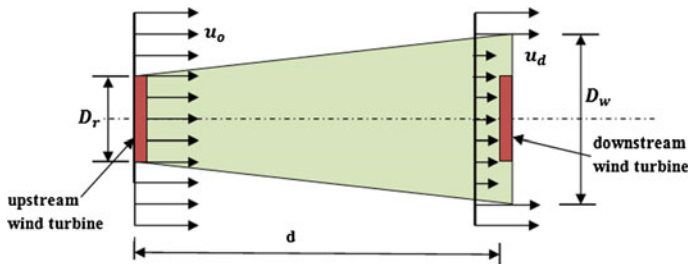


Fig. 1 Representation of the Jensen wake decay model

$$P_{\text{wind farm}} = \sum_{i=1}^{Nt} 0.3 \times u_i^3. \quad (3)$$

The yearly cost (C_w) of one wind farm is obtained using the following equation [3],

$$C_w = Nt \left(\frac{2}{3} + \frac{1}{3} e^{-0.00174Nr^2} \right), \quad (4)$$

where Nt = total turbines.

The objective WFLO problem is to minimize the cost of power generated per kW to maximize the yearly profit of wind farm. So, the mathematical model of present problems is as follows:

$$\text{minimize} \left(\frac{C_w}{P_{\text{wind farm}}} \right), \quad (5)$$

subject to maintaining the minimum distance between turbines is 200 m and no turbine is placed outside of wind farm boundaries.

As describe above, the wake affects sustainable to the power output of wind farms. This effect can be represented in terms of efficiency:

$$\eta_{\text{wind farm}} = \frac{P_{\text{ideal}}}{P_{\text{wind farm}}}, \quad (6)$$

where P_{ideal} = power output of wind farm in ideal condition (no wake effect).

3 Application of Teacher-ABC (T-ABC) Algorithm

A hybrid variant of ABC algorithm and TLBO knew as Teacher-ABC (T-ABC) algorithm was developed and introduced to solve the WFLO problem. TLBO has two solution search phases; one is teachers' phase and the second is learners' phase [16] while ABC algorithm has an employed bee phase and scout bee phase [17]. It has been observed from the literature of TLBO and ABC that both of these algorithms possess the different search method to reach the optimum solution. In TLBO, the properties of teacher are used by the student to improve their mean results; hence, it tries to move the global optimum solution toward the mean of the solution that leads to high exploitation capability. Learner phase relying on other learners and solution is updated by considering the vector difference of two randomly selected solutions for the search space that bears the stronger exploration capability for solving multimodal problems. However, it is proved that excessive exploitation will produce a purely local search that leads to premature convergence of the

algorithm when solving complex multimodal problem containing numerous local optimum solutions. Although ABC algorithm is sound at exploration, the search technique of ABC would generate a candidate solution by moving the prior one toward another randomly selected solution from the population that leads to poor exploitation. The detail description and solution updating strategy of TLBO and ABC was described in Refs. [16, 17], respectively. Hence, to take the benefits of the strong component of ABC algorithm and to enhance the capability of TLBO algorithm, the present study explores and experiments the hybridization of TLBO with the search technique of ABC. This hybridization improves the effectiveness and performance of TLBO for solving the complex problem. Hybridization of TLBO is carried out in the learner phase. The learners' phase of TLBO is replaced by the search technique of ABC. This leads to hybrid variants of TLBO; teaching phase with ABC knew as Teacher-ABC (T-ABC) that is explored as follows.

Solution updating strategy of Teacher Phase of TLBO algorithm

$$S_{ab}^{New} = S_{ab}^{old} + r_{ab}(T_b - T_F M_b), \tag{7}$$

where $a = 1, 2, \dots$, number of population, $b = 1, 2, \dots$, number of design variable, M_b is the mean result of the learners in a specific subject, T_b is the teacher and T_F is teaching factor which is random variable and its value is decided as given as $T_F = \text{round}[1 + \text{rand}(0, 1)\{2 - 1\}]$ [16]. This random value of teaching factor may be 1 or 2. The best function evaluations at the end of the teacher phase are kept and input to the ABC phase.

Solution updating strategy of ABC algorithm

$$S_{ab}^{New} = S_{ab}^{old} + \varnothing_{ab}(S_{ab}^{old} - S_{cb}), \quad \text{where } a \neq c, \tag{8}$$

where $a \in \{1, 2, \dots, \text{number of population}\}$, $b \in \{1, 2, \dots, \text{number of design variable}\}$, $c \in \{1, 2, \dots, \text{number of population}\}$ and \varnothing_{ab} is a uniformly generated random number and its value laying between -1 and 1 [17].

After the ABC phase, the greedy selection is applied and selects the best solution. This practice is continuing until the termination condition is not satisfied. The best solution to this problem is the location of turbine that gives the maximum power output.

4 Results and Discussion

To achieve the objective of WFLO problem, it is required to maximize the energy (power) output of a farm. The present study used the square grid having the dimension $2 \text{ km} \times 2 \text{ km}$ for turbine placement. Unlike the grid-based approach, where farm area is divided into 10×10 grid and the turbine is positioned at the center of the square cell, present study gives the flexibility to the turbine to be placed at any available location by just maintaining the at least 200 m distance to

Table 1 Wind turbine characteristics

Hub height of turbine (h)	60 m
Rotor diameter of turbine (D_r)	40 m
Turbine thrust coefficient (C_T)	0.88
Ground surface roughness (h_0)	0.3

satisfy the rule of thumb spacing. When turbine has placed on the grid, the turbine positioning does not effectively utilize the available wind farm area and this approach introduces the sub-optimality into solution space. Compared to grid-based approach, the unrestricted placement effectively uses the available wind farm area and helps in reducing wake effect yielding a better output of a wind farm. Initially, the turbine placed randomly using the optimization algorithm. Once the turbines are placed, the distance between turbines is calculated and check for the constraints of 200 m (distance between two turbines). If the constraints are not satisfied, then affected turbine is shifty by the step size of 100 m in both x - and y -directions. This process is continuing until given set of turbines are not positioned in a farm. Once the turbines are placed, the turbines under wake effect or having the less velocity are identified. These identified turbines are removed from the current location and shifted in such a way that they are under the no wake effect or minimal wake effect. Once the placement process is complete, the sum of a power output is calculated.

The present study considers the two wind scenario of uniform (case (a)) and variable (case (b)) wind direction considering the identical wind speed (12 m/s). The characteristic of turbines used in present study is given in Table 1. A hybrid variant of ABC algorithm and TLBO algorithm known as Teacher-ABC (T-ABC) algorithm is used to optimize the present problem. The results are calculated for both cases ((a) and (b)) considering 10 runs for population size = 50, function evaluations = 20,000. The best value of 10 runs is considered as a result of WFLO problem.

4.1 Case (a)

The present case considered an identical wind velocity (12 m/s) flowing from the identical wind direction. The wind velocity of downstream turbines will change only when turbines are affected by the wake effect from the upstream turbine. The wind is flowing from the identical direction; hence, the wake created by the upstream turbines depended only on the downstream space. The placement of turbine is flexible throughout the farm area; this will help to place the turbines such that they are less affected by the wake of the upstream turbine and reduce the consequence of wake losses on the output of a farm. The optimization process was carried out for 30 turbines; the result in the form of power output and efficiency was obtained and compare it with results reported in Refs. [4, 7, 14]. The comparative results obtained through new hybrid T-ABC algorithm and results reported in the literature are reported in Table 2. The illustration of the position of turbines in a

Table 2 Performance comparison for case (a): (i) Turner et al., (ii) Grady et al., (iii) Wan et al. and (iv) present study (T-ABC)

	i	ii	iii	iv
Objective function value	0.00149	0.001544	0.001447	0.001433
Number of turbines (N_t)	30	30	30	30
Efficiency (%)	95.16	92.01	98.13	99.08
Power output ($P_{wind\ farm}$)	14,800	14,310	15,262	15,410

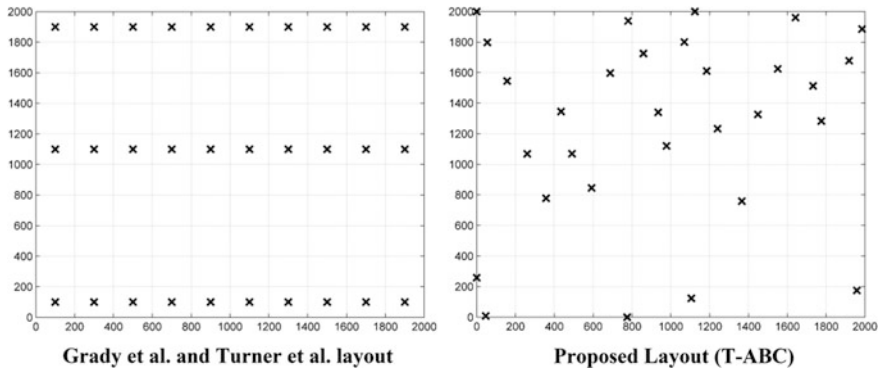


Fig. 2 Wind farm layout configuration for case (a)—30 wind turbines

farm is visualized in Fig. 2. It is clear from Table 2 that present unrestricted approach with T-ABC obtained nearest 100% farm efficiency while grid-based approach obtains the 95.16% efficiency. The $\eta_{wind\ farm} = 99.08\%$ and $P_{wind\ farm} = 15,410\text{ kW}$ is achieved using T-ABC algorithm.

4.2 Case (b)

This case considered an identical wind velocity (12 m/s) but adds a more practical approach of erratic wind directions. The wind is flowing from 36 directions with equal likelihood of occurrence. Hence, in this case, the relative distance between turbines must be broadened as long as possible so that the effect of wake in all the wind direction can be reduced. The optimization process was carried out for 39 turbines; the result in the form of power output and efficiency was obtained and compare it with results reported in Refs. [4, 7, 14]. Table 3 shows the comparative performance of a wind farm for case (b). The illustration of the position of wind turbines in a wind farm is visualized in Fig. 3. It is discovered from Fig. 3 that proposed layout has most of the turbines placed at the outer edge of the boundary. It is clear from Table 3 that the unrestricted positioning of a turbine generates the more power compared to fix grid approach; also, reported results show the better

Table 3 Performance comparison for case (b): (i) Turner et al., (ii) Grady et al., (iii) Wan et al. and (iv) present study (T-ABC)

	i	ii	iii	iv
Objective function value	0.00147	0.001567	0.001483	0.001447
Number of turbines (N_t)	39	39	39	39
Efficiency (%)	90.7	85.17	89.69	92.2
Power output ($P_{wind\ farm}$)	18,336	17,220	18,133	18,603

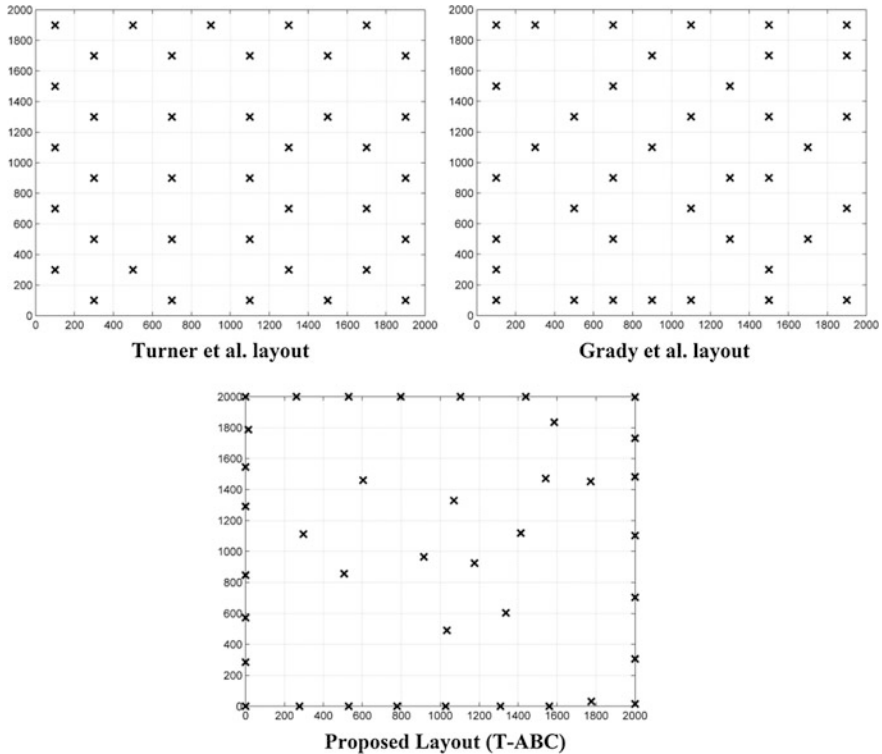


Fig. 3 Wind farm layout configuration for case (b)—39 wind turbines

power output compared previously reported micro-sitting approach. The efficiency of wind farm obtained by using T-ABC algorithm is 92.02%, and power output is 18,603 kW. Grady et al. and Turner et al. use the fix grid approach and reported the 85.17 and 90.7% and power output 17,220 and 18,336 kW, respectively. Wan et al. consider the continuous (unrestricted) positioning of turbines and develop the 18,133 kW power. The power output of wind farm is enhanced by 1.44, 7.43 and 1.43% compared to Grady et al., Turner et al. and Wan et al., respectively, which was significant especially the design of a large-scale wind farm.

5 Conclusion

Present study introduced a novel optimization technique known as Teacher-ABC (T-ABC) for solving the WFLO problem with consideration of unrestricted positioning of turbine in a farm. In unrestricted placement, the turbine is free to place at any available location by maintaining the safe distance among the two adjacent turbines and helps to reduce the wake effects on each other. It is concluded that Teacher-ABC (T-ABC) algorithm with the unrestricted placement of turbine can optimize the position wind turbines in better way compared to previous studies with unrestricted placement or grid-based placement. The results express the enhanced performance in power output of the farm by the unrestricted placement approach and newly developed optimization method with the given set of turbines. The present approach is seen to better alternative for the positioning of turbines in a farm compared to the conventional grid-based approach.

References

1. Patel, J., Savsani, V., Patel, R.: Maximizing energy output of a wind farm using teaching-learning-based optimization. In: ASME 2015 9th International Conference on Energy Sustainability collocated with the ASME 2015 Power Conference, the ASME 2015 13th International Conference on Fuel Cell Science, Engineering and Technology, and the ASME 2015 Nuclear Forum 2015 Jun 28 (pp. V002T19A004-V002T19A004), American Society of Mechanical Engineers (2015)
2. Gebraad, P., Thomas, J.J., Ning, A., Fleming, P., Dykes, K.: Maximization of the annual energy production of wind power plants by optimization of layout and yaw-based wake control. *Wind Energy* (2016)
3. Mosetti, G., Poloni, C., Diviacco, B.: Optimization of wind turbine positioning in large windfarms by means of a genetic algorithm. *J. Wind Eng. Ind. Aerodyn.* **51**(1), 105–116 (1994)
4. Grady, S.A., Hussaini, M.Y., Abdullah, M.M.: Placement of wind turbines using genetic algorithms. *Renew. Energy* **30**(2), 259–270 (2005)
5. do Couto, T.G., Farias, B., Diniz, A.C.G.C., de Moraes, M.V.G.: Optimization of wind farm layout using genetic algorithm. In: Tenth World Congress on Structural and Multidisciplinary Optimization, Orlando, Florida, USA, pp. 19–24 (2013)
6. Huang, H.S.: Distributed genetic algorithm for optimization of wind farm annual profits. *IEEE International Conference on Intelligent Systems Applications to Power Systems ISAP 2007*, pp. 1–6 (2007)
7. Wan, C., Wang, J., Yang, G., Zhang, X.: Optimal siting of wind turbines using real-coded genetic algorithms. In: *Proceedings of European wind energy association conference and exhibition* (2009)
8. Jensen, N.O.: *A note on wind generator interaction* (1983)
9. Ozturk, U.A., Norman, B.A.: Heuristic methods for wind energy conversion system positioning. *Electr. Power Syst. Res.* **70**(3), 179–185 (2004)
10. Chowdhury, S., Zhang, J., Messac, A., Castillo, L.: Unrestricted wind farm layout optimization (UWFLO): investigating key factors influencing the maximum power generation. *Renew. Energy* **38**(1), 16–30 (2012)

11. Yin, P.Y., Wang, T.Y.: A GRASP-VNS algorithm for optimal wind-turbine placement in wind farms. *Renew. Energy* **48**, 489–498 (2012)
12. Bilbao, M., Alba, E.: Simulated annealing for optimization of wind farm annual profit. In: 2009 2nd International Symposium on Logistics and Industrial Informatics, IEEE, pp. 1–5 (2009)
13. Marmidis, G., Lazarou, S., Pyrgioti, E.: Optimal placement of wind turbines in a wind park using Monte Carlo simulation. *Renew. Energy* **33**(7), 1455–1460 (2008)
14. Turner, S.D.O., Romero, D.A., Zhang, P.Y., Amon, C.H., Chan, T.C.Y.: A new mathematical programming approach to optimize wind farm layouts. *Renew. Energy* **63**, 674–680 (2014)
15. Patel, M.R.: *Wind and solar power systems: design, analysis, and operation*. CRC press (2012)
16. Rao, R.V., Savsani, V.J., Vakharia, D.P.: Teaching–learning-based optimization: a novel method for constrained mechanical design optimization problems. *Comput. Aided Des.* **43**(3), 303–315 (2011)
17. Karaboga, D., Basturk, B.: A powerful and efficient algorithm for numerical function optimization: artificial bee colony (ABC) algorithm. *J. Global Optim.* **39**(3), 459–471 (2007)

Fault Diagnosis in Smart Distribution System Using Smart Sensors and Entropy

Mangal Hemant Dhend and Rajan Hari Chile

Abstract Power quality and reliability of electric power supply have become indispensable in today's digital world. Advanced measurement, sensing and communications are available in smart grid environment. Using advanced infrastructure, tools and techniques, modern researchers are trying to devise sophisticated methods for fault diagnosis. This paper proposes a technique using nonconventional symlet mother wavelet function to carry out fault diagnosis process. The technique is discussed for extracting entropy of fault transient signal and is used for pattern recognition. The algorithm is presented which is developed using MATLAB software for fault identification, classification and location tasks. The method is implemented on a 9-bus system model, and the results are discussed. The results show effectiveness of symlet nonconventional wavelet function for feature extraction task. The performance indicates the applicability of the method to fault identification, classification and location tasks. The result proves superiority of the method over other methods of feature selection. The method is useful for real-time monitoring and automation purpose of power system if developed further.

Keywords Entropy • Fault diagnosis • Signal decomposition • Smart grid
Smart sensors • Wavelet technique

M.H. Dhend (✉)

Electrical Engineering Department, AISSMS College of Engineering,
Pune, Maharashtra, India
e-mail: mangaldhend1@gmail.com

R.H. Chile

Instrumentation Engineering Department, SGGS College of Engineering and Technology,
Nanded, Maharashtra, India
e-mail: rhchile@yahoo.com

© Springer Nature Singapore Pte Ltd. 2018

S. SenGupta et al. (eds.), *Advances in Smart Grid and Renewable Energy*,

Lecture Notes in Electrical Engineering 435, https://doi.org/10.1007/978-981-10-4286-7_62

1 Introduction

Faults in power system deteriorate the quality of power delivery and the overall operation of power system. Therefore, it is required to perceive different faults and isolate them quickly as far as possible. The ability of precisely locating a fault in distribution system can assist to expedite system restoration, repair process and reduce duration of outages. For this purpose, a number of methods were developed in the past for the detection and location of faults. At present, research is going on to discover comparatively prevailing and efficient fault diagnosis technology to increase power quality and reliability by using smart meters or advanced metering infrastructure (AMI) [1]. Nowadays, smart meters or sensors are widely being installed in smart grid system. If used with latest communication technology, they can play a very important role in fault diagnosis task. For this purpose, they can be placed intentionally at different locations of distribution system apart from using only at consumer end [2, 3]. Up till now, only some fault location algorithms using this technology have been introduced by the researchers which can be used in smart grid system. Feature extraction from fault transient signal using wavelet analysis is a very effective technique which is finding vast applications in fault diagnosis task as it offers frequency as well as time information of a signal. A number of mother wavelet functions have been tried in the literature, but this paper proposes the use of nonconventional but advanced symlet mother wavelet function for extracting the entropy from the fault signal and uses it to carry out fault diagnosis process effectively.

2 Proposed Technique

The proposed technique is based on ephemeral knowledge of the transient signal and uses measurement of post-fault current signal to predict the fault location. After receiving currents which are sensed by smart sensors placed at different locations, the acquired current signal is decomposed. Up till now, different mother wavelet functions such as Morlet, Daubechies, and continuous ones with different features at different resolution levels [4–7] have been used. The novel idea of this work is to use advanced version of Daubechies function symlet. It is used in this work because in frequency domain it retains bandwidth characteristics similar to ideal filter and in time domain it has shortness and good smoothness [8]. In previous research for analysis and detection of voltage events, square of magnitude, mean value and peak magnitude of features such as skew, energy and standard deviation of wavelet coefficients are proposed [9]. But these give several fault estimations; therefore, in this work the feature index term is formed by finding sum of absolute value of entropies. The detail coefficient of fourth level of scaling is used for this purpose. The entropy is calculated by estimating squares of the coefficients of the DWT and then multiplying it by logarithmic function.

Let $S(m)$ be the discrete signal under transient condition. This signal is transformed at instant t and scale i . It has a high-frequency component coefficient $D_i(t)$ and a low-frequency component coefficient $A_i(t)$ [10, 11]. If sampling frequency is f_s , the frequency band of the information contained in signal components $D_i(t)$ and $A_i(t)$ obtained by reconstruction is as follows

$$D_{i(t)} : [2^{-(i+1)}f_s, 2^{-i}f_s] \tag{1}$$

$$A_{i(t)} : [0, 2^{-(i+1)}f_s] \quad (i = 1, 2, \dots, k) \tag{2}$$

The sum of all components of signal gives the original signal $S(m)$.

$$S(m) = D_{1(m)} + A_{1(m)} = D_{1(m)} + D_{2(m)} + A_{2(m)} = D_{i(m)} + A_{i(m)} \tag{3}$$

The non-normalized Shannon entropy can be calculated as follows

$$E_i = - \sum E_{it} \log E_{it} \tag{4}$$

where E_{it} is the wavelet energy spectrum at scale j and instant k and it is defined as follows

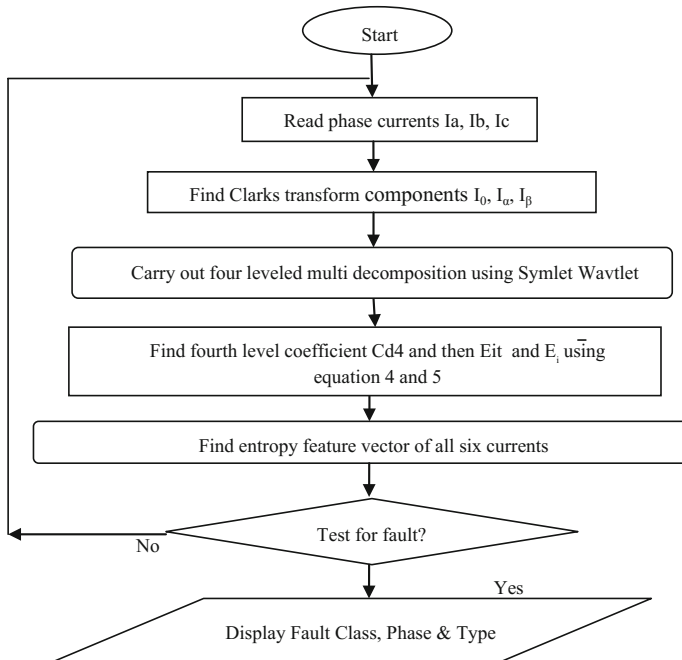


Fig. 1 Flowchart of the proposed method

$$E_{it} = |D_{i(t)}|^2 \quad (5)$$

Figure 1 represents the sequence of steps of the proposed method.

3 Simulation and Results

The above technique is implemented on a sample test system. Fault transient currents are found out by simulating the test model, and the technique is developed using MATLAB 2013a program.

3.1 Test System and Waveforms of Features

The system used in the study has three machines and 9 buses. The machine models are used to simulate generators. Smart sensor in the system gives current signals under normal and transient conditions at a sampling frequency of 10 kHz.

Figure 2 shows the 9-bus test system used to simulate 5 types of class as line to ground (LG), line to line (LL), double line to fault (DLG), all line short circuits (LLL), all line to ground (3LG). By simulating these faults on test model, six currents, namely three phase currents after fault I_a , I_b and I_c and three modal transform components I_α , I_β and I_0 , are obtained. Then coding is done using MATLAB software to get six entropies as mentioned above. Figure 3 shows patterns of entropy under fault condition with the help of which results obtained are compared.

3.2 Fault Classification

An examination of all possible types of fault in three-phase system (AG, BG, CG, AB, BC, CA, ABG, BCG, CAG and ABCG) is carried out. The sum of absolute entropies of wavelet coefficients of the Clarke components I_α , I_β and I_0 is used to investigate the type of fault if it is 3LG, LG, DLG or LL fault.

Table 1 shows that the maximum value of sum of entropies for LG and DLG fault is different and has quite significant divergence which can be used to classify these faults. Table 2 gives the values of entropies of I_0 monitored at S1 for various faults at S1. It is seen that the sum of entropy for 3LG is much more than that of LL (bold values). Hence, these 3LG and LL faults can be easily separated.

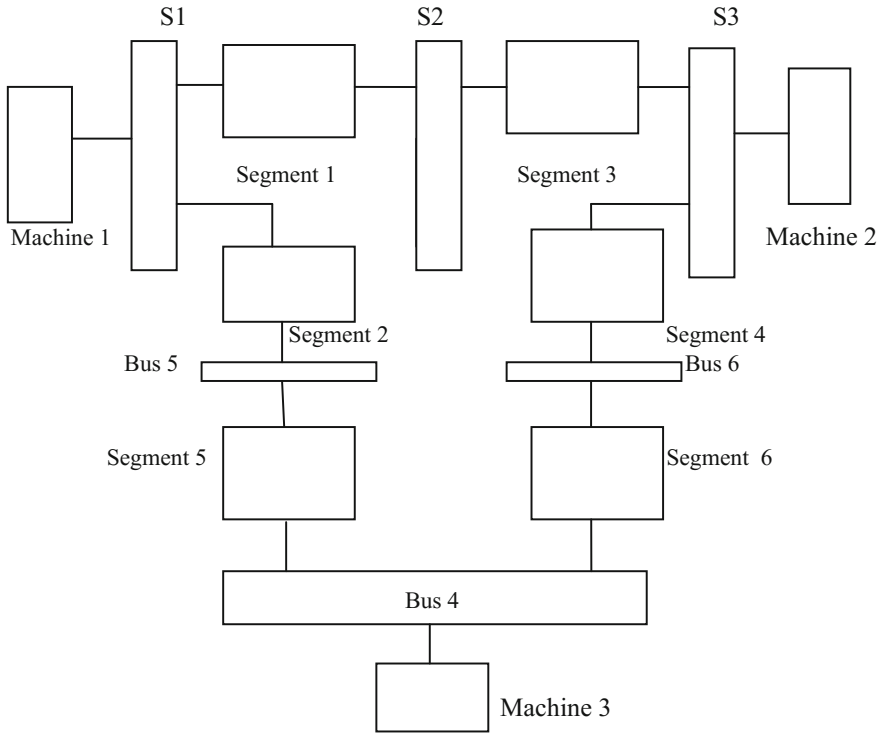


Fig. 2 3-Machine 9-bus test system

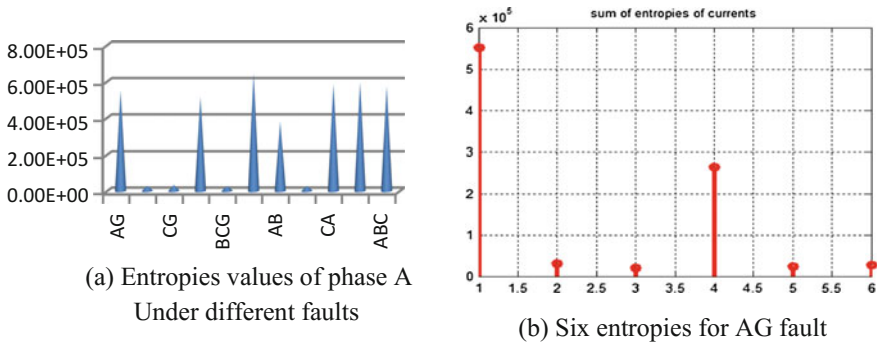


Fig. 3 Entropies found for different faults

3.3 Faulted Phase Identification

Table 3 shows absolute sum of entropies of three phases. The faulted phase can be identified by comparing entropy values of three phases. The phase is faulty for

Table 1 Entropies for a fault at S1

Fault type		Sum of entropies of I_α	Sum of entropies of I_β	Comment
LG	AG	2.63e+5	2.63e+4	Entropies for different types of faults have wide range of difference
	BG	1.03e+5	1.6e+5	
	CG	7.99e+4	3.22e+5	
DLG	ABG	3.86e+5	1.63e+5	
	BCG	8.99e+4	1.835e+5	
	CAG	5.62e+5	3.3e+5	

Table 2 Entropy values of current I_0 for different faults monitored at S1

Type of fault	Fault class	Sum of entropies of current I_0
3LG	ABCG	6.79e+03
LG	AG	2.68e+04
	BG	2.61e+04
	CG	5.52e+04
LL	AB	8.86e-03
	BC	4.22e-03
	CA	3.21e-03
DLG	ABG	5.1e+4
	BCG	2.35e+04
	CAG	2.822e+04

Table 3 Entropies of I_a , I_b and I_c monitored at S1 for a fault at S1

Fault type	Sum of entropies of I_a	Sum of entropies of I_b	Sum of entropies of I_c
AG	5.513620e+5	3.152668e+4	2.019247e+4
BG	2.801085e+4	5.410749e+5	2.187418e+4
CG	3.279891e+4	3.430722e+4	8.535038e+5
ABG	5.160687e+5	5.524566e+5	2.305803e+4
BCG	2.809992e+4	5.663252e+5	9.438287e+5
CAG	6.472343e+5	3.081593e+4	8.936408e+5
ABCG	5.963154e+5	5.615310e+5	9.825324e+5
AB	3.807531e+5	2.893592e+5	1.998773e+4
BC	2.773703e+4	6.851542e+5	5.710859e+5
CA	5.863740e+5	3.007570e+4	6.757615e+5
ABC	5.756683e+5	5.611808e+5	1.001927e+6
Comment	Entropies of currents of faulted phase (bold values) are maximum than that of non-faulted phase		

which entropy value is largest as compared to remaining phases. For example, for fault AG as shown in Table 3 entropy value of phase current I_a is maximum (shown in bold) as compared to phases B and C. Hence, it can be identified easily that fault has occurred on phase A.

3.4 Fault Location

The values of entropies vary depending upon distance of faulted segments. Table 4 gives features for 3LG fault, and from these values, it is seen that smart sensor near to faulted segment gives maximum sum of entropies of current I_0 as compared to values given by smart sensors located at far distances or buses. Table 5 gives entropy values found from current I_0 monitored with smart sensors at different locations of S1, S3, bus 4 and bus 6 for faults at different locations such as segment 1, segment 2, etc. It can be seen that the value of entropy monitored near to fault location gives maximum value as compared to other values. Therefore, if fault occurs at, say, segment 4, then smart sensor near to bus 4 gives highest values (bold) as compared to values at S1, S2 and bus 6. Therefore, faults can be located accurately with maximum values of entropies. And it is not giving multiple fault estimations as compared to other feature values seen in previous literature.

4 Results' Discussion

It is seen that the values of entropies vary depending upon distance of faulted segments. Fault classification is achievable as values found for different types of faults fall within certain range which can be differentiated for each class. Fault location is achieved easily as values of entropies found are different for pre- and post-segment. It is also observed that smart sensor nearer to faulted bus gives maximum values of sum of entropies of I_0 as compared to sensors located at far distance from faulted bus.

Table 4 Fault monitored at S3 and S1 for 3LG fault at various locations

Fault segment	Sum of entropies of I_0 at S3	Sum of entropies of sum of I_0 at S1	Sum of entropies of sum of I_0 at bus 5
1	133.5381	10260.08	736.4925
2	37.63512	1026.008	3144.570
3	603.3754	1486.713	736.4925
4	603.3754	304.0855	741.0778
5	30.40447	56.84377	1341.521
6	30.40447	56.84377	1341.521

Table 5 Entropy values of currents I_0 monitored at different locations

Fault segment	Monitored at S1	Monitored at S3	Monitored at bus 4	Monitored at bus 6
1	8080.22	457.05	430.52	653.34
2	16602.37	595.47	97.35	60.88
3	2463.12	1969.67	627.15	98.06
4	97.35	627.15	2450.92	42012.68
5	700.43	32.53	3201.49	1676.39
6	212.892	25.12	6563.84	10589.46

5 Conclusion

In the deployment of smart grid system, current distribution systems are changing in its infrastructure due to addition of renewable distributed generations. So distribution system monitoring and automation methodology need use of advanced technologies with advanced sensors and communication devices for effective fault diagnosis task. It has been demonstrated in this work that with the use of smart sensors, features of entropies of wavelet coefficients can be extracted from fault signals using symlet as mother wavelet function. It is found that this mother wavelet function gives more sturdy results and eliminates the drawbacks of multiple locations of faults as seen in existing methods of using conventional mother wavelet functions and features. From the result obtained, it can be seen that the proposed method of using smart sensors and nonconventional mother wavelet function symlet is effective for fault identification, classification and fault location. This can be further investigated for increasing the speed, robustness and accuracy of fault diagnosis process in real-time applications.

References

1. Trindade, F.C.L., Nascimento, K.V., Vieira, J.C.M.: Fault location in distribution systems based on smart feeder meters. *IEEE Trans. Power Deliv.* **29**(1), 251–259 (2014)
2. Dhend, M., Chile, R.: Innovative scheme for smart grid distribution system. In: *IEEE PEL Society's International Future Energy Electronics Conference (IFEEC)*, Taiwan (2015)
3. Dhend, M.H., Chile, R.H.: Smart distribution monitoring system for smart grid. In: *International Conference on Computing, Communication of Electrical, Electronic Devices and Signal Processing (CCEED)*, India, pp. 1025–1028 (2015)
4. Panigrahi, B.K., Pandi, V.R.: Optimal feature selection for classification of power quality disturbances using wavelet packet-based fuzzy k-nearest neighbor algorithm. *IET Gener. Transm. Distrib.* **3**, 296–3063 (2009)
5. Hu, G.-S., Zhu, F.-F., Ren, Z.: Power quality disturbance identification using wavelet packet energy entropy and weighted support vector machines. *Expert Syst. Appl.* **35**, 143–149 (2008)
6. de Apráz, M., Barros, J., Diego, R.I.: A laboratory for time–frequency analysis of power quality disturbances using wavelets. *14th IEEE Harmonics and Quality of Power (ICHQP)*, pp. 1–5 (2010)

7. Eristi, H., Demir, Y.: An efficient feature extraction method for classification of power quality disturbance. *International Conference Power System Transients*, pp. 1–6 (2009)
8. Dhend, M.H., Chile, R.H.: Efficient fault diagnosis in smart grid using non conventional mother wavelet function. Paper Selected for IEEE International Conference on Asia Pacific Power and Energy, Xian, China (2016)
9. Dhend, M.H., Chile, R.H.: Fault diagnosis methodology in smart grid with distributed energy generation. Paper selected for IEEE International Conference on Renewable Energy Research and Applications, Birmingham, UK (2016)
10. El-Zonkoly, A.M.: Fault diagnosis in distribution networks with distributed generation. *Electr. Power Syst. Res.* **81**, 1482–1490 (2011)
11. Li, Z., Li, W., Liu, R.: Applications of entropy principles in power system: a survey. *IEEE/PES Transmission and Distribution Conference and Exhibition*, pp. 1–4 (2005)

Topologies of a DC–DC Converter for Micro-grid Application and Implementation of Parallel Quadratic Boost Converter

T. Arunkumari, V. Indragandhi and S. Sreejith

Abstract The sustainable energy resources, namely PV, wind, fuel chambers or vitality stowage strategies like ultra-capacitors or battery management, produce output voltage at the limit of about 12–70 VDC. The grid can be connected to the energy sources whose voltage level can be altered depending on the electrical standards. As the first step, AC mains voltage requirement should be fulfilled, to attain this boost-up of voltage up to adequate level where the DC to AC conversion is attained to balance the utility rating. The another challenge in this energy generation is maintaining efficiency, and this efficiency is affected at the step-up process of DC to DC conversion. This manuscript is intensive on high efficiency and advanced topologies of boost-up mode DC to DC converters with increased voltage ratio. The difference depends on the existence or absence of transformer nodes. And also a new topology of DC to DC converter is implemented, and it is designed using MATLAB/Simulink. A droop control strategy is used to parallel two converters in load-sharing point.

Keywords DC–DC converter · Droop control · High step-up · Micro-grid Photovoltaic · Wind

1 Introduction

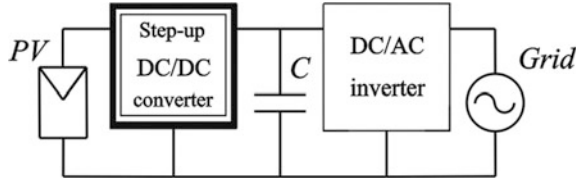
Renewable energies are becoming more popular due to the exhaustion of predictable fossil resources. This renewable energy is capable of providing the source without exhaustance [1]. The renewable energy produced in nature has less voltage

T. Arunkumari (✉) · V. Indragandhi · S. Sreejith
School of Electrical Engineering, VIT University, Vellore, India
e-mail: aak.thi90@gmail.com

V. Indragandhi
e-mail: arunindra08@gmail.com

S. Sreejith
e-mail: sreejith.s@vit.ac.in

Fig. 1 PV source with DC–DC step-up converter



output which is not sufficient for distribution. In order to overcome and improve the usage of this renewable energy step-up of that voltage is needed. And for boost-up condition a converter is needed. Here the DC to DC converters play a vital role in power production. High voltage gain with DC to DC converters and also with increased efficiency is widely used in the generation of conventional energy schemes. Designer's aspect conflicting limits like less in cost and high consistency. The key obligation is to improve the energy level and to reduce the maintenance. The nature of the high gain in voltage is to achieve an appropriate DC voltage level [2]. Power line conditioning is improved, since DC–DC converter with boost-up mode attains high efficiency with high gain (Fig. 1).

In Sect. 2.1, ultra-high converter working is described. In Sects. 2.2 and 2.3, ZVT and quadratic converters are reviewed. In Sect. 2.4, MCB converter is discussed in detail. Sections 2.5 and 2.6 include high voltage gain converters and three-phase bidirectional converter. Section 2.7 briefs about the ULC converter. Comparison is made in Sect. 3. Section 4 concludes work.

2 Topologies of DC to DC Converter

This topology is majorly classified into isolated DC converters and non-isolated DC converters. And as the next category they are classified as buck mode, boost mode, buck–boost mode converters. Here buck mode converters are utilized to reduce voltage range, while boost mode converters are utilized to increase voltage range. Buck–boost converters perform the operation simultaneously as it is required. Here the topologies are reviewed in boost converter capable of providing high voltage ratio and efficiency.

2.1 Ultra-high Step-up Converter

Predictable boost isolated converters can deliver high gain at the period of exciting duty proportions which consequences in heavy energy strain on the control buttons and supplementary circuit apparatuses. The conventional resolution for this drawback is usage of transformer topographies with appropriate turn's ratio [3, 4]. But usage of transformers decreases effectiveness and rise in weight and price.

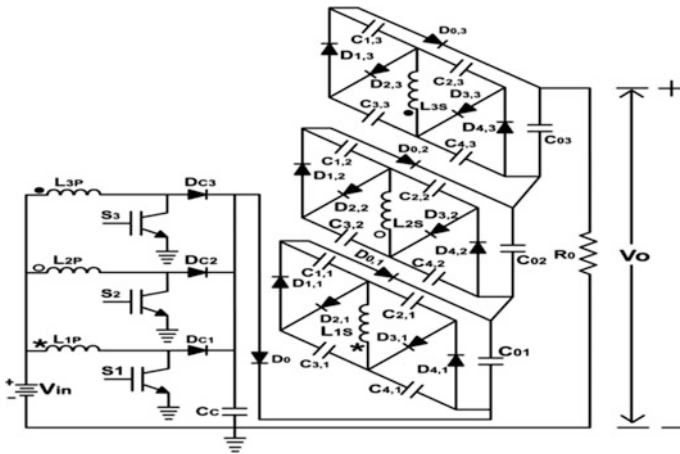


Fig. 2 Ultra-high step-up converter

So, transformer-less converter with high ratio is the finest substitute to the conventional result [5]. And so the new topographies have been arising to overwhelmed these victims and stabilize the voltage. The voltage improvement is found with the help of inductor volt second balance. Vitality escaped at the time of duty cycle is also utilized for calculation [6].

The topology used here is interleaved converter. The converter is the assortment of interleaved boost converter (IBC), coupled inductor (CI) for current control and switched capacitor (SC) for voltage regulation. The increased voltage gain (step-up) ratio is attained. The input voltage from renewable resource is 60 V, and the output achieved by the converter is 6.6 kV. This converter is utilized for hybrid power production. The circuit includes three sections of IBC with three SC systems. The primary and secondary winding plays a major role in SI system. To attain increased gain, series connection must be implemented between the output port capacitors of each SC system and the IBC. There are four operating modes. The working condition of former sections will operate under the delay at an angle of $2\pi/S$; S defines the number of phases engaged. This converter delivers high voltage gain with less switch strain of power rating 1 kW [7]. The converter is shown in Fig. 2.

2.2 ZVT Converter

The distributed renewable vitality production system, which integrates the fuel cell, the micro-turbines, the PV module, is considered as an important key to develop the consistency, improve power system quality and attain the flexible structure of the scheme by using few advanced control techniques. So the boost converter is used in different topologies in modern converter system [8].

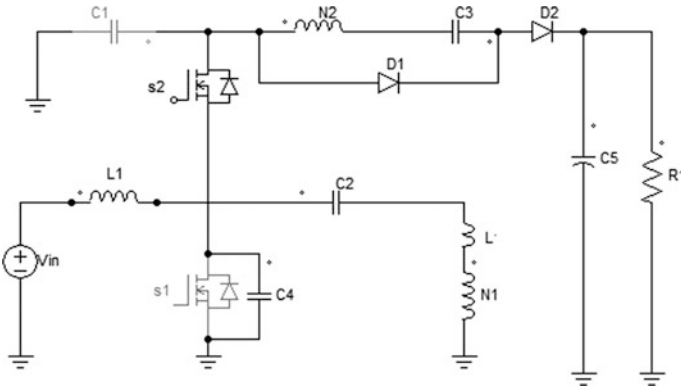


Fig. 3 ZVT converter

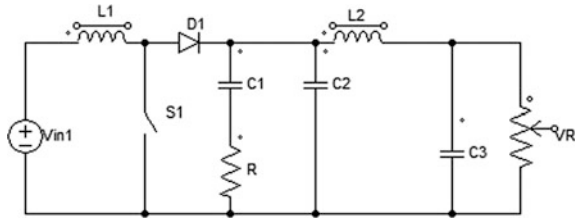
ZVT converter is the mixture of predictable step-up converter followed by voltage multiplier (VM) which is connected along the predictable converter. The VM block generates a type of voltage strain of total power apparatus less than the limited output as converter voltage. And so, the less voltage-ranged power converter strategies can be utilized to decrease the transmission losses and to increase the power scheme consistency. Furthermore, zero-voltage switching (ZVS), soft-switching operation is attained for the key switch in the total switching conversion. Zero-current switching (ZCS) and its off situation are given to diodes in [9]. So, the power converter scheme losses and the diode loss such as reverse recovery are reduced widely. Input ripple current is also decreased. The given voltage to the converter is 36 V, and the boost-up output voltage is 380 V. The converter is shown in Fig. 3.

The diodes used in the predictable step-up converter are substituted by the dynamic switch S_1 . The control switches S_1 and S_2 operate with irregular process to control capacitive voltage C_4 . Soft-switching feature of ZVS is attained for the control switches S_1 and S_2 because of the additional parallel capacitor C_s , the VM device containing a blocking capacitor C_3 , a SC C_2 and the step-up transformer. The snaking n_1 and n_2 are the number of turns present in isolation process. L signifies transformer inductance. Turns ratio is given as n_2/n_1 . There are 7 operating modes of the ZVT converter. Each operates on their own duty cycle ratio and interval.

2.3 MCB Converter

A boost mode device is essential to increase the low-level voltages of conventional sources when utilized in micro-grid [10]. But the boost converter with magnetic stuff plays a major role and creates high efficient voltage gain. And so the converter

Fig. 4 MCB converter



with magnetic property is designed. This converter is enhanced with equivalent series resistance [11]. The converter utilizes four state models and shows 4th least performance. The magnetic coupling with the improved ESR capacitance also enables utilization of small size inductors and decreases the heaviness and capacity of the scheme [12]. The RHP value zero is totally removed in this converter with improved ESR capacitance, and henceforth, it displays a least phase enactment. This helps in arrangement of linear system and easiest control in design. The MCB circuit is represented in Fig. 4. It has high stepping ratio. Usage of fewer state variables designs the mathematical investigation of this converter simpler. The magnetic coupling amid the inductors together with the increased ESR capacitance enables the utilization of small size inductors, which decreases the mass and capacity of the system.

2.4 High Voltage Gain Converter

The SC method has been utilized in [13] to lift the given in voltage as essential output voltage. This impression is satisfactory toward the improvement of less range power converters; meanwhile, numerous modifications with numerous voltage strain and several capacitors are necessary [14].

The high voltage gain converter attains soft switching, and the integrated topography is utilized so that supreme voltage withdrawal from the PV cells, energy storage device with two operating modes, voltage boost-up can be attained in a primary mode conversion [15]. It does not need any extra supplementary circuit for ZVS operation. The circuit design is quite simple, the voltage stress is limited, and this is the main advantage of this circuit. The different mode conversion such as PV mode, battery mode, high voltage mode is integrated in single mode. The input voltage given is 20 V, and it is boosted up to 380 V. The structure is less complex, voltage strain is reduced, and high efficacy is attained. The converter is shown in Fig. 5.

2.5 Three-Phase High Step-up Bidirectional Converter

In three-phase connection, there occur many problems due to heavy load and conversion and so, various methods have been raised to overcome this problem.

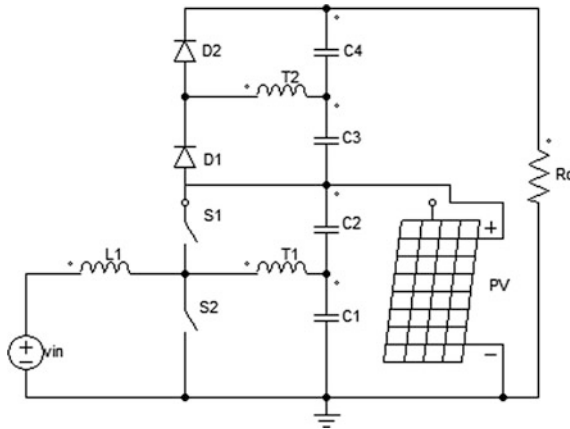


Fig. 5 High voltage gain converter

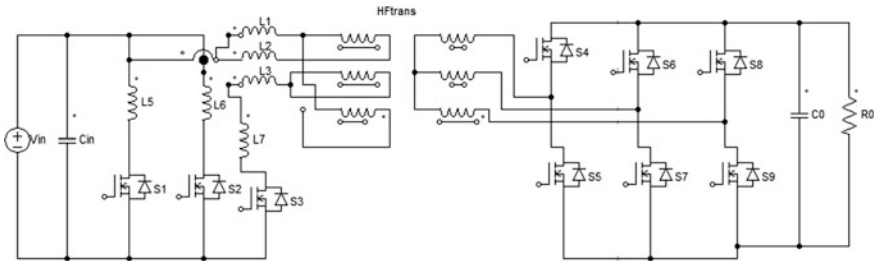


Fig. 6 Three-phase high step-up bidirectional converter

The intrinsic switch off-state voltage strain subject with current mode converters is removed by ancillary inflection in the absence of active mode clamping [16] or snubbers. It reaches commutation limit or voltage clamp with ZVS or ZCS [17, 18] by secondary switch without the presence of additional circuit. All the diodes used in this type of converter commute naturally at the time the currents reach zero. The converter is shown in Fig. 6.

This converter [19] is utilized to exchange the energy among buses of various voltage limits and also in the need for high step-up voltage. This converter attains ZCS for all initial switches, while ZVS of other switches. In the absence of active clamping, ZCS is attained with the help of ancillary modulation where the final voltage is reflected, thereby eradicating the turn-off voltage spear concern related to current-fed type converters. The input voltage is 12 V, and it is stepped up to 320 V. Identical current division among the 3 phases above high-frequency (HF) sequences decreases the highest current strains and transmission losses in devices. The input ripple and output ripple current is reduced ultimately.

2.6 ULC (Unregulated Level Converter) Converter

The distributed renewable vitality production system, which integrates the fuel cell, the micro-turbines and the PV arrays, is considered as an actual resolution to increase the high voltage transmission limit of bidirectional converters attained by altering the turns of the transformer, like fly back model and forward-fly back model. ULC converters have an easy and less rate alignment [8]. On the other hand, it is appropriate for reduced-power diligences because of high voltage strain and leakage inductance vitality. In addition to it, usage of heavy-voltage transformers with a more turn ratio results in numerous issues [20]. And the ULC converter is invented in the absence of transformer to overcome this issue.

The topography utilized is ULC parallel with a 2-phase topography of interleaved charge-pump converter. Due to the modest control techniques, this converter attains high ratio of voltage. In ejection setup, the topography behaves as a voltage-double step-up converter to attain high ratio of (48–400 V). In charge setup, the converter acts as 2 parallel voltage divider, step-down converter to attain high conversion ratio of (400–48 V). The converter is shown in Fig. 7. In excess, the two-stage [21] scheme merits by decreasing voltage strain of dynamic switches, which allows one to approve lesser voltage ranging apparatus to distinct decreasing both the switching loss and transmission losses. Due to the decreases in voltage strain, high efficiency can be attained. For attaining the high power density and efficacy, an ULC converter is established. Subsequently, it requires only a smaller inductor with high-frequency filtration (L_a and L_b). It can considerably step up the power at weak section. Moreover, by withdrawing voltage regulation toward other strong side section, bidirectional converter for the low part with immovable ratio of 2:1 below charge mode working or 1:2 ratio below discharge mode working, can attain strong efficacy with a comparatively less input voltage in total load limits. For the high-side setup, the scheme charge-pump converter is the same as a predictable buck–boost mode converter excluding two dynamic switches along series and a charge-pump capacitance working in the power scheme. The circuit scheme is

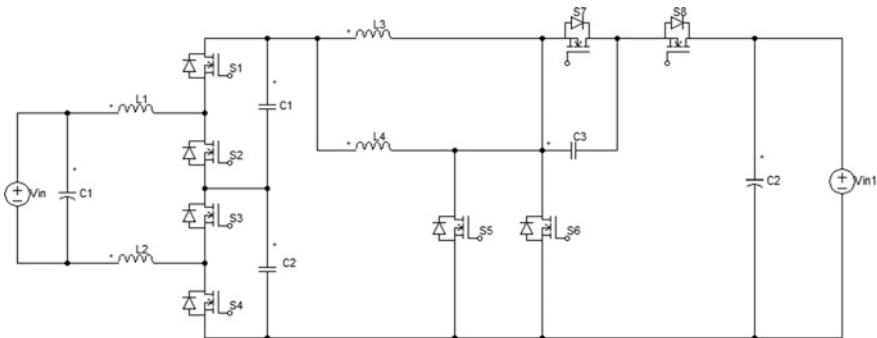


Fig. 7 ULC converter

modest, and it attains the same high ratio with lesser duty cycle. Henceforth, it decreases the transmission losses of the switch, to improve the efficacy of the total two-way converter distinct.

2.7 Proposed Methodology Parallel Quadratic Boost Converter

The isolated converters are forward mode, fly back type, push-pull mode, half-bridge model and full-bridge schemes. They can alter the transformer winding to attain high conversion ratio of voltage. Though the key switches utilized here will agonize a large voltage strain and large power indulgence. They occur at the transformers leakage inductance [22]. The price rises consequently because of the additional switch and large range driver. The level of duty cycle range beyond its working limit also upshot in grave reverse-recovery mode and electromagnetic interference losses [23]. The converter which utilizes the coupled inductor method with active clamp model is projected [24]. But the efficacy and the voltage ratio attained is less. To overcome this, a quadratic boost converter (QBC) is proposed.

QBC attains high voltage conversion rate with suitable duty ratio and with less voltage strain on the key switch. The vitality stowed in the leakage inductance can be reprocessed to the capacitor at the output port. The input voltage given to this converter is 20–40 V, and the voltage is boosted up to 400 V as output [24]. During high-line input, the efficiency is 93.3% and low-line input efficiency is 89.3%. The converter is shown in Fig. 8.

The converter can be alienated into predictable boost converter and boost fly back converter, usually coined as first step-up mode and second step-up mode. The characteristics of this converter are: (1) The QBC is efficiently prolonged to a high boost-up ratio and the first boost-up mode also aided in the current ripple decrement

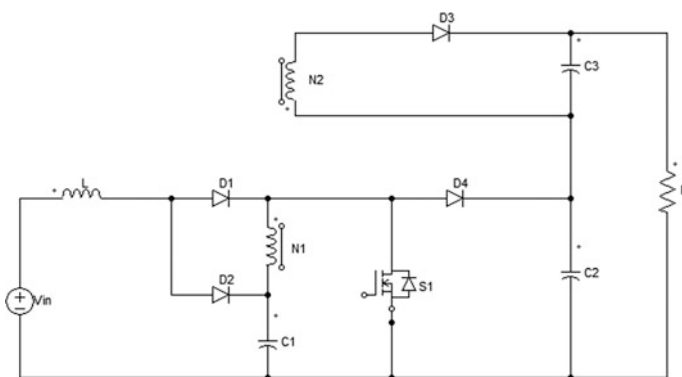


Fig. 8 Quadratic boost converter

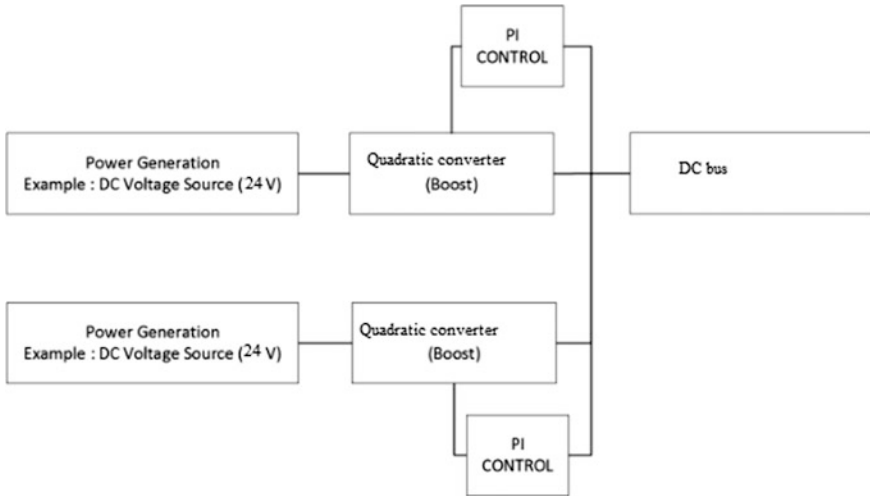


Fig. 9 Control block for proposed methodology

at the input; (2) the vitality of the leakage inductance can be reprocessed, which decreases the voltage strain on the dynamic switch, and also the renovation productivity is knowingly increased. This converter operates below continuous conduction mode. It operates in five modes.

In proposed methodology, the two quadratic boost converters are coupled in cascade setup to the renewable sources and the two voltages of the converter are made equal and the output is derived. Usually when two converters are paralleled, the output voltage may vary or circulating currents may occur. Here droop control method is used to overcome this circulating current with the help of resistance droop.

Here the input of the converter is given as 24 V, and the output attained is 48 V. The two boost converters are connected in parallel. MOSFET switch is used for control operation. PWM pulse generator and PID control strategy are utilized. The MATLAB/Simulink model is designed and verified for the output. The operations are followed as represented in Fig. 9.

3 Comparison Chart

From Table 1, the efficiency of the above-reviewed converters is given. Among them, the ultra-high converters play major conversion ratio, but the drawback is their efficiency that is not constant. The quadratic boost converter also plays a major role in conversion with high efficiency. All the above converters are best suitable for high voltage ratio conversion.

Table 1 Comparison chart

Parameter	Converter						
	Ultra-high converter	ZVT	Quadratic converter	MCB	High voltage gain	Three-phase high step-up	ULC
Voltage ratio	60 V to 6.6 kV	20–40 V to 400 V	45 V to 380 V	20 V to 380 V	20 V/380 V	12 V to 320 V	20 V to 400 V
Efficiency	Not constant	93–89.3%	96%	–	95.6%	High	93%
Switching voltage	Reduced	Less	Less	Less	Less	Zero	Less

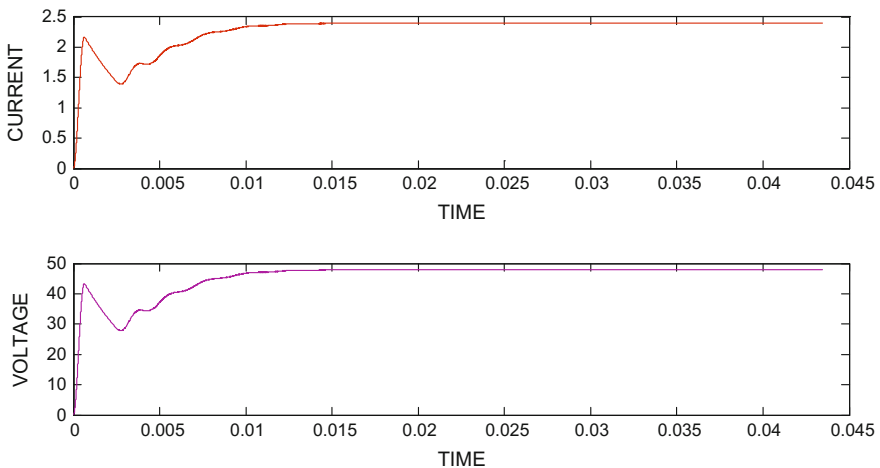


Fig. 10 Output waveform for single quadratic converter

4 Results and Discussion

A parallel DC–DC converter of quadratic boost topology is simulated using MATLAB/Simulink. A 24-V input voltage converter is paralleled, and the boost-up voltage 48 V is achieved. The implementation of the parallel quadratic converter does not require any communication channel. The converter voltage is made equal, and the circulating current is eliminated with the help of droop control strategy. The converter individual plot is signified in Fig. 10. The parallel converter plot is characterized in Fig. 11.

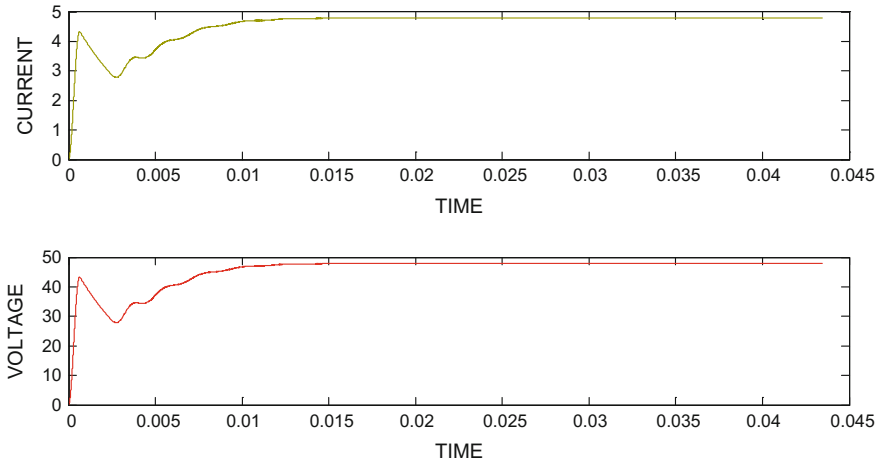


Fig. 11 Output waveform for current and voltage when connected in parallel

5 Conclusion

This review investigated the literature to know about the use of converters in the renewable system. Several studies have been made to design and implement DC–DC converters which are highly efficient. The advantage and the drawbacks of the converters are provided to understand their efficiency and the ratio conversion. The implementation of quadratic boost converter in parallel condition has high efficiency and high voltage conversion ratio. This review will help researchers to design converters with suitable limits and reduced semiconductor devices.

References

1. Blaabjerg, F., Iov, F., Kerekes, T., Teodorescu, R.: Trends in power electronics and control of renewable energy systems. 14th International Power Electronics and Motion Control Conference, 1, k1–19 (2010)
2. Calais, M., Agelidis, V.G.: Multilevel converters for single phase grid connected photovoltaic systems-an overview. *Int. Sympos. Indust. Electron.* **224–229**, 66 (1996)
3. Tomaszuk, A., Krupa, A.: High efficiency high step-up DC/DC converters—a review. *Bull. Pol. Acad. Sci. Tech. Sci.* **59**, 1239–1250 (2011)
4. Dawidziuk, J.: Review and comparison of high efficiency high power boost DC/DC converters for photovoltaic applications. *Bull. Pol. Acad. Sci. Tech. Sci.* **59**, 1239–1250 (2011)
5. Meneses, D., Blaabjerg, F., García, O.: Review and comparison of step-up transformer less topologies for photovoltaic AC-module application. *IEEE Trans. Power Electron.* **28**, 2649–2663 (2013)
6. Zhao, Q., Lee, F.C.: High-efficiency, high step-up dc-dc converters. *IEEE Trans. Power Electron.* **18**, 65–73 (2003)

7. SriRevathi, B., Prabhakar, M.: Analysis and design of ultra-high step up converter for DC microgrids. In: Annual IEEE India Conference, pp. 1–6 (2013)
8. Jin, K., Yang, M., Ruan, X., Xu, M.: Three-level bidirectional converter for fuel-cell/battery hybrid power system. *IEEE Trans. Ind. Electron.* **57**, 1976–1986 (2010)
9. Li, W., Li, W., Deng, Y., He, X.: Single-stage single-phase high-step-up ZVT boost converter for fuel-cell microgrid system. *IEEE Trans. Power Electron.* **25**, 3057–3065 (2010)
10. Park, K.B., Moon, G.W., Youn, M.J.: Nonisolated high step-up boost converter integrated with sepic converter. *IEEE Trans. Power Electron.* **25**, 2266–2275 (2010)
11. Samavatian, V., Radan, A.: A novel low-ripple interleaved buck–boost converter with high efficiency and low oscillations for fuel cell applications. *Int. J. Electr. Power Energy Syst.* **62**, 5560–5568 (2014)
12. Garg, M., Singh, R.K., Mahanty, R.: Magnetically coupled boost converter with enhanced equivalent series resistance filter capacitor for DC microgrid. *IET Power Electron.* **9**, 1943–1951 (2016)
13. Chun C.Y., et al.: A novel single-switch resonant power converter for renewable energy generation applications. In: Proceedings of IEEE/ IAS Industrial and Commercial Power Systems Technical Conference (I&CPS), vol. 50, pp. 1322–1330 (2013)
14. Abutbul, O., Gherlitz, A., Berkovich, Y., Ioinovici, A.: Step-up switching-mode converter with high voltage gain using a switched-capacitor circuit. *IEEE Trans. Circ. Syst. I: Fundam. Theory Appl.* **50**, 1098–1102 (2003)
15. Lakshmi, T.S., Rama Rao, P.V.V.: High voltage gain boost converter for micro grid application. *IEEE Trans. Power Electron.* 323–328 (2012)
16. Prasad, A.R., Ziogas, P.D., Manias, S.: Analysis and design of a three-phase offline DC-DC converter with high-frequency isolation. *IEEE Trans. Ind. Appl.* **28**, 824–832 (1992)
17. Sobrayen, L., Rathore, A.K.: Three-phase soft-switching bi-directional DC-DC converter for low voltage high power applications. In: IEEE 8th International Power Electronics and Motion Control Conference (IPEMC-ECCE Asia), pp. 90–97 (2016)
18. Miura, Y., Kaga, M., Horita, Y., Ise, T.: Bidirectional isolated dual full-bridge dc-dc converter with active clamp for EDLC. In: Energy Conversion Congress and Exposition (ECCE), 2010 IEEE, Atlanta, GA, pp. 1136–1143 (2010)
19. Wu, T.F., Chen, Y.C., Yang, J.G., Kuo, C.L.: Isolated bidirectional full-bridge DC–DC converter with a flyback snubber. *IEEE Trans. Power Electron.* **25**, 1–5 (2010)
20. Yang, L.S., Liang, T.J., Lee, H.C., Chen, J.F.: Novel high step-up dc-dc converter with coupled-inductor and voltage-doubler circuits. *IEEE Trans. Ind. Electron.* **58**, 777–782 (2011)
21. Lai, C.M., Lin, Y.C., Lin, Y.J.: Newly-constructed bidirectional DC/DC converter topology with high voltage conversion ratio for vehicle to DC-micro grid (V2DCG) System, pp. 1–8 (2015)
22. Papanikolaou, N.P., Tatakis, E.C.: Active voltage clamp in flyback converters operating in CCM mode under wide load variation. *IEEE Trans. Ind. Electron.* **51**, 632–640 (2004)
23. Wai, R.J., Duan, R.Y.: High-efficiency DC/DC converter with high voltage gain. *IEE Proc. Inst. Elect. Eng. Electr. Power Appl.* **152**, 793–802 (2005)
24. Tseng, K.C., Liang, T.J.: Novel high-efficiency step-up converter. *IEE Proc. Inst. Elect. Eng. Electr. Power Appl.* **151**, 880–885 (2004)

Quantum Streaming Instabilities in Multi-component Plasma with Dust Particles

U. Deka, K. Choudhury and P.K. Karmakar

Abstract Streaming instabilities in quantum dusty plasmas composed of multi-ionic species are investigated by applying quantum hydrodynamic model. The growth characteristics in two separate cases of ion streaming and dust streaming are discussed. Implications and applications are highlighted.

Keywords Streaming instability · Quantum hydrodynamics · Multi-ion dusty plasma · Quantum plasma

1 Introduction

Quantum plasma has aroused a lot of interest among the scientists and engineers from various fields of science and engineering from the beginning of this century [1–3]. The driving force for the growth of research in this area is because of the advancement in the technology for building micro- and nano-electronic devices and its role in other disciplines of physics, e.g., dense astrophysical systems and laser-produced plasmas [2–4]. The electron gas in an ordinary metal is actually quantum plasma. The impetus in the degree of miniaturization and robustness of today's electronic components vastly depends upon the theoretical development in the field of quantum plasma. The rationale of application of the principle of quantum mechanics is validated by the fact that the de Broglie wavelength of the charge carriers is on an average equivalent to the size of the system [5–9], which is confirmed by numerical methods [10] too. Hence, application of quantum mechanics (e.g., tunneling) is justified and is going to be fundamental in the manufacturing of the futuristic electronic components in the coming years [11, 12].

U. Deka (✉) · K. Choudhury
Department of Physics, Sikkim Manipal Institute of Technology, Rangpo 737136,
Sikkim, India
e-mail: udeka1@rediffmail.com

P.K. Karmakar
Department of Physics, Tezpur University, Napaam, Tezpur 784028, Assam, India

Therefore, it is certain that transport models based on classical physics will be inappropriate to describe such quantum effects. Hence, it will be necessary to apply quantum transport equations like the Schrödinger–Poisson or the Wigner–Poisson equations to understand the basic properties and transport mechanism of such physical systems [11–15].

The occurrence of quantum plasmas is seen in the context of some astrophysical objects satisfying the requisite conditions. In case of extremely high dense objects like white dwarfs, where the density is few tens of order of magnitudes higher than the density of solids, even though the temperature is very high but it is still lesser than the electron Fermi temperature. A white dwarf behaves as a natural source of hot fusion plasma (10^8 K), because of its large density. It still behaves quantum mechanically in spite of its extreme temperature.

The quantum mechanical effects on plasma are invoked through two models—the Wigner model and the Hartree model derived from the Wigner–Poisson and Schrödinger–Poisson equations, which represent the statistical and hydrodynamic behaviors, respectively.

Manfredi [1] in his work has given an elaborate discussion about different paths for the inclusion of the quantum effects on the modeling of electrostatic collisionless plasmas. The complete kinetic model is provided by Wigner model [15–17]. The Wigner formalism was further considered in terms of N one-particle Schrödinger equations, coupled with Poisson's equation that gives rise to the Hartree formalism. This method is comparable to the 'multi-stream' approach in classical plasma physics. The physical consideration for application of quantum mechanics to understand some of the plasma phenomena has been vividly described by the authors [2]. It was very lucidly shown that the fluid models can be derived from kinetic descriptions of charged particle systems using the Wigner–Poisson formalism.

In one of the pioneering works [8] by Haas and Manfredi, they used the statistical representation of the N particles using N pure states, each described by a wave function to represent the 'multi-stream' model. They investigated one- and two-stream cases deriving the dispersion relation for two-stream instability using the Schrödinger–Poisson [1] formalism. The outcome of the numerical simulation and from linear analysis in strongly nonlinear domain further established that the dynamics of quantum plasma can be described by self-consistent nonlinear Schrödinger–Poisson system.

Haas et al. have put forward a quantum multi-stream model under nonlinear Schrödinger–Poisson formalism and analyzed the dispersion relations for one- and two-stream instabilities in their work [9]. In fact, it has been also shown that in multi-stream quantum plasma, application of kinetic theory leads to the damping of instabilities in one- and two-stream instability. The kind of damping is similar to that of Landau damping [5].

Again, Ali and Shukla as mentioned in Ref. [4] studied the instability due to streaming of ions and dust particles. They pointed out that a generalized dielectric response in the case of unmagnetized quantum dusty plasma deviates appreciably as compared to similar phenomenon in absence of quantum affects. The application of

quantum effects was limited to the electrons as they were inertialess. However, the dynamics of the ions and the dust particles were discussed using classical physics only. As in many astrophysical cases, there may be situations encountered where there is a plasma system consisting of multiple ions and dust particles.

In this work, we have proposed a model to see the quantum effect on multi-component ionic plasma. Our model of plasma system is composed of electrons, two different ions, and dust particles. We have further analyzed how streaming instability depends on the mass of different ionic species and its variation.

2 Theoretical Modeling

In this work, we have considered multi-component quantum plasma along with dust particles. We have discussed earlier about the basics of quantum plasma and the criteria under which we define a plasma to be quantum in nature. Further, we have defined three dimensionless parameters, which helps us to distinguish between classical and quantum plasma. But before we dig further into this problem, we would like to mention a few things about dusty plasmas. Dusty plasmas are composed of electrons, ions, and negatively charged dust particles having large spectra of applications varying from space to industries. The dust particles are found to exist under different conditions varying from low temperature laboratory plasma to space and astrophysical plasmas. Dust particles can have either negative or positive charges depending upon the mechanism of charging like electron-ion sticking on the dust particles surface from the background plasma, ultraviolet radiations, electrons emission due to secondary processes, and thermionic emission.

Dusty plasmas are stable under equilibrium plasma and become unstable under non-equilibrium plasmas due to the availability of free energy. The amplitudes of the collective modes grow or damp exponentially with respect to time if the sign of the imaginary term in the wave frequency is positive and decay if the sign is negative. By multi-component plasma, we mean the plasma consists of multiple types of ions (Ar-N₂, Ar-H₂, etc.), electrons, and dust particles as well.

3 Mathematical Modeling

We have considered multi-species quantum plasma composed of electrons, two species of singly charged ions, and negatively charged dust particulates. The charge neutrality condition at equilibrium is $\sum_j q_j n_{j0} = 0$, where q_j is the charge ($-e$ for electrons, e for ions, and $-Z_{d0}e$ for dust particulates); Z_{d0} is the number of electrons residing on the dust particle; n_{j0} is the equilibrium number density.

Here, only electrostatic perturbations are taken into account in the absence of external magnetic field. Quantum hydrodynamic model is used to describe the dielectric response function of the streaming plasma species. The linearized equation of continuity is given below.

$$\frac{\partial n_{j1}}{\partial t} + n_{j0} \frac{\partial U_{j1}}{\partial x} + U_{j0} \frac{\partial n_{j1}}{\partial x} = 0 \quad (1)$$

The linearized equation of motion can be written as,

$$\left(\frac{\partial U_{j1}}{\partial t} + U_{j0} \frac{\partial U_{j1}}{\partial x} \right) = -\frac{q_j}{m_j} \frac{\partial \varphi_1}{\partial x} - \frac{1}{m_j n_{j0}} \frac{\partial P_j}{\partial x} + \frac{\hbar^2}{4m_j^2 n_{j0}} \frac{\partial^3 n_{j1}}{\partial x^3} \quad (2)$$

The linearized Poisson's equation is given as,

$$\frac{\partial^2 \varphi_1}{\partial x^2} = -4\pi \sum_j q_j n_{j1} \quad (3)$$

where $n_{j1}(n_{j0})$ is the perturbed (unperturbed) density, $U_{j1}(U_{j0})$ is the perturbed (unperturbed) flow velocity, φ_1 is the perturbed electrostatic potential. We have considered an isothermal equation of state, and the isothermal pressure of the quantum plasma is given by $P_j = n_{j1} k_B T_j$ where T_j is the temperature of the corresponding species, k_B is the Boltzmann constant. Quantum statistical effects are neglected in our calculation. The standard nonlinear Schrödinger–Poisson system is used to derive the equations from (1) to (3), describing the dynamics of the quantum plasma. The last term in the right-hand side of Eq. (2) signifies the quantum diffraction effects and its genesis lies in the quantum correlation of density fluctuations. Here, we are using the perturbations as

$$n_j = n_{j0} + n_{j1}, \quad (4)$$

$$U_j = U_{j0} + U_{j1} \quad (5)$$

and

$$\varphi = \varphi_1 \quad (6)$$

Assuming a form of plane wave solution $\exp(ikx - i\omega t)$ for the perturbed quantities, where $k(\omega)$ is the wave number (angular frequency) of the propagating waves. We evaluate n_{j1} and U_{j1} from (1) to (2), which is given below.

$$n_{j1} = \frac{kn_{j0}}{(\omega - kU_{j0})} U_{j1} \quad (7)$$

and,

$$U_{j1} = \frac{1}{(\omega - kU_{j0})} \left[\frac{q_j}{m_j} k\varphi_1 + \frac{k_B T_j}{m_j n_{j0}} k n_{j1} + \frac{\hbar^2}{4m_j^2 n_{j0}} k^3 n_{j1} \right] \quad (8)$$

Using Eqs. (8) and (7) and on further simplification, we will get

$$n_{j1} = \frac{q_j n_{j0}}{m_j} \left[\frac{k^2 \varphi_1}{(\omega - kU_{j0})^2 - V_{ij}^2 k^2 - \frac{\hbar^2 k^4}{4m_j^2}} \right], \quad (9)$$

where $V_{ij} = \sqrt{\frac{k_B T_j}{m_j}}$ is the thermal speed.

Using Eqs. (3) and (9), the generalized form of the dielectric response in quantum dusty plasma is derived as given below.

$$\left[1 - \sum_{j=e,i1,i2,d} \frac{\omega_{pj}^2}{(\omega - kU_{j0})^2 - k^2 V_{ij}^2 - \frac{\hbar^2 k^4}{4m_j^2}} \right] = 0, \quad (10)$$

where $\omega_{pj} = \sqrt{4\pi q_j^2 n_{j0} / m_j}$ is the plasma frequency. Equation (10) is the generalized form of dielectric response function in quantum dusty plasma. Equation (10) can be further expanded as

$$1 - \frac{\omega_{pe}^2}{(\omega - kU_{e0})^2 - \Omega_e^2} - \frac{\omega_{pi1}^2}{(\omega - kU_{i10})^2 - \Omega_{i1}^2} - \frac{\omega_{pi2}^2}{(\omega - kU_{i20})^2 - \Omega_{i2}^2} - \frac{\omega_{pd}^2}{(\omega - kU_{d0})^2 - \Omega_d^2} = 0, \quad (11)$$

where $\Omega_e^2 = k^2 V_{te}^2 + \hbar^2 k^4 / 4m_e^2$, $\Omega_{i1}^2 = k^2 V_{ti1}^2 + \hbar^2 k^4 / 4m_{i1}^2$, $\Omega_{i2}^2 = k^2 V_{ti2}^2 + \hbar^2 k^4 / 4m_{i2}^2$ and $\Omega_d^2 = k^2 V_{td}^2 + \hbar^2 k^4 / 4m_d^2$.

The analysis of the two cases, ion streaming instability and dust streaming instability, is presented in the following section.

3.1 Ion Streaming Instability

Applying the approximations $|\omega - kU_{e0}\rangle\langle\langle\Omega_e, |\omega - kU_{i10}\rangle\rangle\Omega_{i1}, |\omega - kU_{i20}\rangle\rangle\Omega_{i2}$, and $\rangle\rangle kU_{d0}, \Omega_d$, we can write Eq. (11) as

$$1 + \frac{\omega_{pe}^2}{k^2 V_{te}^2 + \hbar^2 k^4 / 4m_e^2} - \frac{\omega_{pi1}^2}{(\omega - kU_{i10})^2} - \frac{\omega_{pi2}^2}{(\omega - kU_{i20})^2} - \frac{\omega_{pd}^2}{\omega^2} = 0 \tag{12}$$

or

$$1 - \frac{\Omega_{IA1}^2}{(\omega - kU_{i10})^2} - \frac{\Omega_{IA2}^2}{(\omega - kU_{i20})^2} - \frac{\Omega_{DA}^2}{\omega^2} = 0, \tag{13}$$

where

$$\Omega_{IA1} = \omega_{pi1} \sqrt{\left(k^2 V_{te}^2 + \frac{\hbar^2 k^4}{4m_e^2}\right) / \left(\omega_{pe}^2 + /k^2 V_{te}^2 + \frac{\hbar^2 k^4}{4m_e^2}\right)},$$

$$\Omega_{IA2} = \omega_{pi2} \sqrt{\left(k^2 V_{te}^2 + \frac{\hbar^2 k^4}{4m_e^2}\right) / \left(\omega_{pe}^2 + /k^2 V_{te}^2 + \frac{\hbar^2 k^4}{4m_e^2}\right)}$$

are the ion acoustic frequencies for ion 1 and ion 2, respectively, and $\Omega_{DA} = \omega_{pd} \sqrt{\left(k^2 V_{te}^2 + \frac{\hbar^2 k^4}{4m_e^2}\right) / \left(\omega_{pe}^2 + /k^2 V_{te}^2 + \frac{\hbar^2 k^4}{4m_e^2}\right)}$ is the dust acoustic frequency. From the above expressions and considering the ions to be singly charged and representing $m_{i2}/m_{i1} = \epsilon$, we can show that

$$\Omega_{IA2} = \frac{m_{i1}}{m_{i2}} \Omega_{IA1} = \frac{\Omega_{IA1}}{\epsilon}. \tag{14}$$

Let us consider, $\omega = kU_{i10} + \delta$ and $\omega = kU_{i20} + \delta'$, $\Omega_{DA} \sim kU_{i10}$. If we take the temperature of both the ions to be equal, then the flow velocity is proportional to the mass of the ions. So, we consider $U_{i10} \sim \alpha U_{i20}$ (where $\alpha = 1/\sqrt{\epsilon}$). Then from Eq. (13), we get

$$1 - \frac{\Omega_{IA1}^2}{(\delta)^2} - \frac{\Omega_{IA1}^2}{\epsilon^2 (\delta')^2} - \frac{(\omega - \delta)^2}{\omega^2} = 0$$

or

$$\delta^3 = \frac{1}{2} \Omega_{IA1}^2 kU_{i10} \left[1 + \frac{1}{\epsilon^2 \left(\frac{\delta'}{\delta}\right)^2} \right]. \tag{15}$$

As the flow velocities are inversely proportional to the mass of the respective ions, so we consider $(\delta'/\delta) \propto \alpha$, and so, on solving Eq. (15), we will have three values of δ , as given below.

$$\delta = \left(\frac{\Omega_{IA1}^2 k U_{i10}}{2} \right)^{1/3} \left(1 + \frac{1}{\epsilon} \right)^{1/3}, \left(\frac{-1 + i\sqrt{3}}{2} \right) \left(\frac{\Omega_{IA1}^2 k U_{i10}}{2} \right)^{1/3} \left(1 + \frac{1}{\epsilon} \right)^{1/3},$$

and $\left(\frac{-1 - i\sqrt{3}}{2} \right) \left(\frac{\Omega_{IA1}^2 k U_{i10}}{2} \right)^{1/3} \left(1 + \frac{1}{\epsilon} \right)^{1/3}.$

The real and imaginary parts of the second root can be written as

$$\omega_r = -\frac{1}{2^{4/3}} [\Omega_{IA1}^2 k U_{i10}]^{1/3} \left(1 + \frac{1}{\epsilon} \right)^{1/3} \quad \text{and}$$

$$\omega_i = \frac{\sqrt{3}}{2^{4/3}} [\Omega_{IA1}^2 k U_{i10}]^{1/3} \left(1 + \frac{1}{\epsilon} \right)^{1/3}$$

respectively. The normalized form of the real part can be written as

$$\omega'_r = \omega_r / \omega_{pi1} = -\frac{1}{2^{4/3}} \left[\frac{K' \omega_{pi1}^2 (K'^2 V_{te}^2 + K'^4 H^2 / 4)}{(K'^2 V_{te}^2 + \omega_{pe}^2 + K'^4 H^2 / 4)} \right]^{1/3} \left(1 + \frac{1}{\epsilon} \right)^{1/3}; \quad (16)$$

Similarly,

$$\omega'_i = \frac{\sqrt{3}}{2^{4/3}} \left[\frac{K' \omega_{pi1}^2 (K'^2 V_{te}^2 + K'^4 H^2 / 4)}{(K'^2 V_{te}^2 + \omega_{pe}^2 + K'^4 H^2 / 4)} \right]^{1/3} \left(1 + \frac{1}{\epsilon} \right)^{1/3}. \quad (17)$$

The normalizing parameters used are given below.

$$\omega'_{r,i} = \omega_{r,i} / \omega_{pi}, \omega'_{pi1} = 1, \omega'_{pe} = \omega_{pe} / \omega_{pi1}, K' = k U_{i10} / \omega_{pi1},$$

$$V'_{te} = V_{te} / U_{i10}, H = \hbar \omega_{pi1} / m_e U_{i10}^2.$$

3.2 Dust Streaming Instability

To solve the streaming instability in the presence of dust particles, we consider the approximations $|\omega - k U_{e0}| \langle \langle \Omega_e, \omega \rangle \rangle k U_{i10}, \Omega_{i1}$, and $\langle \langle \omega \rangle \rangle k U_{i20}, \Omega_{i2}$, and using Eq. (11), we derive the following equation.

$$1 + \frac{\omega_{pe}^2}{k^2 V_{te}^2 + \hbar^2 k^4 / 4m_e^2} - \frac{\omega_{pi1}^2}{(\omega)^2} - \frac{\omega_{pi2}^2}{(\omega)^2} - \frac{\omega_{pd}^2}{(\omega - kU_{d0})^2} = 0 \tag{18}$$

or

$$1 - \frac{\Omega_{IA1}^2}{\omega^2} \left[1 + \frac{1}{\epsilon^2} \right] - \frac{\Omega_{DA}^2}{(\omega - kU_{d0})^2} = 0. \tag{19}$$

Considering $\omega = kU_{d0} + \Delta$ with $\Delta < kU_{d0}$ and $kU_{d0} \sim \Omega_{IA1}$ and using Eq. (19), we have

$$1 - \frac{(\omega - \Delta)^2}{\omega^2} (1 + 1/\epsilon^2) - \frac{\Omega_{DA}^2}{\Delta^2} = 0$$

or

$$\Delta^3 = \frac{1}{2} \Omega_{DA}^2 kU_{d0} \left[\frac{\epsilon^2}{1 + \epsilon^2} \right]. \tag{20}$$

The roots of Eq. (20) are

$$\Delta = \left(\frac{\Omega_{DA}^2 kU_{d0}}{2} \right)^{1/3} (\epsilon^2 / 1 + \epsilon^2)^{1/3}, \left(\frac{-1 + i\sqrt{3}}{2} \right) \left(\frac{\Omega_{DA}^2 kU_{d0}}{2} \right)^{1/3} (\epsilon^2 / (1 + \epsilon^2))^{1/3}$$

and

$$\left(\frac{-1 - i\sqrt{3}}{2} \right) \left(\frac{\Omega_{DA}^2 kU_{d0}}{2} \right)^{1/3} (\epsilon^2 / (1 + \epsilon^2))^{1/3}.$$

The second root can be written as

$$\omega_r = -\frac{1}{2^{4/3}} (\Omega_{DA}^2 kU_{d0})^{1/3} (\epsilon^2 / (1 + \epsilon^2))^{1/3} \quad \text{and}$$

$$\omega_i = -\frac{\sqrt{3}}{2^{4/3}} (\Omega_{DA}^2 kU_{d0})^{1/3} (\epsilon^2 / (1 + \epsilon^2))^{1/3}.$$

Introducing the normalized parameters as

$$\omega'_{r,i} = \omega_{r,i} / \omega_{pd}, \omega'_{pd} = 1, \omega'_{pe} = \omega_{pe} / \omega_{pd},$$

$$K' = kU_{d0} / \omega_{pd}, V'_{te} = V_{te} / U_{d0}, H = \hbar \omega_{pd} / m_e U_{d0}^2.$$

We can have the normalized equations as

$$\omega'_r = \omega_r / \omega_{pd} = -\frac{1}{2^{4/3}} \left[\frac{K' \omega_{pd}^2 (K'^2 V_{te}^2 + K'^4 H^2 / 4)}{(K'^2 V_{te}^2 + \omega_{pe}^2 + K'^4 H^2 / 4)} \right]^{1/3} [\epsilon^2 / (1 + \epsilon^2)]^{1/3} \quad (21)$$

Similarly,

$$\omega'_r = \frac{\sqrt{3}}{2^{4/3}} \left[\frac{K' \omega_{pd}^2 (K'^2 V_{te}^2 + K'^4 H^2 / 4)}{(K'^2 V_{te}^2 + \omega_{pe}^2 + K'^4 H^2 / 4)} \right]^{1/3} [\epsilon^2 / (1 + \epsilon^2)]^{1/3} \quad (22)$$

3.3 Numerical Analysis

The results obtained in the previous chapter are solved numerically to understand different physical processes responsible for the instability when quantum effects are included. For numerical calculation of the growth rates and angular frequencies, we have considered some typical parameters, which represent dense astrophysical plasmas: $m_e = 9.1 \times 10^{-28}$ g, $m_{i1} = 2 m_p$ (for H₂ ion), $m_{i2} = 28 m_p$ (for N₂ ion), $m_{i3} = 40 m_p$ (for Ar ion) [where ‘ m_p ’ is the mass of proton], $m_d = 4.008 \times 10^{-6}$ g, $n_{e0} \approx n_{i0} = 1.0 \times 10^{19}$ cm⁻³, $T_e = 10^5$ K, and dust charge state $Z_{d0} = 10^4$. The growth rate equations as mentioned in the previous section, i.e., Eqs. (16), (17), (21), and (22), are solved numerically.

The real and the imaginary parts of the angular oscillation frequencies for the different cases are solved to find the behavior of growth rate due to streaming instabilities. The different cases include pure classical case, i.e., without the inclusion of the quantum effect and the quantum case. We have studied the two situations for two different plasma configurations of Ar–N₂ and Ar–H₂ plasma. We have also studied the effect of the presence of dust particles on both the multi-component plasma system. The graphical outputs from our numerical analysis are given below.

4 Results and Discussions

In Fig. 1a–c, normalized growth rates are plotted against normalized wave numbers. In Fig. 1a, the growth rate is initially observed to increase sharply with the increase in normalized wave number. We can observe that the growth rate starts saturating from $\tilde{K} \approx 0.001$ for both the plasma system considered here, with the increase in value of \tilde{K} . Here, ion streaming speed is considered as the variable parameter, but for the different values of normalized speed, the curves superimpose

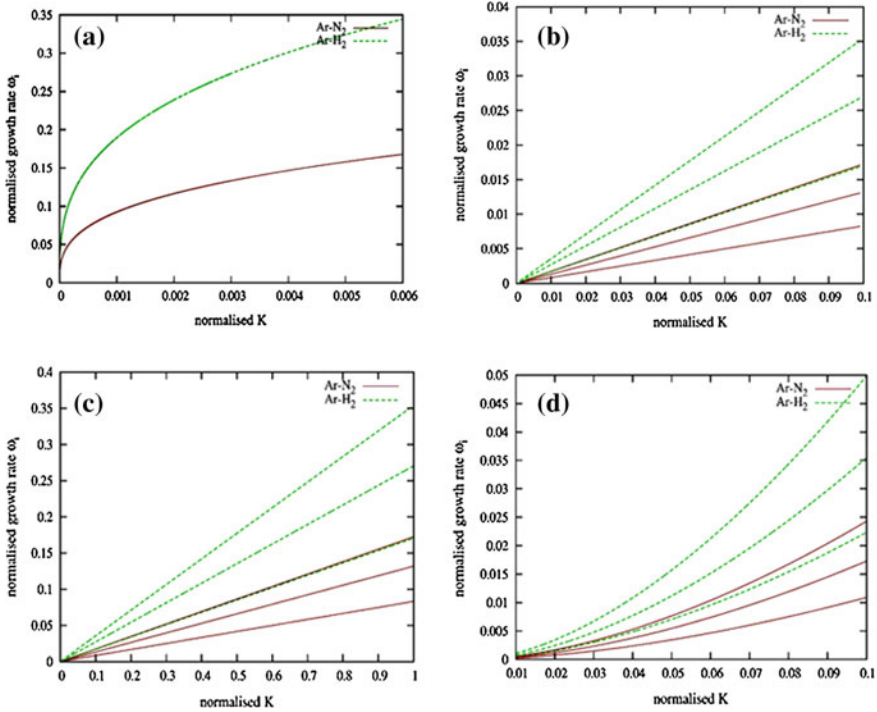


Fig. 1 Normalized growth rates, $(\tilde{\omega}_i = \omega_i/\omega_{pi})$ are plotted against the normalized wave number $(\tilde{K} = KU_{i0}/\omega_{pi})$ with **a** different ion streaming speeds $U_{i0} = 0.0001\omega_{pi}$, $U_{i0} = 0.0003\omega_{pi}$, $U_{i0} = 0.0006\omega_{pi}$; **b** and **c** in pure classical case ($H = 0$) with changing electron, thermal speed $\tilde{V}_{te} = 0.01, 0.02, 0.03$ and $U_{i0} = 0.01\omega_{pi}$; **d** in pure quantum case ($\tilde{V}_{te} = 0$) and varying H ($H = 0.3, 0.6, 1$) keeping $U_{i0} = 0.01\omega_{pi}$

on each other and we get a single line for each plasma system. In Fig. 1b, pure classical case with the quantum parameter $H = 0$ has been considered.

Here, linear growth rate has been observed with no signs of saturation for the smaller values of \tilde{K} as well as for the higher values of \tilde{K} (Fig. 1c). In Fig. 1d, pure quantum case with the electron thermal velocity $\tilde{V}_{te} = 0$ has been considered. A moderate growth rate can be observed in this case too, with distinct lines for each value of the variable parameter, though the thermal velocity of the electrons is zero. In Fig. 2a–c, normalized growth rates are plotted against normalized wave numbers. In Fig. 2a, the growth rate is initially observed to increase rapidly with the increase in normalized wave number. At a very small value of \tilde{K} for both the plasma system considered here, shows a sign of saturation as the \tilde{K} value increases. Here, ion streaming speed is considered as the variable parameter, but for the different values of normalized speed, the curves superimpose on each other and we get a single line for each plasma system.

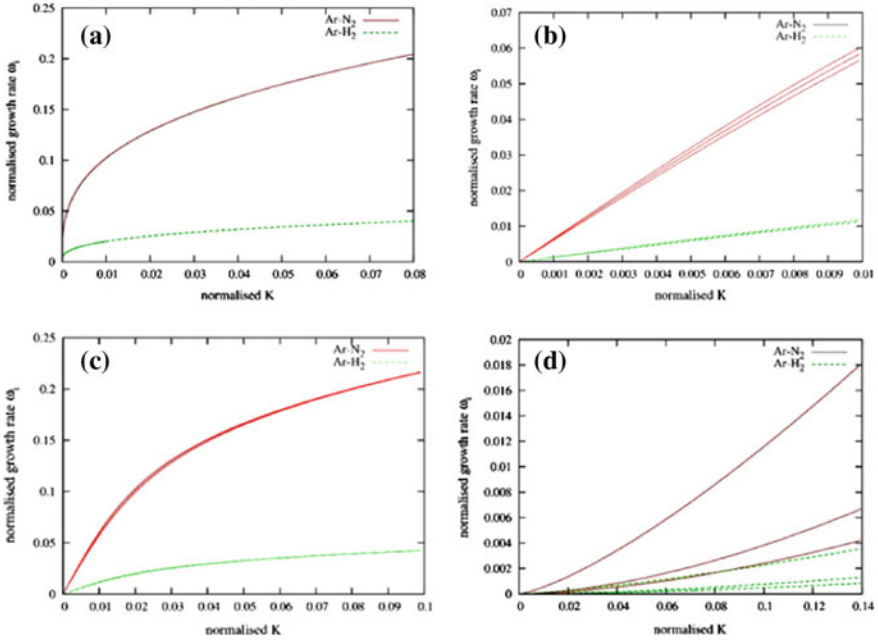


Fig. 2 Normalized growth rates ($\tilde{\omega}_i = \omega_i/\omega_{pd}$) are plotted against the normalized wave number ($\tilde{K} = KU_{i0}/\omega_{pd}$) with **a** different dust streaming speeds $U_{d0} = 0.001 \omega_{pd}$, $U_{d0} = 0.004 \omega_{pd}$, $U_{d0} = 0.008 \omega_{pd}$; **b** and **c** in pure classical case ($H = 0$) with changing electron, thermal speed ($\tilde{V}_{te} = 17, 18, 19$) and $U_{d0} = 0.001 \omega_{pd}$; **d** in pure quantum case $\tilde{V}_{te} = 0$ and varying H ($H = 0.03, 0.06, 0.1$) keeping $U_{d0} = 0.14 \omega_{pd}$

In Fig. 2b, pure classical case with the quantum parameter $H = 0$ has been considered. Here, linear growth rate can be observed with no signs of saturation for the lower range of \tilde{K} . But for the higher values of \tilde{K} (Fig. 1c), three distinct lines for each plasma system for the variable parameter \tilde{V}_{te} merge into one and a sign of saturation too can be witnessed, which was not observed in the case of ion streaming instability. In Fig. 2d, pure quantum case with the electron thermal velocity, $\tilde{V}_{te} = 0$ has been plotted. A moderate growth rate can be observed in this case too, even though the thermal velocity of the electrons is zero. Three different lines for each plasma system can be observed due to the variable parameter H .

Figure 3a–c clearly shows that the growth rate due to ion streaming instability in a plasma having heavier multiple ion species is significantly more compared to a plasma consisting of a relatively lighter ion species. But the case is vice versa when dust streaming instability is taken into consideration. Figure 3d represents the growth rate variation during dust streaming instability.

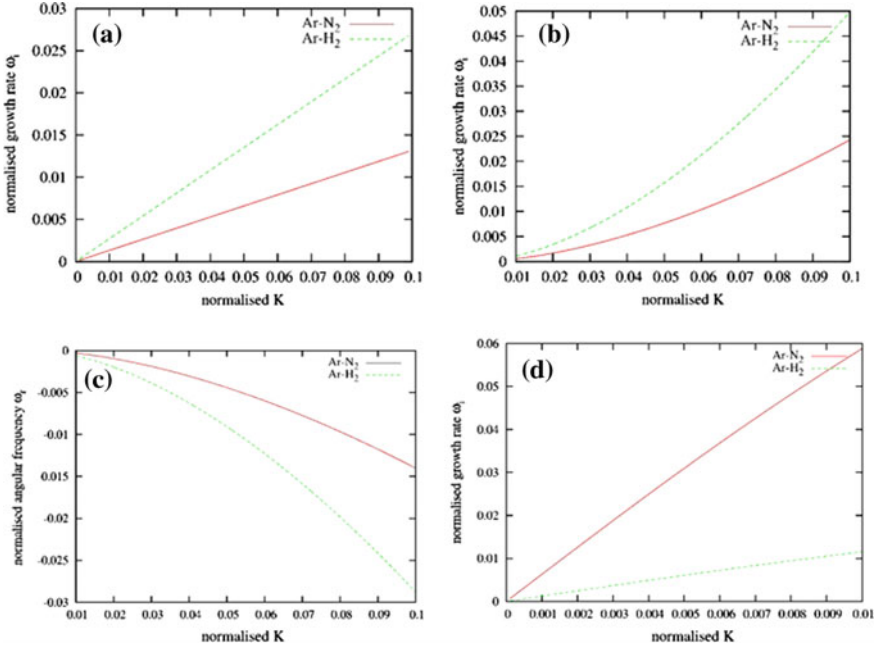


Fig. 3 Normalized growth rates ($\tilde{\omega}_i = \omega_i/\omega_{pi}$) are plotted against the normalized wave number ($\tilde{K} = KU_{i0}/\omega_{pi}$); **a** in pure classical case ($H = 0$) with electron, thermal speed ($\tilde{V}_{te} = 0.02$); **b** in pure quantum case $\tilde{V}_{te} = 0$ and H ($H = 1.0$) keeping $U_{i0} = 0.01\omega_{pi}$; **c** normalized angular frequency ($\tilde{\omega}_r = \omega_r/\omega_{pi}$) are plotted against the normalized wave number ($\tilde{K} = KU_{i0}/\omega_{pi}$) with ($\tilde{V}_{te} = 0$) and H ($H = 1.0$) keeping $U_{i0} = 0.01\omega_{pi}$. Normalized growth rates ($\tilde{\omega}_i = \omega_i/\omega_{pd}$) are plotted against the normalized wave number ($\tilde{K} = KU_{i0}/\omega_{pi}$); **d** in pure classical case ($H = 0$) with electron, thermal speed $\tilde{V}_{te} = 18$

5 Conclusions

Here, in this work, a general dielectric response of multi-component quantum dusty plasma has been presented using the QHD model and Poisson's equation. The conclusions that can be inferred from this analysis are mentioned below. In such plasma, the mass of the ions has got a significant effect on the growth rate, hence the instability.

It can be clearly seen from the plots that instability in a plasma containing heavier species grows slowly compared to a plasma consisting of their lighter counter parts in the case of ion streaming and vice versa for dust streaming instability. Two specific cases of instability of ion streaming and dust streaming are presented here. The analytical and numerical calculations both show that the thermal speeds, streaming speeds, and the quantum effects have a dominant role on the profile of the growth rates and the real angular frequencies.

Quantum effects are only applicable to the electron density perturbation, and the ion species and negatively charged dust particles are treated classically. The presence of the dust particles has affected the instability of the system on a whole and has modified the growth rate.

In pure classical treatment, the linear growth rate, which was observed is unphysical. With the inclusion of the quantum effect we come closer to a more real situation where the growth rate slowly approaches toward saturation. In the pure quantum case, we can clearly see that though the normalized thermal velocity of the electrons are zero, we can still experience instability. It is interesting to note that finite growth rate can be observed even in absence of electron thermal velocity when quantum effects are included, as seen from Fig. 2d. However, the growth rates may be very small compared to the situations when electron thermal velocity is non zero. Such effect is absent in the case of pure classical case and this typical behavior may be attributed to the quantum effect. An analog may be drawn from the quantum oscillators in which the zero-point energy is nonzero. Also, we observe that in the case of hydrogen atom, the ground state energy is finite. Finally, the results may be helpful to delve upon the underlying cause of dense astrophysical objects with quantum dusty plasmas containing multiple ions and streaming dusts.

References

1. Manfredi, G.: How to model quantum plasmas. *Field Inst. Comm.* **46**, 263–287 (2005)
2. Haas, F.: *Quantum Plasmas: An Hydrodynamic Approach*. Springer Science & Business Media (2011)
3. Shapiro, S.L., Teukolsky, S.A.: *Black Holes, White Dwarfs, and Neutron Stars*. Springer, Berlin (2004)
4. Ali, S., Shukla, P.K.: Streaming instability in quantum dusty plasmas. *Eur. Phys. J. D* **41**, 319–324 (2007)
5. Gurnett, D.G., Bhattacharjee, A.: *Introduction to Plasma Physics*. Cambridge University Press, Cambridge (2005)
6. Shukla, P.K., Eliasson, B.: Nonlinear collective interactions in quantum plasmas with degenerate electron fluids. *Rev. Mod. Phys.* **83**, 885–906 (2011)
7. Landau, L.D., Lifshitz, E.M.: *Statistical Physics*. Pergamon Press, New York (1980)
8. Manfredi, G., Haas, F.: Self-consistent fluid model for a quantum electron gas. *Phys. Rev. B* **64**(1–7), 075316 (2001)
9. Haas, F., Garcia, L.G., Goedert, J.: Quantum ion-acoustic waves. *Phys. Plasmas* **10**, 3585–3866 (2003)
10. Kiusalaas, J.: *Numerical Methods in Engineering with MATLAB*. Cambridge University Press, Cambridge (2005)
11. Jung, Y.D.: Quantum-mechanical effects on electron–electron scattering in dense high-temperature plasmas. *Phys. Plasmas* **8**, 3842–3844 (2001)
12. Opher, M., et al.: Nuclear reaction rates and energy in stellar plasmas: the effect of highly damped modes. *Phys. Plasmas* **8**, 2454–2460 (2001)
13. Flower, D.R., Middleton, M.J.: Electron attachment to interstellar grains. *Mon. Not. R. Astron. Soc.* **352**, 837–840 (2004)
14. Andreev, P.A., Kuzmenkov, L.S.: Ion acoustic and dust acoustic waves at finite size of plasma particles. *Phys. Plasmas* **22**(1–9), 032104 (2015)

15. Melrose, D.B.: Quantum Plasma dynamics. Springer, New York (2006)
16. Klimontovich, V.L.: Kinetic Theory of Nonideal Gases and Nonideal Plasmas. Pergamon Press, New York (1982)
17. Bonitz, M.: Kinetic theory for quantum plasmas. AIP Conf. Proc. **1421**, 135–155 (2012)

5.8-GHz Antenna Array Design for Satellite Solar Power Station

Deepak Kumar and Kalpana Chaudhary

Abstract In this work, a basic and low-cost microstrip antenna array with reduced size has been designed and tested. In the implementation level, a microstrip array antenna was realized to obtain the desired gain and directivity at a preferred frequency of 5.8 GHz. The compact antenna array consists of 2×2 elements microstrip patch antenna. Using simple and manual tuning method in electromagnetic full-wave momentum by Agilent Advanced Design Software, a direct control of the antenna's resonant frequency was obtained.

Keywords Microwave · Power · Microstrip antenna · Array · Satellite solar power station

1 Introduction

There is a population increase in worldwide. Modern civilization more depends on the technology equipment that requires higher electrical energy production [1]. Most of the power plants in the world are fossils fuel based. It has issues like global warming and their limited resources for few decades. Therefore, there is a requirement of green energy resources. Thus, the extensive involvement of renewable energy resources for higher electrical power generation is performed everywhere in the world. Solar power is abundantly available on the earth in the form of heat and light. Solar photovoltaic is to convert solar irradiance into electrical energy. However, solar irradiance varies arbitrarily in the daytime, and in night it goes extinct. Therefore, solar photovoltaic is not suitable for base load power [1, 2]. P. Glaser proposed satellite solar power station (SSPS) technique in 1968 [3]. In a satellite solar

D. Kumar (✉) · K. Chaudhary
Department of Electrical Engineering, Indian Institute of Technology BHU,
Varanasi 221005, India
e-mail: Deepak.rs.eee14@iitbhu.ac.in

K. Chaudhary
e-mail: kchaudhary.eee@iitbhu.ac.in

power station, space satellite collects solar energy photovoltaic that converts it into electrical energy. The electrical energy is then converted into microwave power and beaming that microwave power wirelessly to receiving antennas on Earth [2–4]. The receiving antenna connected rectifiers that convert microwave energy back to electrical energy. In this way, power is available to supply terrestrial grid after suitable processing. Therefore, it is suitable to replace conventional sources of energy. SSPS has several benefits over terrestrial solar power due to unhindered and undistorted solar irradiance available in space. On the terrestrial solar system, the SSPS has at least threefold increases in electricity generation capacity. However, SSPS has some technology challenges and major economic issues to implement [4].

2 Satellite Solar Power Station Research Worldwide

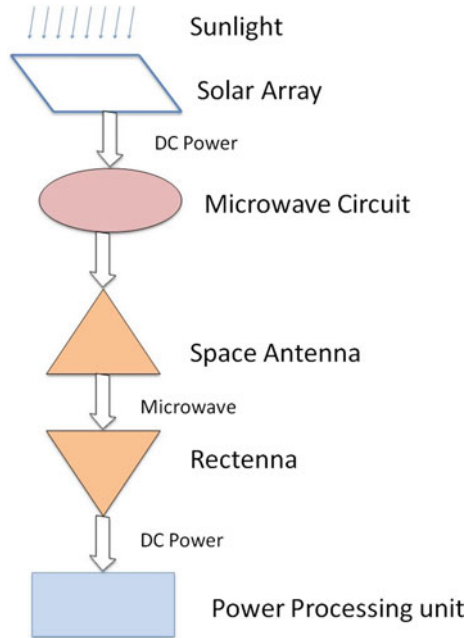
Many space research organizations have investigated SSPS, and researchers are working on the development of its realization techniques. Wireless power transfer for such large distance is a challenge that needs experimental performance. In the early phase, National Aeronautics and Space Administration (NASA) and Department of Energy (DOE) jointly suggested a SSPS reference model. While in 1997, the Fresh-Look-SSPS provided an improved model [4, 5]. The recommended Sun Tower SSPS model has numerous pioneering ideas that reduce SSPS feasibility operation as well as the levelized cost of energy. In the year 2001, Japanese Aerospace Exploration Agency (JAXA) reported 5.8-GHz SSPS operation model. The model utilized enhanced microwave technology. The chosen frequency 5.8 GHz is in the atmospheric attenuation frequency window [5].

The SSPS application in base load and non-base load power plant, a comparative study and analysis were performed by “European space research agency” in 2005. The study compared SSPS and land-based solar thermal with hydrogen storage. It concludes that, for large size (more than 5 GW), SSPS is feasible and economically comparable with land-based power plant [5, 6].

3 System Architecture

In the SSPS space segment, mainly microwave technology is involved. The ground segment is rectenna as shown in Fig. 1; the antenna and rectifier are collectively known as rectenna. As the space transmitting antenna is sending microwave power that must be collected efficiently on the earth rectenna. Thus, high directivity and high gain of the antenna are requisite. On selecting proper antenna array size, one can design highly directive antenna. The microwave power density on the rectenna has a limitation. According to United States Occupational Safety and Health Act (OSHA) workplace, exposure limit for the microwave is 10 mW/cm^2 [6]. The microwave power density limit decides the rectenna size for desired electrical

Fig. 1 Satellite solar power station diagram [2]



power production. The rectenna efficiency is a primary concern for successful wireless power transfer. Therefore, SSPS requires highly efficient and directive rectenna. In low-power rectenna, losses are due to threshold and breakdown voltage and device parasitic [7]. Diode nonlinearity produces harmonics generation. These harmonics can reradiate antenna causing injuries. Appropriate impedance matching is required between antenna and rectifier circuit for maximum power transfer. For microwave frequency in GHz, selection of diode is a tough task.

This work is a design and performance analysis of a 5.8-GHz antenna system considering satellite solar power system (SSPS) [8, 9]. A four-element microstrip antenna array design is implemented on a 1.6-mm FR4 substrate with dielectric constant 4.4 and copper as a conductor of 35 mm thickness. The simulation and design process is performed using Agilent ADS software (ADS). The design process uses ADS toolboxes, microstrip line conversion tool, Smith chart for impedance matching and filter design. The antenna array design uses S11 simulation and EM full-wave simulation in ADS. As a result, high directivity and high gain have been achieved in this design.

4 Antenna Array Design

A 2×2 microstrip patch antenna array is designed using Agilent ADS software. Microstrip has been chosen because of ease of its design and fabrication [9, 10]. Microstrip patch antennas are designed on an FR4 substrate; its specifications are: The height of the substrate is 1.6 mm and dielectric constant 4.4. The conductor

material is 35- μm -thick copper. The antenna is designed with quarter-wave transform matching microstrip lines. Each antenna has a gain of 6 dB. The designed antenna array simulations are performed using ADS EM full-wave simulation tools. Array antenna resonates at 5.8 GHz is confirmed in EM simulation S11 parameter analysis and Smith chart [10].

5 Designed Antenna Performance Result

5.1 Antenna Design Specification

For the antenna design, ADS momentum simulation tool has been used. Antenna length and width has been calculated using ADS microstrip line calculator with conductor and substrate specifications.

The single-patch antenna of size, length 11.75 mm and width 15.74 mm is designed. The single-patch antenna input impedance calculated is 243 Ω . A quarter-wave matching transformer is utilized for matching the antenna with a 50- Ω microstrip line. The 50 Ω has been chosen for the standard connector and coaxial cable connectivity [11]. The matching technique is used for designing four-element antenna array considering equal power division. Antenna spacing more than $\lambda/2$ is adopted in developing process [9–12].

The antenna layout window is generated in EM simulation tool. Figure 2 describes current distribution pattern in the antenna array. The antenna radiation pattern is directive as illustrated in Fig. 3. For radiation pattern calculation, the EM simulation far-field computing facility is used as shown in Fig. 3. The antenna

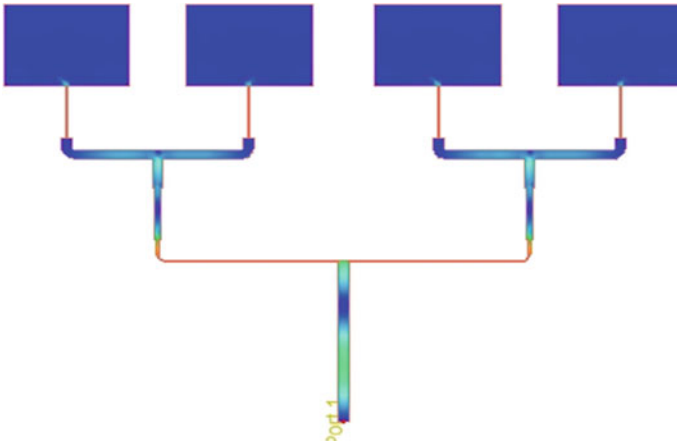


Fig. 2 Current distribution (A/m) at 5.8 GHz

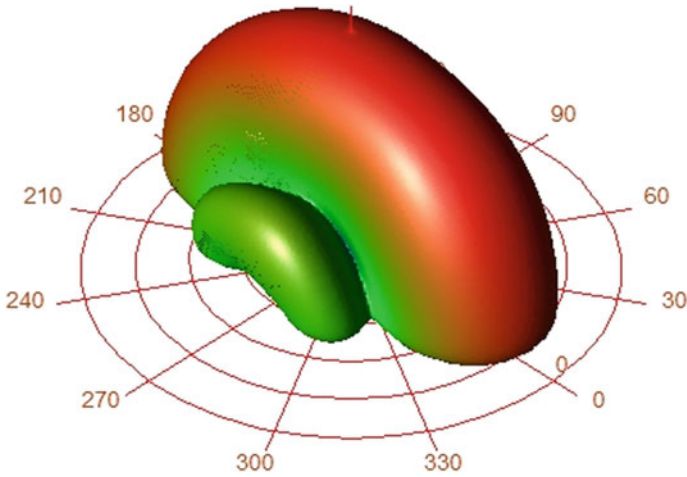


Fig. 3 Radiation pattern

Power radiated (Watts)	0.00175131	
Effective angle (Steradians)	1.18059	
Directivity(dBi)	10.2711	
Gain (dBi)	8.92805	
Maximim intensity (Watts/Steradian)	0.00148342	
Angle of U Max (theta, phi)	34	0
E(theta) max (mag,phase)	1.05721	-95.7255
E(phi) max (mag,phase)	0.000362463	-175.986
E(x) max (mag,phase)	0.87647	-95.7255
E(y) max (mag,phase)	0.000362463	-175.986
E(z) max (mag,phase)	0.591186	84.2745

Fig. 4 Antenna parameter

parameter is shown in Fig. 4. For return loss analysis of antenna array, S11 parameter versus frequency is plotted. At 5.8 GHz, antenna array resonates with return loss below 20 dBm. The S11 parameter and Smith chart are shown in Figs. 5 and 6. The gain and directivity of designed antenna are 8.928 and 10.27 dBi, respectively. The variation of gain and directivity with theta for constant phi value

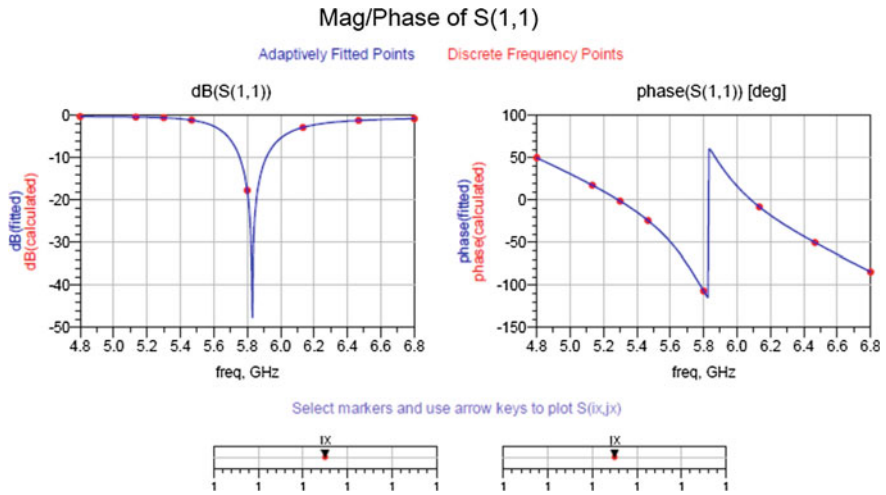


Fig. 5 Mag/phase of $S(1,1)$

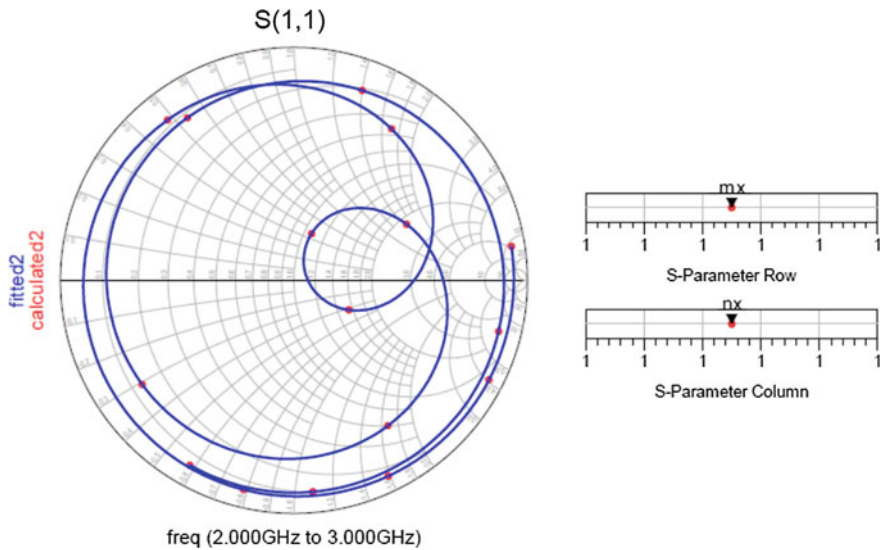


Fig. 6 Smith chart

is shown in Fig. 7. The calculated antenna efficiency is 73.39% as shown in Fig. 7. The radiated power pattern is shown in Fig. 8. In this way, an antenna array with high efficiency as well as high gain and directivity has been designed.

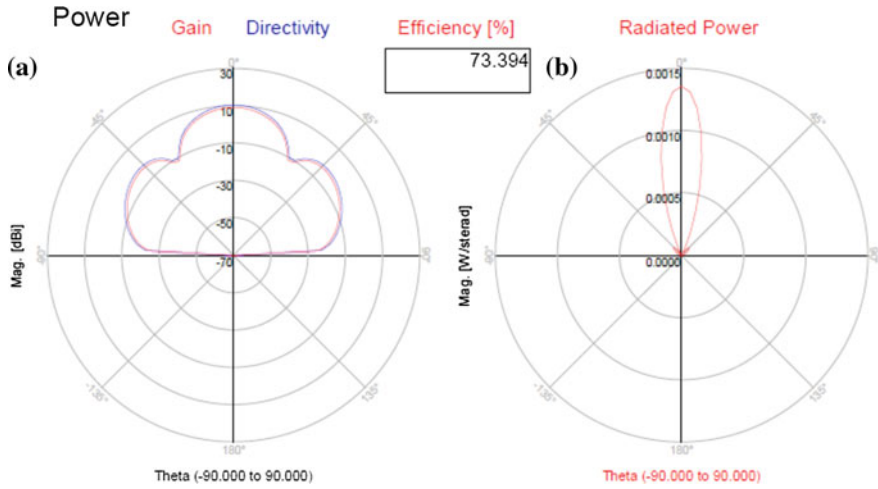


Fig. 7 a Gain and directivity. b Radiated power

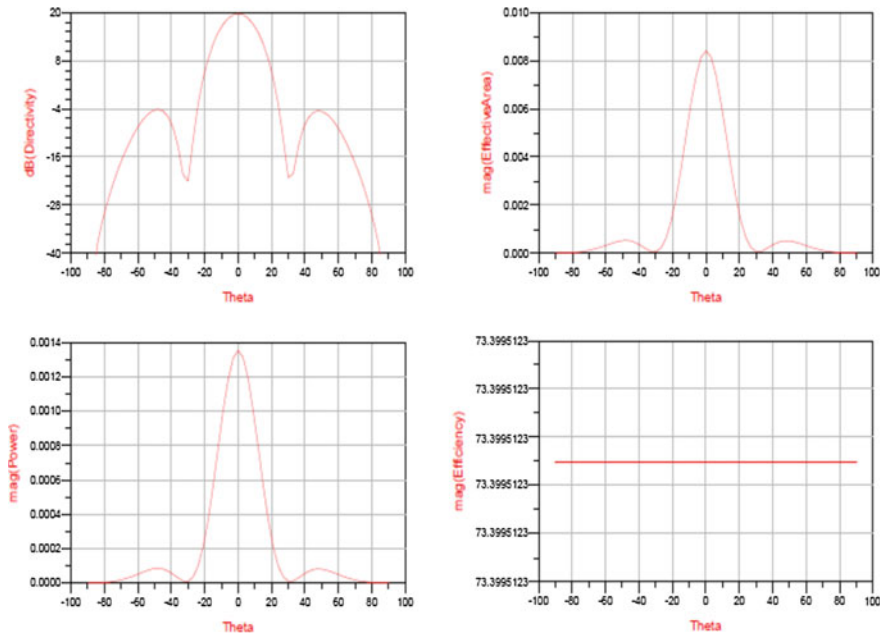


Fig. 8 Antenna gain, directivity, efficiency and power

6 Conclusion

A 5.8-GHz antenna array had been developed, simulated and tested in ADS simulation environment considering highly directive antenna requirements in satellite solar power application. Regardless of the possibility that lone inadequate facility of energy harvesting from a single antenna, it is likewise conceivable to architect components array to get more power. Reducing the size of the antenna array is another aspect, which is implemented in this work. With the increase in frequency and the dielectric constant not varied, the patch antenna size decreases. Initially, a microstrip patch antenna with compact size was planned and executed in ADS software. The antenna hypothetical outline technique is direct; the results obtained from this design demonstrated exceptionally satisfactory exhibitions in the frequency band of intrigue. The high gain and directivity is achieved using antenna array in the design. Further, antenna input port impedance had been matched to 50Ω for circuit integration. The arranged antenna array structure can be viable executed in SSPS microwave technology.

References

1. Hayami, H., Nakamura, M., Yoshioka, K.: The life cycle CO₂ emission performance of the DOE/NASA solar power satellite system: a comparison of alternative power generation systems in Japan. *IEEE Trans. Syst. Man Cybern. Part C: Appl. Rev.* **35**(3), 391–400 (2005)
2. Brown, W.C.: Satellite power stations, a new source of energy. *IEEE Spectr.* **10**(3), 38–47 (1973)
3. Brown, W.C.: The history of power transmission by radio waves. *IEEE Trans. Microw. Theory Tech. MTT* **32**, 1230–1242 (1984)
4. US Department of Energy and NASA: Satellite Power System, Concept Development and Evaluation Program. Reference System Report, Oct 1978 (Published Jan 1979)
5. Johnson, G., Hunt, M.E., Determan, W.R., Hosang, A., Ivanenok, J., Schuller, M.: Design and integration of a solar AMTEC power system with an advanced global positioning satellite. In: *Proceedings of 31th International Energy Conversion Engineering Conference (IECEC)*, vol. 1, p. 623, Washington, D.C., IEEE (1996)
6. Lin, J.C.: Space solar-power stations, wireless power transmissions, and biological implications. *IEEE Microw. Mag.* 36–42 (2002)
7. Lin, J.C.: The new IEEE standard for human exposure to radio-frequency radiation and the current ICNIRP guidelines. *Radio Sci. Bull.* **317**, 61–63 (2006)
8. Akkermans, J.A.G., van Beurden, M.C., Doodeman, G.J.N., Visser, H.J.: Analytical models for low-power rectenna design. *IEEE Antennas Wirel. Propag. Lett.* **4**, 187–190 (2005)
9. Balanis, C.A.: *Antenna Theory-Analysis and Design* (Ch. 14), pp. 840–843. Wiley, New York, NY, USA (2005)
10. Xue, Q., Chin, C.H.K., Chan, C.H.: Design of a 5.8-GHz rectenna incorporating a new patch antenna. *IEEE Antenna Wirel. Propag. Lett.* **4**, 175–178 (2005)
11. McSpadden, J.O., Fan, L., Chang, K.: Design and experiments of a high-conversion-efficiency 5.8-GHz rectenna. *IEEE Trans. Microw. Theory Tech. MTT* **46** (12), 2053–2060 (1998)
12. Suh, Y.H., Chang, K.: A high-efficiency dual-frequency rectenna for 5.8- and 5.8-GHz wireless power transmission. *IEEE Trans. Microw. Theory Tech.* **50**(7), 1784–1789 (2002)

Development of Wireless Data Acquisition and Control System for Smart Microgrid

Lipi Chhaya, Paawan Sharma, Govind Bhagwatikar
and Adesh Kumar

Abstract Smart grid is the most ingenious and experimental technology in the present era. Assimilation of information and communication technologies with electrical infrastructure is the fundamental part of smart grid deployment. Smart grid communication architecture is a methodical framework of networks incorporating varied set of communication standards. Microgrid is the significant component of smart grid as it facilitates and expedites the usage of renewable energy assets. It can resolve the critical problems like unelectrified villages, electricity theft, depletion of fossil fuels, GHG emissions and greenhouse effect. Smart microgrid can function in two modes, namely grid-connected and island mode. It also encompasses hierarchical communication networks for automation of entire system. This paper describes the design and implementation of data acquisition and control system for smart microgrid prototype using IEEE 802.3 and IEEE 802.11 standards.

Keywords Smart grid · Smart microgrid · Data acquisition and control
Wireless communication · Ethernet · Wireless local area network
Wireless monitoring and control · Renewable energy · Solar photovoltaic

L. Chhaya (✉) · P. Sharma · A. Kumar
Department of Electronics, Instrumentation and Control Engineering,
University of Petroleum & Energy Studies, Dehradun, India
e-mail: lipi.chhaya@gmail.com

P. Sharma
e-mail: paawan.sharma@ddn.upes.ac.in

A. Kumar
e-mail: adeshkumar@ddn.upes.ac.in

G. Bhagwatikar
SANY Group, Pune, India
e-mail: gowind.india@gmail.com

© Springer Nature Singapore Pte Ltd. 2018

S. SenGupta et al. (eds.), *Advances in Smart Grid and Renewable Energy*,
Lecture Notes in Electrical Engineering 435, https://doi.org/10.1007/978-981-10-4286-7_66

1 Introduction

A grid is a network that transfers electrical energy from power plants to customer premises. The grid can be made brainy or smart by unification of information and communication technologies with electrical infrastructure. At present, smart grid technology is a significant journey toward reliable and unfailing electricity. Smart grid technology ensures steadfast, proficient, robust and progressive energy distribution structure with numerous features. It is an intelligent power grid with integration of various alternative and renewable energy resources [1–3]. Integration of renewable energy resources will result into reduced carbon footprint and emissions. Supervisory control and data acquisition (SCADA) system is an essential fragment of smart grid technology. Integration of varied set of communication standards requires analysis and optimization for different applications. The use of specific standard can be decided on the basis of coverage area, type of network, security constraints, data rates and bandwidth requirements. Networks can be classified as home area networks (HANs), neighborhood area networks (NANs) and wide area networks (WANs) as per their applications and coverage area [4–6]. Smart grid technology is beneficial for industrial as well as home consumers in many aspects such as monitoring and control of energy usage, time of the day billing cycle, control of home appliances and machines, production and selling of ancillary energy and completely secured automation [7–9]. Consumer electronics appliances communicate their energy consumption statistics to central or main home monitor and regulator or smart meter. Smart meter sends an energy usage statistics to the central electricity grid for monitoring, control, fault detection and billing purposes. Consumer has a choice to operate on a specific energy source for optimization of billing cycle and energy usage. Zigbee, Bluetooth, WirelessHART, Wavenis, Wi-Fi, Ethernet, etc. standards can be used for home as well as industrial applications for short-distance communications using personal or local area networks. The proposed system is designed for data acquisition and control within local area networks for DC microgrid.

2 Design of Developed Prototype

The developed prototype is designed for smart energy management system for wireless local area networks. Figure 1 shows the simplified conceptual block diagram of the developed prototype.

The prototype is controlled by ATMEGA328P microcontroller. In the proposed energy management prototype, three power sources are considered. Depending upon the threshold current value, the DC load will be switched between grid, solar PV or battery. The Hall effect current sensors ACS-712 are used to sense the current from various energy sources. The sensitivity of ACS-712 sensors used in the prototype is 66 mV/A. Figure 2 shows the circuit diagram of developed system.

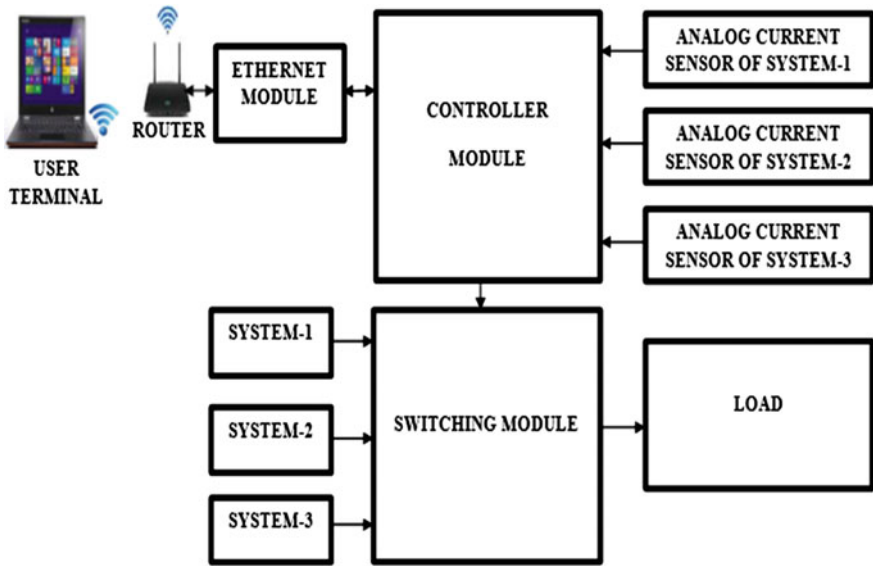


Fig. 1 Block diagram of developed prototype

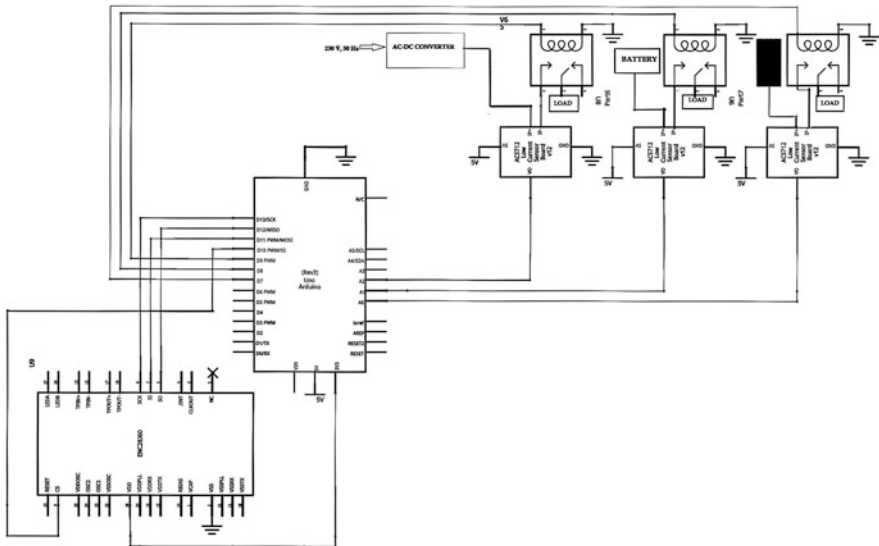


Fig. 2 Schematic diagram of developed prototype (image design with Fritzing)

The designed system can be used for data acquisition and control of home as well as industrial networks. The designed prototype uses IEEE 802.3 and IEEE 802.11 standards for controlling the operation of smart power system. Ethernet is designed for local area network based on IEEE 802.3 standard. ENC28J60 or W5100 Ethernet module can be used for communication. These modules can be used with any microcontroller with inbuilt SPI (serial peripheral interface). W5100 ethernet shield is a stand-alone Ethernet controller with industry standard SPI. It provides encrypted serial communication interface for physical layer security. Ethernet module is attached to LAN port of router for remote wireless communication in local area network. Flowcharts for working of prototype are shown in Fig. 3.

The WLAN router communicates with user terminal. Dynamic host configuration protocol (DHCP) is used for communication between router and user terminals. An intelligent router automatically assigns available IP addresses to avoid IP conflicts. The network can be expanded using network devices. The developed prototype uses wireless-fidelity protected access phase shift keying (WPA-PSK) algorithm and advanced encryption standard (AES) for secured wireless communication. The designed system can be expanded for wide area network (WAN) using port forwarding and configuration of static IP.

3 Results and Discussion

The proposed prototype is designed for remote wireless monitoring of smart microgrid system. An HTML webpage is developed for monitoring and control of energy sources. The data is received at the interval of one second. The system is working successfully in the range of around 50 m in wireless local area network. The developed prototype is tested using all three energy sources. Sequential priorities are given to sources. Initially, the system works on grid. Then, the load can be switched to solar and battery on the basis of threshold current. The prototype represents DC microgrid. It can both operate in grid-connected and island modes. The prototype is tested for local area network using WPA-PSK security mode. Maximum 254 devices can be connected and regulated in the network. The other encryption options such as wired equivalent protocol (WEP), wireless-fidelity protected access temporal key integrity protocol (WPA-TKIP) and WPA2 are also available. Further extension can be achieved by using different network devices such as switches and routers. The user can monitor the data and control an entire system by entering the predefined commands on the webpage as shown in Fig. 4.

This design can also be modified for solar rooftop system. The DC microgrid is considered for the proposed prototype. For AC microgrid, an inverter can be used for conversion. The design can be extended and tested for complete automation of home and industrial network for different environments [10–12]. The developed prototype can be further explored using mesh networks and different communication standards based on applications and requirements [12–15]. The further expansion of the prototype includes web-based monitoring and control of DC microgrid.

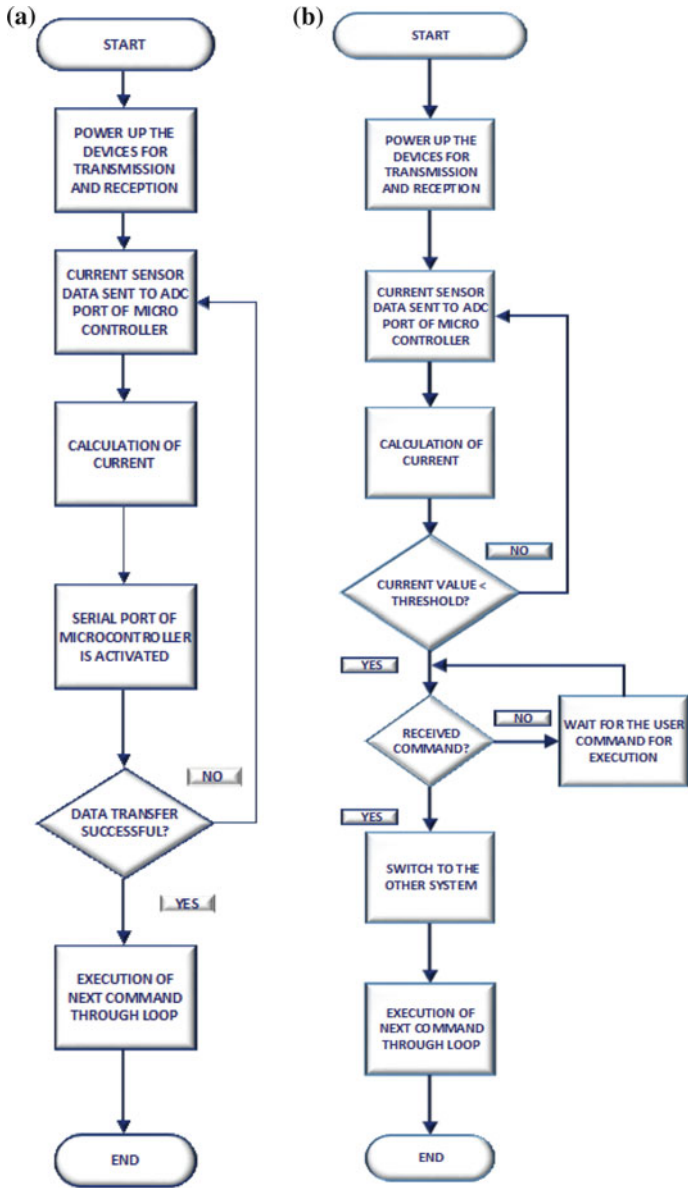


Fig. 3 Flowcharts for a energy monitoring and b control of the prototype

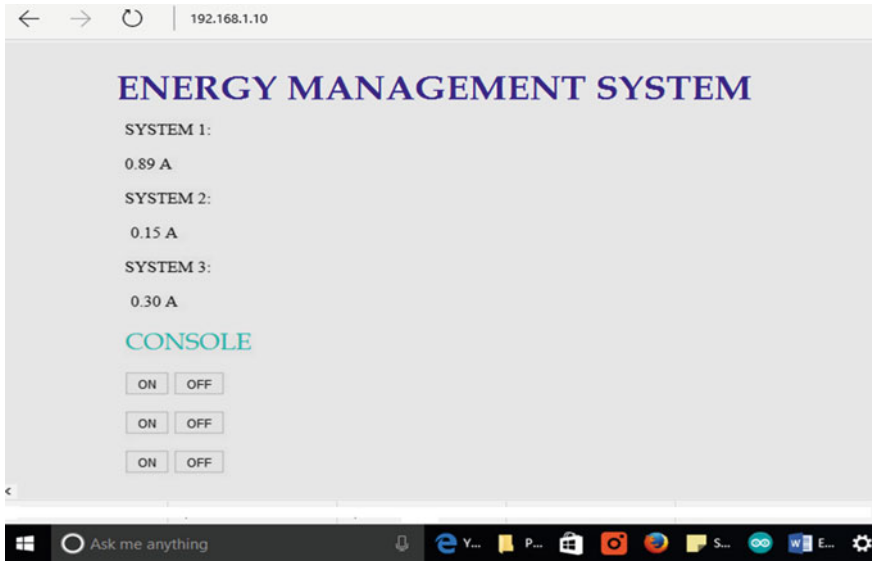


Fig. 4 Snapshot of webpage

4 Conclusion

Data acquisition and control is an integral part of progressive smart grid technology. Design of any monitoring and control system mainly relies on the choice of communication standard. Optimization of communication standard depends on the type of application, security aspects, coverage area, cost and complexity of the network. The developed prototype is an optimized solution for local area network. It can be extended for Internet of Things applications for wide area network. The prototype can also be used for experimental investigation of the preeminent security algorithms against cyber attacks. The developed design is applicable for both home and industrial networks.

References

1. Binti, M.I.N., Wei, T.C., Yatim, A.H.M.: Smart grid technology: communications, power electronics and control system. International Conference on Sustainable Energy Engineering and Application (ICSEEA), Bandung, pp. 10–14 (2015)
2. Erol-Kantarci, M., Mouftah, H.T.: Energy-efficient information and communication infrastructures in the smart grid: a survey on interactions and open issues. *IEEE Comm. Surv. Tutorials* **17**, 179–197 (2015)
3. Huang, J., Wang, H., Qian, Y.: Smart grid communications in challenging environments. *IEEE Third International Conference on Smart Grid Communications*, Tainan, pp. 552–557 (2012)

4. Gungor, V.C., Sahin, D., Kocak, T., Ergut, S., Buccella, C., Cecati, C., Hancke, G.P.: Smart grid technologies: communication technologies and standards. *IEEE Trans. Ind. Info.* **7**, 529–539 (2011)
5. Yan, Y., Qian, Y., Sharif, H., Tipper, D.: A survey on smart grid communication infrastructures: motivations, requirements and challenges. *IEEE Comm. Surv. Tutorials* **15**, 5–20 (2013)
6. Bera, S., Misra, S., Obaidat, M.S.: Energy-efficient smart metering for green smart grid communication. *IEEE Global Communications Conference*, Austin, pp. 2466–2471 (2014)
7. Momoh, J.: Pathway for Designing. *Smart Grid Smart Grid: Fundamentals of Design and Analysis*, pp. 122–139. Wiley-IEEE Press, New York (2012)
8. Landsteiner, C., Andren, F., Strasser, T.: Evaluation and test environment for automation concepts in smart grids applications. *IEEE First International Workshop on Smart Grid Modeling and Simulation*, Brussels, pp. 67–72 (2011)
9. Matsuo, R., Miwa, H.: Grid-connected electric-power control algorithm for promoting the introduction of renewable energy. *International Conference on Intelligent Networking and Collaborative Systems*, Salerno, pp. 163–168 (2014)
10. Farajallah, M., Assad, S.E., Chetto, M.: Dynamic adjustment of the chaos-based security in real-time energy harvesting sensors. *IEEE International Conference on Internet of Things and Cyber, Physical and Social Computing*, Beijing, pp. 282–289 (2013)
11. Piyare, R., Tazil, M.: Bluetooth based home automation system using cell phone. *International Symposium on Consumer Electronics*, Singapore, pp. 192–195 (2011)
12. Bhattarai, B.P., Lévesque, M., Maier, M., Bak-Jensen, B., Pillai, J.R.: Optimizing electric vehicle coordination over a heterogeneous mesh network in a scaled-down smart grid testbed. *IEEE Trans. Smart Grid* **6**, 784–794 (2015)
13. Baig, M.Q., Maqsood, J., Alvi, M.H.B.T., Khan, T.A.: A comparative analysis on home automation techniques. *International Conference on Artificial Intelligence, Modelling and Simulation*, Madrid, pp. 109–114 (2014)
14. Fang, A., Xu, X., Yang, W., Zhang, L.: The realization of intelligent home by ZigBee wireless network technology. *Pacific-Asia Conference on Circuits, Communications and Systems*, Chengdu, pp. 81–84 (2009)
15. Eliasson, J., Zhong, C., Delsing, J.: A heterogeneous sensor network architecture for highly mobile users. *International Conference on Wireless Communication and Sensor Networks*, Allahabad, pp. 1–6 (2010)

Real-Time Implementation of Maximum Power Point Methods for Photovoltaic Systems

Akbar Ahmad and Paulson Samuel

Abstract The eco-friendly solution to the ever expanding demands of the energy supplies has seen a substantial growth of installed renewable energy integration to the grid in the last decade. The major portion of the installed capacity is from the photovoltaic system due to several factors like reduction in capital investment, an increase in efficiency of modules and converters, favorable government policies. The maximum power point tracking enables the maximum utilization of the available power with a constant change in environmental conditions. These techniques are judged on accuracy, speed, efficiency and fewer oscillations. Several strategies have been proposed in the last decade to maximize the power output. The article provides an overview of the operational principle of such techniques. The simulation and real-time hardware implementation have been done using Atmega328 microcontroller to verify the several performance features.

Keywords Maximum power point tracking (MPPT) · Photovoltaic system (PVS) · Real-time implementation (RTI) · Perturb and observe (P&O) Sensors

1 Introduction

Solar PV energy conversion system has seen a tremendous growth in India from 161 MW in 2010 to 4097 MW in 2015 [1]. The motivation for such growth is based on several factors such as the reduction in the capital investment, increase in the efficiency of the PV modules, increased environmental awareness and favorable feed-in tariffs designed by the government. Photovoltaic systems are majorly

A. Ahmad (✉) · P. Samuel
Department of Electrical Engineering, MNNIT Allahabad, Allahabad, India
e-mail: akbar_ree0713@mnnit.ac.in

P. Samuel
e-mail: paul@mnnit.ac.in

classified into the stand-alone system and grid-connected system [2]. The stand-alone systems are useful for remote areas where access to electricity is limited. Although the stand-alone configuration may provide regulated load voltage, but the reliability of such system is not guaranteed because of stochastic nature of sunlight [3]. Its reliability can be improved by the installation of energy storage batteries. The recent advancement in power electronics technology made the integration of a PV system to the grid possible with low losses and high efficiency [4].

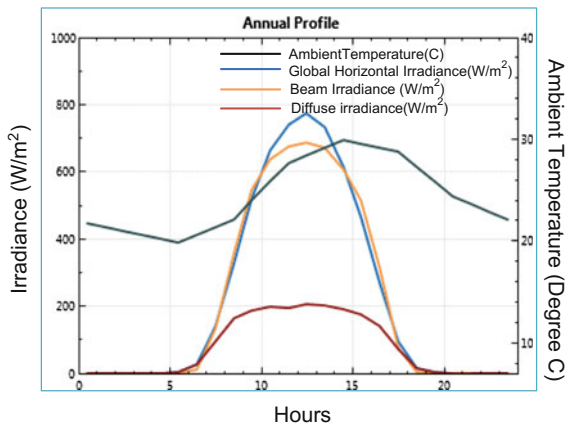
The photovoltaic system consists of highly nonlinear characteristics of power-voltage and current-voltage curves, which are continuously changing with the variation in irradiation and change in temperature as shown in Fig. 1.

The MPPT controller thus plays a vitally important role in sensing and acting in response to rapid changes in the characteristics of the photovoltaic system, thereby ensuring the extraction of the maximum power at all times. The PV source operates in linkage with the DC-DC converter, whose duty cycle is modulated with the tracking dynamics on maximum power point in the curve. The classification of the MPPT algorithm is based on the uniform and nonuniform irradiation [5].

Various methods have been shown in the recent literature for performing the MPP tracking operation under both the uniform incidence of solar radiation and partial shading condition. Each of these methods is different with hardware implementation standards and requirements. An overview of MPP is shown in Fig. 2. Their implementation and operational characteristics are analyzed to show their performance and other features. This will assist the designer of PV power conditioning system to choose the suitable MPP technique for the target application.

In this paper, the real-time implementation of several techniques has been done using the P-V characteristics generated from Agilent E 4360A solar emulator and control using Atmega328 microcontroller. The simulation studies for the same have been verified using MATLAB/Simulink.

Fig. 1 Annual profile for irradiance with variation in ambient temperature



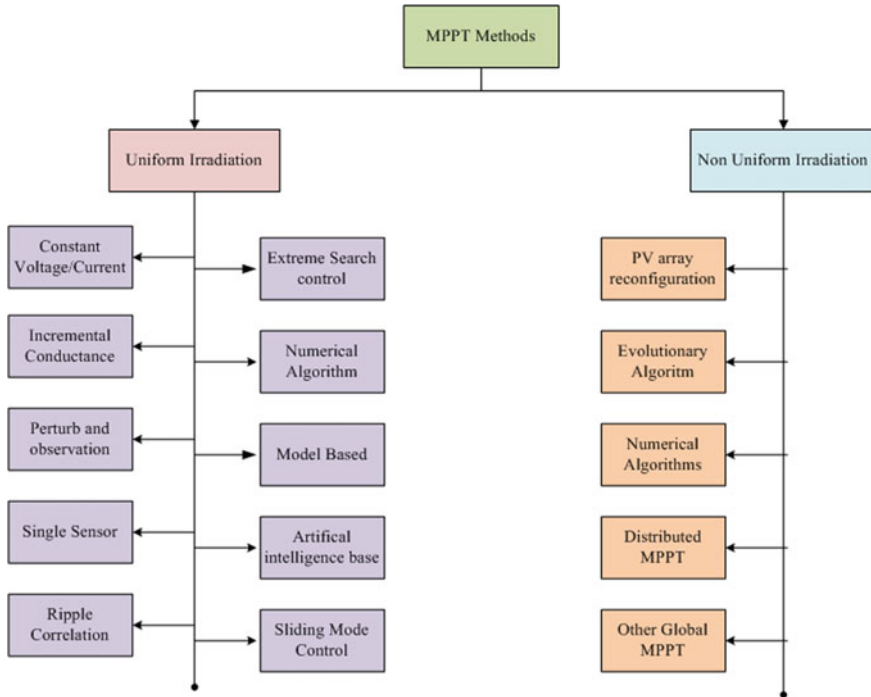


Fig. 2 Classification of MPPT methods based on irradiation

2 MPPT Techniques

The PV source operates in linkage with the DC–DC converter, whose duty cycle is modulated with the tracking dynamics on maximum power point in the curve. The classification of the MPPT algorithm based on the uniform and nonuniform irradiation is analyzed by [5]. Out of several schemes the first and foremost is the perturb and observe which is also termed as hill climbing algorithm [6–8]. The shortcomings of this technique were improved by the incremental conductance method as mentioned in [9]. Due to the ease of implementation, the techniques such as short-circuit current [10], open-circuit voltage, ripple correlation approaches were proposed. The improvement in tracking performance and efficiency of tracking are proposed as adaptive perturb and observe [11] and variable step size incremental method [12–14].

Artificial intelligence-based MPP techniques such as fuzzy and neural network algorithms are applied for achieving the desired operation. The training method with a large set of input for real-time operation is required for such algorithms [15], as the model of the system is highly unpredictable; hence, it offers a huge

disadvantage. The fuzzy-based logic control for the power converters is discussed in [16]. The main advantage of the fuzzy logic-based system is that the knowledge of the approximate model of the system is not necessarily required. However, for achieving the effective performance expert domain knowledge is needed for designing of membership function and its rule-based sets. The optimization techniques such as genetic algorithm and ant colony strategy are applied for parameter tuning in [17].

The PV curve has been generated by using the technical characteristics as mentioned in Table 1. The hardware and simulated characteristics from these data for the change in insolation and temperature are shown in Fig. 3.

Table 1 Electrical ratings of the experimental PV panel

Maximum power (W) P_{max}	15
Voltage at MPP (V) V_{MPP}	13
Current at MPP (A) I_{MPP}	1.27
Open-circuit voltage (V) V_{oc}	17.2
Short-circuit current (A) I_{sc}	1.4

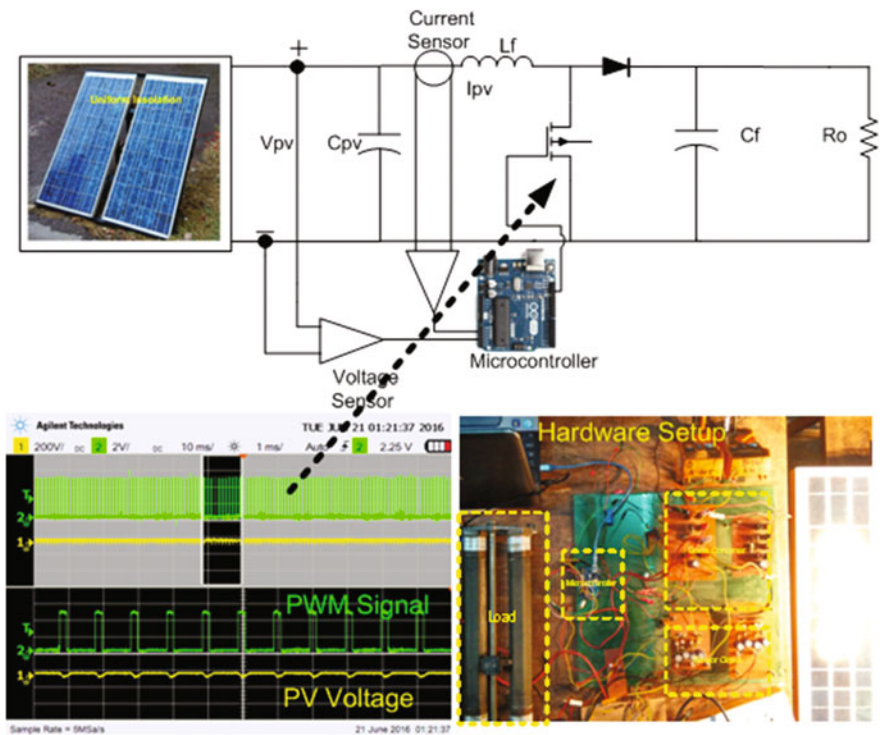


Fig. 3 Detailed experimental setup and DSO output for PWM generation

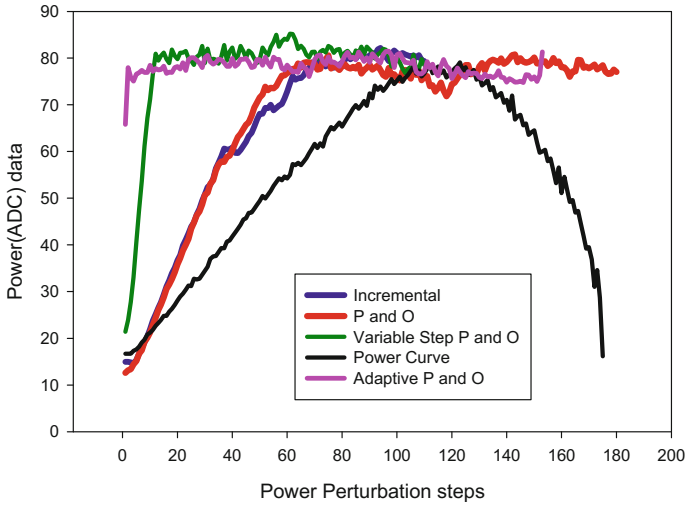


Fig. 4 Comparison of various MPPT techniques

Three experimental PV panels are considered in series to increase the voltage rating, and the current remains the same in the branch. Standard testing conditions are followed for comparison of various MPPT algorithms for the microcontroller. The P&O algorithm is dumped on the microcontroller to observe the MPP and the graph has included for the same as shown in Fig. 4, it can be seen that the oscillations while tracking the MPP is very high and the number of power perturbation steps are also large. The inefficient performance and slow speed became the motivation for the incremental conductance algorithm; the ratio of change in power to the change in voltage is constantly checked value for identifying the MPP location in the P–V curve. This algorithm shows an advantage with lesser oscillation and efficient tracking performance. The variable step P&O was suggested to reduce the number of power steps with improvement in efficiency. In this, the change in duty cycle of the switch is constantly varied in accordance with a change in power.

Adaptive P&O shows improvement with fast speed and reduced oscillation as the duty cycle of the switch is varied with reference to the change in power, just showing major improvement in tracking efficiency. Figure 5 shows the flowchart of the adaptive P&O algorithm which is coded on the microcontroller to observe the change in power with duty cycle variation. The output of the generation of the PWM is shown in Fig. 3. The real-time peak tracking of the I–V and P–V can be seen from Fig. 6, which is observed from Agilent E4360A. The efficiency of the algorithm is observed more than 99% which is very effective.

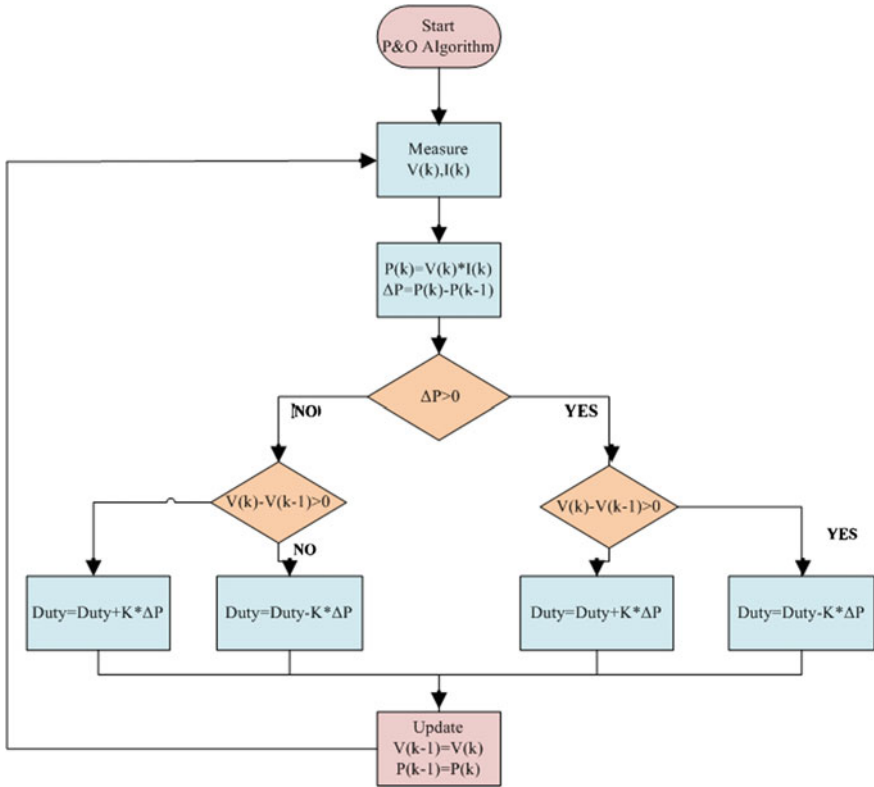
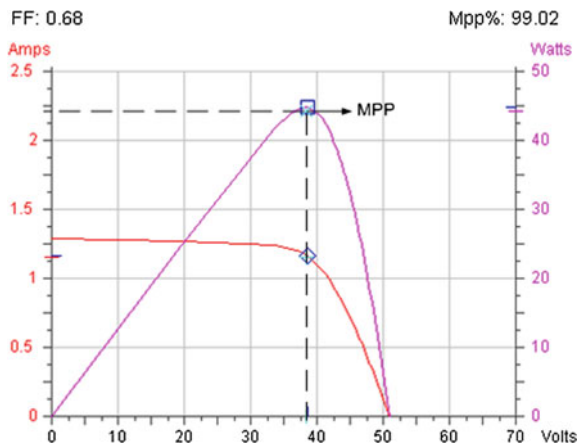


Fig. 5 Flowchart of adaptive P&O algorithm

Fig. 6 Real-time characteristics for I-V and P-V curve tracking



3 Conclusion

The power–voltage curve of the photovoltaic array has a point where the generation of power is at maximum. Under uniform insolation, the point is unique, whereas in the case of the different amount of solar radiations multiple local MPP occurs. It becomes necessary to track this unique point of maxima to reduce the power losses in the photovoltaic energy conversion system. Each method of MPPT has some characteristics, and they can be compared with a common factor like tracking speed and oscillations in power. The real-time implementation of five methods is shown in this paper to compare the efficiency and performance of these techniques, and the adaptive perturb and observe technique has been found to be the fastest of all compared techniques with better efficiency.

References

1. Ahmad, A., Samuel, P., Amar, Y.: Solarizing India: tapping the excellent potential. *Renew. Energy* **9**, 13–17 (2016)
2. David, S.N., Santosh, S.P., Narayanan, L.S.: Control strategy for power flow management in a PV system supplying electrical loads in an air-conditioned bus. *Int. Conf. Power Signals Controls Computation* **60**, 3185–3194 (2014)
3. Peters, M., Schmidt, T.S., Wiederkehr, D., Schneider, M.: Shedding light on solar technologies-A techno-economic assessment and its policy implications. *Energy Policy* **39**, 6422–6439 (2011)
4. Kjaer, S.B., Pedersen, J.K., Blaabjerg, F.: A review of single-phase grid-connected inverters for photovoltaic modules. *IEEE Trans. Ind. Appl.* **41**, 1292–1306 (2005)
5. Koutroulis, E., Blaabjerg, F.: Overview of maximum power point tracking techniques for photovoltaic energy production systems. *Electr. Power Components Syst.* **43**, 1329–1351 (2015)
6. Remy, G., Bethoux, O., Marchand, C., Dogan, H.: Review of MPPT techniques for photovoltaic systems
7. Mastromauro, R.A., Liserre, M., Dell’Aquila, A.: Control issues in single-stage photovoltaic systems: MPPT, current and voltage control. *IEEE Trans. Ind. Informatics* **8**, 241–254 (2012)
8. Femia, N., Petrone, G., Spagnuolo, G., Vitelli, M.: Optimization of perturb and observe maximum power point tracking method. *IEEE Trans. Power Electron.* **20**, 963–973 (2005)
9. González-Morán, C., Arbolea, P., Diaz, G., Gómez-Aleixandre, J.: Modeling photovoltaic DC primary sources as grid connected inverter supplies considering non-linear effects. *IEEE Canada Electr. Power Conf. EPC*, pp. 50–55 (2007)
10. Walker, G.: Evaluating MPPT converter topologies using a MATLAB PV model. *J. Electr. Electron. Eng. Aust.* **21**, 49–55 (2001)
11. Abdelsalam, A.K., Massoud, A.M., Ahmed, S., Enjeti, P.N.: High-performance adaptive Perturb and observe MPPT technique for photovoltaic-based microgrids. *IEEE Trans. Power Electron.* **26**, 1010–1021 (2011)
12. Tey, K.S., Mekhilef, S., Member, S.: Modified incremental conductance algorithm for photovoltaic system under partial shading conditions and load variation. *IEEE J. Ind. Electron.* **61**, 5384–5392 (2014)
13. Amine, A.M., Maaroufi, M., Ouassaid, M.: New variable step size INC MPPT method for PV systems. In: *International Conference Multimedia Computing and System (ICMCS)*, p. 5 (2014)

14. Jain, S., Agarwal, V.: A new algorithm for rapid tracking of approximate maximum power point in photovoltaic systems. *IEEE Power Electron. Lett.* **2**, 16–19 (2004)
15. Sheraz, M., Abido, M.A.: An efficient approach for parameter estimation of PV model using DE and fuzzy based MPPT controller. In: *Proceedings of the IEEE Conference on Evolving and Adaptive Intelligent Systems (EAIS) Linz, Austria*, pp. 1–5 (2014)
16. Afghoul, H., Krim, F., Chikouche, D., Beddar, A.: Tracking the maximum power from a PV panels using of Neuro-fuzzy controller. In: *Proceedings of the IEEE International Symposium on Industrial Electronics (2013)*
17. Adly, M., Besheer, A.H.: An optimized fuzzy maximum power point tracker for stand alone photovoltaic systems: ant colony approach. In: *2012 7th IEEE Conference on Industrial Electronics and Applications ICIEA*, pp. 113–119 (2012)

Deterministic Node Deployment for Connected Target Coverage Problem in Heterogeneous Wireless Sensor Networks for Monitoring Wind Farm

M. Vergin Raja Sarobin and R. Ganesan

Abstract Wireless sensor network (WSN) is recognized a potential monitoring, controlling and communication tool for future power grid, the smart grid. Particularly for wind-based power generation application, the multifunctional wireless sensor nodes are positioned at the possible locations of the wind mill for monitoring. Each wind turbine is said to be a sub-network, where the sensor nodes are deployed at the potential data points to accomplish coverage. Connectivity is then a critical issue because the adjacent wind turbines are very far from each other. Hence, the sensor nodes between adjacent turbines will not be within the communication range. Relay nodes are employed between the turbines to bring up connectivity. We propose a Deterministic Relay node deployment algorithm based on Fermat point and Convex hull (DRFC) to find optimal number of relay nodes. DRFC finds the convex hull and Fermat points recursively until it reaches the centre of target region. The relay nodes are deployed in the Fermat points and also between the Fermat points and the segments to establish connectivity. The DRFC algorithm is analysed mathematically with respect to optimum number of relay node and connectivity.

Keywords Wireless sensor network · Node deployment · Coverage Connectivity · Relay node · Fermat points · Convex hull

1 Introduction

The WSN's low-cost nature brings considerable benefits in health monitoring, environmental and communication technologies [1, 2]. WSNs have been broadly accepted as a remarkable technology that can improve today's electric power

M. Vergin Raja Sarobin (✉) · R. Ganesan
School of Computing Science and Engineering, VIT University - Chennai Campus,
Chennai, India
e-mail: verginraja.m@vit.ac.in

systems, including power generation, transmission, distribution and utilization [3]. But the convolution and density of the complex electric power system may set down the quality of the wireless sensor network. This work is to design WSN more suitable for smart power system.

The wireless sensor nodes can be spread in a large scale over the field of operation of distributed power generation components, transmission equipment or distribution components as an intelligent monitoring platform to monitor the critical parameters such as current, voltage or power readings. The information received from the faulty location will be transmitted immediately to the maintenance centre as required. This will allow the power grid to react to the varying conditions more timely and proactively.

WSNs consist of small battery-powered devices with restricted energy resources [4, 5]. In general after deploying the sensor network, unexpected failure in sensor node or multiple nodes due to harsh environment may result in disjoint sub-networks/segments. For example in battlefield application, part of the WSN may be bombed that results in disjoint segments [6]. Also in wind farm application, the targets are well known and the sensor node deployment is deterministic. But the sensor nodes deployed in the wind turbines cannot communicate between the adjacent turbines because the turbines are far away from each other [7]. This again results in disconnected network. Hence, one of the most important issues that need to be focused is building inter-segment connectivity [8].

Connectivity is achieved by relay nodes incorporated between the turbines or the segments to maintain the information link. These relay nodes help to gather data from the sensors deployed in the wind turbine and forward the same to base station (BS). The challenge here is to optimize the number of relay nodes without affecting connectivity and survivability. The Relay Node Deployment Problem (RNDP) is already proved as an NP-hard problem [9]. DRFC has three phases: (1) Fixed sensor node deployment in wind turbines/segment with the objective of establishing target coverage. (2) Establishing convex hull and Fermat Points (FP) to find the location of relay nodes. (3) Deploy relay nodes to establish inter-segment connectivity. The different phases of DRFC are explained detailed in Sect. 3.

The rest of the paper is organized as follows. Section 2 presents the related work. Section 3 presents the system model, and Sect. 4 elaborates the proposed algorithm. Section 5 comprises the results, and Sect. 6 presents the conclusion.

2 Related Work

Sensor deployment can be random for the regions which are unknown and can be deterministically for the well-known application [10]. Target coverage problem of sensor deployment is handled in this work [11]. Sensor nodes are deployed deterministically in this work so as to achieve maximum network lifetime and

maximum target coverage level. The nodes and the target are static in this paper. But the initial assumption is random deployment. The random deployment is only for simulator. The optimal position is computed and after getting the optimal position, the sensor nodes are deployed in the field and there is no movement of sensor nodes [11]. Connectivity issue is not dealt in this paper.

Connectivity is a major issue, if the targets are highly separated and if multiple sensor node failure occurs. This is handled by deploying additional sensor nodes or by placing relay nodes between the separated targets/segments. Relay nodes in wireless sensor network serve either for routing or connectivity purpose. When placing relay nodes to overcome connectivity issues, the deployment could aim for single tiered or two tiered [12]. In two-tiered relay node deployment, the first level sensor nodes gather information from the target/segment. The relay nodes placed between the segments collect the information from the sensor nodes and send it to base station either through single hop or multi-hop. As a controlled scheme of relay node placement problem, in [13] the system to deploy RNs at a set of candidate spots is proposed. They proposed RNs to ensure survivability and connectivity criteria by considering few constraints on the deployed area. Both the work consider heterogeneous WSN comprising of sensor nodes, base station and RNs. In [14], constrained single-tiered relay node deployment problem is carried out and proposed $O(1)$ -approximation algorithms to place minimum relay nodes. Two-tiered constrained relay node deployment is carried out in [13].

Research has been initiated to exploit WSN in the wind turbine to monitor the mechanical or electrical faults [15–17]. These literatures say that the sensor network topology is designed with respect to single turbine. The work in [18] emphasises target coverage by dense installation of wireless sensors in large operational turbines. Sensor nodes in each turbine communicate the data to the server located at the tower base. The information from the tower base is communicated by wired medium to the control room. This system aims at only turbine level monitoring. The turbine level monitoring paved the way to expand the system to monitor the whole wind farm through wireless multi-hop mesh network. The harsh environmental condition of wind power plant could degrade the performance of WSN by affecting coverage, connectivity and network lifetime. Kishor has addressed these problems and given a solution in [19]. It is stated that some sensor nodes are randomly scattered between two towers. But to provide connectivity for such application, it is enough to transmit the data through transceiver module of the node, and there is no necessity of sensor module. Optimization of scattered sensors is not done here. As an alternative to scattered sensors between turbines, relay nodes are employed between the turbines to improve connectivity [20]. But this work has not considered coverage issue. All the above-said approaches study the need of relay nodes and place it efficiently; they do not emphasis on optimizing their count like DRFC.

3 Problem Statement

3.1 Basic Network Model

Assumptions to design the monitoring system:

- (1) Random deployment of base station in the target region.
- (2) Once the sensor nodes, relay node and base station are deployed, they are assumed to be static.
- (3) The initial energy is considered to be similar for all sensor nodes.
- (4) Communication range, energy and computational power of relay node are relatively higher than that of the sensor nodes.
- (5) The relay nodes are all considered to have similar communication range.
- (6) The first-order radio model is considered to be same as Heinzelman [21].

Energy E_T to transmit m -bit data to a distance ' d ' is shown below in Eq. (1),

$$E_T(m, d) = \begin{cases} mE_{\text{elec}} + \varepsilon_{\text{fs}}md^2 & d < d_r \\ mE_{\text{elec}} + \varepsilon_{\text{mp}}md^4 & d \geq d_r \end{cases} \quad (1)$$

Energy E_R to receive m -bit data is given in Eq. (2),

$$E_R(m) = mE_{\text{elec}} \quad (2)$$

3.2 Problem Statement

In this work, each wind turbine with static sensor nodes for monitoring is considered to achieve target coverage. Each wind turbine is considered as sub-network/segments. Hence, this problem is similar to partitioned network with disconnected segments. One node is defined as the candidate node from each segment, and such candidate nodes have to be connected using relay nodes. Thus, the primary objective of the work is to address connected target coverage (CTC) problem, thereby providing distinctive HWSN deployment scheme for monitoring wind farms. The proposed optimal sensor node deployment scheme is to (1) continuously monitor each and every target and (2) connect all the targets with BS. In addition, the deployment cost will be reduced, in terms of the number of RNs.

4 Proposed DRFC Approach

DRFC focuses mainly on optimum number of relay node computation to reduce deployment cost and to establish connectivity. Connectivity is established here by establishing an efficient inter-segment topology. DRFC operates in three phases. The first phase aims at target coverage by fixing optimum number of sensor nodes in the sub-network/turbine and proceeds with candidate node selection in each sub-network. The second phase of the algorithm has two steps to provide connectivity. In the first step, the border segments are identified by computing convex hull. In the second step, the Fermat points are calculated by considering adjacent border segments towards centre of the deployment area. These two steps are repeated till the number of points to calculate convex hull becomes at most three towards the centre of deployment area. The third phase deploys optimum relay nodes to form a connected inter-segment topology and to reduce deployment cost.

4.1 Target Coverage and Candidate Node Selection

For wind farm monitoring application, the key components of each wind turbine such as gear box, generator and tower are prone to failure. Such components have indeed to be monitored by different types of sensor nodes. The fault detection of the gear box and generator can simply be determined from the change of temperature, vibration and noise. Thus, two sensor nodes capable of measuring temperature, vibration and noise are installed one in gear box and the other in generator of the drive train. The tower is also vulnerable to vibration during high-speed wind. Hence, a vibration sensor node is placed in the midpoint of the tower from the drive train to the tower base. In addition to the above sensor nodes, one sensor node is placed at the tower base which is the candidate node for that particular turbine. The candidate node has higher energy and communication range than that of normal nodes. The candidate node collects the information from the sensor nodes of the corresponding target. By this way, target coverage is achieved by the predetermined sensor nodes deployed on the target itself.

In applications like battlefield, there is huge chance for multiple node failure which leads to partitioned segments. A candidate node is considered in each segment to collect the information from that particular segment and to maintain connectivity with base station. In case of unexpected explosion, multiple node failure may occur. The sensor nodes very close to the affected region identify the sudden drop in communication traffic as they could not reach their neighbours. They become the border nodes of that particular segment. The border node which has more residual energy and more alive neighbours becomes the candidate node as given in Fig. 1. Now the research work becomes connecting one candidate node from each segment using optimum number of relay nodes.

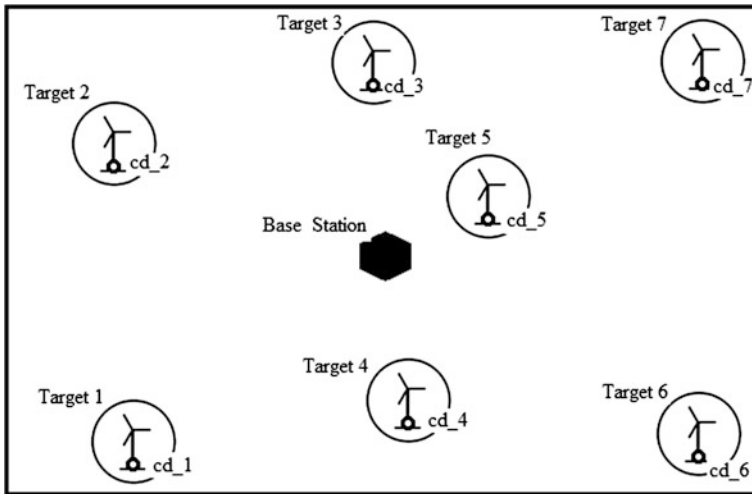


Fig. 1 Partitioned targets with cd_j as candidate node

4.2 Establishing Convex Hull and Fermat Points

Connectivity is the other issue which has to be addressed because the transmission range of the sensor nodes in the segments/targets is very less when compared with the distance between two adjacent targets. Thus, the targets are partitioned as shown in Fig. 1. Connectivity is guaranteed by relay nodes. The RNs are incorporated between the targets to maintain the information link. The shortest path between each segment to the base station at the centre of deployment area is considered as the initial inter-segment topology to deploy relay nodes. It needs 27 relay nodes for the sample topology as given in Fig. 1.

Border Segment Identification Using Convex Hull

The convex hull is computed from the given graph G , by considering the candidate nodes/segments as vertices. It gives the first tier boundary segment CH_0 . With the assumption of at least three non-collinear vertices, the initial closed polygon is formed as shown in Fig. 2. We followed Graham scan algorithm for convex hull formation. Among the n segments, the Grahams convex hull algorithm starts from the bottom-most y -coordinate segment. Sort the rest of $(n - 1)$ segments with a polar angle in counter clockwise direction. Moving from the initial segment until it reaches the same initial segment, right-turns are strictly followed. Figure 2 shows the first level of convex hull (CH_0) with five candidate nodes, Cd_1 , Cd_2 , Cd_3 , Cd_6 and Cd_7 .

Fermat Point Calculation

Fermat points are calculated between adjacent border candidate nodes in CH_0 with respect to BS which is at centre of deployment area. For example for each three

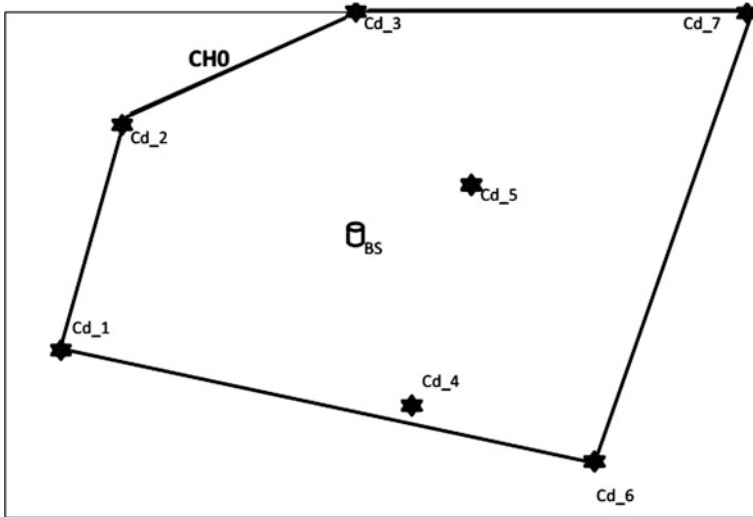


Fig. 2 First round of convex hull formation (CH0)

vertices {Cd₁, Cd₂ and BS}, {Cd₂, Cd₃ and BS}, {Cd₃, Cd₇ and BS}, {Cd₇, Cd₆ and BS}, {Cd₆, Cd₁ and BS}, the Fermat Points (FP) are calculated. Thus, formed FP will be considered as first tier FPs. Figure 3 shows a sample FP calculation strategy for {Cd₂, Cd₃ and BS} with FP₁⁰ emphasized in green colour. Figure 4 shows first tier FPs as {FP₁⁰, FP₂⁰, FP₃⁰, FP₄⁰ and FP₅⁰}.

The following conditions should be satisfied to calculate FPs,

- (i) Consider a triangle with three vertices (ex: ΔCd₂ BS Cd₃ of Fig. 3) to calculate FP.
- (ii) Length of all edges in the triangle (ΔCd₂ BS Cd₃) > R, where R is the communication range of RN.
- (iii) Angles in all the three edges in the triangle <120°.

The above-said two steps of Sect. 4.2 are repeated till the number of points to calculate convex hull becomes at most three towards the centre of deployment region. In the second round convex hull, CH1 is calculated by considering the first tier FPs (FP_j⁰) and remaining segments (ex. Cd₄ and Cd₅ in this case).

Inner convex hulls (ex: CH1 in Fig. 4) are further optimized by the following way,

- (i) If the vertices in outer CH (CH0) have two paths to reach BS at the centre, select the least distance path to reduce relay nodes
- (ii) Also vertices in outer CH have to take common FP path if available

By the above rule, Cd₁ and Cd₂ share FP₁⁰; Cd₆ and Cd₇ share FP₄⁰; and Cd₃ takes FP₃⁰. Here FP₂⁰ is not shared by any vertices in CH0. Thus, it is omitted

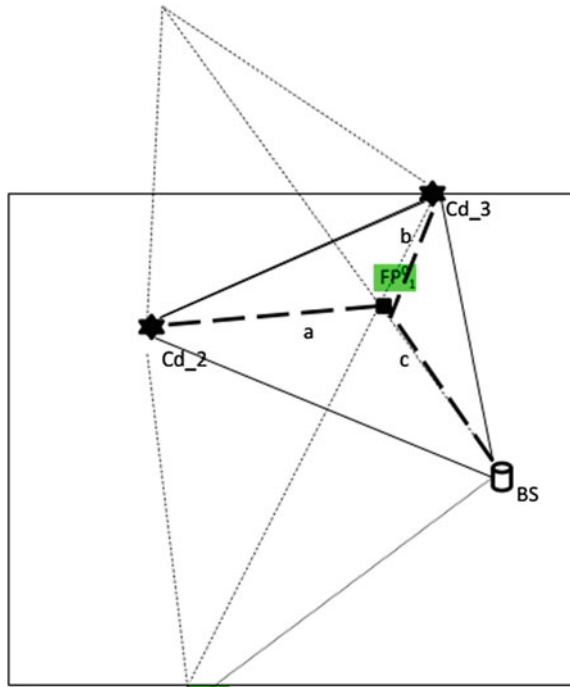


Fig. 3 Sample FP FP_1^0 formation: (is the new shortest path)

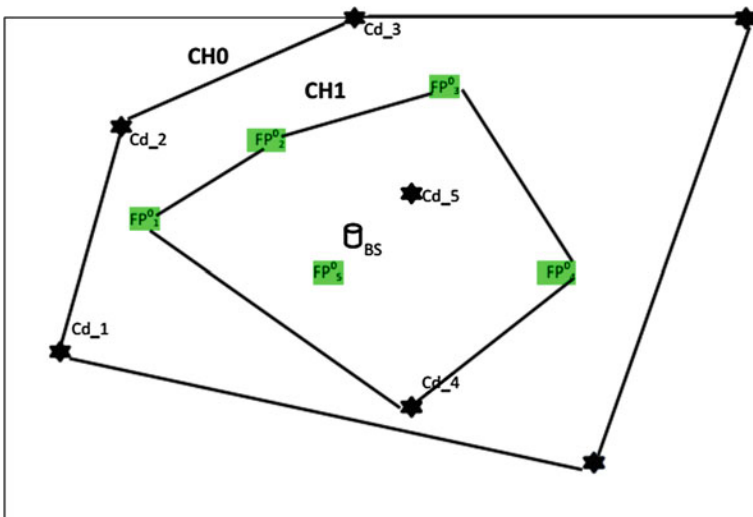


Fig. 4 Second level CH formation (CH1)

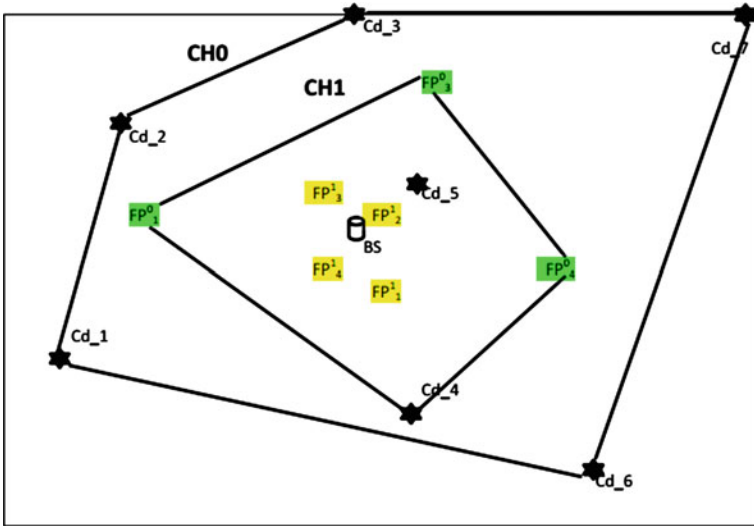


Fig. 5 Optimized inner convex hull (CH1) formation

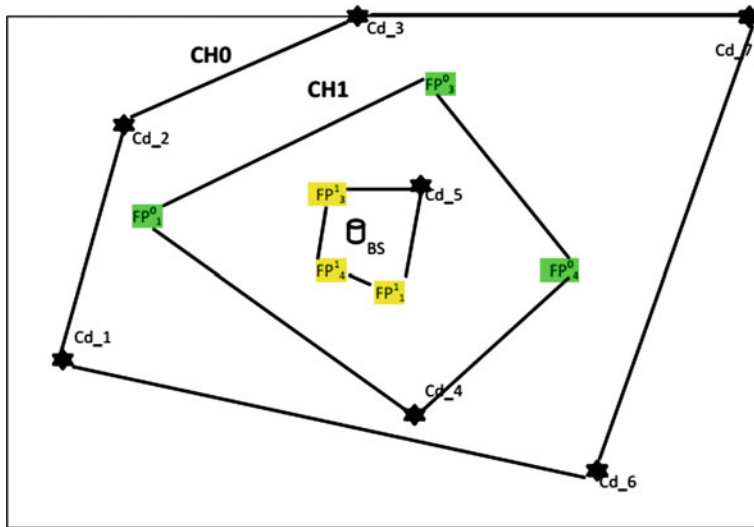


Fig. 6 Optimized inner convex hull (CH2) formation

in second tier FP calculation as given in Fig. 5. The second tier FPs is FP_1^1, FP_2^1, FP_3^1 and FP_4^1 .

Third tier CH (CH2) is formed as shown in Fig. 6. By the above optimized inner convex hull rule, FP_1^0 and Cd_4 share FP_4^1 ; FP_3^0 and FP_4^0 share Cd_5 . The FPs is not formed further as it does not satisfy the second and third condition of FP formation. Finally, Cd_5 and FP_4^1 are connected directly to BS.

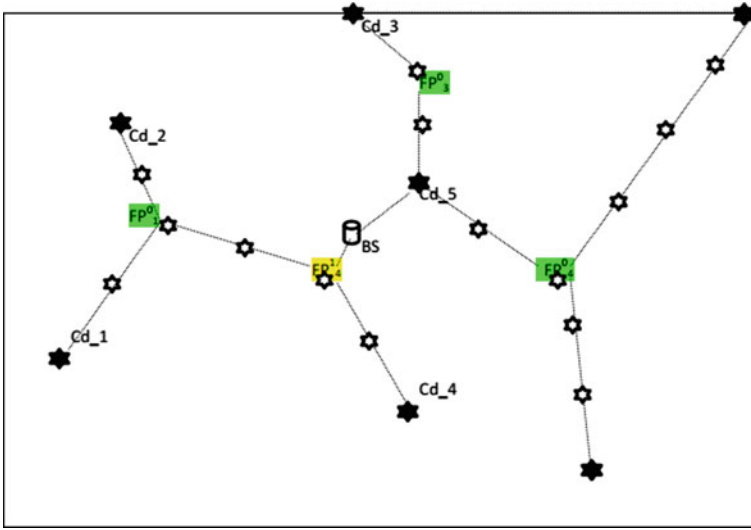


Fig. 7 Final restored topology by DRFC

4.3 Deploy Relay Nodes to Establish Inter-segment Connectivity

The restored topology by DRFC is given in Fig. 7. Additional relay nodes are populated in the resultant path of DRFC algorithm. The total RN deployed using DRFC is only 22 nodes which is very much optimized.

5 Results and Discussion

The performance of proposed DRFC approach is done based on number of relay nodes and average path length. The proposed methodology is simulated in MATLAB 2015b. We are considering a target region as a 2-D grid region with a maximum of $m \times n$ grids in the field. The experiment is performed with a square-shaped network of area size 13×13 units. The number of targets is set to 5–8 for the target region of 13×13 units including base station.

In the $m \times n$ grid field, each grid size is $K/\sqrt{2}$ units both in row and column and the diagonal distance of a single grid is K units. For simplicity, K is equated to 1.414 units, which is scaled to 200 m. Let R be the communication range of RN. The condition for R is $R \geq K$.

If the inter-target distance is equal to R units, only two RNs are placed one in each target zone. If the inter-target distance is greater than R units, RNs are placed with interval R units.

Table 1 Comparison of 1CSCP and DRFC

Number of targets	Average path length (1CSCP)	Average path length (DRFC)	No. of RN (1CSCP)	No. of RN (DRFC)
5	14.52	13.85	13	12
6	18.08	17.01	15	14
7	21.65	21.49	19	19
8	26.5	25.61	23	22

Number of Relay Nodes (N_RN): The performance of DRFC is compared with connected single-cover problem (1CSCP) [13]. The number of RNs required maintaining connectivity is tested with different target setup. In Table 1, the target region of 13×13 with maximum of 8 targets is considered for the study.

Average trail distance: The deployment region is chosen as 13×13 with different target size ranging from 5 to 8. In simple, the average path distance is the optimal path that the targets get connected with base station. In Table 1, the average path distance is compared between 1CSCP and DRFC.

6 Conclusion

In this paper, connected target coverage problem in optimal deployment of heterogeneous wireless sensor network for wind farm is discussed. A novel deployment approach is proposed to overcome the coverage and connectivity issues and to reduce deployment cost. Coverage is a critical problem in WSN which decides perfect monitoring of the target by the sensor nodes. Coverage is guaranteed through optimal sensor node deployment, at the critical points of the target. Connectivity and effective deployment are achieved by DRFC approach based on recursive Fermat points and convex hull formation.

References

1. Ling, Q., Tian, Z., Yin, Y., Li, Y.: Localized structural health monitoring using energy-efficient wireless sensor networks. *IEEE Sensors J.* **9**(11), 1596–1604 (2009)
2. Dyo, V., Ellwood, S.A., Macdonald, D.W., Markha, A., Trigoni, N., Wohlers, R., Mascolo, C., Psztor, B., Scellato, S., Yousef, K.: Wildsensing: design and deployment of a sustainable sensor network for wildlife monitoring. *ACM Trans. Sensor Netw.* **8**(4), 1–33 (2013)
3. Gungor, V.C., Korkma, M.K.: Wireless link-quality estimation in smart grid environment. *Int. J. Distrib. Sensor Netw.* **1**, 1–10 (2012)
4. Akyildiz, I.F., Su, W., Sankarasubramaniam, Y., Cayirci, E.: Wireless Sensor Networks: A Survey. *Comput. Netw. (Elsevier) J.* **38**, 393–422 (2002)
5. Vergin, R.S.M., Linda, A.T.: Improved leach algorithm for energy efficient clustering of wireless sensor network (WSN). *Int. J. Technol.* **7**(1), 50–60 (2016)

6. Lee, S., Younis, M.: Optimized relay node placement for connecting disjoint wireless sensor networks. *Comput. Netw. (Elsevier) J.* **56**(12), 2788–2804 (2012)
7. Erol-Kantarci, M., Mouftah, H.T.: Wireless sensor networks for cost-efficient residential energy management in the smart grid. *IEEE Trans. Smart Grid.* **2**(2), 314–325 (2011)
8. Yang, D., Misra, S., Fang, X.: Two-tiered constrained relay node placement in wireless sensor networks: computational complexity and efficient approximations. *IEEE Trans. Mobile Comput.* **11**(8), 1399–1411 (2012)
9. Misra, S., Majd, N., Huang, H.: Approximation algorithms for constrained relay node placement in energy harvesting wireless sensor networks. *IEEE Trans. Comput.* **63**(12), 2933–2947 (2014)
10. Kulkarni, R.V., Forster, A., Venayagamoorthy, G.: Computational intelligence in wireless sensor networks: a survey. *IEEE Commun. Surv. Tutorials* **13**(1), 68–96 (2011)
11. Mini, S., Udgata, S.K., Sabat, S.L.: Sensor Deployment and scheduling for target coverage problem in wireless sensor networks. *IEEE Sensors J.* **14**(3), 636–644 (2014)
12. Lloyd, E., Xue, G.: Relay node placement in wireless sensor networks. *IEEE Trans. Comput.* **56**, 134–138 (2007)
13. Yang, D., Misra, S., Fang, X., Xue, G., Zhang, J.: Two-tiered constrained relay node placement in wireless sensor networks: efficient approximations. In: *Proceedings of the IEEE Conference on Sensor, Mesh and Ad Hoc Communications and Networks (SECON 2010)*, Boston, MA, June 2010, pp. 323–331
14. Misra, S., Hong, S., Xue, G., Tang, J.: Constrained relay node placement in wireless sensor networks: formulation and approximations. *IEEE/ACM Trans. Netw.* **18**(2), 434–447 (2010)
15. Al-Anbagi, I.S., Mouftah, H.T., Erol-Kantarci, M.: Design of a delay-sensitive WSN for wind generation monitoring in the smart grid. In: *Proceedings of CCECE'11, 2011*, pp. 001370–001373
16. Wang, P., Yan, Y., Tian, G.Y., Bouzid, O., Ding, Z.: Investigation of wireless sensor networks for structural health monitoring. *J. Sensors* 1–7 (2012)
17. Fu, Z.X., Yuan, Y.: Condition health monitoring of offshore wind turbine based on wireless sensor network. In: *IPEC 2012 Conference on Power & energy*, pp. 649–654
18. Swartz, R.A., Lynch, J.P., Sweetman, B., Rolfes, R., Zerbst, S.: Structural monitoring of wind turbines using wireless sensor networks. *Workshop on Sensor Networks for Civil Infrastructure Systems* (2008)
19. Agarwal, D., Kishor, N.: Network lifetime enhanced tri-level clustering and routing protocol for monitoring of offshore wind farms. *IET Wireless Sensor Syst.* **4**(2), 69–79 (2014)
20. Chen, Q., Hu, Y., Chen, Z.: Improved Relay Node Placement Algorithm for Wireless Sensor Networks Application in Wind Farm. *IEEE Smart Energy Grid Engineering (SEGE)*, pp. 1–6 (2013)
21. Heinzelman, W.B., Chandrakasan, A.P., Balakrishnan, H.: An application-specific protocol architecture on wireless microsensor networks. *IEEE Trans. Wireless Commun.* **1**(4), 660–670 (2002)

Kinetic Instability of the Ion Acoustic Mode in Permeating Plasma of Electron–Positron and Ion

U. Deka and K. Shah

Abstract Kinetic instability of the ion acoustic mode is observed in permeating plasma of electron, positron, and ion in a similar background plasma system. The linear growth of the wave is excited only when the streaming speed of the flowing plasma reaches a critical speed for all temperature ratios. Presence of positron, however, only shows a quantitative modification in the critical speed of the flowing plasma.

Keywords Kinetic instability · Ion acoustic mode · Electron–positron plasma
Streaming instability · Growth rate

1 Introduction

The quest of electron–positron plasmas has been an outstanding problem because of its inherent challenges and interwoven physics related to various physical phenomena such as wave propagation, transport properties, and production in laboratory comprising of inferences drawn from theoretical, experimental, and observational mode of investigation [1]. Most of the work in the study of electron–positron plasma was confined to the study in the outburst of short lived very energetic pair particle beams in the early Universe [2–4], proposed to understand the some of the physics of the early Universe. Most of the work in electron–positron plasma is confined to the astrophysics because of many startling observations from the observational astronomy beholding plethora of mysteries yet to be unfolded. Likewise, the unsolved queries related to the radio emission far outside archetypal quasar 3C279 are predicted to be due to circular polarization produced by Faraday

U. Deka (✉) · K. Shah
Department of Physics, Sikkim Manipal Institute of Technology,
Rangpo 737136, Sikkim, India
e-mail: utpal.d@smit.smu.edu.in

K. Shah
e-mail: kz_rhythm@yahoo.com

conversion from electron–positron pairs as component of the plasma jet [5]. Understanding of the physics generation electron–positron plasma in the magnetospheres of magnetars and the related dynamics due to the self consistent radiation is an open question due to experimental limitation [6, 7].

The puzzling facts about the existence of electron–positron plasma in the early Universe and its process of formation in the intergalactic space have led to a wide spectrum of problems related to the plasma dynamics. It is mentioned that persistent flow of electron–positron plasma around hot neutron star is plausibly due to the radiation field around the magnetars [7]. In plasma dynamics, the study of instability is an important aspect. The linear, nonlinear theories of wave propagation in electron–positron plasma have been of great interest for the theoretical plasma physicists. In Ref. [8], it was theoretically argued that electron–proton plasma provides a natural background for the formation of electrostatic solitary waves and hole structures due to streaming instability, which arises due to asymmetric inertia between ions and electrons. In another work, it was shown that both harmonic and spiky waves can exist with the fact that slow waves will have smaller amplitudes, whereas high speed waves moves with large amplitudes [9]. It has been theoretically predicted that turbulence of the electromagnetic waves can be excited in magnetized, collisionless electron–positron plasma using the linear kinetic theory [10]. Linear dispersion theory was used by the authors to predict the existence of two relatively long wavelengths modes that are slightly damped propagate in the presence of a background magnetic field. It has been found that pair-ion plasma has the capability to excite new mode seems to which can become unstable in the presence of shear flow and is quite different from the normal electron–ion plasma [9, 11, 12]. Moreover, the nonlinear mode of the same can form stable vortex structures. The probable cause for such observations may be the uniformity in their masses and magnitude of charges, which reduces the gap in the spacescales and timescales.

The nonlinear modes of the propagation of ion acoustic wave including the higher order compressive and rarefactive solitary waves in presence of positrons have shown interesting results in presence of magnetic field or in its absence. The results derived differ appreciably from the traditional electron–ion plasma [13–17]. It has been shown in some cases that negative soliton, limited in Mach number by double layers, exists over small ranges in β , relative to positron population and Mach number. In uniformly magnetized electron–positron–ion plasma, the percentage of positron density directly affects the amplitude of solitary potential structures. The obliquely propagating soliton in magnetized plasma propagates with subsonic speed, while in the unmagnetized case it is supersonic in nature.

The study of various instabilities in electron–positron plasma is yet another extensive area of research studied by number of authors under various force field configurations. In the study of counter streaming pair plasma for cold electrons, it is observed that instabilities are observed only for two lowest longitudinal and lowest transverse modes out of the two longitudinal and four transverse modes derived from the dispersion relation. Moreover, unique behaviors of modes reconnection are also observed for certain particular condition [18].

In yet another important article [19], the application of kinetic theory reveals that when electron–positron pairs are generated due to back reaction on highly relativistically electromagnetic wave. These waves may damp because of the pairs that are produced and are accelerated by the electromagnetic field of the wave itself. However, kinetic theory predicts that when electromagnetic waves propagates in ultra-relativistic electron–positron plasmas, then such envelopes may collapsed and may be confined into a localized region [20]. At the same time, when an ultra-intense linearly polarized laser pulse is sent in similar plasma, the comparison between the nonlinearity in the interaction and the relativistic light ponderomotive-driven density responses primarily decides the amplitude of the modulation instability [21]. It is seen that when quantum corrections are inserted to two-stream instabilities in electron–positron–ion plasmas, then a new eigen electrostatic mode is generated [22].

The impetus in the theoretical research proposing new modes and new kinds of instability results has created a very high demand for the experimental verifications. The hiccups in laboratory generation of electron–positron plasma have been critically analyzed by Pedersen et al., as mentioned in Ref. [23]. They have proposed an interesting idea for such an experiment in a stellarator. The recent success in the generation of electron–positron plasmas in controlled laboratory experiments by using compact laser-driven setup has overcome extreme hurdles in reproduction neutral matter–antimatter plasmas in the laboratory [24].

The success in experimental production of electron–positron plasma should pave the way for the verification of microinstabilities driving turbulence and transport in electron–ion plasmas [25]. Further, Helander and his co-author pointed out that linear gyrokinetic stability properties of microinstabilities in magnetically confined electron–positron plasmas may be explored by varying parameters such as pressure and magnetic field curvature that can be controlled in laboratory.

The thrust of kinetic instability in electron–positron plasma requires more extensive investigation in view of ion acoustic mode in permeating plasmas. Vranjes and his co-authors studied instability of the ion acoustic mode using a kinetic treatment in case of permeating plasmas has revealed that the temperature and the velocity of the flowing plasma can control the excitation of the instability [26, 27].

In this present work, we have proposed to investigate the kinetic instability of the ion acoustic mode in permeating electron–positron plasma with ions. The work is presented in four sections describing the theoretical modeling, mathematical modeling, results and discussion, and conclusion.

2 Theoretical Modeling

In this work, we have considered warm plasma consisting of static ion, electron, and positron along with flowing ion, electron, and positron is taken under consideration in collisionless and unmagnetized quasineutral plasma. The velocities of

the species are considered in the nonrelativistic range. Further, the static velocity of the species is assumed to be zero. We have adopted the kinetic theory to describe the set of equations governing the plasma system. Finally, the dispersion relation is derived, considering certain temperature range and conditions for the velocity of the streaming plasmas. Such situations are realized in flowing plasmas under astrophysical situations and during explosions, novae and supernovae explosions.

3 Mathematical Modeling

We have considered the equilibrium densities of the flowing and static electron, ion, and positron as given below. Since the whole system is considered to be quasineutral, hence equilibrium densities of singly charged ion and positron are considered to be half of the equilibrium density of the electron.

$$n_{feo} = n_{fo}; n_{fio} = n_{fpo} = \frac{n_{fo}}{2} \tag{1}$$

$$n_{seo} = n_{so}; n_{sio} = n_{spo} = \frac{n_{so}}{2} \tag{2}$$

In general,

$$T_{fe} \neq T_{se} \text{ or } T_{fi} \neq T_{si} \text{ or } T_{fp} \neq T_{sp} \tag{3}$$

The plasma distribution function is given by,

$$f_{jo} = n_{j0} \left(\frac{m_j}{2\pi K_B T_j} \right)^{3/2} \exp \left[-\frac{m_j}{2K_B T_j} \left\{ v_x^2 + v_y^2 + (v_z - v_{jo})^2 \right\} \right] \tag{4}$$

$$v_{Tj}^2 = \frac{k_b T_j}{m_j}$$

The kinetic equation for the collisionless plasma can be written as

$$\frac{\partial f}{\partial t} + \mathbf{v} \cdot \nabla f + \frac{q}{m} (\mathbf{E} + \mathbf{v} \times \mathbf{B}) \left(\frac{\partial f}{\partial \mathbf{v}} \right) = 0 \tag{5}$$

We use the linear perturbations theory to represent $f_j = f_{jo} + f_{j1}$, with f_{jo} as independent of space and time and depends only on velocity to write Eq. (5) as,

$$\frac{\partial f_{j1}}{\partial t} + \vec{v} \cdot \nabla f_{jo} + \frac{q_j}{m} (\vec{\mathbf{E}}_1 + \mathbf{v} \times \mathbf{B}_0) \left(\frac{\partial f_{jo}}{\partial \mathbf{v}} \right) = 0 \tag{6}$$

We use the fourier plane wave expansion of $\sim \exp(-i\omega t + ikz)$ to write Eq. (6) as,

$$-i\omega f_{j1} + \bar{v}ikf_{jo} + \frac{q_i}{m_j} \left[E_1 \frac{\partial f_{jo}}{\partial v} \right] + \frac{q_i}{m_j} \left[(\bar{v} \times \bar{B}) \frac{\partial f_{jo}}{\partial v} \right] = 0 \text{ and obtain}$$

$$f_{j1} = -\frac{iq_j}{m_j(\omega - \bar{v}k)} \left[\bar{E}_1 \frac{\partial f_{jo}}{\partial v} \right]. \tag{7}$$

We consider the standard, the current density expression, and the Maxwell's equations

$$\vec{J} = \sum_j q_j \int \bar{v} f_{j1} \partial^3 \bar{v} \tag{8}$$

$$\nabla \times \mathbf{E} = -\frac{\partial \mathbf{B}}{\partial t} \tag{9}$$

$$\nabla \times \mathbf{B} = \mu_o \mathbf{J} + \frac{1}{c^2} \frac{\partial \mathbf{E}}{\partial t} \tag{10}$$

Considering the flow along the z direction, we will have $\mu_o J_z = \frac{i\omega}{c^2} \bar{E}_z$. Using Eqs. (8)–(9), we can get

$$1 = -\sum_j \frac{\omega_{pj}^2}{n_{jo}k^2} \int \frac{1}{(\omega/k - v_z)} \frac{\partial f_{jo}}{\partial v_z} d^3v \tag{11}$$

where $\omega_{pj} = \frac{q_j^2 n_{jo}}{\epsilon_o m_j}$ and f_{j0} is given by

$$f_{jo} = \frac{n_{jo}}{(2\pi)^{3/2} V_{Tj}^3} \exp \left[-\frac{1}{2V_{Tj}^2} \left\{ v_x^2 + v_y^2 + (v_z - v_{jo})^2 \right\} \right]. \tag{12}$$

Now, by using the plasma distribution function as given in Eq. (12), the generalized dispersion relation can be derived as given below.

$$1 = \sum_j \frac{\omega_{pj}^2}{n_{jo}\omega V_{Tj}^2} \int_{-\infty}^{+\infty} \frac{v_z(v_z - v_{jo})}{(\omega - kv_z)} f_{jo} d^3v \tag{13}$$

Now, Eq. (13) for electron, positron, and ions with limits of integration going from $-\infty$ to $+\infty$ can be written as

$$1 = \left(\frac{\omega_{pe}^2}{n_{eo}\omega V_{Te}^2} \int \frac{v_z(v_z - v_{eo})}{(\omega - kv_z)} f_{eo} + \frac{2\omega_{pp}^2}{n_{po}\omega V_{Tp}^2} \int \frac{v_z(v_z - v_{po})}{(\omega - kv_z)} f_{po} + \frac{2\omega_{pi}^2}{n_{io}\omega V_{Ti}^2} \int \frac{v_z(v_z - v_{io})}{(\omega - kv_z)} f_{io} \right) \partial v_x \partial v_y \partial v_z$$

Using Eqs. (12) and (13) and on solving, we rewrite the dispersion relation in terms of the plasma dispersion function $Z(b_j)$ as,

$$1 + \sum_j \frac{1}{k^2 \lambda_{dj}^2} [1 - Z(b_j)] = 0 \tag{14}$$

$$Z(b_j) = \frac{b_j}{(2\pi)^{1/2}} \int_{-\infty}^{+\infty} \frac{\exp(-\zeta^2/2)}{b_j - \zeta} d\zeta \tag{15}$$

where $b_j = [\omega - kv_{jo}/kv_{Tj}]$, $\zeta = [v_z - v_{jo}/v_{Tj}]$ and $\frac{v_z}{v_{Tj}}, \frac{v_{jo}}{v_{Tj}}$ are the normalized velocities and $\sum_j \frac{1}{k^2 \lambda_{dj}^2} = \frac{1}{k^2} \left[\frac{1}{\lambda_{de}^2} + \frac{1}{\lambda_{dp}^2} + \frac{1}{\lambda_{di}^2} \right] \equiv \frac{1}{k^2 \lambda_d^2}$.

Further substituting the value of ζ and b_j , we can rewrite Eq. (15) as,

$$Z(b_j) = \frac{(\omega - kv_{jo}/kv_{Tj})}{(2\pi)^{1/2}} \int_{-\infty}^{+\infty} \frac{\exp(-(v_z - v_{jo}/v_{Tj})^2/2)}{(\omega - kv_{jo}/kv_{Tj}) - (v_z - v_{jo}/v_{Tj})} dv_z \tag{16}$$

Using the integration over Landau contour as mentioned in standard text books [28], the generalized dispersion equation for the ion acoustic wave in plasma comprising of static electron, positron, and ion and flowing electron, positron, and ion may be obtained as given below.

$$1 + \frac{1}{k^2 \lambda_d^2} + i \left(\frac{\pi}{2} \right)^{1/2} \left\{ \frac{\omega \omega_{pe}^2}{k^3 V_{Te}^3} \exp\left(-\frac{\omega^2}{2k^2 V_{Te}^2}\right) + \frac{\omega \omega_{pp}^2}{k^3 V_{Tp}^3} \exp\left(-\frac{\omega^2}{2k^2 V_{Tp}^2}\right) \right. \\ \times \left. \frac{\omega \omega_{pi}^2}{k^3 V_{Ti}^3} \exp\left(-\frac{\omega^2}{2k^2 V_{Ti}^2}\right) \right\} - \left\{ \frac{\omega_{pe}^2}{\omega^2} + \frac{\omega_{pe}^2}{\omega^2} + \frac{\omega_{pe}^2}{\omega^2} \right\} \\ - \frac{3}{2} \left\{ \frac{k^2 V_{Te}^2 \omega_{pe}^2}{\omega^4} + \frac{k^2 V_{Tp}^2 \omega_{pp}^2}{\omega^4} + \frac{k^2 V_{Ti}^2 \omega_{pi}^2}{\omega^4} \right\} = 0 \tag{17}$$

For static electron, positron and ion and flowing electron, positron and ion, Eq. (17) can be written as,

$$\begin{aligned}
& 1 + \frac{1}{k^2 \lambda_d^2} + i \left(\frac{\pi}{2} \right)^{1/2} \left[\frac{\omega \omega_{pse}^2}{k^3 V_{Tse}^3} \exp \left(-\frac{\omega^2}{2k^2 V_{Tse}^2} \right) + \frac{\omega \omega_{pfe}^2}{k^3 V_{Tfe}^3} \exp \left(-\frac{\omega^2}{2k^2 V_{Tfe}^2} \right) \right. \\
& + \frac{\omega \omega_{psp}^2}{k^3 V_{Tsp}^3} \exp \left(-\frac{\omega^2}{2k^2 V_{Tsp}^2} \right) + \frac{\omega \omega_{pfp}^2}{k^2 V_{Tfp}^3} \exp \left(-\frac{\omega^2}{2k^2 V_{Tfp}^2} \right) \\
& \left. + \frac{\omega \omega_{psi}^2}{k^3 V_{Tsi}^3} \exp \left(-\frac{\omega^2}{2k^2 V_{Tsi}^2} \right) + \frac{\omega \omega_{pfi}^2}{k^3 V_{Tfi}^3} \exp \left(-\frac{\omega^2}{2k^2 V_{Tfi}^2} \right) \right] \\
& - \left\{ \frac{\omega_{pfe}^2}{\omega^2} + \frac{\omega_{pse}^2}{\omega^2} + \frac{\omega_{pfp}^2}{\omega^2} + \frac{\omega_{psp}^2}{\omega^2} + \frac{\omega_{pfi}^2}{\omega^2} + \frac{\omega_{psi}^2}{\omega^2} \right\} \\
& - \frac{3}{2} \left\{ \frac{k^2 V_{Tfe}^2 \omega_{pfe}^2}{\omega^4} + \frac{k^2 V_{Tse}^2 \omega_{pse}^2}{\omega^4} + \frac{k^2 V_{Tfp}^2 \omega_{pfp}^2}{\omega^4} \right. \\
& \left. + \frac{k^2 V_{Tsp}^2 \omega_{psp}^2}{\omega^4} + \frac{k^2 V_{Tfi}^2 \omega_{pfi}^2}{\omega^4} + \frac{k^2 V_{Tsi}^2 \omega_{psi}^2}{\omega^4} \right\} = 0
\end{aligned} \tag{18}$$

In the first term of the imaginary part under the condition $V_{Tsi}^2 \ll |\omega| \ll V_{Tse}^2, V_{Tsp}^2$ and $(\omega - kV_{fo}) \ll kV_{fje}, kV_{fjp}, kV_{fji}$, the exponential term had been expanded for the static electron and static positron, the second part is also obtained on expanding the exponential term. Similarly, we consider only the first term and ignore the rest of the terms for flowing electron, ion, and positron case also. In case, the third term in the exponential is retained as it is and not expanded and considering the equation for static ion only.

Now, we modify the second term of the Eq. (17) related to the terms having $\frac{1}{\omega^2}$ for which only the static ion is considered, and similarly, the third term of the same equation having $\frac{1}{\omega^4}$ term for which also we consider only the static ion. Inserting these modifications, we can draw the equation as,

$$\begin{aligned}
& 1 + \frac{1}{k^2 \lambda_d^2} - \frac{\omega_{psi}^2}{\omega^2} - \frac{3}{2} \frac{k^2 V_{Tsi}^2 \omega_{psi}^2}{\omega^4} + i \left(\frac{\pi}{2} \right)^{1/2} \\
& \left[\left(\frac{\omega \omega_{pse}^2}{k^3 V_{Tse}^3} + \frac{\omega \omega_{psp}^2}{k^3 V_{Tsp}^3} \right) + (\omega - kV_{fo}) \left(\frac{\omega_{pfe}^2}{k^3 V_{Tfe}^3} + \frac{\omega_{pfp}^2}{k^3 V_{Tfp}^3} + \frac{\omega_{pfi}^2}{k^3 V_{Tfi}^3} \right) \right. \\
& \left. + \frac{\omega \omega_{psi}^2}{k^3 V_{Tsi}^3} \exp \left(-\frac{\omega^2}{2k^2 V_{Tsi}^2} \right) \right] = 0
\end{aligned} \tag{19}$$

Equation (19) is the required dispersion relation in the ion acoustic mode in permeating plasma in presence of positron. To further simplify the above mentioned equation, we consider the following new parameters.

$$a = \frac{\omega_{pfe}^2}{k^3 V_{Tfe}^3}, b = \frac{\omega_{pfi}^2}{k^3 V_{Tfi}^3}, c = \frac{\omega_{pfp}^2}{k^3 V_{Tfp}^3}, d = \frac{\omega \omega_{pse}^2}{k^3 V_{Tse}^3}, e = \frac{\omega \omega_{psp}^2}{k^3 V_{Tsp}^3}$$

We can show that,

$$\frac{a}{b} = \left(\frac{m_e}{m_i}\right)^{1/2} \times \left(\frac{T_{fi}}{T_{fe}}\right)^{3/2} \ll 1, \frac{a}{c} = \left(\frac{m_p}{m_i}\right)^{1/2} \times \left(\frac{T_{fi}}{T_{fp}}\right)^{3/2} \ll 1$$

We assume that the temperature of the electron and positron is almost same and higher than that of the ion due to the same mass of the electron and positron but smaller than the mass of ion. Therefore, the ratios considered $\frac{a}{b}$ and $\frac{a}{c}$ is always less than unity. Similarly, we can show that

$$\frac{d}{(\omega - kV_{fo})b} = \left(\frac{T_{fi}}{T_{se}}\right)^{3/2} \times \left(\frac{m_e}{m_i}\right)^{1/2} \ll 1.$$

Now, introducing limits of the above ratios, Eq. (19) may be written as,

$$\Delta = 1 + \frac{1}{k^2 \lambda_d^2} - \frac{\omega_{psi}^2}{\omega^2} - \frac{3 k^2 V_{Tsi}^2 \omega_{psi}^2}{2 \omega^4} + i \left(\frac{\pi}{2}\right)^{1/2} \left[(\omega - kV_{fo}) \left(\frac{\omega_{pfi}^2}{k^3 V_{Tfi}^3}\right) + \frac{\omega \omega_{psi}^2}{k^3 V_{Tsi}^3} \exp\left(-\frac{\omega^2}{2k^2 V_{Tsi}^2}\right) \right] = 0 \tag{20}$$

The real and the imaginary part of the dispersion equation for the acoustic wave can be written as,

$$\begin{aligned} \text{Re}\Delta &= 1 + \frac{1}{k^2 \lambda_d^2} - \frac{\omega_{psi}^2}{\omega^2} - \frac{3 k^2 V_{Tsi}^2 \omega_{psi}^2}{2 \omega^4} \\ \text{Im}\Delta &= \left(\frac{\pi}{2}\right)^{1/2} \left[(\omega - kV_{fo}) \left(\frac{\omega_{pfi}^2}{k^3 V_{Tfi}^3}\right) + \frac{\omega \omega_{psi}^2}{k^3 V_{Tsi}^3} \exp\left(-\frac{\omega^2}{2k^2 V_{Tsi}^2}\right) \right] \end{aligned}$$

The growth rate from Eq. (20) is given as

$$\begin{aligned} \omega_i &\cong -\text{Im}\Delta(k, \omega_r) / [\partial \text{Re}(\Delta) / \partial \omega]_{\omega \cong \omega_r} \\ \omega_i &= -\left(\frac{\pi}{8}\right)^{1/2} \times \frac{\omega_r^3}{(1 + 3k^2 V_{Tsi}^2 / \omega_r^2) k^2 V_{Tfi}^2} \\ &\times \left[\frac{(\omega_r - kV_{fo})}{kV_{Tfi}} \left(\frac{\omega_{pfi}^2}{\omega_{psi}^2}\right) + \frac{\omega_r \omega_{psi}^2}{kV_{Tsi} \omega_{psi}^2} \right. \\ &\left. \times \frac{V_{Tfi}^2}{V_{Tsi}^2} \exp\left(-\frac{\omega_r^2}{2k^2 V_{Tsi}^2}\right) \right] \end{aligned} \tag{21}$$

Using, $\frac{V_{T\bar{f}i}^2}{V_{Tsi}^2} = \frac{T_{\bar{f}i}}{T_{si}}$ and $\frac{\omega_{\bar{f}i}^2}{\omega_{\bar{p}si}^2} = \frac{n_{fo}}{n_{so}}$, Eq. (21) can be simplified as

$$\omega_i = -\left(\frac{\pi}{8}\right)^{1/2} \times \frac{\omega_r^3}{(1 + 3k^2 V_{Tsi}^2 / \omega_r^2) k^2 V_{T\bar{f}i}^2} \times \left[\frac{(\omega_r - kV_{fo})}{kV_{T\bar{f}i}} \left(\frac{n_{fo}}{n_{so}}\right) + \frac{\omega_r}{kV_{Tsi}} \times \frac{T_{\bar{f}i}}{T_{si}} \exp\left(-\frac{\omega_r^2}{2k^2 V_{Tsi}^2}\right) \right] \quad (22)$$

Again, the frequency of the ion acoustic wave is given by,

$$\omega_r^2 = \left(k^2 \lambda_d^2 \omega_{\bar{p}si}^2 / 2\right) \left[1 + (1 + 12\lambda_{si}^2 / \lambda_d^2)^{1/2}\right] \quad (23)$$

In the above equation,

$$\frac{\lambda_{si}^2}{\lambda_d^2} = \lambda_{si}^2 \left[\frac{1}{\lambda_{di}^2} + \frac{1}{\lambda_{de}^2} + \frac{1}{\lambda_{dp}^2} \right] \quad (24)$$

where $\lambda_{de}^2 = \frac{\epsilon_0 K_B T_e}{n_o e^2}$ and $\lambda_{dp}^2 = \frac{\epsilon_0 K_B T_p}{n_o / 2 e^2}$.

Since the $T_e \sim T_p$, then $\lambda_{dp}^2 = \frac{2\epsilon_0 K_B T_e}{n_o e^2}$, which will give $\lambda_{dp}^2 = 2\lambda_{de}^2$. Now, inserting $\frac{\lambda_{de}^2}{\lambda_{di}^2} \ll 1$, Eq. (24) becomes $\frac{\lambda_{si}^2}{\lambda_d^2} = \frac{3\lambda_{si}^2}{2\lambda_{de}^2}$. Now, by using this approximation, Eq. (23) can be rewritten as,

$$\omega_r^2 = (kc_s^2 / 2) \left[1 + \left(1 + 18 \frac{T_{si}}{T_{se}}\right)^{1/2}\right]$$

We now substitute $\omega_r = \sqrt{2} kc_s$ in Eq. (22) to find,

$$\omega_i = \left(\frac{\pi}{8}\right)^{1/2} \times \frac{\sqrt{2} k^3 c_s^3}{(1 + 3k^2 V_{Tsi}^2 / 2k^2 c_s^2) k^2 V_{T\bar{f}i}^2} \times \left[\frac{(kV_{fo} - (\sqrt{2}kc_s))}{kV_{T\bar{f}i}} \left(\frac{n_{fo}}{n_{so}}\right) - \frac{\sqrt{2}c_s}{V_{Tsi}} \times \frac{T_{\bar{f}i}}{T_{si}} \exp\left(-\frac{2k^2 c_s^2}{2k^2 V_{Tsi}^2}\right) \right]. \quad (25)$$

Further assuming $\frac{3k^2 V_{Tsi}^2}{2k^2 c_s^2} \ll 1$ and replacing $\frac{V_{\bar{f}i}}{V_{Tsi}}$ by $\sqrt{\frac{T_{\bar{f}i}}{T_{si}}}$ and using $c_{se} = \sqrt{\frac{k_B T_{se}}{m_i}}$, $V_{T\bar{f}i} = \sqrt{\frac{k_B T_{\bar{f}i}}{m_i}}$, $\frac{C_{se}}{V_{T\bar{f}i}} = \sqrt{\frac{T_{se}}{T_{\bar{f}i}}}$ Eq. (25) can be rewritten as,

$$\omega_i = \left(\frac{\pi}{4}\right)^{1/2} \times kc_s \left(\sqrt{\frac{T_{se}}{T_{fi}}}\right)^3 \times \left[\left(V_{fo}/\sqrt{2}c_{se} - 1\right) \left(\frac{n_{fo}}{n_{so}}\right) - \left(\frac{T_{fi}}{T_{si}}\right)^{3/2} \exp\left(-\frac{c_{se}^2}{V_{fo}^2}\right) \right] \tag{26}$$

Equation (26) gives the growth rate of the acoustic wave.

4 Numerical Analysis

Equation (26) is solved numerically to observe the variation of the growth rate by varying some of the important parameters. It is to be noted that the temperature and streaming speed has a very important affect on the growth rate. The nature of the growth primarily depends upon the normalized streaming speed, normalized density, and temperature as given in Eq. (26).

Further, in most of the astrophysical conditions, it is more important to find the affect of temperature and the streaming speeds. Henceforth, the variation of the growth rate w.r.t. the varying streaming speed has been plotted for a given temperature ratio at a fixed normalized density. The density of the flowing plasma is normalized with the density of the static plasma, i.e., the background plasma. The variation is shown in Fig. 1a, b. The variations are observed for the normalized speed for a given temperature ratio, τ . The normalized streaming speed is varied for a range of 0.1–1.4 and beyond in Fig. 1b for three different temperature ratio of τ equal to 1.00, 1.25, and 1.75. Similar variations are also observed for different values of τ .

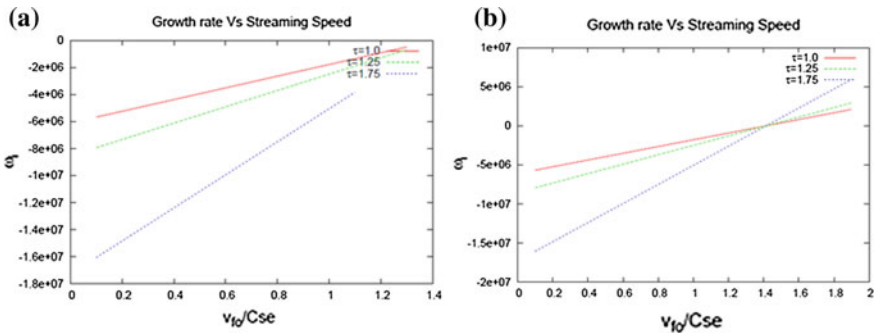


Fig. 1 Variation of the growth is plotted against the normalized streaming speed. **a** The normalized streaming speed is varied up to a value of 1.4 and **b** the normalized streaming speed is varied beyond 1.4, which appears to be critical value

The temperature of static electron and static ion is considered to be 10^5 K and 10^3 K, respectively. The growth rate (ω_i) is seen to be a function of temperature ratio (depending basically on the temperature of flowing ion), flow velocity (V_{f0}), and density of the plasma species considered (n_{f0}, n_{s0}). As shown in Fig. 1, the growth rate for all the values of τ is initially negative and starts becoming positive when for $V_{f0}/C_{se} \rightarrow 1.4127$, which indicates that the growth rate described under the linear theory is observed when the flow velocity ratio V_{f0}/C_{se} reaches a critical value.

5 Results and Discussion

The complete expression for the growth rate is given in given in Eq. (25). However, under the condition of $\frac{3k^2 V_{f0}^2}{2k^2 C_s^2} \ll 1$, the expression for the growth rate is simplified as given in Eq. (26). From Eq. (26), it is evident that the growth rate depends upon number of parameters of the considered plasma system. The growth rate is affected whenever there is a variation on the following ratios, (i) temperature ratio of the static electrons to the flowing ions (ii) temperature ratio of the flowing ions to static ions (iii) equilibrium density ratio of the flowing to static plasma, and (iv) ratio of streaming velocity of the ion beam to the ion acoustic speed. It is being observed that the introduction of the positrons modifies the growth rate quantitatively.

From Fig. 1, we can observe that the growth rate is negative until the streaming speed of the flowing plasma reaches a critical value as mentioned in the previous section. It indicates that the wave gets excited and grows when the streaming speed of the flowing plasma for almost all the temperatures for the considered normalized density of $n_{s0}/n_{f0} = 1.66$ reaches 1.4127. This is an interesting result observed from our calculation. Using a root finding method, we find that the critical normalized streaming speed lies at approximately 1.4127. From this, we can confer that all waves in the flowing plasma may not exhibit instability. Only those ion acoustic waves whose velocity crosses a threshold value only becomes unstable. Hence, we can confer that the streaming speed acts as the free source of energy only after a minimum threshold value. Further, we note that the threshold value for excitation of the instability is same for all temperature ranges. The nature of growth rate remains linear throughout for all velocity ranges.

We would also like to mention that the presence of positrons modifies the threshold value only quantitatively. The nature of instability remains the same without significant variation in the instability condition, when compared to the instability as derived in Ref. [27]. It is noted that, as the temperature ratio τ increases, the growth rate decreases. The plausible reason for only quantitative modification may be that the presence of the positively charge ions, which are more massive than the positrons. It will be more fruitful to include the ions as some impurities to electron–positron plasma and investigate the effect of fractional densities of the ions maintaining an overall quasineutrality condition.

6 Conclusion

When an ion acoustic wave is excited in flowing electron–positron plasma with ion in presence of similar background plasma, it is observed that the certain acoustic modes can grow linearly. The growth rate primarily depends upon the streaming speed of the flowing plasma and the temperature ratio of the different plasmas, i.e., the flowing and static plasma. The permeation of plasma can be the source for the instability of an acoustic mode only after attaining a particular threshold value. The presence of positrons, though do not exhibit any such qualitative modification in the growth rate but small quantitative modification, is observed. The plausible cause may be their similar mass as that of the electrons does not affect the wave propagation as compared to any other positive ions or dusts in the system.

References

1. Ruffini, R., Vereshchagin, G., Xue, S.S.: Electron–positron pairs in physics and astrophysics: from heavy nuclei to black holes. *Phys. Reports* **487**, 1–140 (2010)
2. Abdo, A.A., et al.: Fermi observations of high-energy gamma-ray emission from GRB 080916C. *Science* **323**, 1688–1693 (2009)
3. Lyne, A.G., et al.: A double-pulsar system: a rare laboratory for relativistic gravity and plasma physics. *Science* **303**, 1153–1157 (2004)
4. Tavani, M., et al.: Discovery of powerful gamma-ray flares from the crab nebula. *Science* **331**, 736–739 (2011)
5. Wardle, J.F.C., Homan, D.C., Ojha, R., Roberts, D.H.: Electron-positron jets associated with the quasar 3C279. *Nat.* **395**, 457–461 (1998)
6. Istomin, Y.N., Sobyenin, D.N.: Electron–positron plasma generation in a magnetar magnetosphere. *Astro. Letts.* **33**, 660–672 (2007)
7. Beloborodov, A.M.: Electron–positron flows around magnetars. *Astrophys. J.* **777**, 114–132 (2013)
8. Jao, C.S., Hau, L.N.: Formation of electrostatic solitons and hole structures in pair plasmas. *Phys. Rev. E.* **86**, 056401(1-8) (2012)
9. Lu, G., Liu, Y., Yu, M.Y.: Exact electrostatic waves in electron–positron plasmas. *Phys. Scr.* **81**, 045503(1-5) (2010)
10. Gary, S.P., Karimabadi, H.: Fluctuations in electron–positron plasmas: linear theory and implications for turbulence. *Phys. Plasmas* **16**, 042104(1-7) (2009)
11. Saleem, H., Vranjes, J., Poedts, S.: On some properties of linear and nonlinear waves in pair-ion plasmas. *Phys. Letts. A* **350**, 375–379 (2006)
12. Stenflo, L., Shukla, P.K., Yu, M.Y.: Nonlinear propagation of electromagnetic waves in magnetized electron–positron plasmas. *Astrophys. Space Sci.* **117**, 303–308 (1985)
13. Baluku, T.K., Hellberg, M.A.: Ion acoustic solitary waves in an electron–positron–ion plasma with non-thermal electrons. *Plasma Phys. Control Fus.* **53**, 095007(1-16) (2011)
14. Mahmood, S., Mushtaq, A.H.: Ion acoustic solitary wave in homogeneous magnetized electron–positron–ion plasmas. *New J. Phys.* **5**, 28.1–28.10 (2003)
15. Bahamida, S., Annou, K., Annou, R.: Ion-acoustic solitons in electron positron non-thermal plasma. In: 34th EPS Conference on Plasma Physics, vol. 31F, pp. 4.139(1-4) (2007)
16. Gill, T.S., Singh, A., Kaur, H., Saini, N.S., Bala, P.: Ion-acoustic solitons in weakly relativistic plasma containing electron–positron and ion. *Phys. Letts. A* **361**, 364–367 (2007)

17. Jao, C.S., Hau, L.N.: Two-dimensional electrostatic solitary structures in electron–positron plasmas. *New J. Phys.* **17**, 053047 (1-10) (2015)
18. Verdon, M.W., Melrose, D.B.: Wave dispersion in a counter streaming, cold, magnetized, electron–positron plasma. *Phys. Rev. E* **77**, 046403(1-10) (2008)
19. Bulanov, S.S., Fedotov, A.M., Pegoraro, F.: Damping of electromagnetic waves due to electron–positron pair production. *Phys. Rev. E* **71**, 016404(1-11) (2005)
20. Liu, Y., Liu, S.Q., Dai, B.: Modulational behavior of electromagnetic waves in ultra-relativistic electron–positron plasmas. *Astrophys. Space Sci.* **346**, 149–153 (2013)
21. Hu, Q.L., Xiao, G.L., Yu, X.G., Wang, Z.G., Luo, X.B.: Modulational instability of ultra-intense linearly polarized laser pulse in electron–positron plasmas. *Phys. Letts. A* **377**, 2594–2597 (2013)
22. Mushtaq, A., Khan, R.: Linear and nonlinear studies of two-stream instabilities in electron–positron–ion plasmas with quantum corrections. *Phys. Scr.* **78**, 015501(1-5) (2008)
23. Pedersen, T.S., et al.: Plans for the creation and studies of electron–positron plasmas in a stellarator. *New J. Phys.* **14**, 035010(1-13) (2012)
24. Sarri, G., et al.: Generation of neutral and high-density electron–positron pair plasmas in the laboratory. *Nat. Commun.* **6**(6747), 1–8 (2015)
25. Helander, P.: Microstability of magnetically confined electron–positron plasmas. *Phys. Rev. Lett.* **113**, 135003(1-4) (2014)
26. Vranjes, J., Poedts, S., Ehsan, Z.: Kinetic instability of ion acoustic mode in permeating plasmas. *Phys. Plasmas* **16**, 074501(1-4) (2009)
27. Vranjes, J., Poedts, S.: Ion acoustic mode in permeating plasmas. *J. Phys. Conf. Series* **511**, 012010(1-4) (2010)
28. Bittencourt, J.A.: *Fundamentals of Plasma Physics*. Springer, Berlin (2013)

Comparative Study and Yield Productivity of Nano-paint and Nano-fluid Used in a Passive-Type Single Basin Solar Still

Amrit Kumar Thakur, Deepak Agarwal, Prashant Khandelwal and Saty Dev

Abstract Water is necessary for all living beings. It is particular the most important factor for the sustenance of mankind. More than 66% of the earth is covered with water in which 97% of available water from various sources stands brackish which includes some harmful microbes, and 2% water is frozen in the form of icy masses and freezing tops. Solar still (SS) is a device used to convert brackish water into distilled water, but it has very limited productivity which is the major concern. To improve the yield of simple solar still (SS) in this work, black paint is mixed with Al_2O_3 + water to make it nano-paint and it is coated outside the glass cover of solar still. Al_2O_3 can be placed inside water sink to increase the vaporization rate, and due to this, yield productivity increases. Experiments were conducted from 25 June to 27 June for common depth of 0.01 m for simple solar still and nano-fluid in water basin of solar still and nano-paint with nano-fluid both combined for SS in climatic conditions of Jaipur, India. The theoretical performance of the passive solar still and nano-paint and nano-fluid in solar still is compared with effectiveness and yield productivity. Simple solar still gives the water output of 4.47 L for 0.01 m water

A.K. Thakur (✉)

Department of Mechanical and Automobile Engineering, Arya College of Engineering and IT, SP 42, Riico Industrial Area, Kukas, Jaipur 302028, Rajasthan, India
e-mail: amritt1@gmail.com

D. Agarwal

Mechanical Engineering Department, Apex Institute of Engineering and Technology, Jaipur, Rajasthan, India
e-mail: deepak_agarwal7@rediffmail.com

P. Khandelwal · S. Dev

Mechanical Engineering Department, Arya College of Engineering and IT, Jaipur, India
e-mail: Prashant.khandelwal605@gmail.com

S. Dev

e-mail: satyadevyadav08@gmail.com

© Springer Nature Singapore Pte Ltd. 2018

S. SenGupta et al. (eds.), *Advances in Smart Grid and Renewable Energy*,

Lecture Notes in Electrical Engineering 435, https://doi.org/10.1007/978-981-10-4286-7_70

depth whereas simple SS with Nano fluid give output of give output of 5.25 L and SS with Nano fluid in water basin and Nano paint on glass cover of SS give yield of 5.56 L for all three cases for same water depth.

Keywords Nano-paint • Nano-fluid • Solar still • Evaporation • Effectiveness

1 Introduction

Water is necessary for all living beings. It is particular the most important factor essential constituent for the sustenance of mankind. More than 66% of the earth is covered with water in which 97% available water from various sources stands brackish which includes some harmful microbes, and 2% is solidified in icy masses and glacial freezing tops. Subsequently, just 1% from the total available water is used for consumption and household [1, 2]. Underground water in many regions is not generally used as drinking water just because of excessive amount of dissolved solid and mineral in water. The majority of the human illnesses are because of contaminated or non-filtered water. For improving eminence of drinking water, several approaches are used by people but these approaches use energy via themselves such as reverse osmosis and boiling through electrical energy. Among the various available methods, solar energy will be a good source especially in western and northern parts of India where temperature reaches above 40 °C in summer. The yearly sun-powered vitality that achieves the world's surface is roughly 3,400,000 EJ [3]. Desalination is the process which is used to improve water quality by removing excess salt and mineral from water to make it suitable for domestic use and other purposes. The world's aggregate renewable energy sources utilized for desalination is just around 0.02% of the total vitality available [4]. Solar still (SS) is a device used to convert brackish water into distilled water, but it has very limited productivity which is the major concern. Various methods and designs have been studied from research papers [5–14] and implemented for this experimental work to achieve optimum results.

2 Methodology

In this work, an impassive-type solitary sink solar still has been studied. Fabrication and Research work has been carried out at Jaipur, Rajasthan, under the Indian climatic conditions for month of June, 2016. In this work, glass cover of solar still has been black painted, then Al_2O_3 + water which is mixed with black paint and

this mixture has been painted on glass cover to increase its absorptivity of still. Al_2O_3 + water is placed inside water sink to increase the vaporization rate, and it increases effectiveness and yield of SS.

3 Explanation of Experimental Setup and Observations

The complete layout of experimental setup is shown in Fig. 1 in which glass is black painted and thermocouple is fixed on to it for measuring temperature. The experimental setup is installed at Jaipur, India (26.9124°N latitude, 75.7873°E longitude). Solar stills are south fronting to collect the maximum solar radiation. The SS having sink area of 1 m² is made up by using an aluminum sheet of 1.8 mm thickness. Boundaries of solar still is protected by a 2.5 cm thickened plywood and thermocol to protect side heat losses to surrounding. To increase the absorption of solar radiation, basin liner is blackened on its upper and lower surfaces and it also mixed with Al_2O_3 (nano-fluid) + water to form nano-paint. The glass cover of the still is of 4 mm thick and inclined at the angle 26° as from past work angle should be equal to latitude of experimental site to achieve maximum productivity of still. Experimentations are conducted in interval period of 7:00 a.m.–7:00 a.m. for 24 h on typical days in June 2016 but temperature reading of different thermocouples has been used from 7 a.m. to 7 p.m., as in night its reading is almost negligible, only complete night yield productivity in liter from 7 p.m. to 7 a.m. has been considered. The temperatures are recorded by using three J-type thermocouples. The ambient temperature is recorded by using temperature meter (J-type). Pyranometer with accuracy of $\pm 25 \text{ W/m}^2$ and range of 0–1750 W/m^2 has been used to monitor the solar radiation. The comparative performance of simple SS&SS with nano-fluid and SS with nano-fluid and nano-paint has been analyzed at the water depths of 0.01 m.



Fig. 1 Experimental setup picture

4 Mechanism

Solar emanation is conveyed over single slant SS shield, and then, temperatures of water in basin of still rise. Black paint done on glass cover of still increases its absorptivity and rate of convection increases. Nano-fluid Al_2O_3 has been used in water basin to increase the rate of evaporation. Nano-fluid has the ability to absorb heat, it is very helpful when value of solar radiation decreases, then stored heat of nano-fluid gives a better yield, and it also increases the night productivity. In this work, nano-paint has been formed with the help of black paint mixed with Al_2O_3 + water which is coated on to outer surface of glass cover of SS which increases the heat absorbing capacity of SS as compared to both cases. The location of various thermocouples is shown in table below.

Thermocouple	Position
T ₁	Upper glass surface
T ₂	Ambient air temperature
T ₃	Absorber plate temperature

5 Results and Discussion

Thermal effectiveness: Generally, thermal effectiveness of arrangement under dynamic method of action is considered as

$$\eta = \frac{M_{se} \cdot l \times 3600}{(A_{sa}) \cdot Ir(t)}$$

where $Ir(t)$ = solar energy on glass shield of SS, l = latent heat of evaporation = 2270000.00 J/kg, M_{se} = full day yield, A_{sa} = basin area = 1 m².

Figures 2, 3, and 4 show the temperature distribution of solar still at various locations which is measured by thermocouple. From graph, it was observed that for depth of 0.01 m when simple SS is used, absorber plate has highest temperature value of 73 °C at 1 p.m. and ambient temperature has lowest value. When Al_2O_3 is used in basin of SS, temperature of absorber plate reaches a value of 76 °C at 12 noon for depth of 0.01, and when nano-paint is used in glass of SS with nano-fluid in water basin, then 79 °C highest temperature was achieved by lower glass surface which is 81 °C at 12 noon.

Figures 5, 6, and 7 show the global radiation and production of distilled water. Wind velocity plays a very important role in productivity of SS. For simple SS with water depth of 0.01 m, radiation reaches a value of 3.37 MJ/m² at 12 noon and it gives a yield of 0.42 L at 1 p.m. When nano-fluid is used in water basin then at depth of 0.01 m, radiation attains a value of 3.61 MJ/m² at 1 p.m. to give yield of

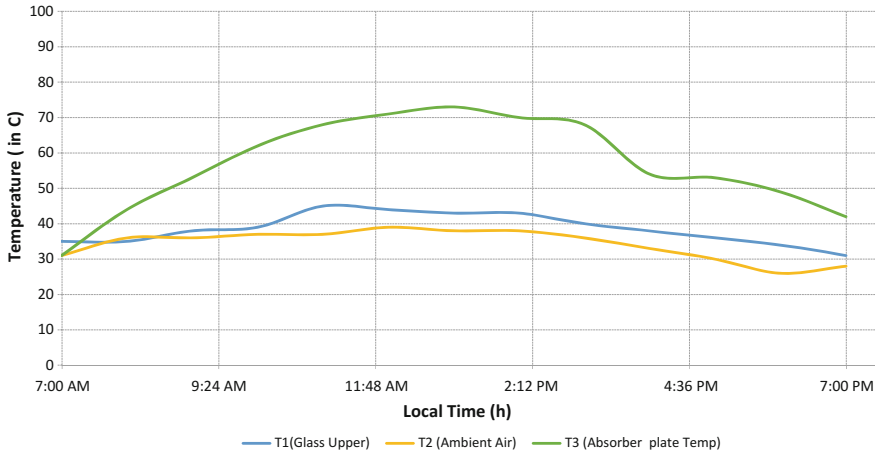


Fig. 2 Temperature of simple SS on June 25, 2016, for 0.01 m depth

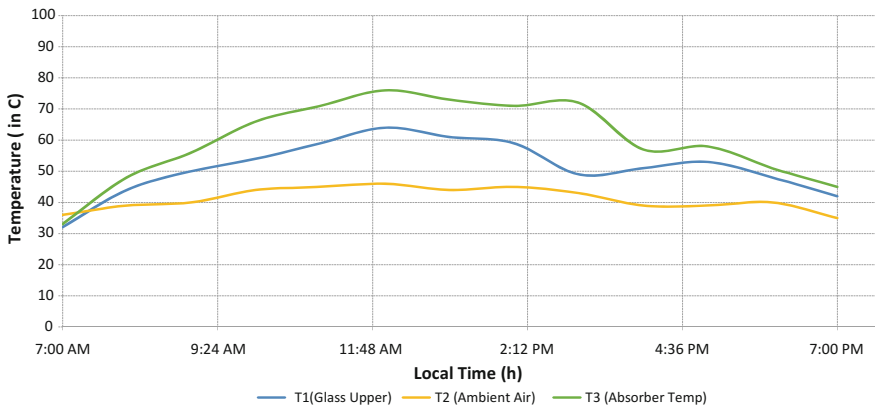


Fig. 3 Temperature of simple SS with nano-fluid on June 26, 2016, for 0.01 m depth

0.49 L. For nano-paint, radiation has maximum value of 3.62 MJ/m² at 1 p.m. and production is highest at 12 noon of 0.50 L (Fig. 8).

Full day production		Full day efficiency
Depth 0.01 (simple SS)	4.47 L	39.03%
Depth 0.01 (nano-fluid)	5.25 L	44.14%
Depth 0.01 (nano-paint)	5.56 L	46.75%

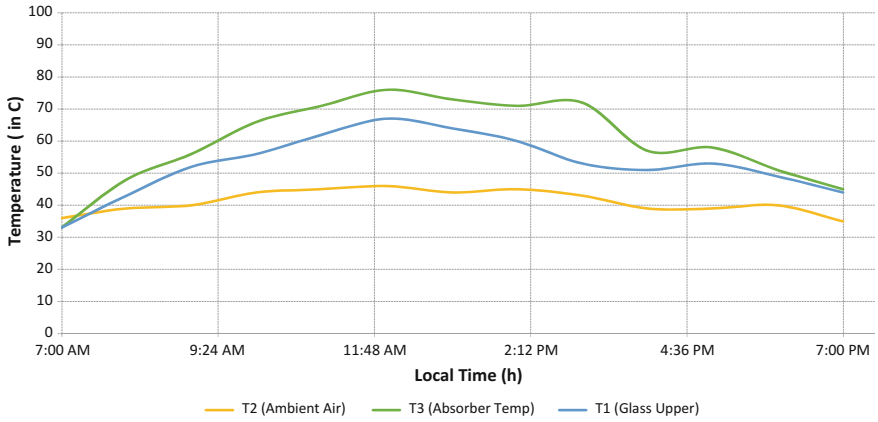


Fig. 4 Temperature of SS with nano-paint and nano-fluid on June 27, 2016 for 0.01 m depth

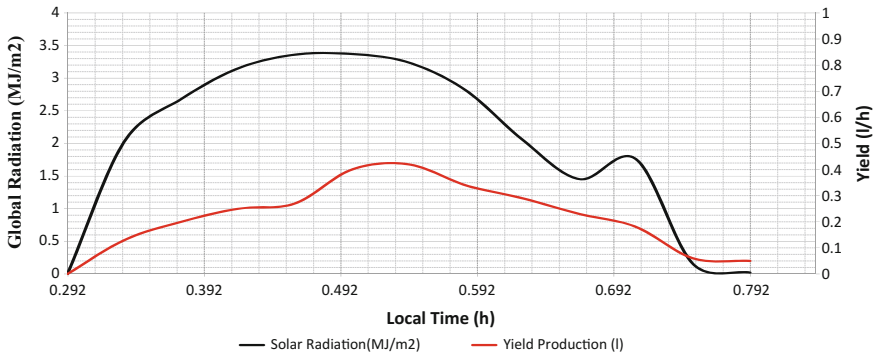


Fig. 5 Solar radiation and yield production of simple SS for 0.01 m depth

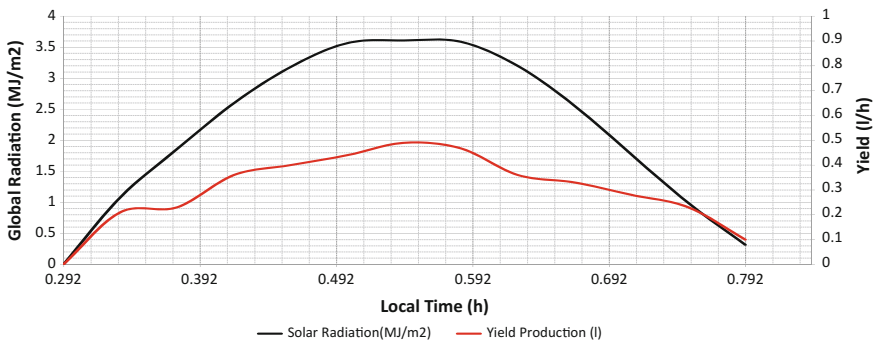


Fig. 6 Radiation and yield production of simple SS with nano-fluid for 0.01 m depth

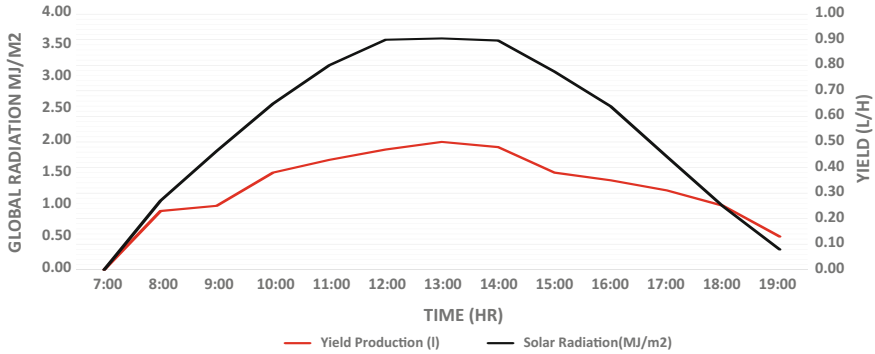


Fig. 7 Radiation and yield production of SS with nano-paint and nano-fluid for 0.01 m depth

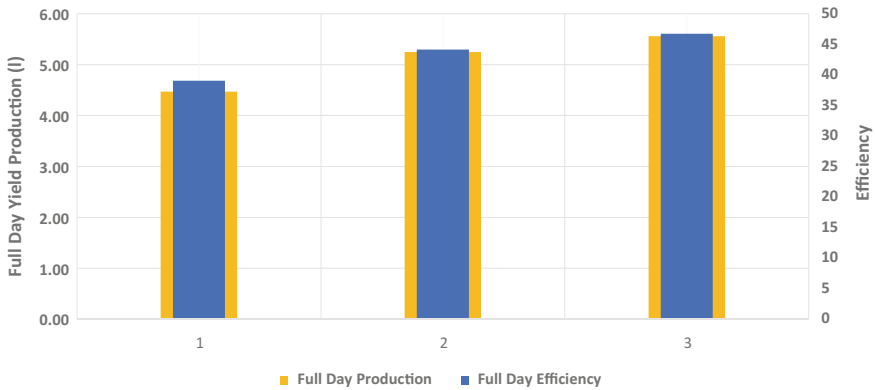


Fig. 8 Full day production and efficiency for (1) simple SS (2) SS with nano-fluid (3) SS with saint

6 Conclusion

When nano-fluid is mixed with black paint and coated on to glass surface, it gives highest yield and thermal efficiency. In this research objective, nano-fluid and nano-paint have been combined in an experiment to determine a better yield of solar still. Following conclusions have been observed from the experimental results:

- Nano-fluid has energy-absorbing properties due to which night productivity in both the cases of SS increased due to the fact that at the time of high radiation, it absorbs energy and when it is needed, supplied back it to the system.
- Wind velocity has huge impact on condensation and evaporation rate and directly helps to achieve better yield.
- Absorber plate is made up of Al sheet which has better thermal conductivity as compared to G.I sheet and gives improved yield productivity.

7 Future Recommendations

- Various designed Concentrator can be used with Nano painted SS and other good yield designed still for achieving better results.
- Forced circulation can be used to improve rate of reaction and productivity of SS.

References

1. Tabrizi, F.F., Dashtban, M., Moghaddam, H., Razzaghi, K.: Effect of water flow rate on internal heat and mass transfer and daily productivity of a weir-type cascade solar still. *Desalination* **260**, 239–247 (2010)
2. Rufuss, D.D.W., Iniyani, S., Suganthi, L., Davies, P.A.: Solar stills: a comprehensive review of designs, performance and material advances. *Renew. Sustain. Energy Rev.* **63**, 464–496 (2016)
3. Seddegh, S., Wang, X., Henderson, A.D., Xing, Z.: Solar domestic hot water systems using latent heat energy storage medium: a review. *Renew. Sustain. Energy Rev.* **49**, 517–533 (2015)
4. Gugulothua, R., Somanchia, N.S., Sri Rama Devi, R., Banoth, H.B.: Experimental investigations on performance evaluation of a single basin solar still using different energy absorbing materials. *Aquat. Procedia* **4**, 1483–1491 (2015)
5. Velmurugan, V., Gopalakrishnan, M., Raghu, R., Srithar, K.: Single basin solar still with fin for enhancing productivity. *Energy Convers. Manag.* **49**, 2602–2608 (2008)
6. Dev, R., Tiwari, G.N.: Characteristic equation of a passive solar still. *Desalination* **245**, 246–265 (2009)
7. Uma Maheswari, C., Vinodh Reddy, B., NavyaSree, A., Vishnuvardhan Reddy, A., Siva Prasad Reddy, A., Raghu Ram Prasad, C., Harish Kumar Varma, B.: CFD analysis of single basin double slope solar still. *Invent. J. Res. Technol. Eng. Manag.* **1**, 1–5 (2016)
8. Jamar, A., Majid, Z.A.A., Azmi, W.H., Norhafana, M., Razak, A.A.: A review of water heating system for solar energy applications. *Int. Commun. Heat Mass Transf.* **280**, 320–330 (2016)
9. Kaviti, A.K., Yadav, A., Shukla, A.: Inclined solar still designs: a review. *Renew. Sustain. Energy Rev.* **54**, 429–451 (2016)
10. Panchal, H.N., Shah, P.K.: Char performance analysis of different energy absorbing plates on solar stills. *Iranica J. Energy Environ.* **2**, 297–301 (2011)
11. Badran, O.O.: Experimental study of the enhancement parameters on a single slope solar still productivity. *Desalination* **209**(1), 136–143 (2007)
12. Asbik, M., Ansari, O., Bah, A., Zari, N., Mimet, A., El-Ghetany, H.: Exergy analysis of solar desalination still combined with heat storage system using phase change material (PCM). *Desalination* **381**, 26–37 (2016)
13. Gugulothua, R., Somanchia, N.S., Sri Rama Devi, R., Banoth, H.B.: Experimental investigations on performance evaluation of a single basin solar still using different energy absorbing materials. *Aquat. Procedia* **4**, 1483–1491 (2015)
14. Mousa, H., Gujarathi, A.M.: Modeling and analysis the productivity of solar desalination units with phase change materials. *Renew. Energy* **95**, 225–232 (2016)